2mil4

CR-134586

R73AEG443

QUIET ENGINE PROGRAM
TURBINE NOISE SUPPRESSION

VOLUME II
Treament Selection, Installation, and Test Results

PRICES SUBJECT TO CHANGE

by

A. Clemons
H. Hehmann
K. Radecki

GENERAL ELECTRIC COMPANY

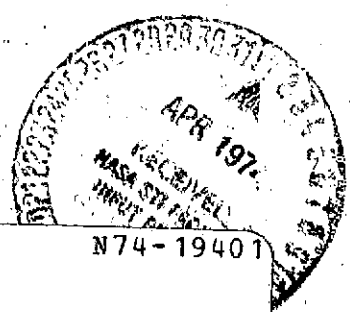

Prepared For

National Aeronautics and Space Administration

NASA Lewis Research Center
Contract NASA3-12430

1. Report No.	2. Government Accession No.	3. Recipient's Catalog No.
NASA CR- 134586		

4. Title and Subtitle	5. Report Date
QUIET ENGINE PROGRAM TURBINE NOISE SUPPRESSION Volume II - Treatment Selection, Installation, and Test Results	December 1973 6. Performing Organization Code

7. Author(s)	8. Performing Organization Report No.
A. Clemons, H. Hehmann, and K. Radecki	R73AEG443 10. Work Unit No.

9. Performing Organization Name and Address	11. Contract or Grant No.
General Electric Aircraft Engine Group Cincinnati, Ohio 45215	NASA 3-12430 13. Type of Report and Period Covered

12. Sponsoring Agency Name and Address	14. Sponsoring Agency Code
National Aeronautics and Space Administration Washington, D.C. 20546	Contractor Report

15. Supplementary Notes

Project Manager, E.W. Conrad, V/STOL & Noise Division
NASA Lewis Research Center, Cleveland, Ohio 44135

16. Abstract

Acoustic treatment was developed for jet engine turbine noise suppression. Acoustic impedance and duct transmission loss measurements were made for various suppression systems. An environmental compatibility study on several material types having suppression characteristics is presented. Two sets of engine hardware were designed and are described along with engine test results which include probe, farfield, near field, and acoustic directional array data. Comparisons of the expected and the measured suppression levels are given as well as a discussion of test results and design techniques.

17. Key Words (Suggested by Author(s))	18. Distribution Statement
Acoustic Treatment, High Temperature Turbine Noise	Unclassified - Unlimited

19. Security Classif. (of this report)	20. Security Classif. (of this page)	21. No. of Pages	22. Price*
Unclassified	Unclassified		

* For sale by the National Technical Information Service, Springfield, Virginia 22151

TABLE OF CONTENTS

VOLUME II

TABLE OF CONTENTS (Concluded)

LIST OF ILLUSTRATIONS - CONTINUED

LIST OF ILLUSTRATIONS - CONTINUED

LIST OF ILLUSTRATIONS - CONTINUED

LIST OF ILLUSTRATIONS - CONTINUED

LIST OF ILLUSTRATIONS - CONTINUED

LIST OF ILLUSTRATIONS - CONTINUED

LIST OF ILLUSTRATIONS - CONTINUED

LIST OF ILLUSTRATIONS - CONTINUED

LIST OF TABLES

INTRODUCTION

The program providing for the development of acoustic treatment for turbine noise suppression as initiated by NASA and the General Electric Company's Aircraft Engine Group has been divided into two phases, each of which is contained in a separate volume. The first phase investigated potential suppression materials, Volume I. The second phase, as contained in Volume II, is concerned with the installation of the treatment in Quiet Engines A and C, the measured PNL suppression values, a comparison of the measured vs. predicted suppression, and conclusions resulting from the program.

SECTION I

HIGH TEMPERATURE ACOUSTIC TREATMENT DESIGN

A. QEP DESIGN REQUIREMENTS

1. Acoustic

The peak attenuation frequency is of prime consideration in optimizing the design of any suppression configuration. Peak suppression for the Helmholtz-type resonator systems occurs at a zero acoustic reactance value for normal incidence sound. However, when the treatment is subjected to airflow as in a lined duct or as in jet engines the optimum reactance changes to some value less than zero. The curve in Figure 235 defines the wall impedance of a lined duct for maximum sound attenuation from an analysis by Rice.[8]

The optimum reactance and resistance are seen to be functions of the sound wave length and the distance between treated surfaces, H/λ. Thus, these two parameters reduce the number of possible design considerations in any optimum suppressor design effort.

The initial effort in defining the acoustic requirements for both engines A and C was to define the turbine noise spectra. The turbine design parameters required for a precise spectrum were not available at this time. Annoyance weighted pure tone spectra were generated to identify the tuning requirements for the treatment configurations. The data available at this phase of the program are listed in Table IV.

The turbine blade passing frequencies are determined by the blade number per stage and the predicted approach power and take-off power fan rpm, and can be seen in the table.

The predicted shapes of the weighted turbine spectra are given in Figures 236 and 237. These were established by making the following assumptions:

- Pure tones were of equal sound pressure levels. (5 dB above broadband noise level)
- Flat broadband noise SPL
- 30 NOY curve weighted at 50 cycles (to determine the required decibel adder to produce a spectra for perceived noise)

The flat broadband noise spectra is given as the x-axis in the figures. Tones 5 dB greater in amplitude are superimposed. Upon application of the 30 NOY curve, the weighted spectra is produced. It is this spectra shape that must be suppressed in order to reduce the PNL.

Table IV. Predicted Engine A and C Low Pressure Turbine Blade Passing Frequencies.

ENGINE A

STAGE	TAKEOFF	APPROACH	NUMBER OF BLADES	BPF AT TAKEOFF	BPF AT APPROACH
1	3271 RPM	1868 RPM	166	9050 Hz	5150 Hz
2	3271 RPM	1868 RPM	142	7750 Hz	4420 Hz
3	3271 RPM	1868 RPM	126	6850 Hz	3920 Hz
4	3271 RPM	1868 RPM	112	6100 Hz	3500 Hz

ENGINE C

STAGE	TAKEOFF	APPROACH	NUMBER OF BLADES	BPF AT TAKEOFF	BPF AT APPROACH
1	4705 RPM	2615 RPM	118	9250 Hz	5150 Hz
2	4705 RPM	2615 RPM	130	10K Hz	5660 Hz

If it is assumed that turbine noise is more of a factor in the noise level at approach than at takeoff, then the following conclusion with respect to treatment design can be made. Engine A acoustic treatment should have a resonance frequency centered between the four pure tones (approximately 4200 Hz). Then, the engine C treatment should have a resonance of approximately 5300 Hz. Both resonator designs should have a broad absorption bandwidth capability due to the expected characteristics of the spectra.

Since the design of the treatment is also related to the geometry in the area of treatment application it is necessary to know the engine geometry in order to evaluate and select the final treatment design. The engine geometry for engines A and C is given in Figures 238 and 239, respectively. The average treatment length to duct height ratio is 3.0 for engine A and 3.7 for engine C.

2. Aero/Mechanical

Up to now, most of the emphasis in jet engine noise suppression has been on the design of treatment configurations for suppressing fan and compressor generated noise. With the treatment of turbine noise a new environment is introduced. Thus many materials suitable for fan suppression are eliminated due to the constraints of the environment, with the primary reason being the increased temperature.

The predicted temperature and the Mach number distributions for engines A and C at approach power are given in Figures 240 and 241. A temperature of 590° K (600° F) was selected as the mean value and was used throughout the testing program in the High Temperature Acoustic Duct Facility. The average Mach number selected using the predicted values was 0.25.

Many materials and types of suppression devices were evaluated. A rating in respect to their merits in withstanding the environment as well as to their weight and cost was made. These results are presented in the Environmental Compatibility section of this report.

B. ENVIRONMENTAL COMPATIBILITY

Bulk sound absorbers comprise a wide range of materials. These include bonded or unbonded metal, glass or ceramic fibers, and porous metal or porous ceramic materials. A list of possible materials is indicated in Tables V and VI. Shown in the tables are the material types and sources along with a few characteristics of each material. While a large number of bulk materials are available, many are quite similar in composition and characteristics often making the justification of selecting any one material over others difficult.

The structural reliability and suitability of bulk sound absorbers to design conditions must be considered. While the adequacy of a given material can only be determined by appropriate testing, some general observations can be made. The problem of leaking of fuel and the possibility of extremely high

Table V. Typical Sound Absorber Materials.

Designation	Vendor	Composition	Description	Max. Temp	Bulk Density	Price/lb	Comments
Bulk Fireous Materials Kaowool	Babcock & Wilcox Co. Augusta, Georgia	$45Al_2O_3$-$52SiO_2$- $1.3FE_2O_3$-$1.7TiO_2$	Fiber Mat 2.8 Micron Avg Dia	---	96 & 160_3 kgs/M^3 (6 & 10 lb/ft^3)	*	Sound absorption coefficient for 1" thickness & 6 lb/ft^3: 2000 cps - 0.82 4000 cps - 0.7 6000 cps - 0.78
Fiberfrax Felt	Carborundum Co. Niagara Falls, N.Y.	$50.9Al_2O$-$46.8SiO_2$- $1.2B_2O_3$-$0.8Na_2O$	Fibermat 2-40 Micron Dia	1530 ° K (2300° F)	96 & 160 kgs/M^3 (6 & 19 lb/ft^3)	*	50-180 ksi Fiber Strength
Fiberfrax Block	Carborundum Co. Niagara Falls, N.Y.	$50.9Al_2O_3$-$49.4SiO_2$ $1.2B_2O_3$-$0.8Na_2O$ Inorganic Binder	Pressed Fiber Block	1530° K (2300° F)	256-320 kgs/M^3 (16-20 lb/ft^3)	*	---
Cerafelt/Thermoflex	Johns Manville Manville, N.J.	$50.3Al_2O_3$-$49.4SiO_2$ $0.14Fe_2O_3$-$0.02TiO_2$- 2.3 Organic Binder	Fibermat 3 Micron Avg Dia	1530° K (2300° F)	48-384 kgs/M^3 (3-24 lb/ft^3)	$1.50/lb est	---
Fiberchrome	Johns Manville Manville, N.J.	Similar to cerafelt but with small amt of Cr_2O_3 added	Fibermat 3 Micron Avg Dia	1530 ° K (2300° F)	64-160 kgs/M^3 (4-10 lb/ft^3)	*	---
Micro-Quartz	Johns Manville Manville, N.J.	Porous Quartz Fiber	Fibermat 3 Micron Drawn "E" Glass Fiber, Leached & Felted into Mat	Unspecified	48-96 kgs/M^3 (2-6 lb/ft^3)	~$25/lb ($5-6/ft^2@1/2")	---
WRP - XZQ Dyna-Quartz	Refractory Products Co. Evanston, Illinois Johns Manville Manville, N.J.	$34Al_2O_3$-$64SiO_2$- 1.1 Inorganic Proous Quartz Fiber	Fibermat Sintered Micro Quartz	1530° K (2300° F) Unspecified	272-304 kgs/M^3 (17-19 lb/ft^3) 72-160 kgs/M^3 (4.5-10 lb/ft^3)	$1.50/lb est	---
S-Glass Fiber Mat	Owens Corning Fiberglass Granville, O.	$25Al_2O_3$-$64SiO_2$- 10 MgO	Fibermat/Cloth ~9.5 Micron Dia (375×10^{-6} in.) Continuous Filament	1088° K (1500° F) Static 810° K (1000° F) Dyn.	80 kgs/M^3 (5 lb/ft^3)	~$45/lb ($12-14/ft^2@1/2")	Contains inorganic lubricant for resistance to thread abrasion
Porous Ceramics Glass Rock Foam	Glass Rock Products, Inc Atlanta, Georgia	Sintered Fused Quartz	65-80% Porosity 0.0156 Avg Pore Size	1200°-1370° K (1700°-2000° F) Continuous	480-800 kgs/M^3 (30-50 lb/ft^3)	~$0.95/lb	Low expansion; excellent thermal shock resistance
Cercor	Corning Glass Works	Proprietary	Triangular Parallel holes: 0.075" base X 0.040" height X 0.005 wall 78% porosity (typical)	1370° K (2000° F) Intermittent	500 kgs/M^3 (31 lb/ft^3)	Specific quotation only	Other configurations available; low expansion; excellent thermal shock resistance current application for continuous regenerative type heat exchangers for auto gas turbines
CER-VIT	Owens-Illinois, Inc	Proprietary Glass-Ceramic C-126	Porous with 0.030" Dia Parallel Holes thru the Specimen Thickness; 0.005" Wall Thickness Between Pores	1370° K (2000° F)	1470 kgs/M^3 (92 lb/ft^3)	~$32/lb	$500/ft^2 as 1/2" flats $3000/ft^2 as 1/2" machined to contour

Table VI. Typical Sound Absorber Materials.

Designation	Vendor	Composition	Description	Max Temp	Bulk Density	Price/lb	Comments
Porous Ceramics Foamed Al_2O_3	Astromet Assoc, Inc Cincinnati, Ohio	Al_2O_3	Porosity to 95%	1923° K >(3000° F)	200-1000 kgs/M^3 (12.5-62 lb/ft^3)	Quotation Only	Not in commercial production; Process based on use of polyurethane foam as carrier
Foamed ZrO_2	Astromet Assoc, Inc Cincinnati, Ohio	ZrO_2	Porosity to 95%	2478° K >(4000° F)	280-1400 kgs/M^3 (17.5-87 lb/ft^3)	Quotation Only	Not in commercial production; Process based on use of polyurethane foam as carrier.
Foamed ZrO_2	National Beryllia Corp Haskell, N.J.	ZrO_2	Porosity 75 - 85%	2478° K >(4000° F)	800-1400 kgs/M^3 (50-87 lb/ft^3)	Quotation Only	Not in commercial production
Porous Metals Foamed Metals	Astromet Assoc, Inc Cincinnati, Ohio	Ni, HS-25 Hastelloy X	Foamed Powder Metals in polyurethane foam carrier	810°-1088° K >(1000°-1500° F)	1760-5350 kgs/M^3 (110-333 lb/ft^3)	Quotation Only	Cu, Ag, W, Mo & Ta also have been made as sintered powder metal foams. Not in commercial production.
Sintered Metal Fibers	Brunswich Corp	Type 304, 310, 316L & 347 SS, Hastelloy X, etc.	Sintered Metal Fibermat; 4-25μ Fiber Dia available; 8μ typical; 30-55% porosity typical	810°-1088° K >(1000°-1500° F)	2880-5550 kgs/M^3 (180-344 lb/ft^3) SS Typical	Quotation Only ~$15-25 lb/$ft^2$ @ 0.38cm-0.050cm (0.015 in-0.020 in) Thickness	Composite material with supporting metal elements on one or both sides are specifically constructed to meet engineering requirements
Rigi Mesh	Aircraft Porous Media Glencove, LI, N.Y.	Type 304, 316, 347 SS and N155 L605, etc.	Sintered wire screen 18-120μ pore size 45-72% porosity	1088° K >(1500° F)	2220-4330 kgs/M^3 (140-270 lb/ft^3) Typical	~$35-55/lb est Quotation Only	Available in wide range materials and composite construction details to meet specific engineering requirements

combustion temperatures within the absorber material is of significant concern to the use of bulk absorbers. Wirt[9] points to experience wherein exhaust system porous sound absorption materials have soaked up fuel during false starts. During subsequent engine startup, the oxygen-rich exhaust is forced deep within the porous absorber material and combustion occurs internally with very little provision for heat release through the low conductivity absorber material. Internal melting of refractory fibers can result. The successful use of bulk-type absorbers will require extensive testing under simulated or actual engine exhaust conditions. Particular consideration will be given (1) to the method of supporting the bulk absorber to avoid impact or vibration damage (particularly if it is of a ceramic type), (2) to the possibility of fuel wicking and combustion within the absorber, and (3) to the extent of sonic fatigue damage which might be expected within the absorber.

Various aluminum silicate fiber materials listed in Table V, such as "Fiberfrax", "Cerafelt", and "Fiberchrome", are relatively inexpensive fibers blown from melts of aluminum silicate compositions each having a melting point well over 1533° K (2300° F). Materials of this type would tend to have random fiber lengths and nonuniform diameters and to contain some particulate matter. In addition, small amounts of organic binders necessary for improved handling characteristics tend to burn out at 810° K (1000° F). While the weight change is relatively minor from such burnout, the mechanical properties of the fibrous material can change significantly and result in more rapid degradation by fatigue, or in shifting of the material. Thermal stability characteristics of this type must be considered in the selection of these materials.

Similar fibrous materials are made from drawn "E" glass which is subsequently heat treated and leached to produce a porous high silica fiber mat known as Micro Quartz; like the refractory aluminum silicate fibers, this material is very stable at 810° K (1000° F). Glass fibers made from "S" glass and capable of use at 1090° K (1500° F) have been woven into glass cloth with an inorganic fiber lubricant; they have operated successfully as filter bags at 700° K to 810° K (800-1000° F) for periods of 2-3 weeks under dynamic conditions. More conventional glass fiber mats for thermal and acoustical insulation near room temperature are generally made from glasses with melting temperatures in the 1090° K (1500° F) range and would be marginally serviceable at temperatures near 810° K (1000° F). All the above fibrous materials are available in bulk, blanket, or felted forms. The strength and durability of these can be improved by effecting a degree of bonding between fibers. Examples of this are evident in "QRP-XAQ" (an inorganically bonded refractory fiber mat), "Dyna-Quartz" (a sintered quartz fiber mat), and various bonded, impregnated, surface-sealed, or pressed and bonded refractory fiber materials; these are available from Carborundum Company and others. A wide range of variations in density, strength, and airflow resistance can be achieved in an expected manner by the incorporation of inorganic binders under varying degrees of pressure during cure.

The selection of a particular type of fiber material for ultimate use depends upon acoustic performance tests, observed modes of deterioration under simulated environments, methods of attachment or retention, and a realistic appraisal of the fuel wicking problem. While some degree of property modifications in fiber-type acoustical absorbers is possible, it is

expected that the critical problems of fuel wicking, retention of physical form, and degradation under high intensity acoustically induced vibration will be the principal limiting factors.

Light-weight porous ceramics are available in a wide variety of refractory materials for use as thermal insulators. Porosity is generally achieved by the addition of burnout agents or may also be achieved by various methods of foaming. The possible presence of enclosed pores and dead-end passages which do not provide flow paths for acoustic absorption and the fragile nature of the more highly porous materials are particular problems with such porous ceramics. The brittle nature of ceramics and the generally poor thermal shock resistance of conventional ceramics makes their use difficult in acoustic absorber designs consisting of metal structures, which have greatly different thermal expansion characteristics. The effects of shock, and attachment and brittle failure under flexure must be recognized. Inclusion of porosity lowers the bulk modulus of elasticity and offers some improvement in thermal shock resistance. However, the higher porosity materials are weaker and more friable; their resistance to both foreign object damage and/or erosion from relatively small objects would be seriously reduced from that of dense ceramics. General Electric Company development experience in using porous ceramics for thermal insulation in high velocity hot gas ducts has indicated the attachment problem is formidable. Like the fibrous ceramic sound absorbers, it is expected that the attachment method may very well require a porous metal plate or sheet to retain the ceramic absorber.

A typical porous sintered ceramic material with very low thermal expansion (to resist thermal shock) is "Glassrock" foam. The material is available in block form and can be machined to shape. It has a fine open pore structure and average pore size of 0.157 cm (1/16 in.) at 84 percent porosity. Comprised of fused quartz, it has excellent stability at 810° K (1000° F). Foamed glasses with lower temperature capability than sintered quartz are available from Pittsburgh Corning Corporation. While the porosity is not initially interconnected, the thin cell walls can be broken open by a recompression process. These sound absorbers, however, deteriorate rapidly above 700° K (800° F). A foamed glass with the proper combination of acoustical and mechanical properties at 1313° K (1000° F) is not known to be commercially available.

Glass-ceramics such as "Cer-Cor" and "Cer-Vit" are developed from special glass compositions which, after being formed in the glassy state, can be heat treated to precipitate crystalline ceramic phases from the glass matrix, McMillan[10]. A wide range of materials with differing properties can be developed. The crystalline ceramic has all the fabrication advantages of its initial glassy form. It can be cast, pressed, blown, drawn, or shaped by other glass forming methods and then heat treated to develop the crystalline ceramic phase. As powdered glass frit, it can be impregnated into combustible carriers and sintered to form many complex components. These processing capabilities permit the development of very fine-textured, high porosity materials with controlled structures (such as triangular-shaped honeycomb cells) in which high density is achieved in uniform thickness walls. Furthermore, materials with very low expansion coefficients can be made from glass-ceramic compositions to assure thermal shock resistance. Airflow characteristics could be

developed to cover a wide range of requirements because of the versatility of fabrication methods. Currently this type of glass-ceramic honeycomb is available only in thick planar sections from which contoured parts could be machined. Precontoured ceramic honeycomb is not available.

A bulk absorber with the necessary airflow resistance and both the ductility and thermal strain capabilities of metals would offer a decided advantage (with the exception of weight) over ceramic bulk absorbers. Foamed metals of this type have been developed by the General Electric Company with porosity ranging from 60 to 90 percent. Nickel and copper foam metals in this density range can be procured commercially and other metal alloys could be prepared as foamed metals, if necessary.

Sintered porous metal materials have been made in stainless steel, iron, nickel, and titanium and in other alloys which are available as metal powders. Wide ranges of porosity and flow resistance are possible. The very open structures of the low density foams, however, cannot be achieved.

Sintered metal fibers, and rolled and sintered wire screens provide metallic sound absorption materials which, in general, should be of improved strength relative to sintered powder metal sound absorbers with equivalent flow capacity. Since the fibers or wire are fully dense and are sintered to adjacent metal at many points along their length, their mechanical properties would tend to be more reliable and their strain capacity greater than a sintered powder metal sound absorber with equivalent airflow characteristics. Since materials of this type are engineered structures which differ in porosity, average pore sizes, internal structure, and airflow characteristics, it is difficult to make comparisons other than those of a general nature without having available detailed engineering test information on composition, structure, mechanical properties, and acoustic properties. For long time applications at 810° K (1000° F) where oxidation of stainless steels and nickel-base superalloys is not a serious problem, these types of metal bulk absorbers should be superior to ceramics in reliability, attachment, FOD resistance, and thermal shock. While the use of titanium, as sintered fibers or as sintered powder materials, would result in significant decreases in weight over similar stainless steel or nickel-base bulk absorbers, it was not seriously considered because of (1) its contamination and embrittlement at 310° K (1000° F) or slightly higher temperatures over long periods of time, and (2) the possibility of fires occurring as the result of hot starts or of fuel wicking and internal combustion within the bulk absorber.

Sound-absorption systems involving resonant panels at the exhaust airflow surfaces can be constructed from (1) perforated sheet metal or other porous metal media for the front face, (2) metal honeycomb or other types of core structures for the center, and (3) solid metal sheet for the rear face. The design and acoustical characteristics of such systems provide a wide range of possible configurations. However, all require the use of formable sheet metal alloys which (1) are sufficiently strong and oxidation resistant at elevated temperatures, (2) can be joined readily by brazing and/or welding, and (3) are of reasonable cost.

The 0.2% yield strengths and rupture stresses for failure in 10,000 hours for four potential alloys are shown in Figure 242 as a function of temperature. Solution-strengthened alloys of good forming and welding characteristics have been selected for consideration. Note that the alloys become limited in creep and rupture characteristics at temperatures much over 810° K (1000° F). These property curves present a relative comparison of the areas for selection of allowable design stresses for each material. The composition of these alloys, their relative cost, density and room temperature tensile ductilities are shown in Table VII.

Inco 625 is generally recommended for all-metal sound structures of the types of designs suggested elsewhere in this report. Its strength characteristics are very good for a formable nickel-base, solution-strengthened alloy. It is much superior in strength to the stainless steels, such as Type 321, to the more economical nickel-base alloy Inco 601, and to Hastelloy X, which is used extensively for much higher temperature applications. The recommended alloy is very formable in the types of operations necessary to develop three dimensional contours in exhaust nozzle sound absorbers. It is much more formable than Hastelloy C and other alloys which may require the use of intermediate anneals between forming operations. The excellent toughness, resistance to notch effects, and high fatigue strength of Inconel 625 also favor its use. While its cost is relatively high with respect to other formable alloys, its advantages in the above respects encourage its ultimate selection provided that the design can most effectively utilize its strength advantages.

The technology for forming, assembling, and brazing complex stainless steel and high temperature alloy honeycomb sandwich panels is well established at several locations within the United States. Welded honeycomb core panels have been prepared by the Stresskin[11] approach. Corrugated core ribbons with flanged edges are roller-spot-welded to the surface sheets, and core nodes are subsequently spot welded as each core ribbon is sequentially added to the core. These all-welded panels can be subsequently formed into various shapes and, with appropriate techniques, can be joined by various welding methods. The expected design and manufacturing versatility in fabricating and joining such structures offers potential advantages which should be given careful cost comparison considerations in detailed design studies.

Cores of similar acoustical performance have been prepared in glass-epoxy systems. Flat epoxy-glass cores can readily be formed and cured in contact with accurate metal mold surfaces. Curvature in the rigidized (corrugated direction) is achieved by providing a series of equally spaced parallel saw cuts at right angles to the corrugations. After forming the core to its three dimensional shape, the cuts in alternate corrugated surfaces are sealed for acoustical purposes. The front and rear fiber glass-epoxy face sheets can accommodate themselves to the minor irregularities of the corrugation edges and the organic adhesives provide additional and reasonable clearance tolerance at the bond lines between surface sheets and the core.

Table VII. Potential Alloys for Sound Absorption Structures.

ALLOY	CHEMICAL COMPOSITION - WEIGHT %										DENSITY Kgs/M^3	DUCTILITY* %		SHEET COST
	C	Cr	Ni	Co	Fe	Mo	W	Cb+Ta	Al	Ti		Elong	% RA	
INCO 625	0.1	21.5	BAL	1.0	05.0	9.0	-	3.65	0.40	0.4	8442	70-80	70-80	3.29
HASTELLOY X	0.1	22.0	BAL	1.5	18.5	9.0	0.6	-	-	-	8221	40+	-	4.64
TYPE 321SS	0.08	18.0	9.5	-	BAL	0.5	-	-	-	0.2	8027	45-75	65-80	1.36
INCO 601	0.05	23.0	BAL	-	14.1	-	-	-	1.35	-	8055	40+	60+	1.93

* ROOM TEMPERATURE 291°K (64°F)

As contrasted to the glass-epoxy system, the more rigid nature of a contoured corrugated sheet metal core, and the more precise fit ups required in brazing make the need for precision much greater in the preparation of these cores. Because of the deep convolutions, in this type of metal core, allowance would be required for gathering of metal, and multiple dies for progressive forming would probably be required. Explosive or other high energy rate processes might also be attempted in an effort to minimize spring back effects which would otherwise decrease the accuracy of the core. High accuracy is needed for precision braze fit ups. The formation of the core by methods similar to those used for epoxy-glass corrugated cores would result in at least two problems. First, fit up problems would exist along the bond lines where the core maintained a broken straight line configuration (a chord-arc effect); second, problems would occur in sealing the alternate corrugation core slots without either distorting the core or plugging areas which are to be left open.

Once corrugated cores of good dimensional characteristics are available, additional manufacturing development and evaluation would be necessary to establish the machining, trimming, fit-up, and brazing processes necessary to produce reliable hardware.

As a means of relatively rating the merits of various bulk absorber materials and competing brazed honeycomb-type designs, each were evaluated by engineering judgement in the following categories:

Temperature Capability

Oxidation Resistance

Strength

Vibration Resistance

Thermal Shock Resistance

Thermal Fatigue Resistance

Fluid Compatibility

Liquid Retention

Freezing and Thawing Resistance

Fabricability

Cost

Weight

Repairability

Ratings from 1 to 10 were assigned for each material or each design in each of the above categories. The most favorable rating was 1 and the least favorable was 10. Values were assigned by engineering judgement based upon a general knowledge of the materials and how they might be used in the engine. The rating for each material is given in Table VIII.

In temperature capability and oxidation resistance, the refractory fiber materials and stable refractory oxide materials ranked highest, but, even the lower ranked metal foams and metal alloy honeycomb-type structures had properties sufficient for the application. Only titanium in the form of sintered metal fibers (or porous sintered powder) was considered marginal.

The strength of the bulk ceramic fiber materials was rated poor; that of the porous ceramics was expected to be much better as the sintered density increased. The cellular macroporosity and the more densely sintered ceramic-glass walls of the "Cer-Cor" and "Cer-Vit" type of materials was rated as much higher in strength. Further strength increases were attributed to the porous metals, and the metal brazed structures were logically presumed to have the highest strengths. Vibration characteristics were presumed to closely parallel ratings of strength. The level of acceptable strength and vibration resistance would be a function of the method of attachment and other design considerations, therefore, no unacceptability limit could be specified; however, it is expected that the group of porous ceramics would be particularly susceptible to failure because of inadequate strength, vibration resistance, corrosion resistance, or ductility.

In thermal shock resistance and thermal fatigue, the fibrous materials would not be affected because of their extremely low bulk modulus of elasticity. Likewise, the low expansion materials such as fused quartz and certain glass-ceramic materials such as "Cer-Cor" and "Cer-Vit" should also be resistant. The relatively high thermal expansion ceramics would have a greater tendency to fail in thermal shock or to deteriorate under thermal fatigue. The reduced bulk modulus of the higher porosity materials, however, acts in favor of improving thermal shock resistance; furthermore, thermal shock conditions from 810° K (1000° F) may not be severe enough to cause failure or deterioration. While the limits of acceptability under thermal shock and thermal fatigue cannot be specified, the relative ratings are still valid. The lower thermal expansions of certain ceramics and the ductility and high thermal conductivity of metal alloys are properties which favor the thermal shock resistance, thermal fatigue, and hot spot characteristics of these materials.

Compatibility with fluids is not expected to be a problem with any of the above materials with the exception of some of the fibrous materials, the binders of which may be affected.

Retention of liquids by the fibrous insulators, porous ceramics, and porous metals may result in either combustion of retained fuel within the structure or freezing and thawing damage. These effects are expected to be more severe in the fibrous and porous ceramic materials which would probably

Table VIII. Relative Merits of Materials Processes and Designs.

Fiberous Materials	Temp Capab.	Oxidation Resist.	Strength	Vibration Resistance	Thermal Shock Resistance	Thermal Fatigue Resistance	Fluid Compatibility	Liquid Retention (Fuel, etc)	Freezing Thawing Resistance	Fabricability	Cost	Wt	Repairability	Comments
Refractory Fiber Mat	3	2	10	9	3	3	2	10	6	1	1	1	1	Fuel wicking, water retention, freezing thawing, fiber settling are limiting
Refractory Fiber Block	3	2	8	7	4	4	2	10	8	2	2	2	2	" " " "
Micro Quartz	4	2	10	9	2	2	2	10	6	1	2	1	1	" " " "
Dyna Quartz	4	2	9	7	3	3	2	10	8	2	4	2	2	" " " "
S Glass Mat	7	3	10	8	4	4	2	10	5	1	2	1	1	" " " "
Porous Ceramics														
Sintered Ceramics Quartz	4	1	7	6	2	2	2	8	9	4	3	4	6	Wicking, freezing attachment and FOD are limiting
Cellular Ceramics (low α) CER CORE, CerVit	4	1	4	5	1	1	2	4	6	6	6	2	6	Attachment, FOD & possibly freezing are limiting
Foamed Ceramics (Al_2O_3, ZrO_2)	1	1	8	8	7	5	2	6	6	7	8	3	6	Thermal shock, wicking, freezing and attachment are limiting
Porous Metals														
Foamed Metals (Oxidation Resistant)	5	5	5	4	3	3	1	6	4	7	6	6	4	Wicking and freezing are limiting
Sintered Metal Fiber (Oxid. Resistant)	5	4	4	3	2	2	1	7	3	5	6	7	4	Wicking and freezing are limiting
Rigimesh (Oxidation Resistant)	5	3	2	2	1	1	1	7	3	3	5	7	4	Wicking, freezing are possibly limiting
Structures														
Brazed Honeycomb	5	3	1	1	1	1	1	2	2	2	2	3	3	Generally most reliable
Brazed Double Honeycomb	5	3	1	1	1	1	1	2	2	4	4	3	3	Reliable, increased cost, possible acoustic advantage
Brazed Single Triangular	5	3	1	1	1	1	1	2	2	8	8	3	3	Significantly higher cost and poorer fabricability mainly because of core type as compared to above
Brazed Double Diamond Core	5	3	1	1	1	1	1	2	2	10	10	3	3	Added precision parts stackup required in braze preparation

be used more as thick bulk absorbers because of their lower density. The effects would tend to be less severe in the porous and fiber media which would more likely be used as thin flow control membranes over resonant sound absorption structures.

Fabricability and cost of the bulk fibrous absorbers are quite favorable. The porous ceramics are more expensive and the fabrication of large areas with unusual shapes and special attachment methods can increase their cost. The porous metal absorbers, while more amenable to fabrication and joining than the ceramic absorbers, can have significant costs associated with their manufacture and fabrication. The cost of the progressively more complicated honeycomb-type sound absorbers increases rapidly when the problems of complex core manufacture are faced.

The lightest weight sound absorbers should be the bulk absorbers followed by honeycomb structures and then the more dense porous ceramic and porous metal sound absorbers.

The repair or replacement of fibrous bulk sound absorbers retained by sheet metal covers should be most economical, followed by the ease of repair and maintenance of the highly reliable honeycomb structures. Porous ceramics and either foam or fiber metal structures will probably be the most difficult to maintain and repair, particularly if the method of attachment exposes them to the direct exhaust gas stream where more frequent damage can be expected.

Unless outstanding sound-absorption characteristics are obtained with bulk porous sound absorbers, their use should be drastically limited by a concern for such problems as wicking of fuel and combustion within the absorber, freezing and thawing resistance, shifting of absorber material, degradation of the absorber by vibration or thermal fatigue, and damage by foreign objects. The more reliable metal honeycomb-type sound absorbers provide a direct approach to sound-absorption structures which should better meet the requirements of strength, oxidation resistance, fatigue, thermal stress, drainability, fabricability, cost, weight, and repairability. The possibility of developing more effective sound absorbers through the use of multiple-degree-of-freedom structures may require the development of methods for forming complex cores, but such developments seem more amenable to success than does the solution of problems involving the use of ceramic materials.

The next step in more efficient sound-absorption systems would appear to be the use of multiple-degree-of-freedom double-layer brazed honeycomb structures. While this type of construction would be somewhat more difficult than current single-layer brazed honeycomb sound-absorption structures, it would utilize current technology and would require only a reasonable growth in manufacturing methods. The advent of more complicated systems involving the fabrication of intricate cores must be based upon lead time necessary for the development of manufacturing technology and methods for forming the cores and resolving the problems anticipated in brazing these complex structures.

C. ENGINE TREATMENT RECOMMENDATIONS

1. Engine A

The turbine treatment recommended for engine A was selected on the basis of acoustical characteristic, manufacturing technique requirements, cost, and other considerations as outlined in Table IX. The bulk fibrous absorbers were not serious contenders because of the problems they encounter as stated in the Environmental Compatability section. The suppression predictions for the configurations, as defined in Figure 243, show that the Cer-Vit material offers approximately 2 PNdB more suppression than any of the other leading treatment configuration candidates. The suppression predictions were calculated by applying the measured transmission loss values for each system to the predicted unsuppressed turbine noise spectra given in Figures 244 and 245.

These predicted spectra are somewhat different from those used in the initial phase of the program. The spectra shown are, respectively, pure turbine noise and turbine/compressor noise combined. These were generated using a semiempirical turbine noise prediction procedure[12] based on a vortex noise model which has proven to give good agreement with noise measurements. The engine cycle data required as input in using this prediction method are given in Table X. The tables show that the turbine rpm for the takeoff and approach conditions has changed relative to the data given in Table IV.

The predicted 1/3-octave band spectra were weighted by adding an annoyance level which is a function of the frequency. From the weighted spectra, the frequency range controlling the perceived noise level (PNL) is easily identified. Thus, the treatment tuning frequency is defined as that which gives the maximum reduction in the perceived noise level (ΔPNL). It is evident from the weighted spectra for engine A that a wide suppression bandwidth and a treatment designed to peak in the 4000 Hz to 5000 Hz range is required.

The suppression values that were applied to the predicted turbine spectra are given in Figures 246 - 251. These suppression values are for a treated-length-to-duct-height ratio of 3.0 which corresponds to the engine turbine exhaust duct treated-length-to-duct-height ratio (L/H). This actual L/H ratio was not measured in the acoustic duct. However, the values for the L/H ratio of 3 were interpolated from duct measurements representing L/H values of 4.5 and 2.25. The suppression in terms of the calculated ΔPNL indicates that MDOF No. 3 and SDOF No. 18 configurations give about the same suppression. The PNdB suppression calculated for the turbine plus the compressor noise is shown in Figure 252. The addition of the compressor noise produces a spectrum which has no sharp peak, and is flat relative to the spectrum for turbine noise only. A spectrum of this type demands a suppressor material having a good suppression bandwidth capability in order to give a significant reduction in the perceived noise level. This, then, means better suppression values can be obtained from the MDOF and bulk-type absorber systems. The figure shows the MDOF No. 3 resonator system to be as effective as the Cer-Vit material and substantially better than the best SDOF design. The MDOF No. 3 configuration is described in Figure 10. The core geometry is seen to be triangular in

Table IX. Hot End Treatment Evaluation.

Type of Treatment (Thickness)	Weight kgs/M^2 (lb/ft^2)	Current Relative Cost	Producibility	Reliability, Maintainability and Versatility
Bulk Absorber (Cerafelt) 3.81 cm (1.5 in.)	--	.6	• Simple to manufacture	• Lacks durability, limited life • Has temperature limitations
Single Layer Honeycomb 1.27 cm (0.5 in.)	9.3 (1.9)	1	• Producible by known manufacturing techniques	• Reliable, long-life configuration
Double Layer Honeycomb 1.27 cm (0.5 in.)	14.1 (2.9)	1.5	• More difficult than single layer honeycomb but still within present state of the manufacturing art	• Reliable, long-life configuration • Can be manufactured as structural nozzle component or incorporated as removable panels • Occupying relatively large volume could be a disadvantage
Cer-Vit 1.27 cm (0.5 in.)	13.9 (2.85*) (Cer-Vit Only)	Not Available	• Experimental material which is presently expensive but has potential for becoming economical in production quantities • Requires separate design and testing program to develop retention techniques	• Brittle material with non-structural characteristics • May have limited life with best of developed retention techniques
Triangular Core 0.635 cm (0.25 in.)	13.2 (2.7)	3.0	• Requires expensive tooling and lengthy manufacturing development • Requires advanced manufacturing techniques to produce sound economical component • Great difficulty in maintaining required gaps for good braze joints • Vendors will not undertake manufacturing of this configuration without prior development program • Potential configuration for large lot quantities	• Reliable long-life configuration if good braze joints can be produced • Can be manufactured as structural nozzle component or incorporated as removable panels • Small thickness very attractive for variable nozzles

* Overall weight will be highly dependent upon required retention configuration.

Table X. Revised Cycle Engine A and C Low Pressure Turbine Blade Passing Frequencies.

ENGINE A

STAGE #	TAKEOFF RPM	APPROACH RPM	# BLADES	BPF @ T/O	BPF @ APPR.
1	3288	2164	166	9100 Hz	6000 Hz
2	3288	2164	142	7750 Hz	5100 Hz
3	3288	2164	126	6900 Hz	4550 Hz
4	3288	2164	112	6130 Hz	4000 Hz

ENGINE C

STAGE #	TAKEOFF RPM	APPROACH RPM	# BLADES	BPF @ T/O	BPF @ APPR.
1	4605	3008	118	9050 Hz	6040 Hz
2	4605	3008	130	10000 Hz	6680 Hz

shape with alternate walls perforated with narrow slits. This type of geometry presents complex problems in manufacturing. To produce such a piece of hardware requires special tooling and calls for advanced manufacturing techniques. These requirements as described in Table IX lead to higher cost in development. The cost relative to SDOF systems is increased by a factor of 3.

The MDOF system having a triangular-core geometry can be redesigned with a different core geometry, yet have equivalent acoustic characteristics. By changing to the sandwich or double-layer honeycomb, the acoustic properties for MDOF No. 3 can be duplicated. This configuration is that of the double sandwich II configuration as described in Figure 11. Figure 253 gives the predicted acoustic reactance for both configurations and shows that the parameter that controls the absorption bandwidth and the peak attenuation frequency is the same for both designs. The amplitude of suppression is governed by the porosity parameters which can be made the same for both systems. From Table IX, the producibility of the double-layer honeycomb is described as being more difficult than SDOF, yet it is still within the present state of the manufacturing art. The cost is reduced by 100 percent relative to the cost of the MDOF triangular-core configuration, but is still 50 percent higher than the more simple SDOF system.

Based on the information that has been presented above, the double sandwich configuration, Figure 254, was recommended to be the engine A turbine treatment configuration. This sacrificed cost and weight increases in favor of an advanced configuration offering better acoustic suppression characteristics.

2. Engine C

The turbine treatment recommended for the engine C vehicle is based on both the suppression prediction for the different suppression systems, as shown in Figures 246-251 and 255-257, and the other comparative information outlined in Table IX. The suppression predictions for engine C, as for engine A, were calculated by applying duct transmission loss values to the predicted turbine noise spectrum. The predicted unsuppressed turbine noise for engine C is given in Figure 258 and the turbine/compressor spectrum is given in Figure 259. As was the case for engine A, the duct suppression values were interpolated for the L/H value that corresponds to the L/H for the engine turbine exhaust geometry. It is important to note that the revised engine cycle data of Table X (acquired after updated design inputs) have resulted in a shift of the optimum tuning frequency from 5.0 kHz to 6.3 kHz. The revised cycle data, therefore, changed the emphasis in the peak frequency of suppression in duct testing.

The ΔPNL values calculated for engine C for eight different treatment configurations are given in Figures 260 and 261. The double sandwich gives the optimum suppression, some 12 PNdB. The SDOF systems are the most favorable from the view point of cost and weight considerations. Since the difference in the suppression between the configurations is so small, when applied to the total spectra as shown in Figure 261, it was felt that all of the configurations would produce the same farfield suppression. Therefore, SDOF No. 19, described in Figure 6, was recommended for engine C.

SECTION II

ENGINE HARDWARE DESIGN AND FABRICATION

A. DESCRIPTION

1. Engine A

The engine A exhaust nozzle design consisted of an inner and outer support shell into which panels which formed the actual nozzle flowpath were bolted. Two sets of panels were constructed. One consisted of a support frame with solid face sheets, and this served as a hardwall base line nozzle. The second set was the double-layer brazed honeycomb acoustic configuration, double sandwich II. The nozzle panel geometry, see Figure 262, was slightly different than the recommended test panel geometry because of material availability at time of construction. That is, the face plate was 0.051 cm (0.020 in.) instead of 0.076 cm (0.030 in.) and the inner plate was 5% porosity instead of 4%.

An engine A exhaust nozzle cross section with the double sandwich II acoustic panels in place, Figure 263, shows the basic construction as well as acoustic treatment length and area. This type of construction, which is flight worthy but not flight weight, was selected over the continuous shell construction because of the difficulty and cost associated with producing a double-layer honeycomb as a continuous shell. Figure 264 is a photograph of the assembled engine A nozzle.

2. Engine C

Two separate exhaust nozzles were constructed for engine C. One was the hard-wall base-line nozzle which consisted of an inner and outer exhaust cone. The second nozzle was the acoustically treated version where single-layer brazed honeycomb had been selected for the treatment. At the time, manufacture of a single-layer brazed honeycomb continuous shell was within the state of the art, and this type construction was selected. It has the advantage over the engine A nozzle design of being truly flight weight. Figure 265 is a cross section of the engine C acoustic nozzle and shows treatment length and area. The honeycomb geometry, Figure 266, is similar to a test panel honeycomb geometry, SDOF No. 19, but not identical because of material availability at time of manufacturing. Figure 267 is a photograph of the engine C acoustic nozzle assembled on the engine.

B. STRUCTURAL ANALYSIS

The following factors were examined to assure the integrity of the engine A honeycomb panels and engine C honeycomb shells:

- Gross structure stress
- Local failure modes in the honeycomb
- Mechanical vibration

A similar analysis, where applicable, was also conducted on the engine A support shells and hardwall panels, and engine C hardwall nozzle. However, since no new analysis techniques were used, the analysis procedures and results will not be discussed.

Contributions to the gross structural stresses include gas loading, maneuver loading, and thermal gradients through the honeycomb thickness. Of the three, the thermal gradient was the primary stress contributor. The calculated face sheet temperatures vs. time for engines A and C are given in Figures 268 and 269, respectively. These distributions are based on a 3 minute throttle delay start. The maximum gross honeycomb stresses, due to all three contributors, are given in Figure 270. The figure also gives the 0.2% YS for the honeycomb material (Inco 625) and the calculated failure stress limits associated with the following local instabilities (also see Figure 271):

- Intracellular buckling (dimpling)
- Wrinkling of face sheet
- Core crushing

These local instability limits were calculated using techniques outlined in References 13 and 14.

Mechanical vibration of the engine A honeycomb panels and engine C honeycomb shells was considered and no problem areas were discovered.

C. MANUFACTURING PROCEDURE

The manufacturing techniques used for engines A and C honeycomb nozzle hardware is similar to that outlined in Section I on Panel Fabrication. Face sheets and thin-foil resistance-welded honeycomb core were fabricated from Inconel 625 alloy. This nickel-base alloy has very good high temperature strength in the 1000° F range and has excellent formability.

Brazed alloy AMI 930, a nickel-base alloy containing 23 manganese, 7 silicon, and 3 copper, was selected as the high temperature brazing alloy because of its compatibility with the 625 alloy and its ability to be welded without detrimental effects after brazing. Sheet metal components were formed by punching, drawing, and annealing to achieve the desired shape of the individual components that went into the braze assembly.

Inspection of engines A and C brazed hardware was performed by x-ray inspection methods. Detailed acceptability requirements were established. These were based upon the ability to detect brazed fillets and to identify the extent of brazed fillet coverage. By shooting the panel obliquely during x-ray exposure, the upper and lower fillets of the two-sheet honeycomb could be readily identified. Inspection of the engine A double-layer honeycomb panels involving four brazed fillets became a more acute problem; however, special techniques were used to make positive identification of individual brazed fillets.

The x-ray inspection revealed some defective braze areas. These areas were repaired by tying the face sheets together by drilling holes through the honeycomb structures and welding small tubes to the face sheets. The repair tube spacing is determined using the same principles used in the local instability analysis. This "fix" produced an unattractive yet seemingly good repair method.

In addition to x-ray inspection, honeycomb sample specimens brazed with each panel were subjected to flatwise tensile tests to assure the brazing process produced quality components. Testing of sheet metal specimens assured that the properties of the base alloy had not been adversely effected.

The most significant aspect of producing high quality brazed honeycomb sound panels is the development of reliable manufacturing processes, and the attention to the details of cleanliness, and precision and process control in production of components. The vendors processing plan, detailing all processing steps and all the controls which the vendor used to assure reliable quality in finished parts, was reviewed with the General Electric Company prior to approval for manufacturing.

SECTION III

ENGINE TESTING

A. INSTRUMENTATION

1. Probes

Three acoustic probes were positioned in a straight line parallel to the engine axis on engine A at the leading and trailing edges of the acoustic treatment section and at the treatment midpoint. The probes were separated by 0.428 m (16.84 in.) and 0.430 m (16.72 in.) fore to aft, respectively. Duct heights within the converging nozzle, Figure 238, varied from 0.216 m (8.5 in.) at the leading edge to 0.244 m (9.6 in.) at the midpoint and 0.279 m (10.98 in.) at the trailing edge. Five immersion positions were used, each of which was at the geometric center of an equal area annular ring. The test procedure called for only one probe at a time to be immersed in the air stream. The others were retracted to the outer passage wall to reduce the potential of noise generation.

Two acoustic probes were used on engine C. They were also positioned in a line parallel to the engine axis, one at the leading edge of the treatment section and the other slightly upstream of the trailing edge. The leading edge probe traversed a flow passage height of 0.187 m (7.37 in.), Figure 239, and utilized seven distinct immersion positions each of which was at the center of an equal area annular ring. The trailing edge probe was located 0.781 m (30.75 in.) from the leading edge probe and traversed a duct height of 0.294 m (11.57 in.) in seven equal area immersions. Only one probe was extended into the flow at a time. The same probes were used on both engines with the exception of the upstream probe of engine A which was not reused.

In the case of probe measurements in a duct with flow and elevated temperature and pressure it should be noted that a correction should be made to the measured sound pressure levels. That is,

$$SPL_{actual} = SPL_{measured} + 20 \log (1 + .707\ M) + 10 \log \frac{P_o}{P_s} \sqrt{\frac{T}{T_o}} \qquad (8)$$

where
- M = Mach number
- P_o = Ambient pressure
- T_o = Ambient temperature
- P_s = Static pressure
- T = Static temperature

These corrections are on the order of 2 dB and cancel when making transmission loss calculations and were therefore omitted from the calculations of power level.

The power level was calculated for the pure tones as well as broadband noise. Transmission loss, defined as the reduction in power level between probe positions was calculated for all configurations. Corrected transmission loss, defined as

transmission loss for a treated configuration minus the transmission loss for the untreated configuration, was also calculated.

2. Directional Acoustic Array

The array was positioned on engine A at angles of 50, 60, 70, 90, 110, 120, and 130 degrees measured from the inlet at a nominal distance of 30.5 m (100 ft.) from the fan rotor. At each of these positions, the array was directed at nine engine locations and the output voltage was tape recorded. These positions and locations are shown in Figure 272.

The array was positioned on engine C at angles of 50, 60, 90, 100, 110, 120, and 130 degrees from the inlet at a nominal distance of 30.5 m (100 ft) from the fan rotor. These positions as well as the nine engine locations at which the array was directed are shown in Figure 273.

The engine locations, in addition to the core nozzle region, were required in order to obtain a complete knowledge of each engine source. The off-axis and side lobe contributions from the other sources could then be removed by application of the array characteristic curves.

The array output was narrowband analyzed with a 20 Hz bandwidth filter over the frequency range of 1.25 to 6.3 Hz. Amplitudes for the array directed at each engine source were tabulated and the array characteristics were applied to obtain the true source component levels.

3. Farfield Microphones

A farfield array, Figure 274, of B&K Model 4133 microphones was positioned on a 45.8 m (150 ft) arc at a height of 12.2 m (40 ft). They were located at angles measured from the inlet of 10 degrees through 160 degrees in 10 degree increments. Data at all angles was simultaneously recorded for all test points. These test data were obtained while complying with the following restrictions which were imposed on acoustic testing:

1. Acoustic data were not taken with steady winds greater than 8.1 km/sec (5 mph) or gusts (above a steady wind) greater than 4.8 km/sec (3 mph);

2. Water or snow accumulation on the sound field prohibited testing;

3. Rain, snow, or fog at the test site prohibited testing;

4. Testing was restricted to conditions where the relative humidity was greater than 30% and lower than 90%;

5. No absolute level acoustic data were taken while aerodynamic instrumentation was installed.

Engine C test restrictions were later modified as follows:

6. Testing was permitted in a crosswind of 11.3 km/sec (7 mph) with gusts of no more than 4.8 km/sec (3 mph). A crosswind being defined as ± 45 degrees from a perpendicular to the engine centerline.

4. Near Field Microphones

Six near field microphones (B&K 4134) were positioned on engine A as shown in Figure 275. They were placed at the height of the engine centerline and pointed upward (grazing incidence). The placement and designation of the near field microphones on engine C is indicated in Figure 276. Their elevation was that of the engine centerline. Near field data from the six microphones were recorded simultaneously.

B. TEST RESULTS

Engines A and C (Figures 277, 278, and 279) were both acoustically tested at Peebles Test Operation using a nominal core nozzle with various turbine treatment configurations. The configurations on engine A consisted of the hardwall baseline, Cerafelt treatment, and the double sandwich II resonator system. Engine C testing involved a hardwall baseline, and the SDOF No. 19 resonator system in the standard nozzle configuration and in a coplanar nozzle configuration. Several aft fan configurations were employed on engine C and these will be shown to have an effect on turbine tone radiation. Descriptions of the treatments and their respective areas are shown in the section on engine hardware fabrication.

Engine A turbine contained four low pressure stages. Engine C utilized a two-stage low pressure turbine. The turbine and compressor stages are listed in Table XI. The high pressure turbine and compressor produced no significant tones measureable by probes in the turbine treatment section or the farfield.

Tests utilizing the probes and the directional acoustic array were conducted at two engine speeds - approach and takeoff - defined as 60% and 90% corrected fan speed, respectively, whereas farfield and near field data were recorded at a number of fan speeds. Pertinent engine parameters from cycle data for both engines are shown in Table XII at the approximate test conditions.

1. Engine A

a. Probe Data

Acoustic probe data were taken downstream of the turbine section on engine A for a baseline hardwall configuration, for the double sandwich II configuration, and for the Cerafelt configuration. Data were recorded at approach and takeoff power. Three probes were used, each immersed to 5 separate depths. A typical probe measurement is shown in Figure 280. This

Table XI. Engines A and C Blade Numbers.

STAGE	COMPRESSOR	H.P.TURBINE	ENGINE A L.P.TURBINE	ENGINE C L.P.TURBINE
1	36	108	166	118
2	26	116	142	130
3	42		126	
4	45		112	
5	48			
6	54			
7	56			
8	64			
9	66			
10	66			
11	76			
12	76			
13	76			
14	76			
15	76			
16	76			

Table XII. Engine A and C Engine Parameters.

	ENGINE A		ENGINE C	
	APPROACH	TAKEOFF	APPROACH	TAKEOFF
PERCENT FAN SPEED, N_{fc}	56.3	89.5	60.0	90.5
LOW PRESSURE TURBINE DISCHARGE TOTAL TEMPERATURE, T_{56}	654°K (718°F)	783°K (950°F)	615.3°K (648°F)	748.4°K (888°F)
LOW PRESSURE TURBINE DISCHARGE MACH NUMBER, M_{56}	.185	.320	.266	.490
JET NOZZLE THROAT AREA, A_8, (m^2)	.372 ($577\ IN.^2$)	.372 ($577\ IN.^2$)	.548 ($850\ IN.^2$)	.548 ($850\ IN.^2$)
JET NOZZLE THROAT MACH NUMBER, M_8	.315	.602	.253	.459
JET NOZZLE THROAT VELOCITY, V_8 (m/sec)	158 (519 ft/sec)	322 (1055 ft/sec)	124 (406 ft/sec)	243 (797 ft/sec)
JET NOZZLE THROAT GAS FLOW, W_8, (kg/sec)	30.4 (67.13 lb/sec)	56.7 (125.1 lb/sec)	36.6 (80.56 lb/sec)	61.9 (136.38 lb/sec)

was taken by the probe at the downstream edge of the double sandwich II treatment configuration. This is not corrected for probe losses. It clearly shows the existence of all four low pressure turbine blade passing frequencies as well as harmonics. The data show no indication of a hump of noise centered at the blade passing frequencies, as will be shown to be evident in all external engine measurements. There is also no evidence of significant high pressure turbine tones.

The power level at the forward probe at approach and takeoff for the untreated and double sandwich II configurations is shown in Figure 281. Broadband noise (1/3-octave band with pure tone omitted) repeatability is good except at low frequencies at approach. Pure tone repeatability is very good. These data are a measure of both source and electronic system repeatability. Corrected transmission loss for pure tones and broadband noise at approach and takeoff is shown in Figure 282. At approach the pure tone suppression, reaching a maximum of 19.5 dB, is much greater than the broadband suppression except at the first stage BPF (6000 Hz). At takeoff, broadband, and pure tone suppression are more nearly equal with pure tone suppression reaching a maximum of 10 dB. Broadband suppression does not equal pure tone suppression due to noise generation along the treatment length. That is, broadband noise is both suppressed and generated in the treated duct. Broadband noise generated upstream of the treatment is suppressed the same as the pure tones, however, the generated noise does not experience the same length of treatment and therefore is suppressed to a lesser degree. Noise may be generated by flow over any irregularities on the surface of the duct such as gaps, holes, or ridges or may be due to boundary layer fluctuations [15].

The transmission loss (Δ PWL) for each of the treatment configurations is shown in Figure 283. It can be seen that for the Cerafelt configuration the broadband PWL at the downstream edge of the treatment is greater than at the leading edge. These levels automatically invalidate the data, preventing any measure of treatment suppression for broadband noise. The increased noise level was believed due to a relatively poor fabrication of the treatment section which resulted in gaps and ridges on the flow surface. These imperfections produced increased noise and turbulence which were recorded by the downstream probe as a noise floor.

Figure 284 shows the corrected transmission loss of the turbine tones as a function of treatment length. This is derived from the three acoustic probes and shows CTL to the midpoint and aft treatment positions. Results for the two treatments are similar for the second and third stage BPF. The Cerafelt data at the fourth stage BPF show the peculiarity of a decrease in corrected transmission loss with increased treatment length. This may be attributed to the relatively small number of probe immersions which for the midstream probe may have allowed a high energy mode to pass undetected. This energy, however, was evidently measured by the downstream probe. It is not untypical for the tone sound pressure level to vary by 10 dB from one immersion to the next, and it was for this reason that the number of immersions was increased from five to seven for engine C.

A comparison of corrected transmission loss at approach for the two treatments is shown in Figure 285. Measurements of Cerafelt suppression were obscured by duct generated noise, which was believed to be due to a relatively poor panel assembly which contained several small gaps and rough spots. The data are therefore shown accompanied by an arrow and means that the suppression is greater than the indicated value, but that the actual magnitude could not be measured due to the presence of a noise floor. The double sandwich II corrected transmission loss is seen to be relatively constant across the spectrum at approximately 13 dB except for the reduced suppression at 6000 Hz. The tone at this frequency, unfortunately, was also the one of greatest power level both treated and untreated. Figure 286 shows the relative power levels of each tone observed by the downstream turbine probe at approach power for both the baseline and the double sandwich II treatment configurations.

It is seen in the treated configuration that the dominant tone corresponds to the first stage low pressure turbine fundamental and that the second, third, and fourth stage tones are approximately of equal power level. The first stage tone also dominates the spectra on a perceived noise level basis.

b. Near Field Data

Narrowband results of engine A for the hardwall core nozzle measured with the near field microphones are shown in Figures 287 through 292 at approach speed. The No. 1 location shows two tones which appear to be compressor generated, at 8300 and 9850 Hz. No other tones are discernable. The tones in the No. 2 location are unidentifiable but may be related to external engine cooling air pumps. These occur at 4300 and 6400 Hz. No tones are seen at position No. 3. Position No. 4 clearly shows the fan second harmonic despite the extensive fan treatment. The No. 5 position which is the first position aft of the plane of the core nozzle does not show the fan tone but does show two turbine tones. These are, respectively, the fourth and third stage low pressure turbine blade passing frequencies. Position No. 6 shows a broadband hump of noise just above 6 kHz in addition to the fourth stage fundamental. The hump occurs centered at the first stage blade passing frequency.

The data at takeoff are shown in Figures 293 through 298. All positions show the presence of the fan fundamental and second and third harmonics. In addition, the fourth harmonic appears at position No. 3. At position No. 4, the band containing the fan third harmonic changes from the sharp tone seen at the forward positions to a hump of noise believed due to the fan struts, since a prior fix involving reducing their number and streamlining the leading edge resulted in substantial noise reduction. This behavior continues for the remaining positions. The frequency does not correspond to any of the turbine stages.

Near field data were not recorded in the treated nozzle configuration on engine A so that no measurements of suppression could be made. The usefulness of these data are therefore, limited. It does, however, show two important points: (1) the third and fourth stage turbine tones at approach radiate from the nozzle, Figure 299, and not the casing, and (2) the first stage

tone is obscured by a noise hump which appears to radiate from a position well downstream of the nozzle (unlike the other two tones).

c. Directional Array Data

Directional acoustic array data were recorded for all three engine A turbine treatment configurations. These consisted of the baseline engine which contained fan frame treatment only, the fully suppressed fan (inlet and exhaust splitter treatment) with the double sandwich II treated core nozzle, and the treated fan frame configuration with Cerafelt core nozzle treatment. Representative array outputs are shown in Figure 300. The engine positions recording the maximum amplitude at the turbine blade passing frequencies are shown.

An analysis of core radiated broadband noise requires utilization of all the array data. That is, in evaluating core nozzle radiated noise, fan radiated noise must be examined. This is due to the nature of the array which only partially rejects off-axis noise sources. Broadband noise data for the engine are presented for two configurations. These are the basically untreated engine (baseline with fan frame treatment) and the fully suppressed engine including double sandwich II turbine treatment. Figures 301 through 306 each shows, for different 1/3-octave bands, the amplitude of sound reaching the receiver radiating from positions along the engine axis. These positions (6 through 1) include, respectively, the fan casing, fan discharge plane, core cowl, core nozzle plane, and positions 0.76 and 1.52 meters (2.5 and 5 ft.) downstream of the core nozzle plane. Data are presented for angles of 90, 110, 120, and 130 degrees relative to the inlet, and at approach and takeoff power. The untreated configuration as well as the treated configuration at approach power each show the fan exhaust radiated noise to dominate, especially toward aft angles. High frequency broadband noise radiates from a region at the fan discharge whereas low frequencies are radiated also from the area 0.92 m (3 ft) aft of the discharge plane. Some of the broadband noise at low frequencies may propagate with the fan flow external to the engine before radiating, or the noise radiating from axial position 4 may actually be core cowl generated noise.

Core radiated noise appears to radiate from a source distributed several feet downstream of the core nozzle plane. The total core noise arriving at an omni-directional receiver such as a farfield microphone would be the sum of the levels at positions 1, 2, and 3, so that at takeoff for the treated configuration, the fan exhaust radiated noise and the core radiated noise would be of comparable amplitude.

The broadband core noise sound pressure level suppression for the double sandwich II configuration is summarized in Figure 307 for the 120 degree angle which is the angle of maximum farfield perceived noise level. The suppression, as seen by the array, peaks at 3.15 kHz at both approach (6.5 dB) and takeoff (4.5 dB).

The broadband suppression results for the Cerafelt configuration are shown in Figure 308. The results show the broadband suppression to peak at

only 1.5 dB at approach and to actually be negative in the lower 1/3-octave bands. These results are as expected after having observed the probe data. That is, the treatment section has actually produced broadband noise in the boundary layer. At takeoff, treatment suppression occurs over the range of 1.6 - 6.3 Hz and peaks at 2 dB in the 3.15, 4.0, and 5.0 1/3 octave bands.

The fourth stage low pressure turbine blade passing frequency was observed in all three configurations at approach. The first stage fundamental, however, was obscured by a hump of noise centered near the first stage blade passing frequency. The hump was also observed in farfield and nearfield data. As seen in Figure 300 the source position appears to have shifted. That is, in the untreated configuration the first stage tone appears to radiate from a position 1.52 meters (5 feet) downstream of the nozzle (position No. 1), whereas in the treated configuration the radiation is from the region 0.76 meters (2.5 feet) downstream of the nozzle. (position No. 2). The nozzle treatment configuration, therefore, appears to affect the radiation characteristics as well as the power level.

The directivity of the fourth stage turbine blade passing frequency at approach is shown in Figure 309 for the three treatment configurations. There is no suppression observed at 130 degrees. At the maximum angle of 120 degrees, the Cerafelt configuration shows 4 dB reduction whereas 11.5 dB reduction is observed for the double sandwich II configuration. The sound pressure level of this tone in the treated configurations is greatly reduced at the midangles. The maximum levels are propagated further aft in the treated configuration than in the untreated configuration.

An analysis of the first stage low pressure turbine blade passing frequency cannot be made since it is either obscured by broadband noise or is modulated into a band of noise. The analysis of this broadband hump of noise is critical since it is a major source contributing to the farfield PNL. A summary of the array measurements of this hump is presented in Figure 310. The upper part of the figure shows the relative amplitudes of the 1/3-octave band centered at the hump's peak frequency for the three configurations. The maximum difference occurs at 130 degrees. The double sandwich II configuration shows 2.5 dB reduction whereas the Cerafelt run is reduced by 6 dB relative to the hardwall. An analysis of the peak amplitude of the hump is made in the lower part of the figure. The treatments rank in the same order, however, a greater reduction is obtained in peak amplitude. The first stage hump is therefore suppressed in amplitude to a greater degree than is its 1/3-octave band level.

d. Farfield Data

Farfield engine data in a 1/3-octave band analysis are of relatively little value in evaluating the turbine noise suppression, since broadband noise is composed of signals arriving from several engine sources simultaneously. The amplitude of the core radiated component cannot be determined.

Nevertheless, farfield suppression on a 1/3-octave band basis is the standard by which the effectiveness of any engine modification or treatment is judged. For this reason 1/3-octave band data measured on a 45.7 m (150 ft) arc and extrapolated to a 61 m (200 ft) sideline are presented. A more comprehensive examination of engine A farfield measurements can be found in Kazin.[16] Data taken in the fan frame treatment engine configuration (fan not fully suppressed) both with and without Cerafelt turbine treatment are presented. Figure 311 shows the power level at approach to be reduced by less than 1 dB in the BPF region. Sound pressure level reduction is observed at both the maximum forward and aft angles, Figures 312 and 313. The maximum suppression (3 dB) is observed at 120 degrees in the 6.3 kHz band. The sound power level suppression at takeoff is shown in Figure 314. This shows 1 dB suppression at 4.0 kHz. The forward angle, Figure 315, shows no suppression over the frequency range of interest (4.0 - 8.0 kHz). The aft angle at takeoff, Figure 316, shows 1 dB suppression from 4.0 to 6.3 kHz due to the application of the turbine treatment. The PNL suppression at the maximum aft angle is approximately 1 PNdB at all four tested engine speeds, Figures 317 through 320. Observed suppression was severely limited by fan noise radiating to the farfield as was shown by the array data.

Data are also shown for the fully suppressed fan configuration both with and without double sandwich II core nozzle treatment. Figure 321 shows the relative values of sound power level at approach speed (60% N_{f_c}). It is apparent that the configuration with core nozzle treatment has an increased power level for frequencies from 0.5 to 10 kHz. These data are further analyzed on a sound pressure level basis in Figures 322 and 323 at the maximum forward and aft angles, respectively. The level is seen to have increased by a greater amount at the forward angle than at 120 degrees. There is in fact moderate suppression at 120 degrees over the frequency range from 2.5 to 6.3 kHz. This strongly indicates that the fan power level has increased between configurations and that the fan levels control the farfield power level. The data at takeoff are shown in Figures 324 through 326. The power level again is seen to have increased with the insertion of treatment (primarily in the 2.0 and 4.0 kHz 1/3-octave bands). These bands incidently contain the fan fundamental and second harmonic, respectively. Both the forward and aft angles show increased levels in these bands which again points to the fan as the cause of increased power level. These results are similarly reflected in the perceived noise level plots as shown in Figures 327 through 330, which show speeds of 60, 70, 80, and 90% N_{f_c}, respectively. The double sandwich II core nozzle configuration shows a distinctly increased PNL value at angles of 40 through 80 degrees and a slight increase at the aft angles. The increased PNL is fan related. The 1/3-octave band data is then of no value in analyzing the effect of the core nozzle treatment and in fact erroneously implies that the core radiated sound power increases.

Narrowband analysis of tones which emanate solely from the core nozzle region is a more accurate means of treatment evaluation than is 1/3-octave band data which is influenced by other engine sources. Narrowband data at the maximum aft angle for the untreated and Cerafelt treatment configurations at approach is shown in Figure 331. The fan frame treatment configuration was used with the Cerafelt treatment. The high amplitude of this fan component presents a noise floor preventing the measurement of the turbine tone suppression. At least 3 dB suppression of the fourth stage tone is observed.

Suppression of 2 dB is observed at the first stage low pressure turbine blade passing frequency. A hump of noise at the first stage BPF is seen in the untreated configuration. This will be examined in greater detail for the configurations involving the fully suppressed fan.

Four sets of engine corrected rpm data were run on engine A for the hardwall and for the double sandwich II treatment in the fully suppressed fan configuration. The were grouped near the approach speed. The data at the two maximum aft angles (120° and 130°) are shown in Figures 332 through 339. In order to make the comparison more direct, the treated data was frequency shifted on the figure such that the blade passing frequencies would coincide. Suppression of the fourth stage tone at 1802 rpm is greater than 10 dB at 120 degrees, whereas, the third and first stage tones are reduced by 4 dB. Humps of noise are evident at the first and fourth stage BPF's. Results are considerably different at 130 degrees, where the treated noise level is generally 2 dB higher than at 120 degrees. Also, the untreated fourth and third stage turbine tones are lower in amplitude while the amplitude of the first stage tone is 3 dB greater than at 120 degrees. Almost no information can be derived from the data at 130 degrees due to a noise floor. The data at 2157 rpm (Figure 334) show at least 10 dB reduction for the fourth stage tone at 120 degrees. There is no apparent change in the first stage level. Again at 130 degrees, there is no significant information. Basically the same results are seen at the higher rpm's with the exception of a reduction in the "first stage hump", especially at 2531 rpm where a 5 dB reduction is seen.

Farfield data, then, show approximately 10 dB reduction of the fourth stage tone at its maximum angle over the speed range of 1800 to 2500 rpm the third stage tone is also reduced, but a noise floor prevents this measurement. The first stage blade passing frequency is shrouded in a hump of noise which peaks near, but not at, that frequency. The hump is slightly reduced due to treatment insertion.

An important observation regarding the noise haystack at 6 kHz is shown by the farfield narrowbands. They show the peak frequency to shift as a function of angle. A linear relationship occurs between angle and frequency. This is most pronounced at the approach speed, Figures 340 and 341, and it is independent of turbine treatment. This phenomena has not been observed on any previously tested engine nor was it observed on engine C. Figure 342 shows the directivity of the hump peak independent of its frequency, for farfield as well as directional array data and both configurations as well as repeat runs. The amplitude peaks at 120 to 130 degrees and drops off fairly rapidly with increasing or decreasing angle.

A possible explanation of the frequency shift is based in part on a report by R. Hayden[17] which investigates lip noise generation at the edge of a nozzle and a flat plate exposed to axial air flow. It is believed that the 6.0 kHz noise hump on engine A is lip noise generated at the core nozzle. Hayden's results were applied to engine A to verify the lip noise generation mechanism.

Hayden shows the generated frequency to be:

$$f = \frac{.25\ V}{\delta_w} \tag{9}$$

for flow on both sides of a trailing edge.

where, V = velocity

δ_w = plate thickness + 2 δ^*

δ^* = $\delta/8$

δ = boundary layer thickness

The generated power level is shown to be proportional to V^6, that is;

$$PWL\ (1/3\ OB) = 10 \log (\delta_w W_c V^6) - 26.5\ dB \tag{10}$$

where

W_c = span length of the edge

The relative velocities of V_{28} (fan discharge) and V_8 (core discharge) are shown in Figure 343. It can be seen that the two velocities near approach (60% N_{f_c}) are approximately equal. This is the speed range in which the noise hump occurs. Shown in Figure 344 is the relationship between the 1/3-octave band of noise centered at the haystack peak frequency and the engine speed or jet velocity. At the lower speeds where V_{28} and V_8 are nearly equal the amplitude is seen to increase as the average velocity to the sixth power. At approximately 65% N_{f_c} there is an apparent change in the source mechanism. The amplitude drops as the hump simply becomes broadband noise and the slope of the increase then becomes a function of $V_{28}{}^6$. Also shown in Figure 344 is the relationship of the peak amplitude of the hump to engine speed. Over the speed range where the hump is significant the peak amplitude appears to be a function of $V_{avg}{}^6$.

The frequency and the power level in the speed region at which the hump occurs therefore agrees with the lip noise theory. A sketch of the core nozzle lip is shown in Figure 345. The geometry becomes complex at high temperatures and is not known exactly so that a value cannot be assigned to δ_w. At high temperatures the nozzle may not be circular so that the lip may not be uniform around the circumference.

It is believed that the lip noise source is actually near 4900 Hz at approach and that the source is moving away from the nozzle with the velocity of the gas flow. This moving source radiates to the farfield producing a Doppler shift at the far field angles. Shown in Figures 340 and 341 is the predicted Doppler shift for this source. Agreement with the measured peak frequency is excellent over the angles from 110 to 150 degrees.

2. Engine C

a. Probe Data

Turbine probe data were recorded on Engine C in the fan frame treatment configuration using the nominal core nozzle. Two acoustic probes were used. One was positioned at the treatment leading edge, while the other was positioned several centimeters forward of the treatment trailing edge. Data from seven immersion positions for each probe were recorded, both for the untreated baseline configuration and for the treated turbine (SDOF No. 19) configuration. Data were taken at both approach and takeoff power. Typical narrowband frequency plots taken at the aft probe at approach are shown in Figure 346.

The calculated power level, for pure tones as well as for broadband noise, at the upstream probe for both treatment configurations is shown in Figure 347. The broadband data show a fairly large amount of scatter whereas the pure tones at approach repeat well. The second stage turbine BPF at takeoff occurs above 10 kHz and was not analyzed. In general, the power level of broadband noise at the upstream probe apparently decreases with the insertion of the acoustic treatment. The corrected transmission loss at both engine speeds is shown in Figure 348. The CTL for broadband noise peaks near 6 kHz, at 6 dB at approach and 10 dB at takeoff. Due to the apparent effect of the treatment on the upstream power level, the corrected transmission loss does not show the overall effect of the treatment. That is, the installation of the treatment resulted in an increase in the low pressure turbine blade passing frequency power levels. The power level reduction at the aft probe due to the treatment is shown in Figure 349. The power level at the aft probe is reduced by a greater amount than is indicated by corrected transmission loss measurements.

The turbine tones are seen to be reduced to a greater degree than broadband noise at the corresponding frequency, reaching 11 dB and 7.7 dB for the first and second stage low pressure turbine blade passing frequencies, respectively. The broadband noise suppression is believed to be limited by the generation of pseudo-sound in the treatment section.

b. Near Field Data

Data were recorded on the nominal core nozzle with both hardwall and SDOF No. 19 (single-degree-of-freedom) treatment configurations. Narrowband analysis was made at approach speed (3200 rpm) and at takeoff (4750 rpm). The data at approach are presented in Figures 350 through 355. Both the baseline and SDOF No. 19 configuration data are presented together to more clearly show the effect of treatment. The fan fundamental as well as harmonics up to the seventh are clearly seen at the first few positions for both configurations. Both the treated and untreated configurations show the presence of two distinct humps of noise at positions 4, 5, and 6. These occur near the blade passing frequencies, which are at 6160 and 6780 Hz for the data in the untreated configuration, and at 6320 and 6960 Hz for the treated configuration. It should be noted that the fan 5th harmonic falls at the same frequency as the turbine second stage BPF.

The amplitude of the hump of noise peaks at position No. 5 which is 0.61 meters (2 ft) aft of the core nozzle. The amplitude of the peak is reduced due to treatment at position No. 5 by 7 dB and by 6.5 dB, at the first and the second stage blade passing frequencies, respectively.

Data taken at takeoff power are shown in Figures 356 through 361. The turbine blade passing frequency fundamentals occur at 9,240 Hz and 10,200 Hz for the untreated configuration and at 9,500 Hz and 10,450 Hz for the treated configuration. The data were only reduced to 10 kHz and therefore does not show the second stage tone. Position No. 5 again records the maximum amplitude of the noise hump, which occurs at the first stage blade passing frequency. No turbine tone is apparent due to the presence of the hump. Treatment is shown to reduce the amplitude of the hump by at least 10 dB. An exact treatment evaluation cannot be made since the hump is not evident in the suppressed configuration.

c. Directional Array Data

Directional acoustic array data were recorded on the fully suppressed fan engine (incorporating fan frame treatment and treated inlet and treated exhaust splitters) for configurations involving the hardwall core nozzle and single degree of freedom (SDOF No. 19) acoustic treatment. Data were taken at both approach and takeoff speeds. In addition, data were recorded with a treated core nozzle in a coplanar nozzle configuration, and in the fan frame configuration which did not utilize the low Mach number fan exhaust duct. These data (corrected for array characteristics) are presented in Figures 362 through 408.

Due to the extended nature of each source, a single engine positioning of the array would not adequately measure each source. For this reason several positions were summed before plotting. The core nozzle data refers to the sum of the nozzle plane level as well as the level at positions 1.52 m (5 ft.) and 3.04 m (10 ft.) downstream of the nozzle. Fan discharge data refer to the sum of measurements made at the fan nozzle and at the core cowl, while fan inlet data are the sum of levels radiating from the inlet plane and a position 1.52 m (5 ft) forward of the inlet. Fan casing radiation data, when plotted, are the sum of the levels observed radiating from the positions on each side of the rotor. In the case of the coplanar nozzle, casing radiation also emerges from the two positions upstream of the core nozzle plane. The output level of a B&K microphone which was mounted on the array is also plotted as is a level which is the summation of the source amplitudes for all nine engine positions. The summation level is consistently lower than that of the B&K microphone. This is due to the fact that the array does not pick up the total energy radiated by the engine. This is partly due to the limited number of engine positions at which array data were taken. In order for the array to pick up all the energy, the number of positions would need to be increased. The optimum number of positions will increase with increasing frequency. A higher number of positions, besides being time consuming and therefore costly, would only be satisfactory over a small frequency range. Too large a number of positions would result in overlapping beam patterns and an erroneously high value of sound pressure level.

Shown in Figure 409 are the relative amplitudes of the core nozzle radiated broadband noise spectra at approach that is recorded by the array at angles of 90, 100, 110, 120, and 130 degrees, respectively. This level was obtained by summing the three aft engine positions, that is, the core nozzle plane and the positions 1.52 m and 3.04 m downstream. Suppression is observed at all angles at frequencies above 2500 Hz.

The fully suppressed engine data appear relatively low at angles of 110 and 120 degrees in the frequency range near 5 kHz, while the coplanar nozzle (both fan and core nozzles exit at the same place) data appear to agree well with the fan frame configuration data. However, the coplanar data also contain a fan noise component so that these data cannot be compared directly with the other configurations. The true level of core radiated noise for the coplanar nozzle is actually lower than shown. Using the average of the treated core configurations (omitting the coplanar) it is seen that the suppression peak occurs at approximately 10 dB for the angles of 110 and 120 degrees in the 4.0 and 5.0 kHz 1/3-octave bands. The suppression in the 6.3 kHz band is 7.5 dB at 110 degrees and 8.5 dB at 120 degrees.

The relative amplitudes of the core radiated noise for the different configurations at takeoff and 120 degrees is shown in Figure 410. No data were recorded with the coplanar nozzle at takeoff. The core radiated noise level varies considerably between the two treated configurations. The approach data are shown in this figure for reference. The apparent turbine noise reduction is considerably less at takeoff than observed at approach. This is due to the noise floor (flow noise and jet noise) which at takeoff is only slightly below the turbine noise level. The peak sound pressure level reduction is 5.5 dB and occurs at 5.0 kHz.

A rough calculation of power level suppression at approach has been made. This was based on the measurements made at these five angles for the untreated and treated turbine in the fully suppressed configuration. This calculation shows suppression of 8.3, 8.9, and 7.0 dB in the 4.0, 5.0, and 6.3 kHz bands, respectively. These values are all in excess of the probe measured corrected transmission loss of 3.5, 5.0, and 6.0 dB at these same frequencies, respectively. The probe data, however, was believed to have reached a noise floor. The probe measured corrected transmission loss for the first and second stage tones (6.0 and 6.5 kHz) has been shown to be 11.0 and 7.7 dB, respectively. The true duct broadband suppression (neglecting the noise floor) is expected to fall within this range. In this event there would be reasonably good agreement between the probe and array measurements of turbine noise suppression.

The relative magnitudes of the major engine broadband noise components at 120 degrees for the fan frame configuration and for the fully suppressed configuration (both of which used two degree of freedom core treatment) are shown in Figure 411. This shows that the core radiated noise is not the major source in the fan frame configuration but that the fan discharge radiated noise controls the spectra at 120 degrees. The fully suppressed fan succeeds in reducing the fan noise to the point that the fully treated configuration is completely dominated by core radiated noise, even though turbine treatment is installed.

The level and directivity of the low pressure turbine tones at approach power for the first and second stages (6.0 and 6.5 kHz, respectively) are shown in Figures 412 and 413. All four engine configurations are shown. The results from the B&K microphone appear reasonable, in that the untreated core produces the greatest amplitude, and the treated core configurations repeat with the exception of the coplanar nozzle configuration. The coplanar configuration results in the first stage tone increasing by up to 5 dB and the second stage tone increasing up to 10 dB relative to the other treated configurations. These results were also observed in the farfield measurements. The array data for the first stage tone produce a similar conclusion (although the coplanar data are nearer in amplitude to that of the untreated core configuration). The second stage tone as observed by the array exhibits several peculiarities which cannot be attributed to the data reduction but may be a problem of the array encountered at this small wavelength. This would be due to the source size and a variation in the speed of sound due to atmospheric gradients. For these reasons the turbine tone array data offers no advantage over a standard microphone in measuring the tone amplitude. It does, however, verify the source location at the core nozzle region as opposed to the turbine casing. The first stage turbine tone suppression over the aft angles is approximately 13 dB as measured with both the array and the B&K microphone. This value is considerably greater than that measured for the broadband noise (7.5 dB and 8.5 dB at 110 and 120 degrees, respectively). The array broadband data are, therefore, probably influenced by a noise floor.

d. Farfield Data

The principle method of farfield analysis involves 1/3-octave band perceived noise levels and sound pressure levels. A comprehensive report on measured farfield data on Engine "C" can be found in Kazin [18]. The fully suppressed fan configuration with treated core results in the lowest level of perceived noise at both approach and takeoff speeds. At approach in this configuration, the perceived noise level, Figure 414, is reduced by 4 PNdB at 120 degrees and 2.5 PNdB at 70 degrees due to the installation of the turbine treatment. The sound pressure level spectra is shown at 70 and 120 degrees in Figures 415 and 416, respectively. The forward angle level is reduced at all frequencie above 1600 Hz. The maximum suppression is 7.5 dB at 2.0 kHz. The aft angle shows suppression at frequencies above 2.0 kHz. The maximum suppression is 8.5 dB and is observed at 4.0 kHz.

The perceived noise level is shown at takeoff speed in Figure 417. The maximum angle is 120 degrees where 2.5 PNdB suppression is observed. At 70 degrees, 2.0 PNdB suppression is observed. Figures 418 and 419 show the SPL spectra at these two angles. Suppression is seen at the forward angle for all frequencies above 1.0 kHz. The maximum suppression is 4.5 dB and is observed at 6.3 kHz. The aft angle shows suppression above 2.5 kHz, with a maximum of 7.0 dB at 10 kHz.

Comparisons of farfield sound pressure level reduction at four engine speeds are shown in Figures 420 to 423 for the fully suppressed configuration. The ΔSPL plotted is the largest value observed irrespective of frequency. The suppression is fairly uniform from 90 through 130 degrees and decreases at smaller and larger angles. The suppression values are similar at all engine speeds.

The farfield narrowbands reveal no pure tones at the turbine blade passing frequencies at takeoff, even with the untreated turbine-fully suppressed fan configuration. At approach, however, the blade passing frequencies were observed. The narrowband plots over the frequency range which include the low pressure turbine blade passing frequencies at approach for four engine configurations are shown in Figure 424 at the aft angle of 120 degrees. The first and second stage tones appear distinctly only in the coplanar treated core configuration. The fully suppressed fan configurations both contain an additional frequency which was seen by the array to originate in the vicinity of the core cowl. The other two fan configurations (shorter fan duct in the fan frame configuration and extended duct in the coplanar configuration) did not generate this tone. It is evident, in the non-coplanar configuration, that a fairly wide bandwidth of noise occurs at the expected second stage blade passing frequency. This is similar to the noise hump which occurred at 6.0 kHz for the first stage tone of engine A. Unlike engine A, however, the frequency of the peak amplitude of the hump does not change with angle in the farfield. The second stage tone in the coplanar configuration (treated core) is, in fact, of an apparently higher amplitude than the tone in the untreated core configuration. This can be explained by an external modulation mechanism caused by the mixing of the jets which effectively changes the pure tone (it is a pure tone as observed at the aft probe position) into a band of noise centered at the blade passing frequency.

This external modulation mechanism makes an analysis of pure tone suppression highly inaccurate. The farfield amplitude of the "tone" has little relationship to the tone power level at the trailing edge of the turbine treatment.

SECTION IV

DISCUSSION OF RESULTS

A. TREATMENT DESIGN

The selection of the single-degree-of-freedom resonator configurations as outlined in Table II covers a wide range of core depths and face plate porosities. With this kind of variation, the acoustic duct test results give data that illustrate, upon analysis, the influence of these different design parameters on the performance of the system.

The first parameter effect is that of porosity as is illustrated in Figure 425. These test results are for five different face plate porosities over a range of 4% to 22% with all other parameters held constant. The maximum peak attenuation occurs for a 7% porosity face plate. Of course, the optimum porosity is a function of such duct environmental factors as Mach number, sound pressure level, and temperature. Thus, since the acoustic resistance of the system is determined from these parameters any change in these values will require a different face plate porosity.

The effect of the duct Mach number is illustrated in Figure 426. The peak attenuation is seen to change with a corresponding change in duct Mach number for most of the configurations. Illustrated in Figure 427 is the Mach number effect on the attenuation versus frequency for the SDOF configuration No. 19. For increasing Mach number (greater than 0.25), the peak attenuation amplitude decreases and is shifted to a higher frequency. The shift in frequency is due to the decrease in acoustic mass at the higher Mach numbers.

The effect of the panel core depth is shown in Figure 428. The absorption for three different depths is given with the other parameters held constant. The peak attenuation frequency is shifted upward for a corresponding decrease in the panel thickness. The amplitude of the attenuation is reduced for decreasing thickness. This is brought about by the increase in the (H/λ) parameter. No appreciable changes can be seen in the suppression band width for this range of core thicknesses. Figure 429 was derived from these data and is extrapolated to cover a wide range of required core depths for desired peak attenuation frequencies.

The effect of face plate thickness is given in Figures 430 and 431. Figure 430 refers to SDOF No. 18 and SDOF No. 23. The only difference in the two systems is face plate thickness of 0.076 cm (0.03 in.) and 0.254 cm (0.01 in.), respectively. The thinner face plate shifts the peak frequency upward with a small decrease in peak amplitude. In Figure 431, for SDOF configurations No. 19 and No. 24, the frequency is also shifted upward, but the peak amplitude is unchanged. No significant change is noticed in the suppression bandwidths due to a change in the face plate thickness.

A design method for future turbine noise suppression sytems is contained in Figures 432 through 436. The procedure is the same as that used in the design of treatment systems for the suppression of fan exhaust and fan inlet radiated noise of jet engines. Due to the temperature difference between the fan exhaust and the turbine exhaust there was a need for data to enable development of a design method for such areas of application as turbine noise. The duct test results and engine test results obtained in this program produced adequate data to extend and further substantiate this design procedure.

The predicted acoustic reactance values for the SDOF configurations plus the predicted optimum reactance ($0.77\ H/\lambda_o$) as given by Cremer[19] for a 20.3 cm (8 in.) duct height are given in Figure 432. This definition of optimum reactance is very close to that given by Rice[8] and was used because of its simplicity. The reactance is shown for four different SDOF resonator systems. The point of intersection of the predicted reactance and the predicted optimum reactance curve determines the peak attenuation frequency for each particular system. The following listing compares the predicted and the measured peak attenuation frequencies for these four systems.

SDOF Panel No.	Predicted Peak Freq.	Measured Peak Freq.
1	3800 Hz	4000 Hz
8	3000 Hz	2500 Hz
18	4600 Hz	4500 Hz
22	6300 Hz	6500 Hz

As can be seen the predicted and the measured results are in good agreement. Thus, from these results, this method of defining peak attenuation frequencies for SDOF systems is substantiated. The peak suppression for the least attenuated mode per (L/H) versus the acoustic parameter (H/λ_o) is given in Figure 433.

The curve for both pure tone and broadband noise suppression was developed from previous acoustic duct data at ambient temperature and from engine test results for fan exhaust radiated noise suppression. The predicted suppression as indicated for broadband noise coincides with the theoretical prediction over a practical design range $1.0 \leq H/\lambda_o \leq 2.5$.

$$\frac{\Delta\ dB}{L/H} = \frac{7}{H/\lambda_o} \qquad (11)$$

The suppression rate as indicated for pure tones corresponds to the maximum attenuation values observed from test results and is on the order of $\frac{10}{H/\lambda_o}$.

The figure gives a comparison of measured attenuation in the acoustic transmission loss duct facility versus the predicted value. The results given in Figure 434 show that the measured farfield pure tone suppression for engines A and C fall below the predicted value. This measured suppression could, however, be limited by other noise sources. The broadband noise suppression measured for engine A can not be used since other radiated engine noise sources interfered with the farfield broadband noise measurements. The broadband noise suppression as measured for engine C agrees with the predictions. In Figure 435 the engine pure tone suppression values as measured by the directional acoustic array and by engine-

mounted acoustic probes are seen to have an average value that agrees with the predicted suppression level. Thus, from both duct and engine data, broadband and pure tone noise, it is evident that the predicted peak suppression levels are in good agreement with measurements. The reliability of the predicted peak attenuation is very important in any design study where emphasis is placed on Δ PNdB.

A requirement in calculating Δ PNdB levels is to utilize a suppression bandwidth curve after establishing the peak suppression frequency and attenuation amplitude. Figure 436 shows a suppression bandwidth curve established from the acoustic duct test results and this curve is compared with farfield 1/3-octave band suppression bandwidth measurements. The suppression bandwidth curve as shown was the best fit curve through all of the SDOF configuration test results. The engine results were based on three different engine speeds with the data taken at an aft angle of 120° on a 61 m (200 ft.) sideline. The engine data indicate a somewhat broader suppression bandwidth at frequency ratios greater than one than that which was established from the duct data, but is less broad at frequency ratios less than one.

Methods for predicting the peak attenuation frequency, suppression amplitude, and suppression bandwidth have been presented. The following is a listing of the order in which the given curves can be used in future turbine suppressor or similar noise suppression configuration design studies.

- Frequency Tuning - Figure 432.
  Requirements are to first generate the optimum reactance curve for a given duct height. Then, by plotting the predicted acoustic reactance for a system, the tuning frequency is determined by the intersection of the two curves.

- Peak Amplitude - Figure 433
  By knowing the L/H and H/λ_o parameters the peak attenuation value can be found.

- Suppression Versus Frequency
  The suppression as a function of frequency is determined after the peak attenuation and center frequency are established by using the suppression bandwidth, Figure 436.

B. ENGINE TESTING

The most satisfactory method of measuring the turbine treatment suppression is with engine acoustic probes mounted upstream and downstream of the acoustic treatment. All farfield measurements are influenced to some degree by sources other than turbine noise, which reduce the signal/noise ratio, thereby preventing measurement of the full treatment effect. The directional acoustic array increases the signal/noise ratio by effectively filtering out much of the other engine sources but the signal/noise ratio is still insufficient. Near field microphones offer some source location information as does the directional array but the level cannot be calculated from these measurements and the noise problem remains. Farfield measurements are the most inadequate since they record all engine sources as they arrive at the microphones.

The final measure of a treatments effect is, of course, the farfield measurements of sound pressure level, power level, and perceived noise level. The sound produced by flow over the treatment is then as vital as the sound suppression, since the resultant level is the overall treatment effect.

1. Engine A, Measurements vs Predicted Suppression

The double sandwich II configuration was simply a variation of MDOF No. 3 configuration, which was predicted to result in suppression of 12 PNdB for the turbine noise component. The evaluation of turbine suppression in PNdB could not be measured due to the contribution of other engine sources. Duct measurements made at the same L/H value indicate that the turbine tone power level suppression should range from 12-15 dB over the frequency range of 2.5 kHz - 6.3 kHz. Probe measurements indicate 12.5 - 16.5 dB suppression from 4 - 5 kHz and 10 - 19.5 dB suppression from 8 - 9 kHz. Only for the first stage BPF (6100 Hz) is suppression (6 dB) less than expected. Broadband noise suppression could not be measured accurately with any of the measurement systems due to the presence of noise floors.

Engine A turbine treatment evaluation was complicated by the presence of a "haystack" of noise occuring near the first stage low pressure turbine blade passing frequency. The haystack was found, by directional array and near field data, to be generated aft of the engine. It is believed to be due to a modulation phenomena induced by the velocity relationship between the mixing fan discharge and core jets. The haystack was produced by a moving source (the mixing jets) and resulted in a Doppler frequency shift in the farfield.

The summary of treatment effects measured by three methods - probe, directional array, and farfield microphone, is shown in Tables XIII and XIV. These results are for the Cerafelt treatment, which was used with the fan frame configuration, and the double sandwich II treatment used with the fully suppressed fan configuration.

The array measurements on the fully treated fan configuration have shown that the fan exhaust radiated noise, that is, duct noise, fan jet and core cowl scrubbing noise, dominates the spectra and consequently prevents the measurement of the full turbine treatment effect in farfield data. This problem is even greater for the Cerafelt turbine treatment configuration in which the fan was not fully suppressed. The probe data for the Cerafelt treatment showed turbine tone power level suppression of at least 11.5 dB. The array and farfield suppression value at the maximum aft angle is considerably less than this value. The array shows the first stage tone to be suppressed by 6.5 dB and the farfield data show fourth stage tone suppression in excess of 4 dB. However, the true pure tone sound pressure level suppression values cannot be determined due to frequency modulation. Broadband suppression of 0-3 dB is observed with the array and with farfield measurements. These values however are limited by other engine sources. The probe data in the Cerafelt configuration show an increase in broadband sound power level over the treatment

Table XIII. Measured Cerafelt Turbine Treatment Suppression on Fan Frame Treated Engine A at Approach (ΔPNL = 1 PNdB).

PURETONES

STAGE	FREQUENCY (KHz)	PROBE (ΔPWL, dB)	DIRECTIONAL ARRAY (ΔSPL, dB @ Max Aft Angle)	FARFIELD (ΔSPL, dB @ Max Aft Angle)
4	4.1	8.5	4.0	>4.0
3	4.6	>11.5	-	-
2	5.1	>11.0	-	-
1	6.1	11.5	6.5	2.0

BROADBAND NOISE

1/3 Octave Band	PROBE (ΔPWL, dB)	DIRECTIONAL ARRAY (ΔSPL, dB @ Max Aft Angle)	FARFIELD (ΔSPL, dB @ Max Aft Angle)
3150	-4.0	0	0.5
4000	-4.0	1.0	1.0
5000	-2.5	1.5	1.0
6300	-5.0	1.0	3.0
8000	-11.5	-	0

Table XIV. Measured Double Sandwich II (2DOF) Turbine Treatment Suppression on Fully Suppressed Engine A at Approach (ΔPNL = 0.5 PNdB).

PURETONES

STAGE	FREQUENCY (KHz)	PROBE (ΔPWL, dB)	DIRECTIONAL ARRAY (ΔSPL, dB @ Max Aft Angle)	FARFIELD (ΔSPL, dB @ Max Aft Angle)
4	4.1	16.5	12	>10
3	4.6	12.5	-	>4
2	5.1	13.5	-	-
1	6.1	6.0	2.5	0

BROADBAND NOISE

1/3 Octave Band	PROBE (ΔPWL, dB)	DIRECTIONAL ARRAY (ΔSPL, dB @ Max Aft Angle)	FARFIELD (ΔSPL, dB @ Max Aft Angle)
3150	1.0	6.5	0.5
4000	2.0	4.0	2.0
5000	3.5	2.0	1.5
6300	3.0	-	1.0
8000	1.5	-	-0.5

length, which was believed to be due to a relatively poor panel assembly that produced sound. Only 1 PNdB suppression was observed due to the insertion of Cerafelt treatment relative to a hardwall configuration. But the perceived noise level was dominated by fan discharge noise in this configuration.

The double sandwich II treatment on engine A resulted in greater suppression than the Cerafelt treatment produced (as measured by the probes, array, and farfield microphones). Maximum suppression (16.5 dB) occurs at the fourth stage blade passing frequency as observed by the probes. The array shows 12 dB suppression at the maximum aft angle and the farfield data show suppression to be in excess of 10 dB. The farfield measurements were limited by a fan-radiated broadband noise floor. Broadband noise reduction is shown to be greatest from the array measurements where 6.5 dB suppression is observed. Probe broadband data are limited by a duct noise floor. Only 0.5 PNdB suppression is observed due to the installation of double sandwich II turbine treatment in the fully suppressed fan configuration. But the farfield measurements were still controlled by fan-radiated noise even though the fan is fully suppressed in this configuration.

2. Engine C, Measurements vs Predicted Suppression

Predictions of engine C sound pressure level and perceived noise level were first made based on fan C farfield data. Engine C was, however, subsequently run using the nominal nozzle and fan frame treatment at approach and takeoff. Both farfield data and turbine probe data were taken with a hardwall turbine and with SDOF No. 19 turbine treatment. These data were used in conjunction with predicted turbine noise, predicted turbine suppression, predicted jet noise, and measured fan C data to arrive at the engine noise components.

The predicted turbine treatment suppression at approach and takeoff power is shown in Figure 437. These predictions are based on the high temperature duct measurements.

An analytical turbine noise prediction procedure based on Smith and Benzakein was made. In light of engine data, however, the initial turbine noise prediction was modified. The fully suppressed fan with the untreated core resulted in a level at approach which was 2.2 PNdB greater than predicted while at takeoff it was 2.9 PNdB greater than predicted.

The originally predicted value of turbine noise sound pressure actually exceeded the farfield measurement for the engine and the probe measured power level, Figure 438. The predicted amplitude was therefore reduced by 2.5 dB at approach and by 2.0 dB at takeoff. In addition to the farfield data showing up this error in the turbine noise prediction, the probe data did not indicate the expected value of corrected transmission loss. For this reason the originally predicted values of turbine treatment suppression were reduced by 3.5 dB for frequencies less than or equal to 6.3 kHz before calculating the predicted engine PNL for the fully suppressed configurations.

The measured farfield suppression values were much less than the 7-9 dB SPL reduction observed in the maximum weighted frequency region from probe and array data. There is, therefore, a noise floor which is not connected with the turbine noise that limits the measured PNL suppression.

A comparison of the acoustic components of engine C is shown in Figures 439 and 440 at approach and takeoff power, respectively. The component levels are shown as they would exist at an angle of 120 degrees at a sideline distance of 61 meters (200 ft). At the approach speed, it is seen that the engine contained low frequency noise that was not present on the fan. This noise is grouped as part of the jet noise and includes both fan and core jet noise, combustor noise, and core duct generated noise produced by flow over irregular surfaces. The fan discharge noise becomes significant at frequencies above 200 Hz. The predicted turbine spectra which has been corrected as explained above is also shown. At takeoff power for the engine configurations consisting of treated fan frame and treated turbine, it is seen that, except at very low frequencies, the fan noise dominates the spectrum.

Future testing was to involve the addition of a low Mach number fan exhaust configuration containing a splitter in addition to both a hardwall and treated turbine. An investigation of the PNL of the components was performed as well as the predicted PNL for the engine in the planned configuration. This information is shown in Tables XV and XVI for approach and takeoff, respectively. At approach, the fully treated configuration is dominated by the turbine noise at high frequencies and the jet noise at low frequencies. The predicted PNL (fully suppressed) is 98.2 PNdB. A complete elimination of the turbine noise component would result in a predicted level of 94.6 PNdB. The engine C farfield data, however, did not attain the predicted values. A comparison of predicted and measured perceived noise levels at the maximum aft angle for approach and takeoff power is shown in Table XVII. It shows predicted PNL to be underestimated by 2 - 3 PNdB.

The application of turbine treatment to engine C results in much greater farfield suppression than observed on engine A. This is due to the lower fan noise of engine C and the higher power level of untreated turbine noise - a combination which permitted the turbine noise to contribute more strongly to the farfield levels.

A summary of the turbine treatment suppression as measured by four systems; probe, nearfield microphones, directional array, and farfield microphones, is presented in Table XVIII. Probe and directional array data show considerably more suppression at the first stage BPF than at the second. Near field data did not indicate the presence of turbine tones in either the treated or untreated turbine configurations. The second stage tone was not detectable in any farfield measurement, including the array, due to the presence of a noise hump centered at the blade passing frequency. The probe data show the first stage tone was suppressed on the order of 11 dB and the second stage tone on the order of 7 dB.

The directional array data show the maximum measure of broadband noise suppression due to the turbine treatment. Suppression at the maximum aft angle

Table XV. Engine C Predicted Perceived Noise Level at Approach Power (120°, 61 Meters (200 ft.) Sideline).

COMPONENT PNL		ENGINE PNL	
103.2	Treated Fan Frame	107.2	Fan Frame Treatment (Actual Data)
101.1	Untreated Turbine	105.5	Fan Frame + Turbine Treatment (Actual Data)
94.4	Treated Turbine	103.5	Fan Frame + LMES Treatment
92.7	Jet Noise	98.2	Fan Frame + LMES + Turbine Treatment
87.7	Treated Fan Frame + Low Mach Number Fan Exhaust Splitter	94.6	Super-Suppressed with Turbine Fully Suppressed

Table XVI. Engine C Predicted Perceived Noise Level at Takeoff Power (120°, 61 Meters (200 ft.) Sideline).

COMPONENT PNL		ENGINE PNL	
115.5	Treated Fan Frame	117.6	Fan Frame Treatment (Actual Data)
105.2	Treated Fan Frame + Low Mach Number Exhaust Splitter	116.6	Fan Frame + Turbine Treatment (Actual Data)
103.7	Untreated Turbine	110.3	Fan Frame + LMES Treatment
103.5	Jet Noise	108.5	Fan Frame + LMES + Turbine Treatment
97.6	Treated Turbine		

Table XVII. Comparison of Predicted and Measured PNL for Engine C at Max Aft Angle.

CONFIGURATION	APPROACH		TAKEOFF	
	PREDICTED	MEASURED	PREDICTED	MEASURED
Fan Frame Treatment	-	107.2*	-	117.6*
	-	106.7	-	117.4
Fan Frame, Treated Core	-	105.5*	-	116.6*
	-	106.6	-	117.3
Repeat Run	-	106.3	-	118.8
Fully Suppressed Fan, Untreated Core	103.5	105.7	110.3	113.2
Fully Suppressed Fan, Treated Core	98.2	101.5	108.5	110.7
Coplanar Nozzle, Treated Core	-	102.5	-	111.1

* B&K Data Reduction Value Used as a Base for Predictions

Table XVIII. Measured Turbine Treatment Suppression on Fully Suppressed Engine C at Approach (ΔPNL = 4.7 PNdB).

PURETONES

STAGE	FREQUENCY (KHz)	PROBE (ΔPWL, dB)	DIRECTIONAL ARRAY (ΔSPL, dB @ Max Aft Angle)	FARFIELD (ΔSPL, dB @ Max Aft Angle)
1	6.0	11.0	13	> 7
2	6.5	7.7	> 2	> 6

BROADBAND NOISE

1/3 O.B.	PROBE (ΔPWL, dB)	NEARFIELD (ΔSPL, dB)	DIRECTIONAL ARRAY (ΔSPL, dB @ Max Aft Angle)	FARFIELD (ΔSPL, dB @ Max Aft Angle)
3150	0.5	4.0	7.5	2.5
4000	3.5	5.5	10.0	8.5
5000	5.0	6.5	10.0	8.0
6300	6.0	7.5	8.5	6.5
8000	4.5	6.5	-	3.0

TABLE 17

MEASURED TURBINE TREATMENT SUPPRESSION ON FULLY SUPPRESSED QEP ENGINE C AT APPROACH (ΔPNL = 4.7 PNdB)

is 10 dB in both the 4.0 and 5.0 kHz 1/3-octave bands. These suppression values drop for farfield, near field, and probe data (in that order) as the data reach consecutively higher noise floors. Perceived noise level suppression at the maximum aft angle is 4.7 PNdB.

SECTION V

CONCLUSIONS

A methodology for the design of acoustic treatment and the prediction of noise suppression was developed for jet engine turbines, based on acoustic duct, impedance tests, and treated engine configuration test results. The design procedure as developed takes into consideration a series of configurations at temperatures and Mach numbers typical of the turbine region.

Both metallic and nonmetallic suppression meterials have been identified for turbine noise suppression applications. Several materials offer improved suppression capabilities, but their application is limited due to installation difficulties and excessive cost.

Affects of turbine noise suppression cannot be fully realized without substantial fan discharge noise suppression. This is evident from the data. Engine C, due to its high amplitude of unsuppressed turbine noise and relatively low amplitude of fan noise, permitted large values of farfield suppression to be measured. On the other hand engine A turbine treatment resulted in almost negligible farfield suppression due to the presence of a strong fan discharge radiated noise source and a relatively low amplitude untreated turbine noise spectra.

The turbine noise suppression values can be measured by several techniques. Pure tone suppression, however, can only be accurately measured by probes within the core nozzle since these tones are modulated in the mixing region and do not appear as tones in the near or farfield. Broadband suppression, however, cannot be measured by the probes due to probe self noise and duct flow noise floors. The most satisfactory measurement of broadband suppression utilizes a directional farfield system which effectively filters out some of the engine broadband sources. All farfield measurements (including directional devices) are influenced by several sources, making evaluation of even very efficient suppression configurations difficult.

Power level suppression on engine A, as measured by acoustic probes, was seen to range from 6 to 19.5 dB for the turbine tones. The power level suppression on engine C was seen to range from 7 to 11 dB for the two strongest turbine tones.

REFERENCES

1. Ingard, Uno and Ising, Hartnut, "Acoustic Nonlinearity of an Orifice," The Journal of the Acoustic Society of America, Feb. 1967.

2. Kazin, S.B., Smith, E.B., and Huber T.R., "A Linear Dynamical Acoustic Liner Model," Technical Memorandum No. 68-331 GE Class 2 (Can be obtained upon request from GE Evendale Technical Information Center).

3. Smith E.B., Benzakein M.J., and Radecki K.P., "Study and Tests to Reduce Compressor Sounds of Jet Aircraft," FAA Technical Report No. FAA DS-68-7.

4. Phillips, B., "Effects of High-Wave Amplitude and Mean Flow," NASA TM X-1582, February 15, 1968.

5. Olson, H.F., "Acoustical Engineering," D. Van Nostrand Company Inc., 1957.

6. Albers, V.M., "Underwater Acoustics Handbook," The Pennsylvania State University Press, University Park, Pennsylvania, 1965, pp. 189-190.

7. Dolph, C.L., "A Current Distribution of Broadside Arrays which Optimizes the Relationship Between Beam Width and Side-Lobe Level," Proceedings of the Institure of Radio Engineers, June, 1946, pp. 335-348; Dolph, C.L., "Discussion on 'A Current Distribution of Broadside Arrays...," Proceedings of the Institute of Radio Engineers, May 1947, p. 492; Krauss, J.D., Antennas, McGraw-Hill Book Co., New York, 1950; and Albers, V.M., "Underwater Acoustics Handbook," The Pennsylvania State University Press, University Park, Pennsylvania, 1965, pp. 188-199.

8. Rice, Edward J., "Attenuation of Sound in Soft Walled Circular Ducts" - NASA TM X 52442, Lewis Research Center, May 20-21, 1968.

9. Wirt, L.S., "Gas Turbine Exhaust Noise and its Attenuation," SAE Paper 1002B, International Automotive Engineering Congress, Detroit, Michigan, Jan. 11-15, 1965.

10. McMillan, P.W., Glass Ceramics, Academic Press, New York, 1964.

11. Kolom, A.L., and Ackley, J.M., "Soundwich - The Sound Attenuating Structure," 1969 Southern Metals Conference, ASM, Noise Abatement Symposium, Grand Bahamas, April, 1969.

12. Benzakein, M.J., Smith, E.B., "Turbine Noise Generation and Suppression," ASME Publication 73 WA/GT-7, November 11-15, 1973.

13. Military Handbook 23.

14. Sullins, R.T., "Manual for Structural Stability Analysis of Sandwich Plates and Shells," NASA Report CR1457, December 1969.

15. Ffowcs Williams, J.F., "The Acoustics of Turbulence Near Sound Absorbing Liners," J. Fluid Mech., Vol. 51, Part 4, February 1972.

16. Kazin, S.B., and Paas, J.E., "NASA/GE Quiet Engine "A" Acoustic Test Results," NASA CR121175, Lewis Research Center, 1973.

17. Hayden, R., "Bolt Beranek and Newman Report," NAS1-9559-14.

18. Kazin, S.B., and Paas, J.E., "NASA/GE Quiet Engine "C" Acoustic Test Results," NASA CR 121176 Lewis Research Center, 1973.

19. Cremer, Lothar. "Theorie der Luftschall - Dämpfung im Rechteckkanal mit Schluckender Wand und das sich Dabei ergebende höchste Dämpfungsmass," Akustische Beihefte, Acustica Vol. 3 Heft 2, 1953.

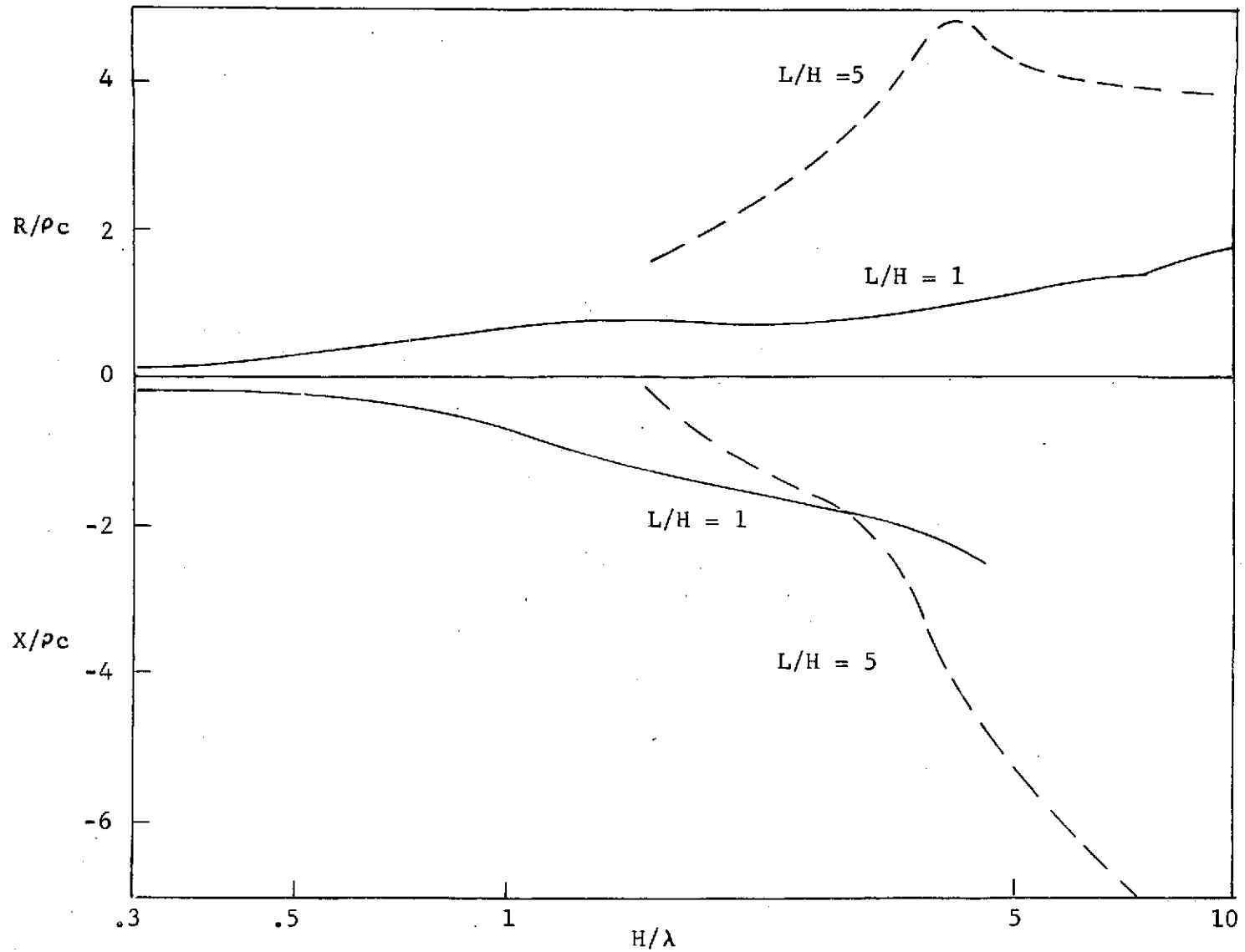

Figure 235. Wall Impedance for Maximum Duct Suppression (Curves from Rice).

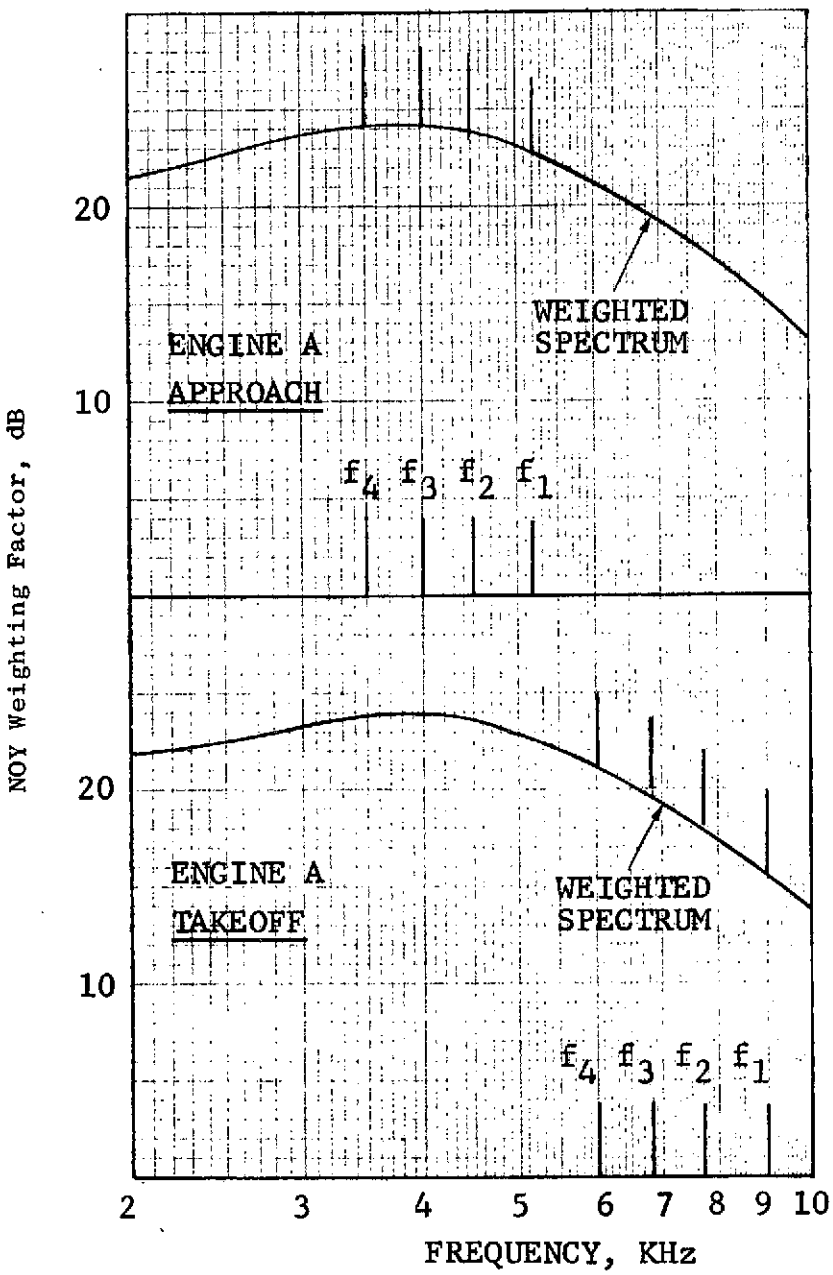

Figure 236. Predicted Turbine Noise Spectrum Shape for Treatment Tuning Requirements, Engine A.

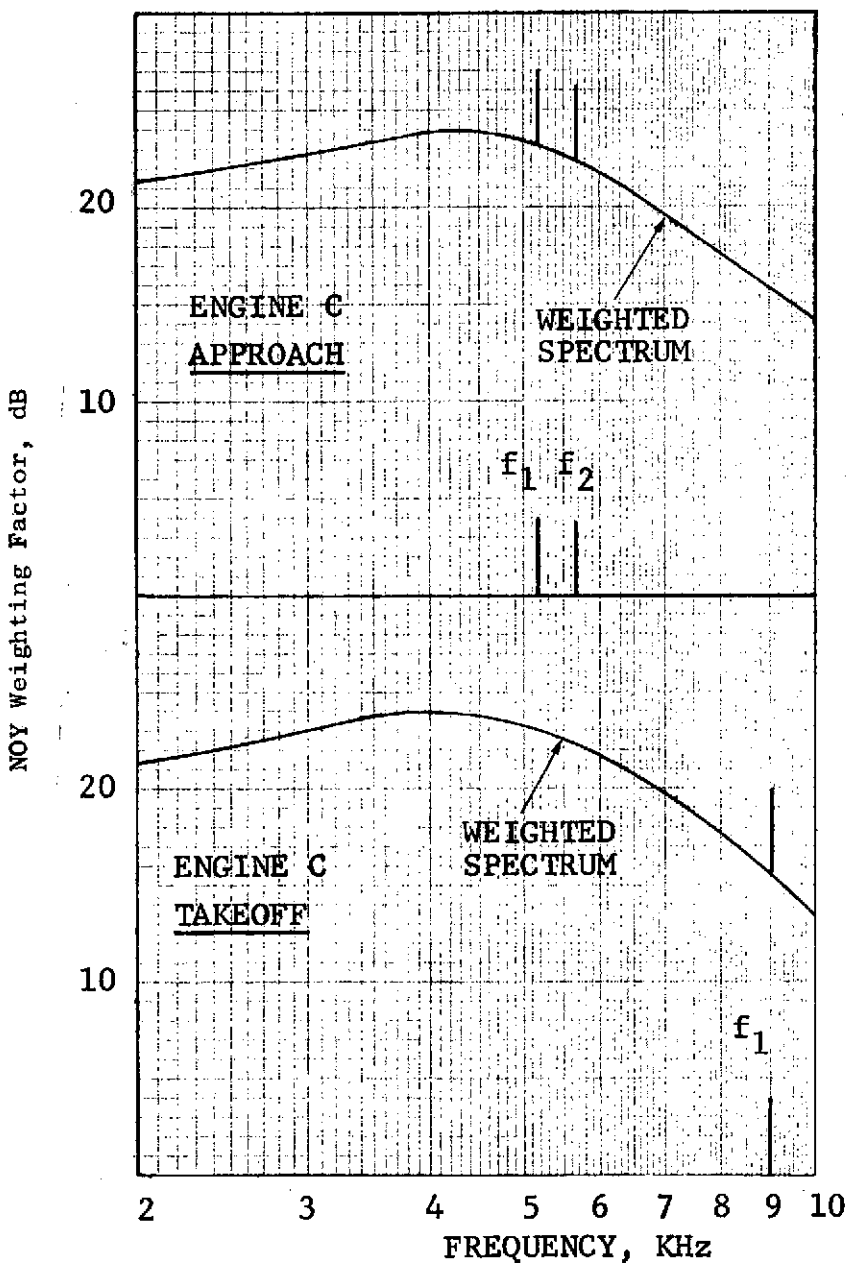

Figure 237. Predicted Turbine Noise Spectrum Shape for Treatment Tuning Requirements, Engine C.

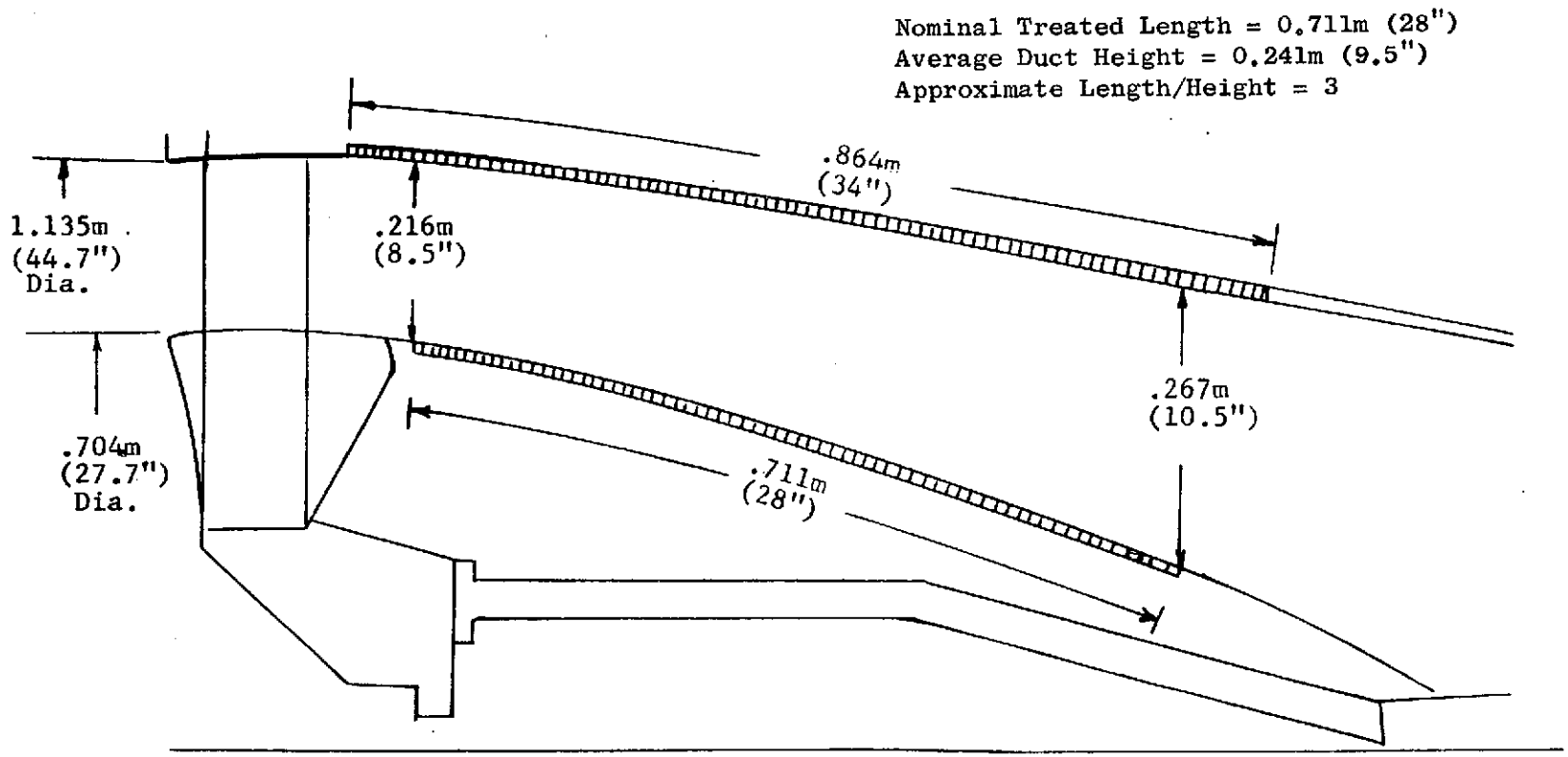

Figure 238. Engine A Acoustically Treated Exhaust Nozzle.

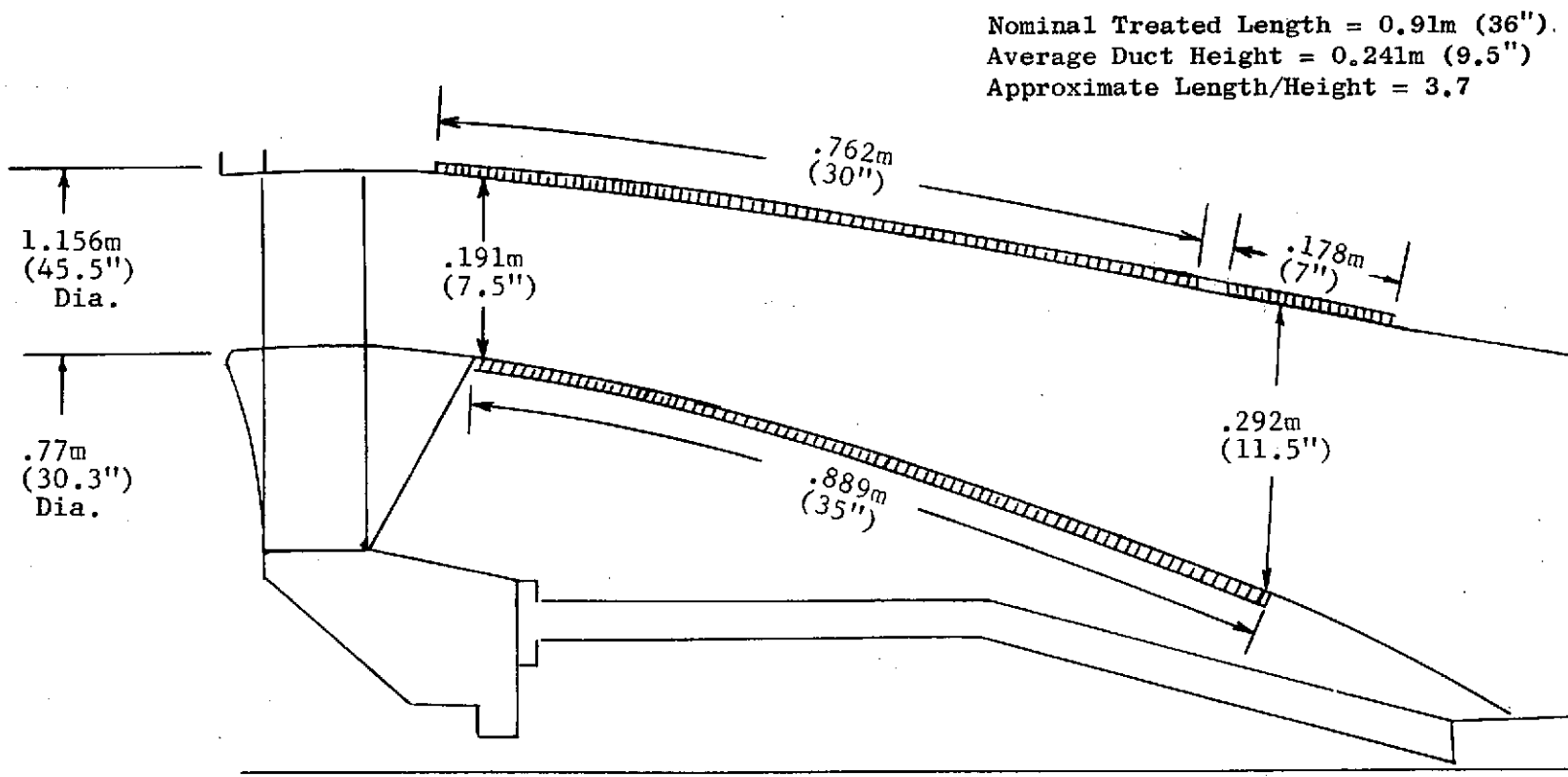

Figure 239. Engine C Acoustically Treated Exhaust Nozzle.

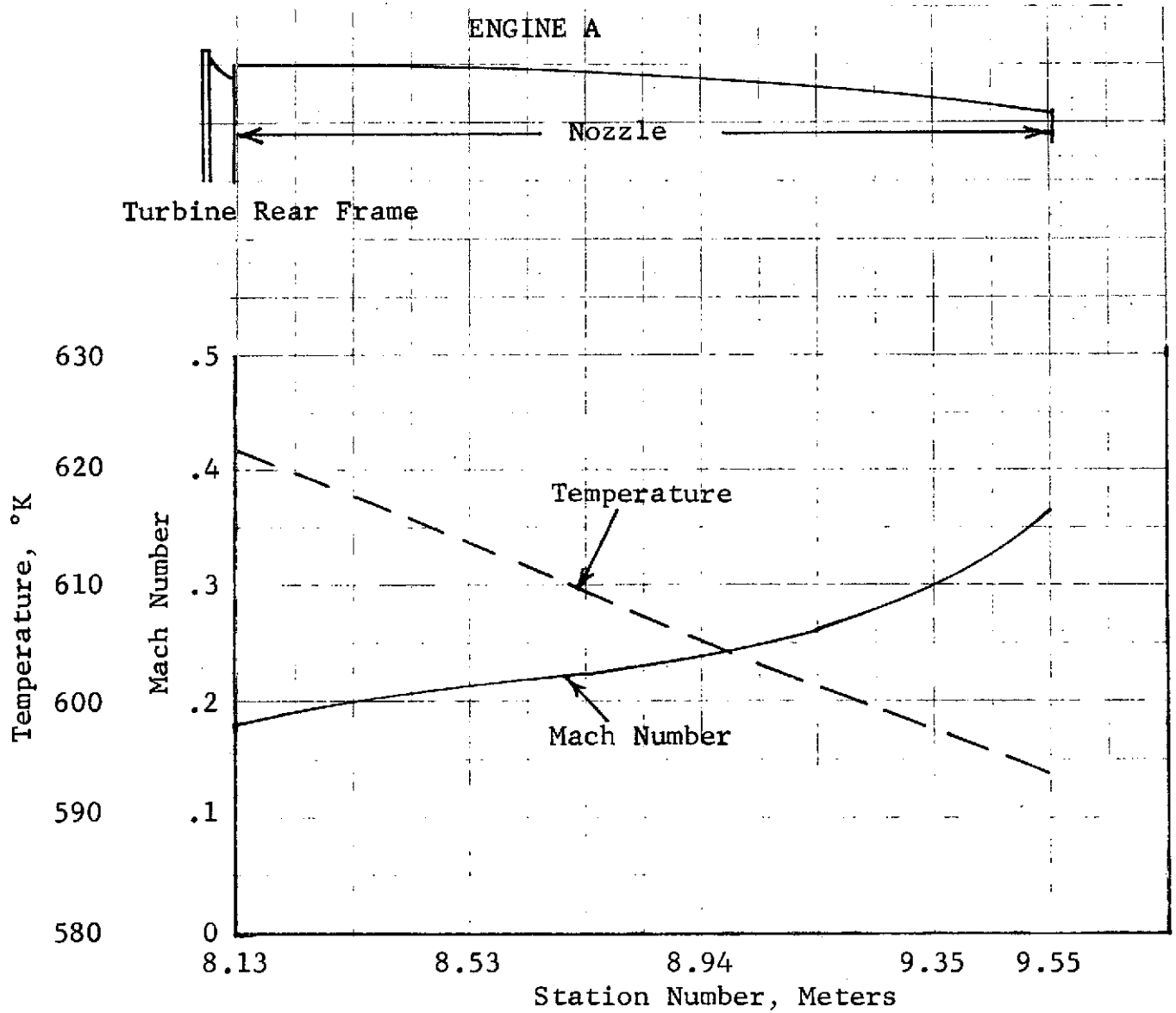

Figure 240. Predicted Engine A Turbine Exhaust Temperature and Mach Number Distributions.

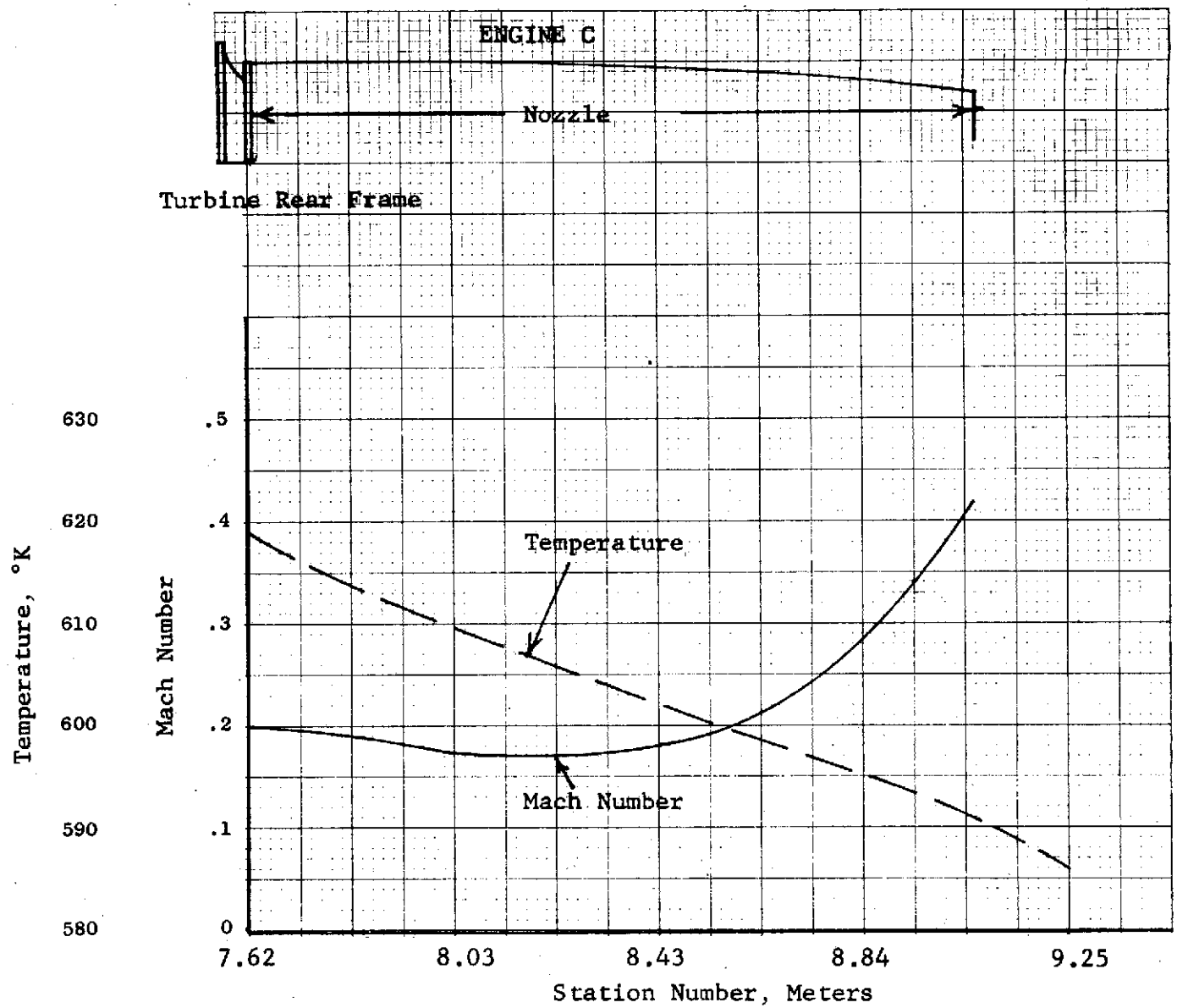

Figure 241. Predicted Engine C Turbine Exhaust Temperature and Mach Number Distributions.

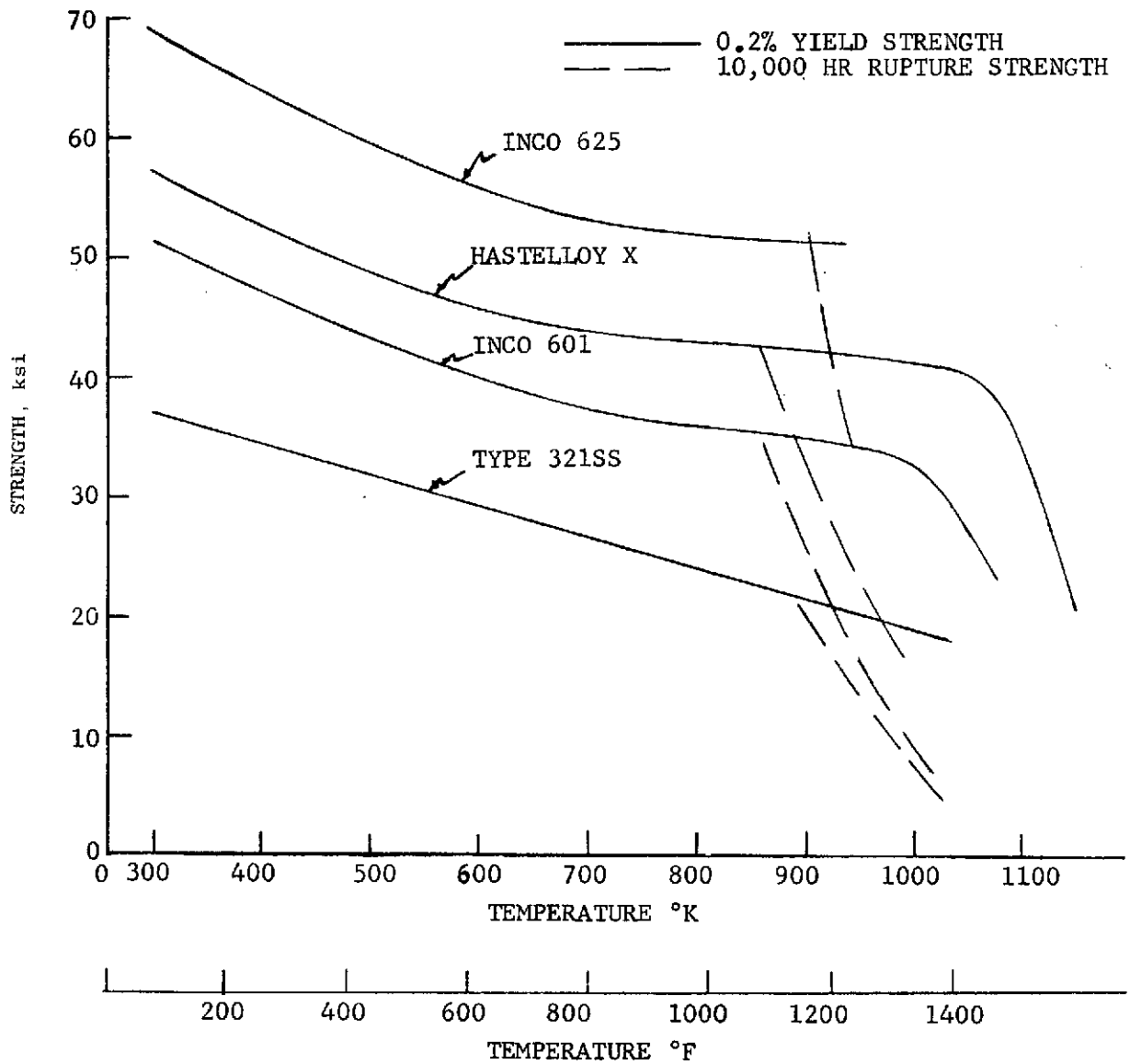

Figure 242. 0.2% Yield and 10,000 Hr Rupture Strengths Vs. Temperature for Possible Hot Exhaust Sound Structures.

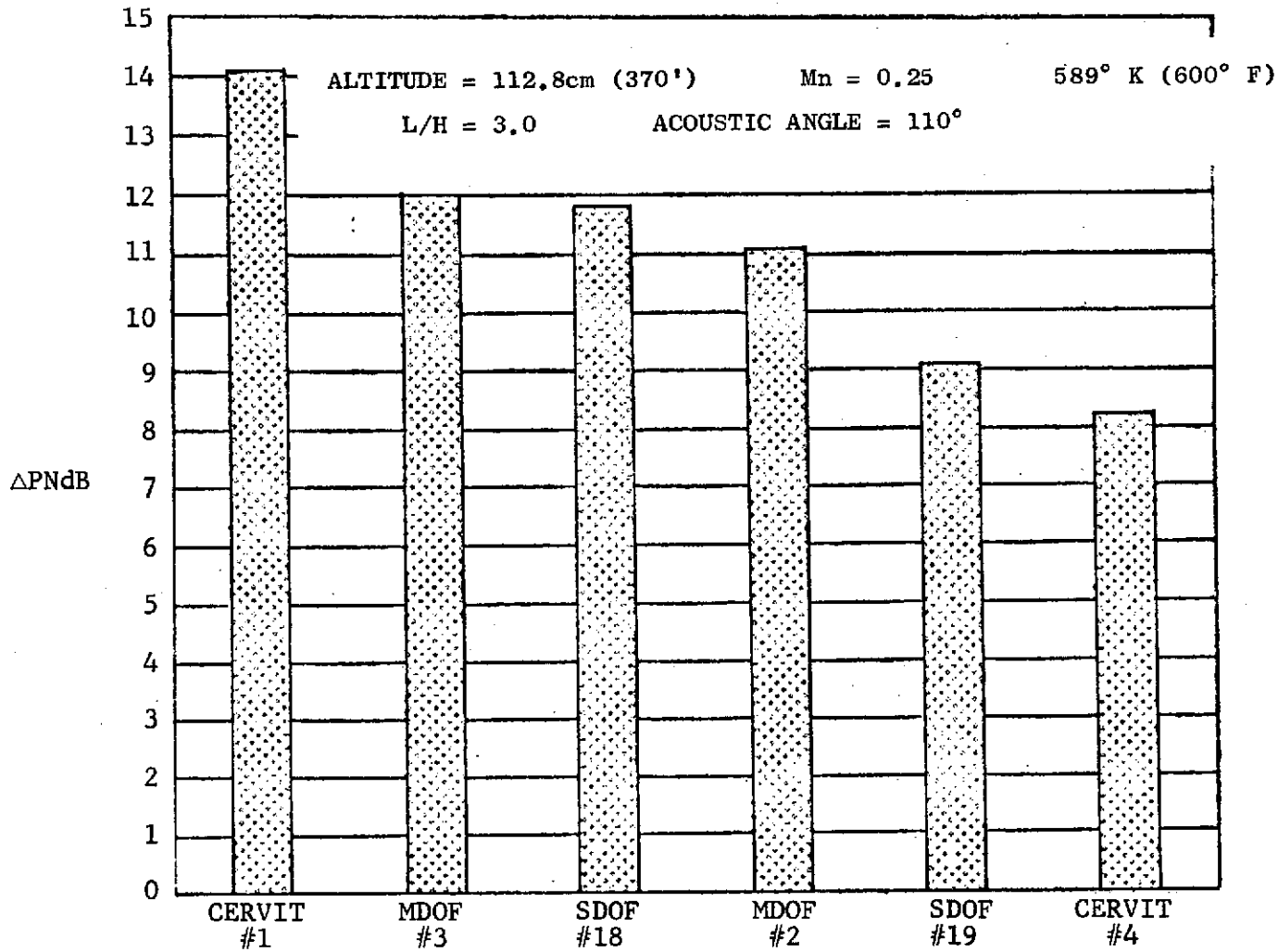

Figure 243. PNdB Suppression for Turbine Noise on Engine A.

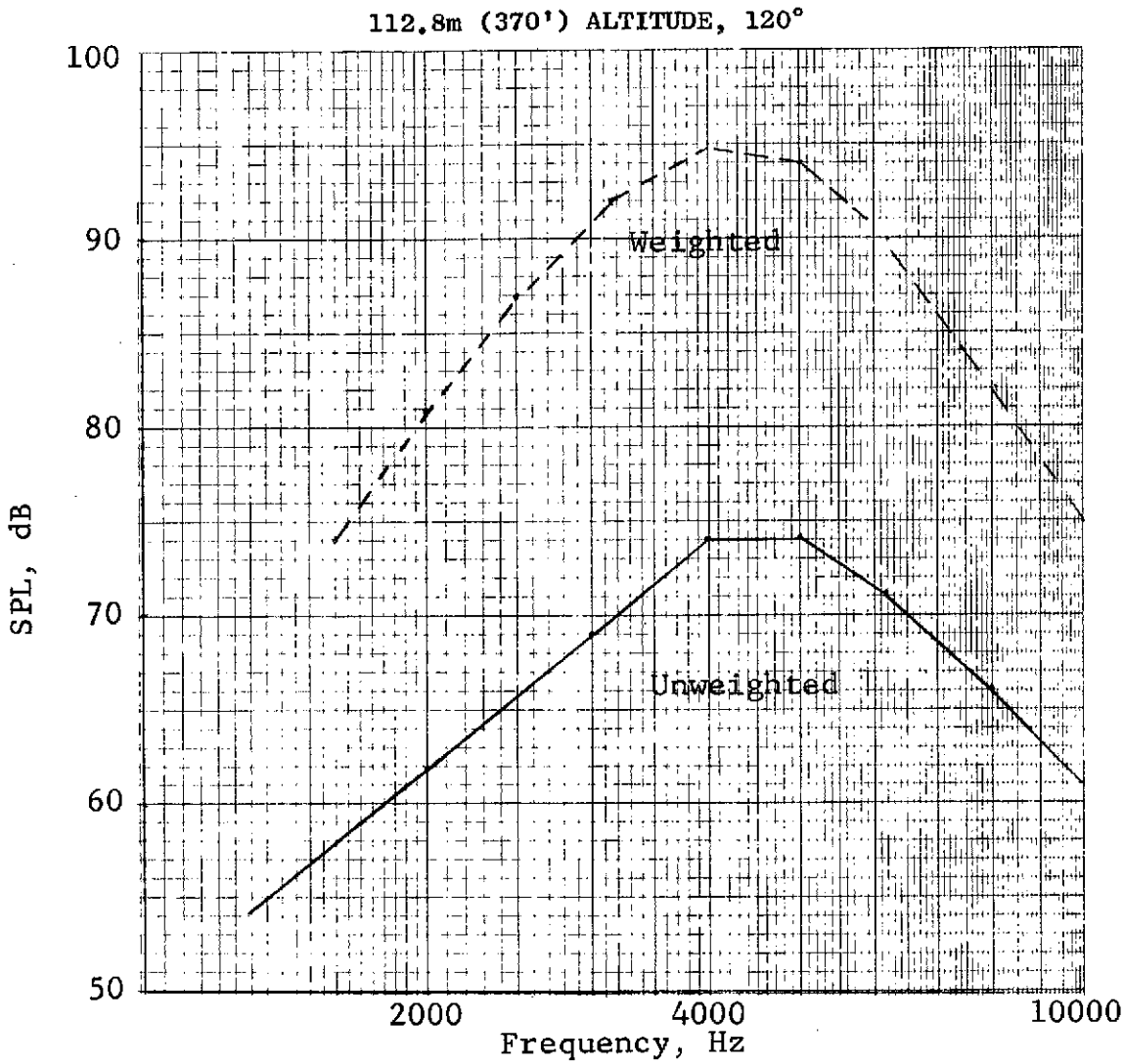

Figure 244. Engine A Predicted Turbine Noise Spectrum at Approach.

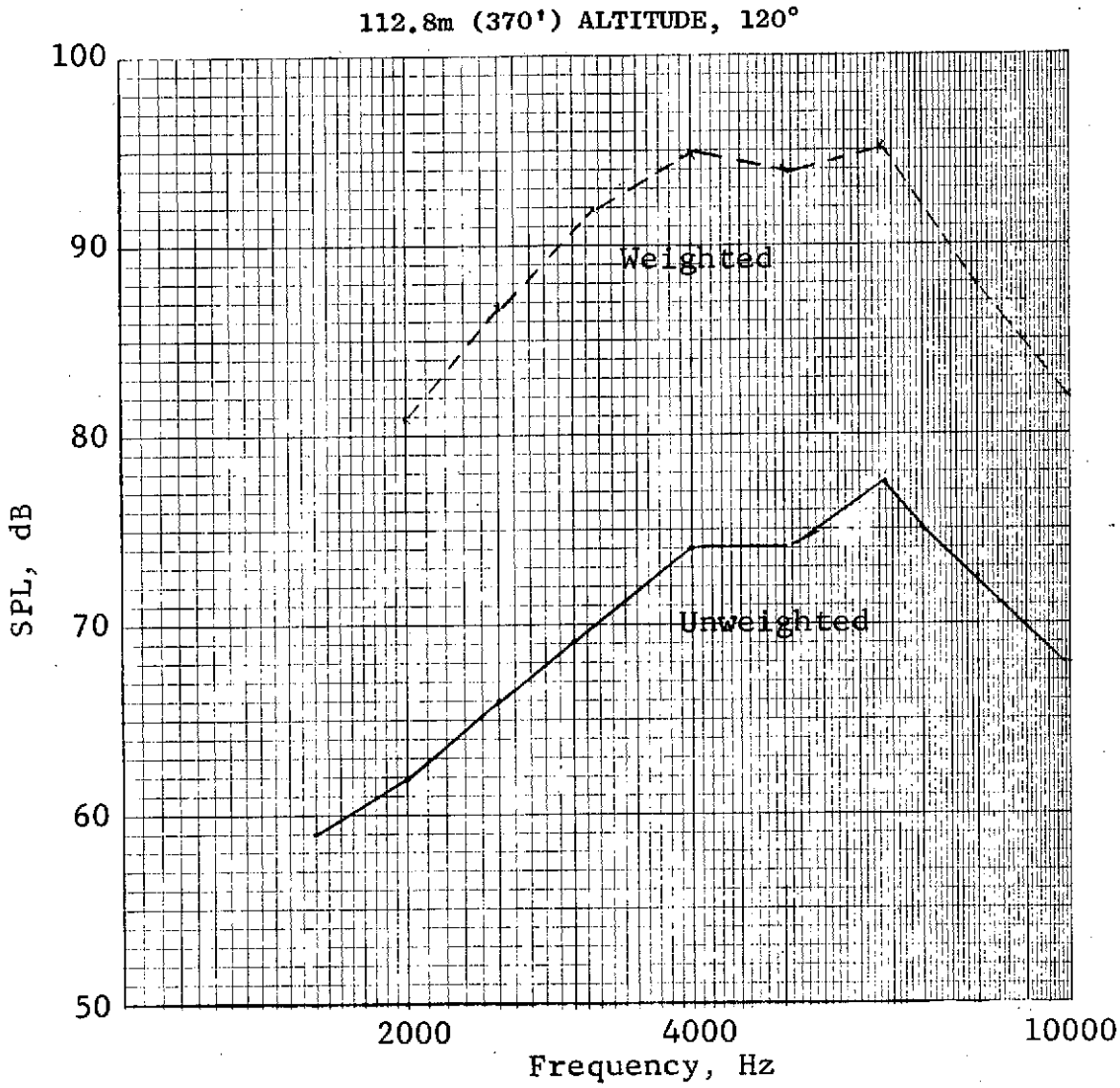

Figure 245. Engine A Predicted Turbine/Compressor Noise Spectrum at Approach.

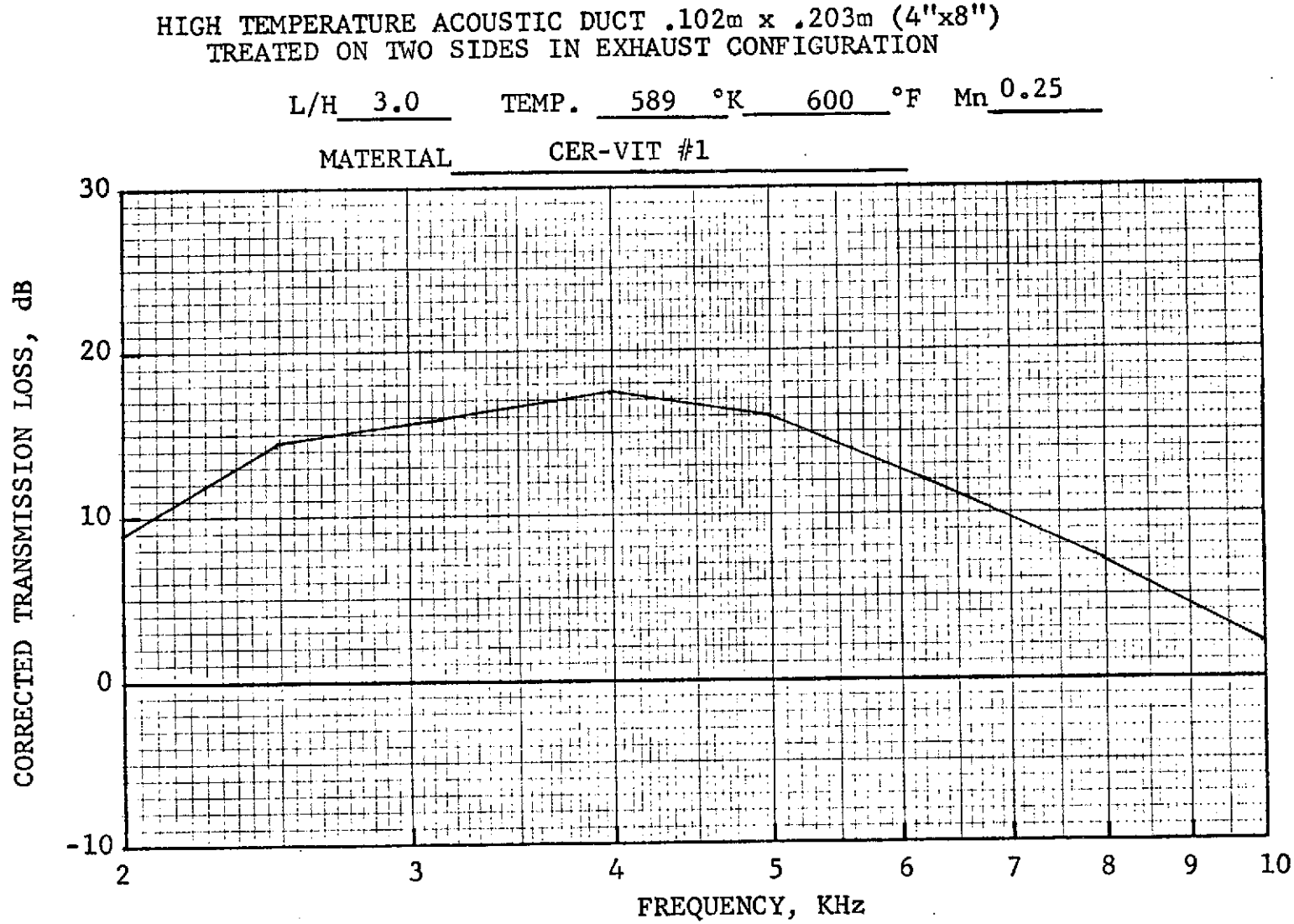

Figure 246. Corrected Transmission Loss Vs. Frequency for CER-VIT No. 1.

HIGH TEMPERATURE ACOUSTIC DUCT .102m x .203m (4"x8")
TREATED ON TWO SIDES IN EXHAUST CONFIGURATION

TEMP. 589 °K 600 °F Mn 0.25

MATERIAL MDOF III

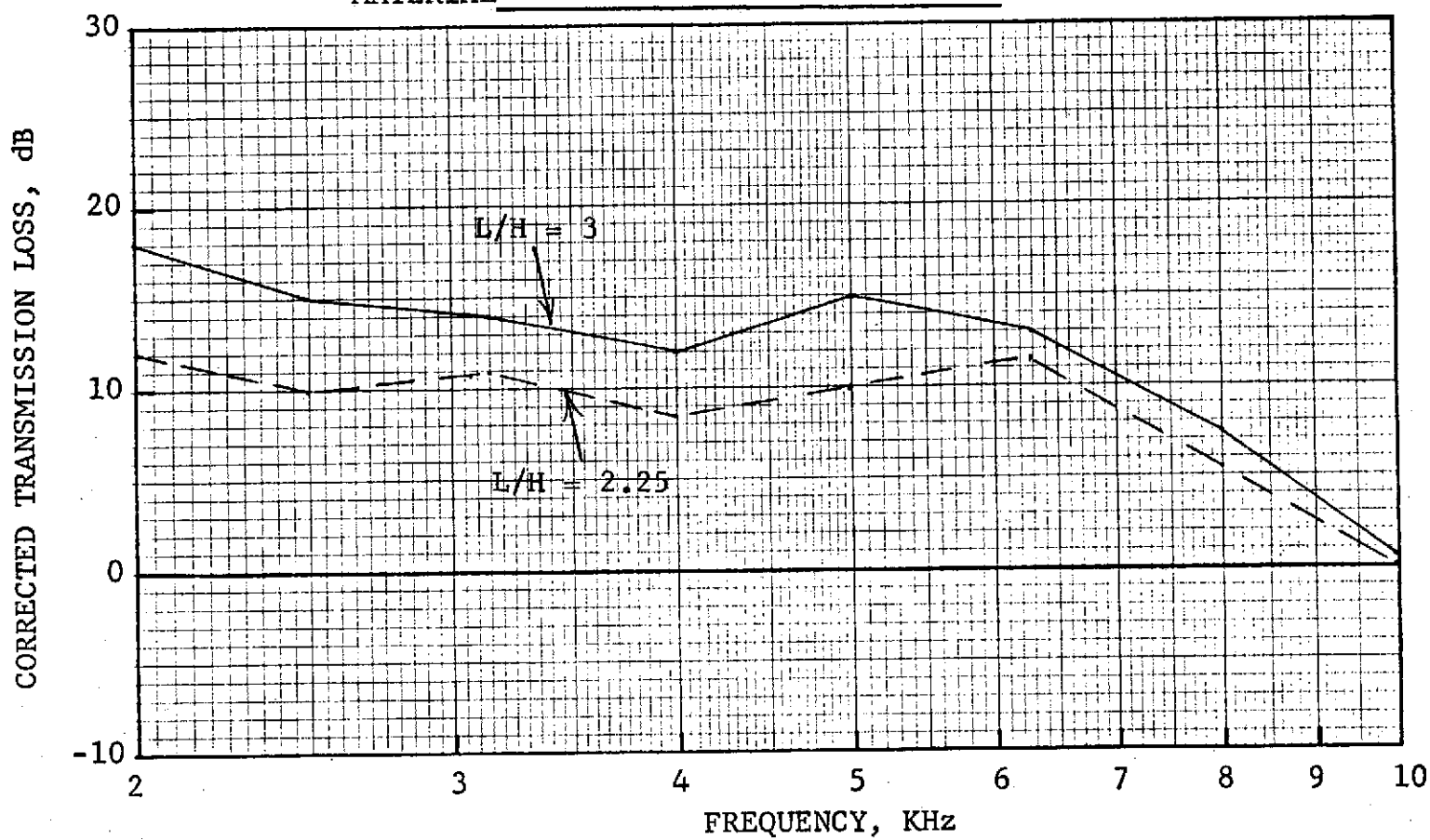

Figure 247. Corrected Transmission Loss Vs. Frequency for MDOF III.

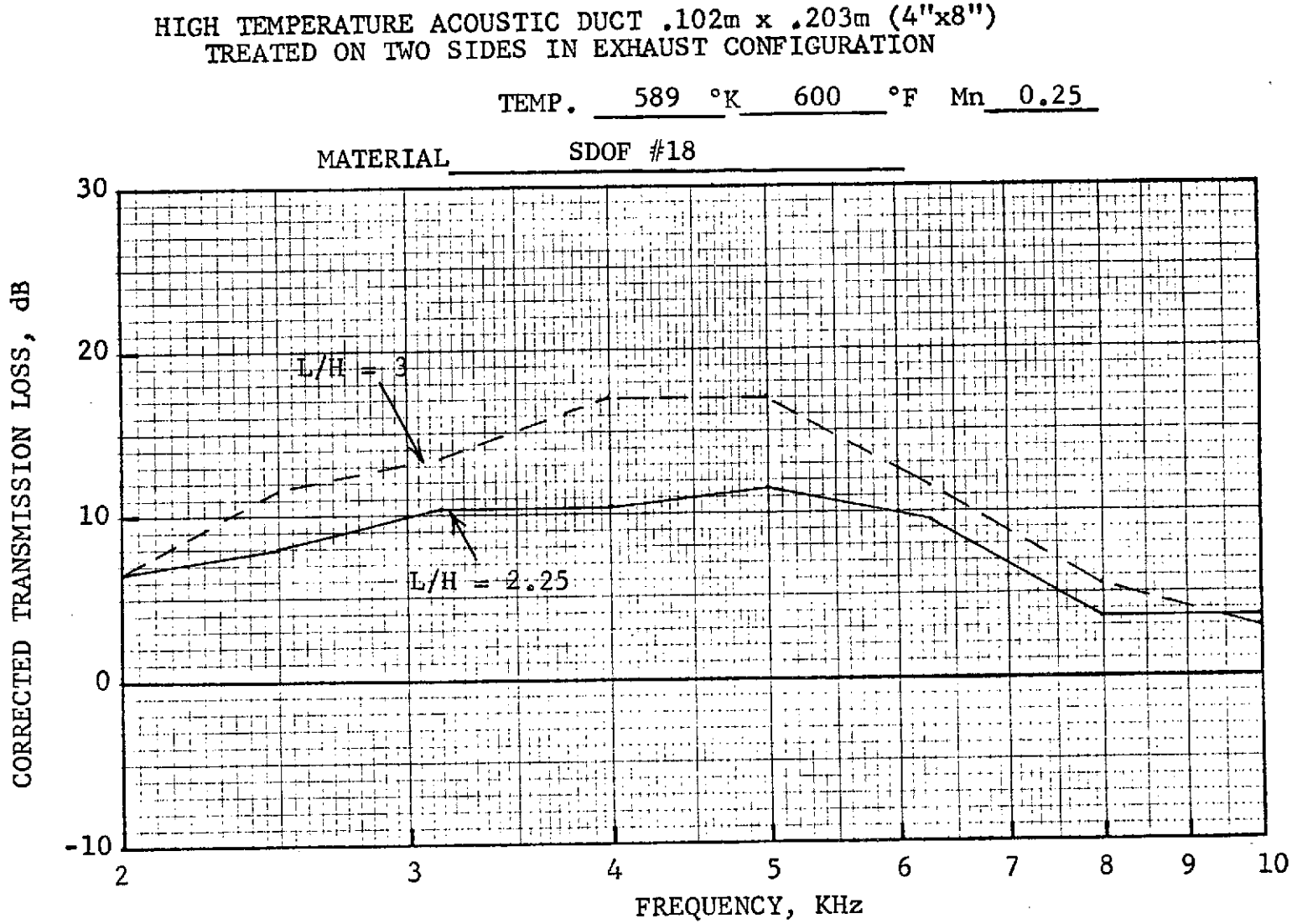

Figure 248. Corrected Transmission Loss Vs. Frequency for SDOF No. 18.

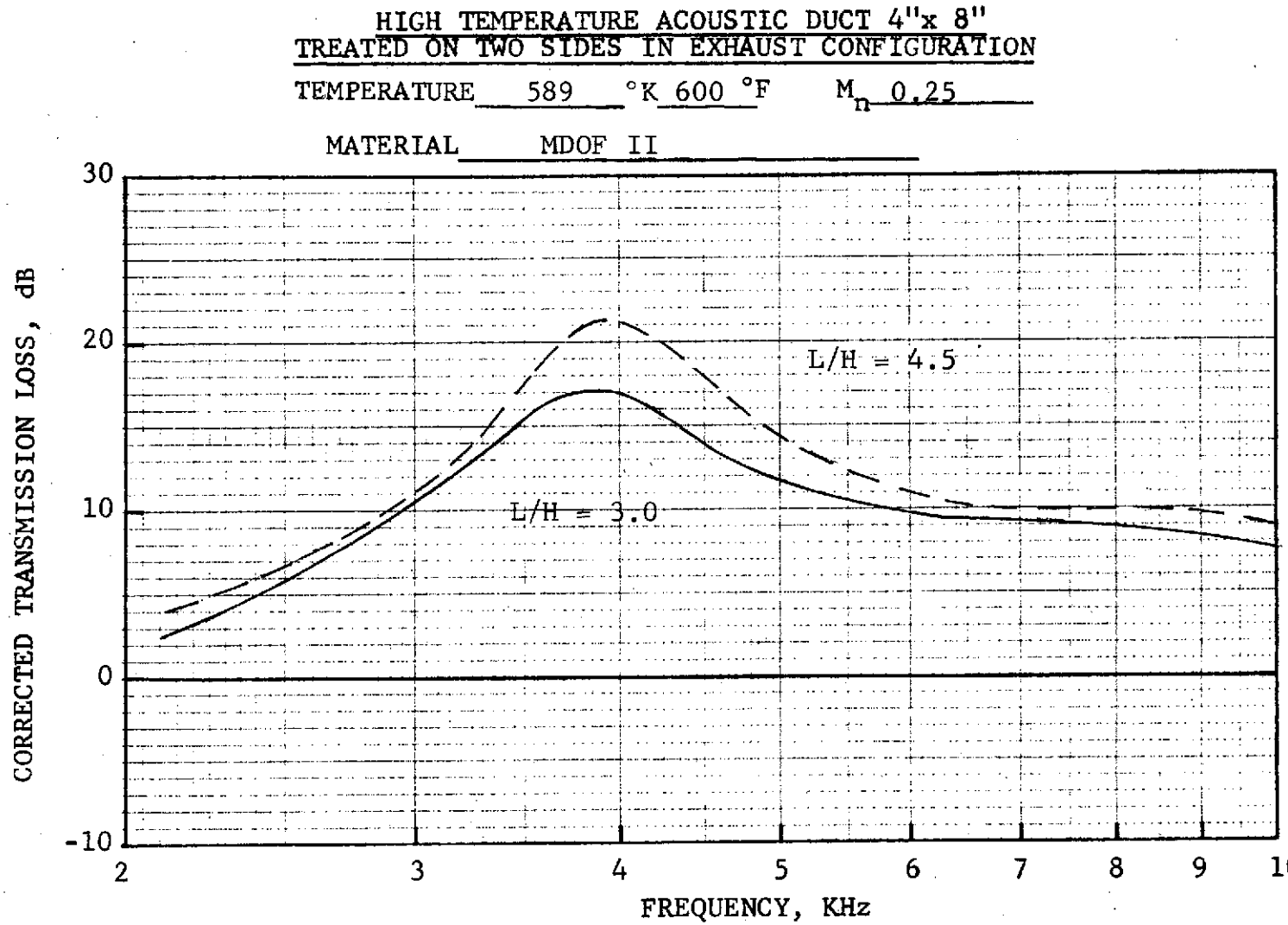

Figure 249. Corrected Transmission Loss Vs. Frequency for MDOF II.

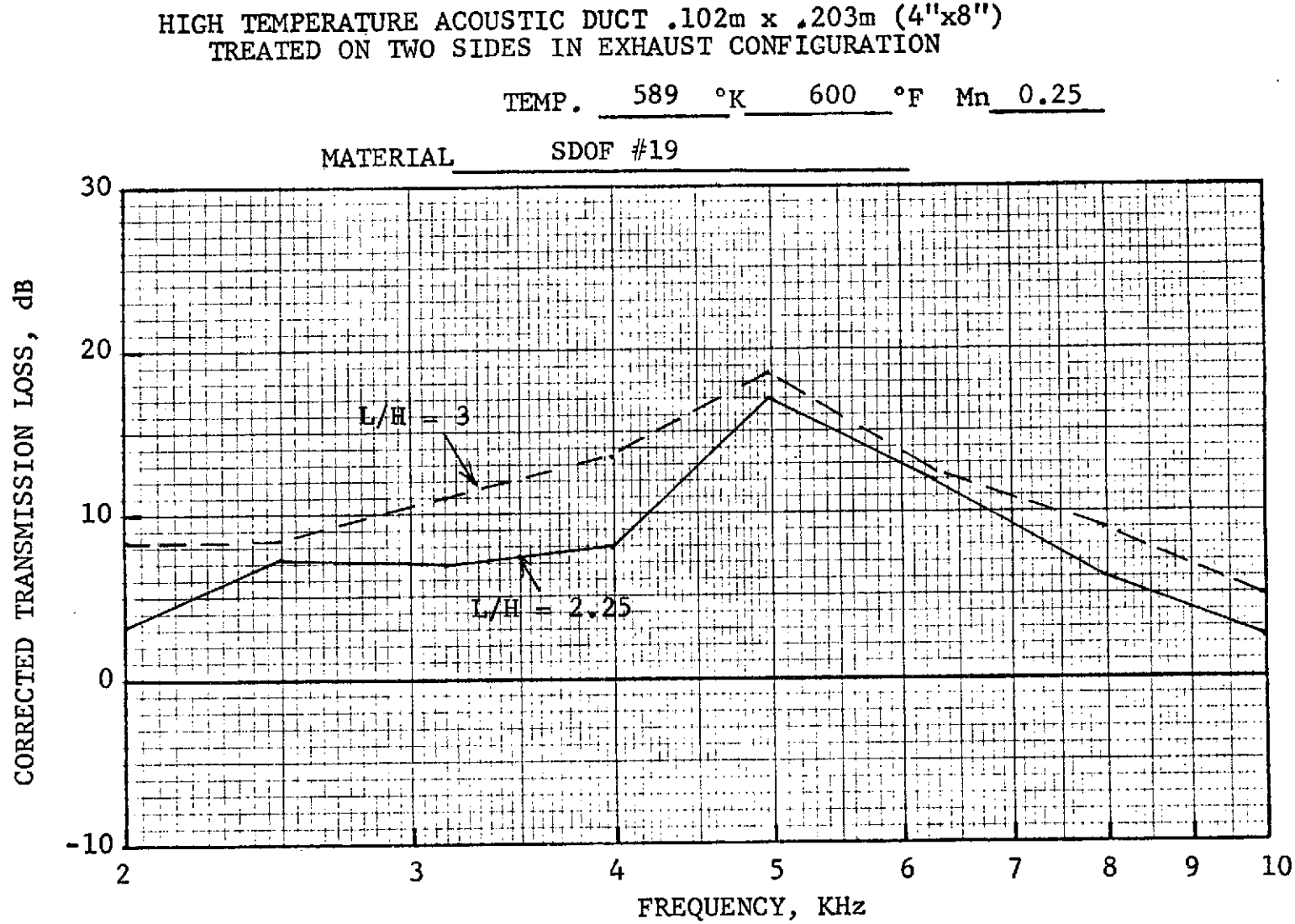

Figure 250. Corrected Transmission Loss Vs. Frequency for SDOF No. 19.

HIGH TEMPERATURE ACOUSTIC DUCT .102m x .203m (4"x8")
TREATED ON TWO SIDES IN EXHAUST CONFIGURATION

L/H 3.0 TEMP. 589 °K 600 °F Mn 0.3

MATERIAL CER-VIT #4

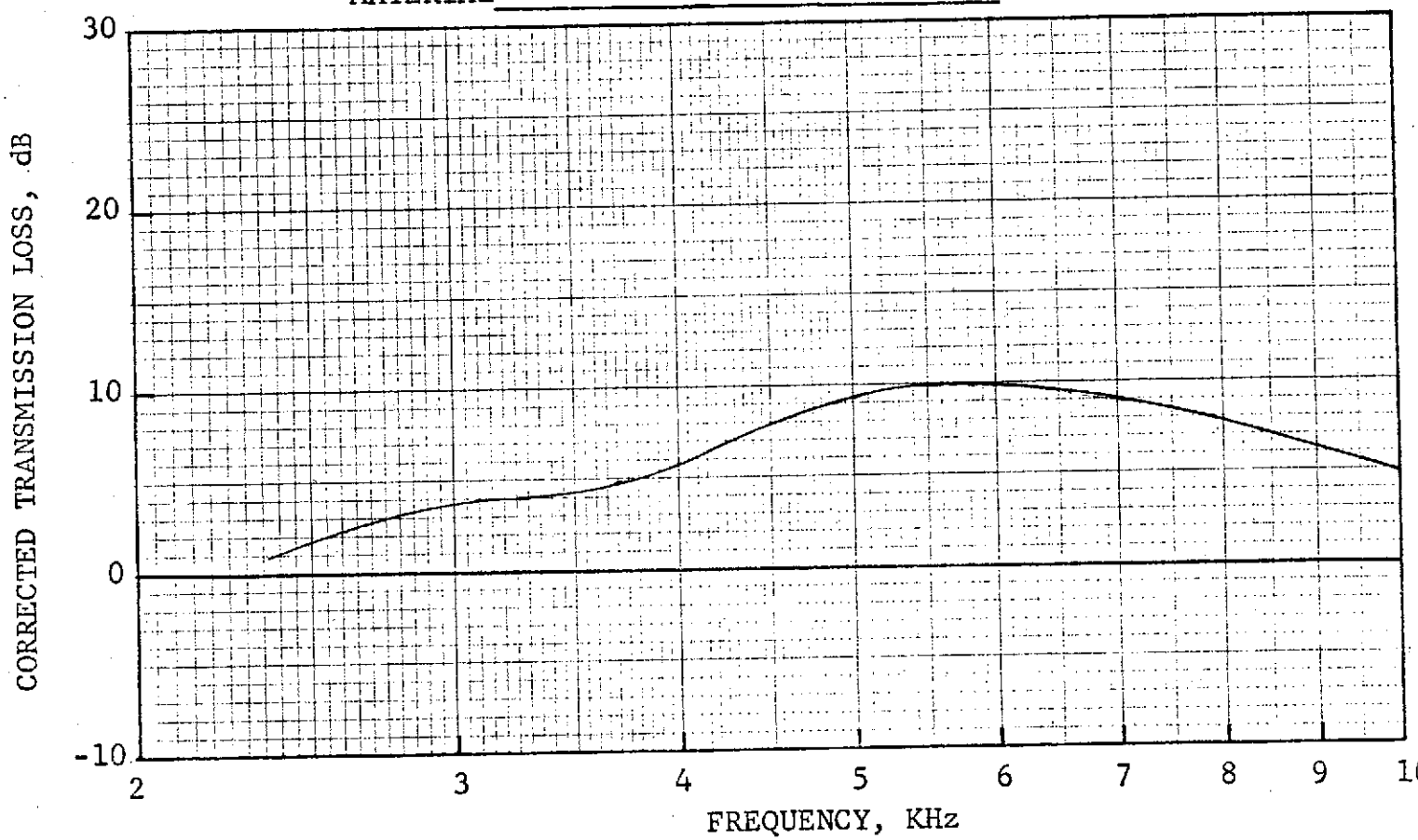

Figure 251. Corrected Transmission Loss Vs. Frequency for CER-VIT No. 4.

ALTITUDE = 112.8m (370') Mn = 0.25 589° K (600° F)

L/H = 3.0 ACOUSTIC ANGLE = 110°

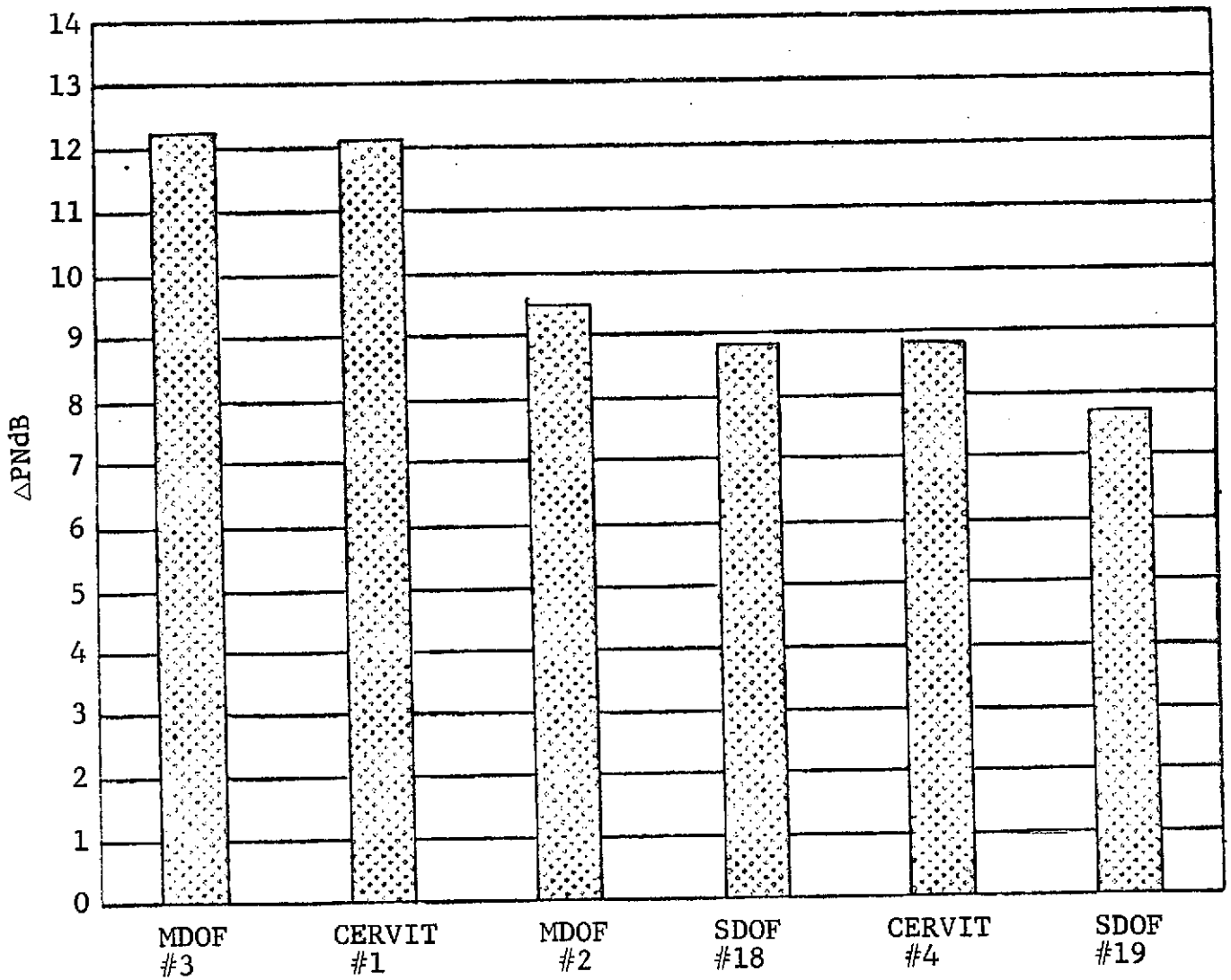

Figure 252. Perceived Noise Suppression for Turbine and Compressor Noise on Engine A.

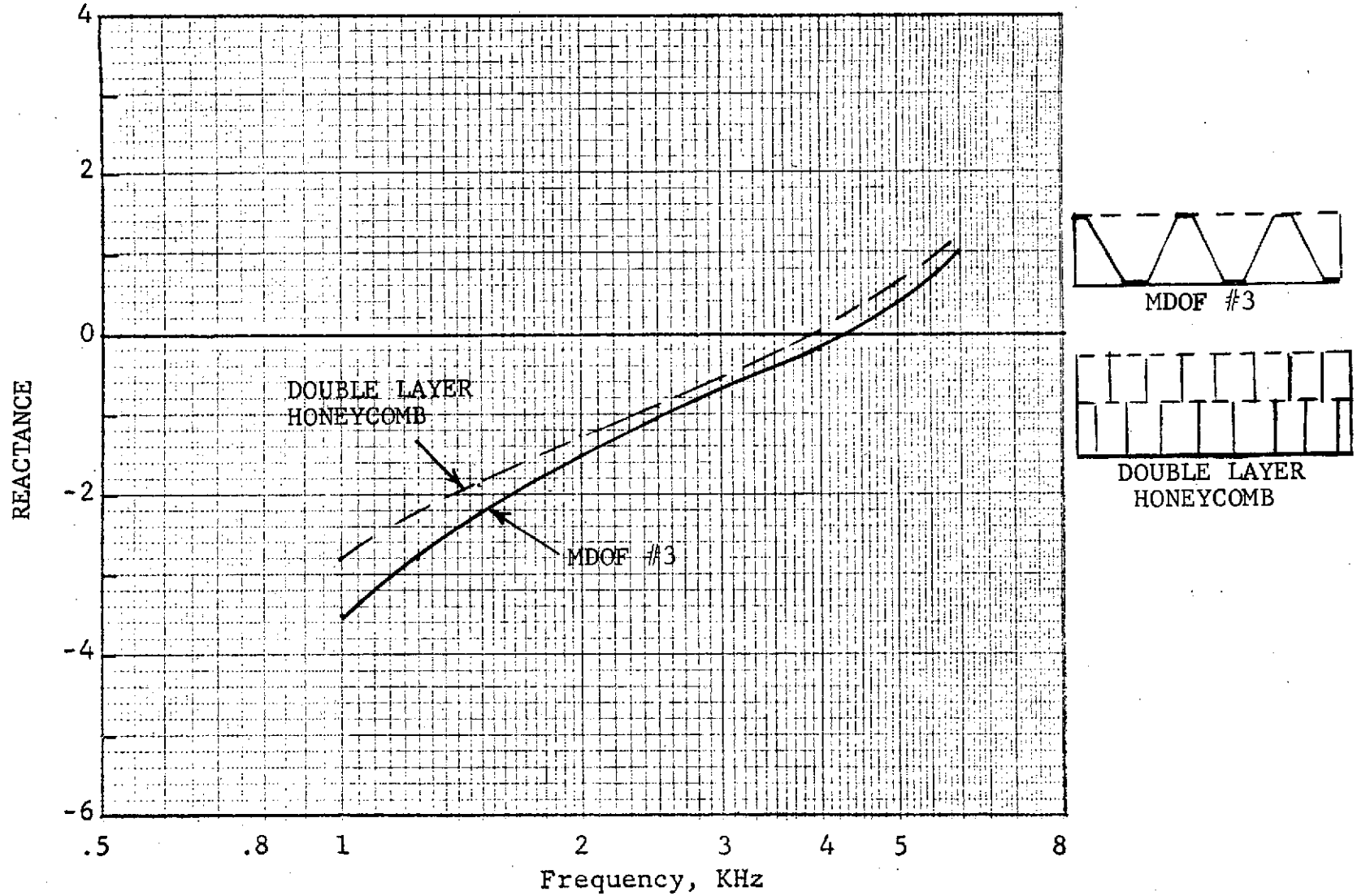

Figure 253. Predicted Reactance for Selected Engine A Turbine Treatment Configurations.

FACEPLATE:
EFFECTIVE OPEN AREA RATIO .07
THICKNESS .076cm (.030")
HOLE DIA. .159cm (.0625")

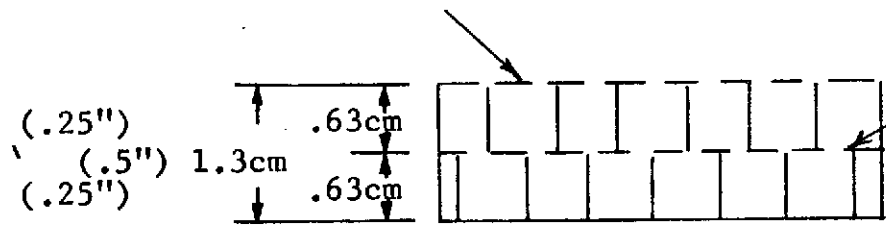

CORE PLATE:
EFFECTIVE OPEN AREA RATIO .04
THICKNESS .076cm (.030")
HOLE DIA. .159cm (.0625")

- BROADBAND SUPPRESSION
- REPRESENTS STATE-OF-ART IMPROVEMENT
- COMPATIBLE WITH ENGINE ENVIRONMENT

Figure 254. Recommended Treatment for Engine A, Double-Layered Honeycomb Sandwich.

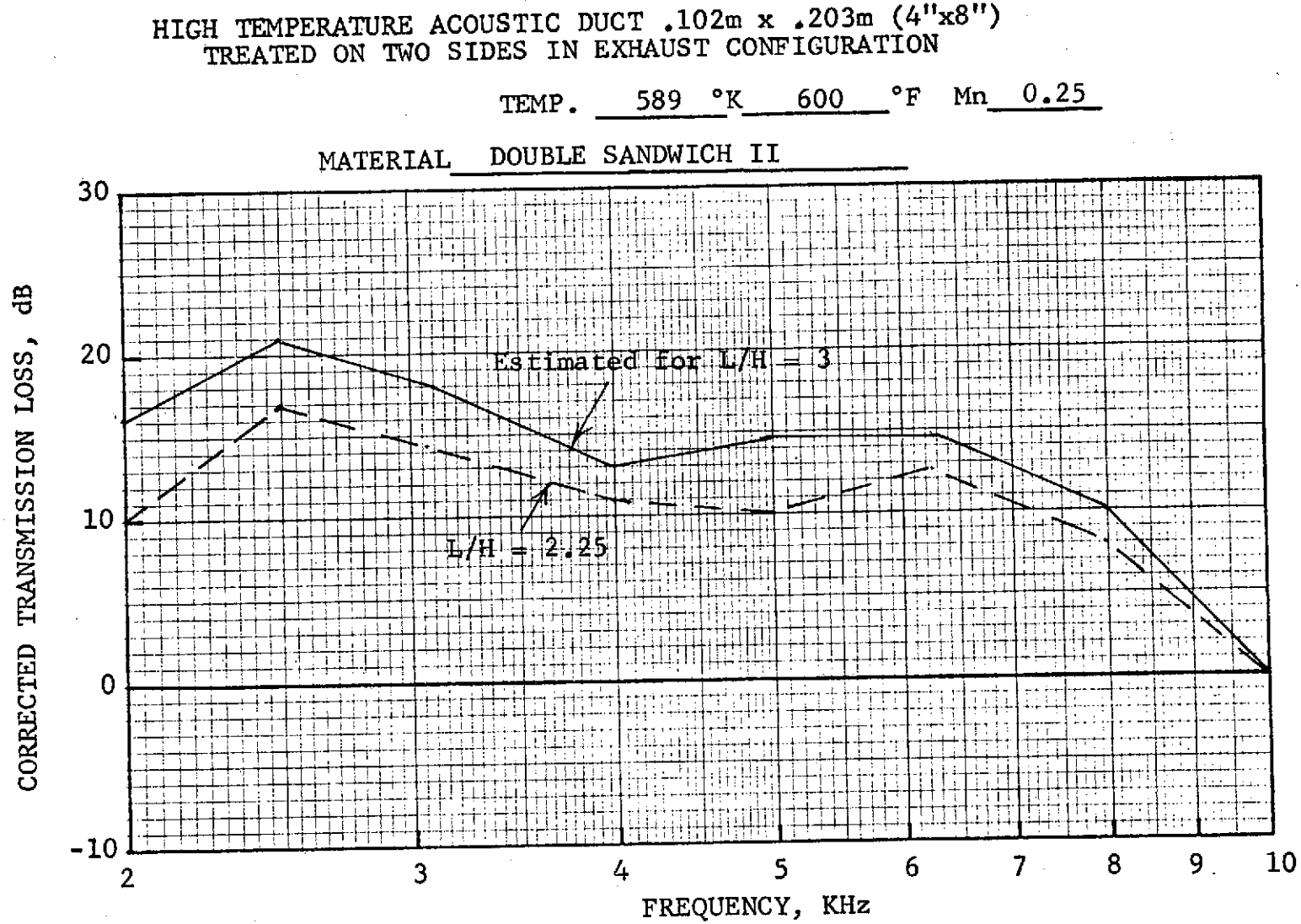

Figure 255. Corrected Transmission Loss Vs. Frequency for Double Sandwich II.

HIGH TEMPERATURE ACOUSTIC DUCT .102m x .203m (4"x8")
TREATED ON TWO SIDES IN EXHAUST CONFIGURATION

TEMP. 589 °K 600 °F Mn 0.25

MATERIAL MDOF I

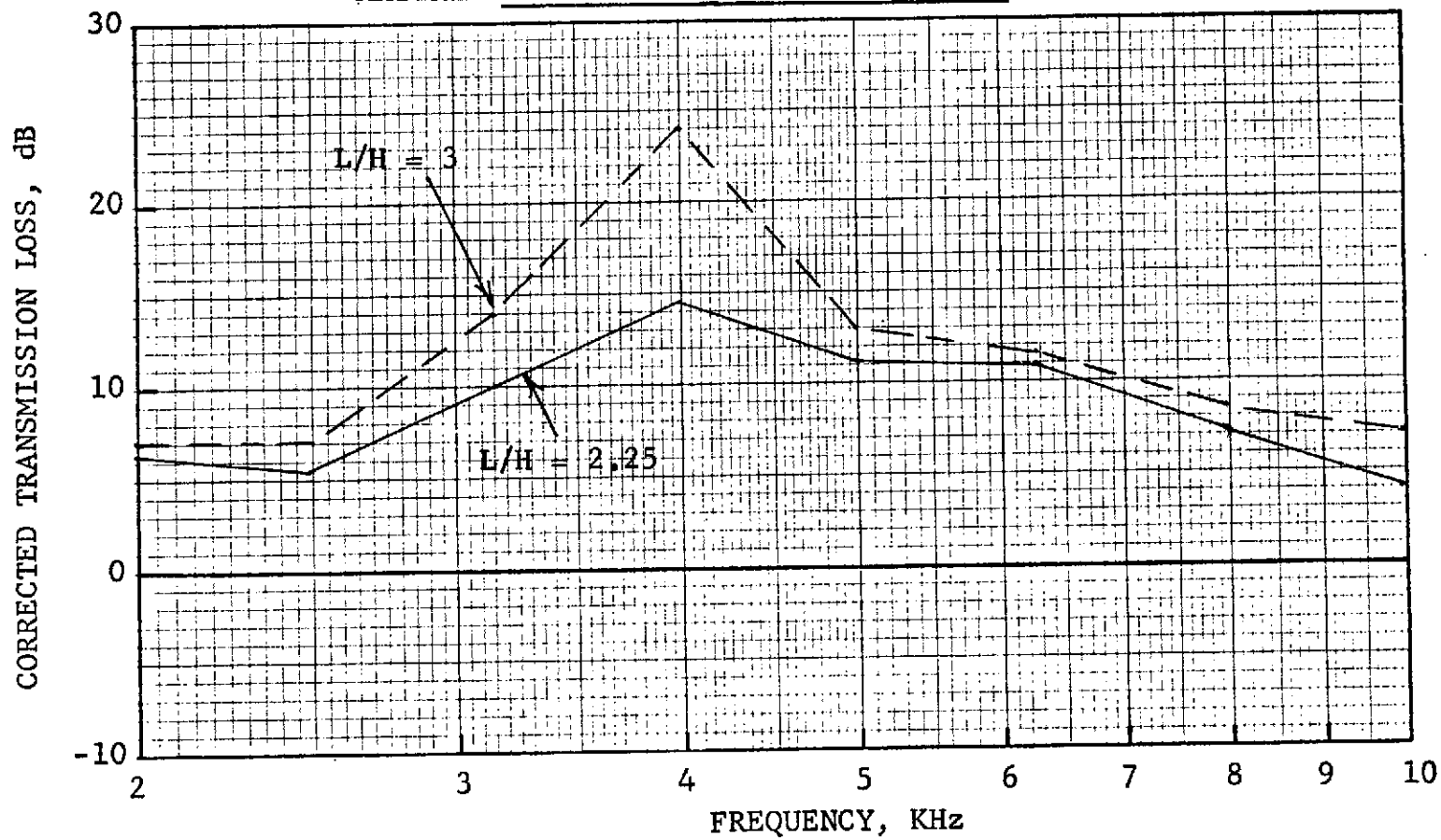

Figure 256. Corrected Transmission Loss Vs. Frequency for MDOF I.

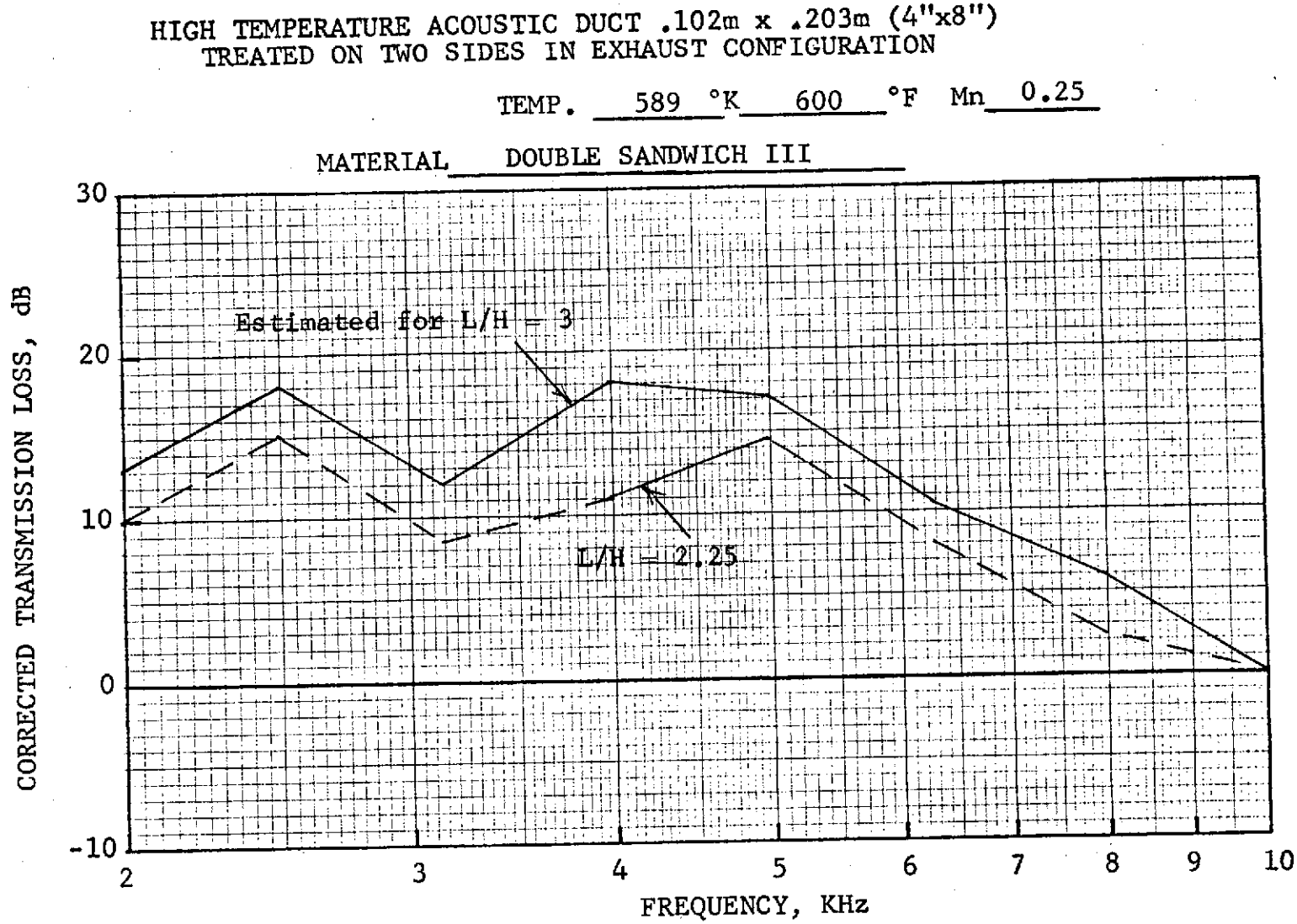

Figure 257. Corrected Transmission Loss Vs. Frequency for Double Sandwich III.

C-2

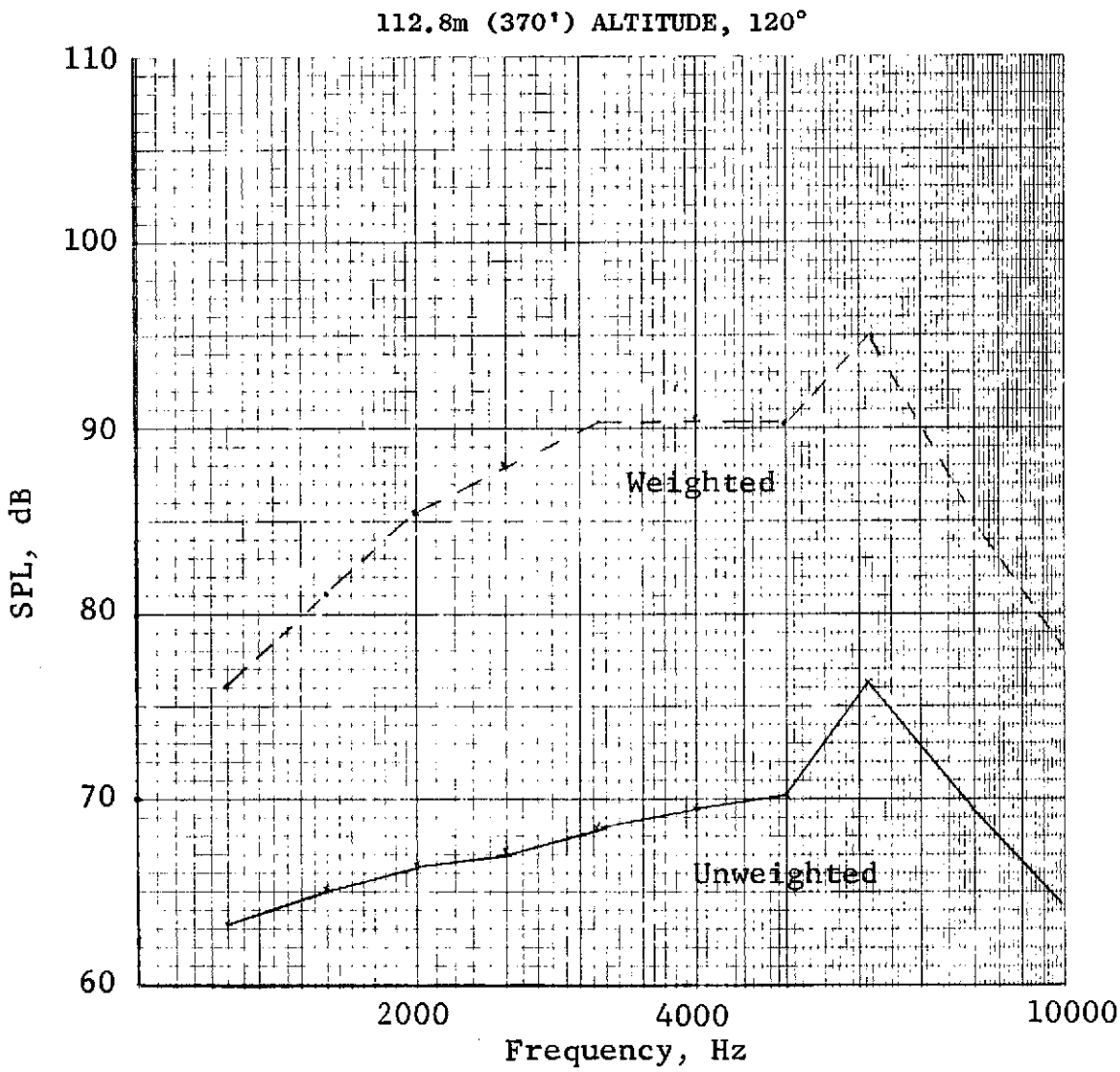

Figure 258. Engine C Predicted Turbine Spectrum at Approach.

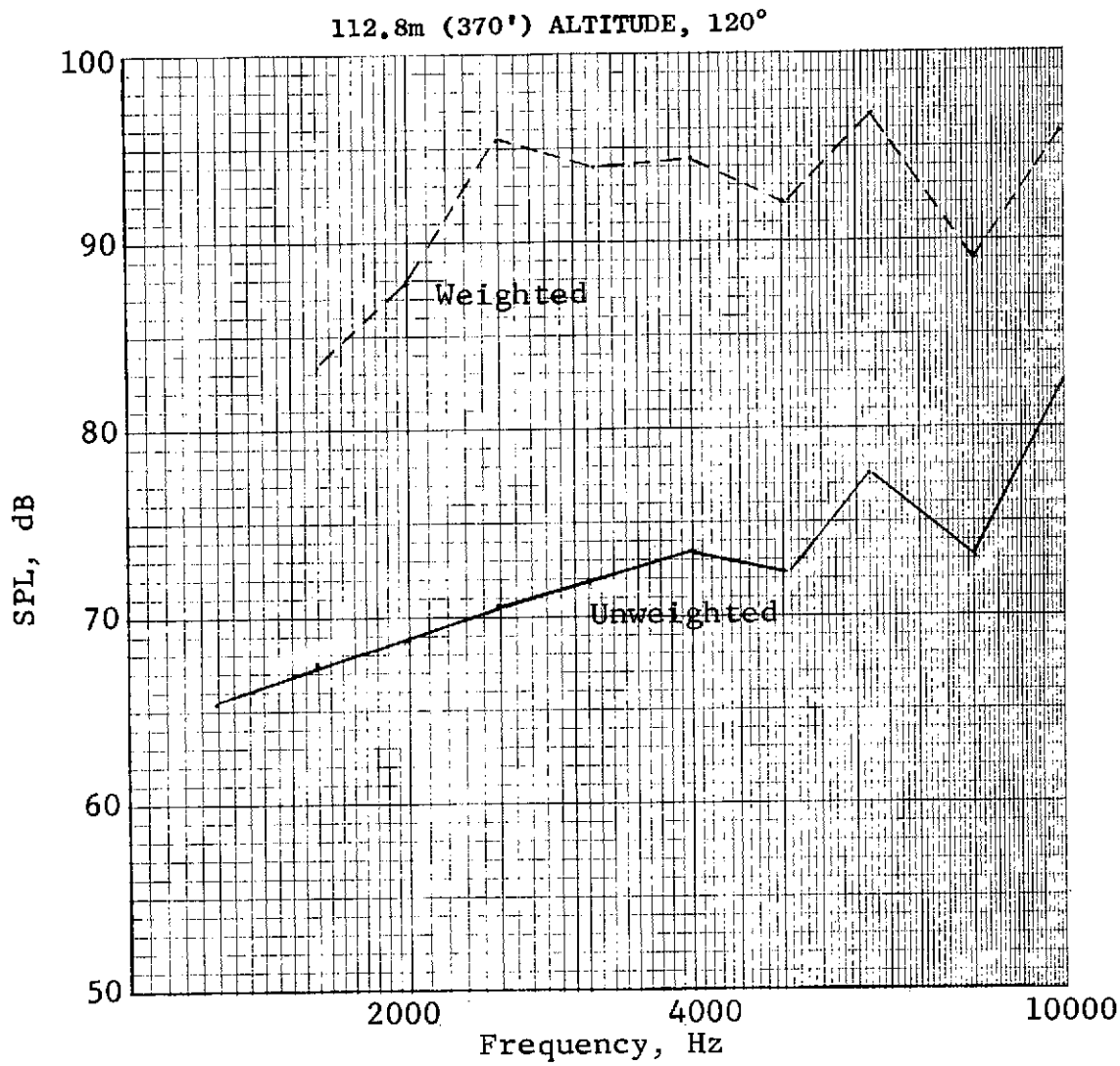

Figure 259. Engine C Predicted Turbine/Compressor Spectrum at Approach.

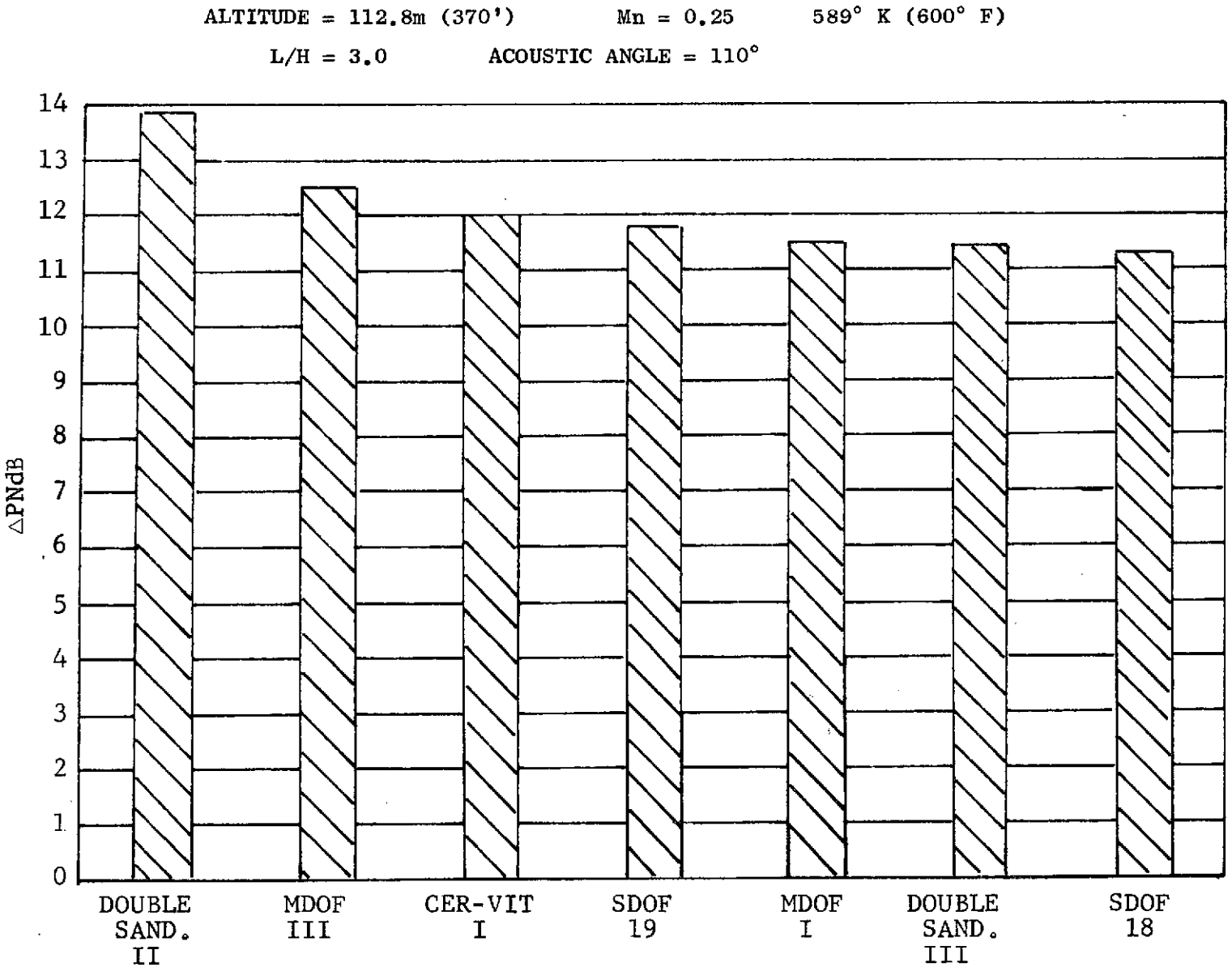

Figure 260. Perceived Noise Suppression for Turbine Noise on Engine C.

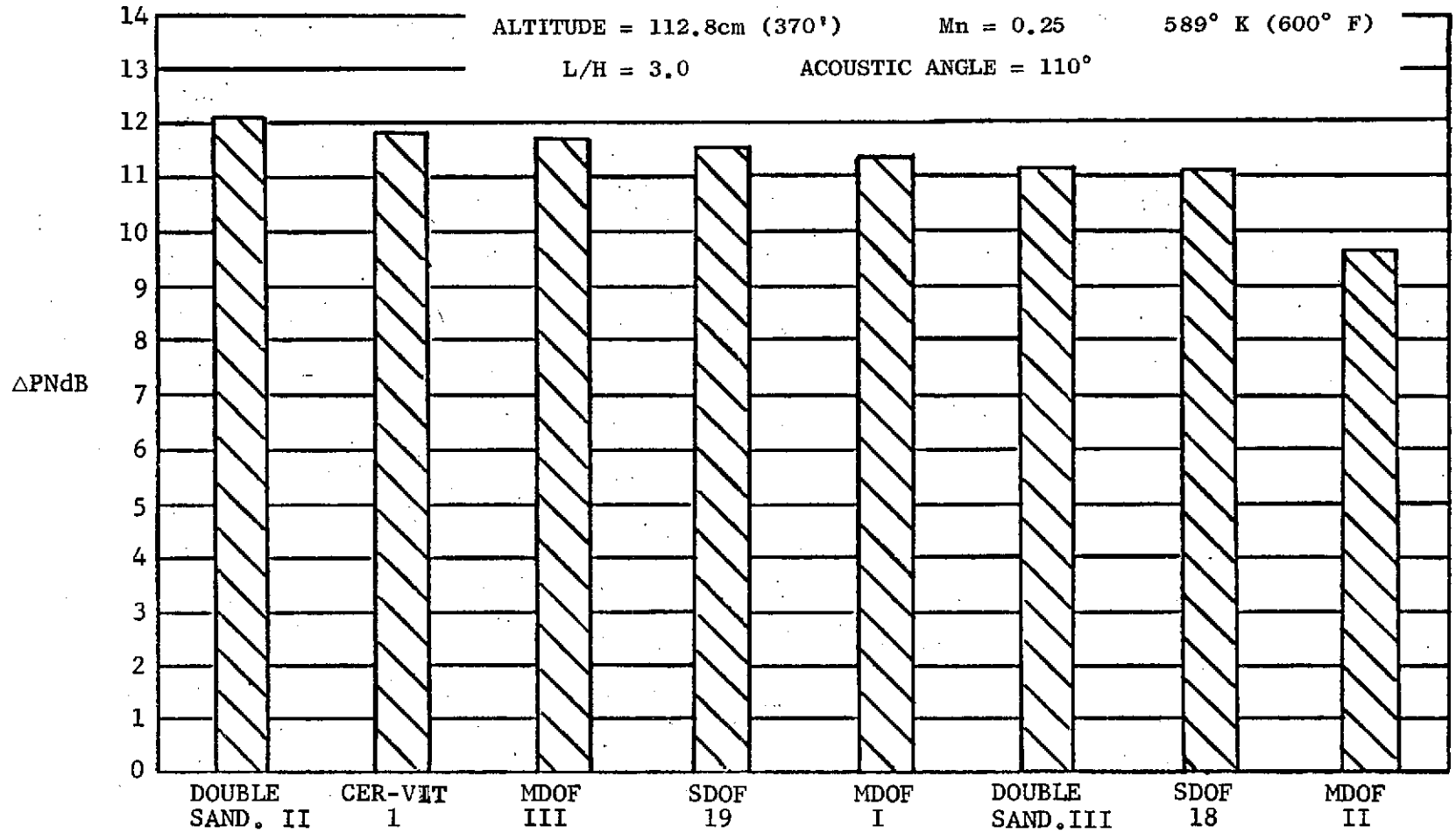

Figure 261. Perceived Noise Suppression for Turbine and Compressor Noise on Engine C.

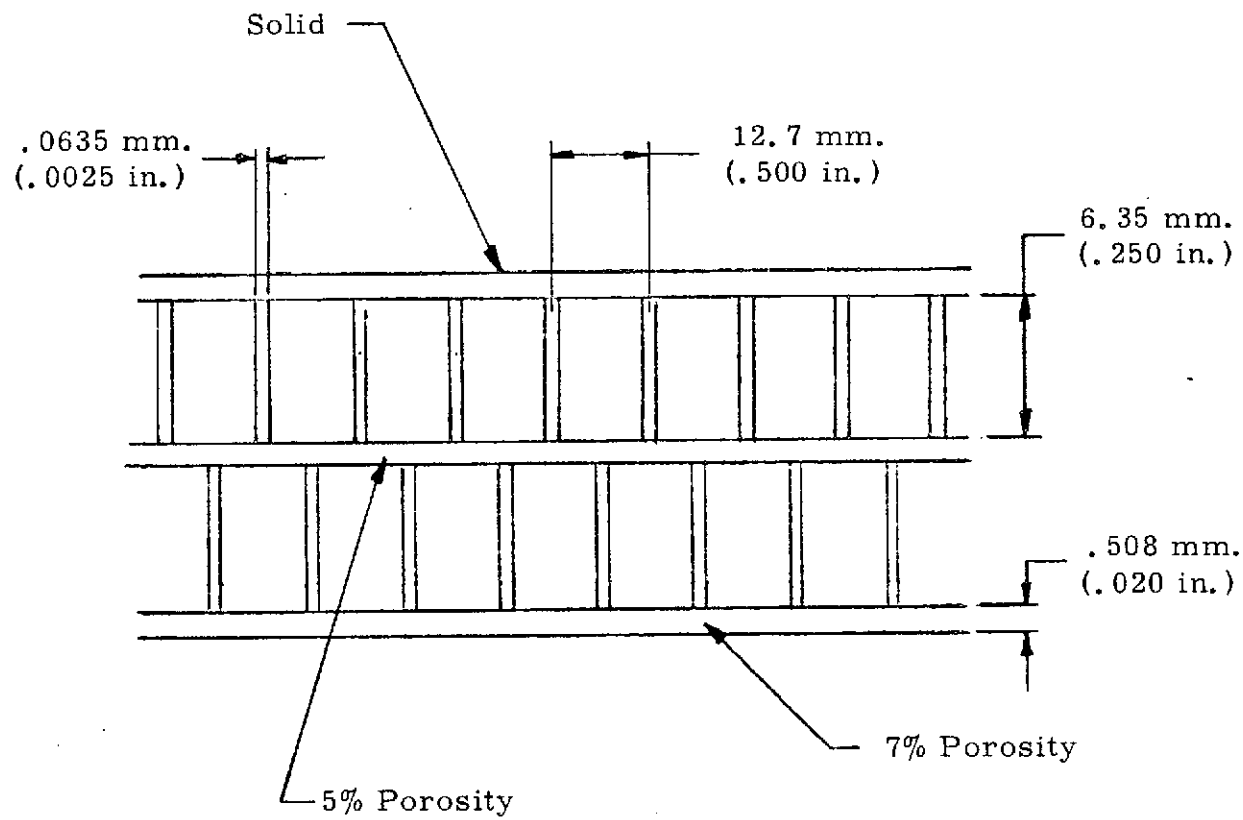

Figure 262. Honeycomb Geometry, Engine A (Double Sandwich II Ref.).

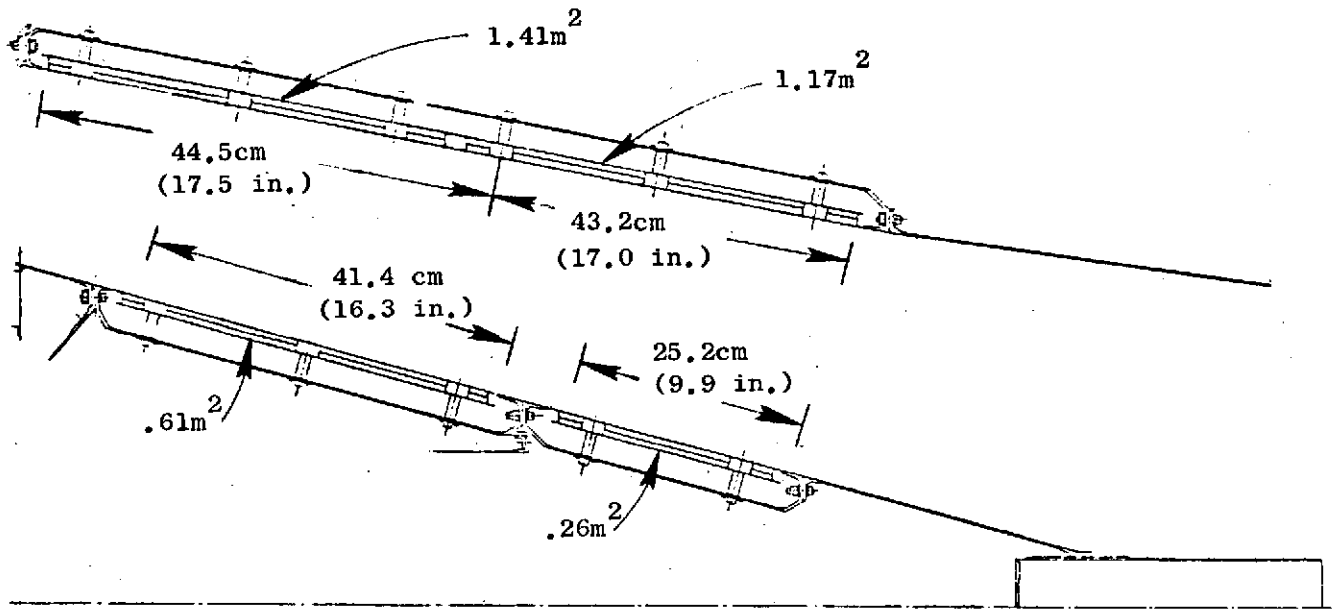

Figure 263. Engine A Exhaust Nozzle Cross Section.

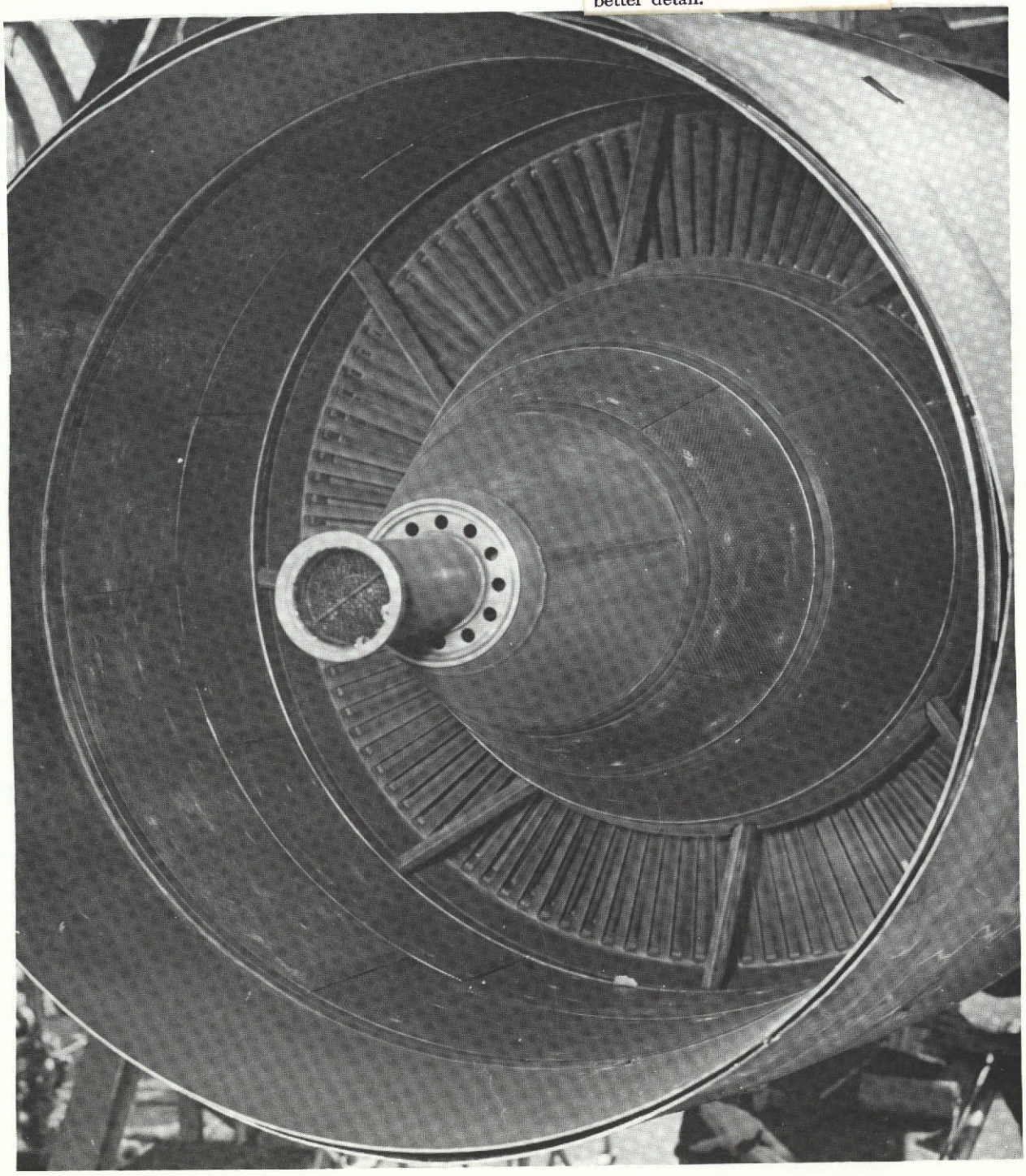

Figure 264. Engine A Exhaust Nozzle Assembly.

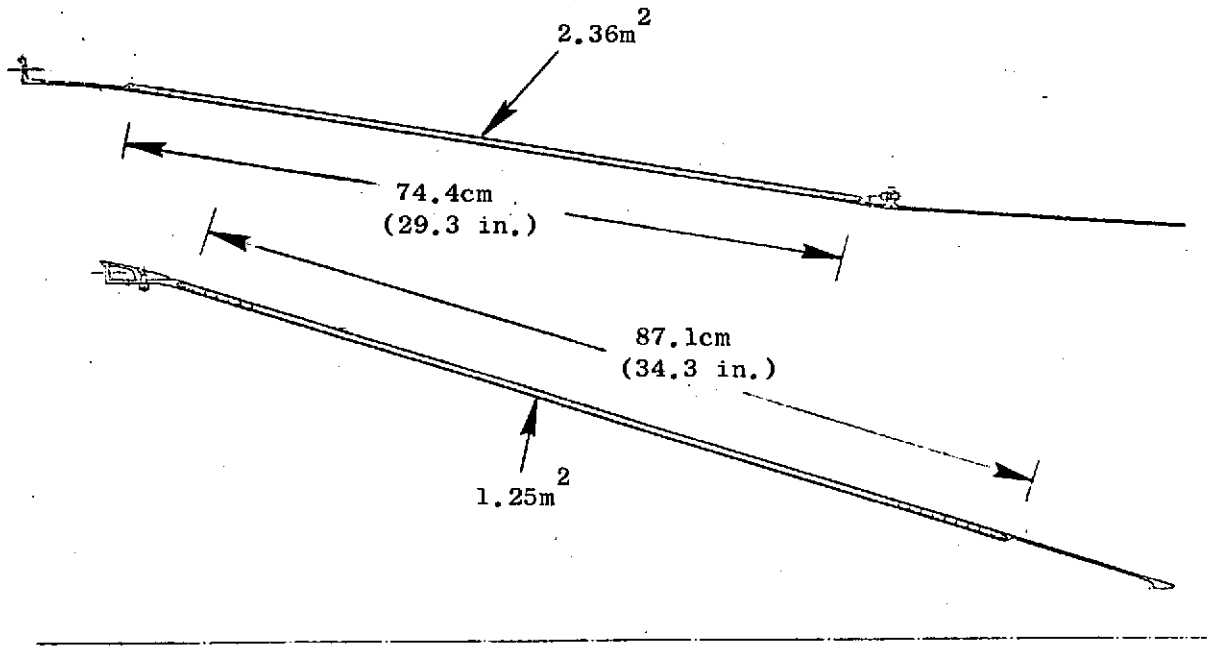

Figure 265. Engine C Exhaust Nozzle Cross Section.

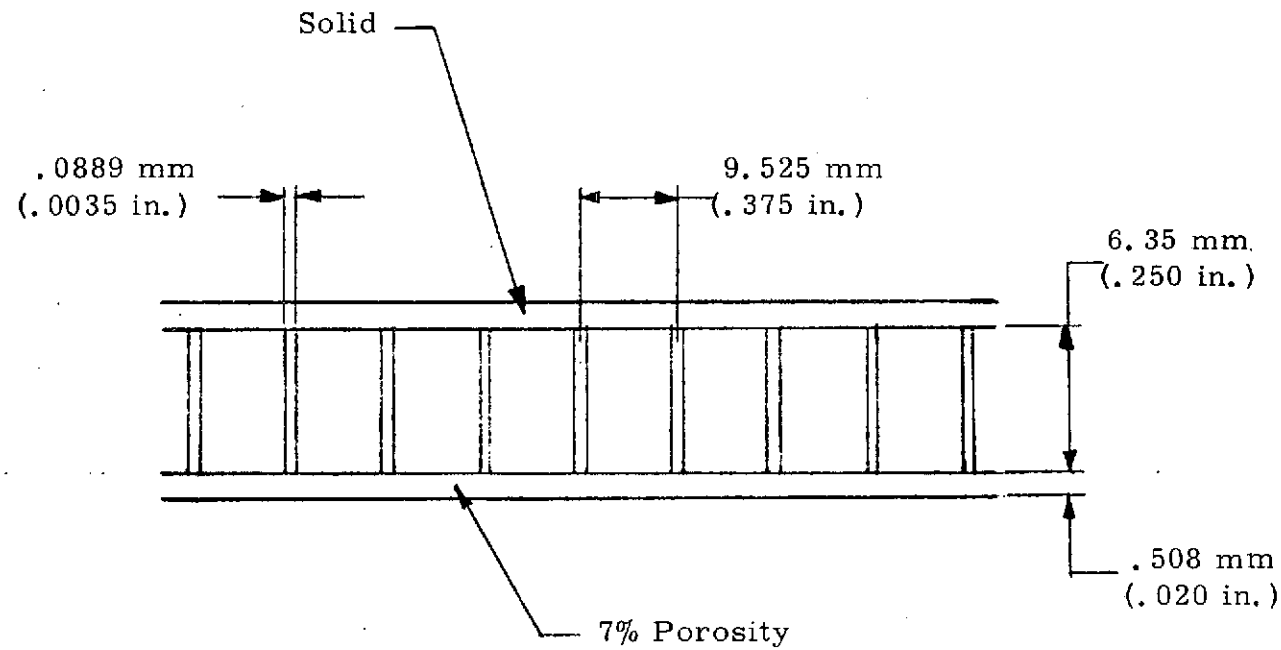

Figure 266. Honeycomb Geometry, Engine C (SDOF #19 Ref.).

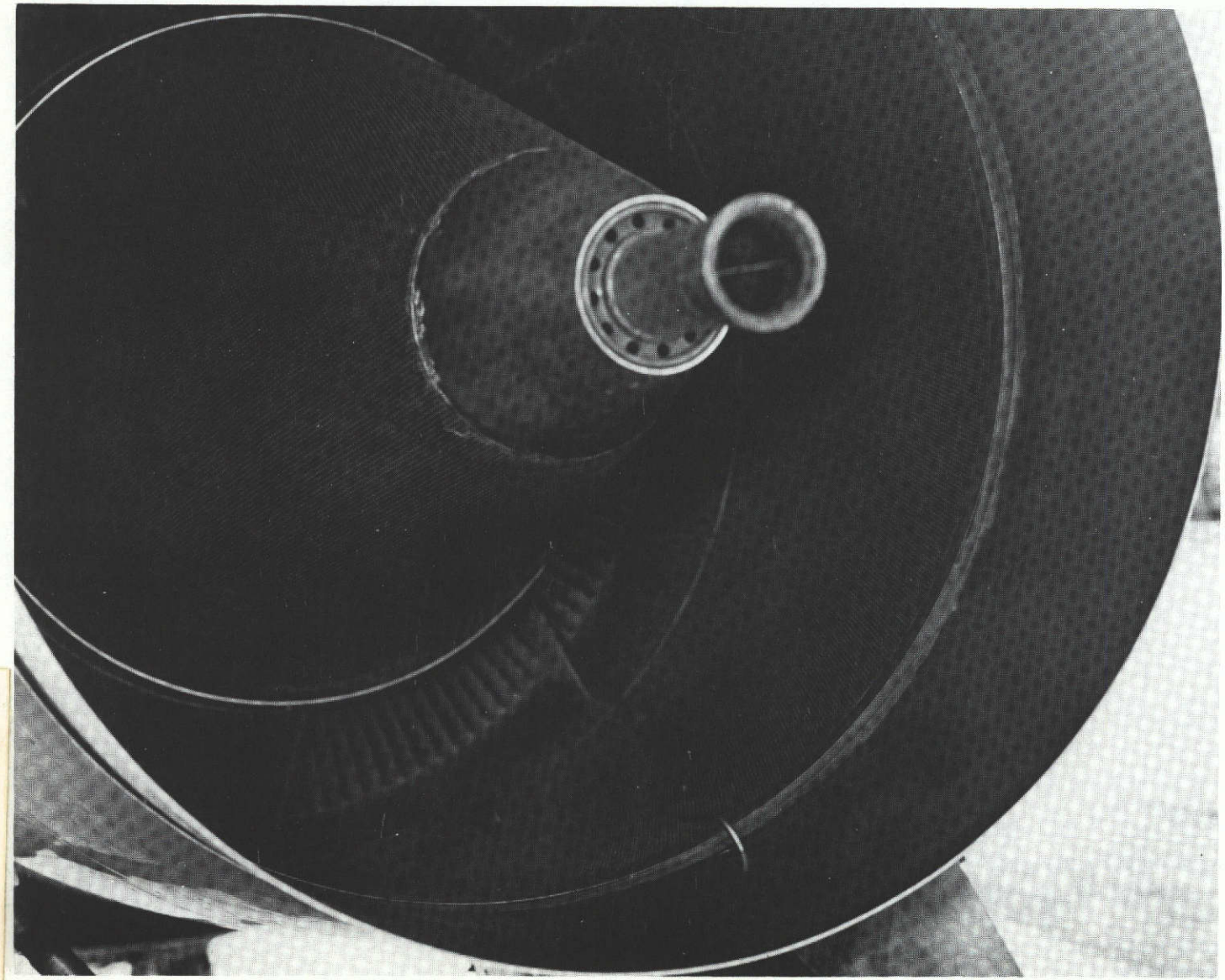

Figure 267. Engine C Exhaust Nozzle Assembly.

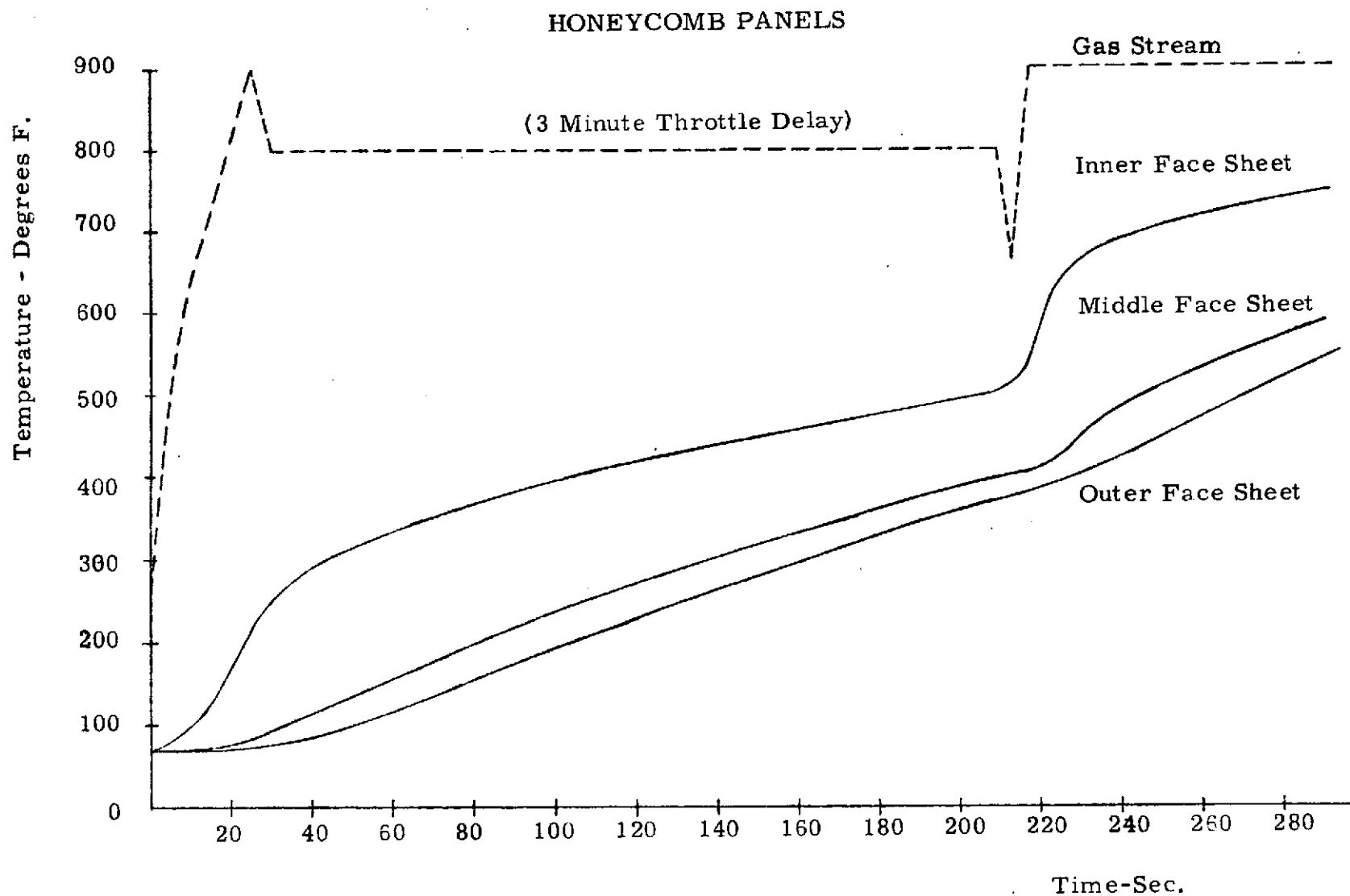

Figure 268. Temperature Vs. Time, Engine A.

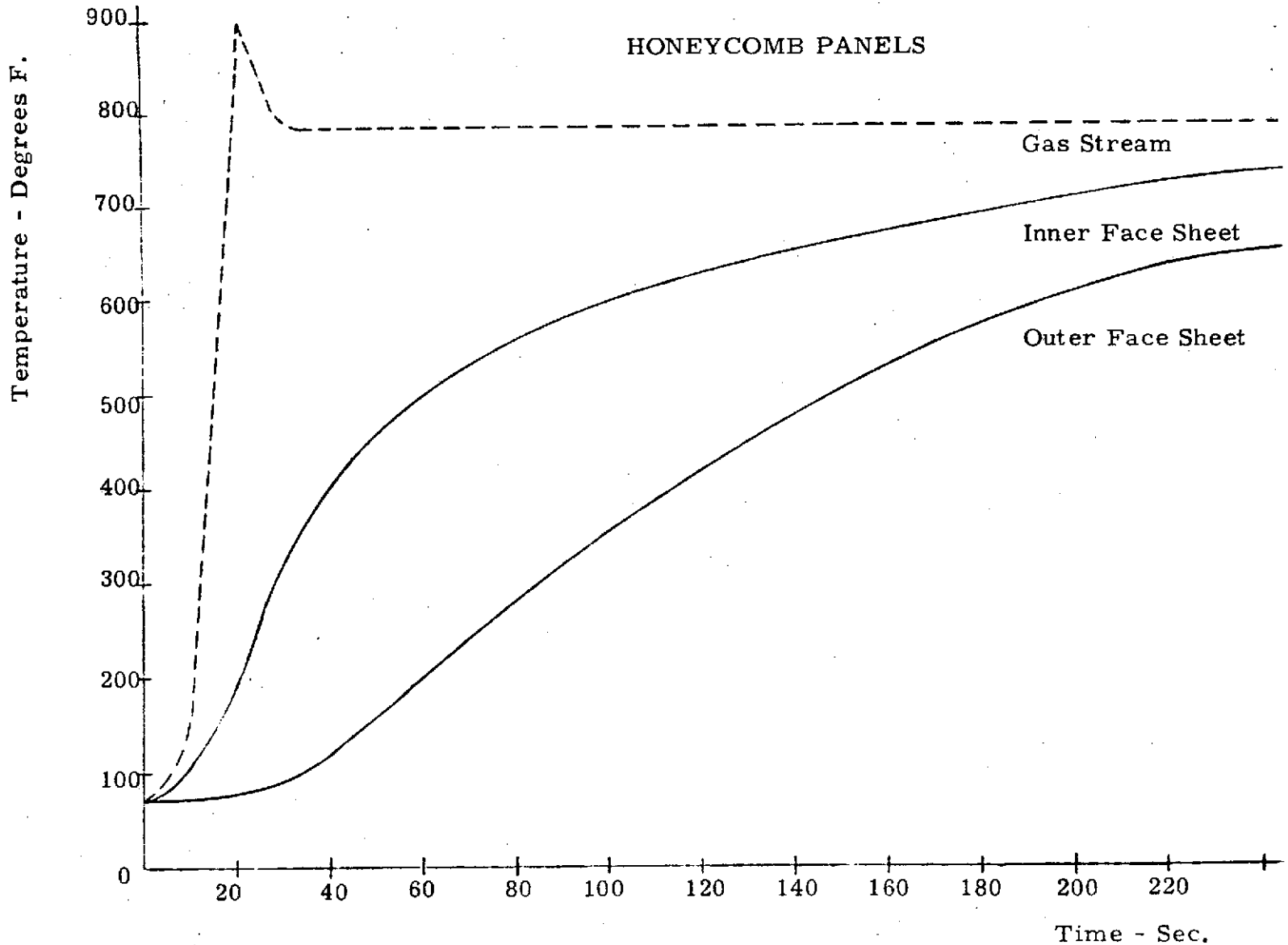

Figure 269. Temperature Vs. Time, Engine C.

Type of Local Instability	Maximum Calculated Honeycomb Stresses KG./cm^3 (PSI)		Failure by Local Instability/Limit KG./cm^3 (PSI)	
	Engine "A"	Engine "C"	Engine "A"	Engine "C"
Intracellular Buckling (Dimpling)	0.48×10^4 (1) (0.69×10^5)	0.28×10^4 (0.41×10^5)	9.91×10^3 (1.41×10^5)	1.24×10^4 (1.77×10^5)
Wrinkling of Face Sheet	0.48×10^4 (1) (0.69×10^5)	0.28×10^4 (0.41×10^5)	3.93×10^4 (5.60×10^5)	1.91×10^4 (2.72×10^5)
Core Crushing	0.14×10^2 (0.20×10^3)		1.75×10^2 (2.50×10^3)	

(1) Assumes Rigid Connection Between Panel and Support Structure. For Sliding Connection Stress is 0.19×10^4 KG/cm^3 (0.27×10^5 PSI).

Figure 270. Calculated and Failure Stress Limits in Honeycomb.

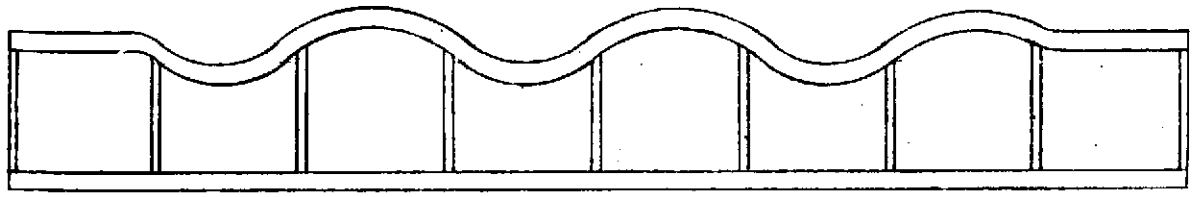

INTRACELL BUCKLING (DIMPLING)

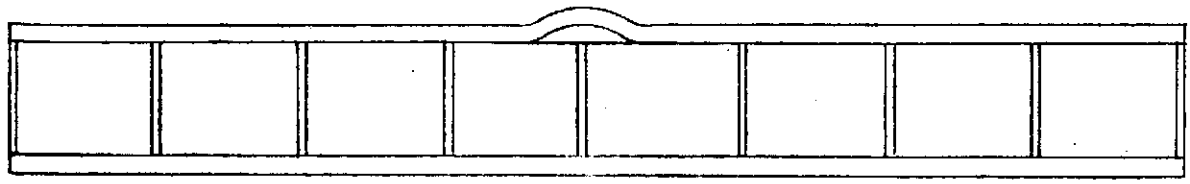

FACE WRINKLING (ADHESIVE BOND FAILURE)

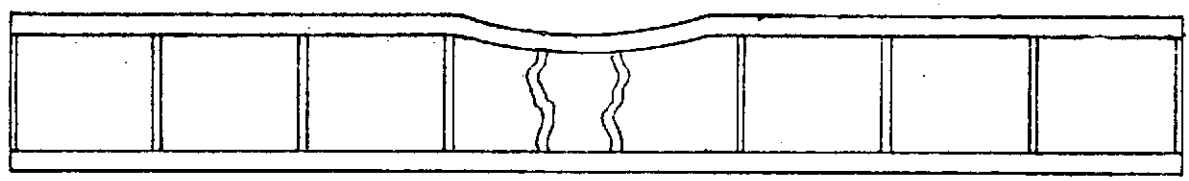

CORE COMPRESSION FAILURE

Figure 271. Modes of Instability Failures in Honeycomb Structures.

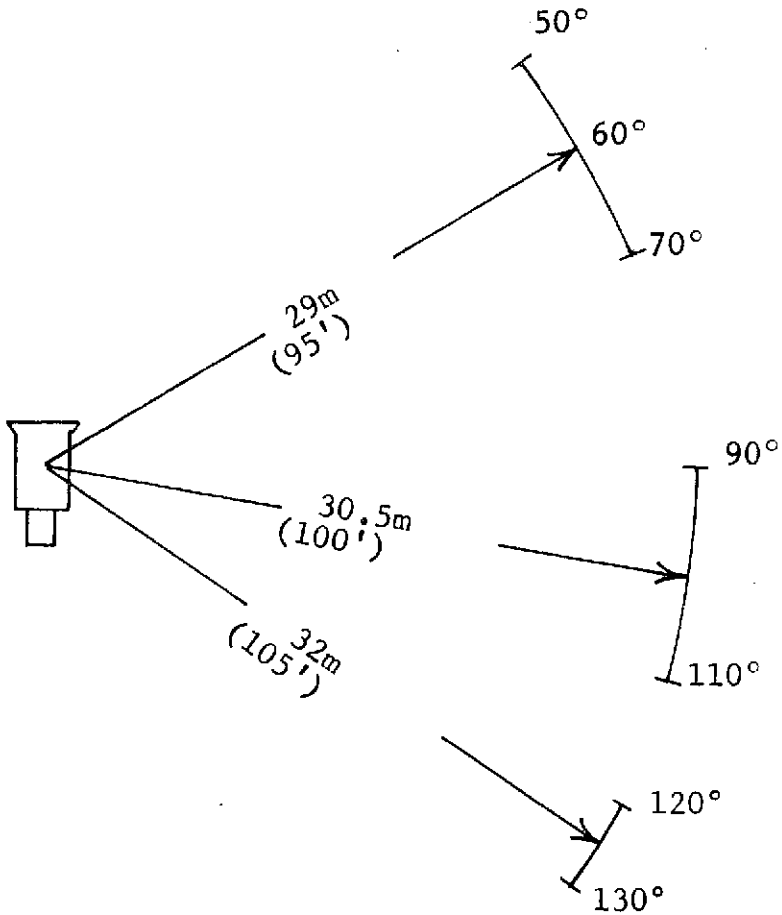

ARRAY ANGULAR POSITIONS

ENGINE POWER SETTINGS

APPROACH: 60% SPEED

TAKEOFF: 90% SPEED

POSITION NO.	ENGINE SOURCE POSITIONS
9	• 1.52m (5') FORWARD OF INLET
8	• 0.76m (2.5') FORWARD OF INLET
7	• INLET PLANE
6	• ROTOR PLANE
5	• FAN DISCHARGE PLANE
4	• TURBINE CASING
3	• CORE NOZZLE EXIT PLANE
2	• 0.76m (2.5') AFT OF EXIT PLANE
1	• 1.52m (5') AFT OF EXIT PLANE

Figure 272. Directional Array Test Locations for Engine A.

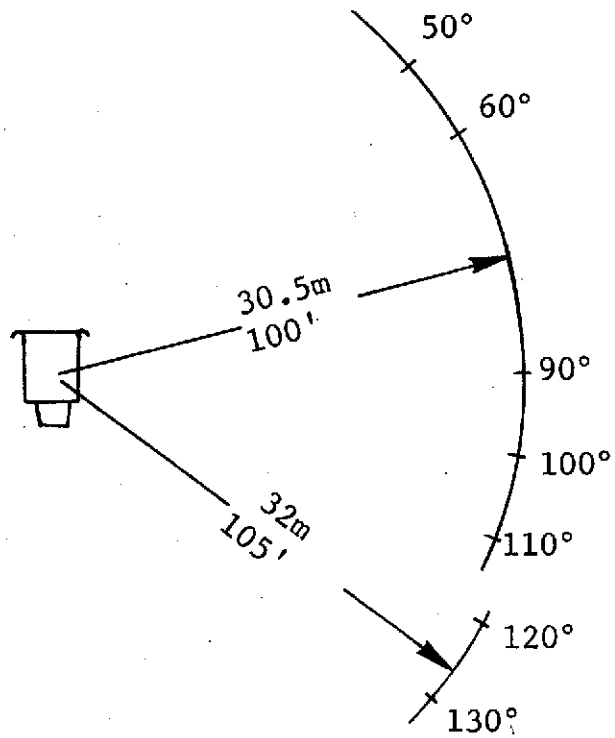

ARRAY ANGULAR POSITIONS

ENGINE POWER SETTINGS

APPROACH: 60%

TAKEOFF: 90%

POSITION NO.	ENGINE SOURCE POSITIONS
9	• 1.52m (5') FORWARD OF INLET
8	• INLET PLANE
7	• .43m (1.4') FORWARD OF ROTOR
6	• AFT FAN COWL
5	• FAN DISCHARGE PLANE
4	• TURBINE CASING
3	• CORE NOZZLE EXIT PLANE
2	• 1.52m (5') AFT OF EXIT PLANE
1	• 3.04m (10') AFT OF EXIT PLANE

Figure 273. Directional Array Test Locations for Engine C.

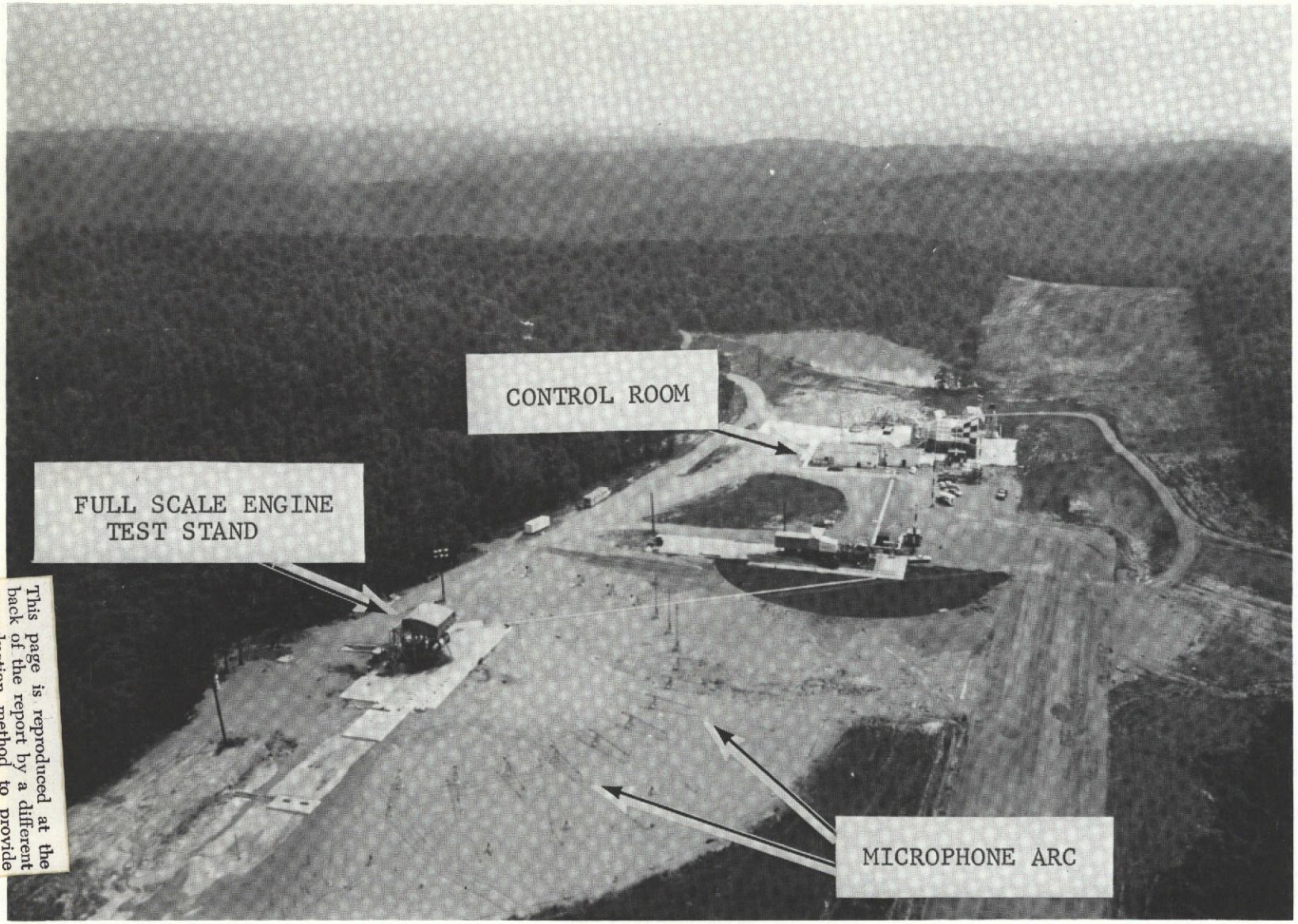

Figure 274. Aerial View of Peebles Sound Field.

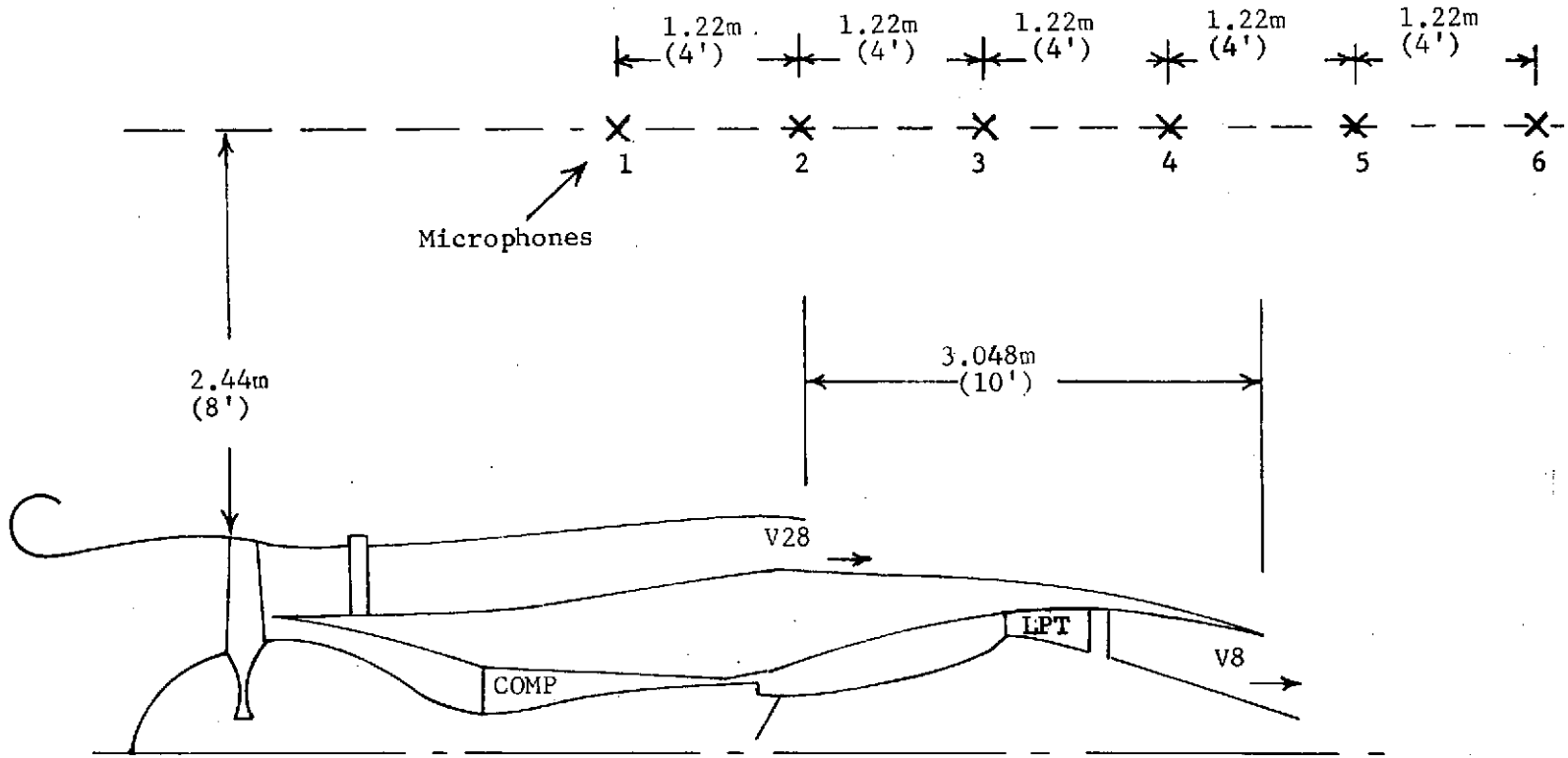

Figure 275. Engine A Nearfield Microphone Locations.

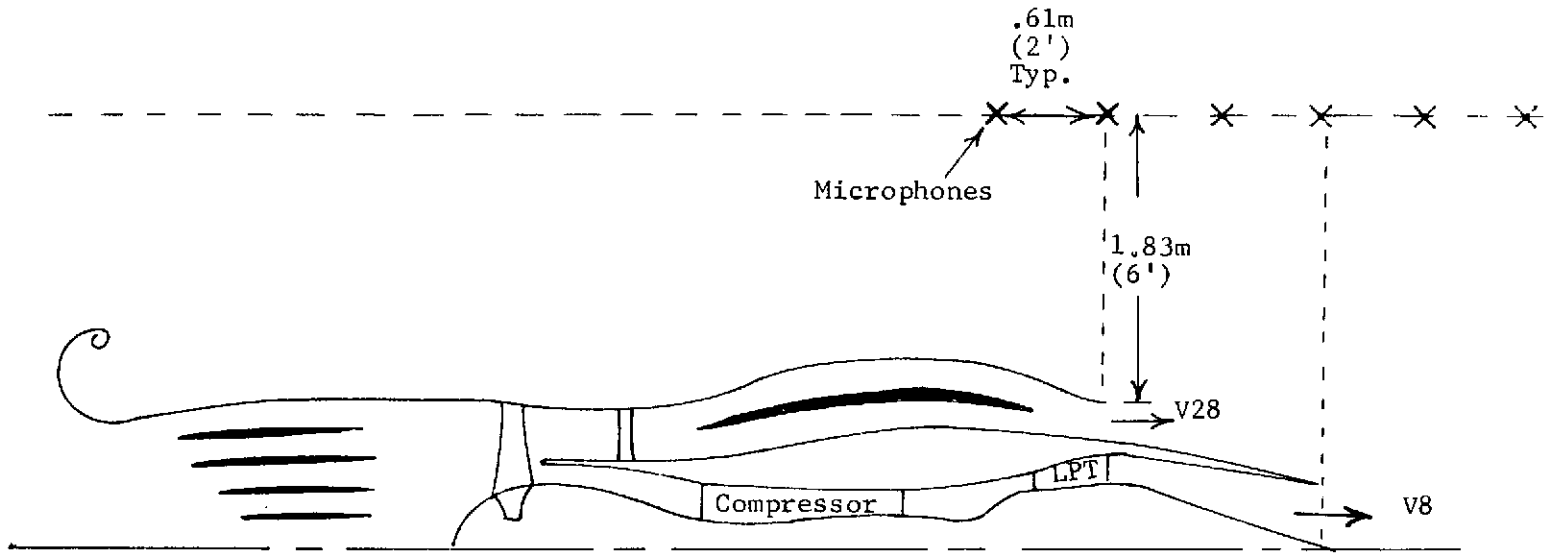

Figure 276. Engine C Nearfield Microphone Locations.

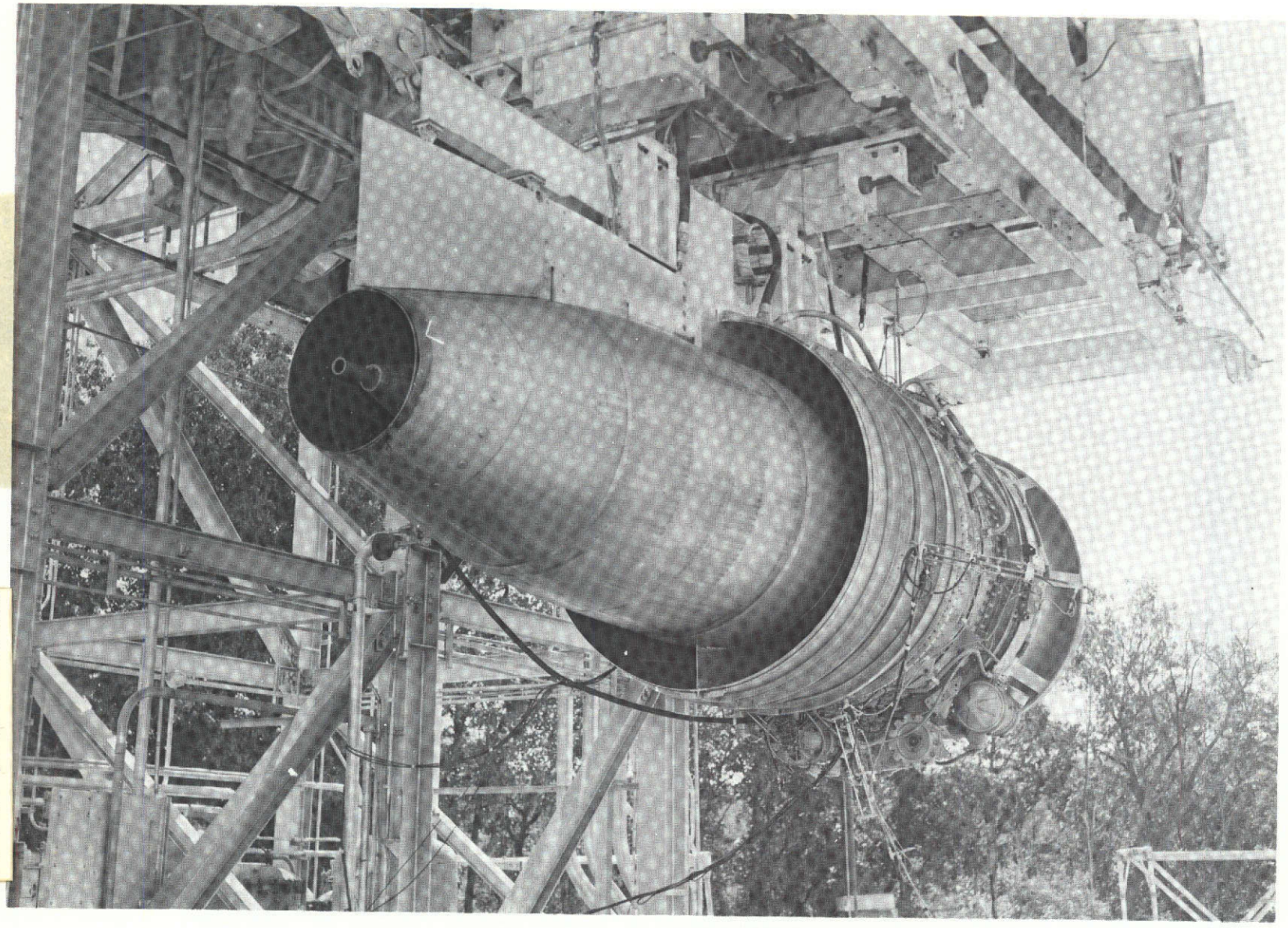

Figure 277. Engine A Mounted on Engine Test Stand.

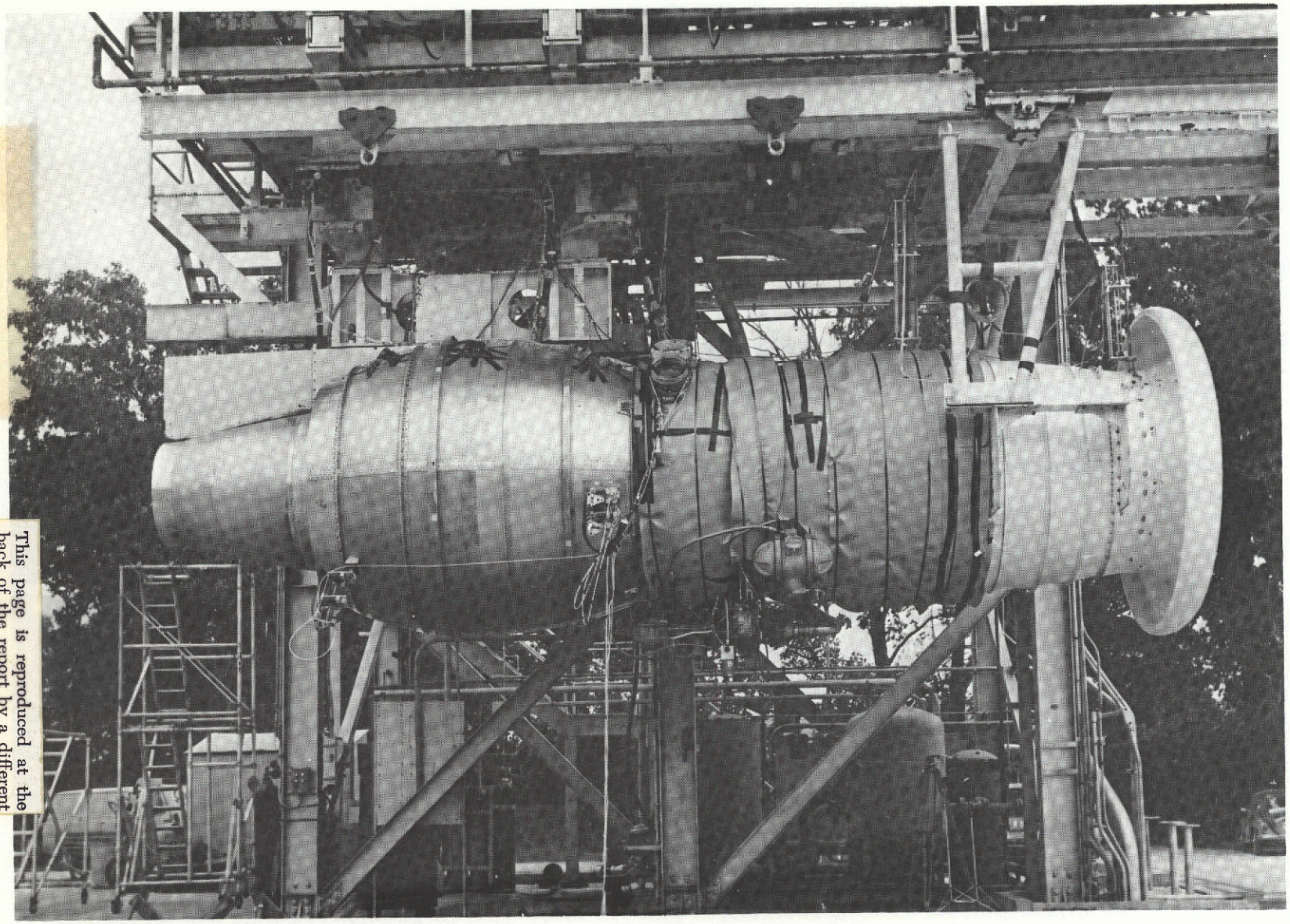

Figure 278. Engine C, Fully Suppressed.

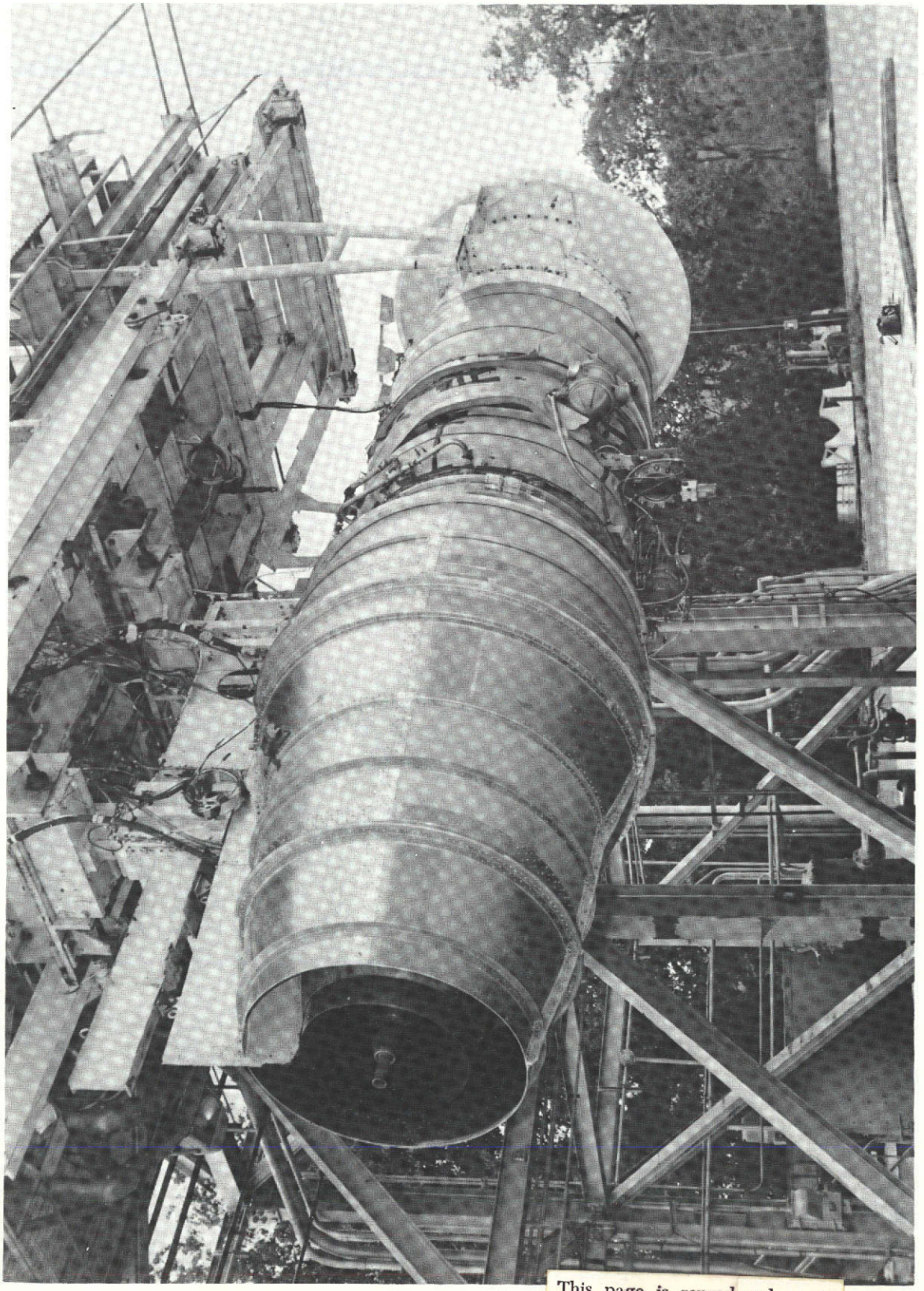

Figure 279. Engine C, Fully Suppressed, Coplanar Nozzle.

This page is reproduced at the back of the report by a different reproduction method to provide better detail.

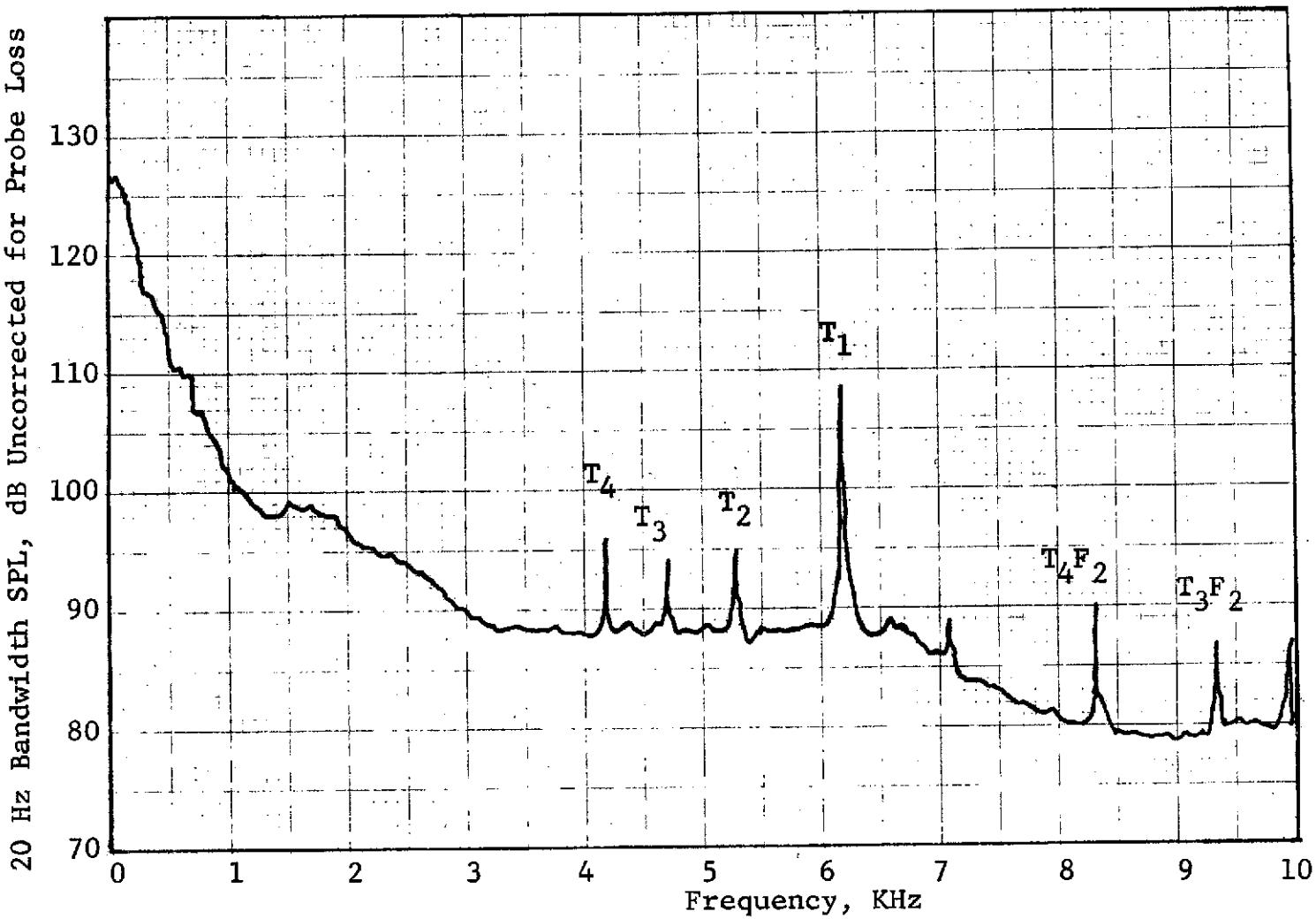

Figure 280. Engine A Typical Acoustic Probe Sound Pressure Level (Data at Duct Center Downstream of 2DOF2 Acoustic Treatment) Approach Power.

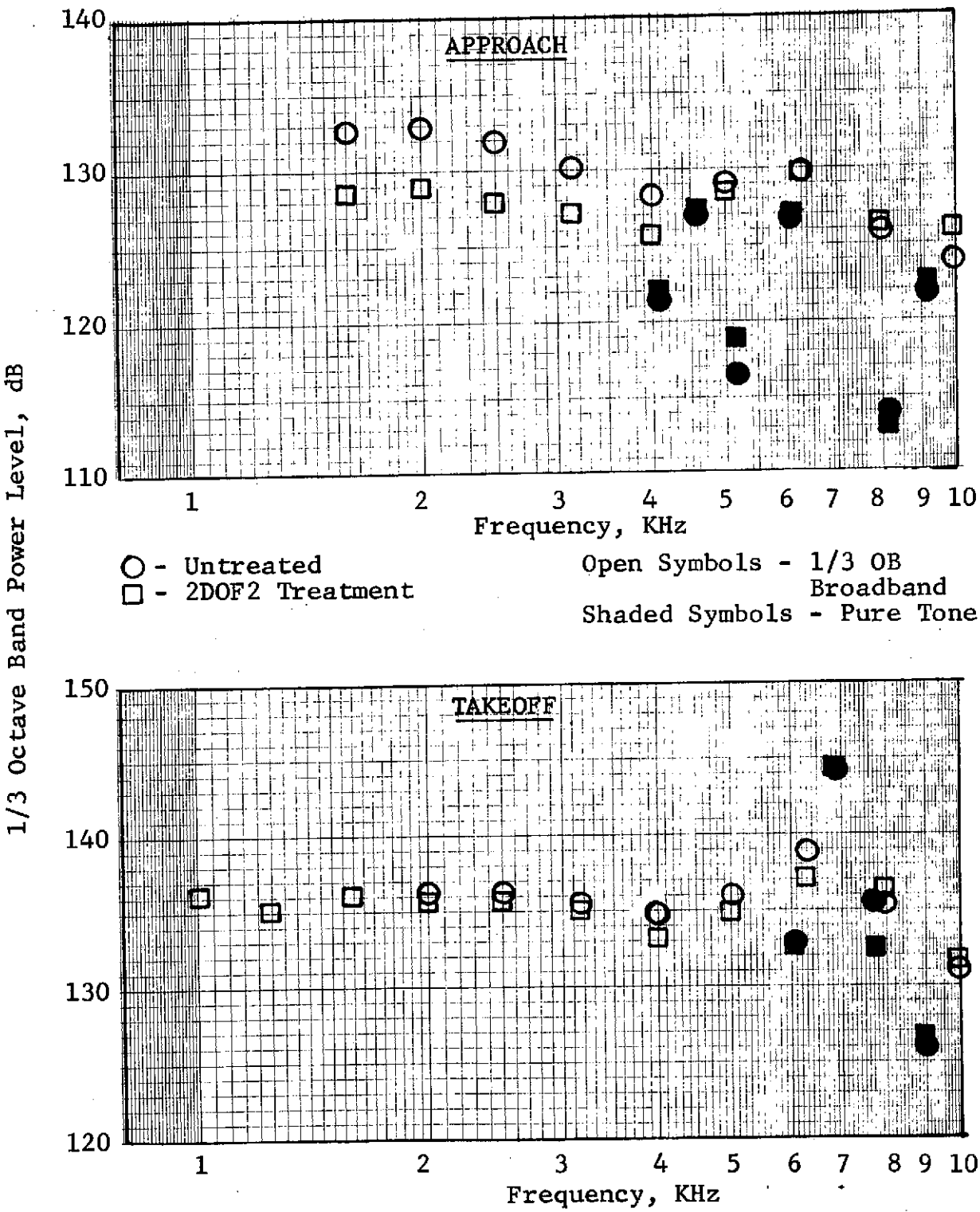

Figure 281. Engine A Power Level at Forward Turbine Probe.

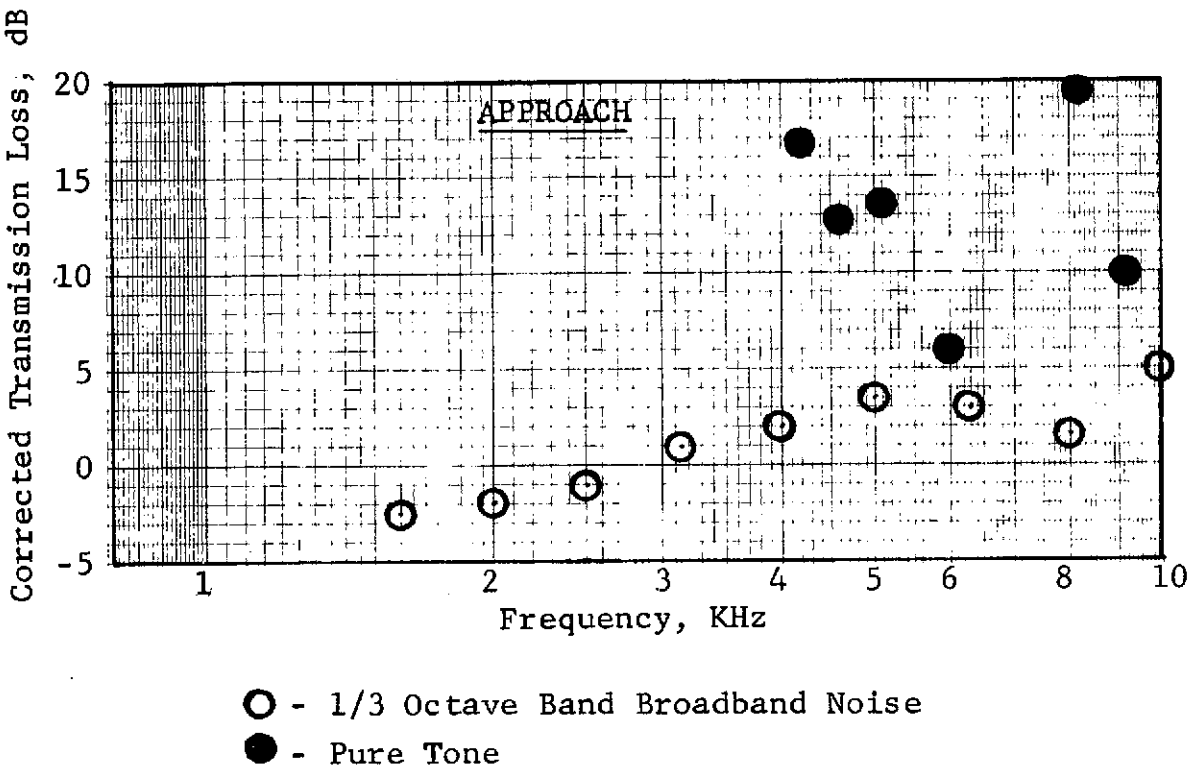

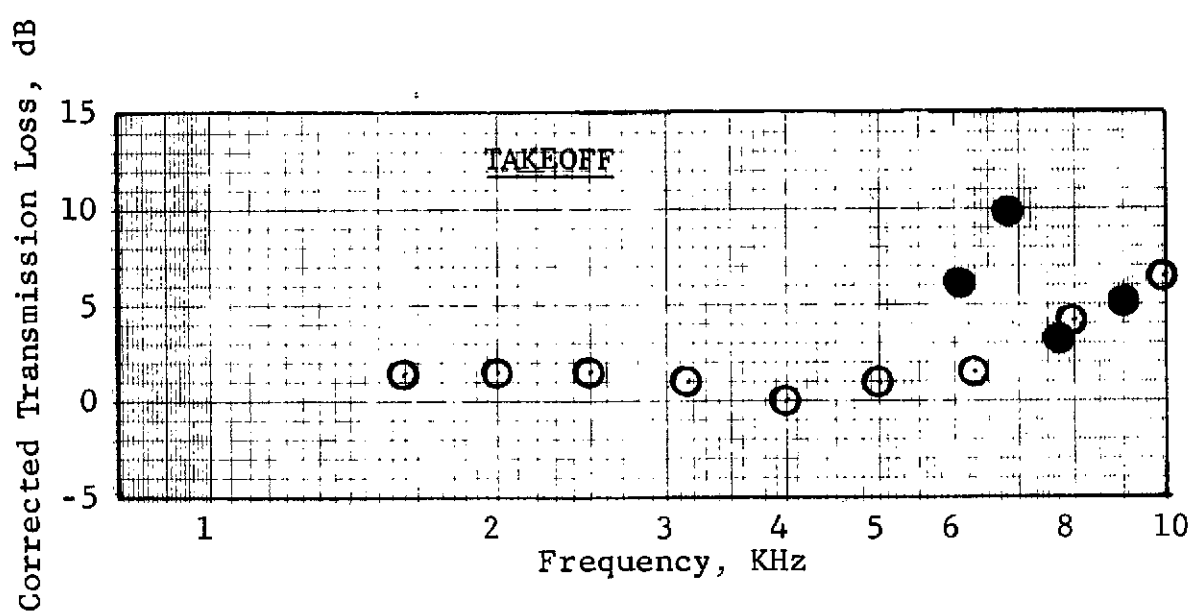

Figure 282. Engine A Turbine Treatment Corrected Transmission Loss (Double Sandwich II).

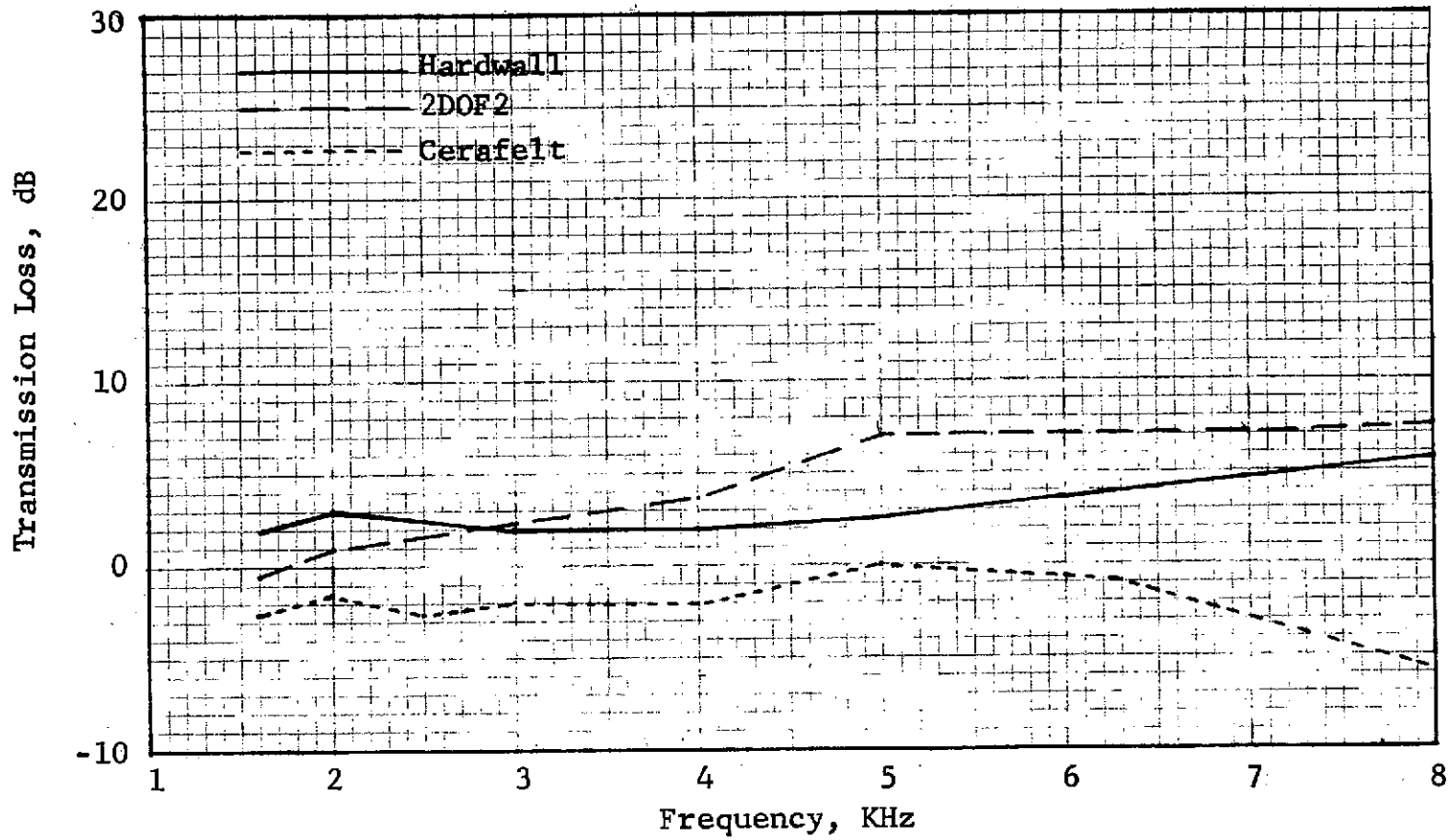

Figure 283. Engine A Broadband Transmission Loss as Measured with Acoustic Probes @ 2175 rpm.

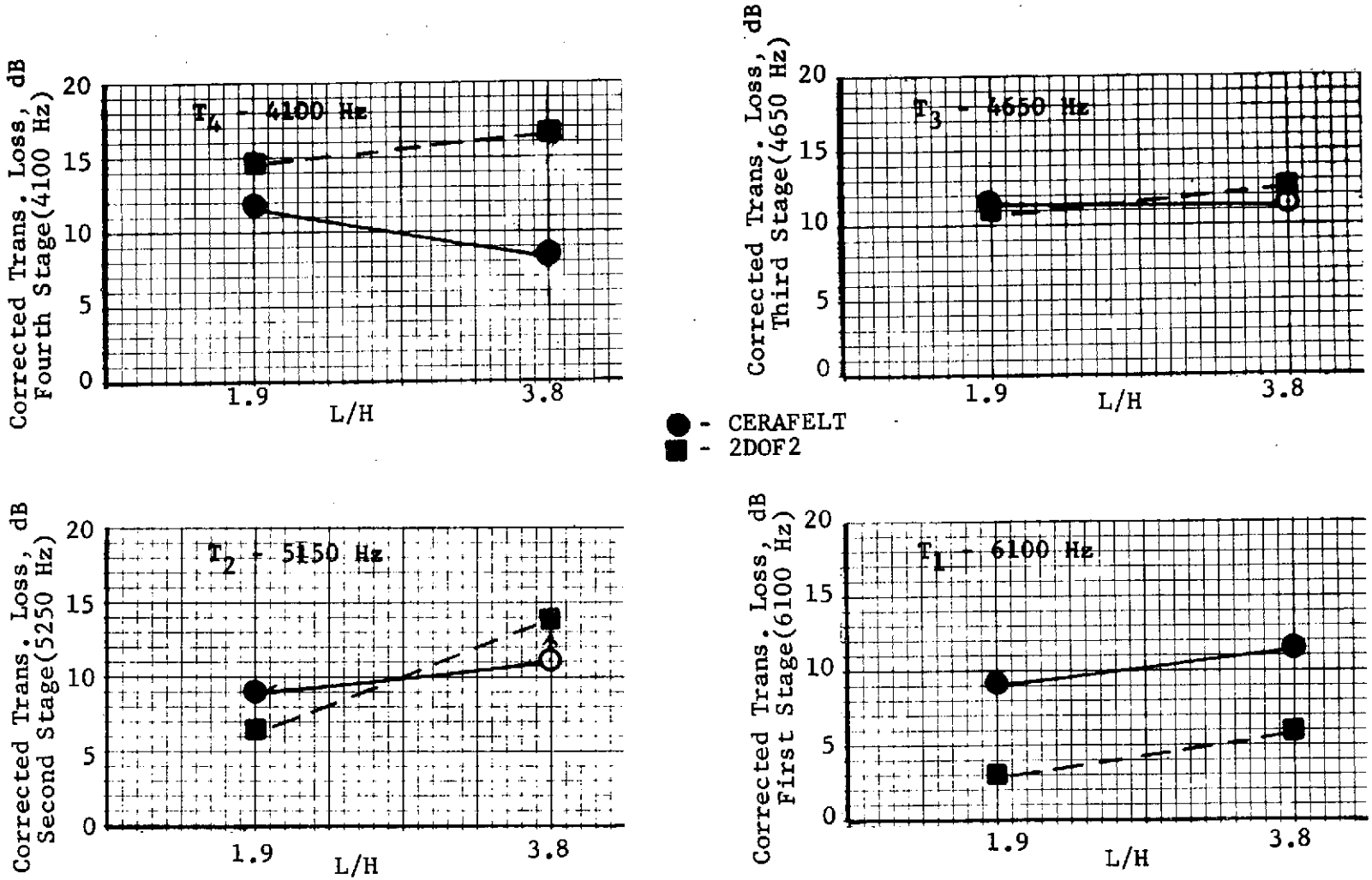

Figure 284. Engine A Corrected Transmission Loss Vs. Treatment Length from Probe Data at Approach Power.

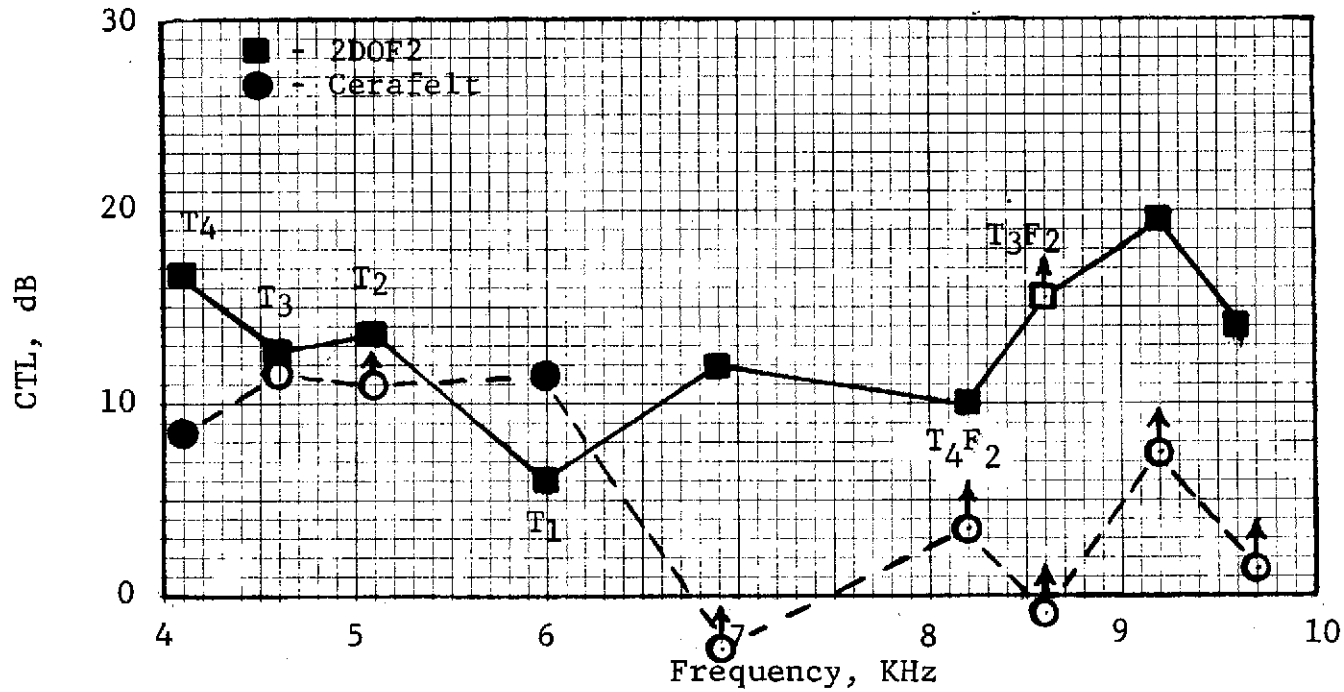

* Open Symbols Indicate
Marginal S/N Ratio

Figure 285. Engine A Corrected Transmission Loss at Approach.

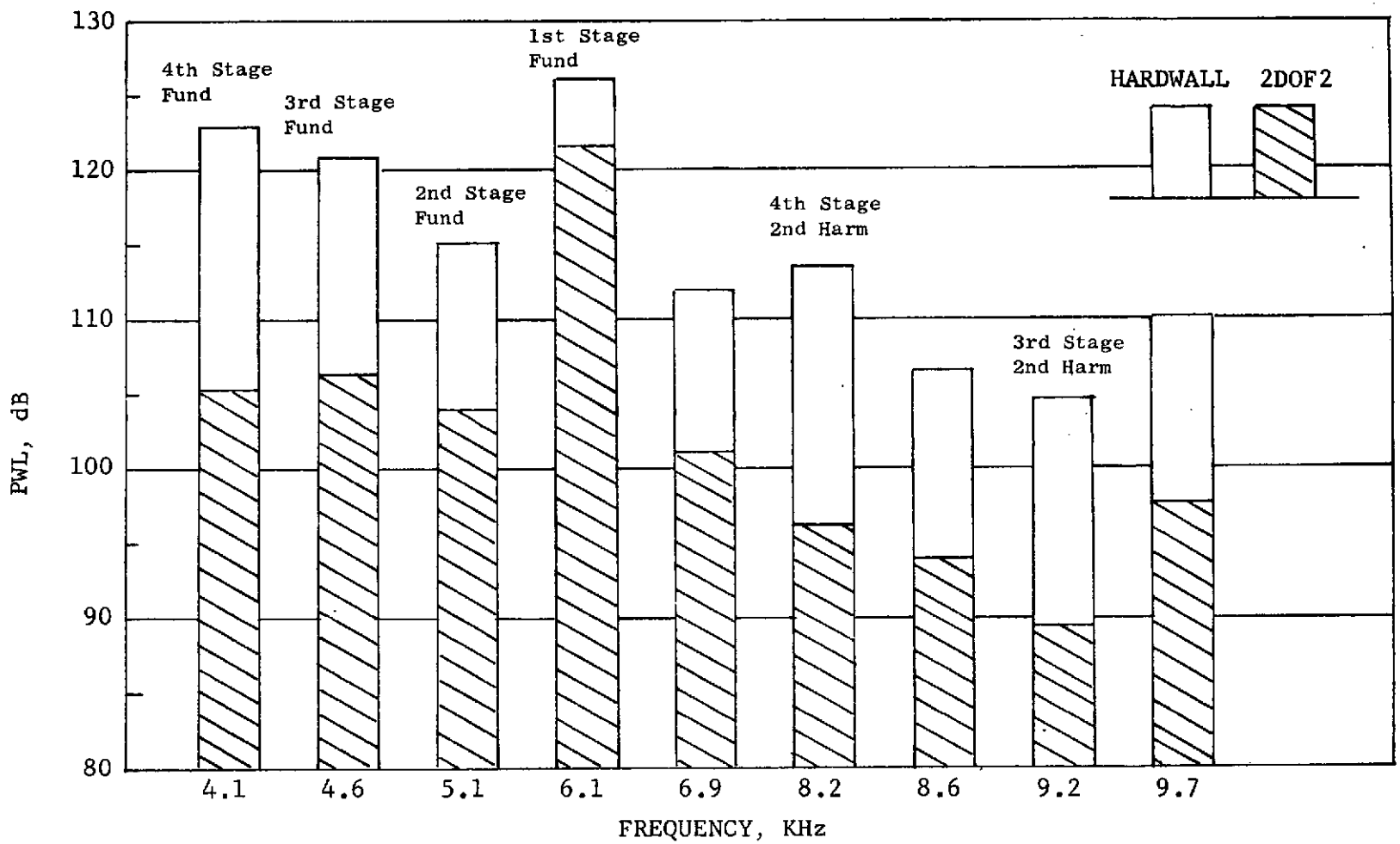

Figure 286. Engine A Power Level of Turbine Tones at Downstream Probe Location at Approach Power.

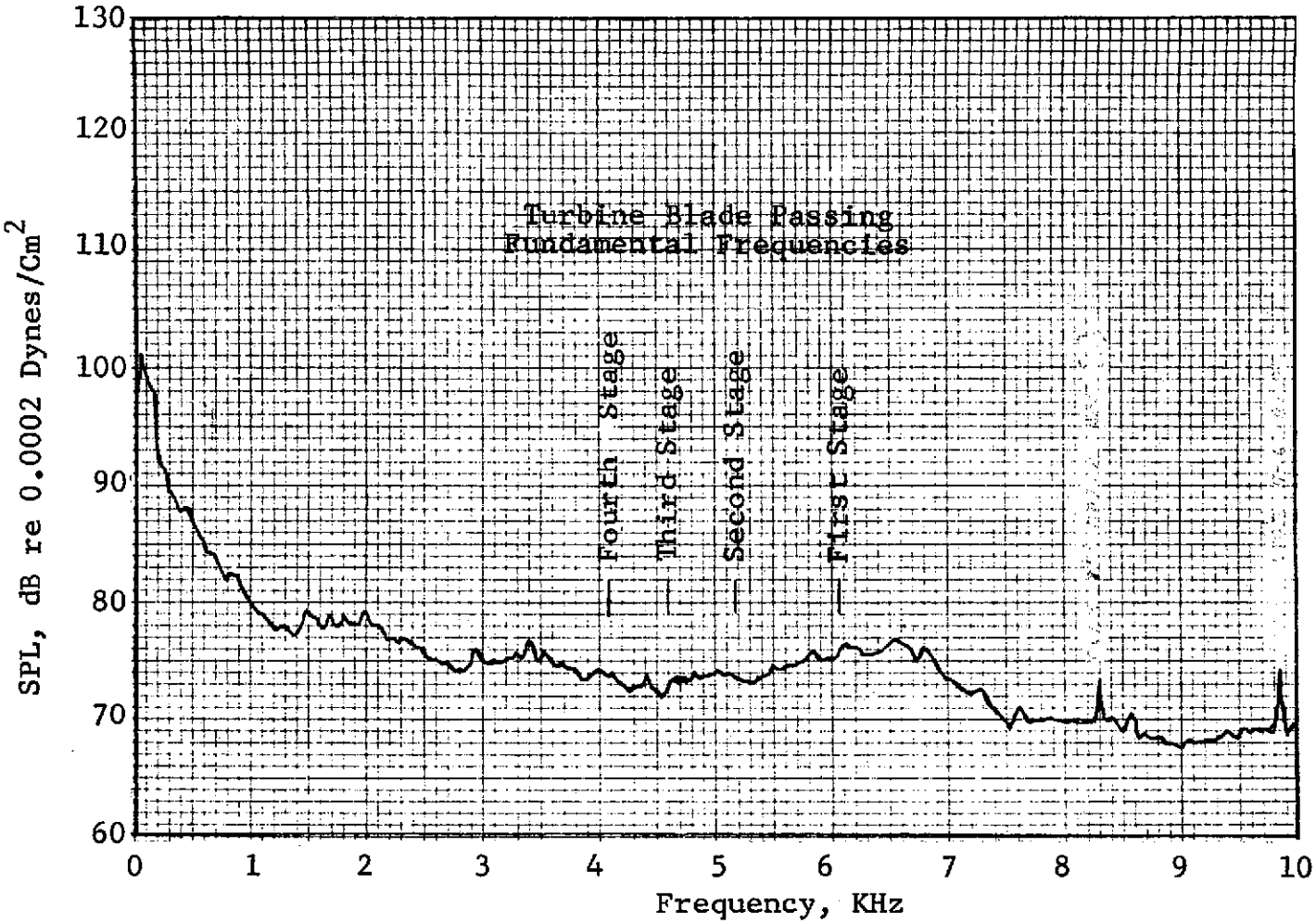

Figure 287. Engine A Nearfield Untreated Turbine Spectra (Approach Power, Position No. 1).

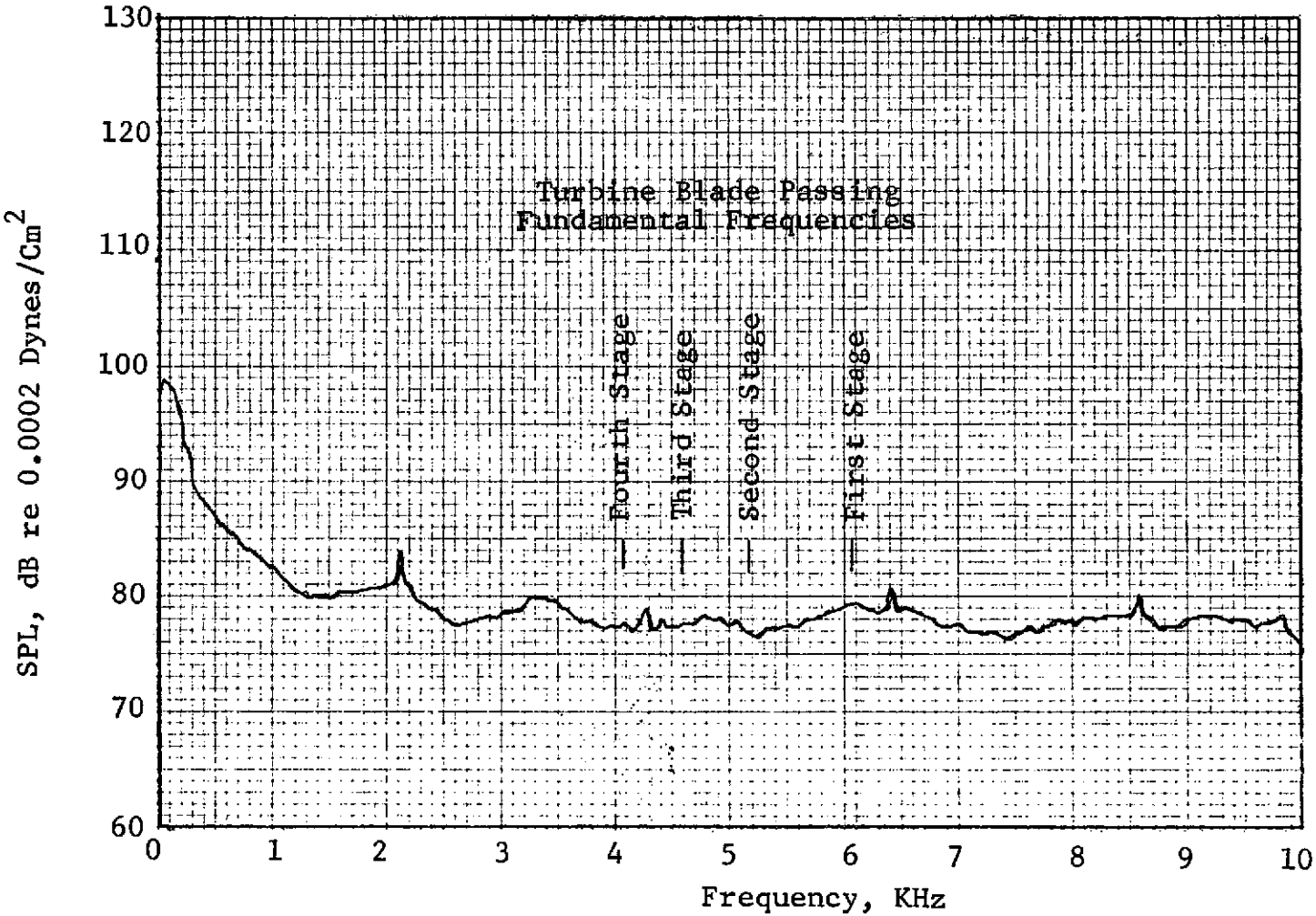

Figure 288. Engine A Nearfield Untreated Turbine Spectra (Approach Power, Position No. 2).

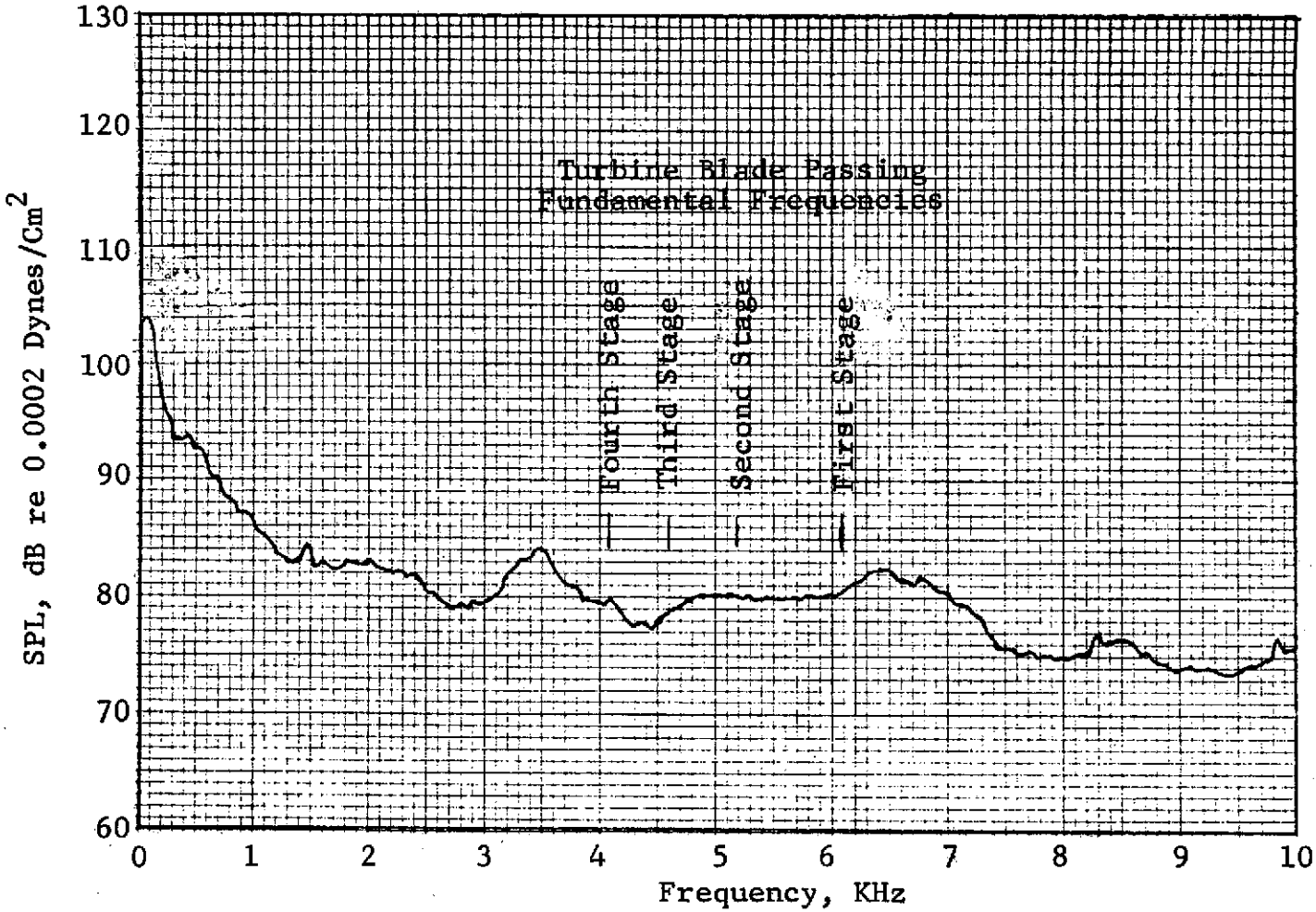

Figure 289. Engine A Nearfield Untreated Turbine Spectra (Approach Power, Position No. 3).

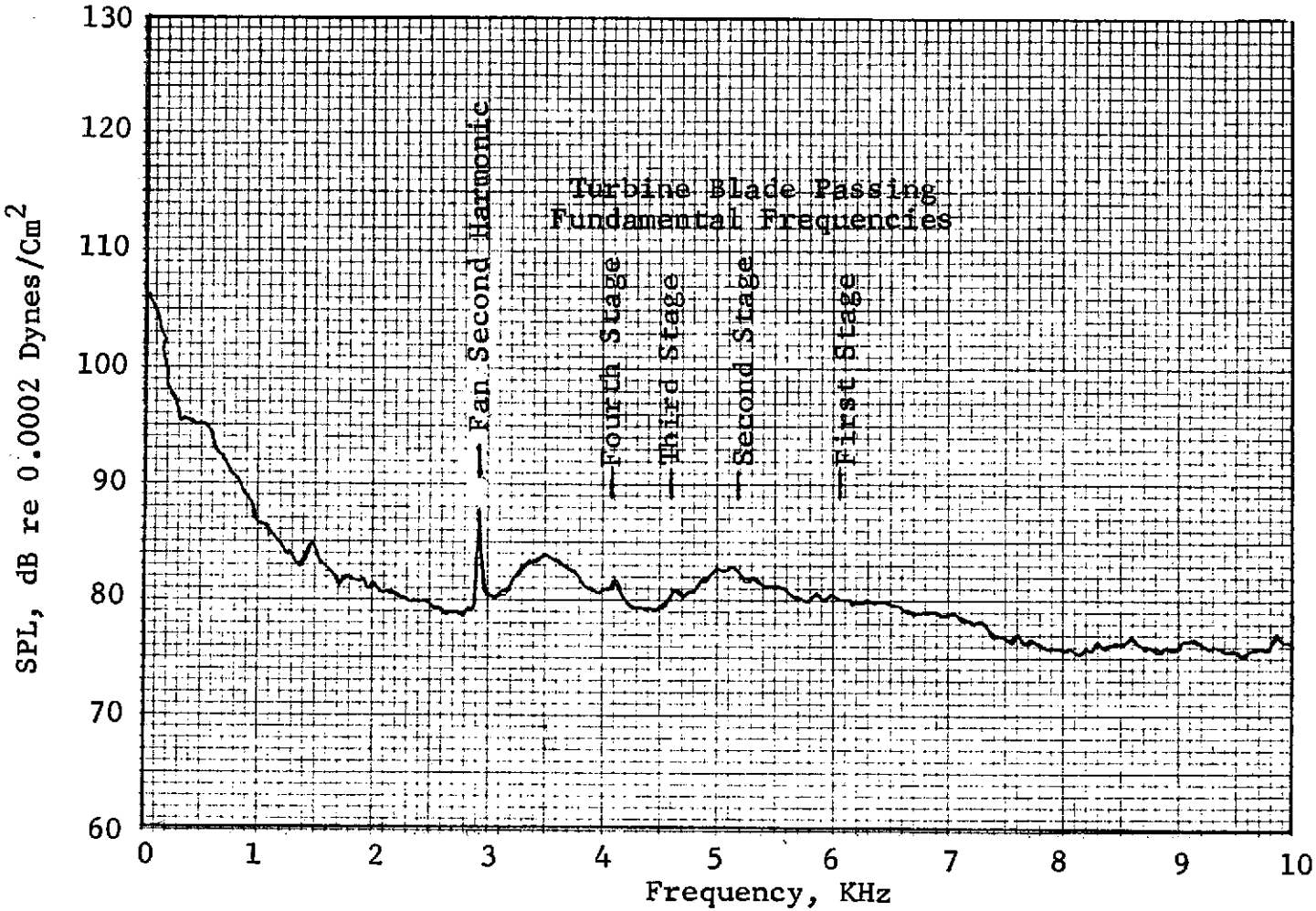

Figure 290. Engine A Nearfield Untreated Turbine Spectra (Approach Power, Position No. 4).

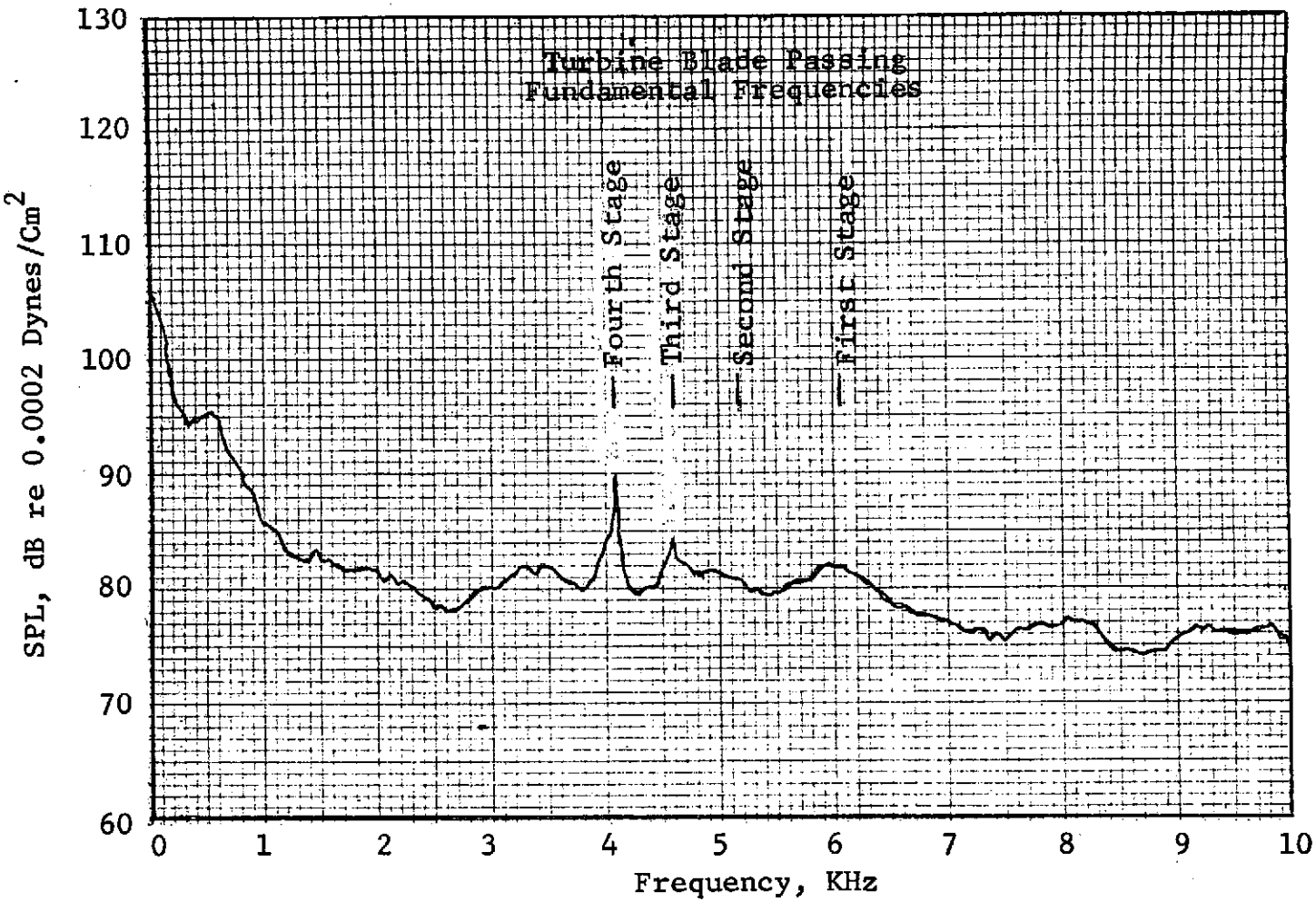

Figure 291. Engine A Nearfield Untreated Turbine Spectra (Approach Power, Position No. 5).

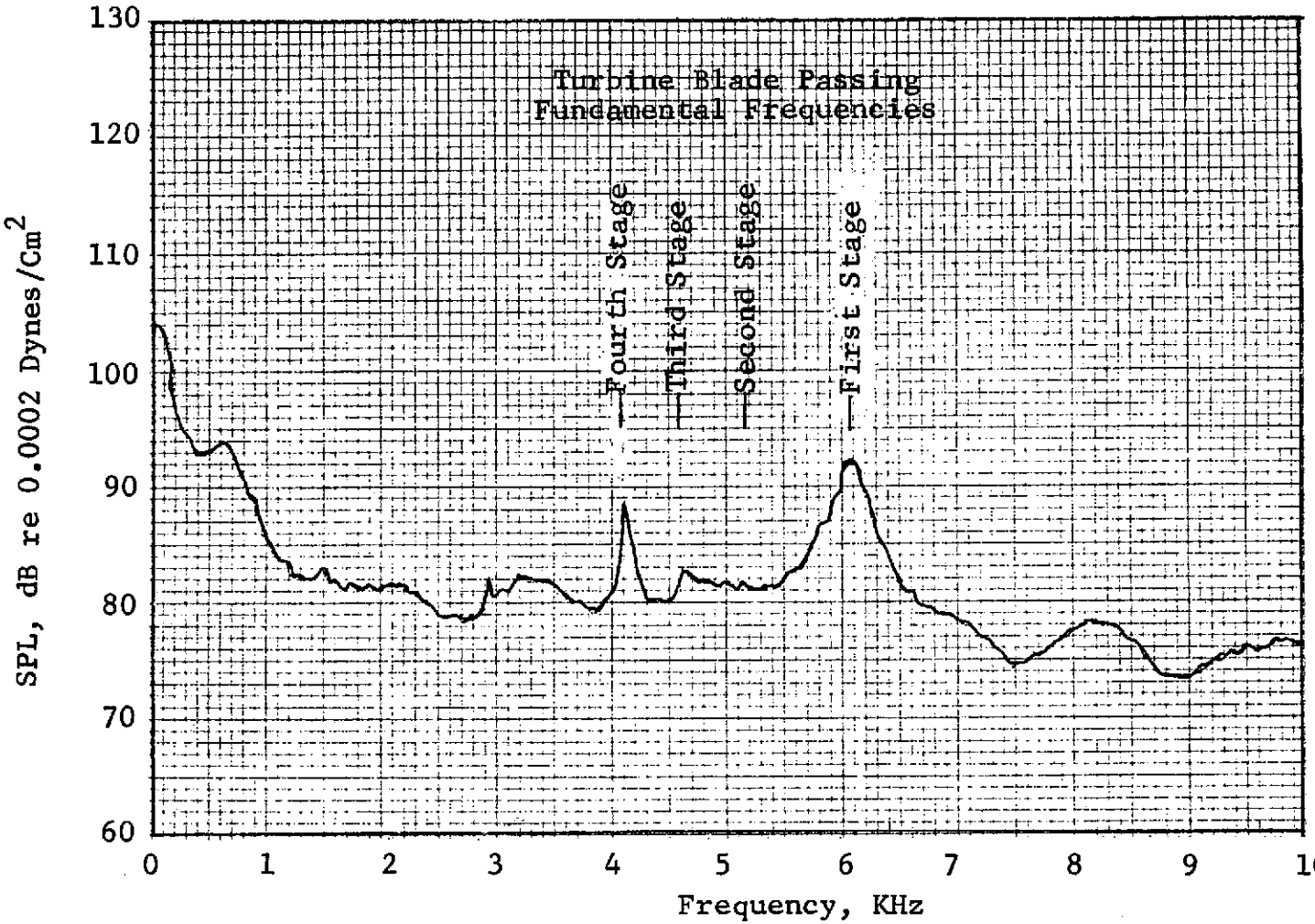

Figure 292. Engine A Nearfield Untreated Turbine Spectra (Approach Power, Position No. 6).

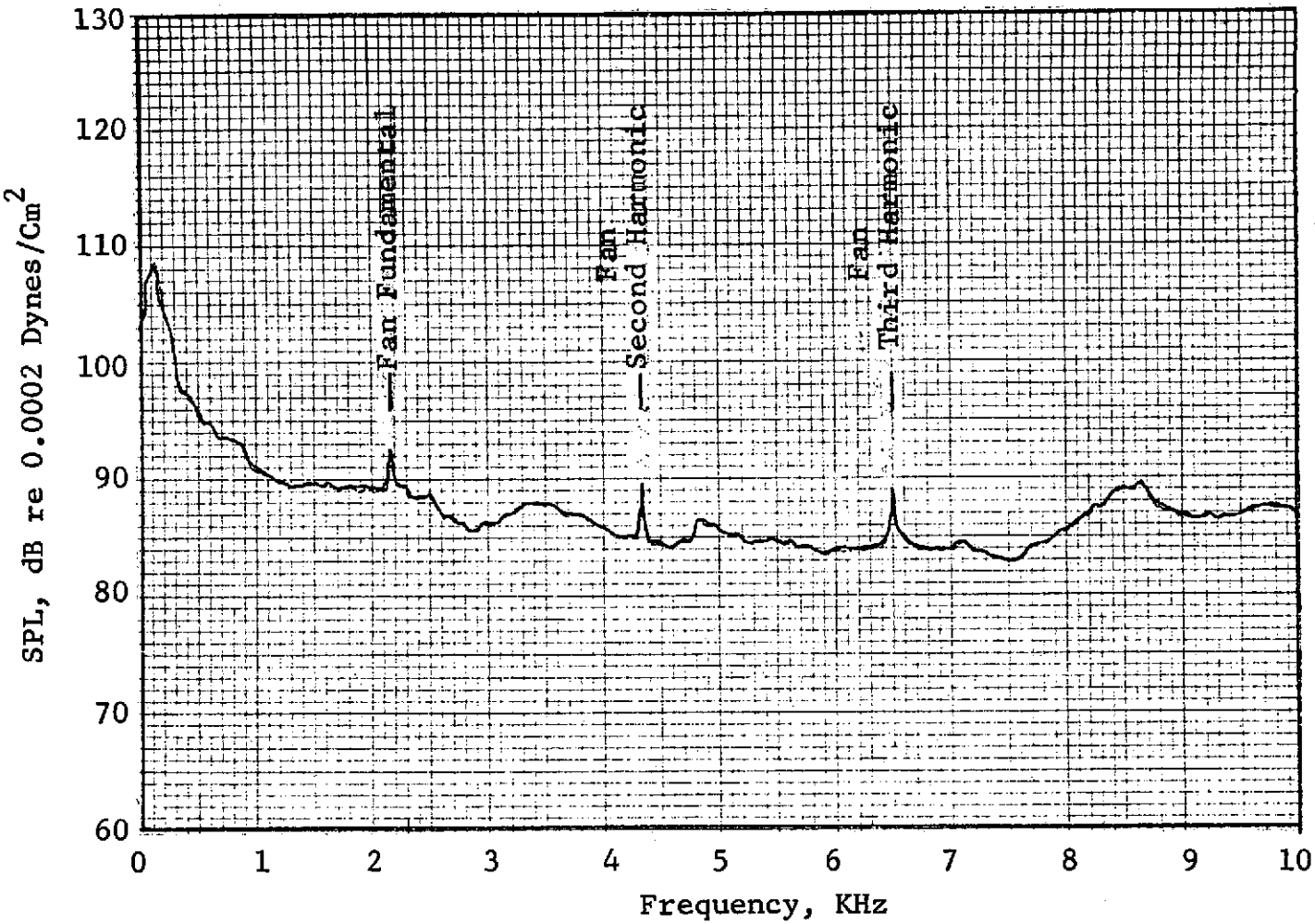

Figure 293. Engine A Nearfield Untreated Turbine Spectra (Takeoff Power, Position No. 1).

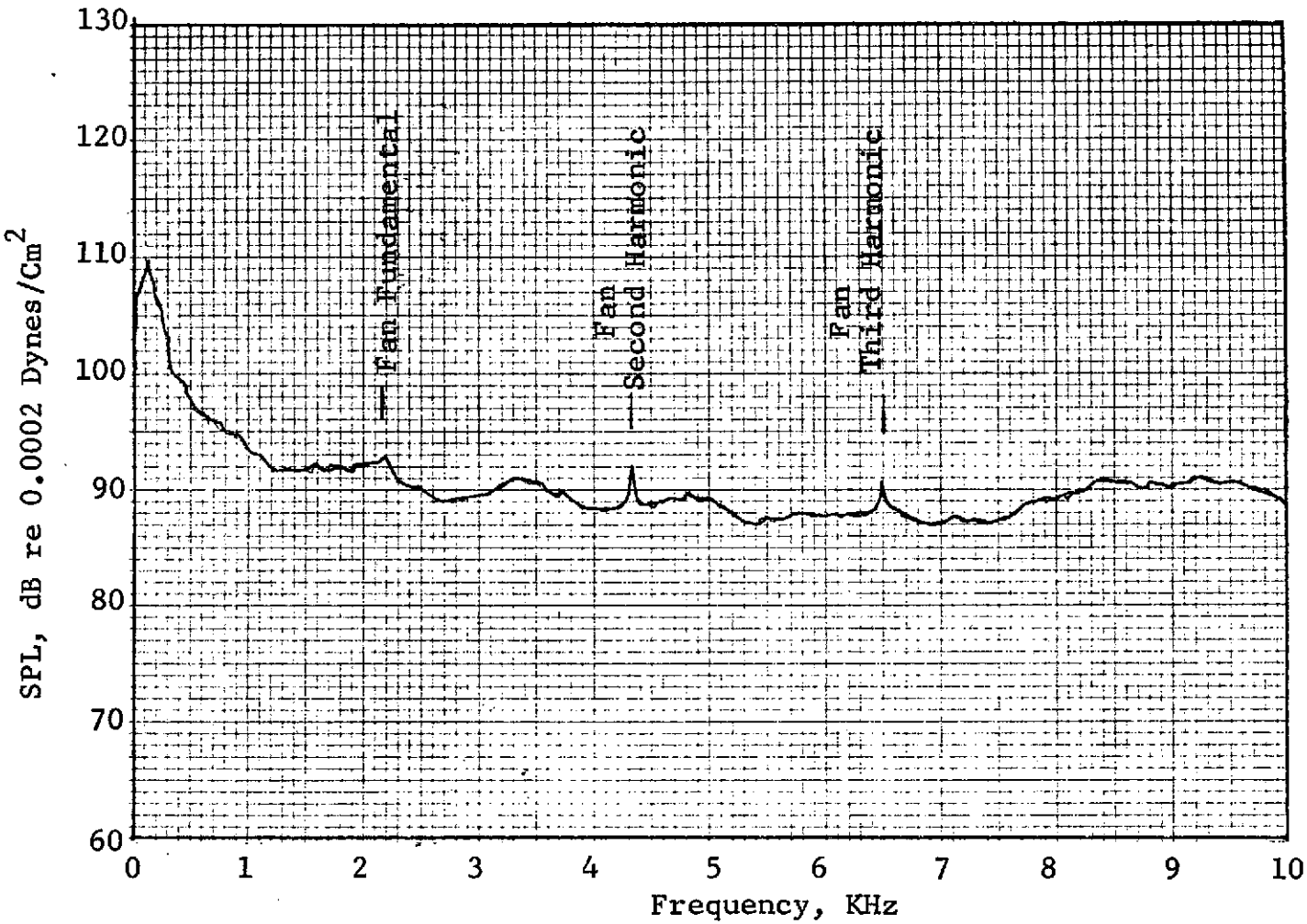

Figure 294. Engine A Nearfield Untreated Turbine Spectra (Takeoff Power, Position No. 2).

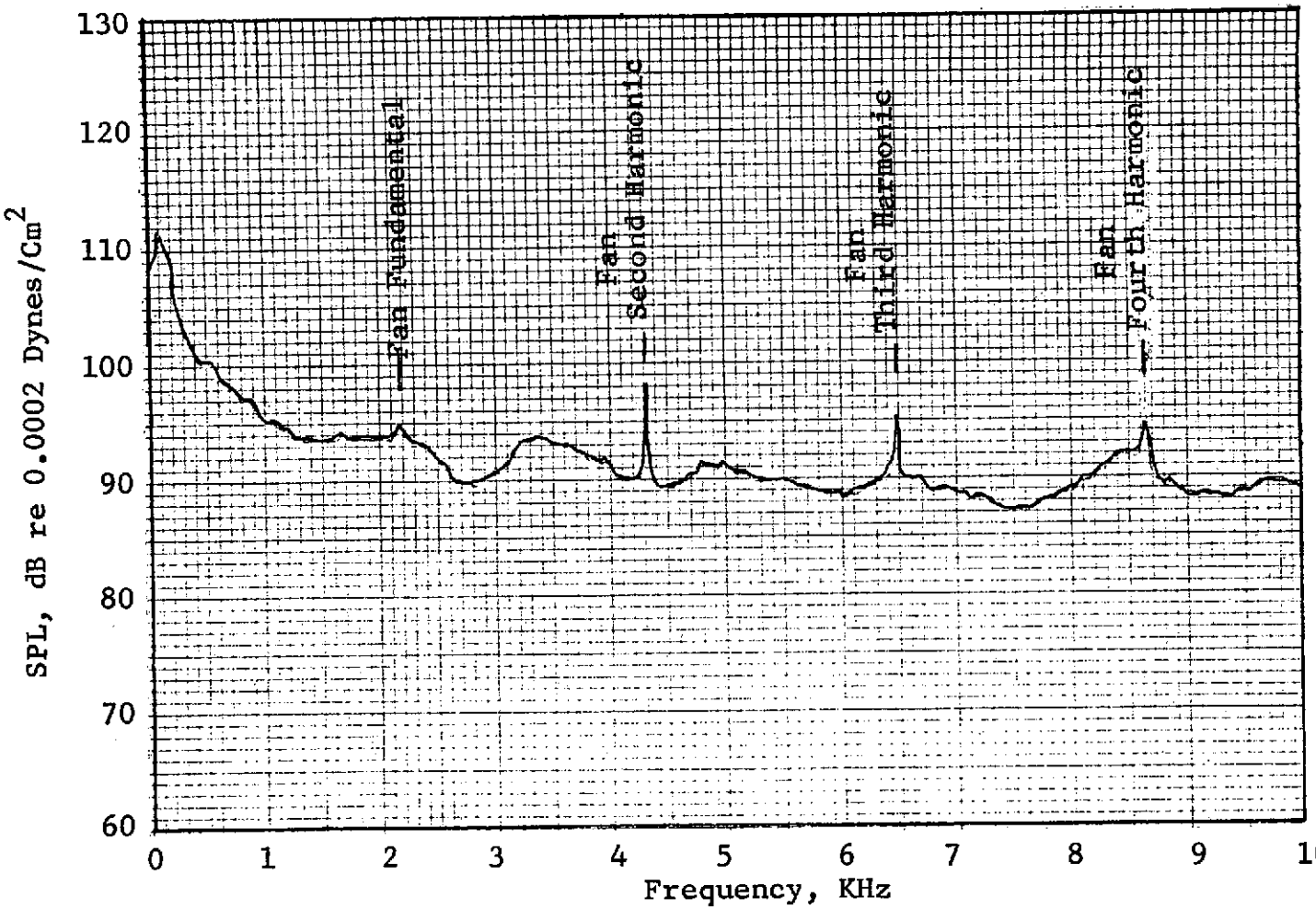

Figure 295. Engine A Nearfield Untreated Turbine Spectra (Takeoff Power, Position No. 3).

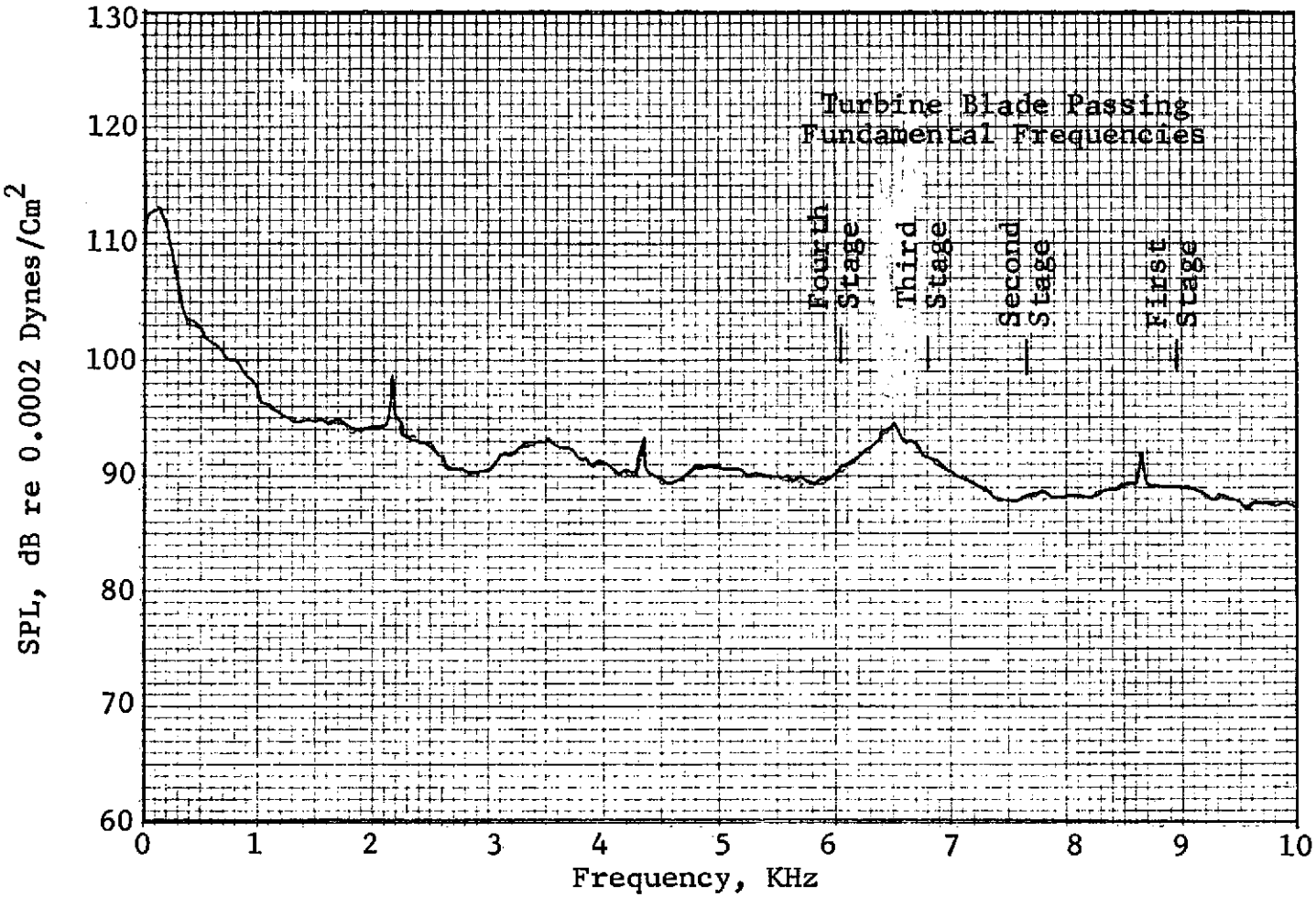

Figure 296. Engine A Nearfield Untreated Turbine Spectra (Takeoff Power, Position No. 4).

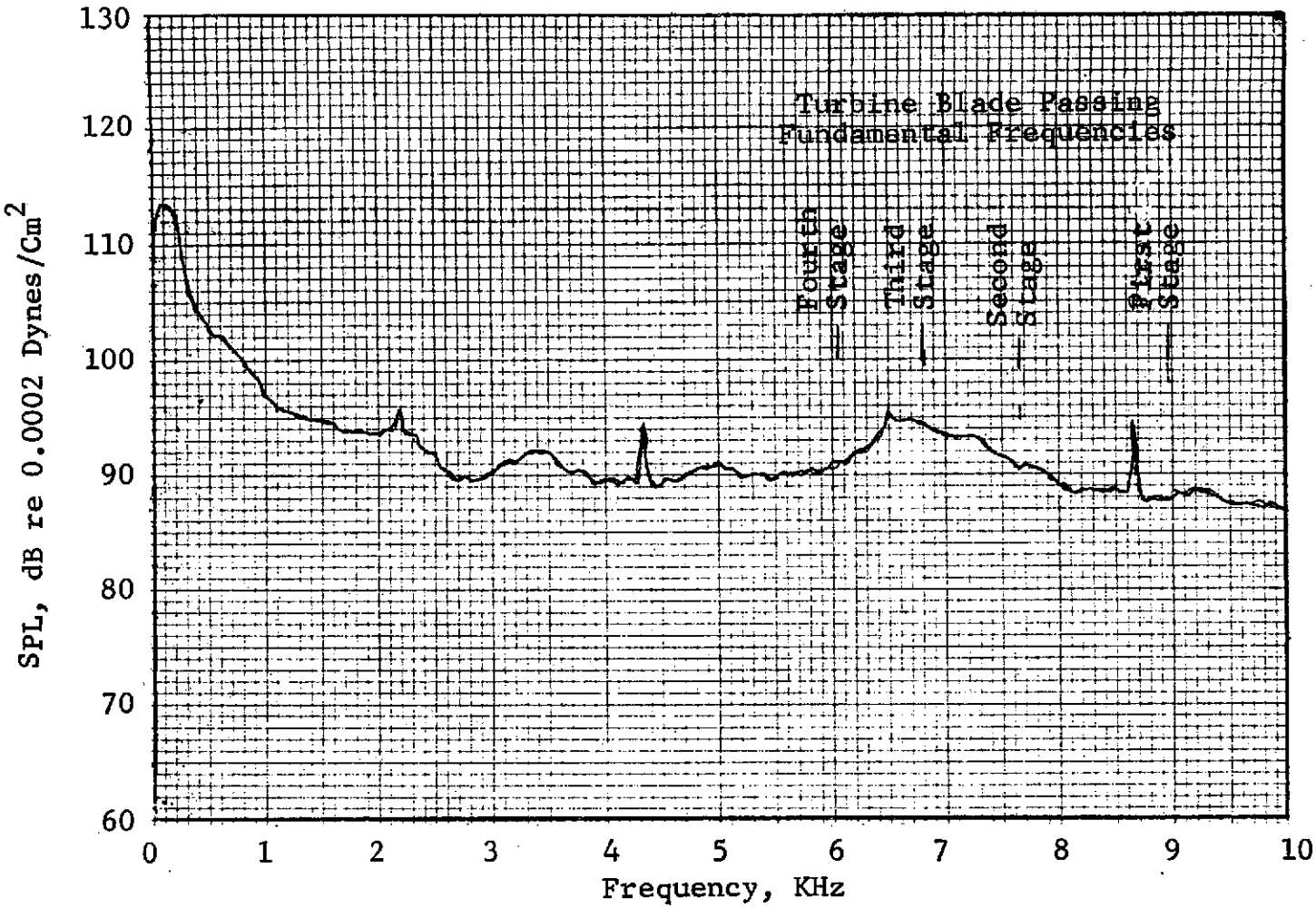

Figure 297. Engine A Nearfield Untreated Turbine Spectra (Takeoff Power, Position No. 5).

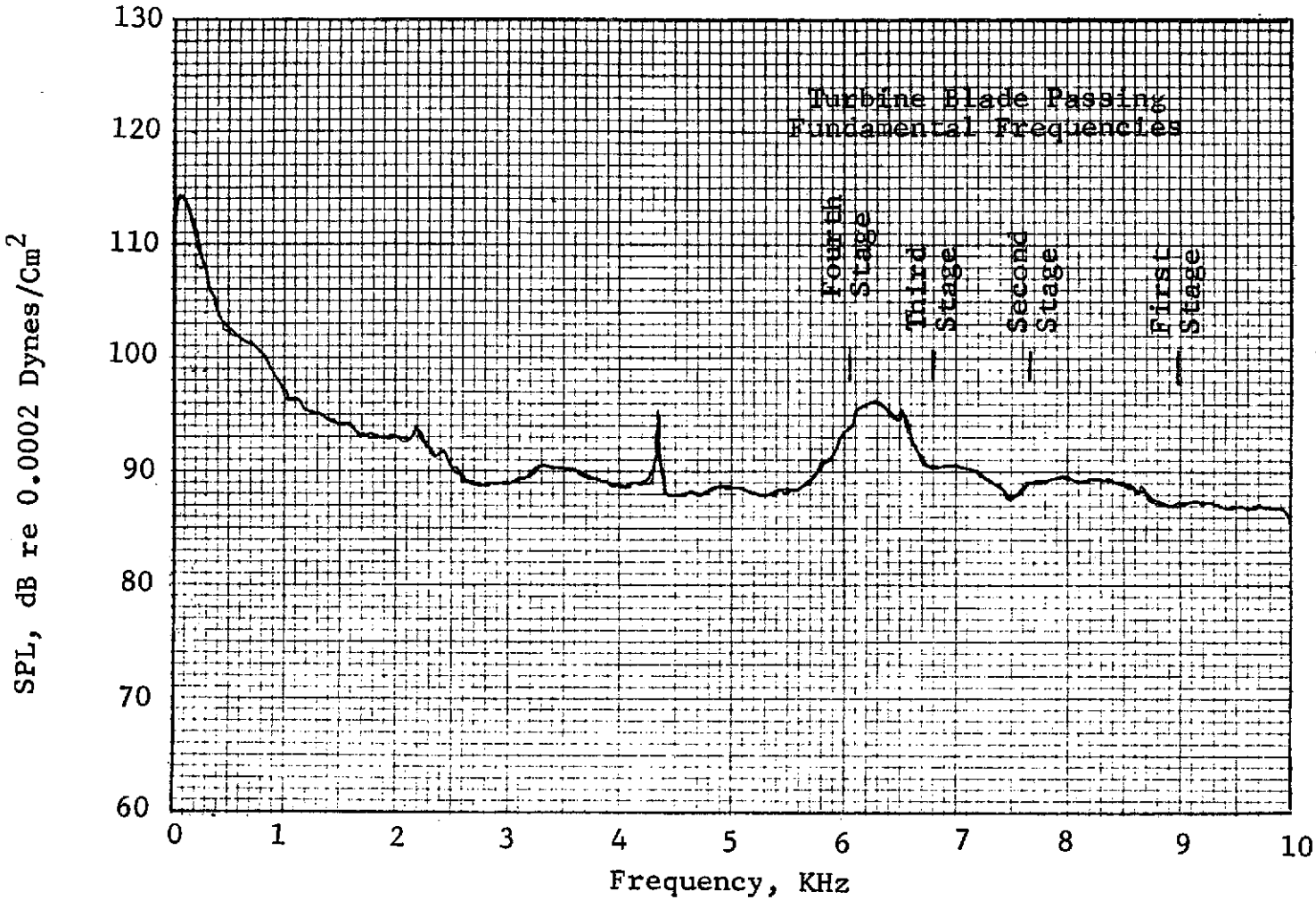

Figure 298. Engine A Nearfield Untreated Turbine Spectra (Takeoff Power, Position No. 6).

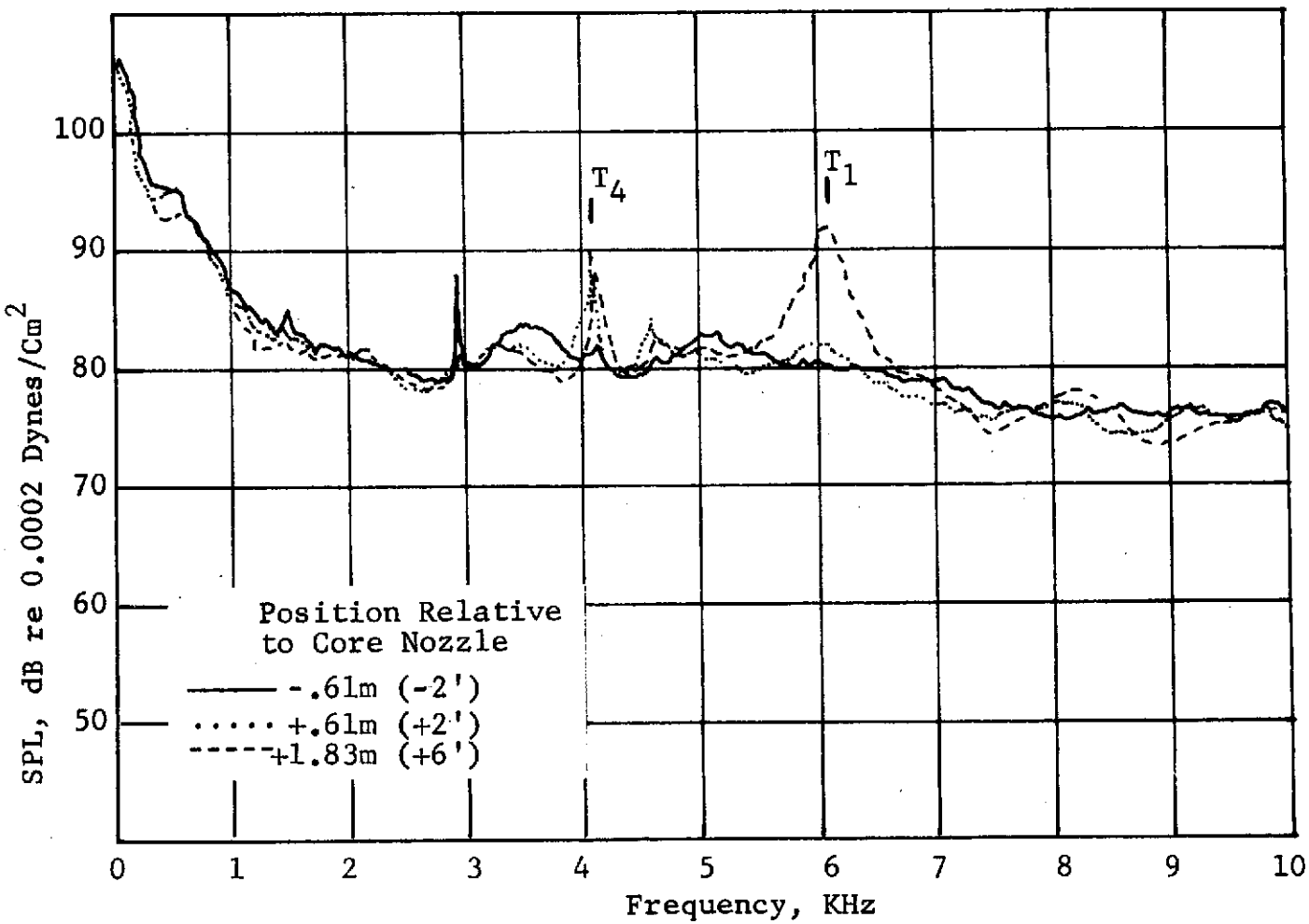

Figure 299. Engine A Directional Array Data at Approach Power, Hardwall Nozzle.

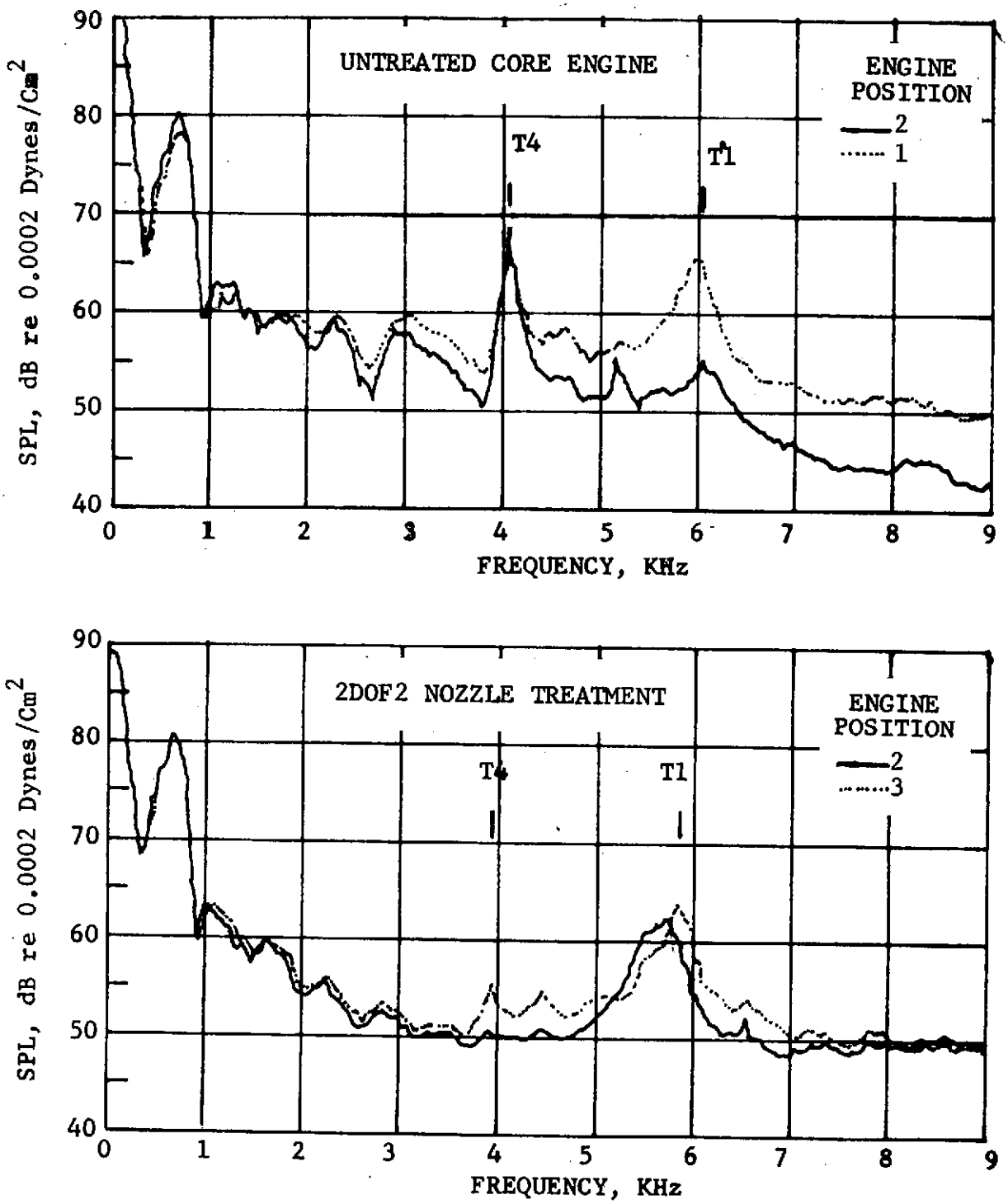

Figure 300. Engine A Directional Array Data at Approach Showing Source Position of Max. Core Noise Radiation 30.5m (100') Radius, 120 Degrees.

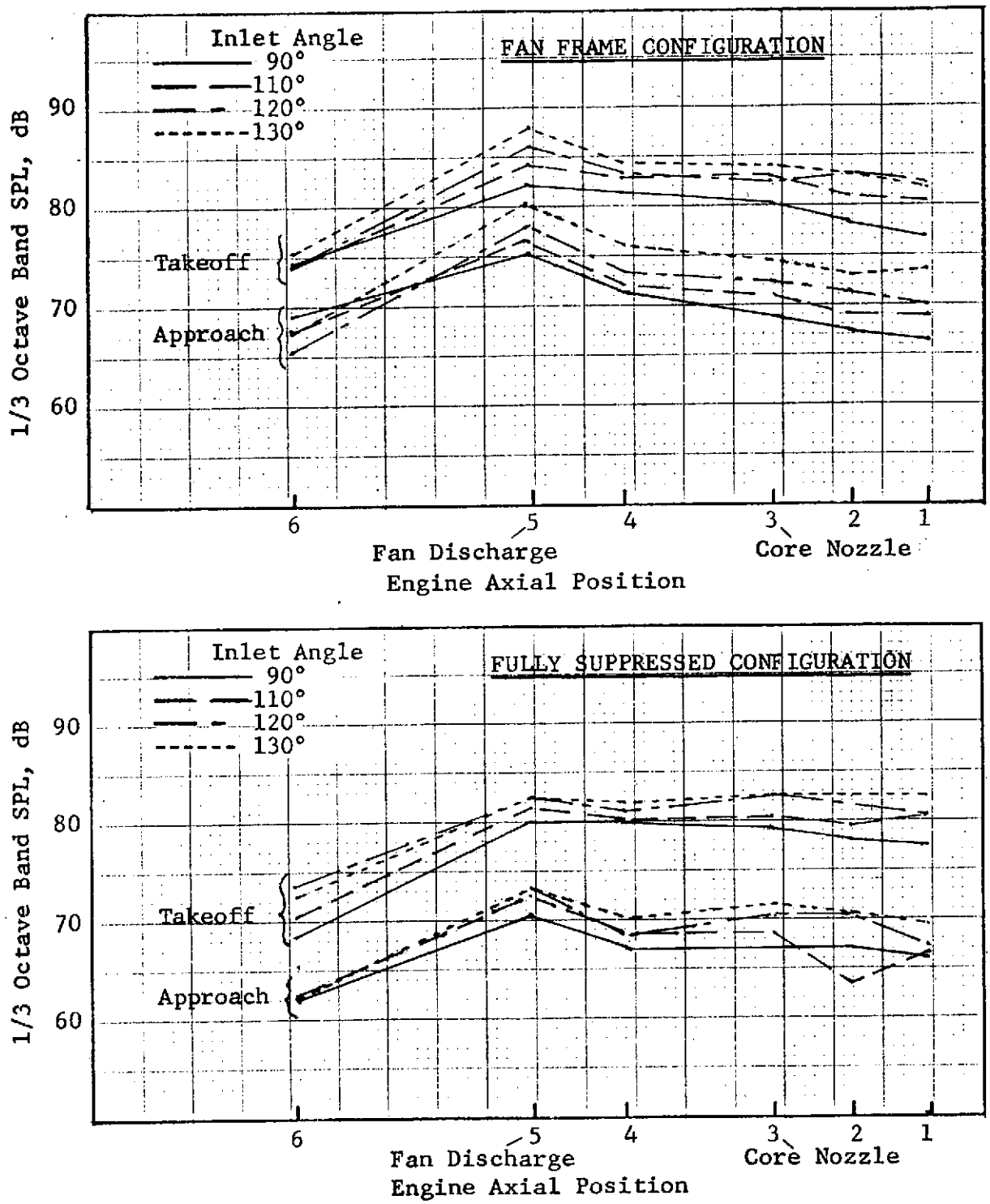

Figure 301. Array Measured Broadband Directivity of Engine A (1600 Hz, 30.5m (100') Radius).

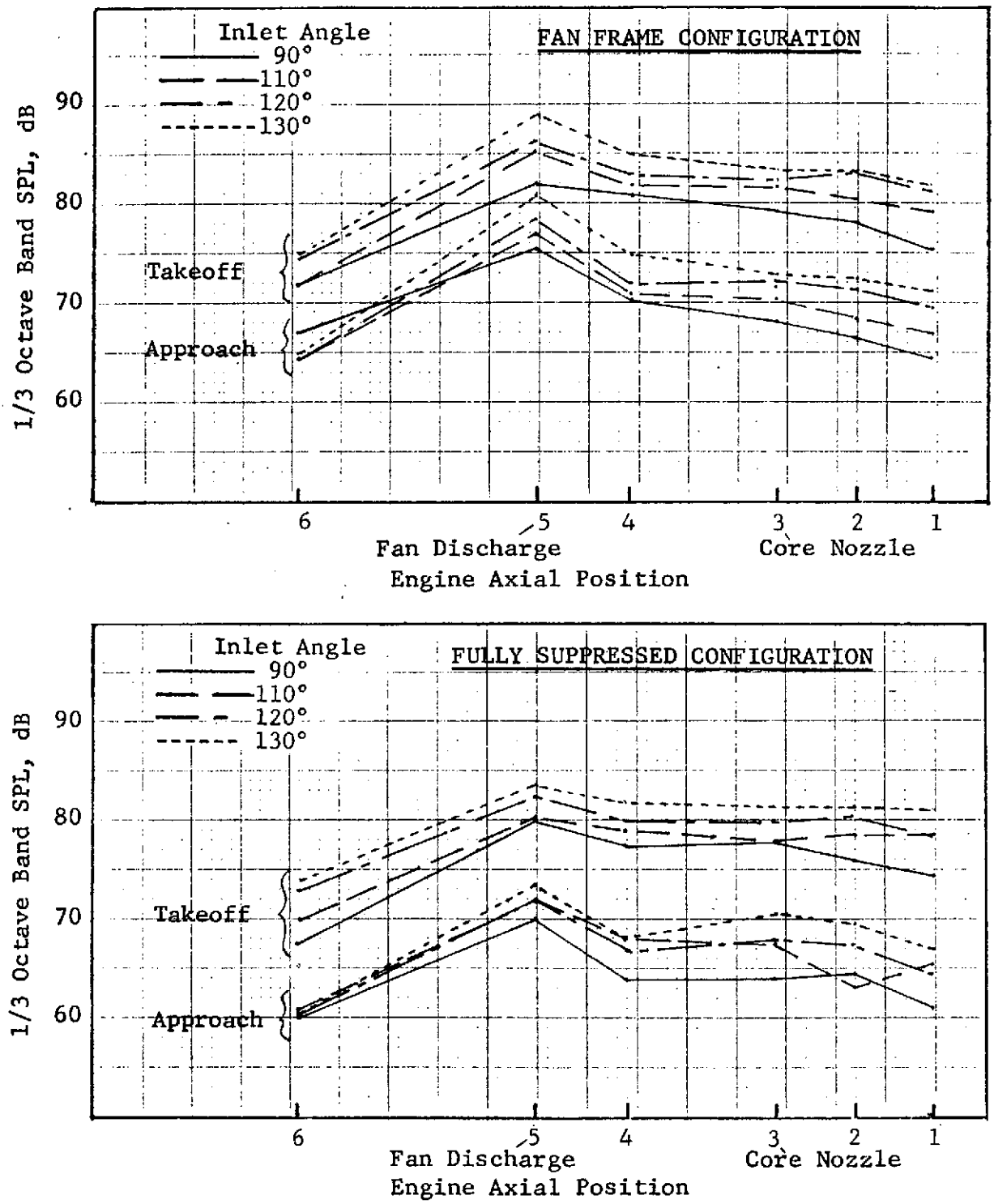

Figure 302. Array Measured Broadband Directivity of Engine A (2000 Hz, 30.5m (100') Radius).

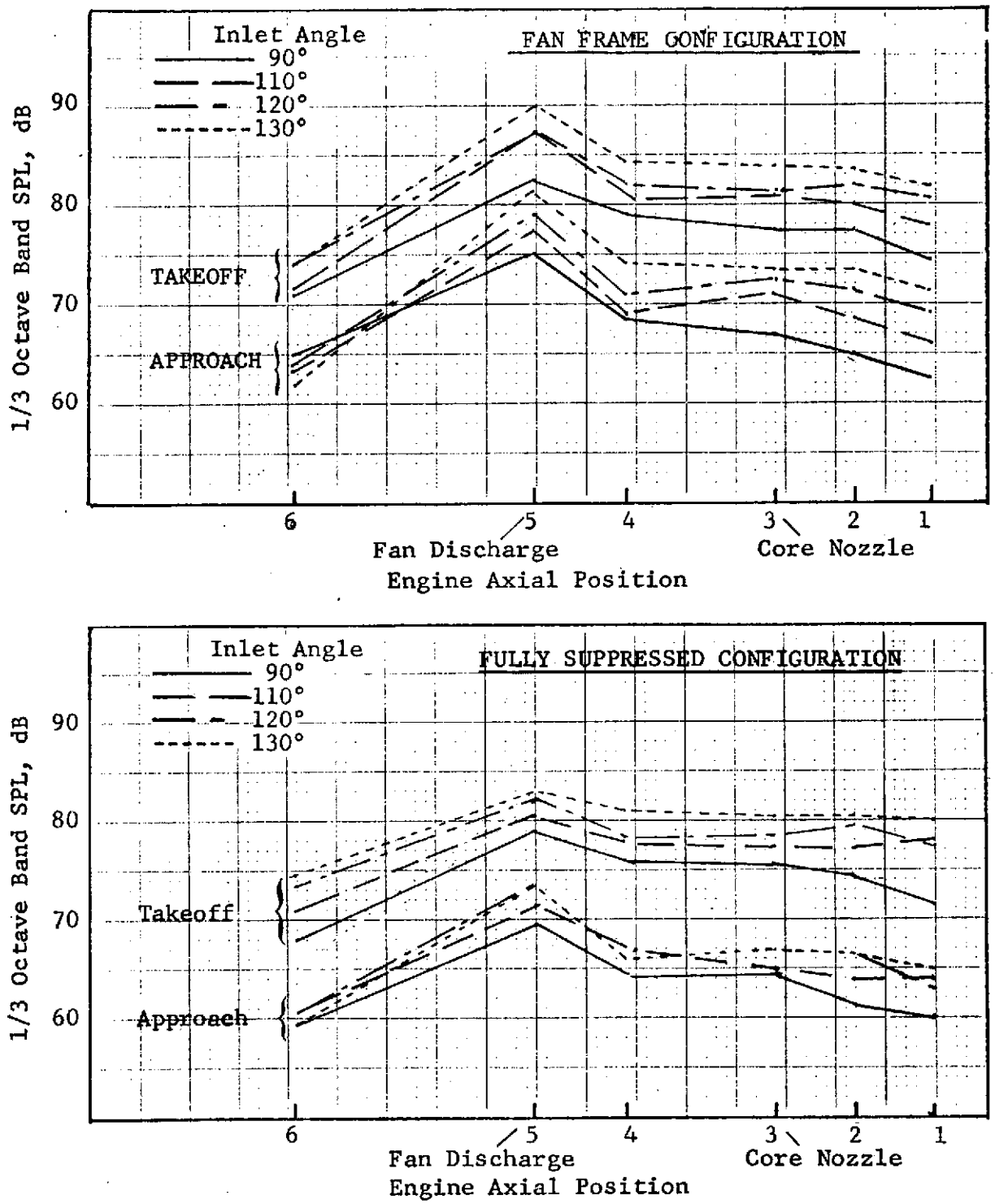

Figure 303. Array Measured Broadband Directivity of Engine A (2500 Hz, 30.5m (100') Radius).

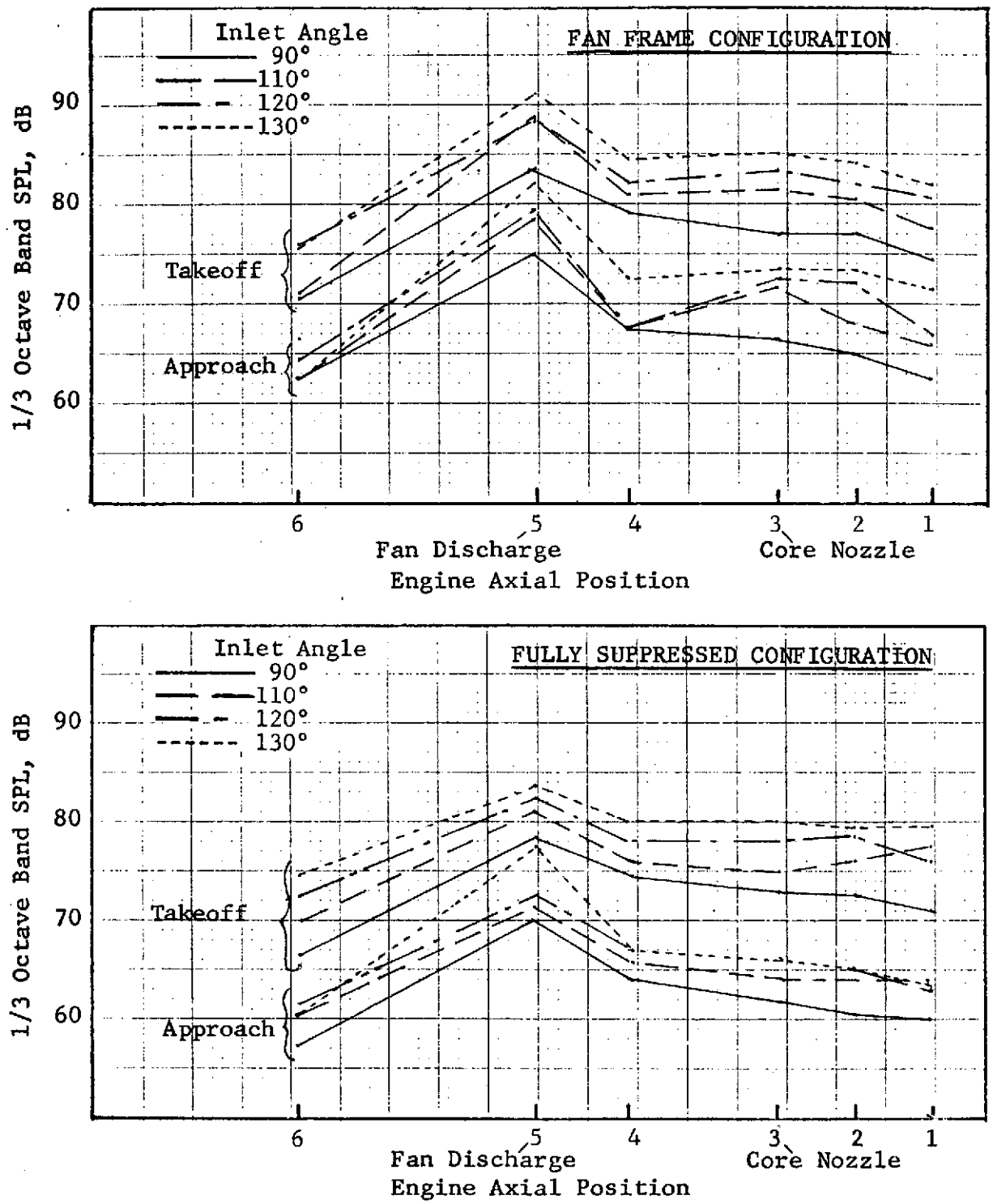

Figure 304. Array Measured Broadband Directivity of Engine A (3150 Hz, 30.5m (100') Radius).

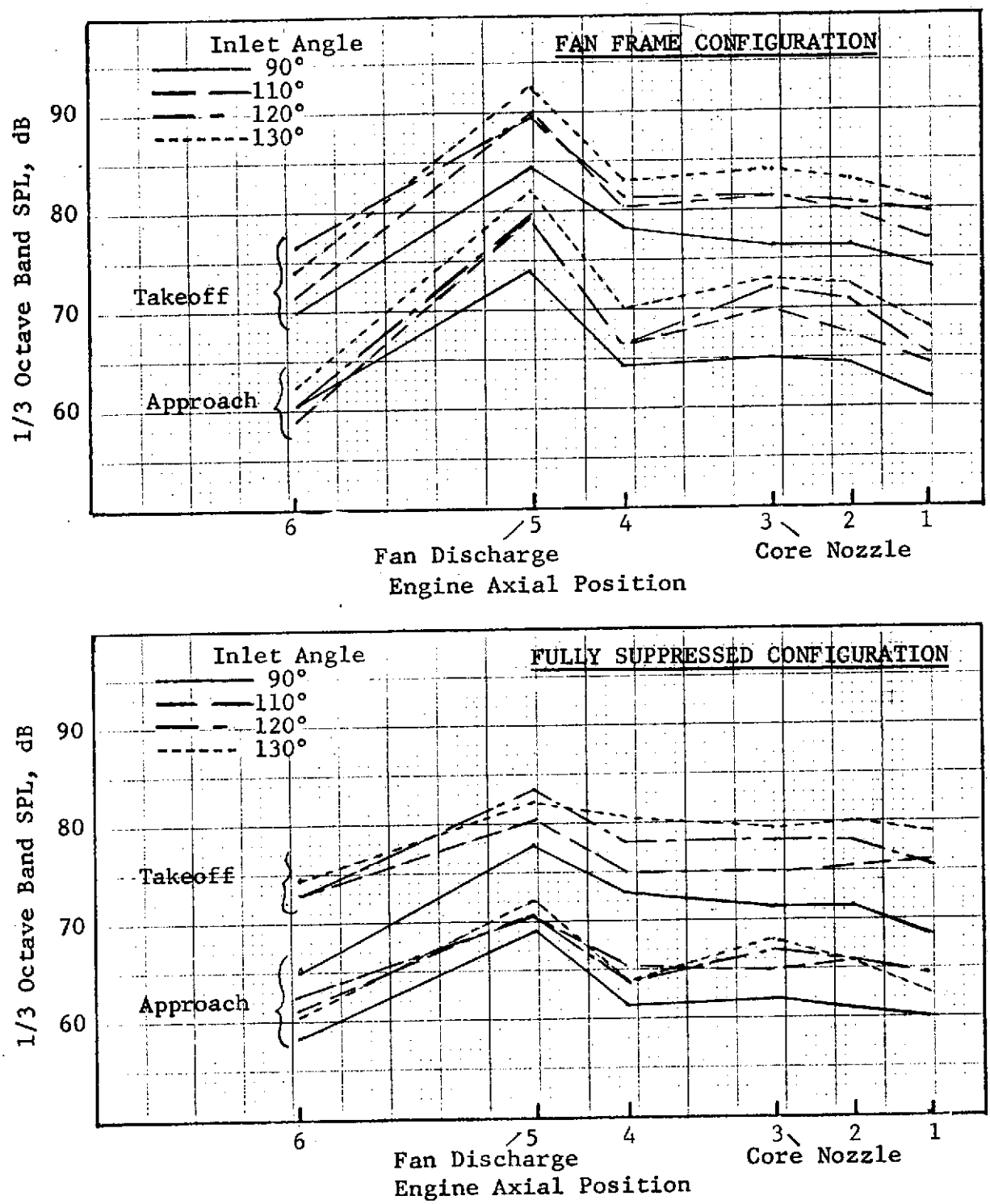

Figure 305. Array Measured Broadband Directivity of Engine A (4000 Hz, 30.5m (100') Radius).

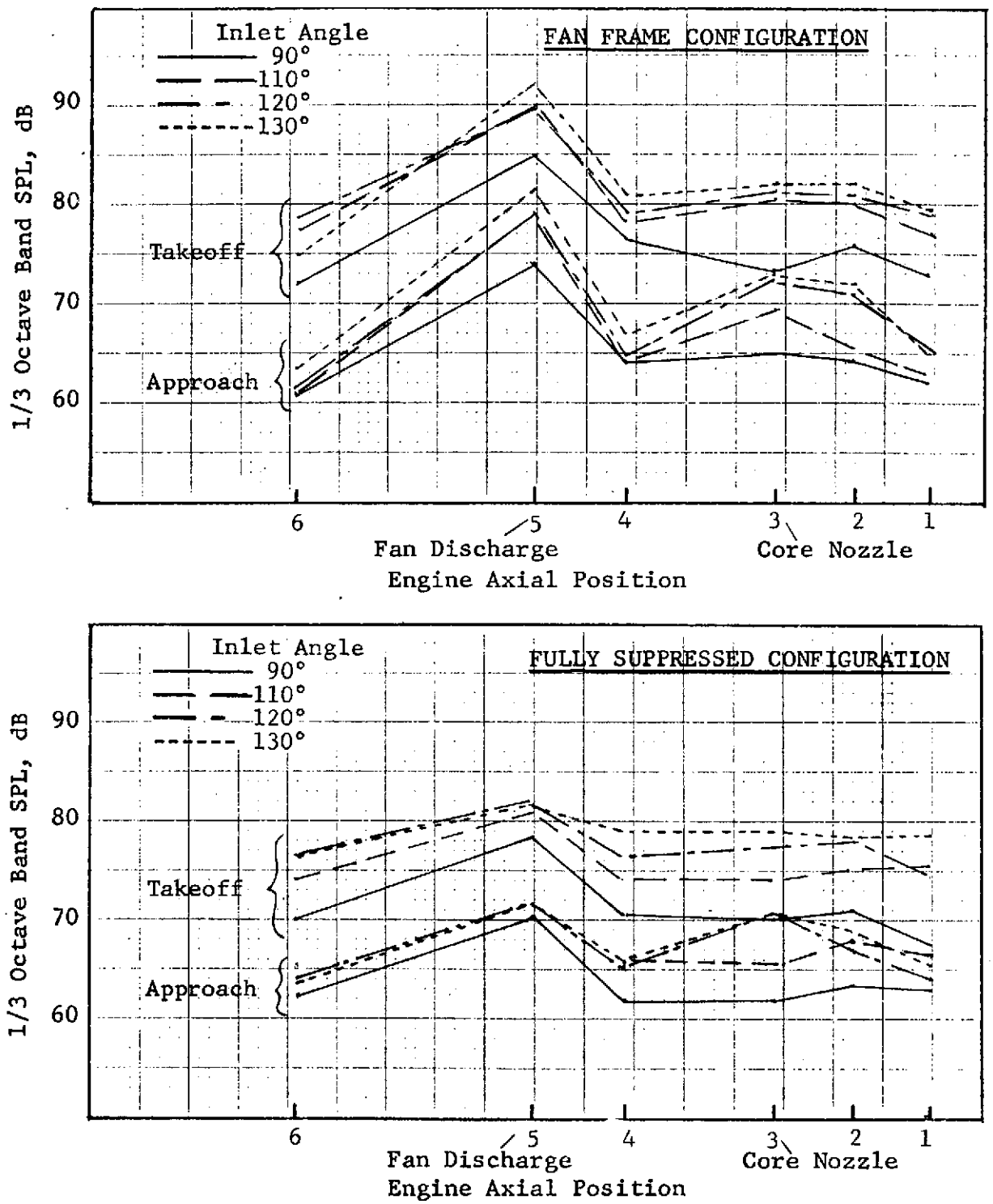

Figure 306. Array Measured Broadband Directivity of Engine A (5000 Hz, 30.5m (100') Radius).

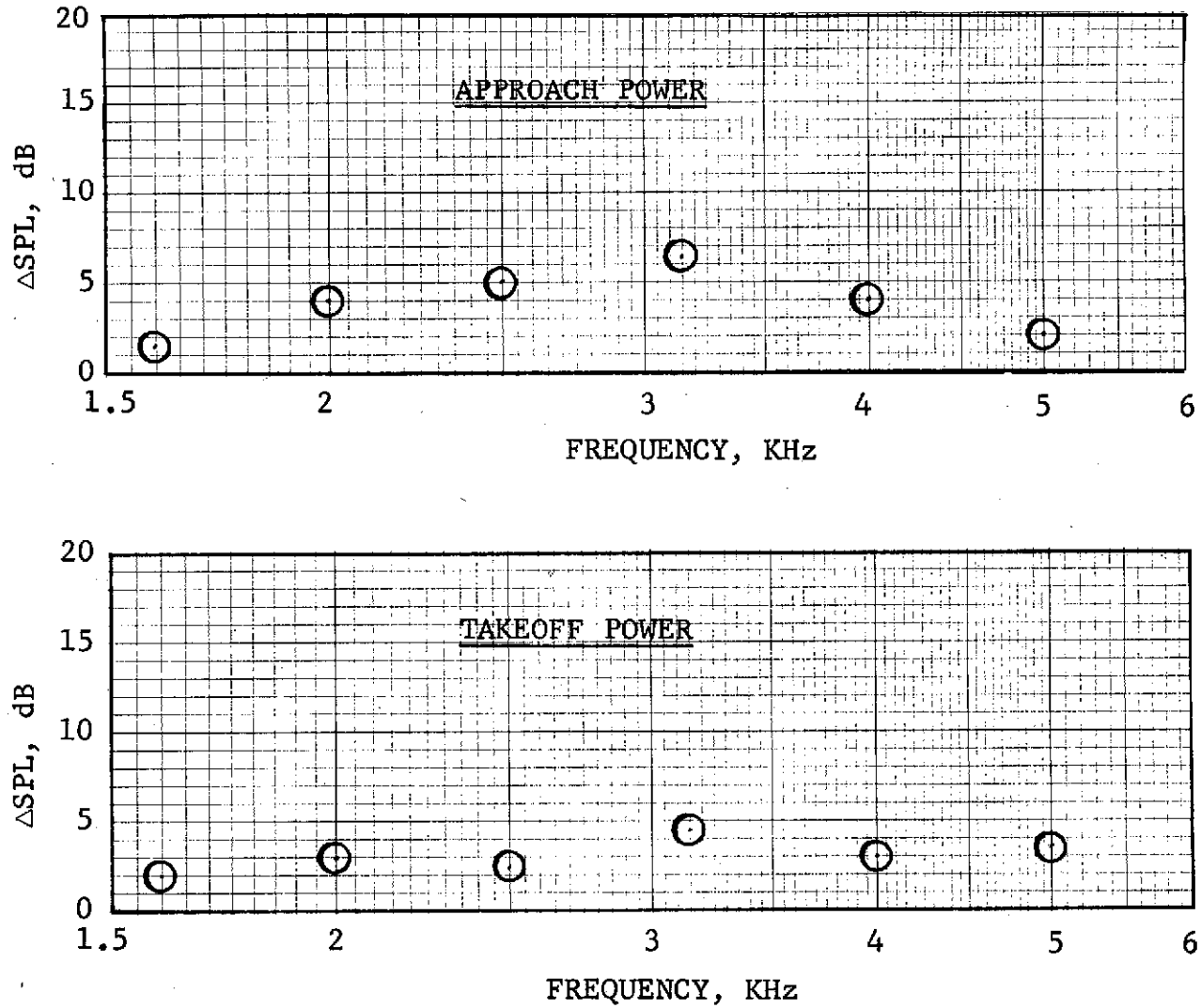

Figure 307. Engine A Directional Array Measured Broadband Core Noise Suppression at 120° (Double Sandwich II Turbine Treatment Vs. Untreated Configuration).

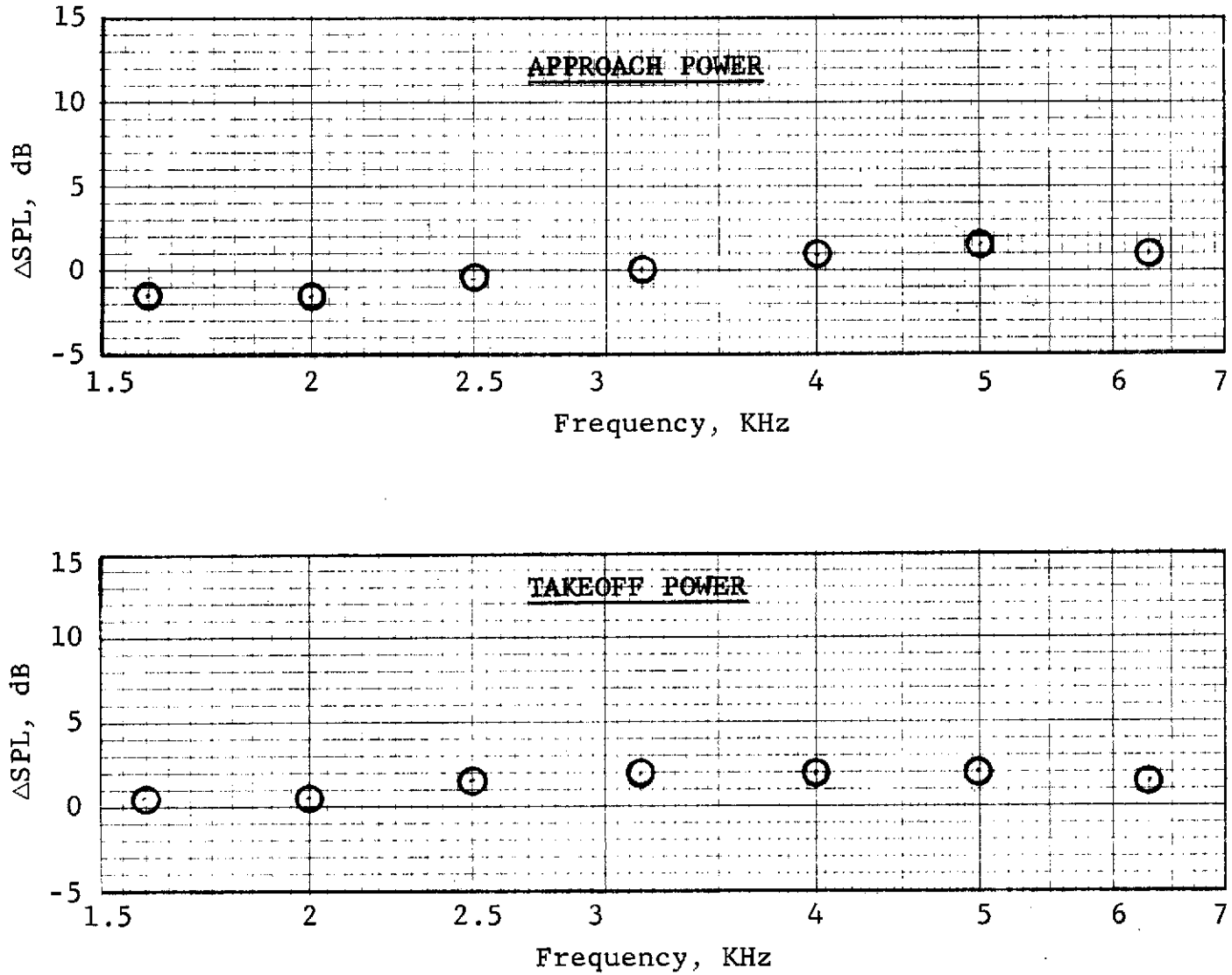

Figure 308. Engine A Directional Array Measured Broadband Core Noise Suppression at 130° (Cerafelt Turbine Treatment Vs. Untreated Configuration).

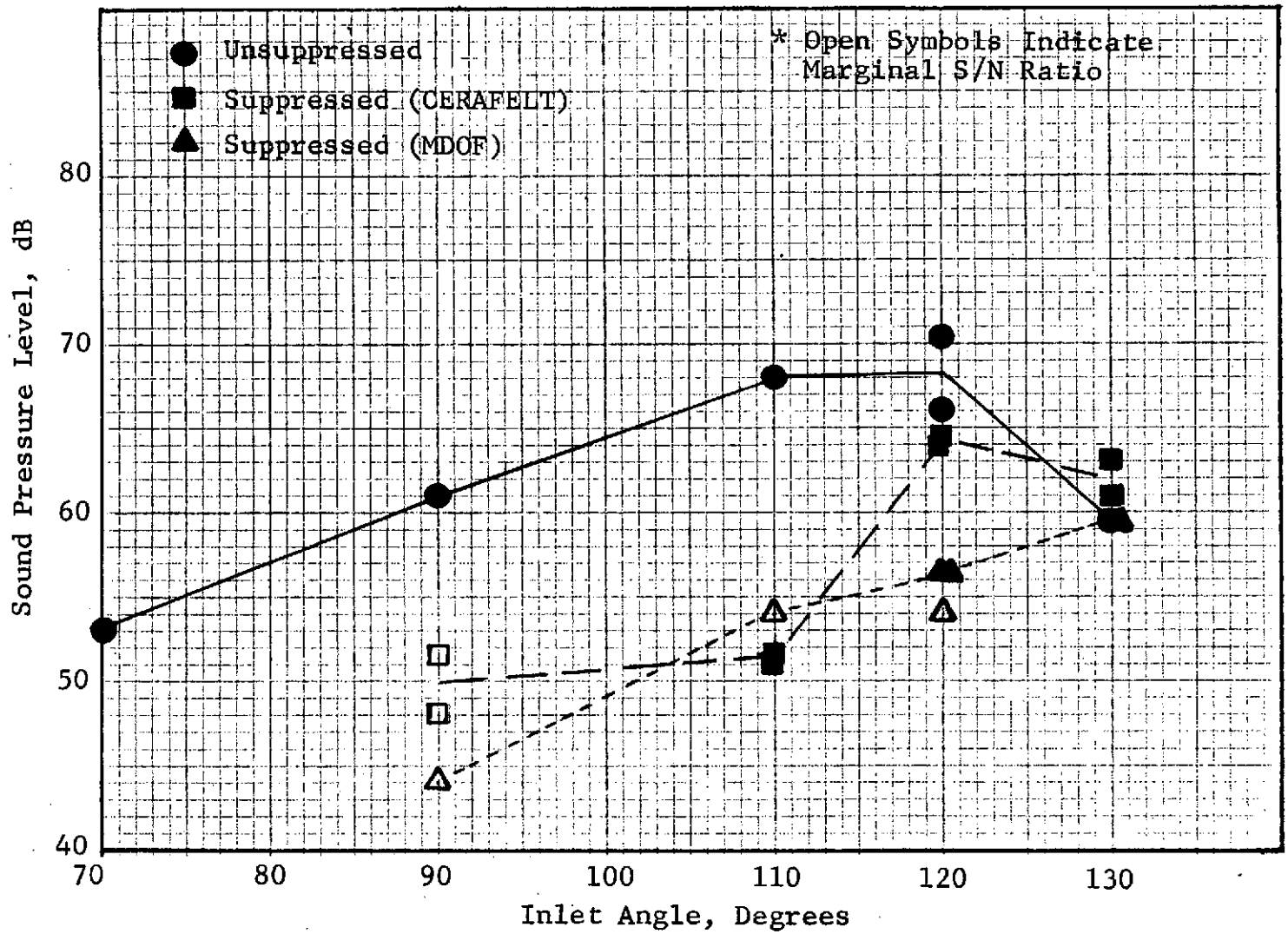

Figure 309. Engine A Fourth Stage Turbine Blade Passing Frequency Directivity at Approach (Approximately 30.5 m (100') Radius).

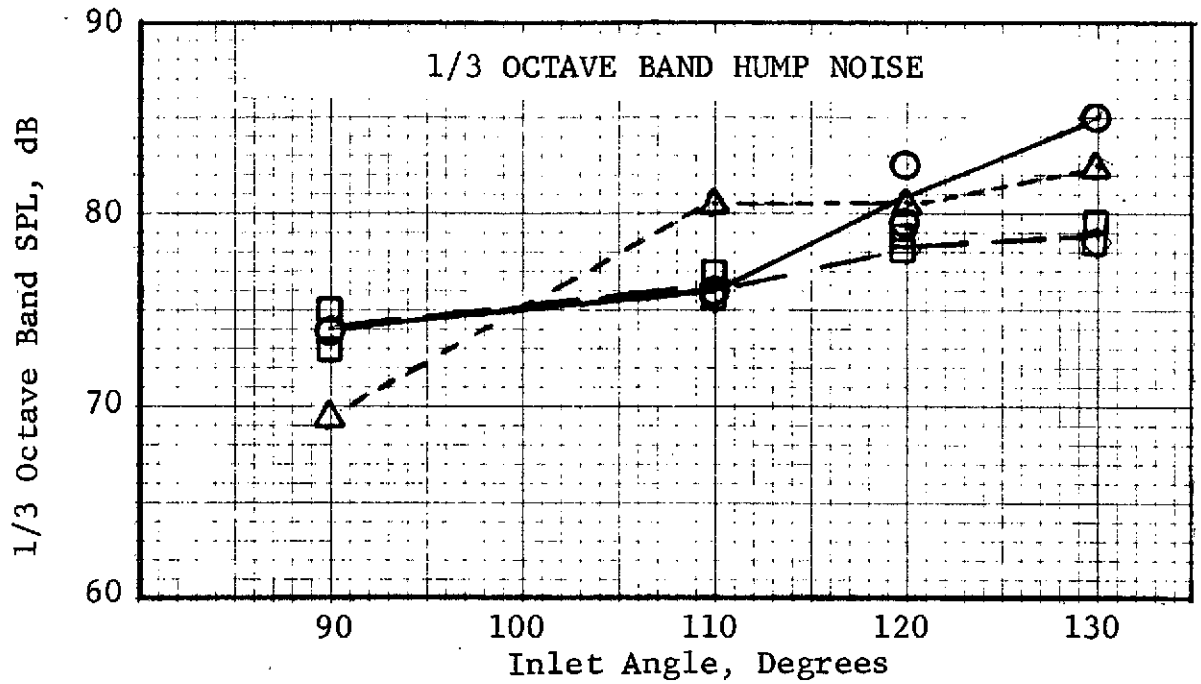

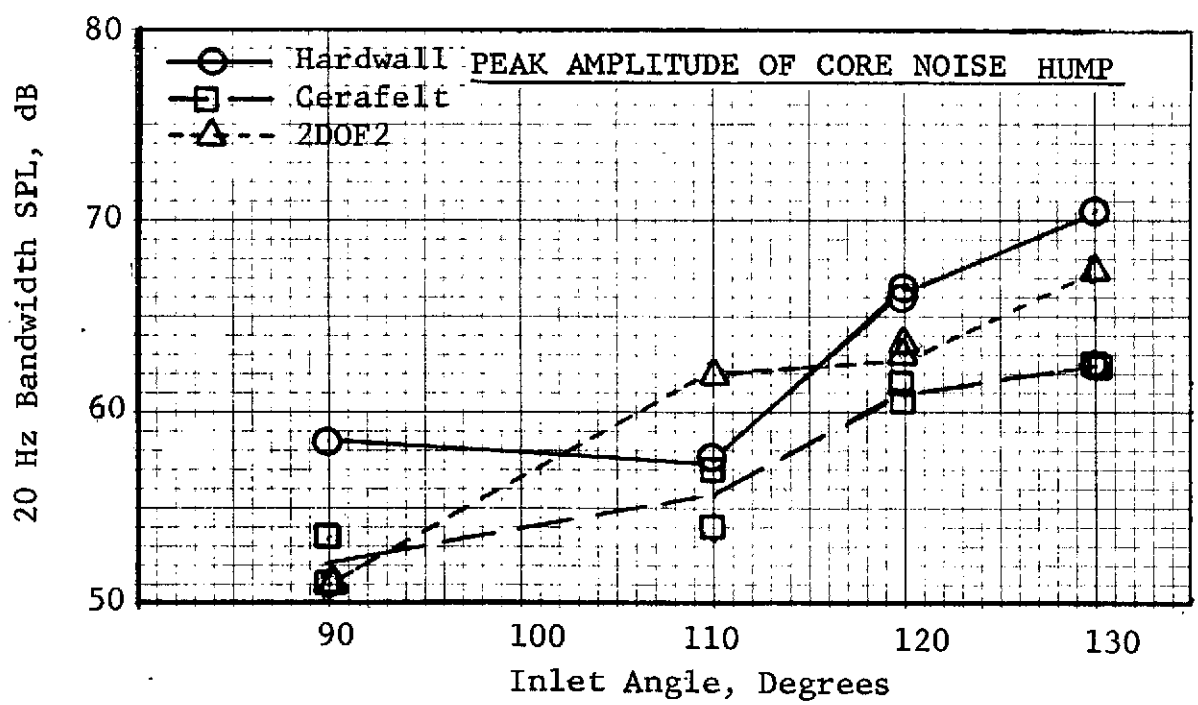

Figure 310. Engine A Suppression of "First Stage Hump" Measured with Directional Array at Approach Power.

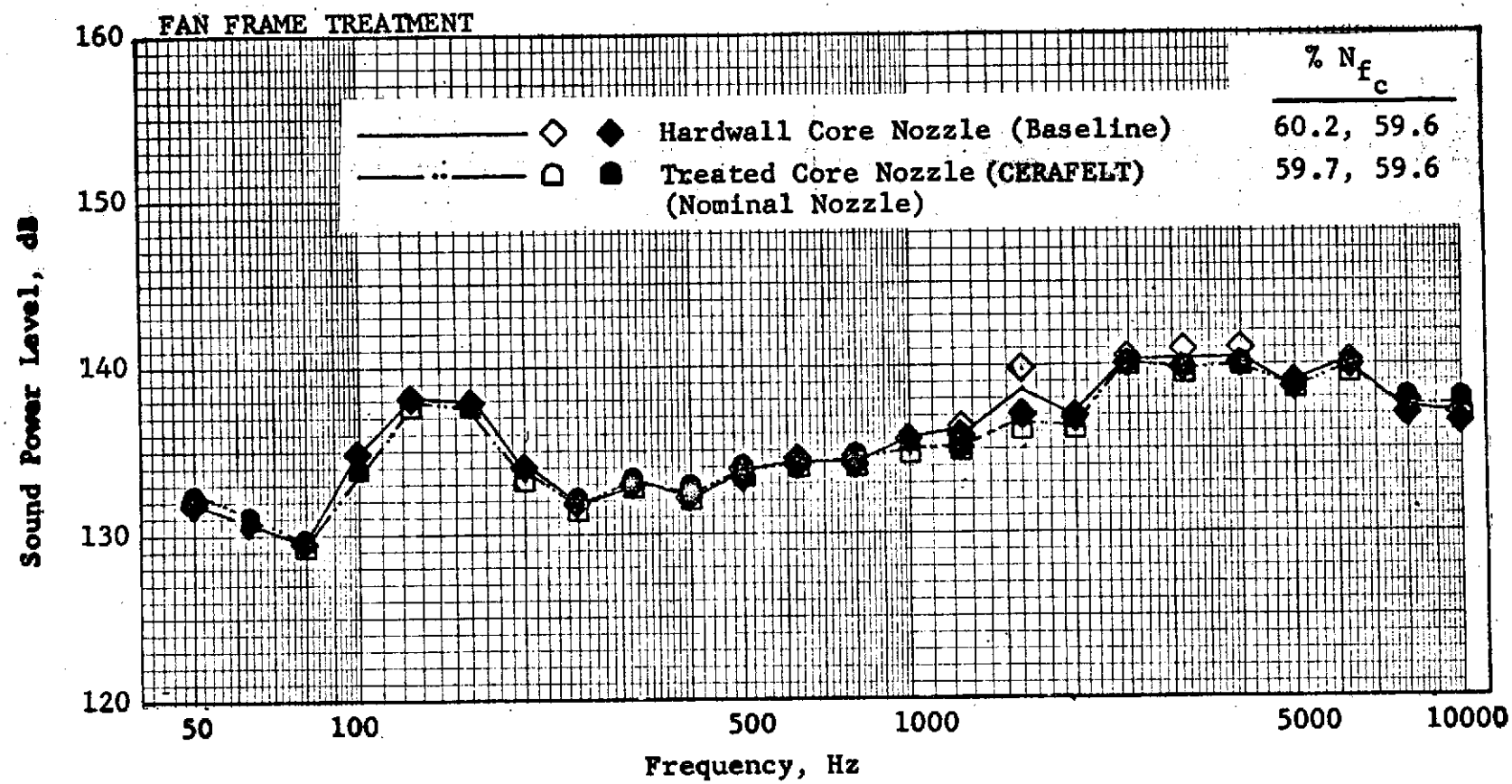

Figure 311. Engine A Sound Power Level Spectra Treated Vs. Hardwall Core Nozzle (Fan Frame Treatment) at 60% N_{f_c} Standard Day.

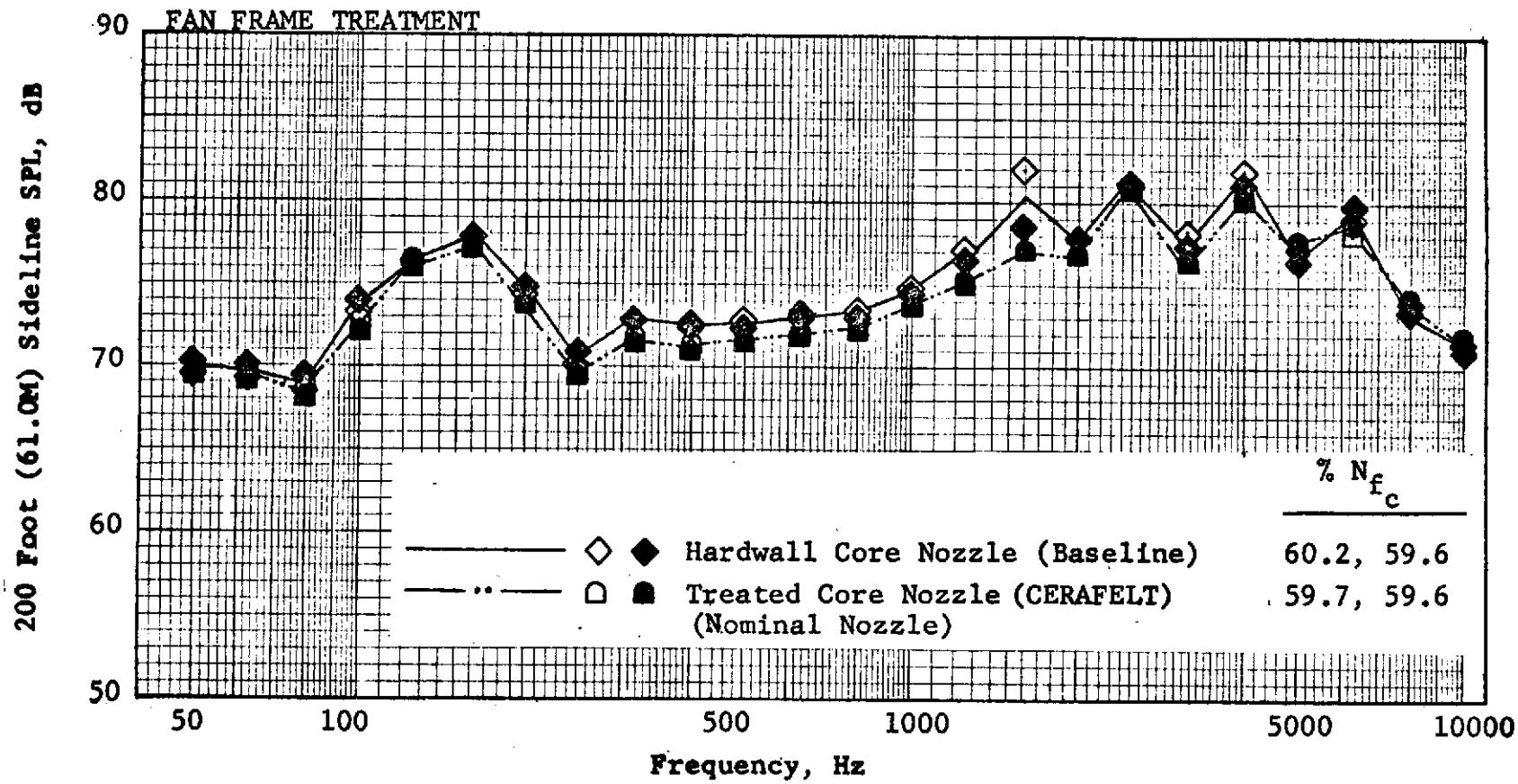

Figure 312. Engine A Sound Power Level Spectra at 50° Treated Vs. Hardwall Core Nozzle (Fan Frame Treatment) at 60% N_{f_c} Standard Day.

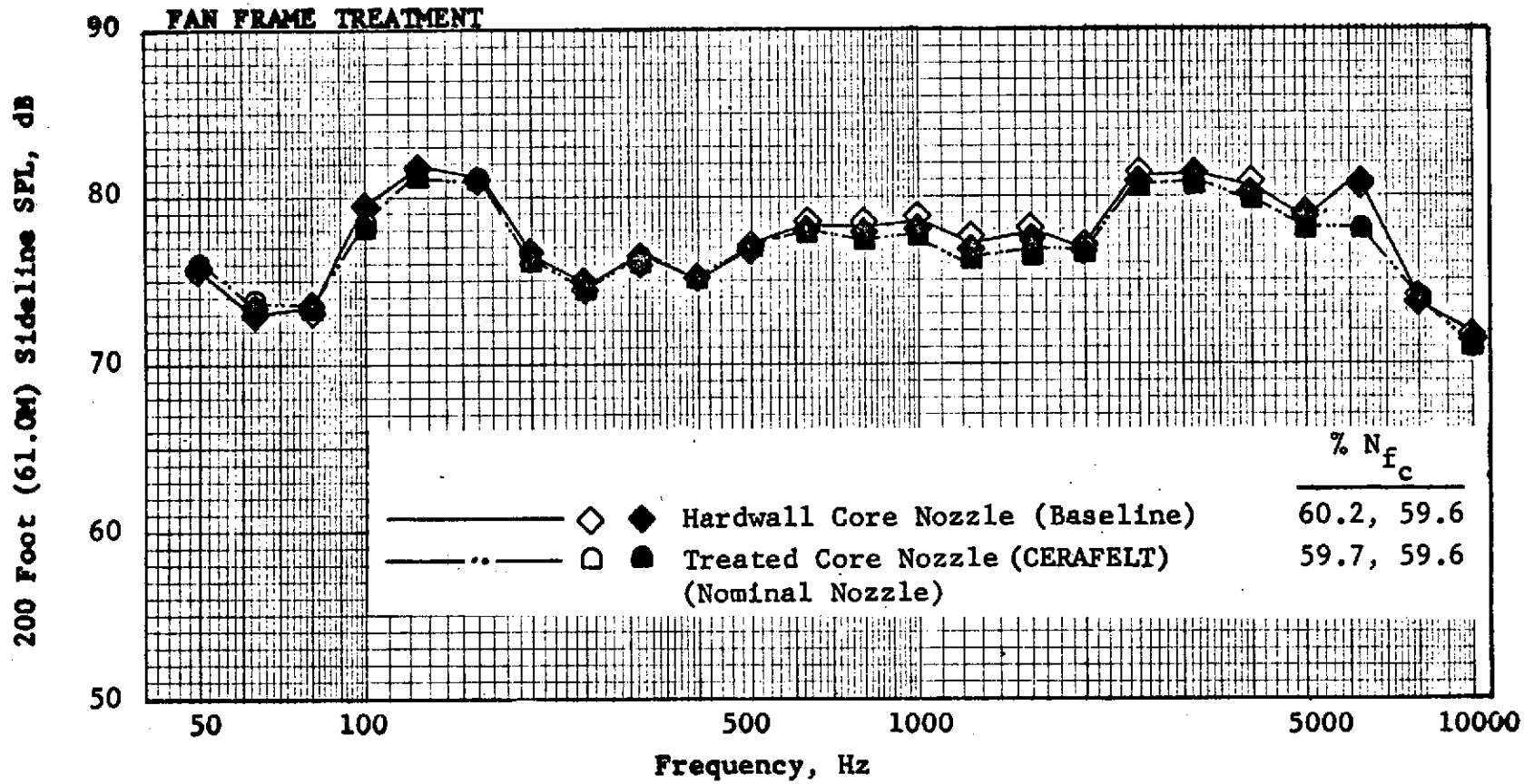

Figure 313. Engine A Sound Power Level Spectra at 120° Treated Vs. Hardwall Core Nozzle (Fan Frame Treatment) at 60% N_{f_c} Standard Day.

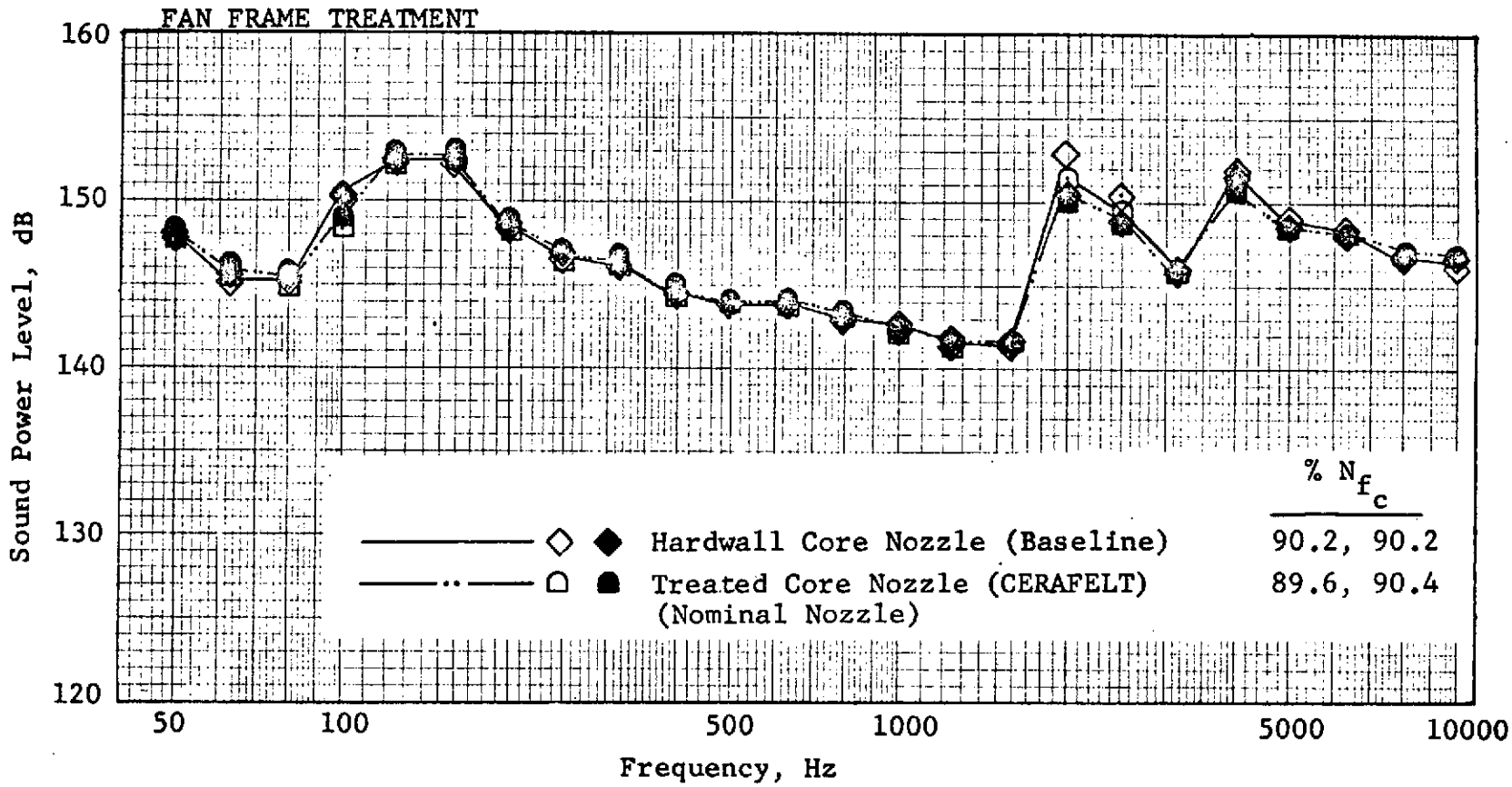

Figure 314. Engine A Sound Power Level Spectra Treated Vs. Hardwall Core Nozzle (Fan Frame Treatment) at 90% N_{f_c} Standard Day.

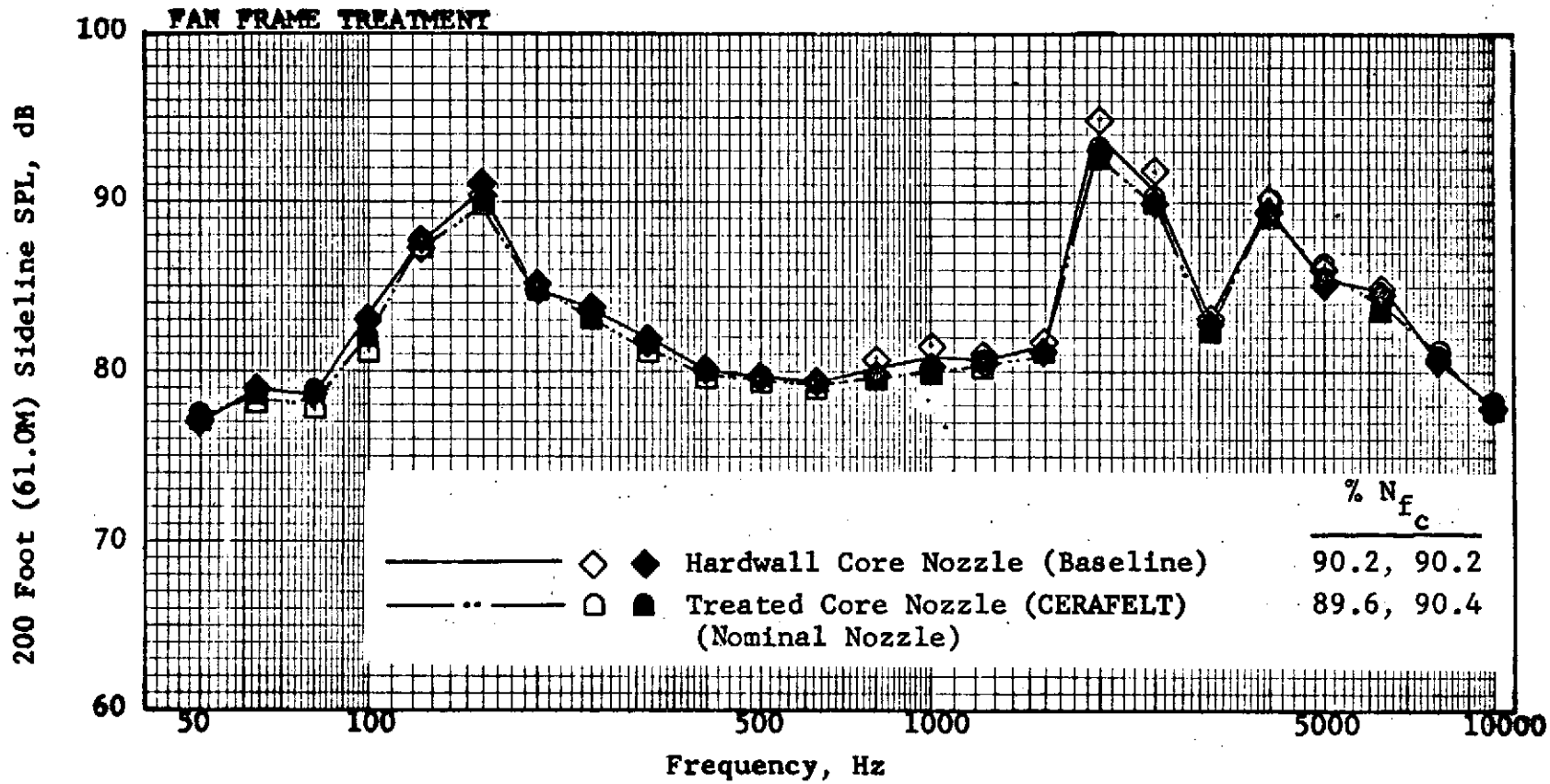

Figure 315. Engine A Sound Power Level Spectra at 50° Treated Vs. Hardwall Core Nozzle (Fan Frame Treatment) at 90% N_{f_c} Standard Day.

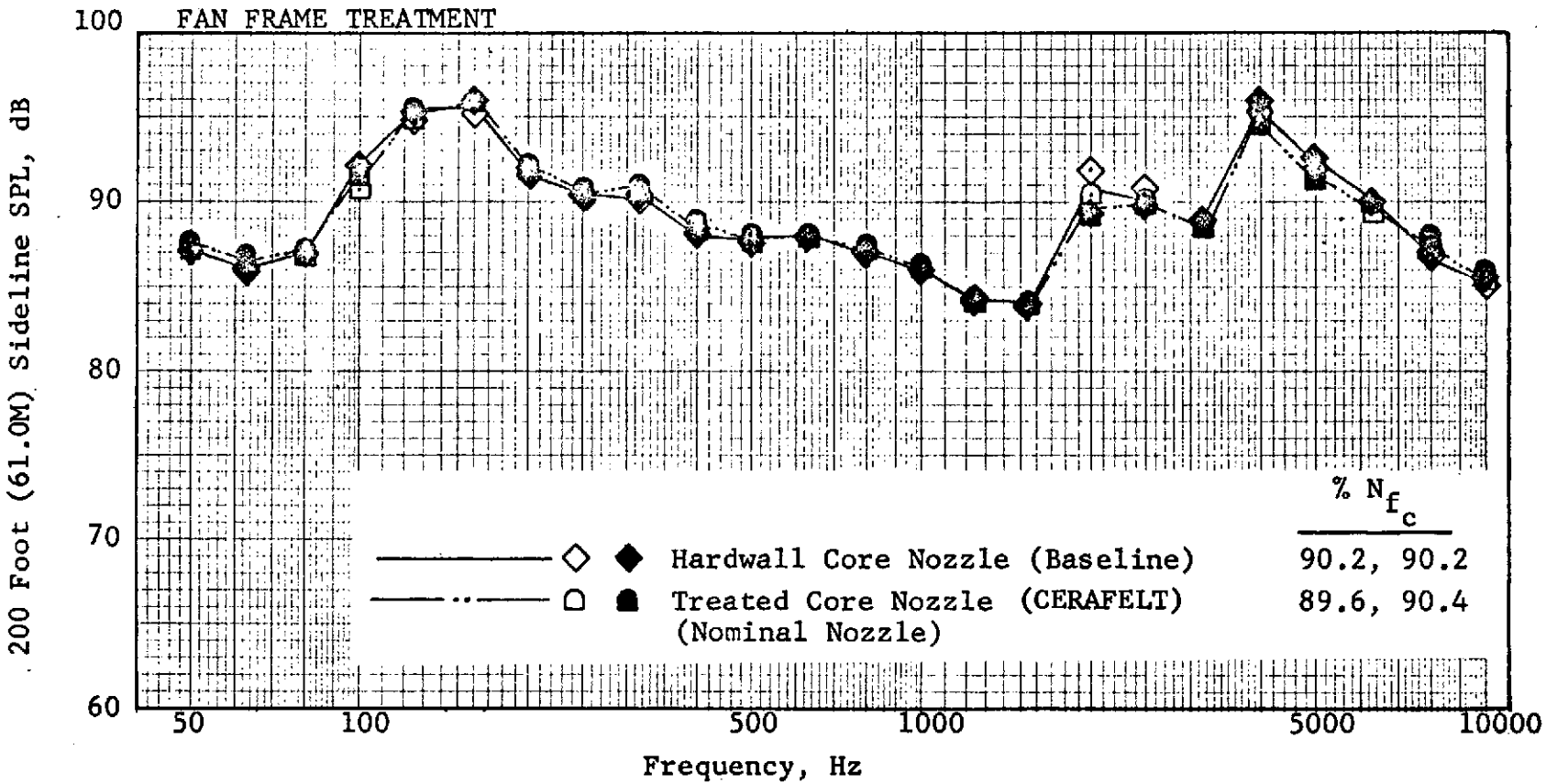

Figure 316. Engine A Sound Power Level Spectra at 120° Treated Vs. Hardwall Core Nozzle (Fan Frame Treatment) at 90% N_{f_c} Standard Day.

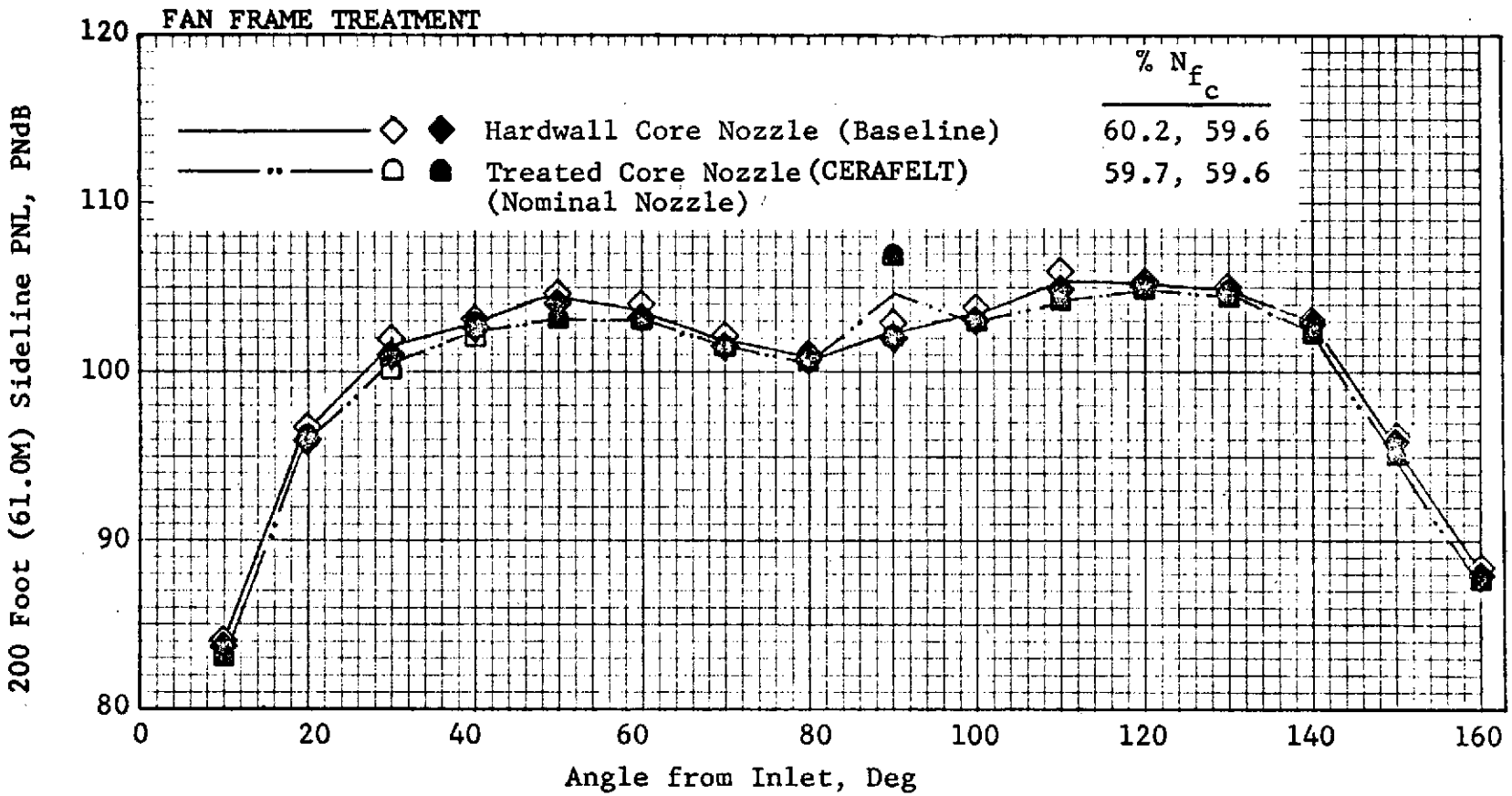

Figure 317. Engine A Perceived Noise Levels for a Single Engine Treated Vs. Hardwall Core Nozzle (Fan Frame Treatment) at 60% N_{f_c} Standard Day.

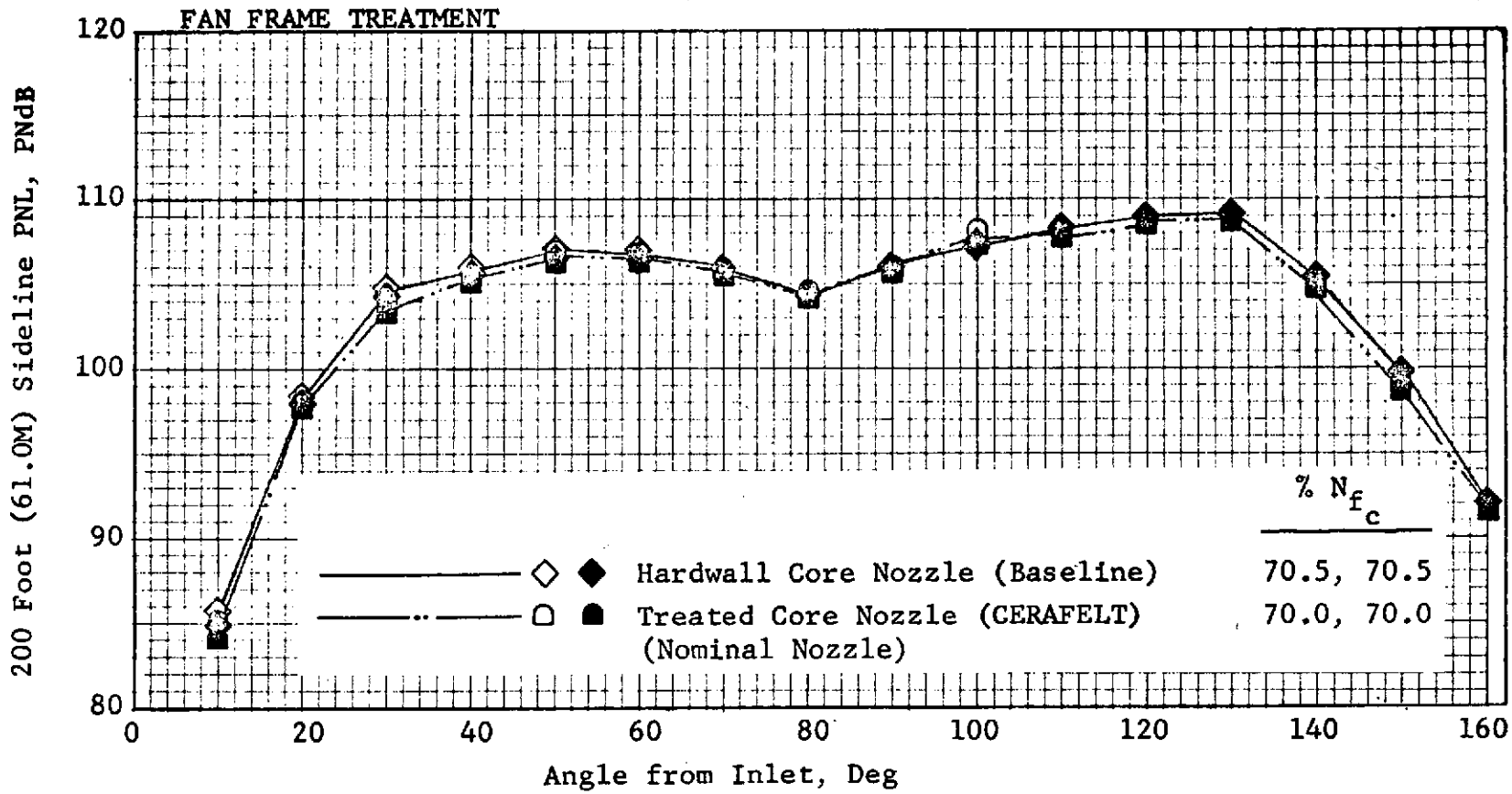

Figure 318. Engine A Perceived Noise Levels for a Single Engine Treated Vs. Hardwall Core Nozzle (Fan Frame Treatment) at 70% N_{f_c} Standard Day.

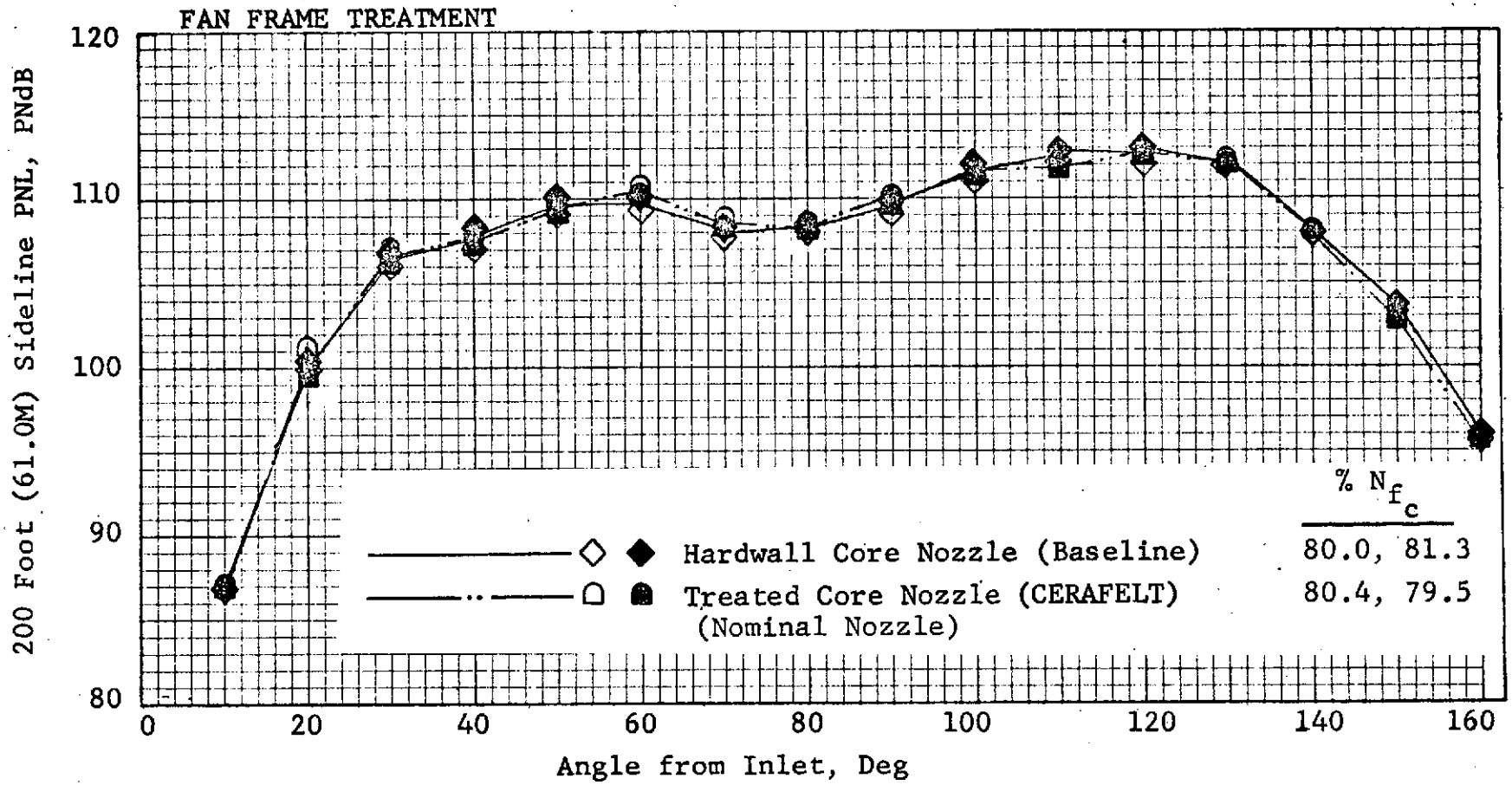

Figure 319. Engine A Perceived Noise Levels for a Single Engine Treated Vs. Hardwall Core Nozzle (Fan Frame Treatment) at 80% N_{f_c} Standard Day.

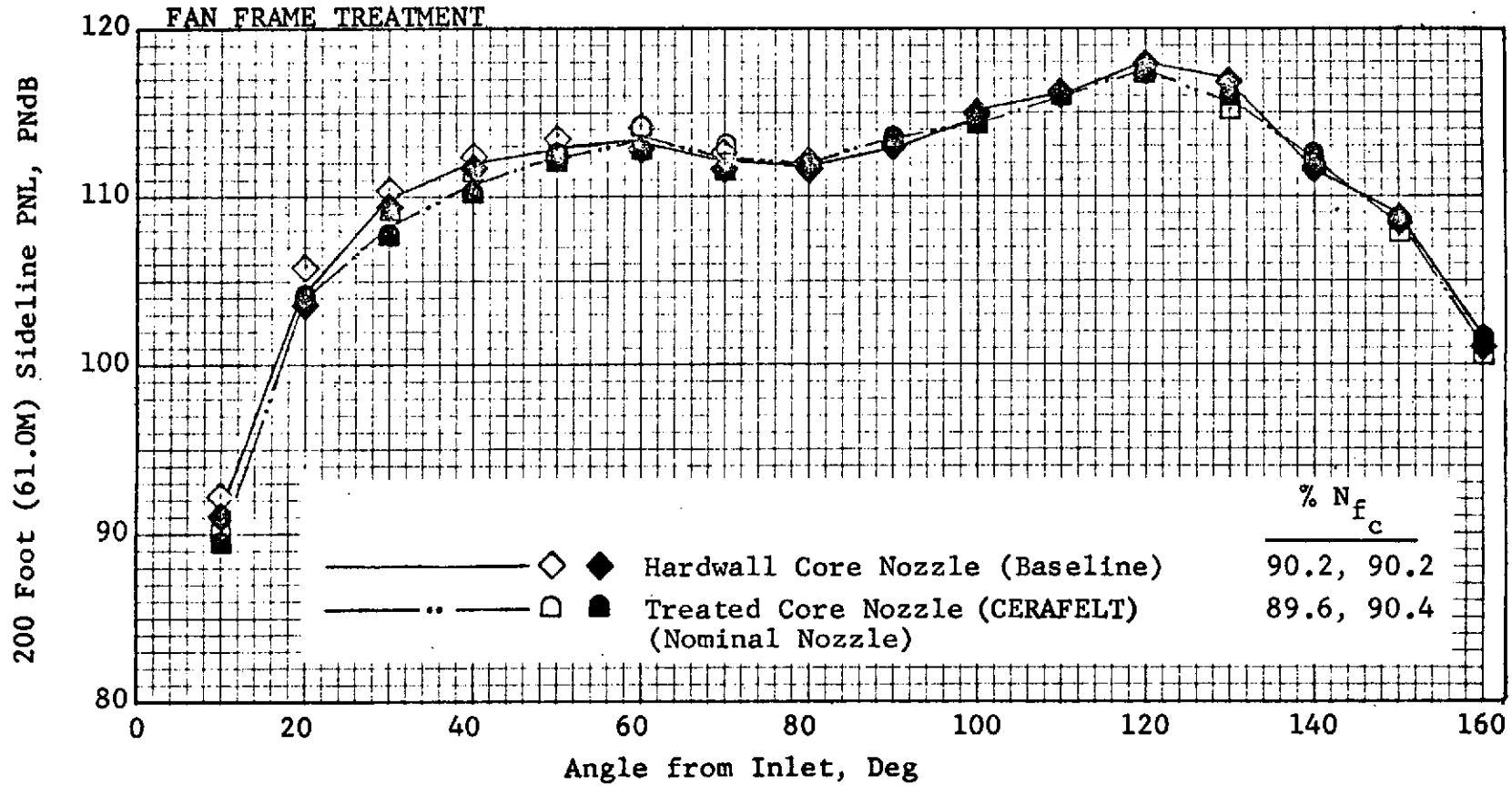

Figure 320. Engine A Perceived Noise Levels for a Single Engine Treated Vs. Hardwall Core Nozzle (Fan Frame Treatment) at 90% N_{f_c} Standard Day.

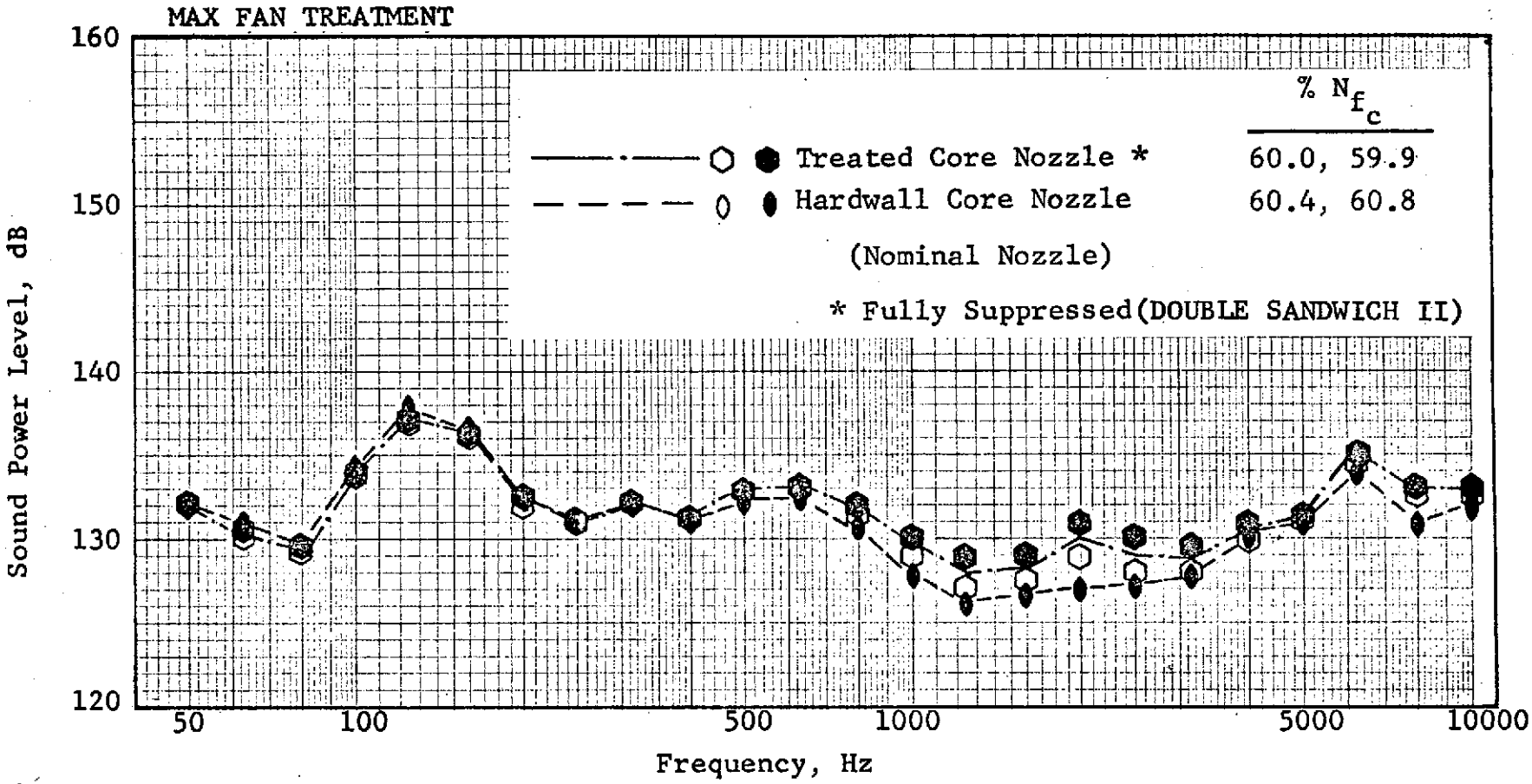

Figure 321. Engine A Sound Power Level Spectra Treated Vs. Hardwall Core Nozzle (Fully Suppressed) at 60% N_{f_c} Standard Day.

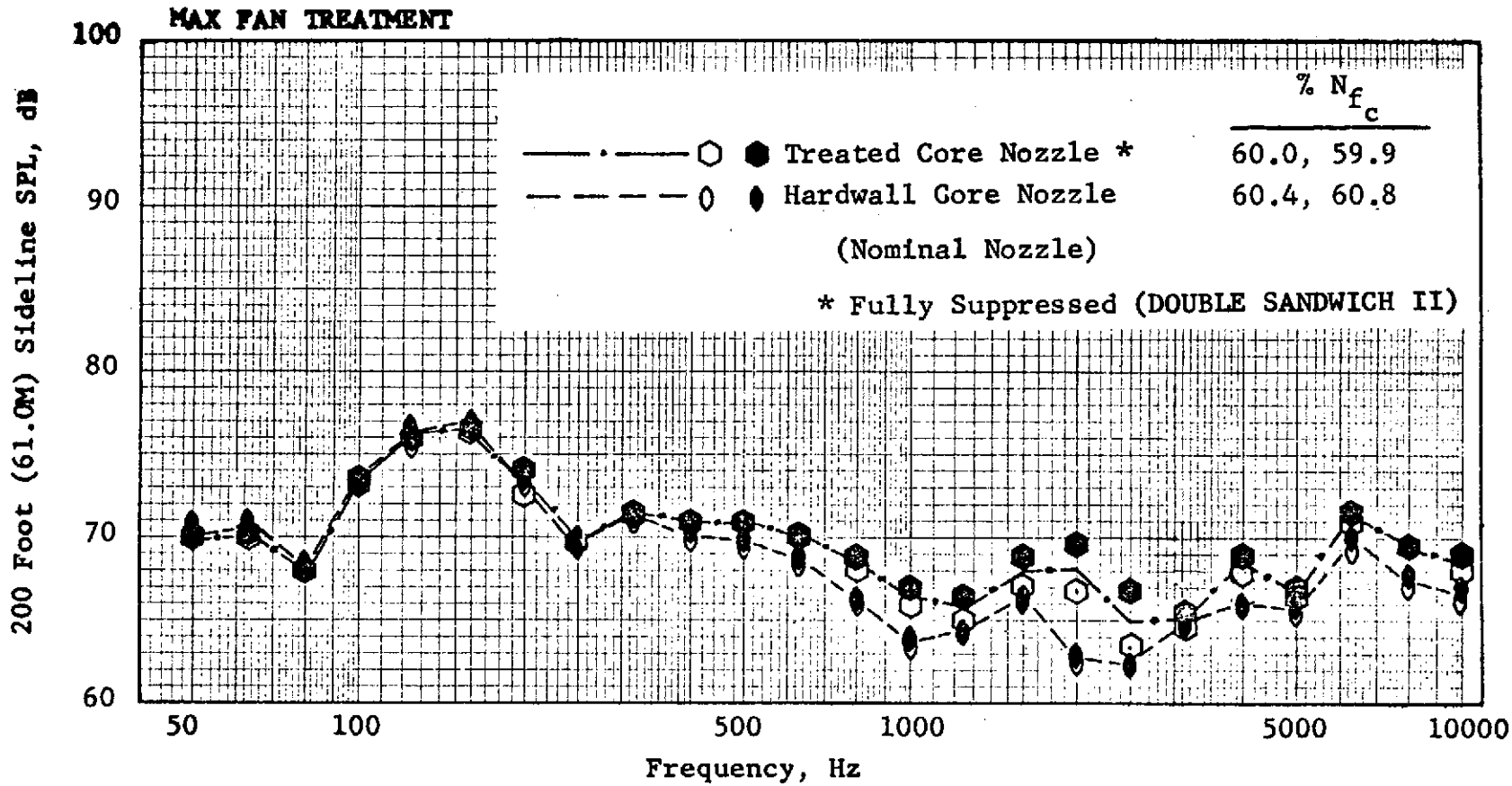

Figure 322. Engine A Sound Power Level Spectra at 50° Treated Vs. Hardwall Core Nozzle (Fully Suppressed) at 60% N_{f_c} Standard Day.

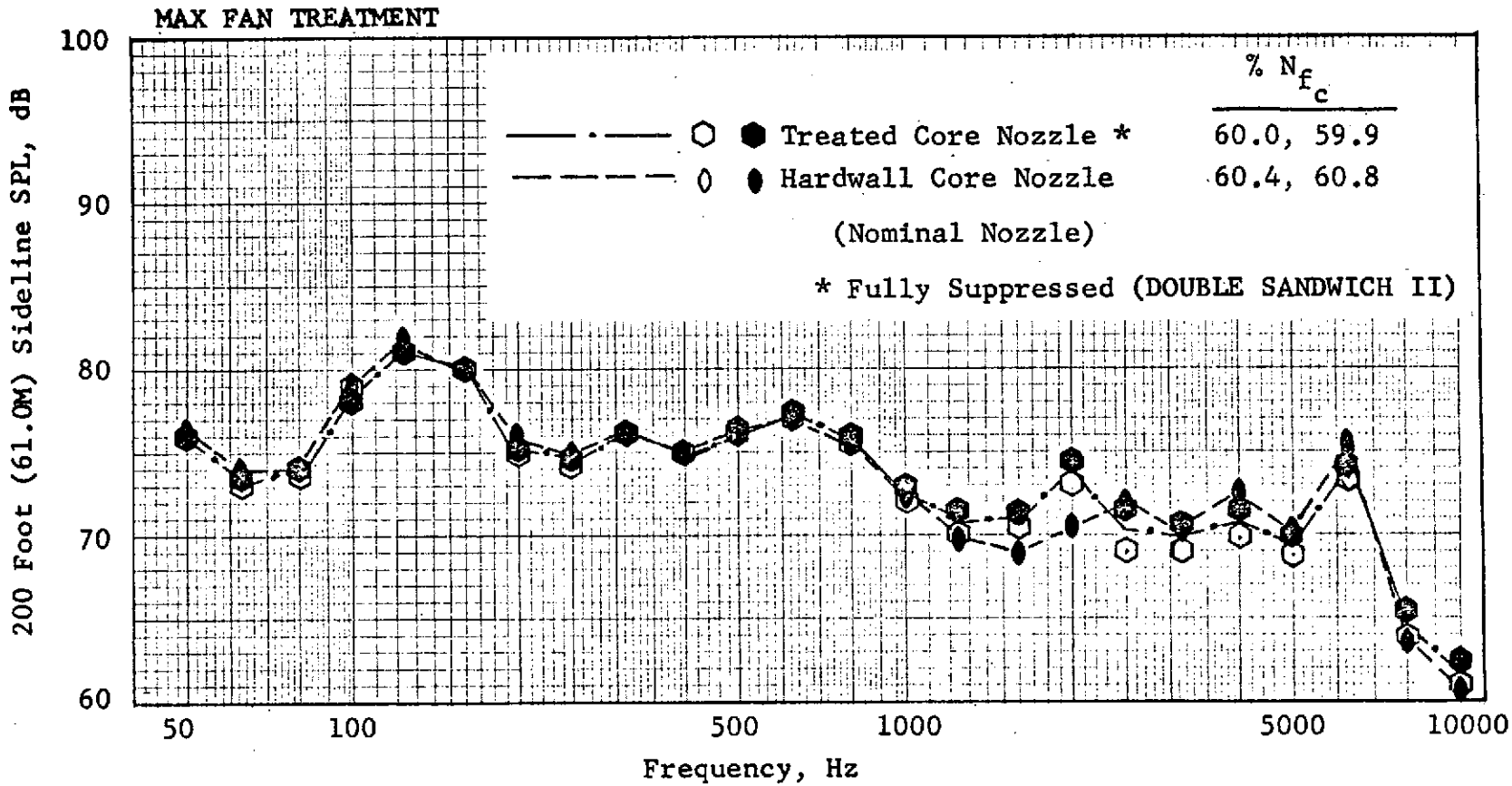

Figure 323. Engine A Sound Power Level Spectra at 120° Treated Vs. Hardwall Core Nozzle (Fully Suppressed) at 60% N_{f_c} Standard Day.

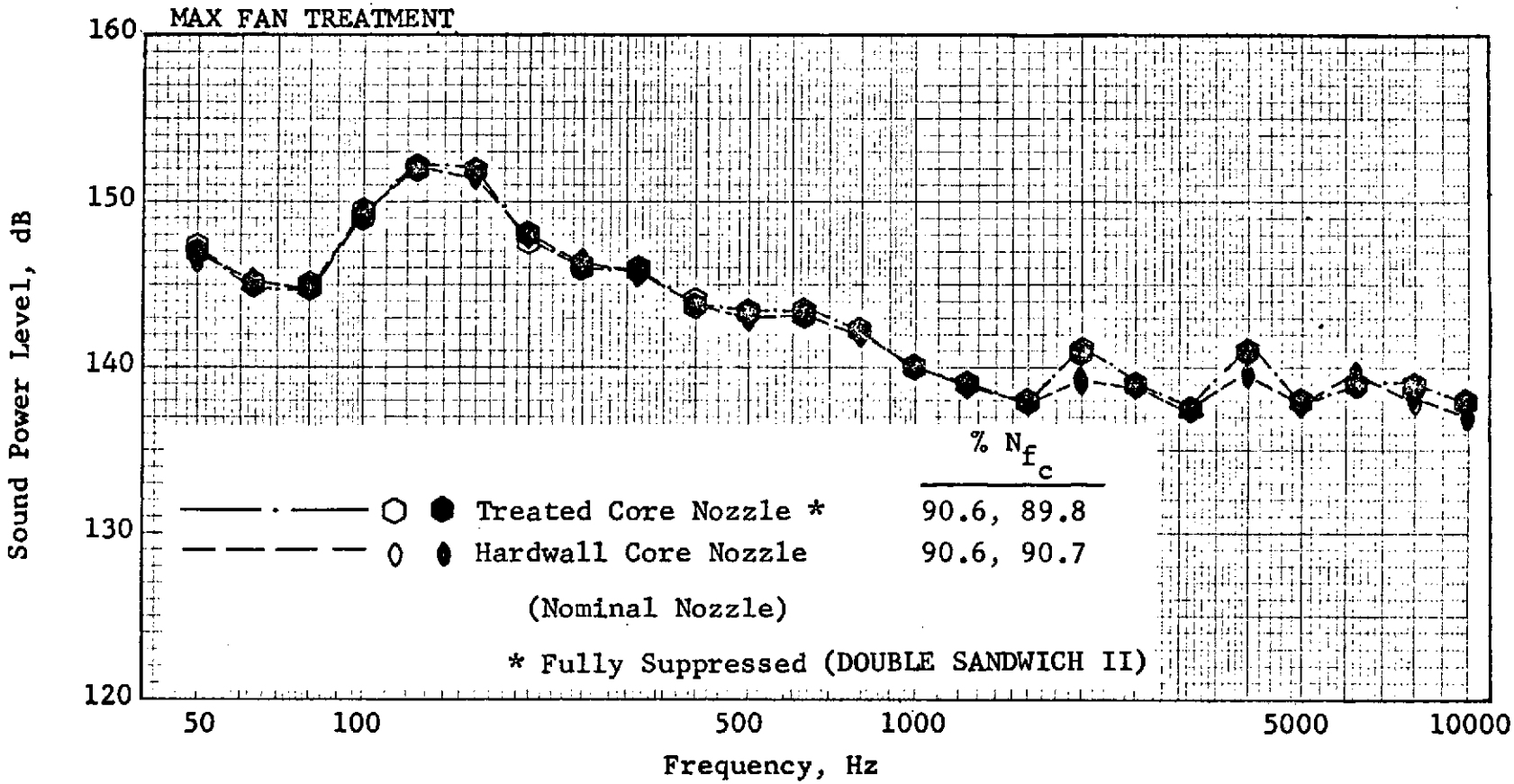

Figure 324. Engine A Sound Power Level Spectra Treated Vs. Hardwall Core Nozzle (Fully Suppressed) at 90% N_{f_c} Standard Day.

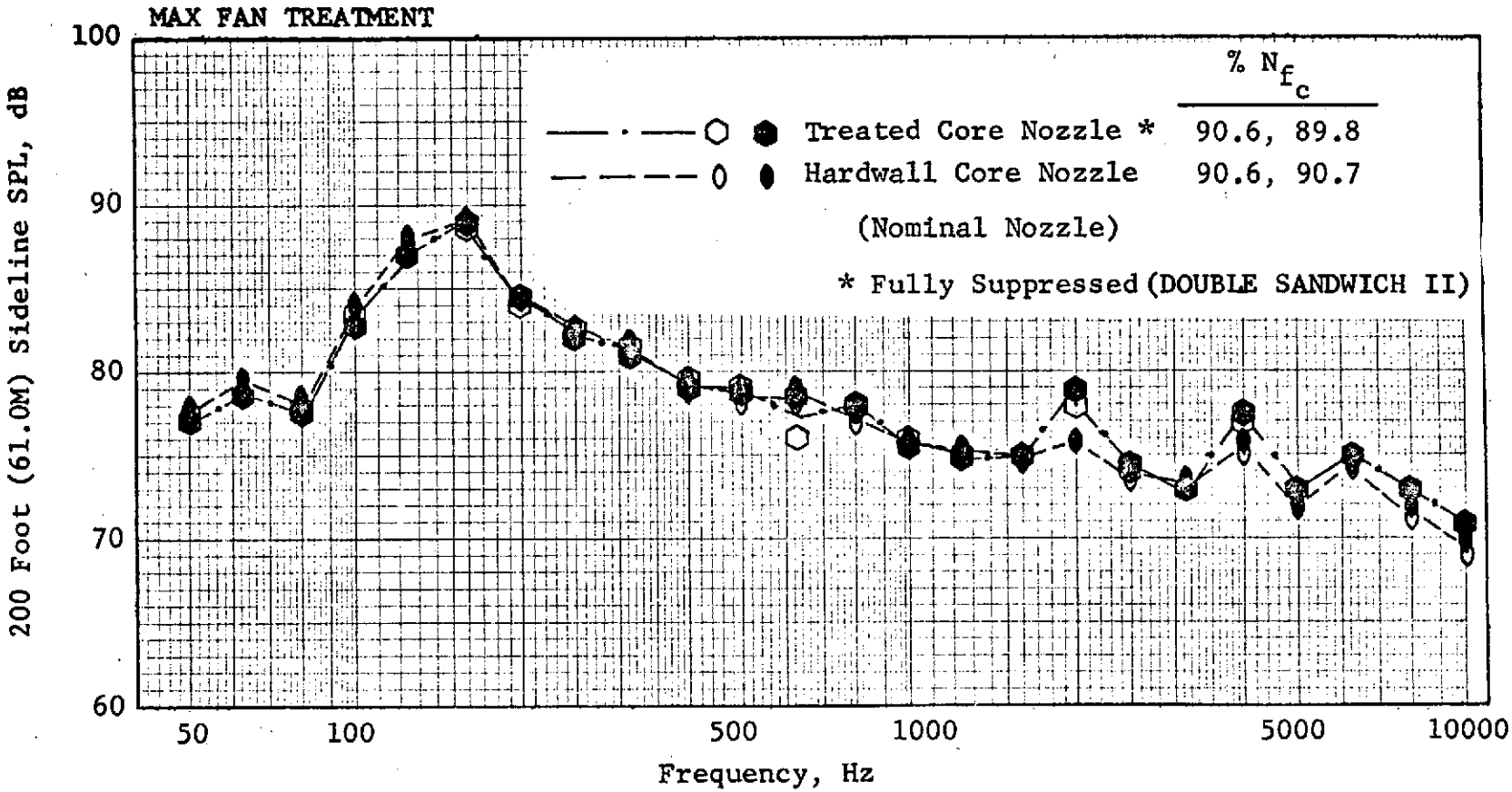

Figure 325. Engine A Sound Power Level Spectra at 50° Treated Vs. Hardwall Core Nozzle (Fully Suppressed) at 90% N_{f_c} Standard Day.

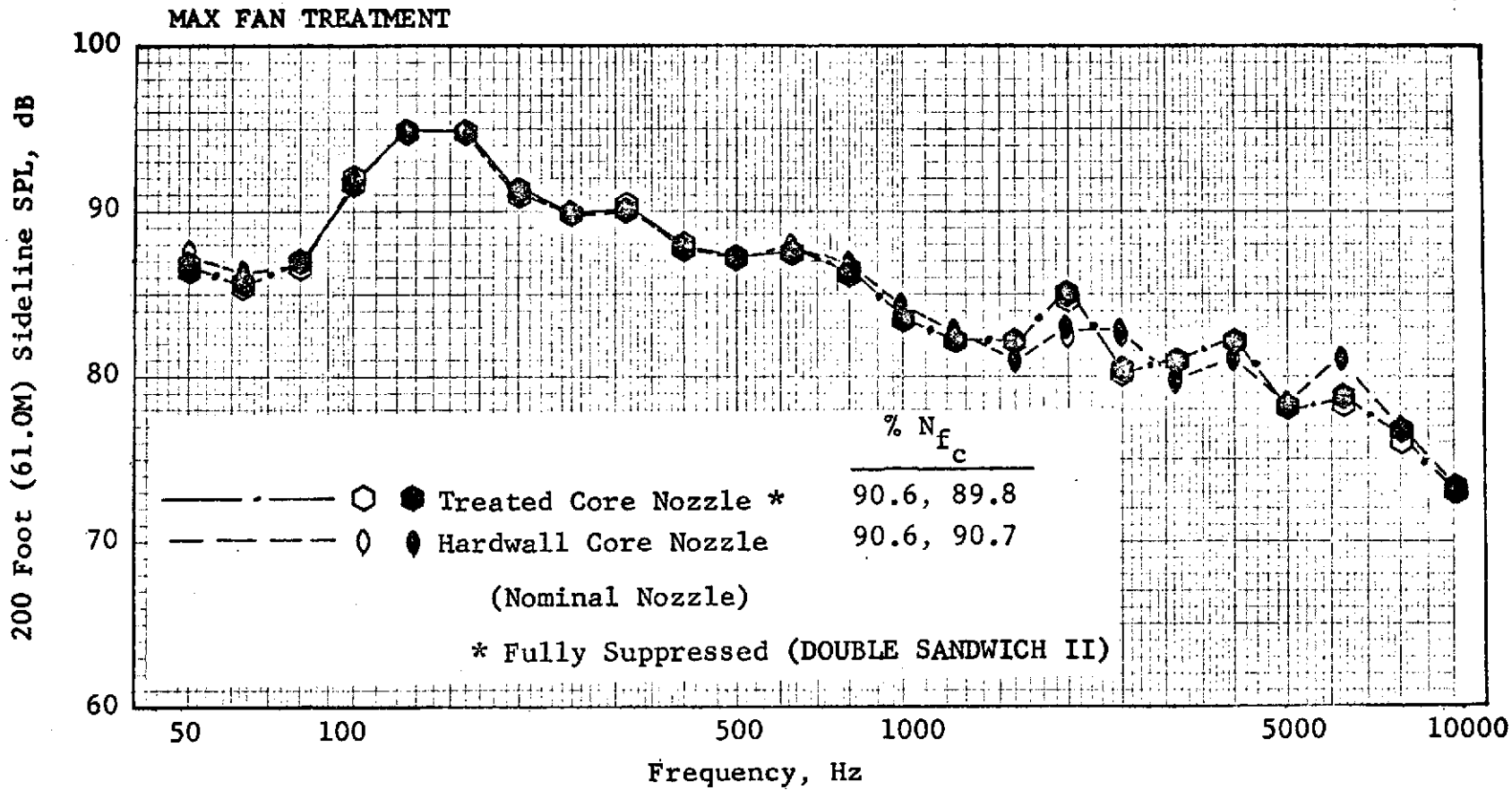

Figure 326. Engine A Sound Power Level Spectra at 120° Treated Vs. Hardwall Core Nozzle (Fully Suppressed) at 90% N_{f_c} Standard Day.

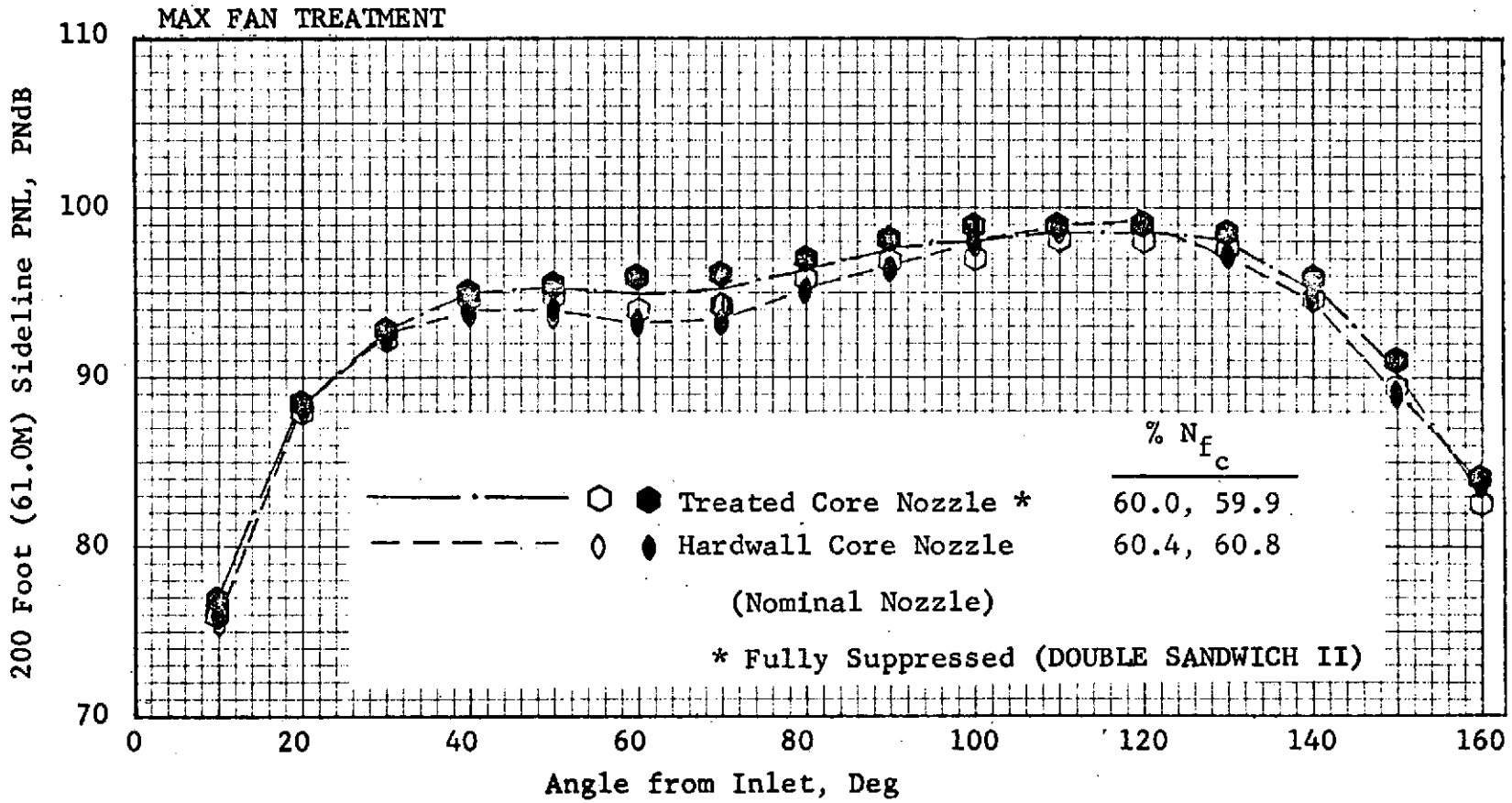

Figure 327. Engine A Perceived Noise Levels for a Single Engine Treated Vs. Hardwall Core Nozzle (Fully Suppressed) at 60% N_{f_c} Standard Day.

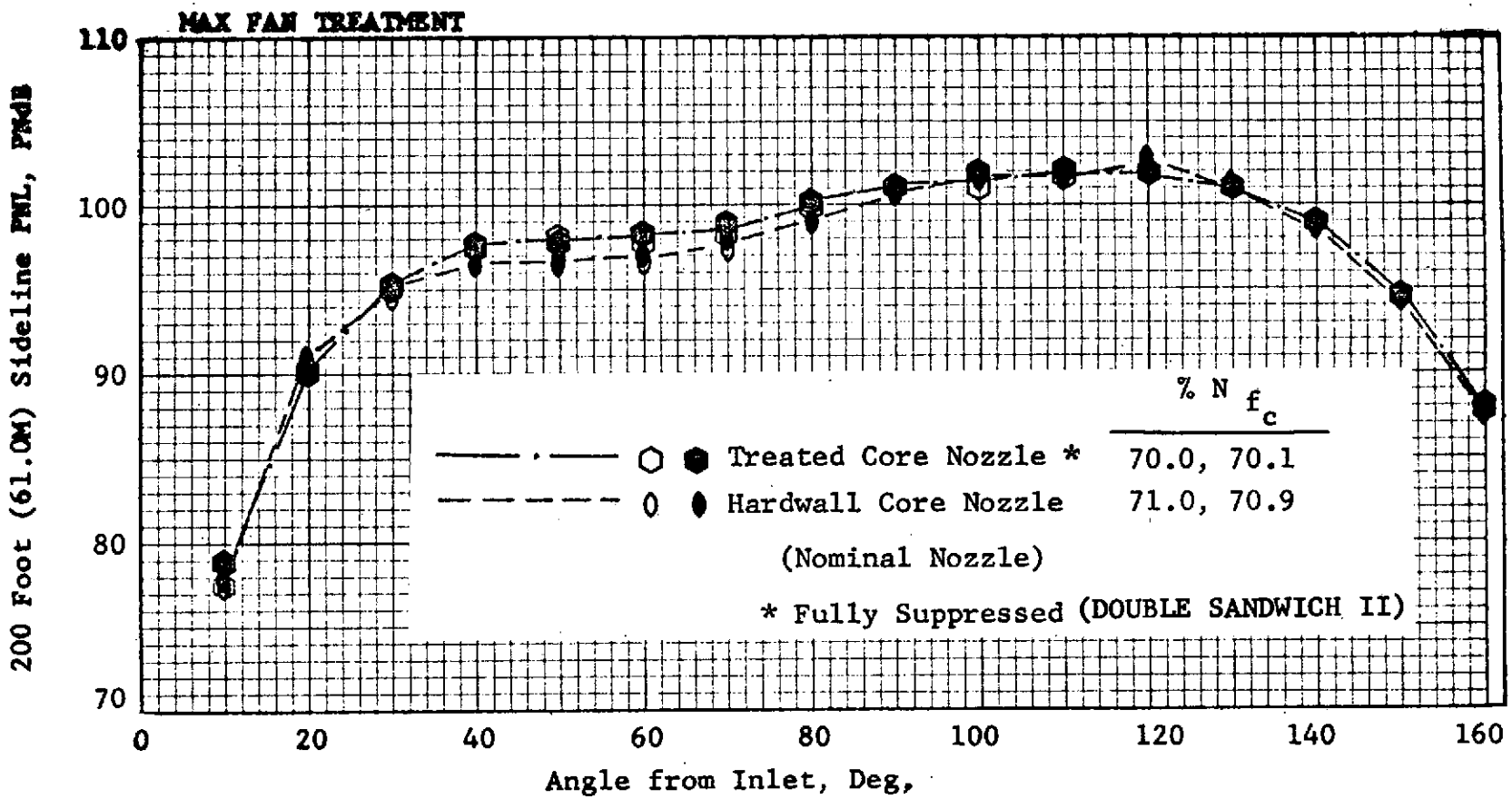

Figure 328. Engine A Perceived Noise Levels for a Single Engine Treated Vs. Hardwall Core Nozzle (Fully Suppressed) at 70% N_{f_c} Standard Day.

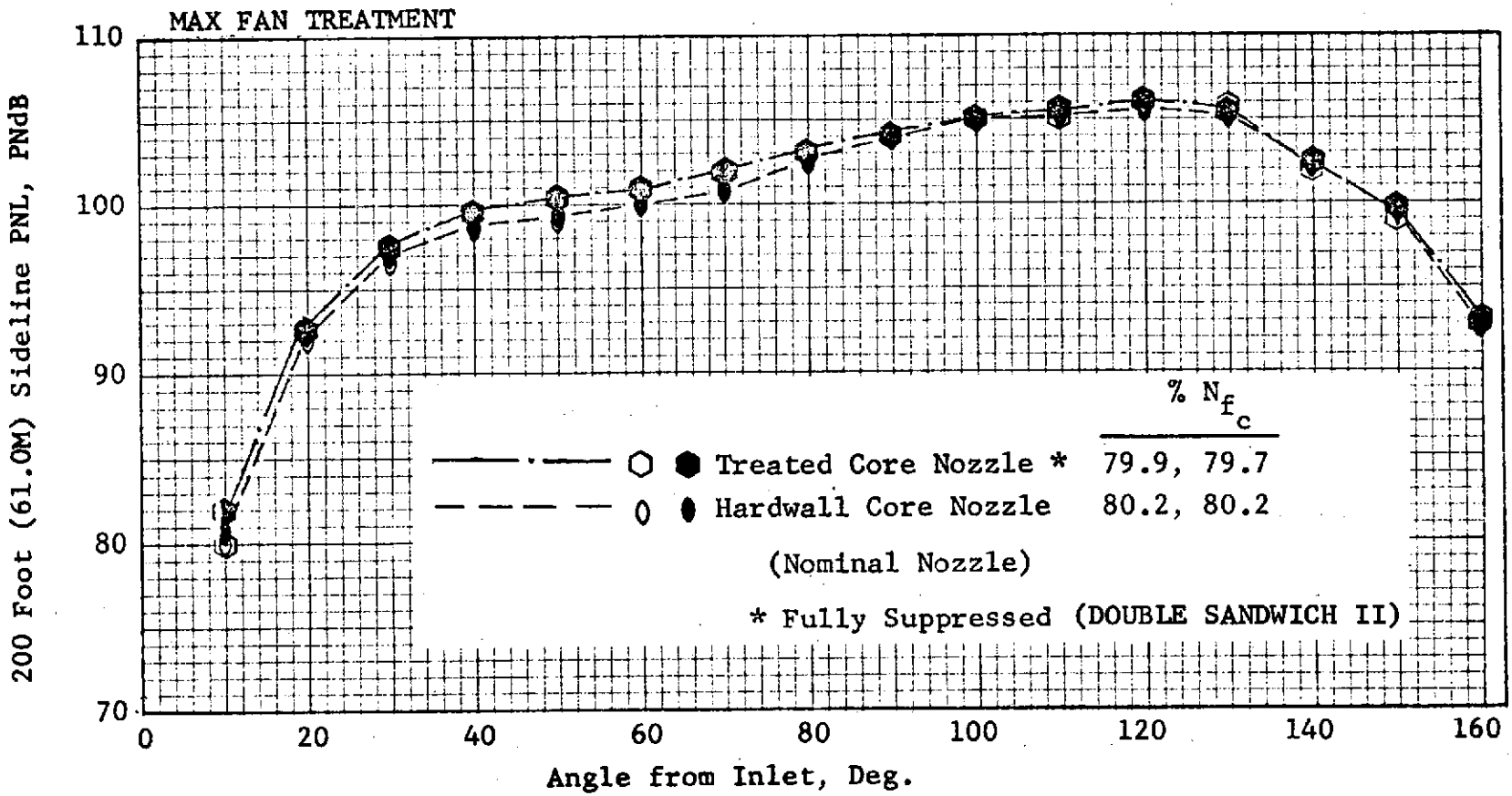

Figure 329. Engine A Perceived Noise Levels for a Single Engine Treated Vs. Hardwall Core Nozzle (Fully Suppressed) at 80% N_{f_c} Standard Day.

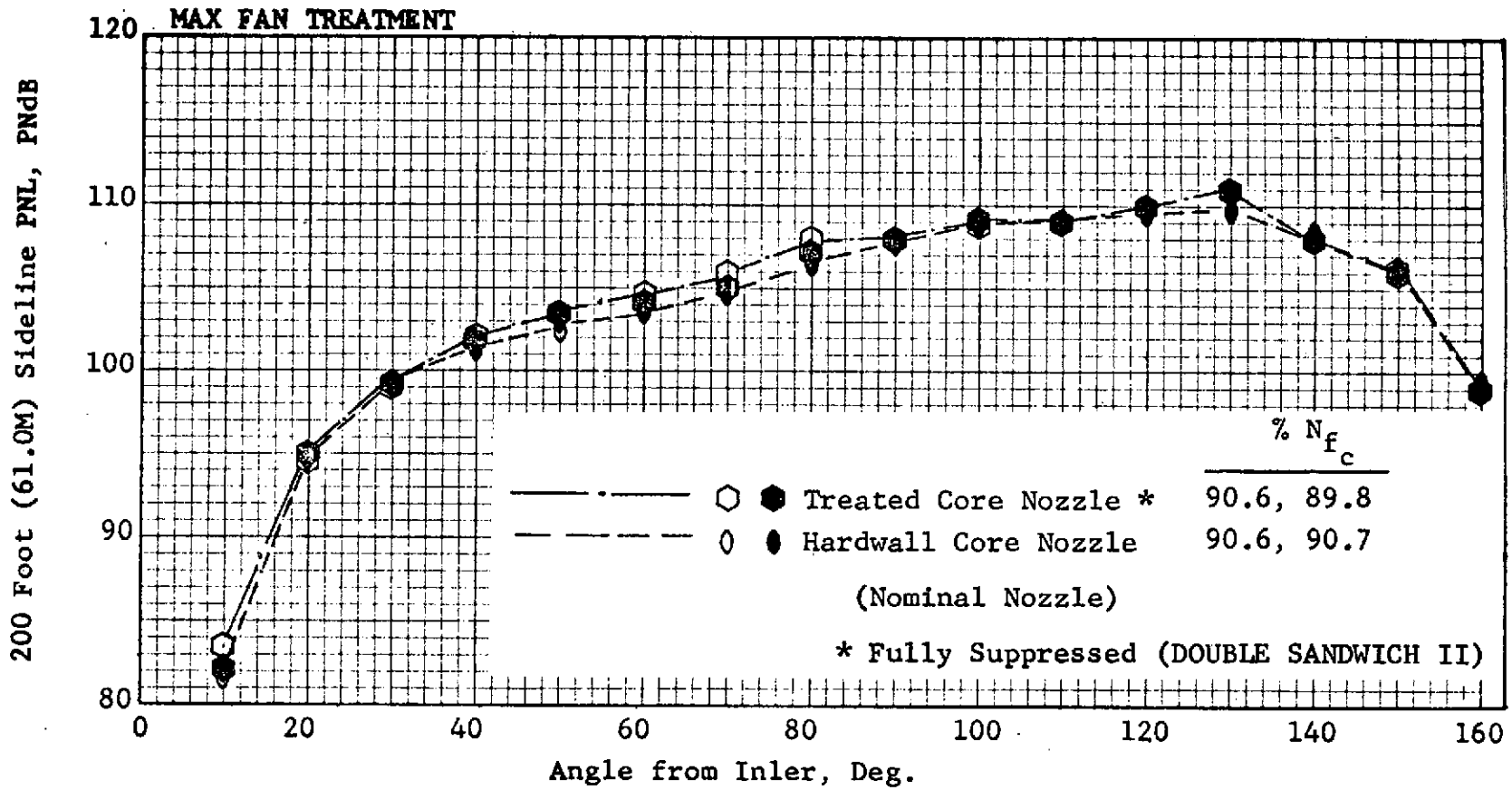

Figure 330. Engine A Perceived Noise Levels for a Single Engine Treated Vs. Hardwall Core Nozzle (Fully Suppressed) at 90% N_{f_c} Standard Day.

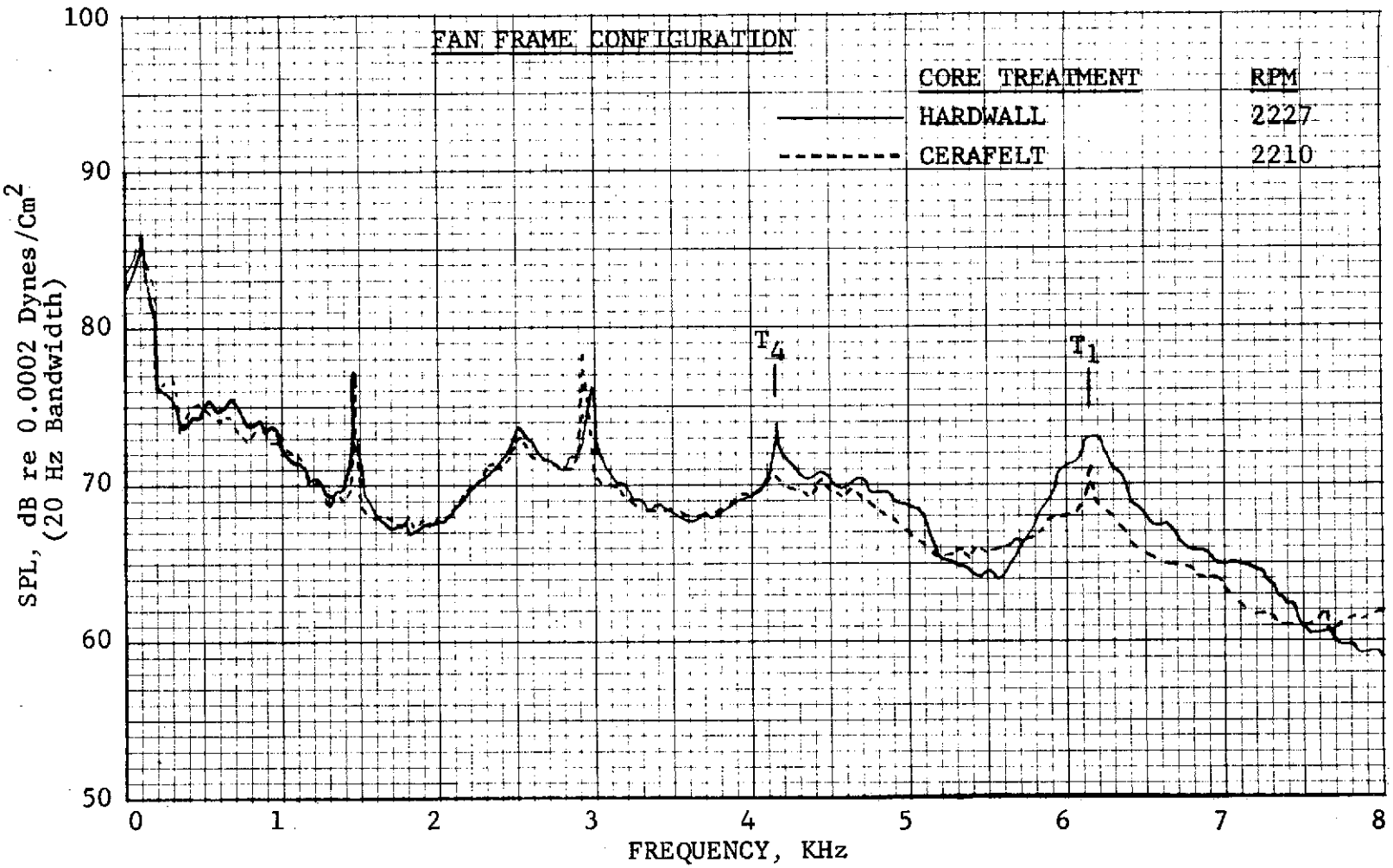

Figure 331. Engine A Farfield Narrowband Spectrum at 120 Degrees.

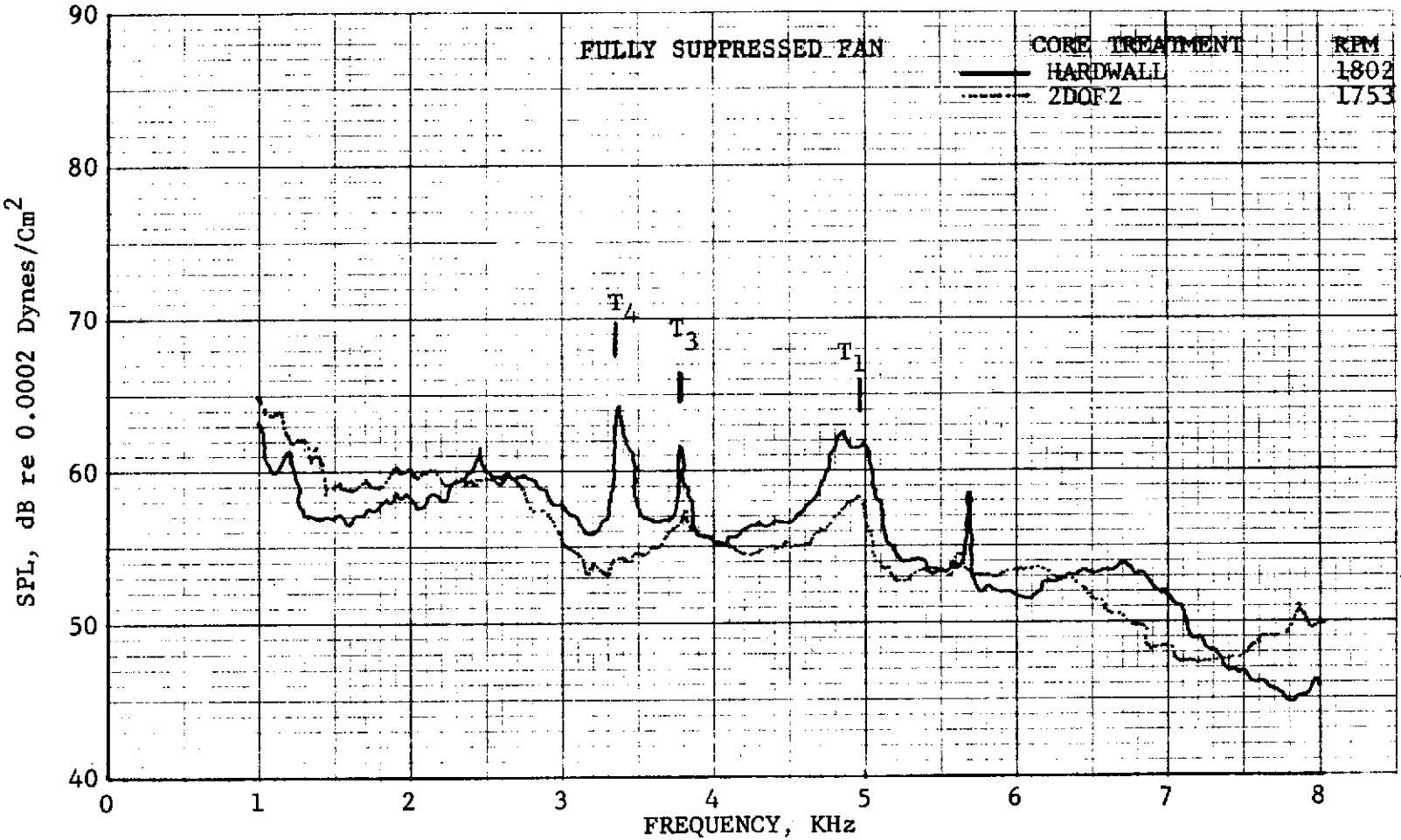

Figure 332. Engine A Farfield Narrowband Spectrum Showing Hump at 120°, 1753 rpm (Treated Data Frequency Shifted to Enable a Direct Tone Level Comparison).

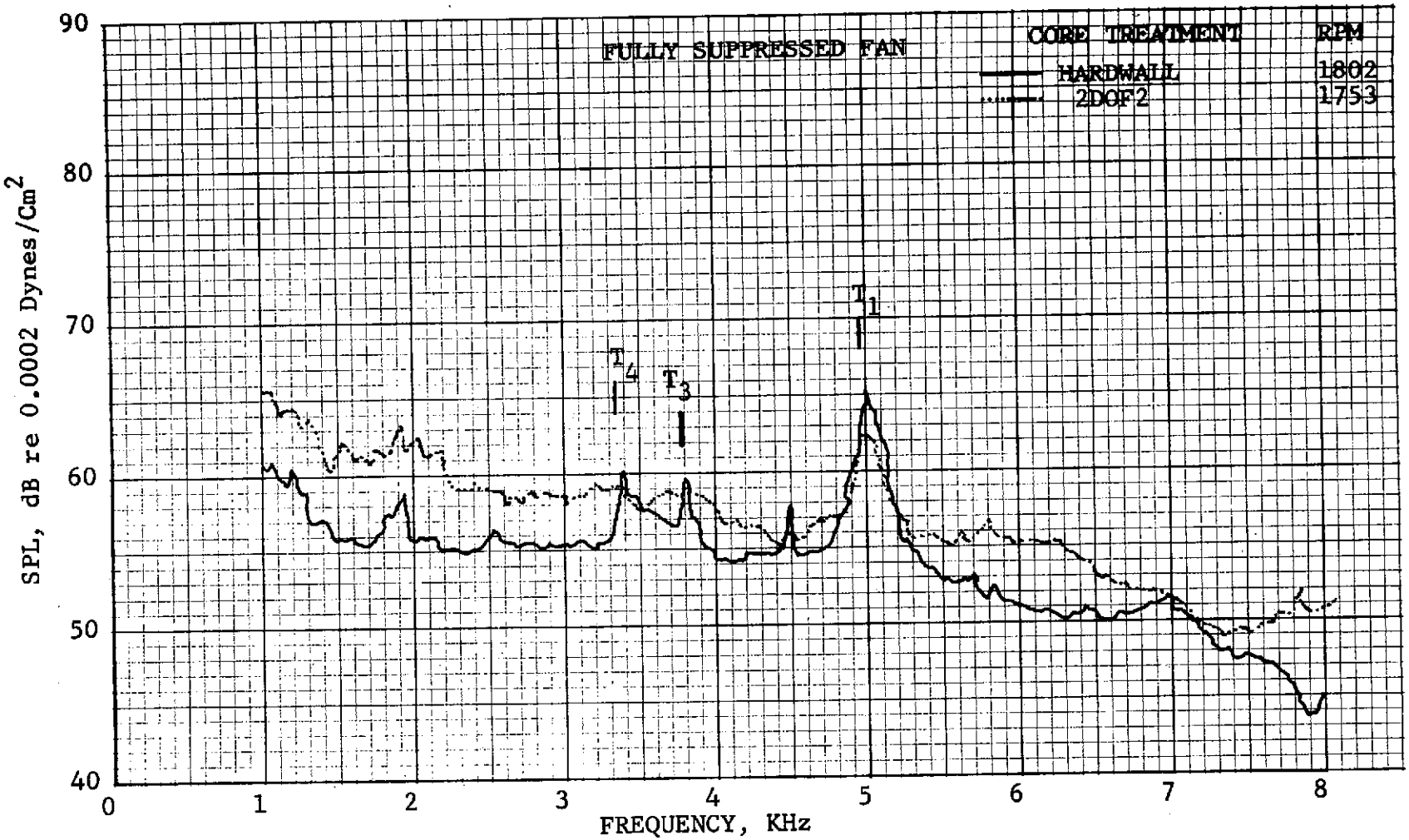

Figure 333. Engine A Farfield Narrowband Spectrum Showing Hump at 130°, 1753 rpm (Treated Data Frequency Shifted to Enable a Direct Tone Level Comparison).

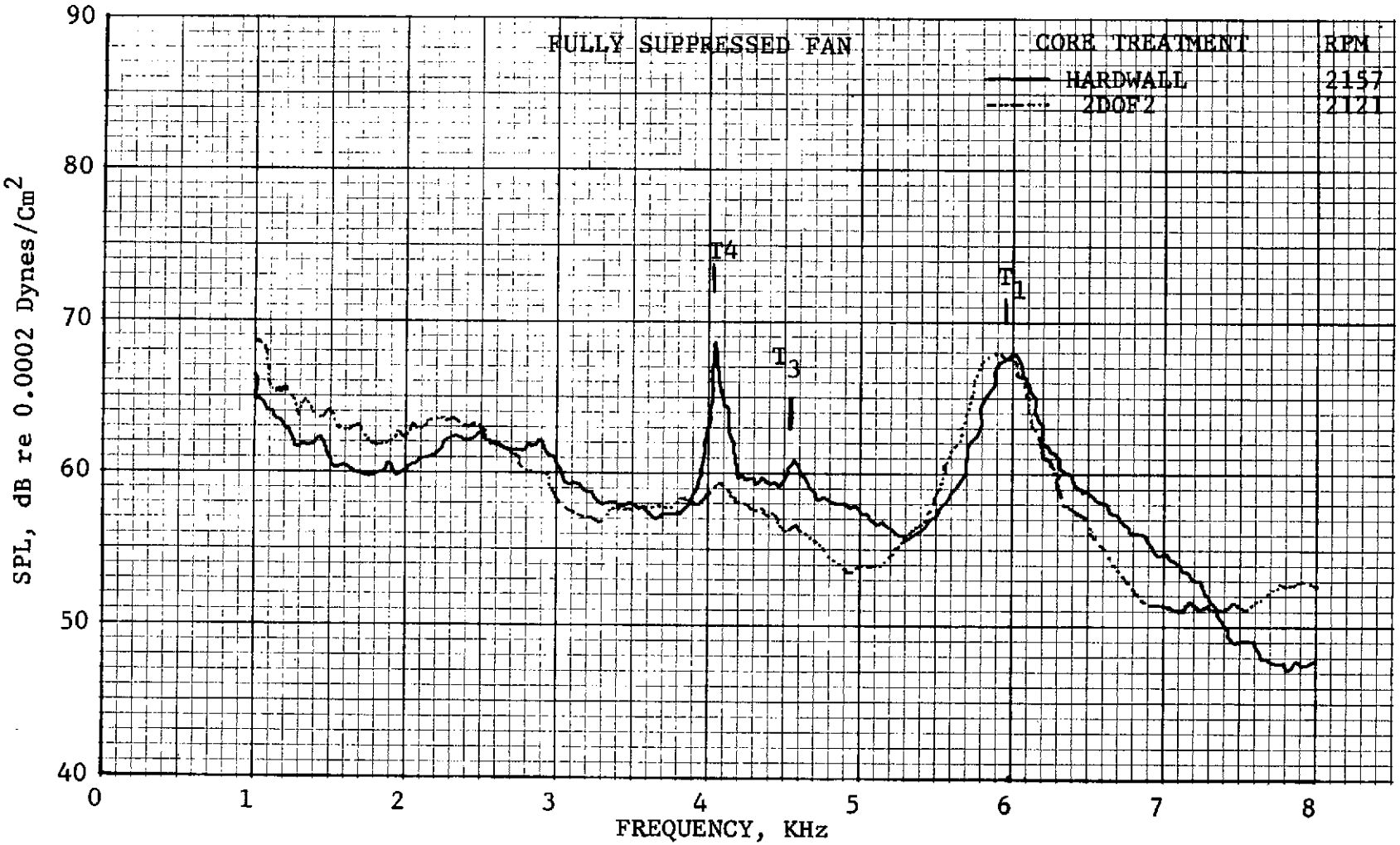

Figure 334. Engine A Farfield Narrowband Spectrum Showing Hump at 120°, 2121 rpm (Treated Data Frequency Shifted to Enable a Direct Tone Level Comparison).

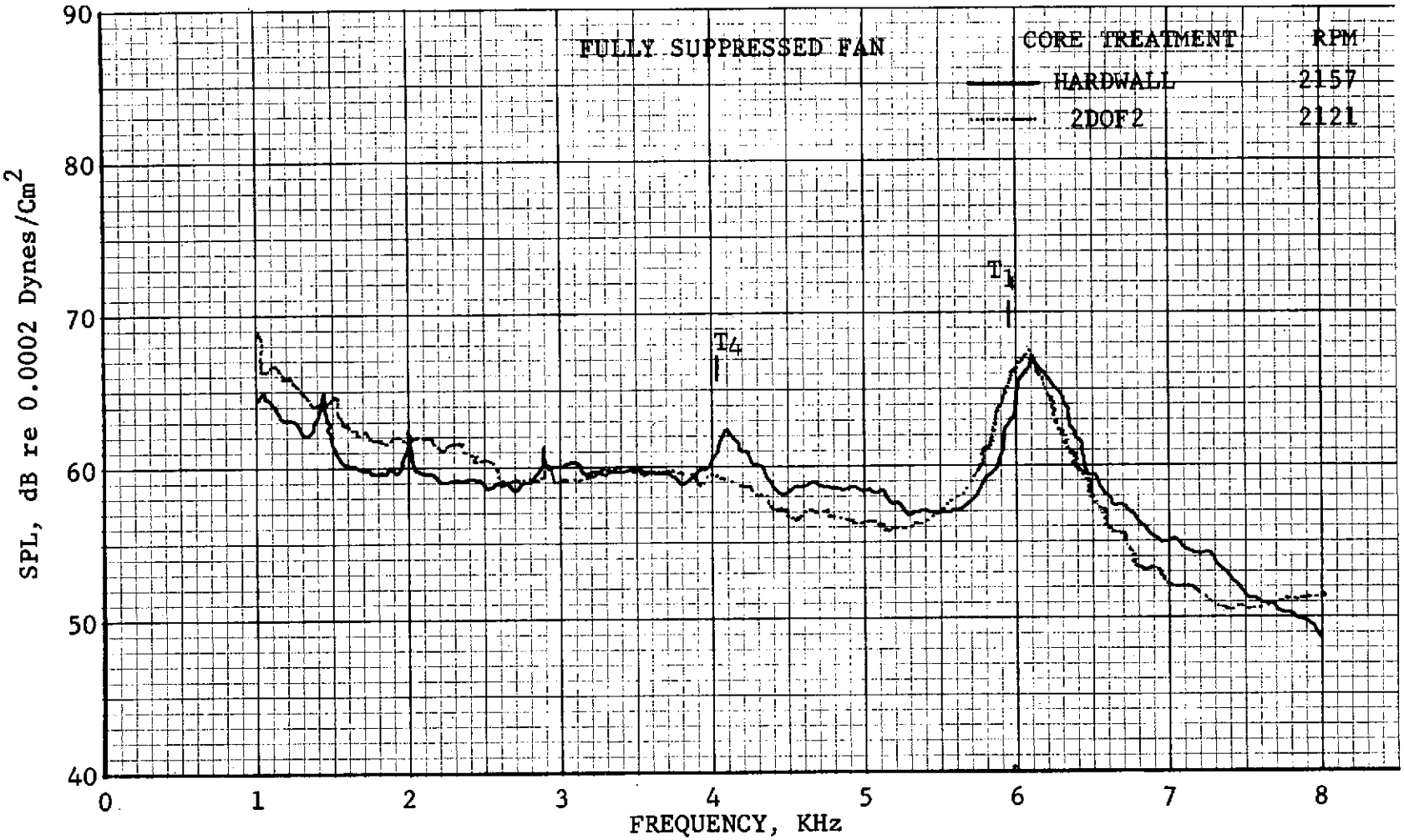

Figure 335. Engine A Farfield Narrowband Spectrum Showing Hump at 130°, 2121 rpm (Treated Data Frequency Shifted to Enable a Direct Tone Level Comparison).

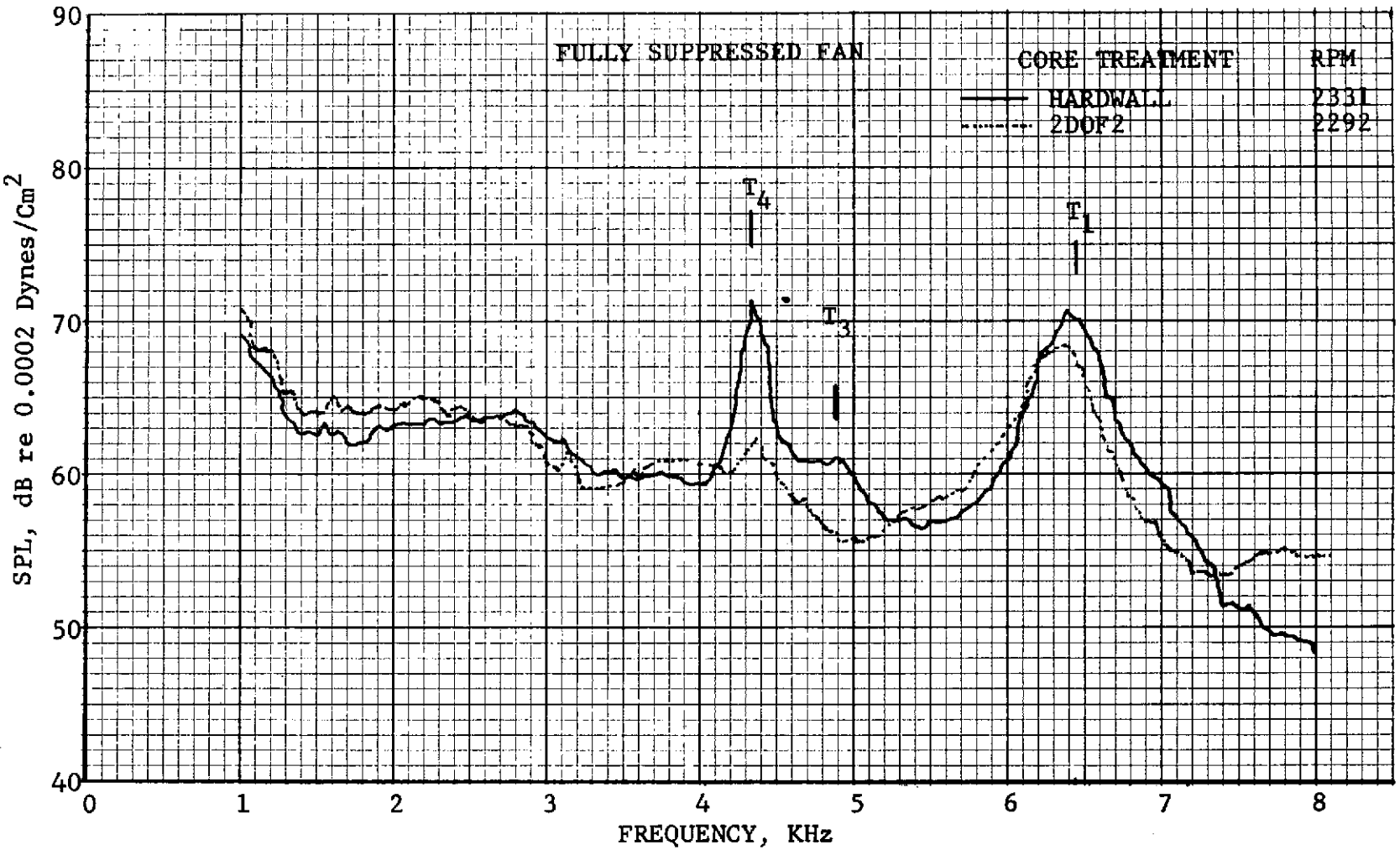

Figure 336. Engine A Farfield Narrowband Spectrum Showing Hump at 120°, 2292 rpm (Treated Data Frequency Shifted to Enable a Direct Tone Level Comparison).

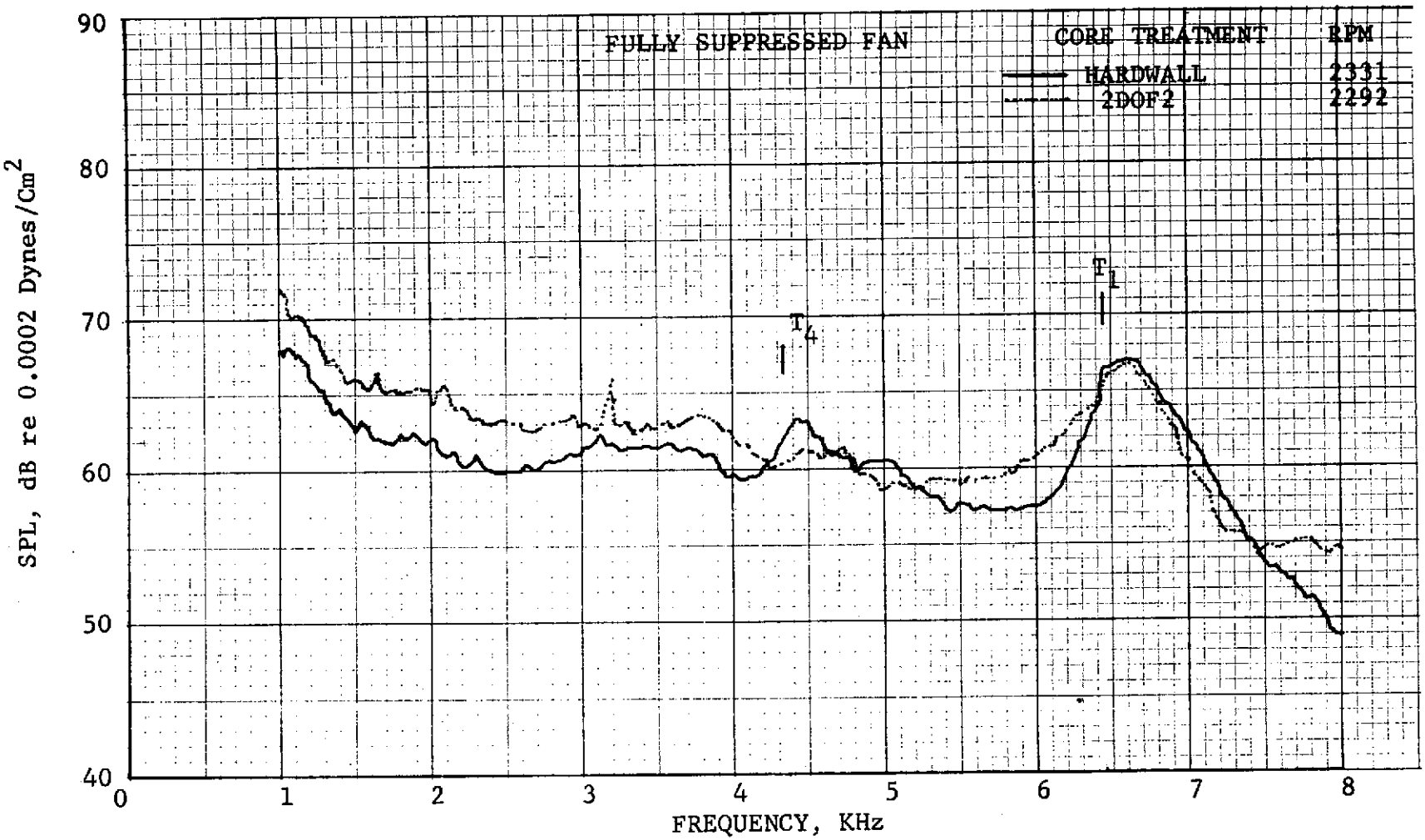

Figure 337. Engine A Farfield Narrowband Spectrum Showing Hump at 130°, 2292 rpm (Treated Data Frequency Shifted to Enable a Direct Tone Level Comparison).

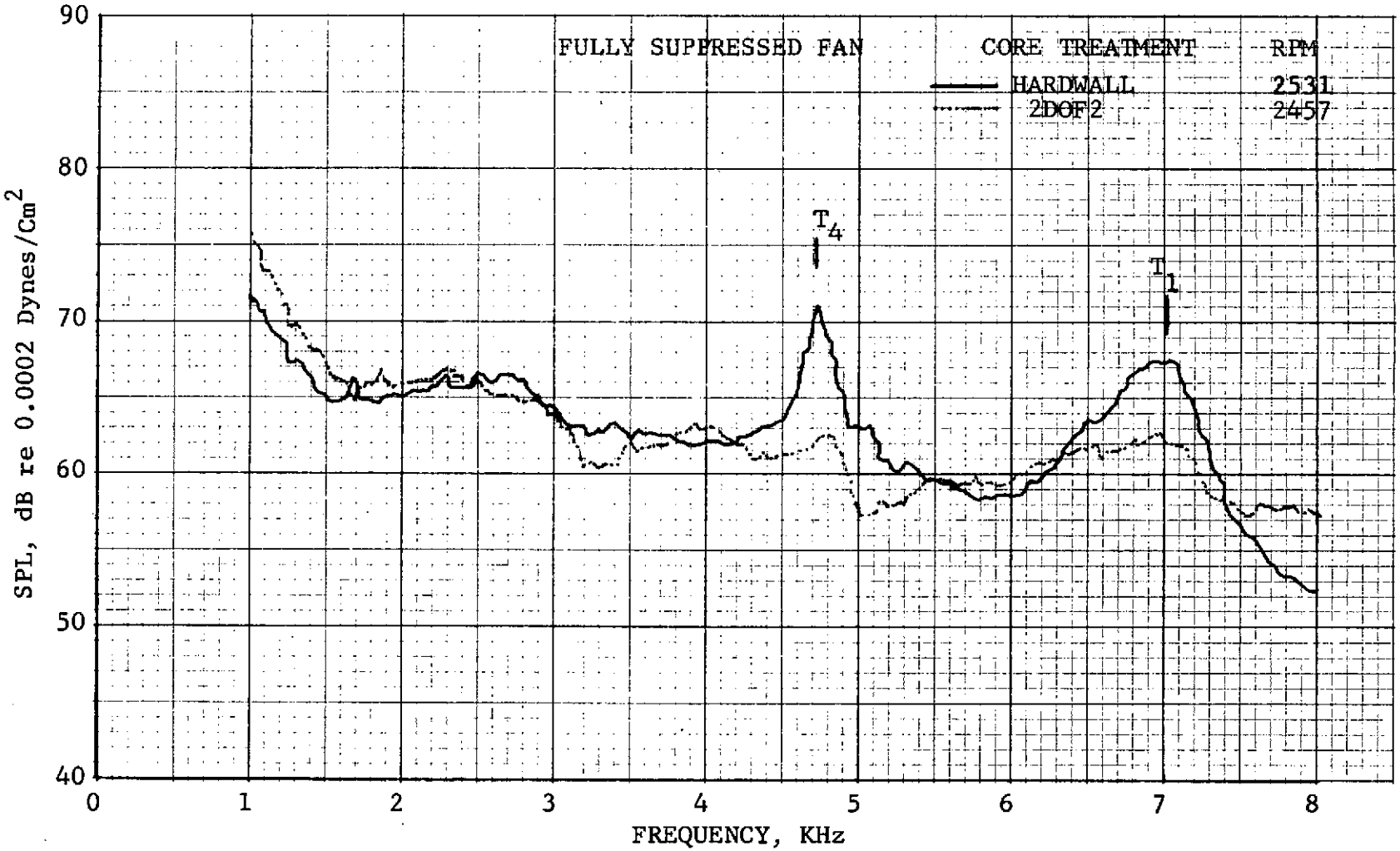

Figure 338. Engine A Farfield Narrowband Spectrum Showing Hump at 120°, 2457 rpm (Treated Data Frequency Shifted to Enable a Direct Tone Level Comparison).

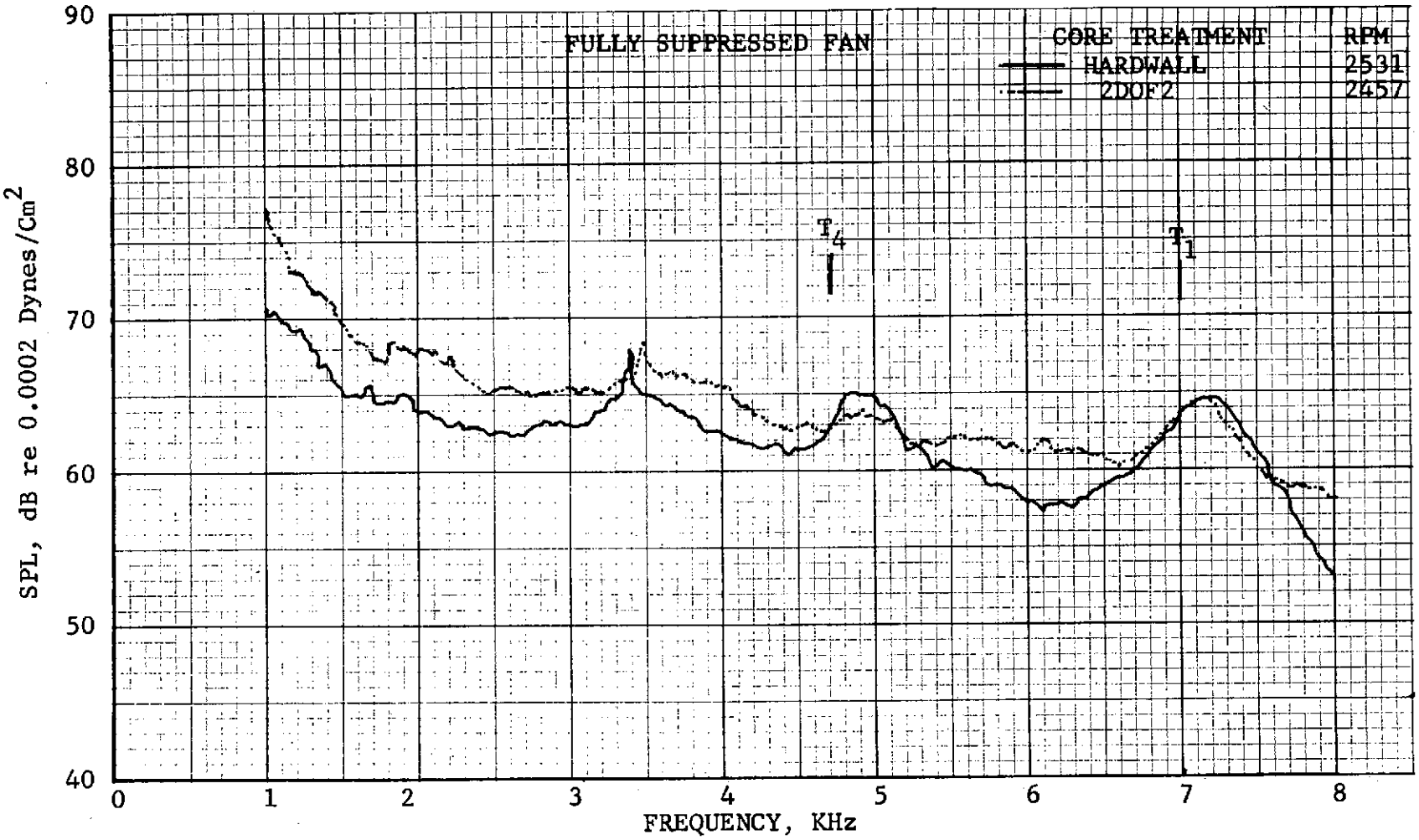

Figure 339. Engine A Farfield Narrowband Spectrum Showing Hump at 130°, 2457 rpm (Treated Data Frequency Shifted to Enable a Direct Tone Level Comparison).

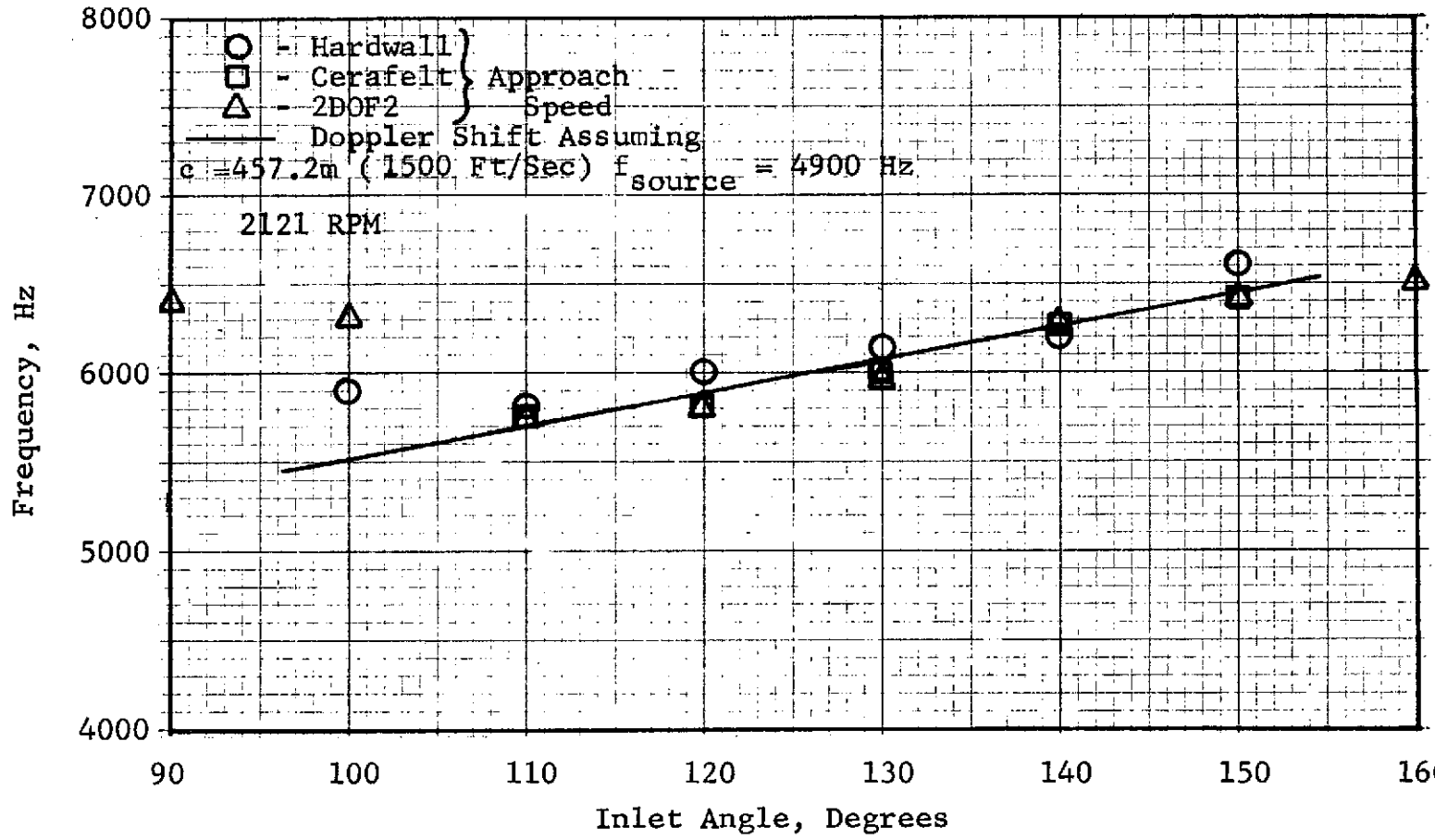

Figure 340. Engine A Hump Center Frequency Shift in the Farfield for Several Treatment Configurations at Approach Speed.

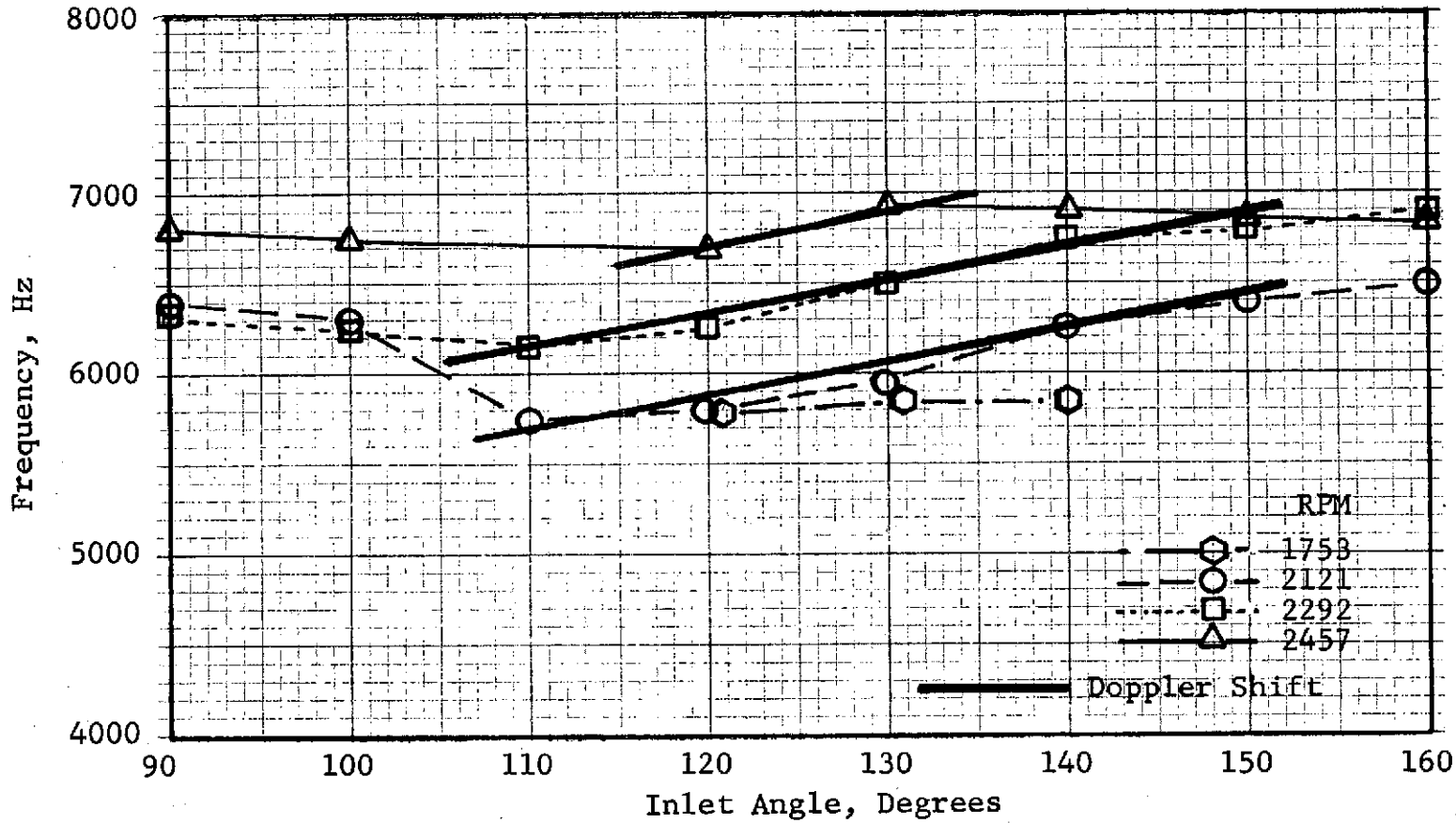

Figure 341. Engine A Hump Center Frequency Shift in the Farfield for 2DOF2 at Several Engine Speeds.

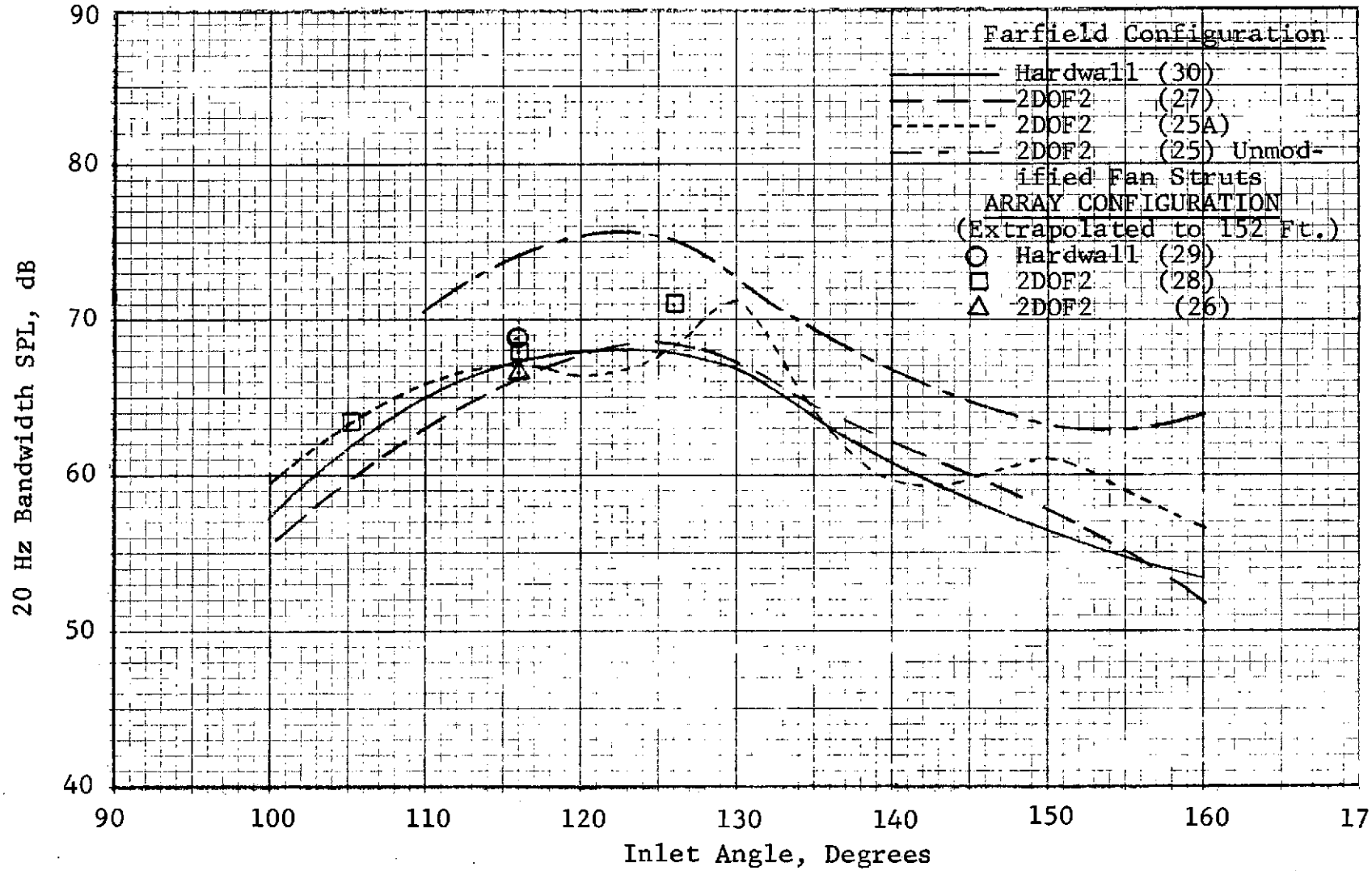

Figure 342. Engine A Directivity of Hump Center Frequency at Approach Speed from Farfield Data and Array Data.

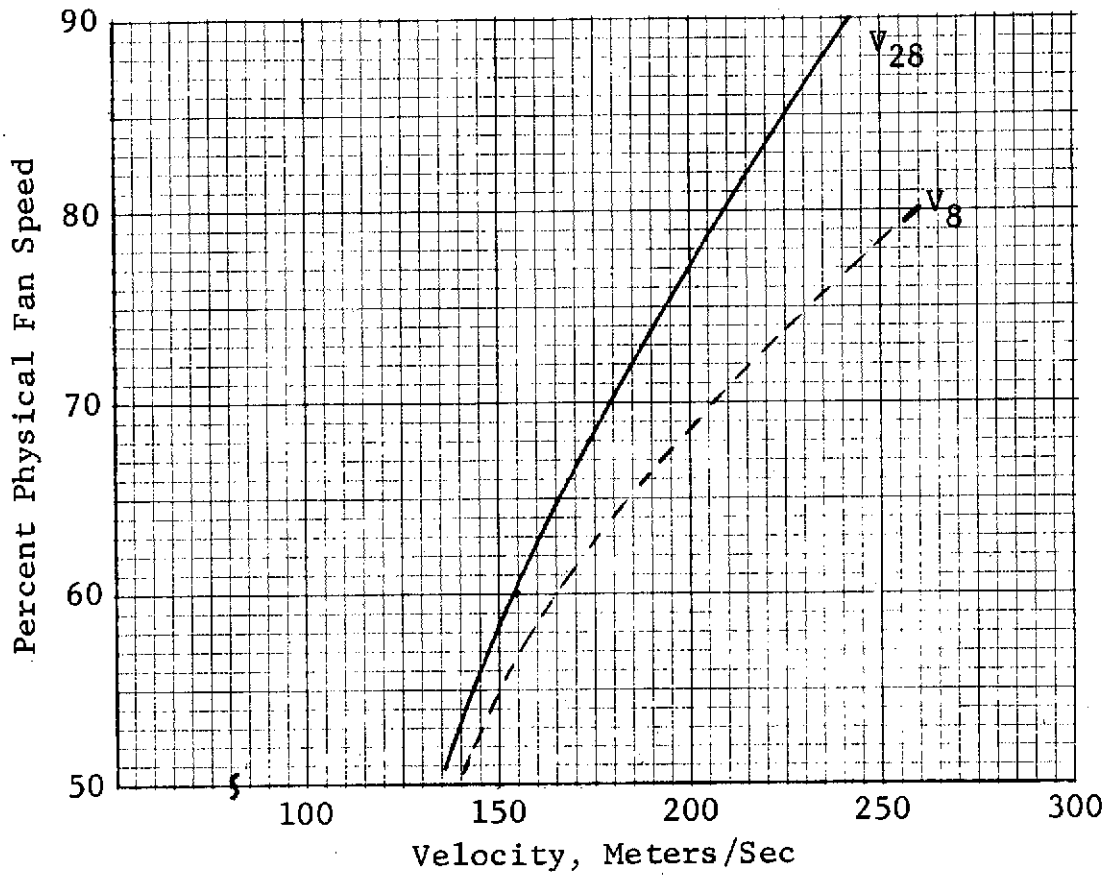

Figure 343. Engine A Fan and Core Discharge Velocity Vs. Percent Physical Fan Speed.

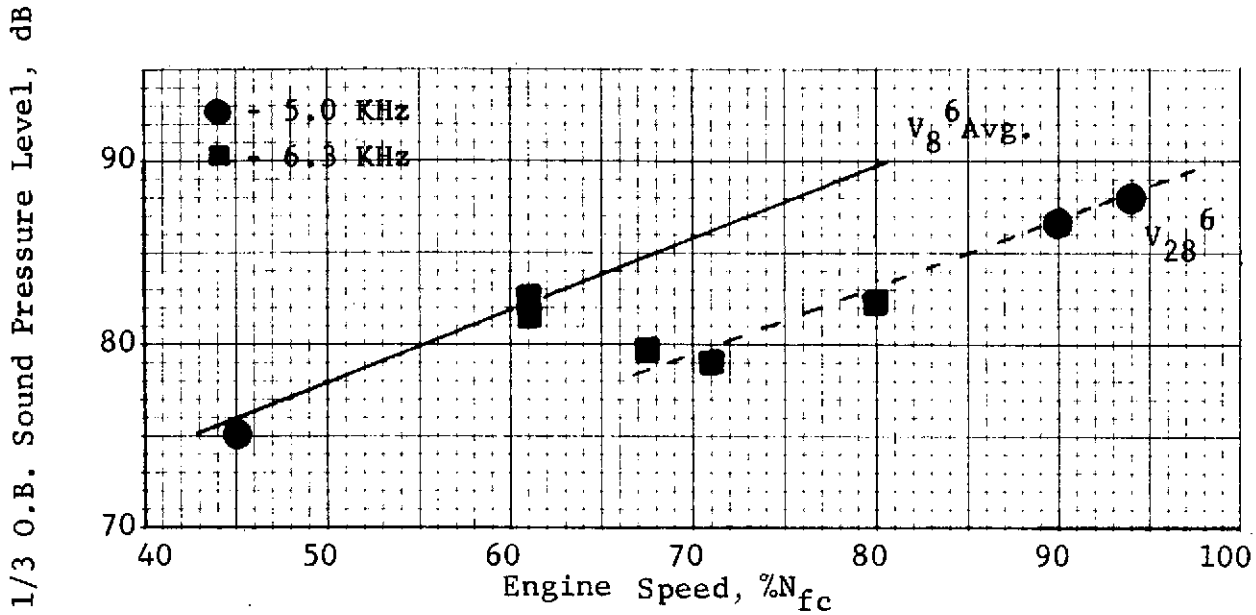

A. 1/3 OCTAVE BAND SPL AT NOISE HUMP

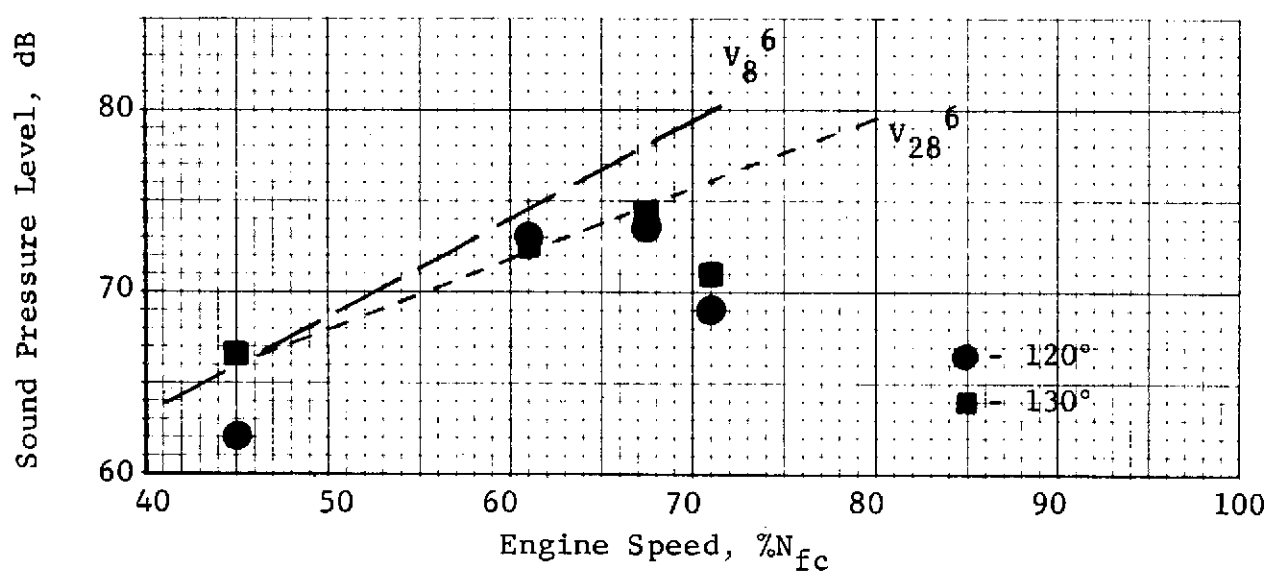

B. PEAK AMPLITUDE OF NOISE HUMP

Figure 344. Engine A Noise Hump - Amplitude Vs. Jet Velocity at Max Aft Angle.

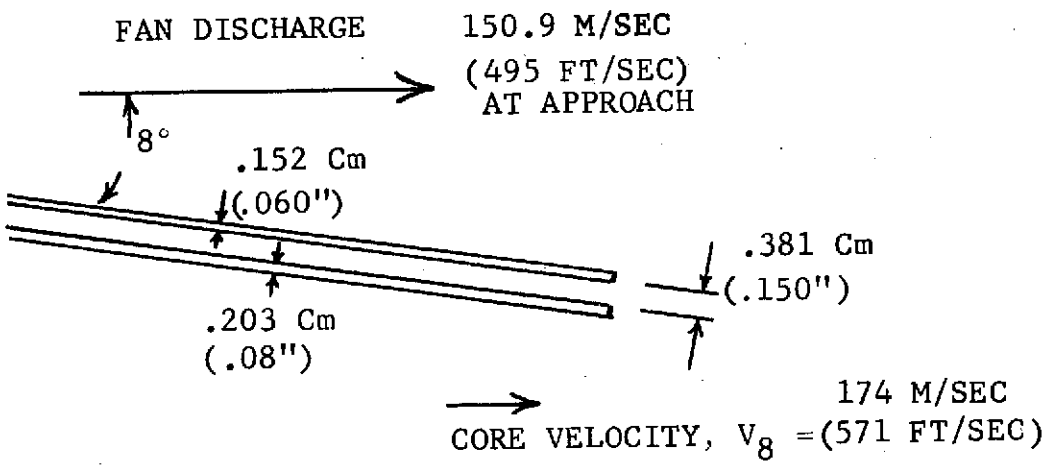

LIP NOISE

$f_o \approx .2V/d$

AVERAGE VELOCITY AT LIP = 162.5 M/SEC (533 FT/SEC)

d = LIP THICKNESS; .152Cm (.06") $\leq$ d $\leq$ .737CM (.29")

$f_{@d=.26}$ = 4900 Hz

Figure 345. Engine A Core Nozzle Lip At Ambient Temperature (Inner Wall Expands During Engine Runs).

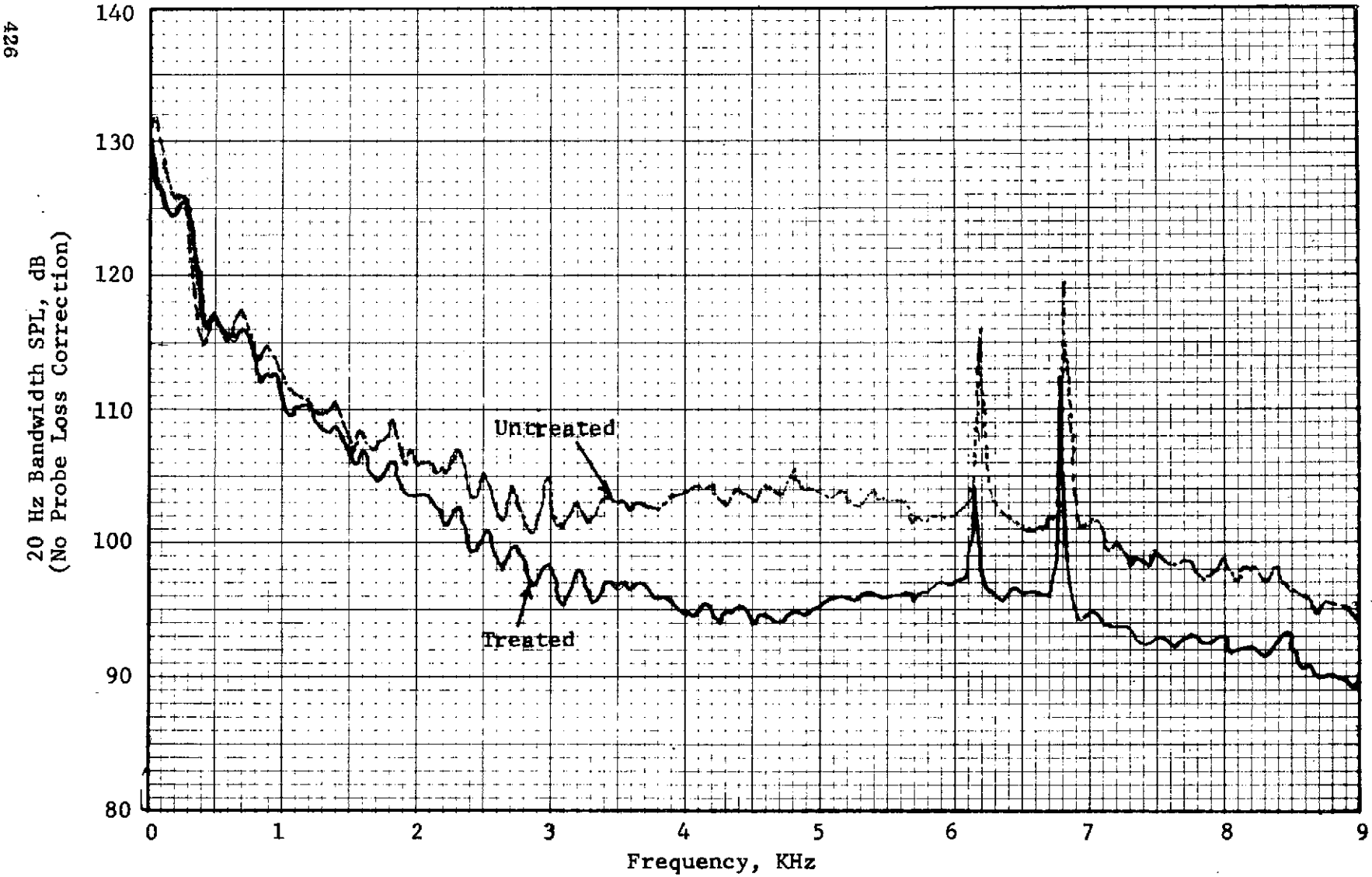

Figure 346. Engine C Aft Turbine Probe Narrowbands at Approach (3150 rpm, Midstream Immersion).

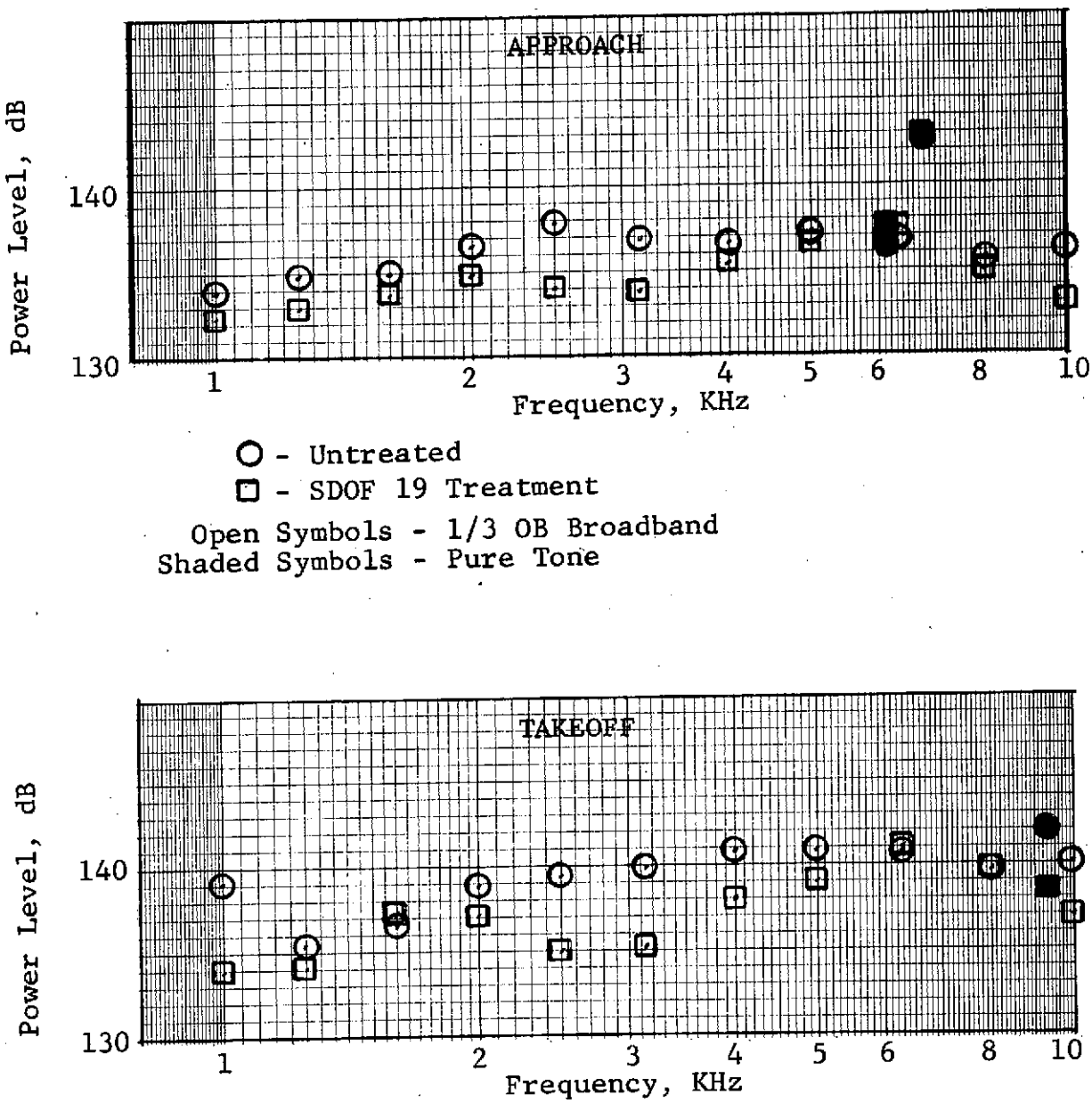

Figure 347. Engine C Power Level at Forward Turbine Probe.

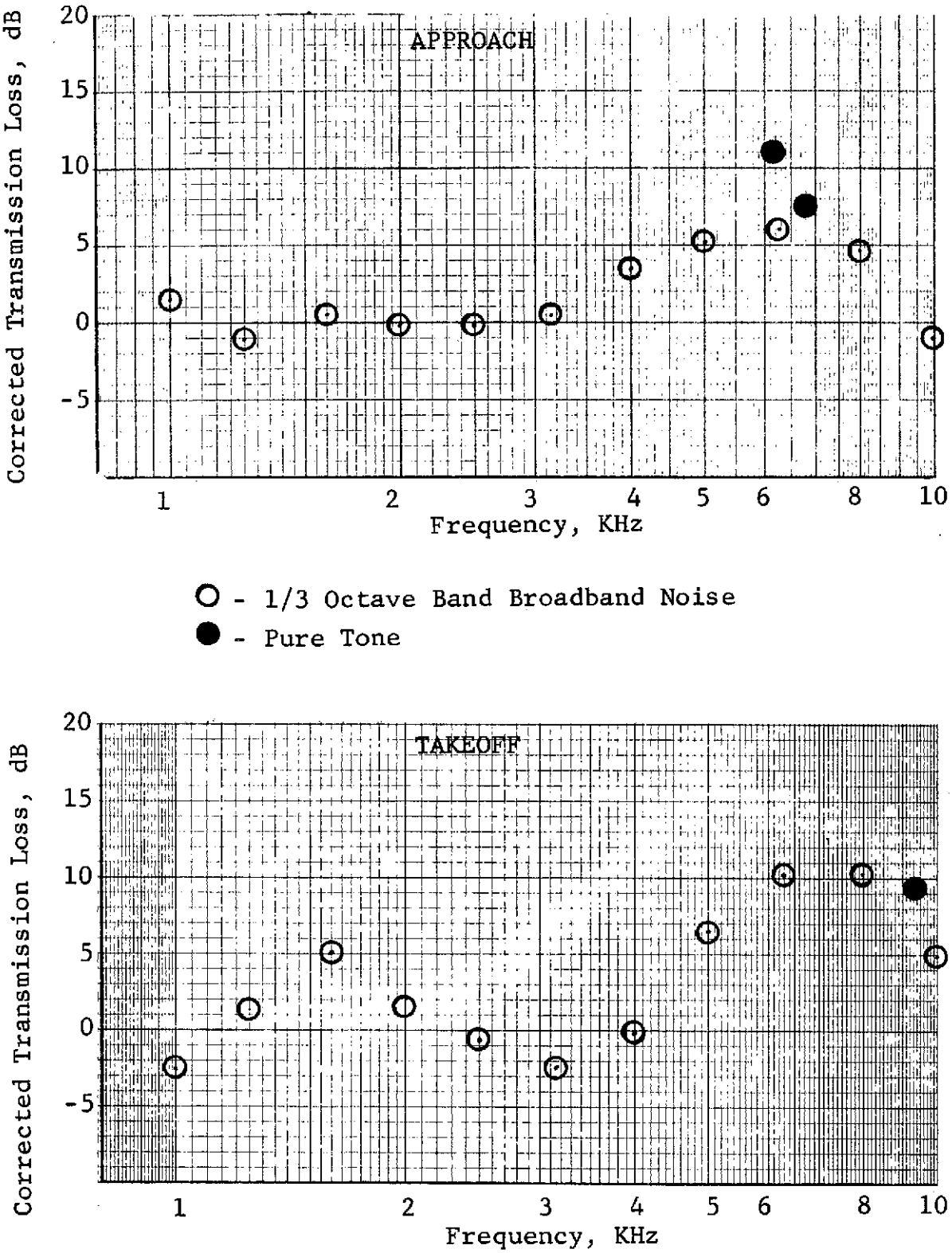

Figure 348. Engine C Turbine Treatment Corrected Transmission Loss.

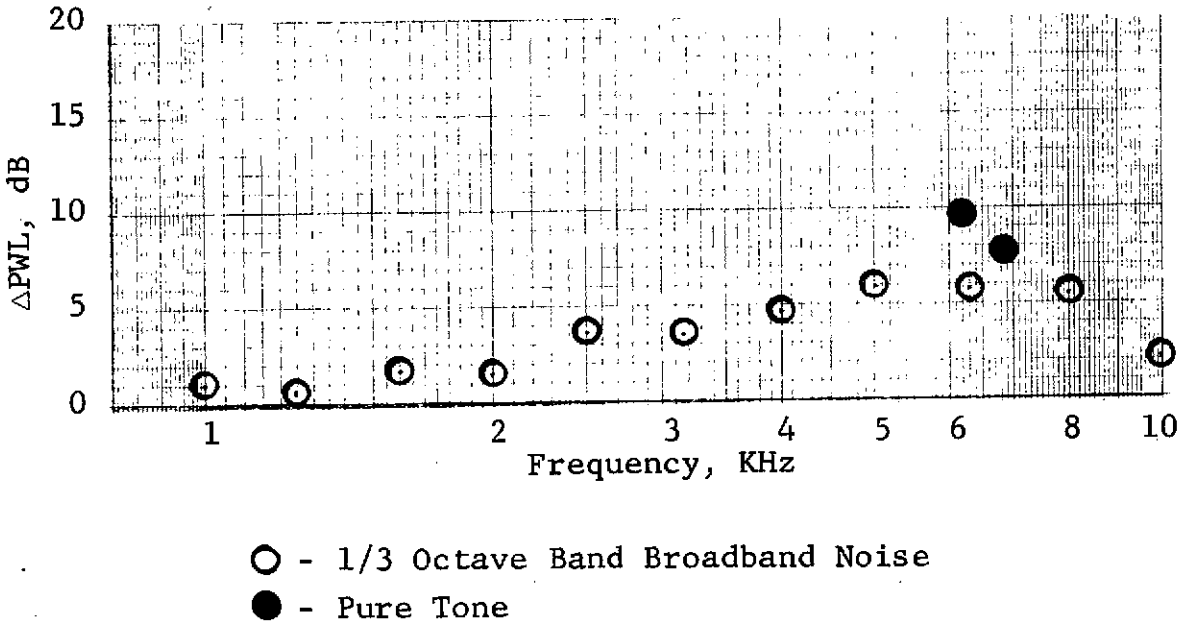

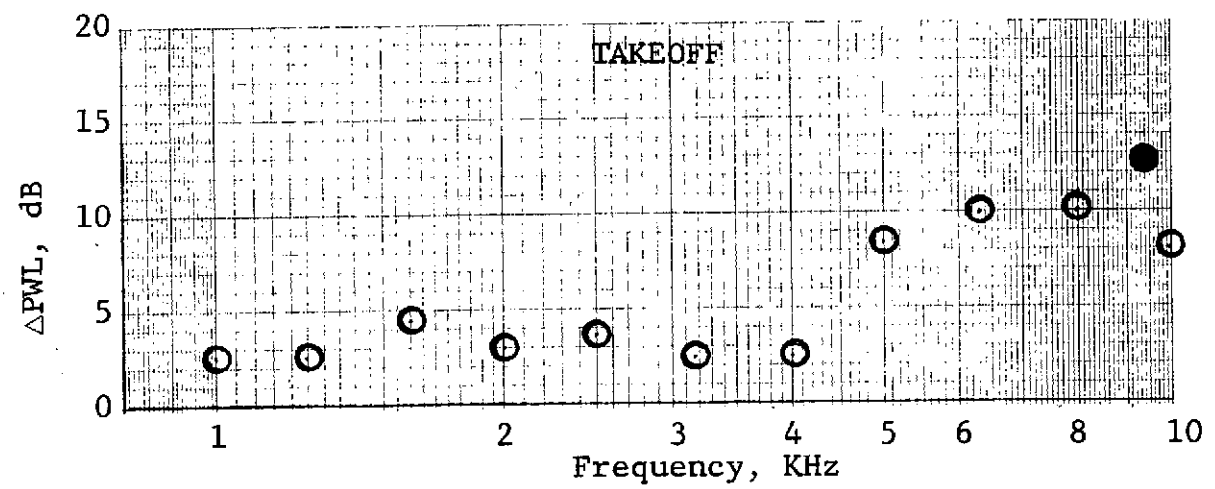

Figure 349. Engine C PWL Reduction at AFT Probe for Turbine Treatment RE Hardwall Turbine Configuration.

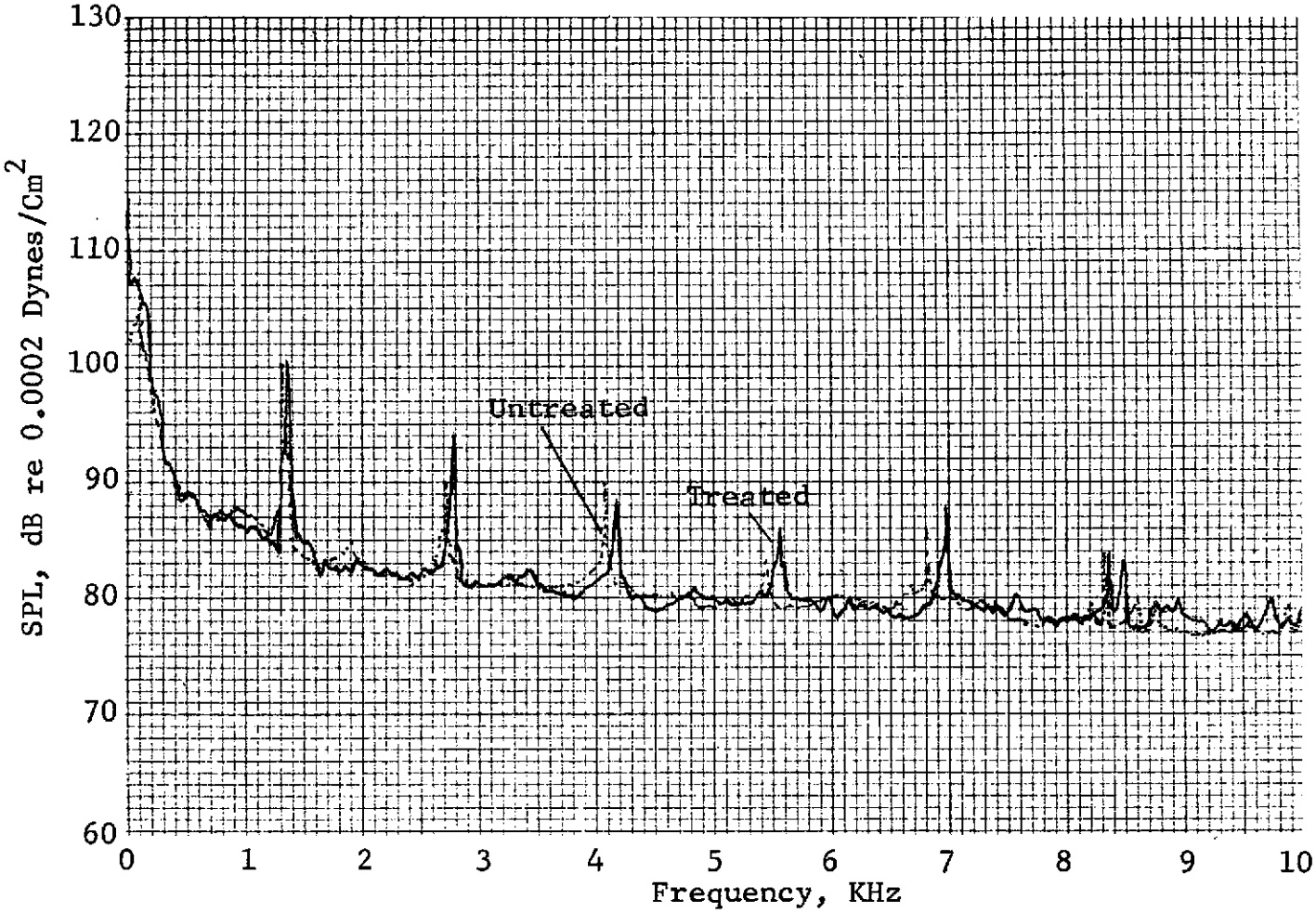

Figure 350. Engine C Nearfield Turbine Treatment Spectra (Approach Power, Position No. 1).

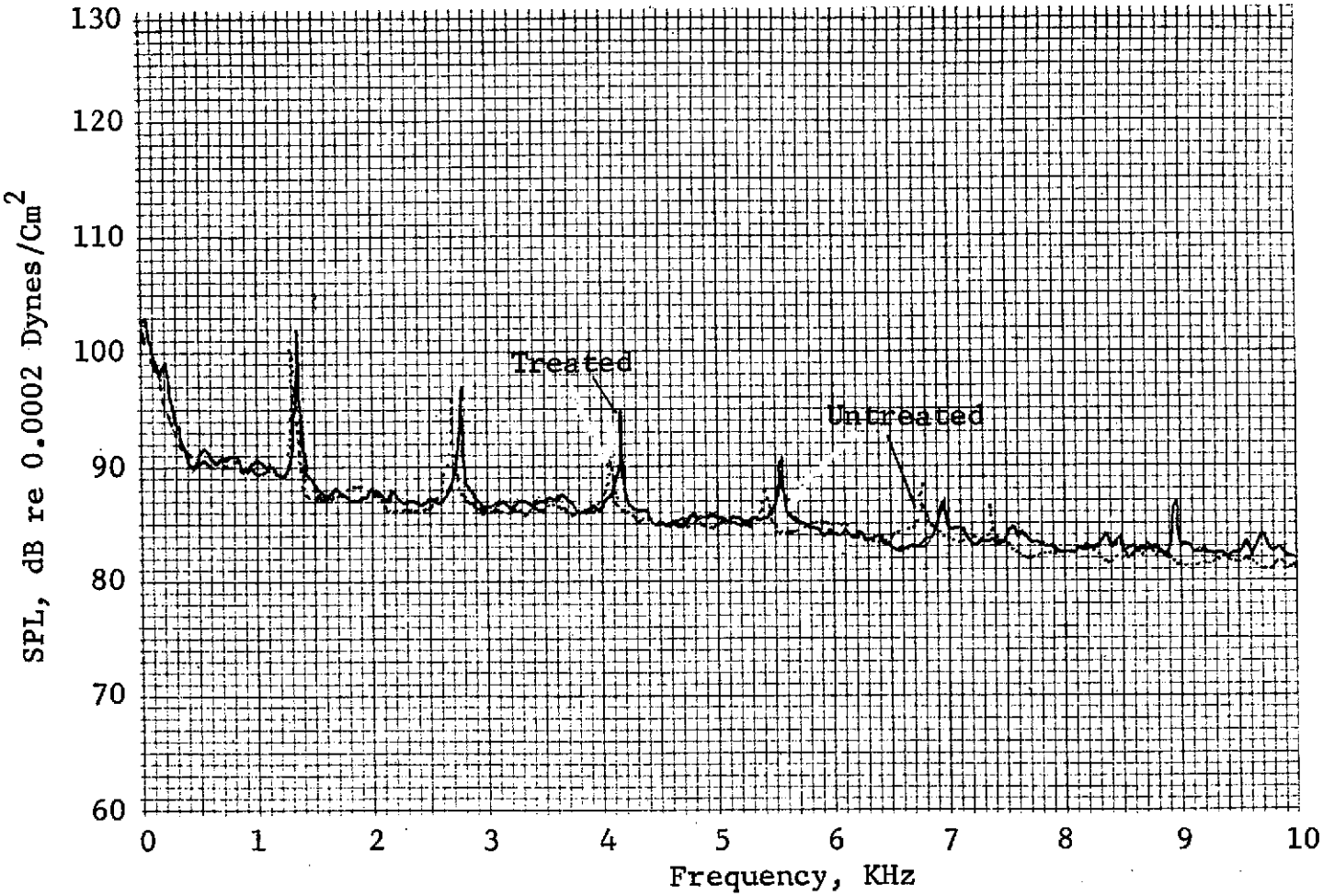

Figure 351. Engine C Nearfield Turbine Treatment Spectra (Approach Power, Position No. 2).

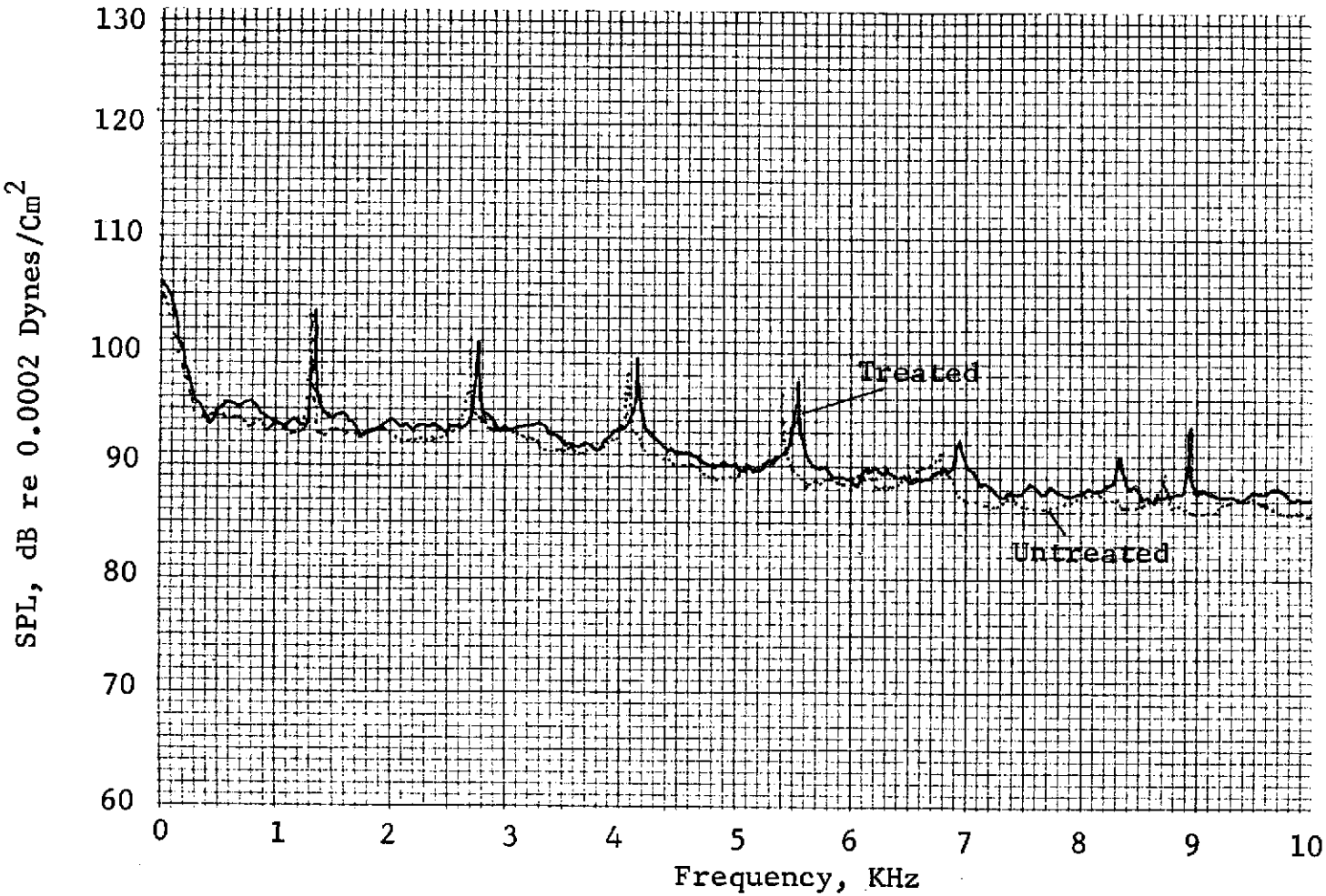

Figure 352. Engine C Nearfield Turbine Treatment Spectra (Approach Power, Position No. 3).

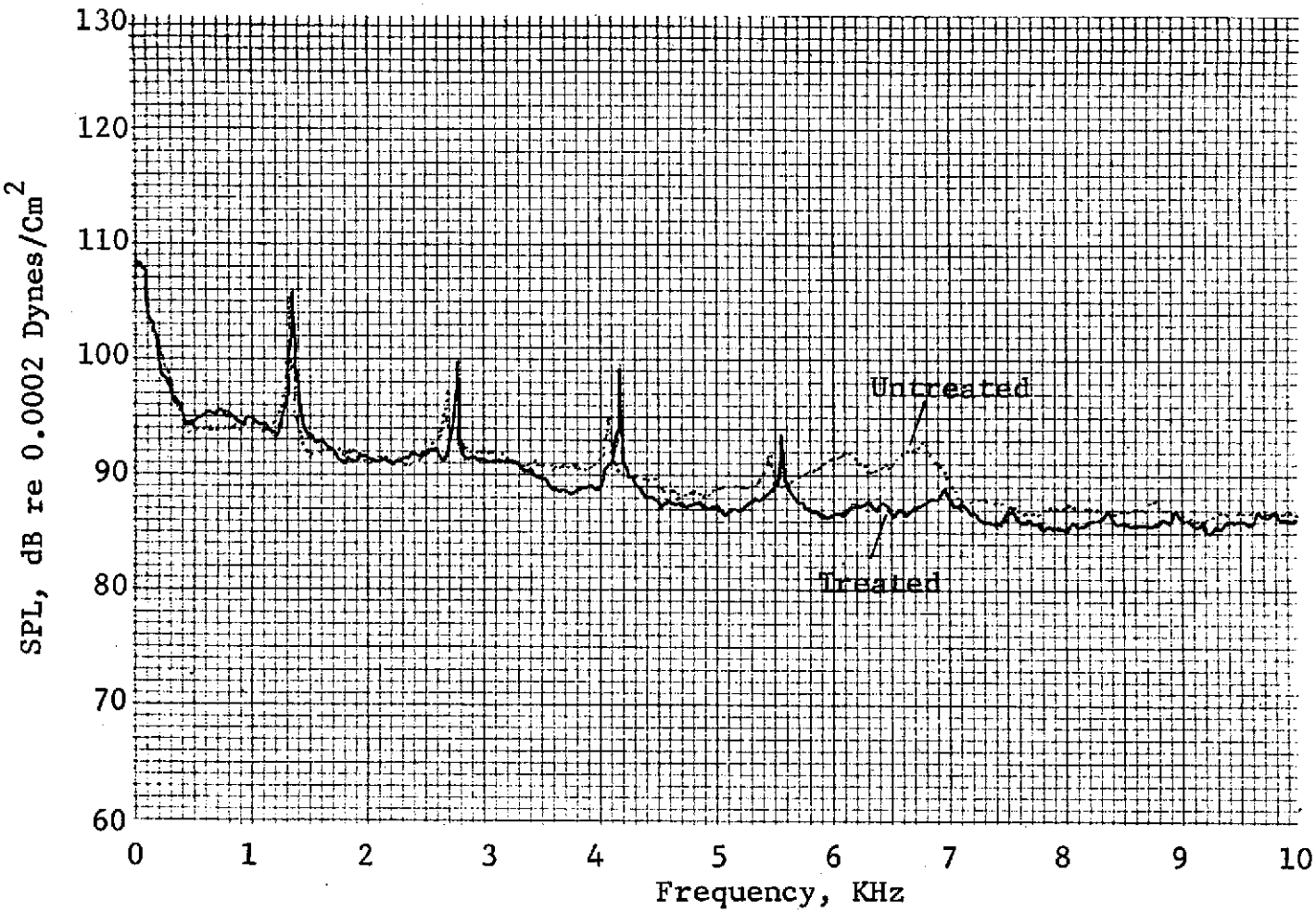

Figure 353. Engine C Nearfield Turbine Treatment Spectra (Approach Power, Position No. 4).

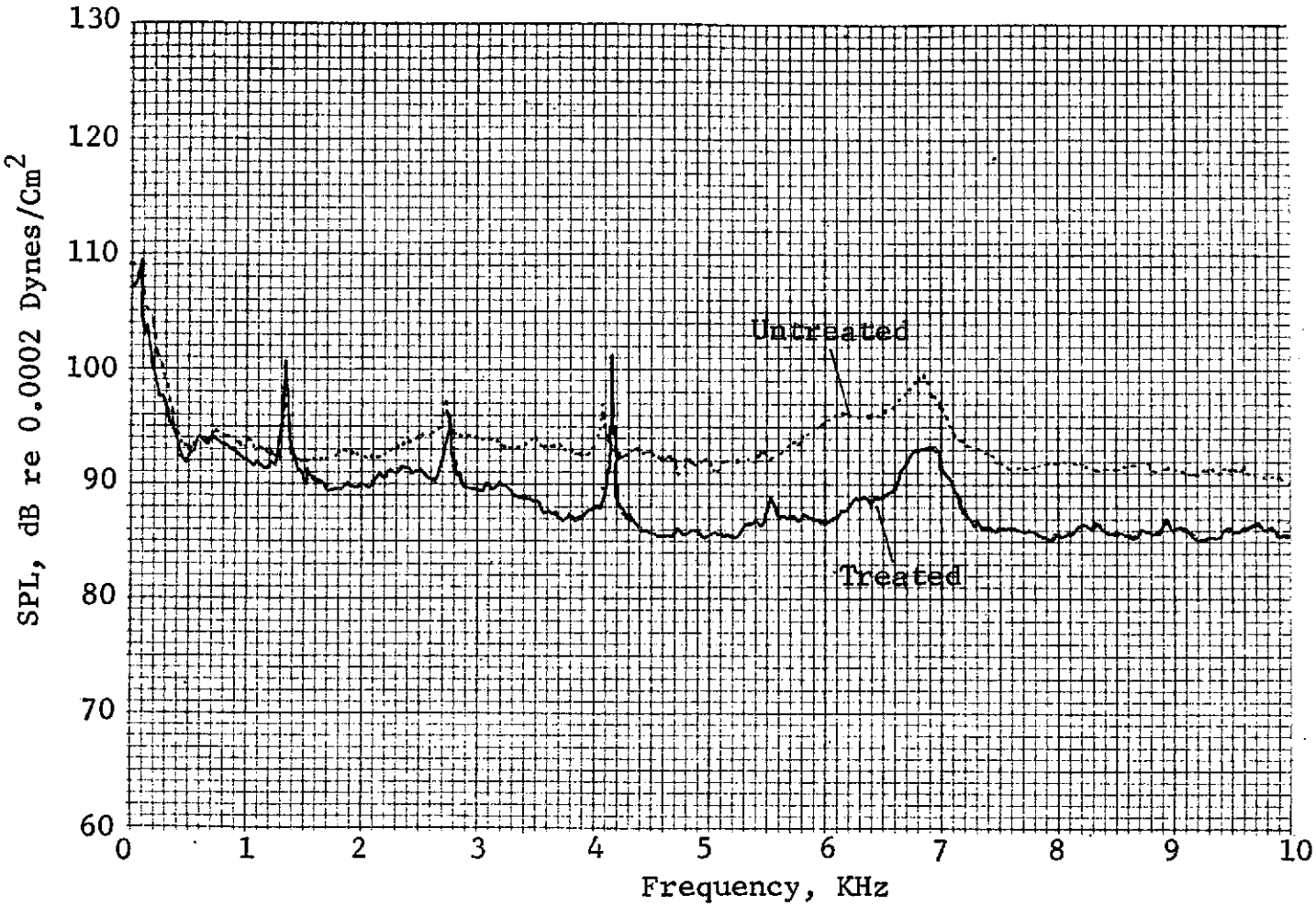

Figure 354. Engine C Nearfield Turbine Treatment Spectra (Approach Power, Position No. 5).

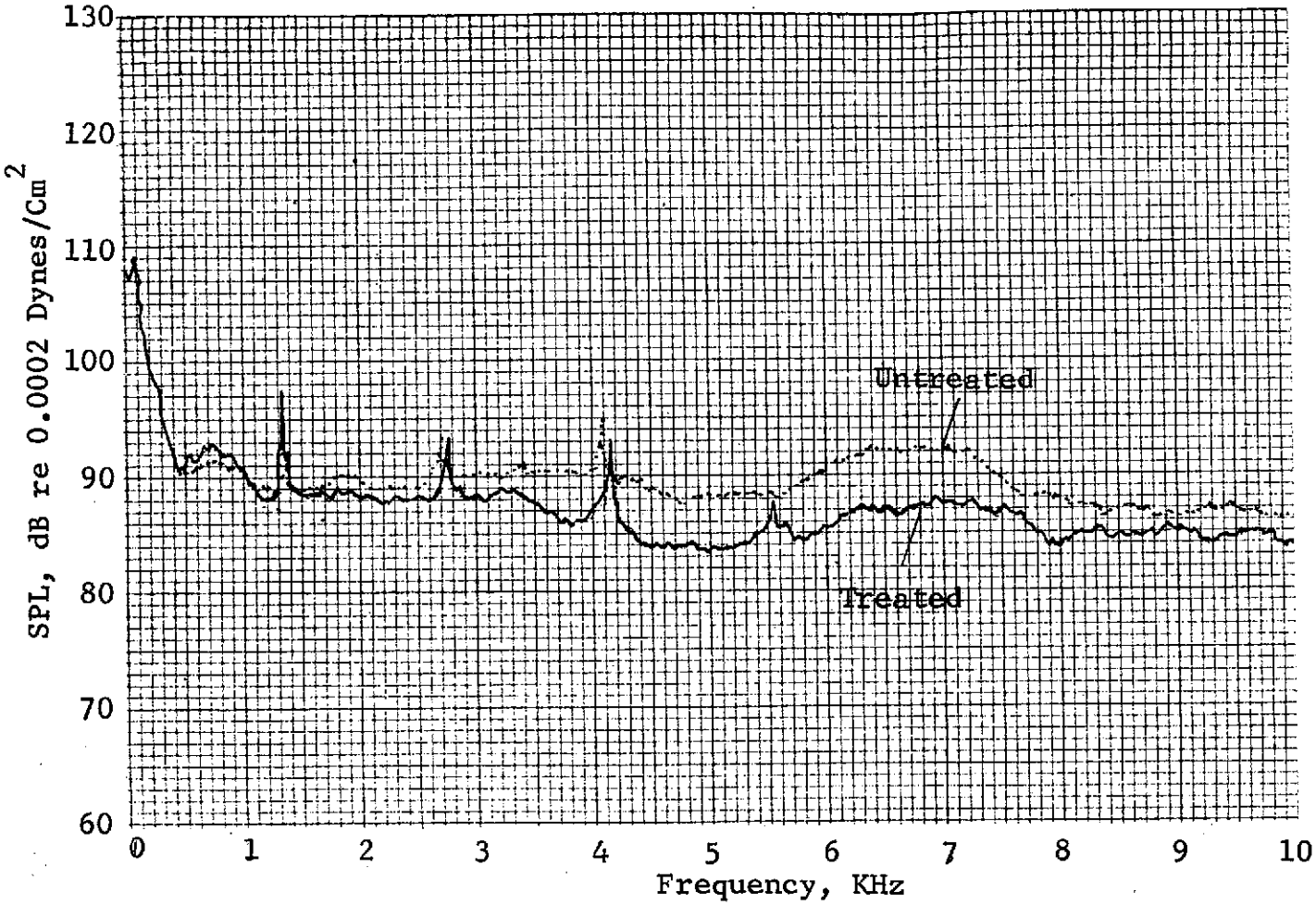

Figure 355. Engine C Nearfield Turbine Treatment Spectra (Approach Power, Position No. 6).

C-22

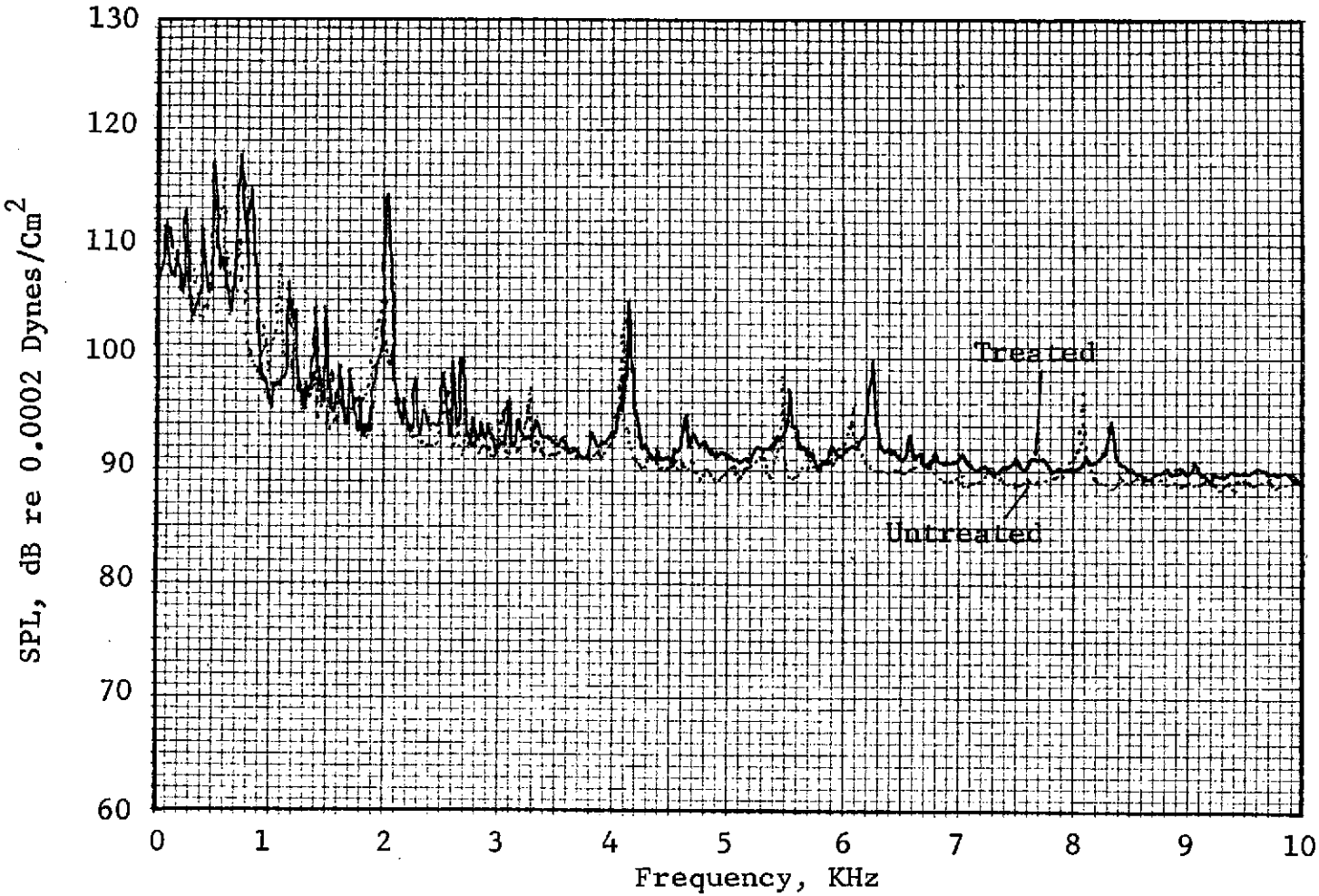

Figure 356. Engine C Nearfield Turbine Treatment Spectra (Takeoff Power, Position No. 1).

C-2

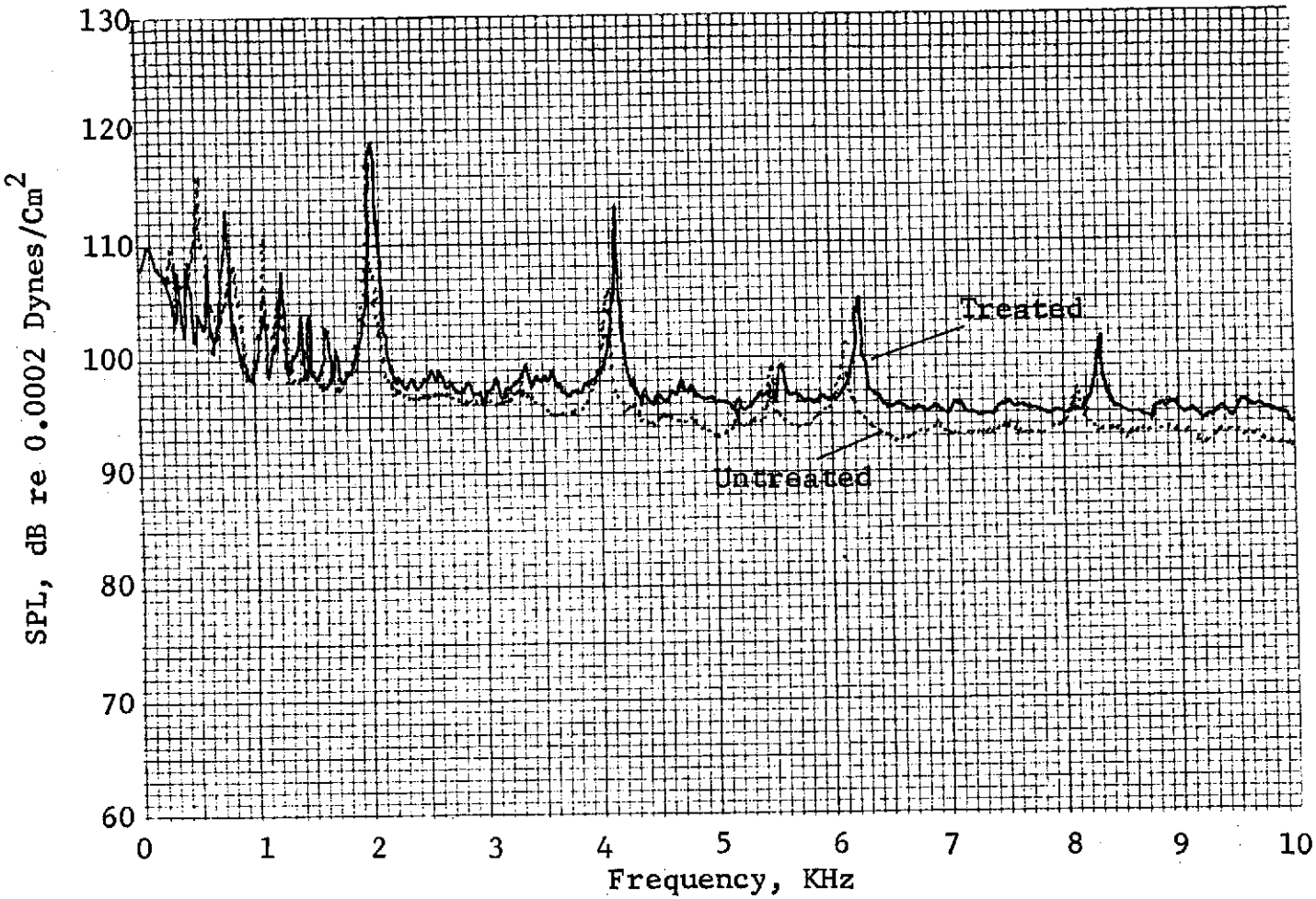

Figure 357. Engine C Nearfield Turbine Treatment Spectra (Takeoff Power, Position No. 2).

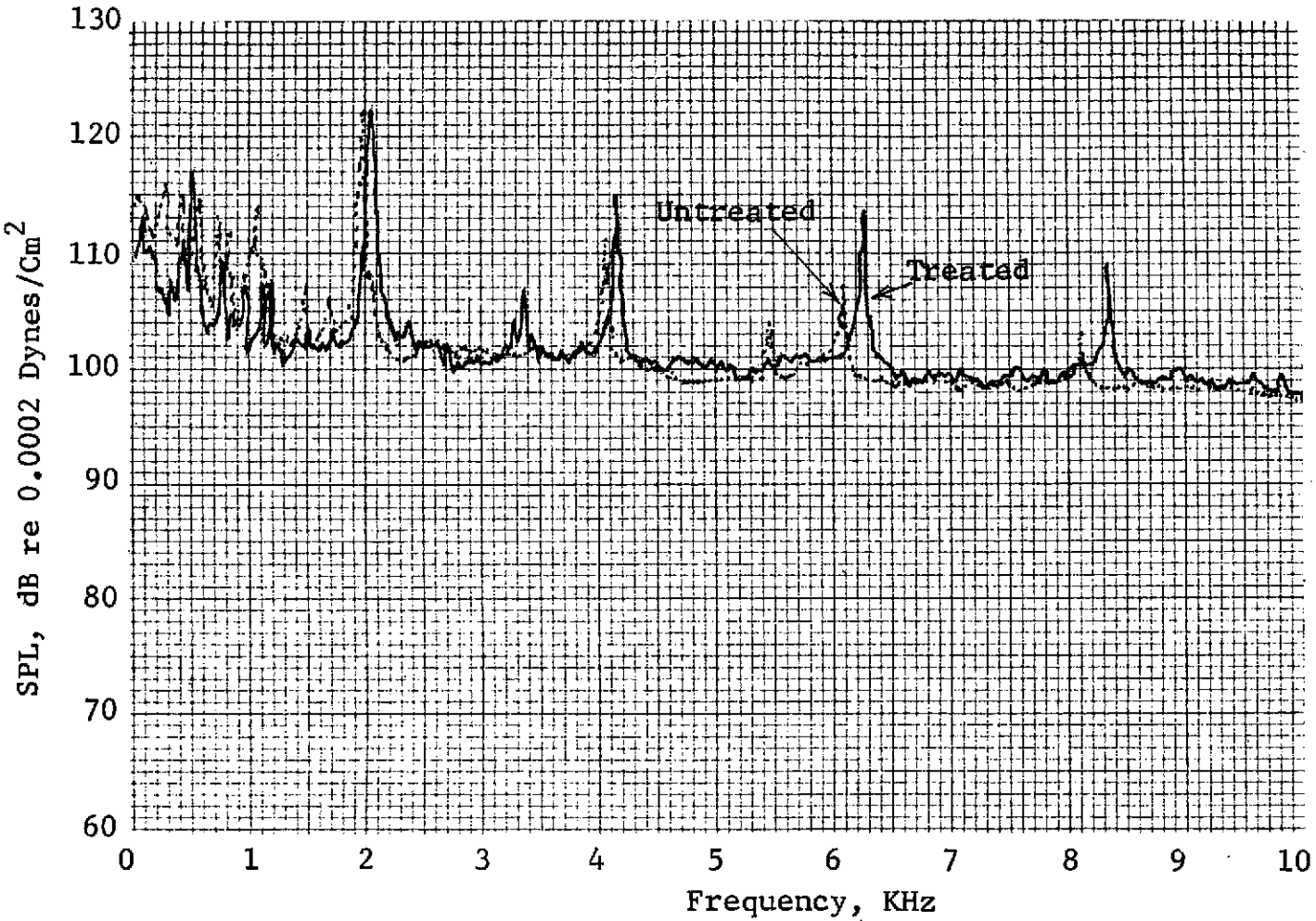

Figure 358. Engine C Nearfield Turbine Treatment Spectra (Takeoff Power, Position No. 3).

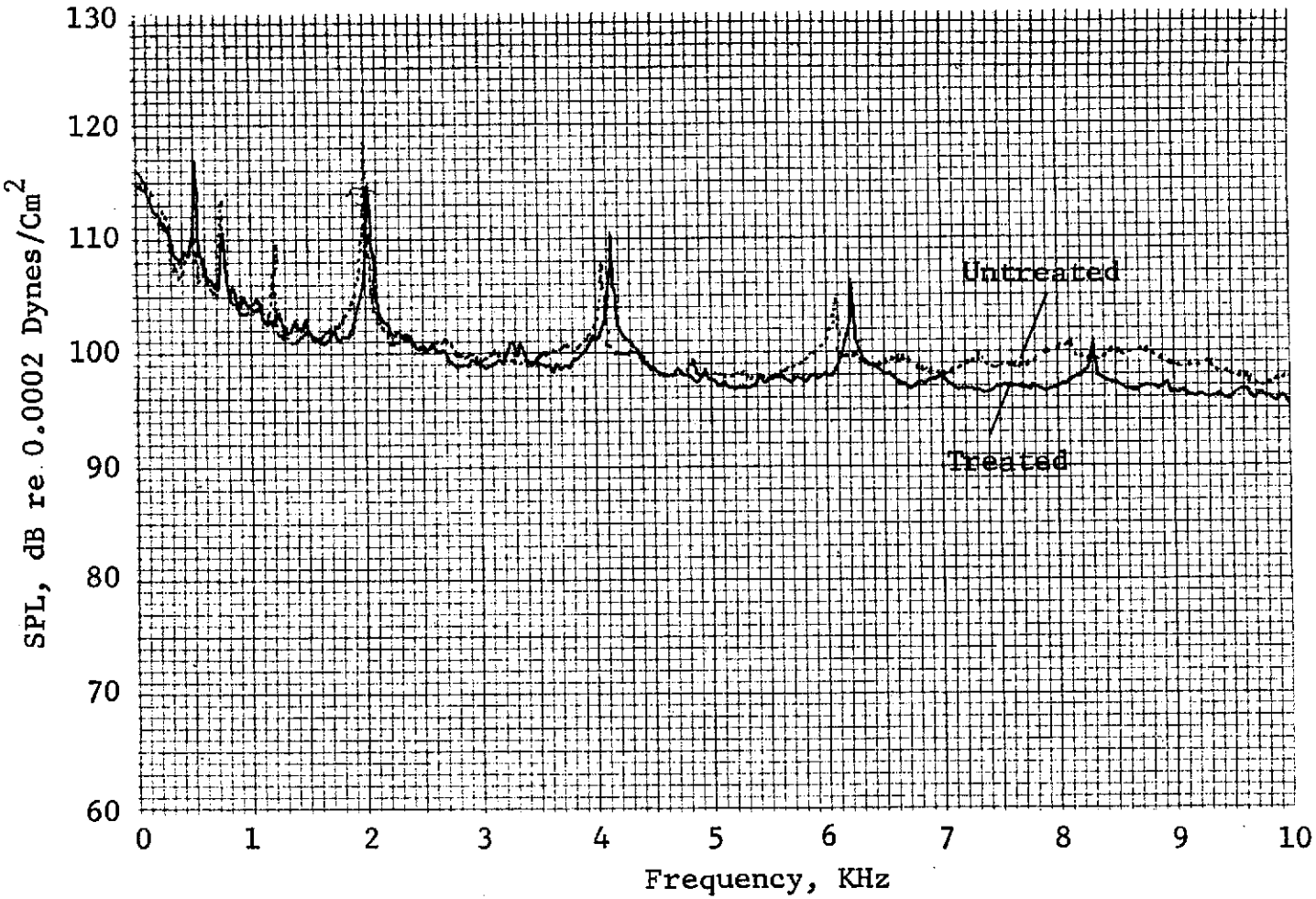

Figure 359. Engine C Nearfield Turbine Treatment Spectra (Takeoff Power, Position No. 4).

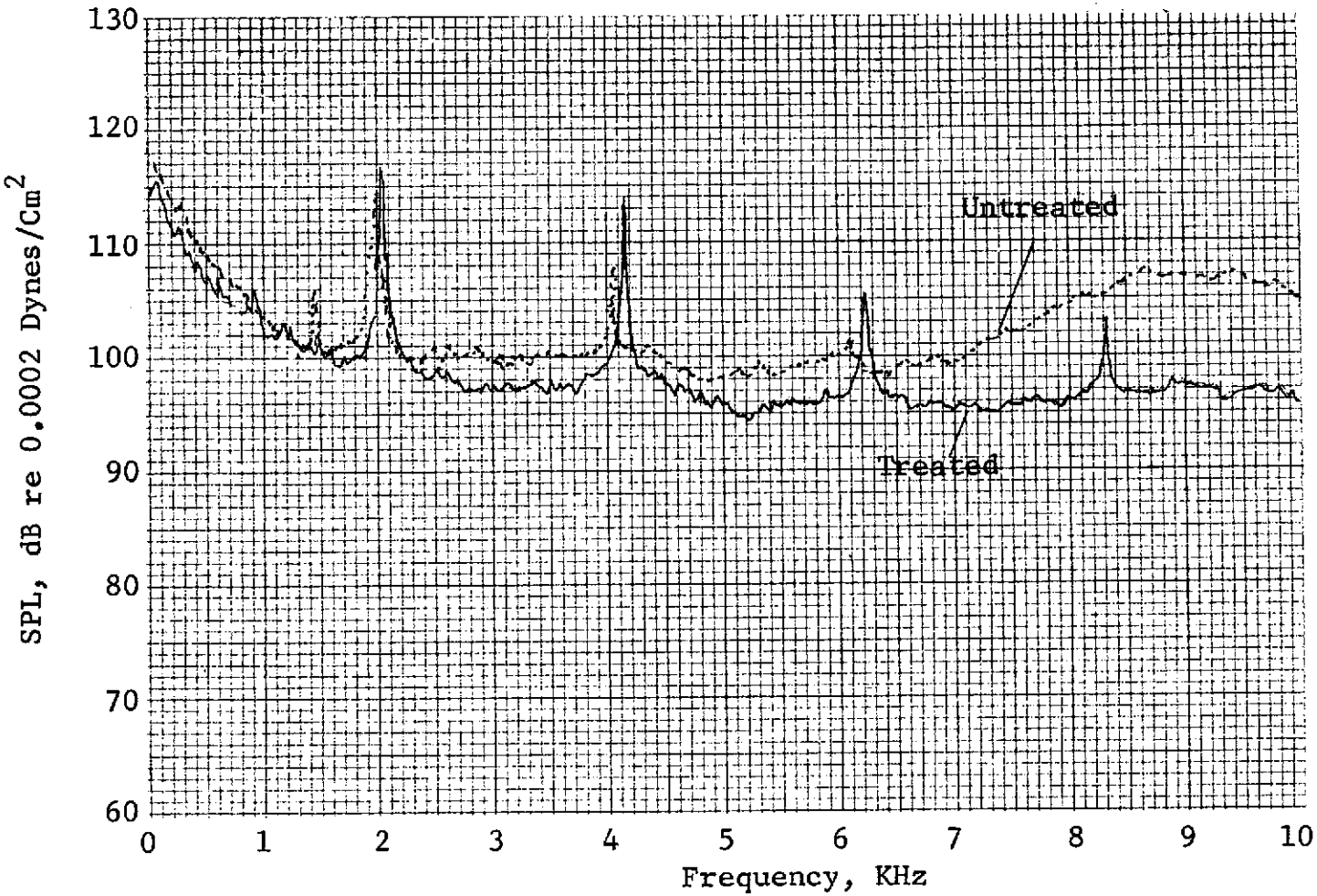

Figure 360. Engine C Nearfield Turbine Treatment Spectra (Takeoff Power, Position No. 5).

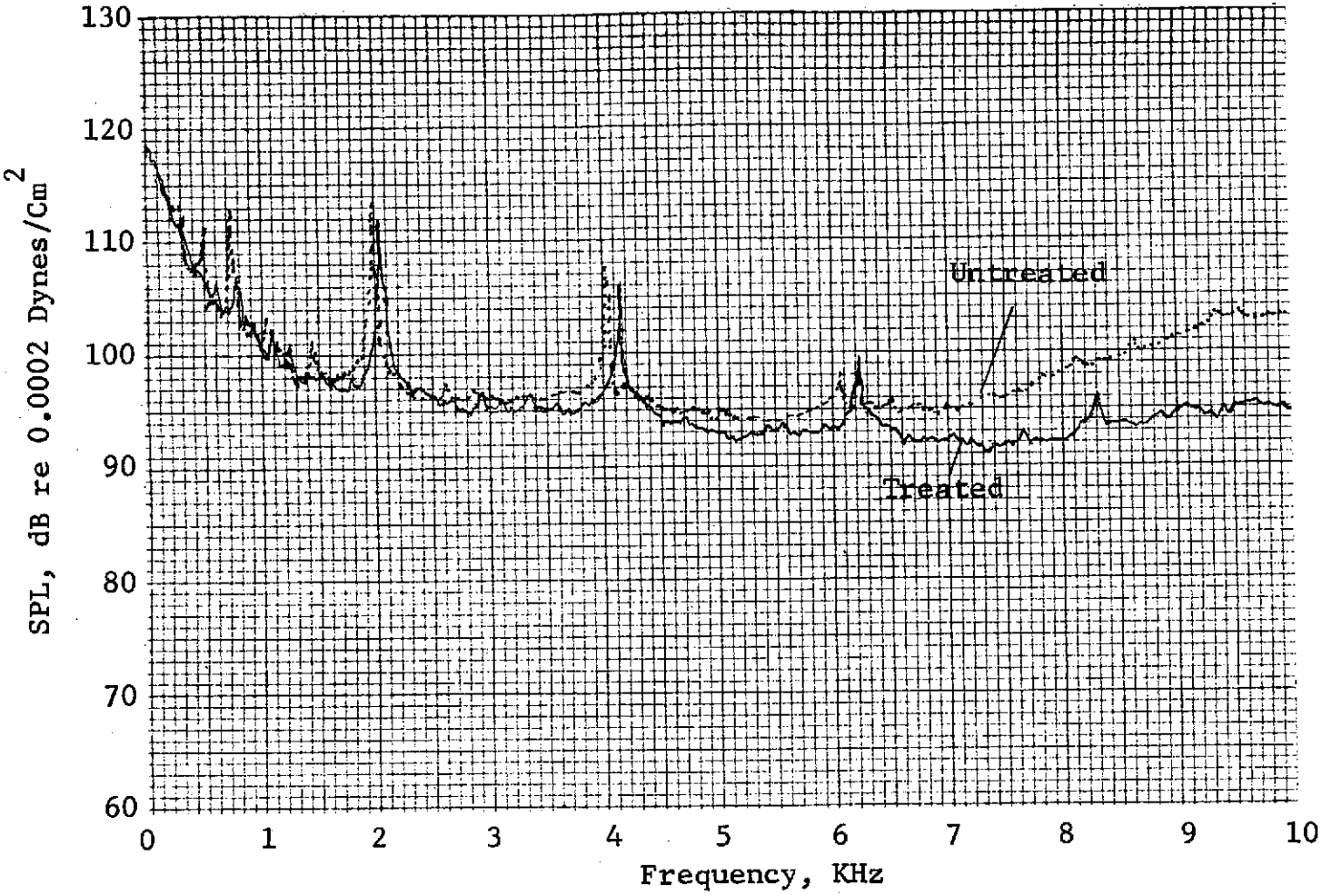

Figure 361. Engine C Nearfield Turbine Treatment Spectra (Takeoff Power, Position No. 6).

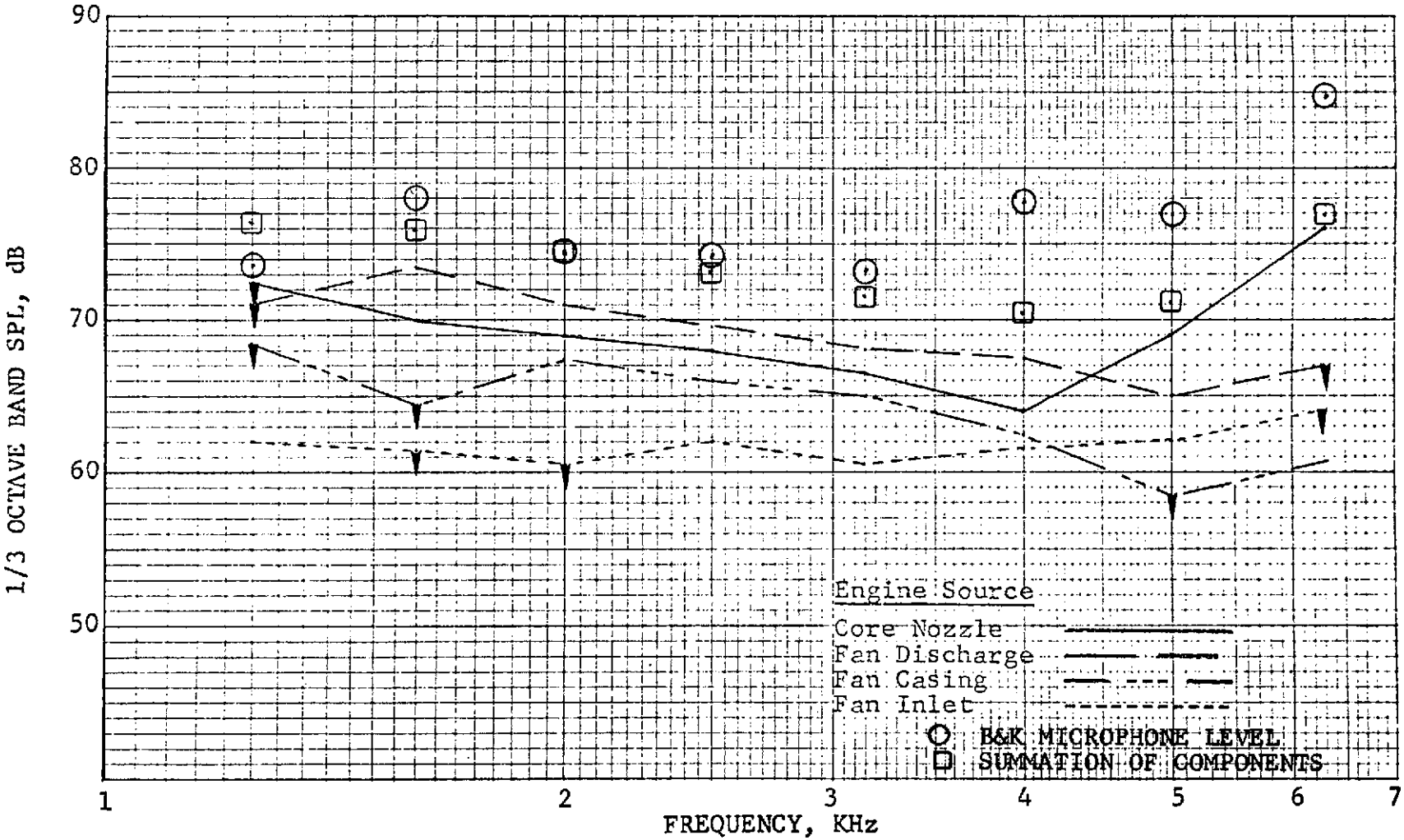

Figure 362. Engine C Broadband Noise Directivity from Directional Array Fully Suppressed Configuration, Approach Speed 50° from Inlet.

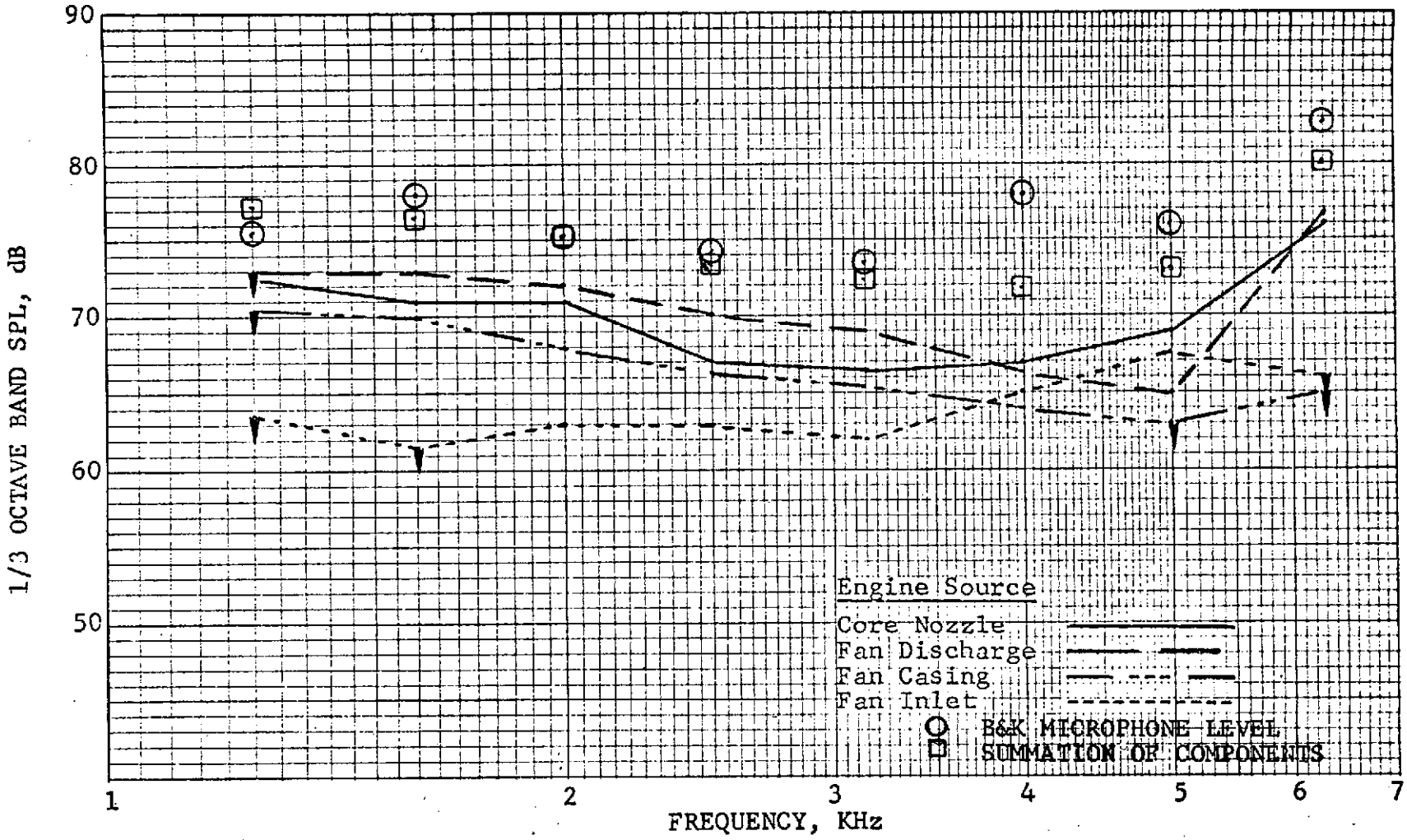

Figure 363. Engine C Broadband Noise Directivity from Directional Array Fully Suppressed Configuration, Approach Speed 60° from Inlet.

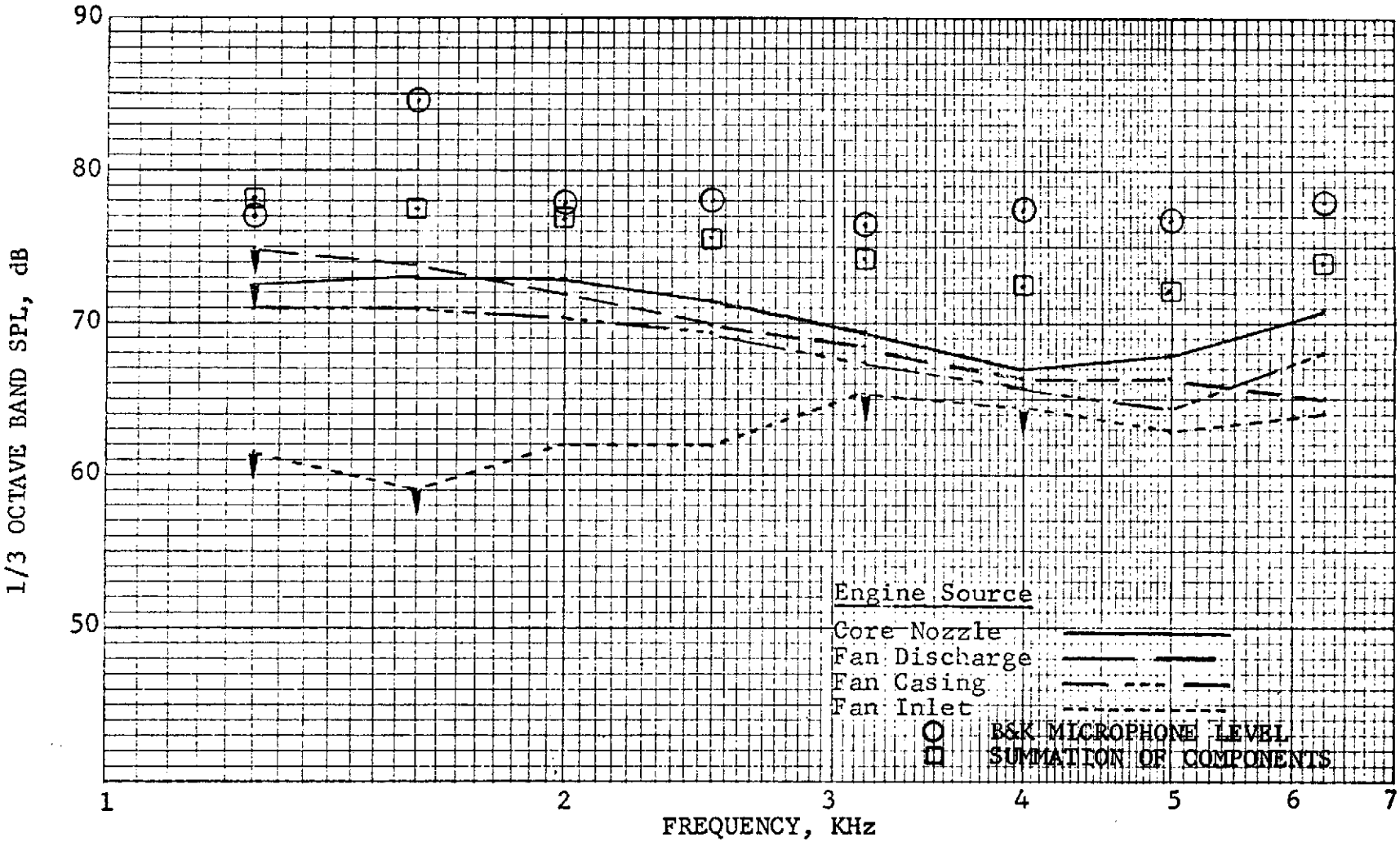

Figure 364. Engine C Broadband Noise Directivity from Directional Array Fully Suppressed Configuration, Approach Speed 90° from Inlet.

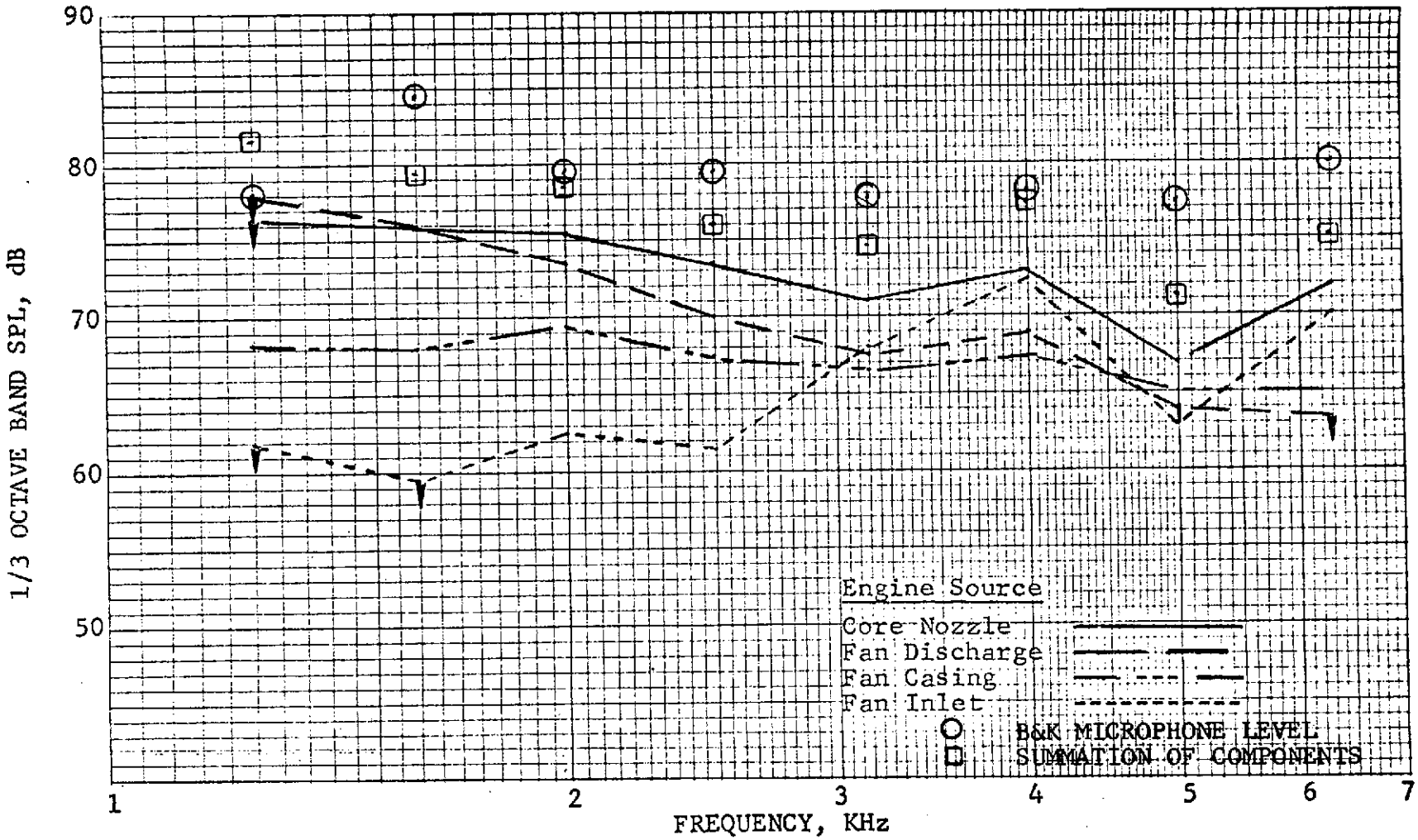

Figure 365. Engine C Broadband Noise Directivity from Directional Array Fully Suppressed Configuration, Approach Speed 100° from Inlet.

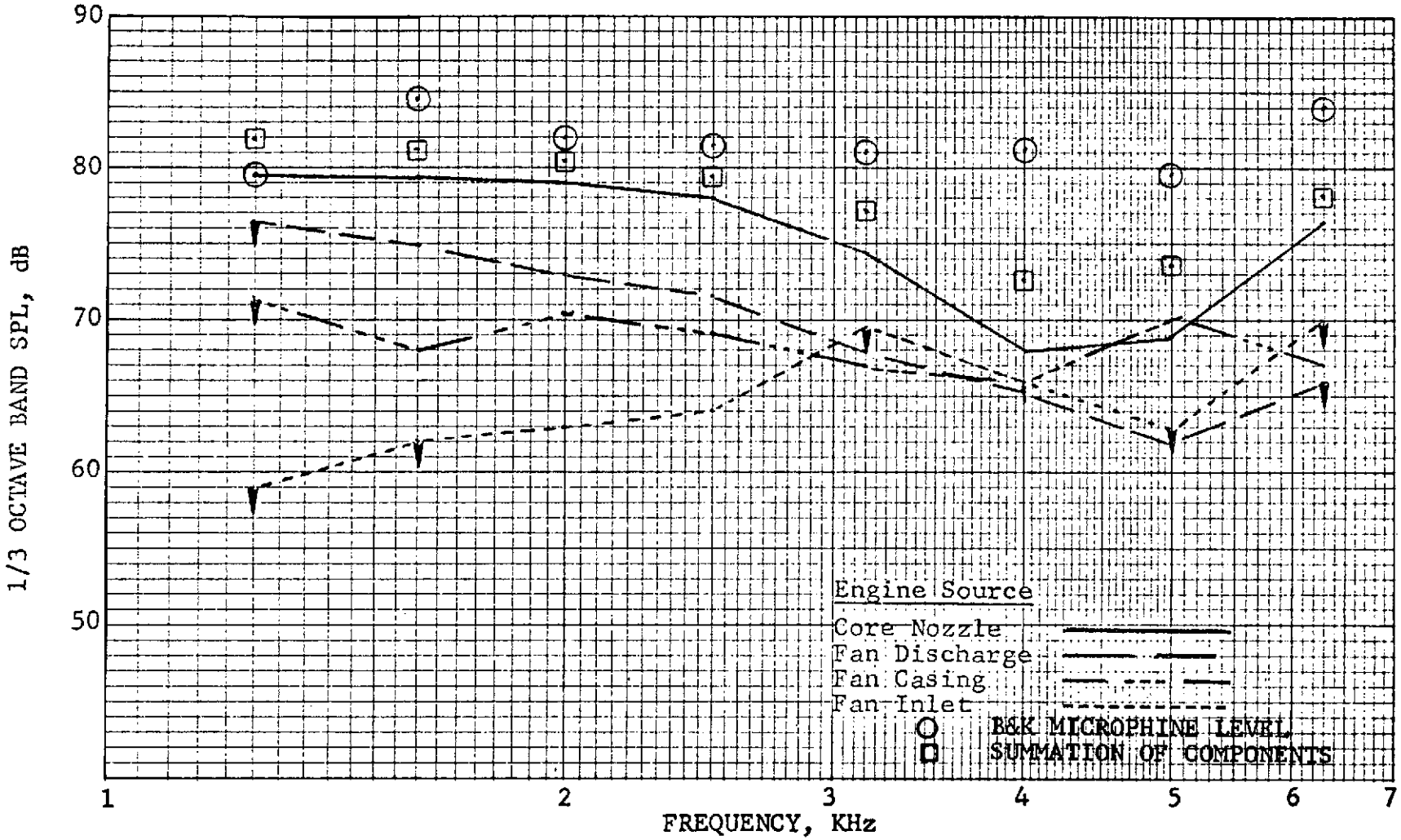

Figure 366. Engine C Broadband Noise Directivity from Directional Array Fully Suppressed Configuration, Approach Speed 110° from Inlet.

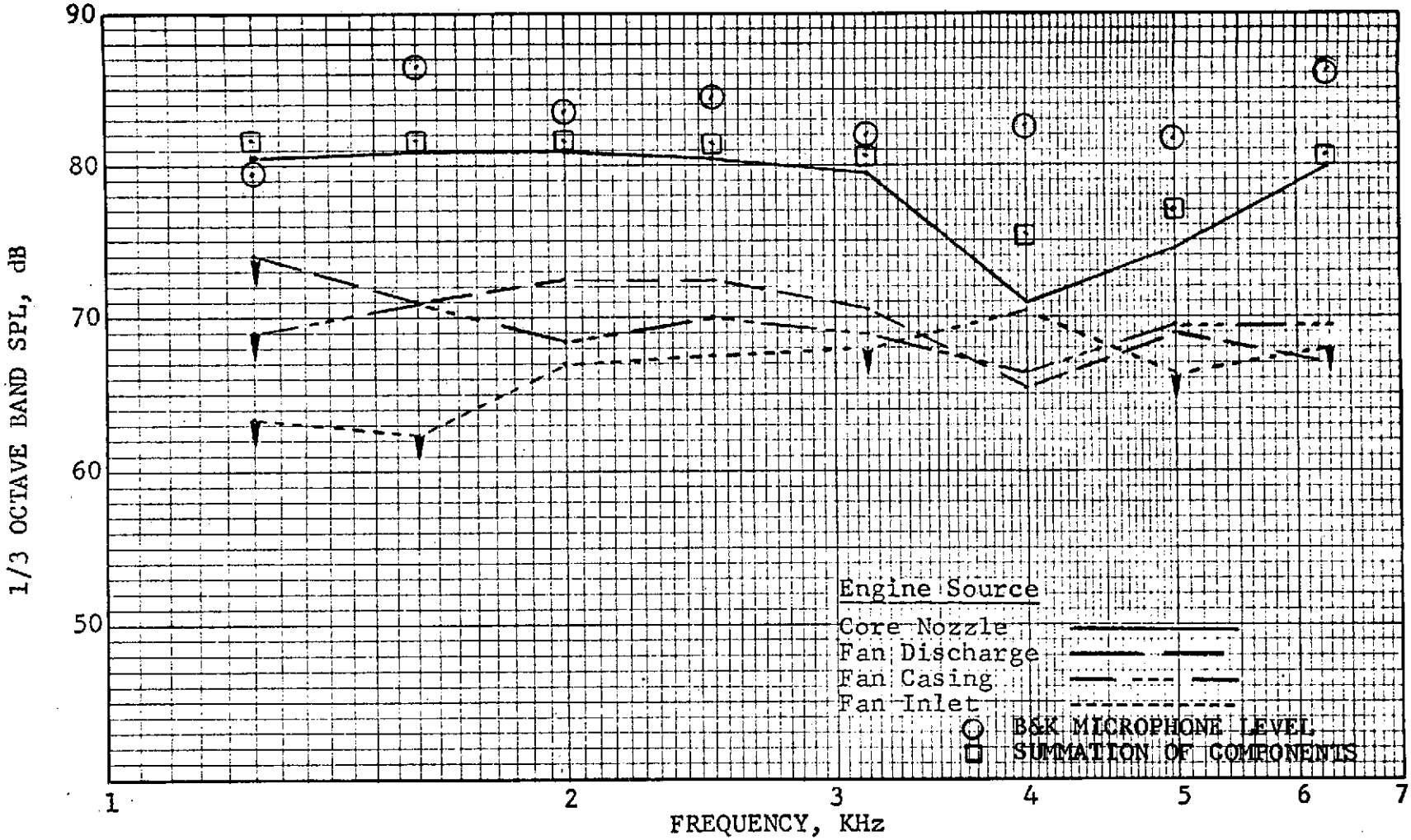

Figure 367. Engine C Broadband Noise Directivity from Directional Array Fully Suppressed Configuration, Approach Speed 120° from Inlet.

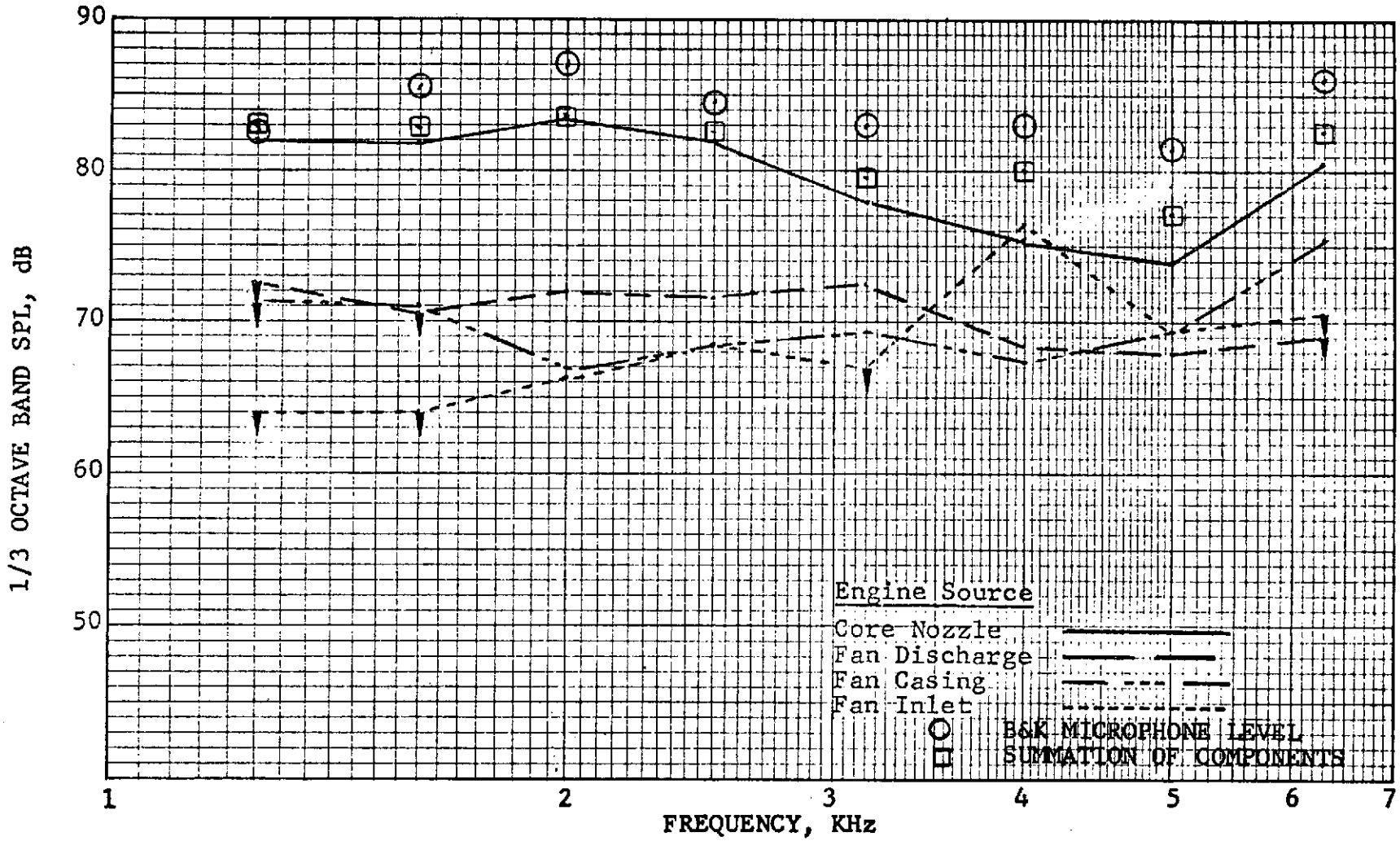

Figure 368. Engine C Broadband Noise Directivity from Directional Array Fully Suppressed Configuration, Approach Speed 130° from Inlet.

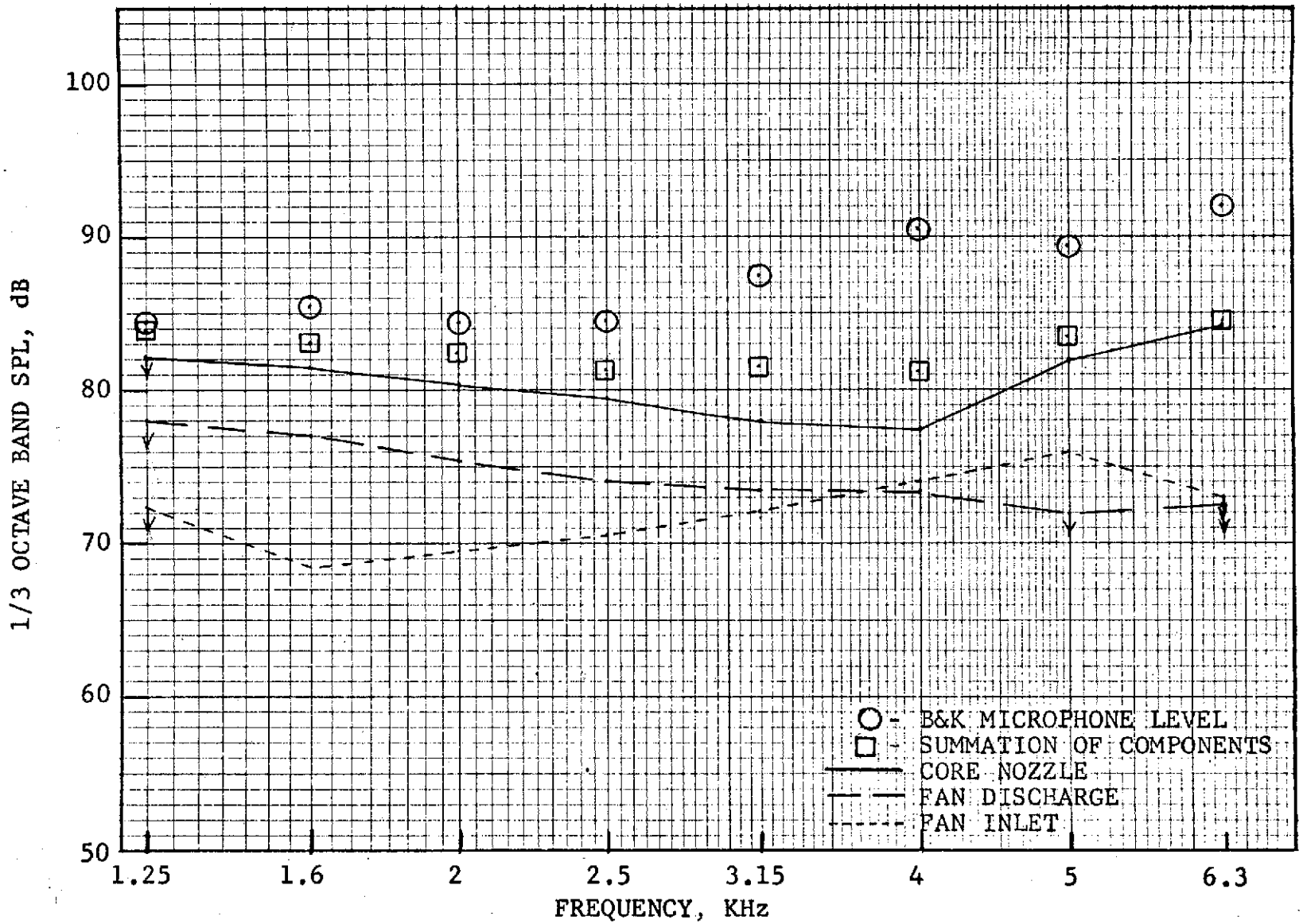

Figure 369. Engine C Broadband Noise Directivity from Directional Array Fully Suppressed Configuration, Takeoff, 50°.

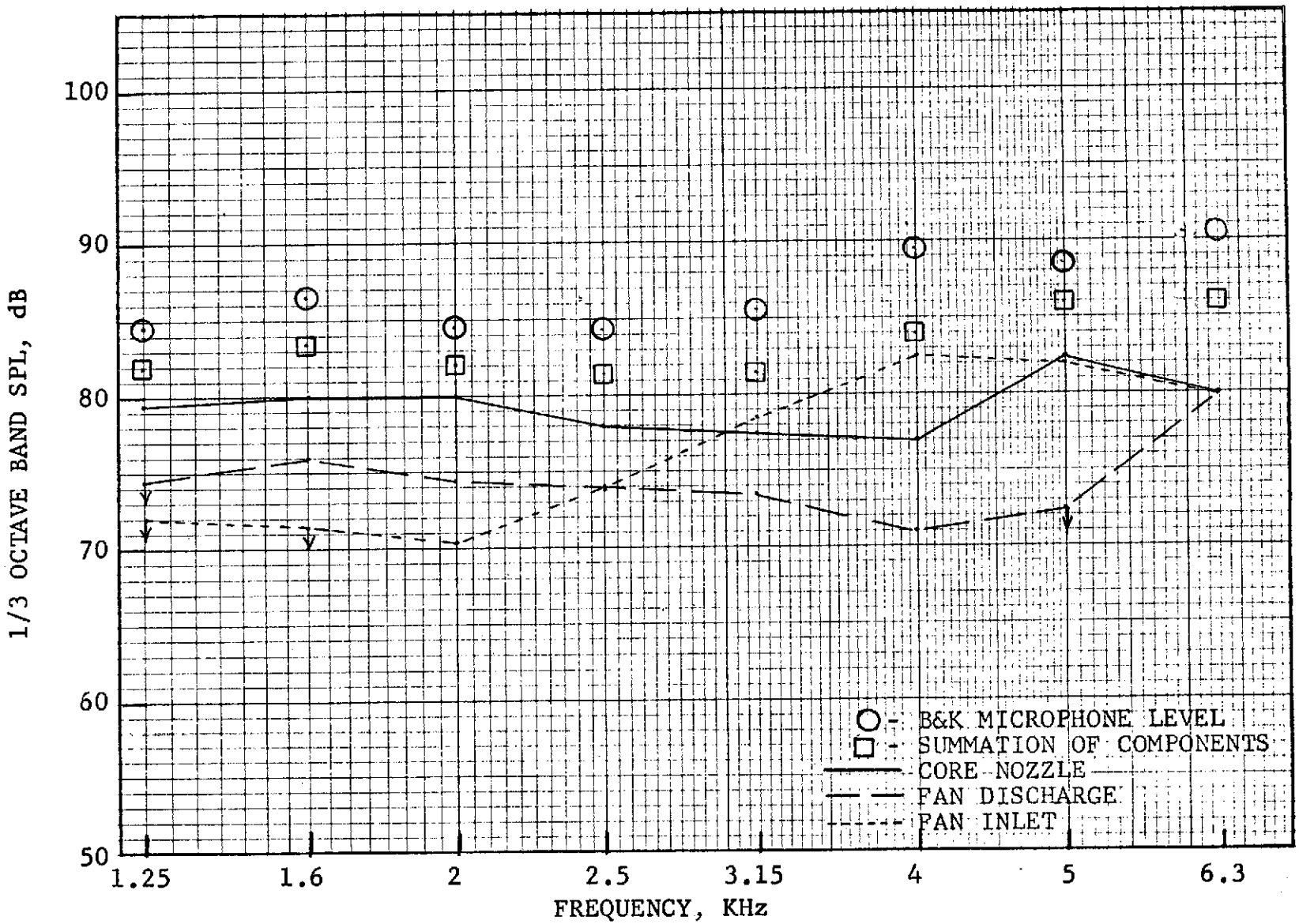

Figure 370. Engine C Broadband Noise Directivity from Directional Array Fully Suppressed Configuration, Takeoff, 60°.

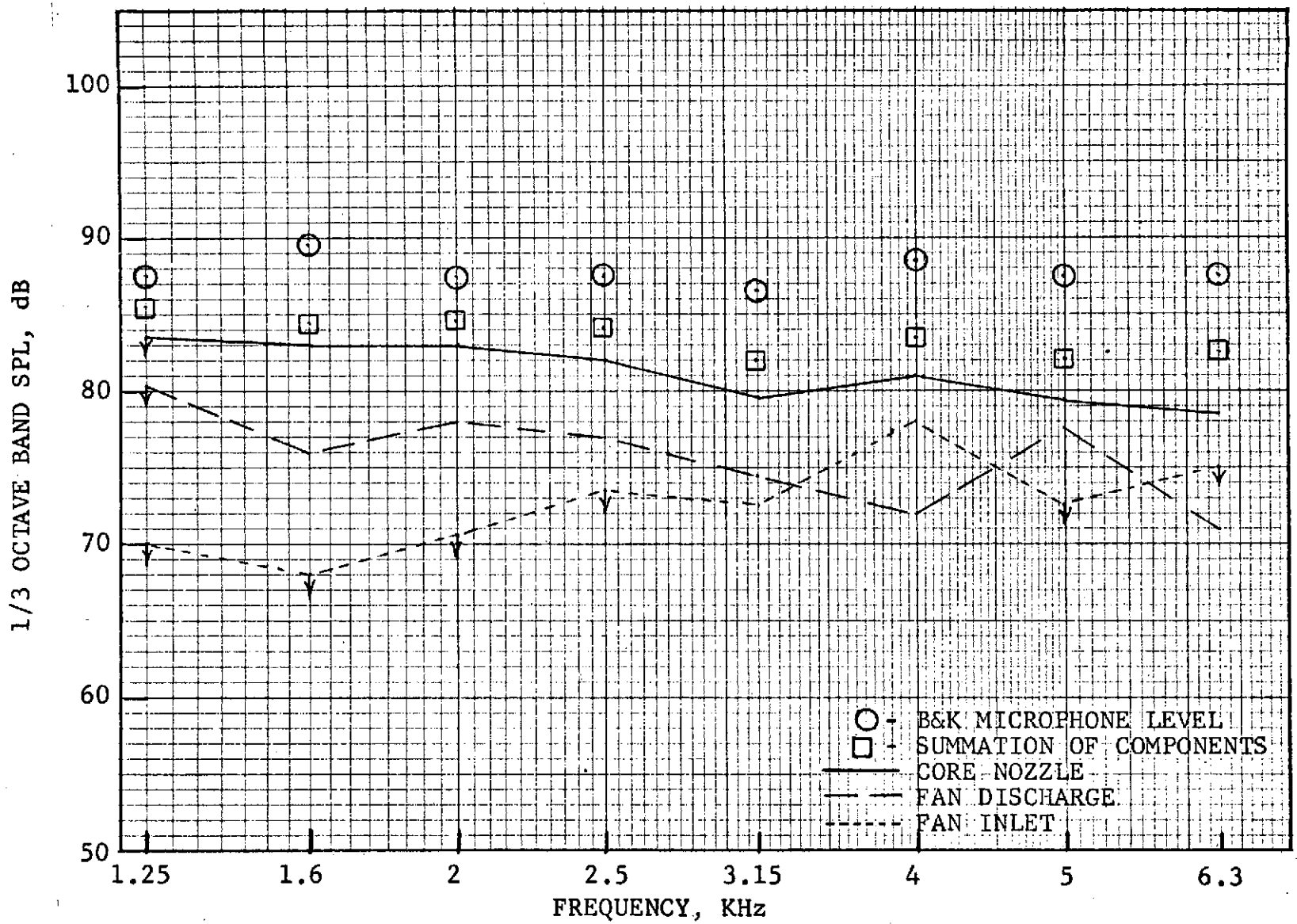

Figure 371. Engine C Broadband Noise Directivity from Directional Array Fully Suppressed Configuration, Takeoff, 90°.

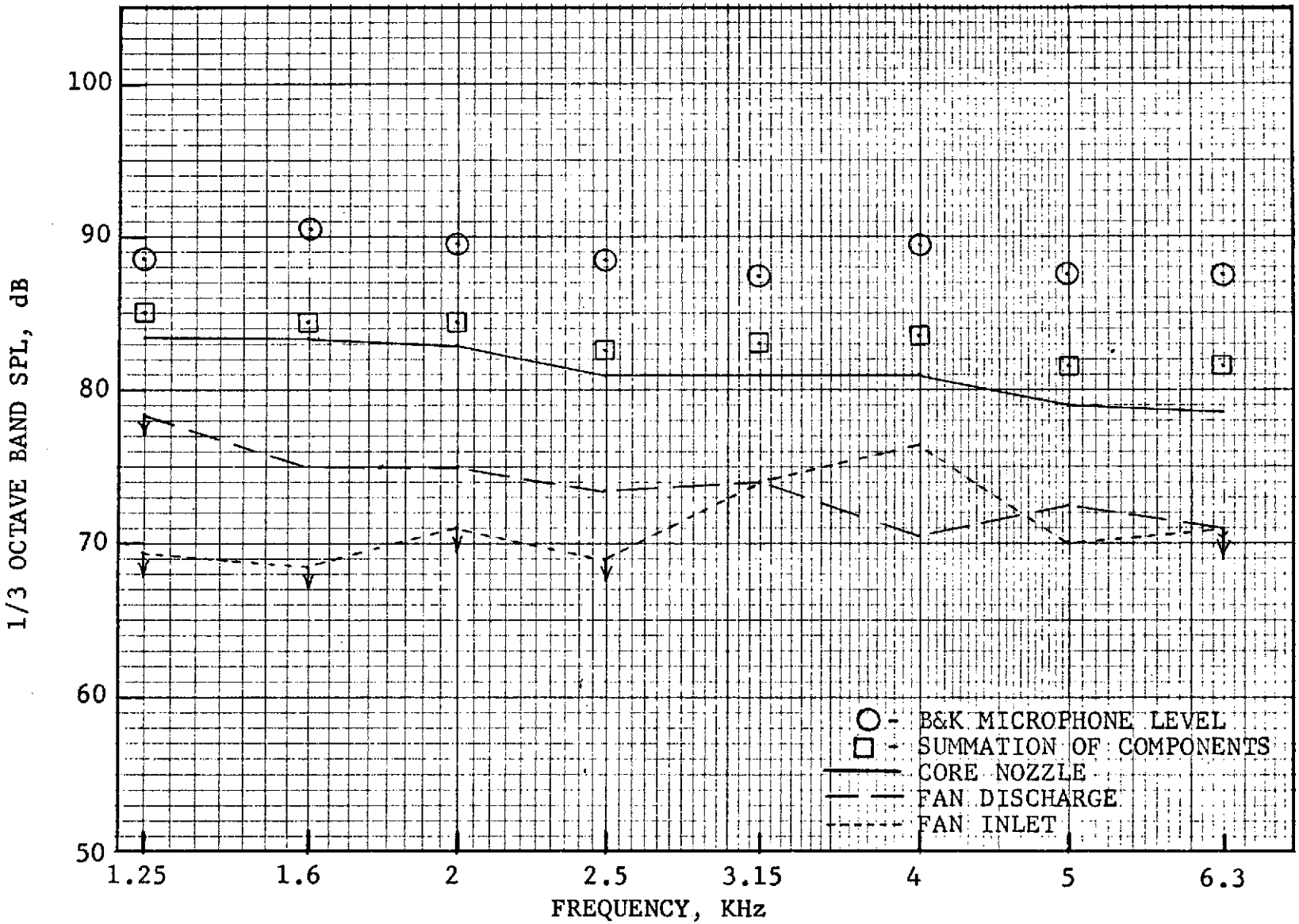

Figure 372. Engine C Broadband Noise Directivity from Directional Array Fully Suppressed Configuration, Takeoff 100°.

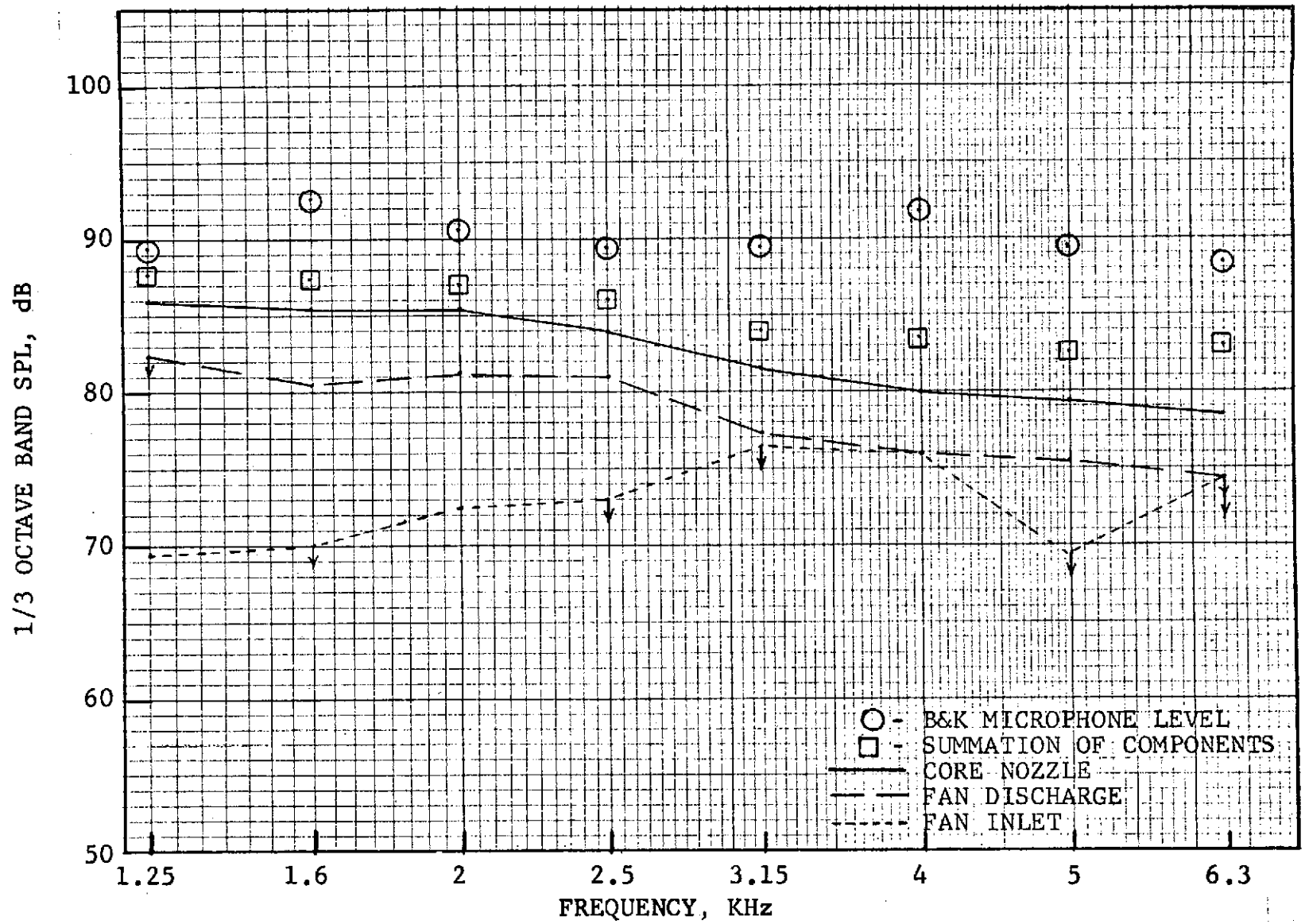

Figure 373. Engine C Broadband Noise Directivity from Directional Array Fully Suppressed Configuration, Takeoff, 110°.

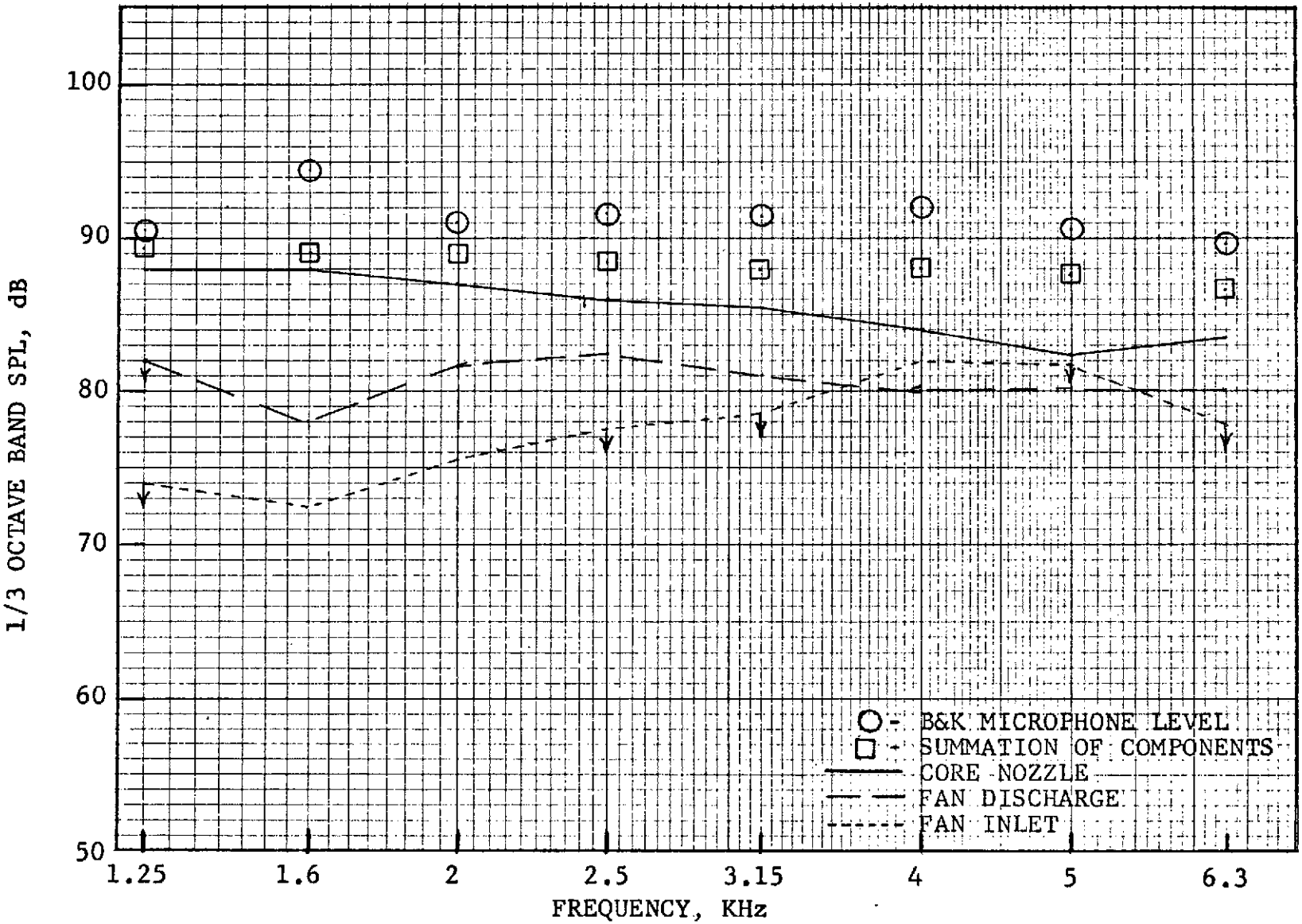

Figure 374. Engine C Broadband Noise Directivity from Directional Array Fully Suppressed Configuration, Takeoff, 120°.

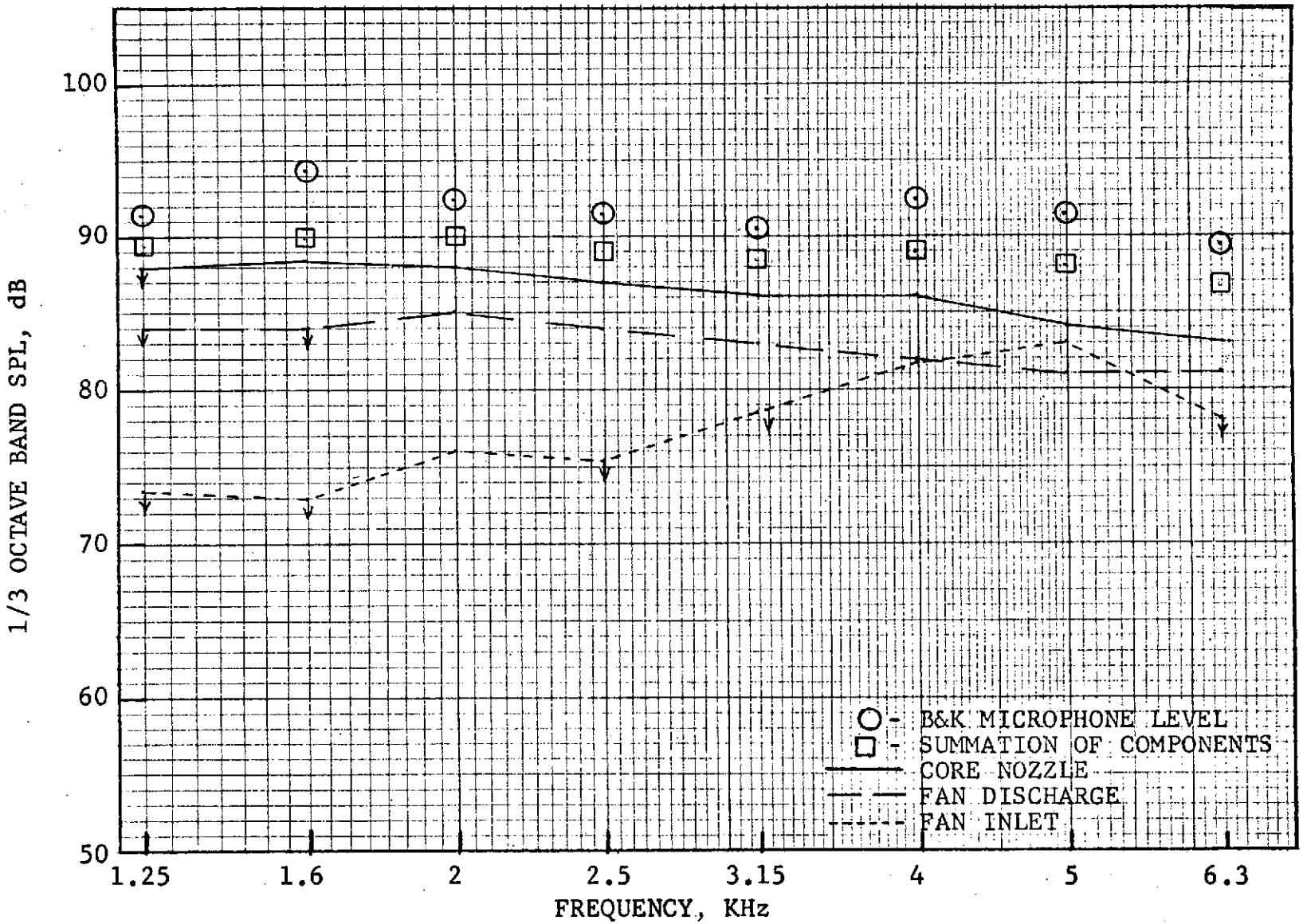

Figure 375. Engine C Broadband Noise Directivity from Directional Array Fully Suppressed Configuration, Takeoff, 130°.

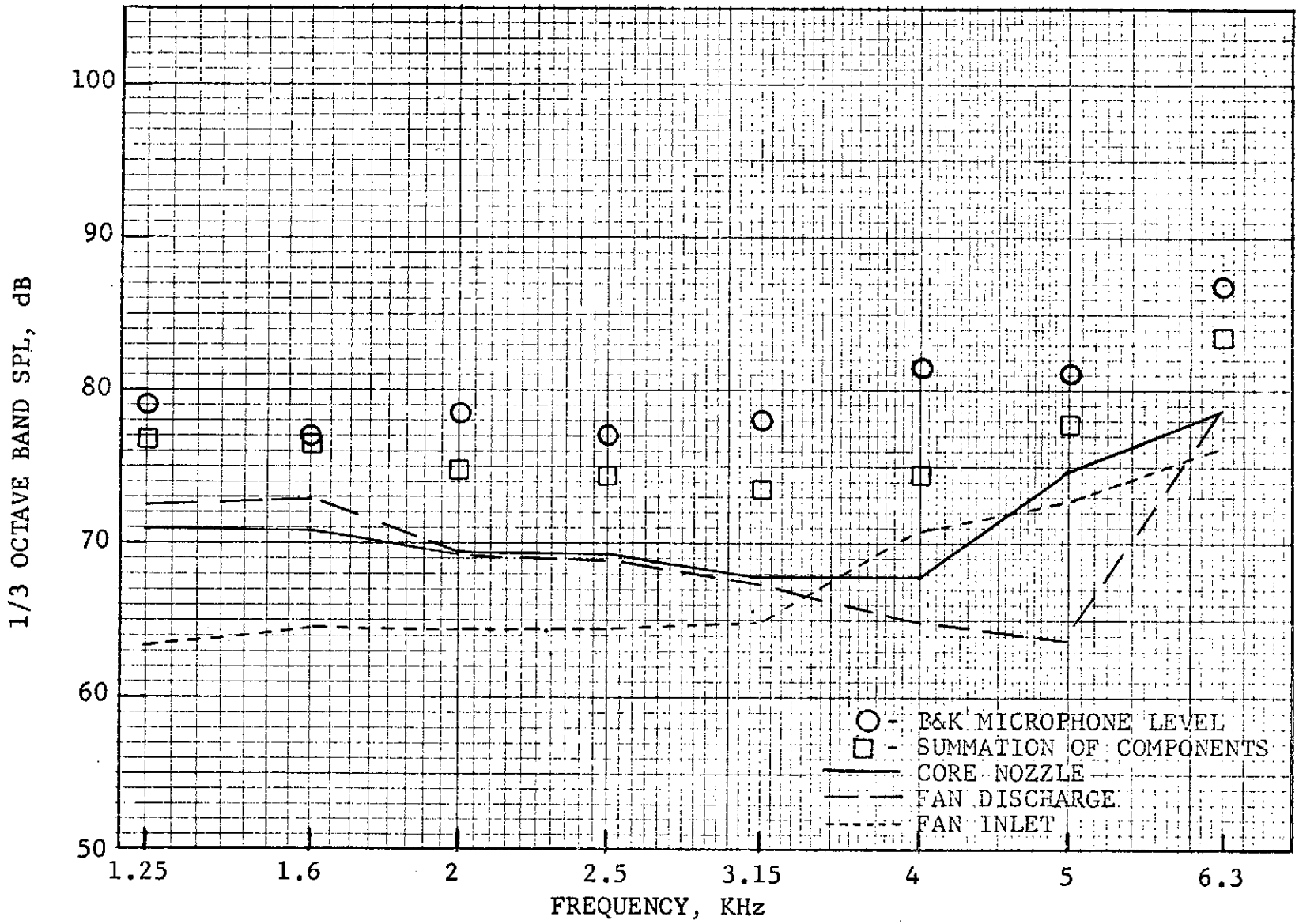

Figure 376. Engine C Broadband Noise Directivity from Directional Array Fully Suppressed Fan, Hardwall Nozzle, Approach Speed 50° from Inlet.

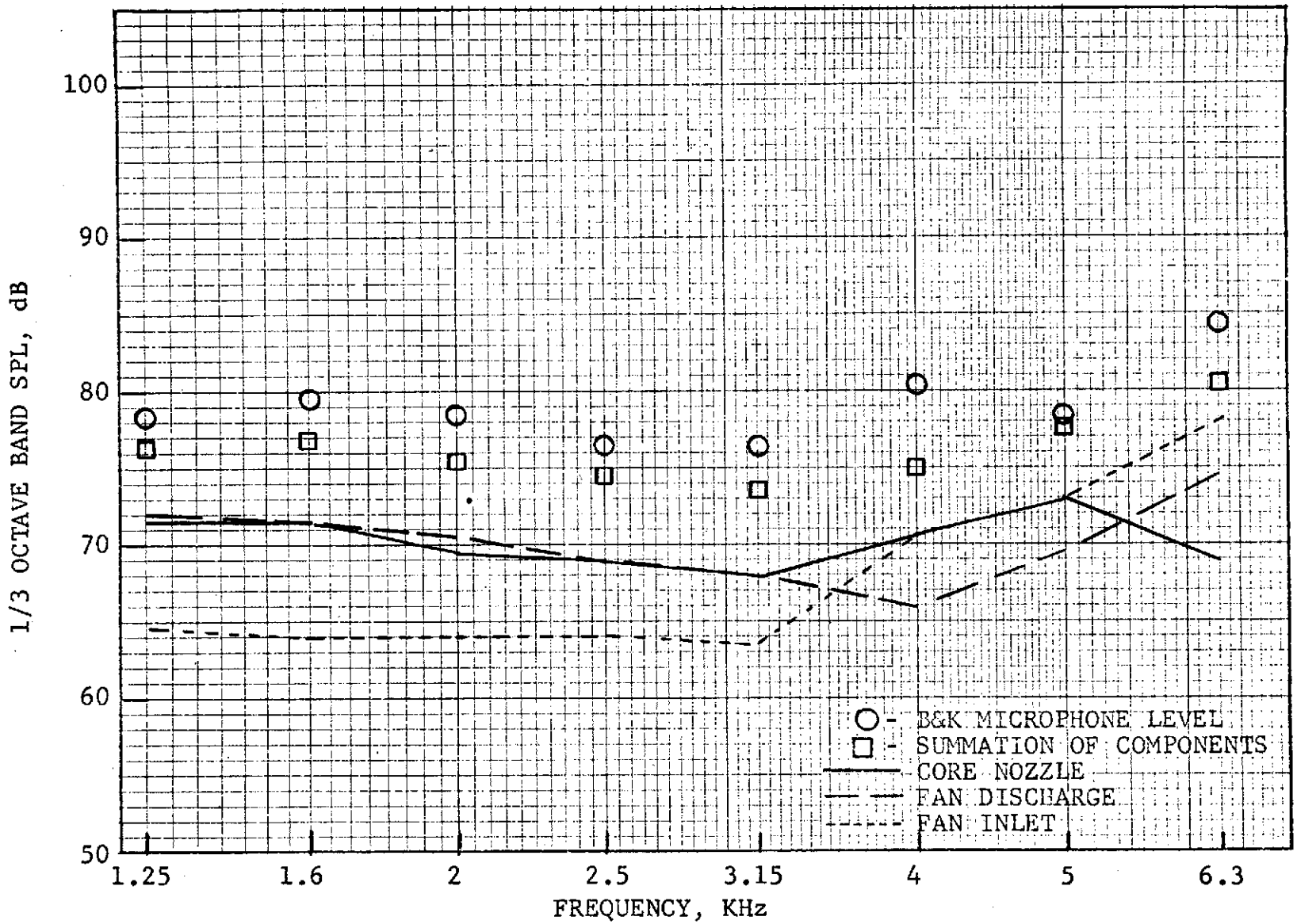

Figure 377. Engine C Broadband Noise Directivity from Directional Array Fully Suppressed Fan, Hardwall Nozzle, Approach Speed 60° from Inlet.

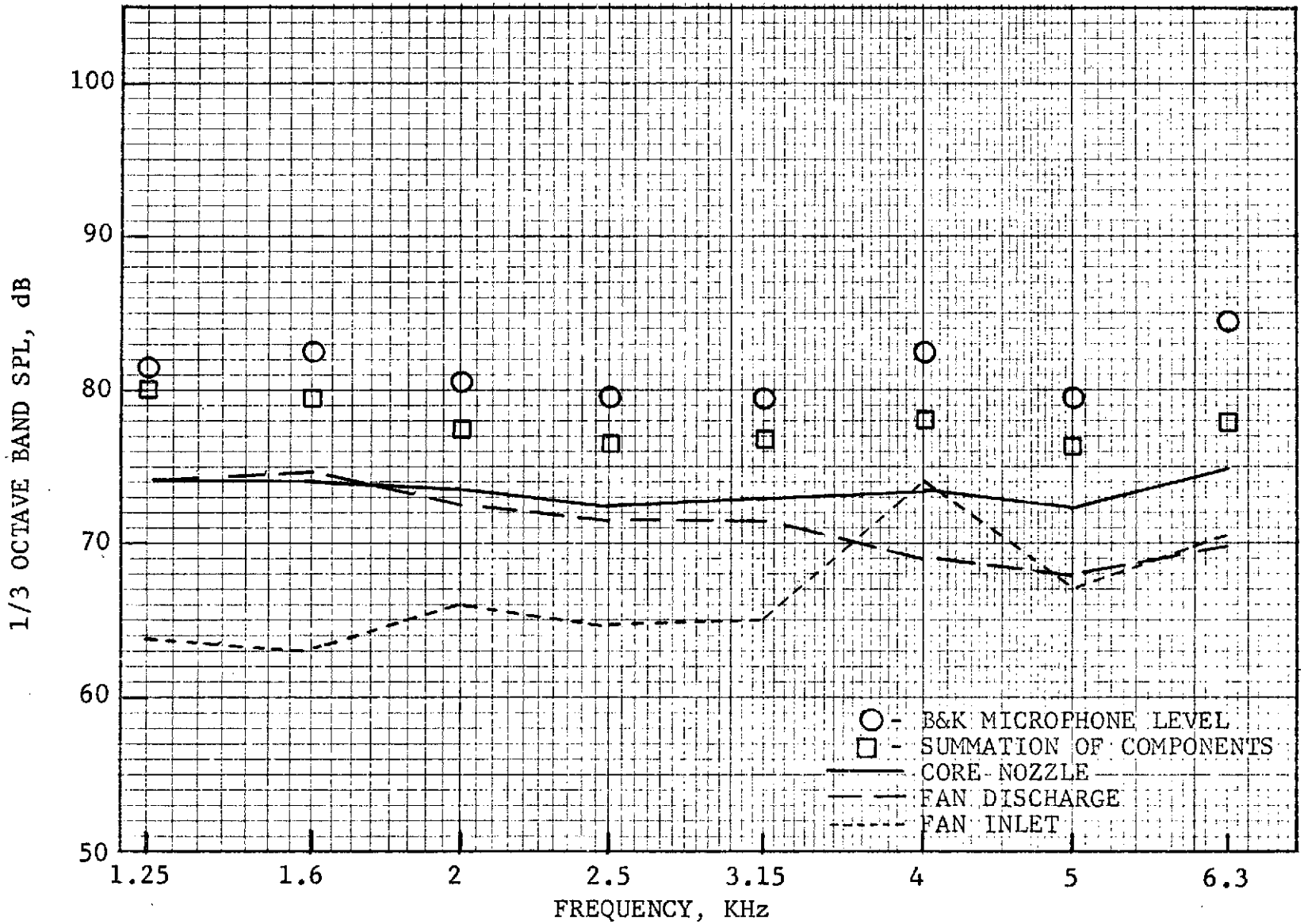

Figure 378. Engine C Broadband Noise Directivity from Directional Array Fully Suppressed Fan, Hardwall Nozzle, Approach Speed 90° from Inlet.

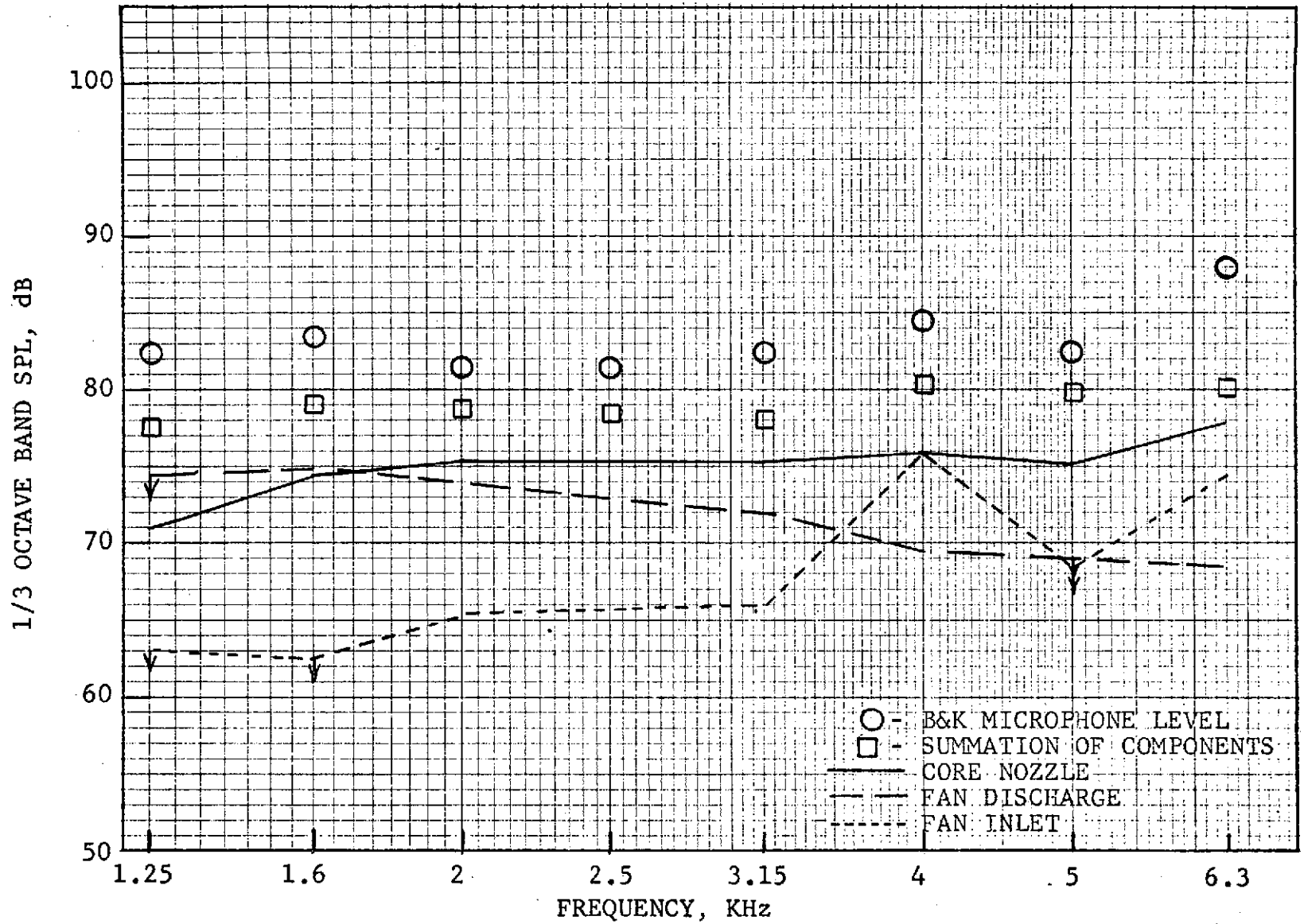

Figure 379. Engine C Broadband Noise Directivity from Directional Array Fully Suppressed Fan, Hardwall Nozzle, Approach Speed 100° from Inlet.

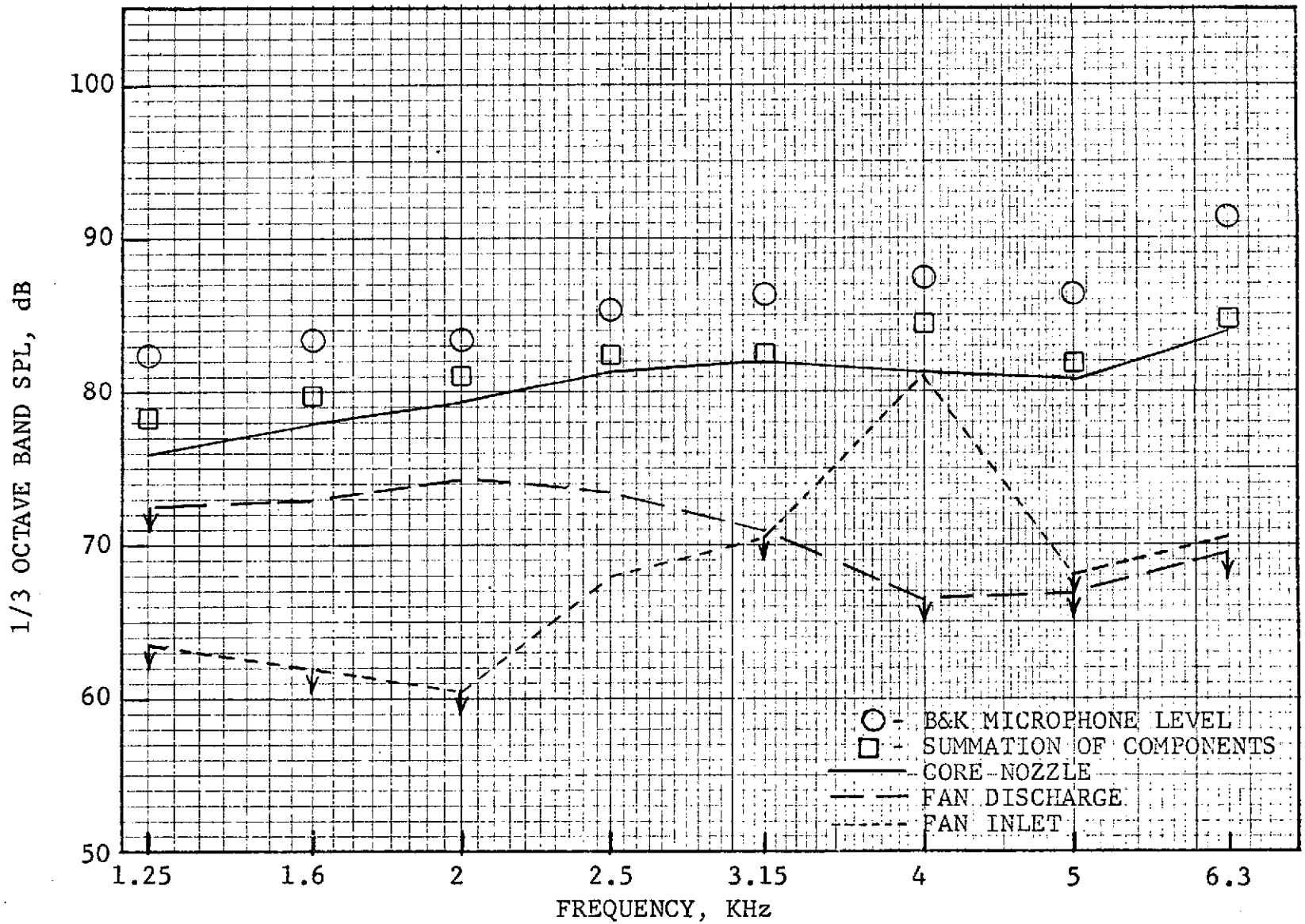

Figure 380. Engine C Broadband Noise Directivity from Directional Array Fully Suppressed Fan, Hardwall Nozzle, Approach Speed 110° from Inlet.

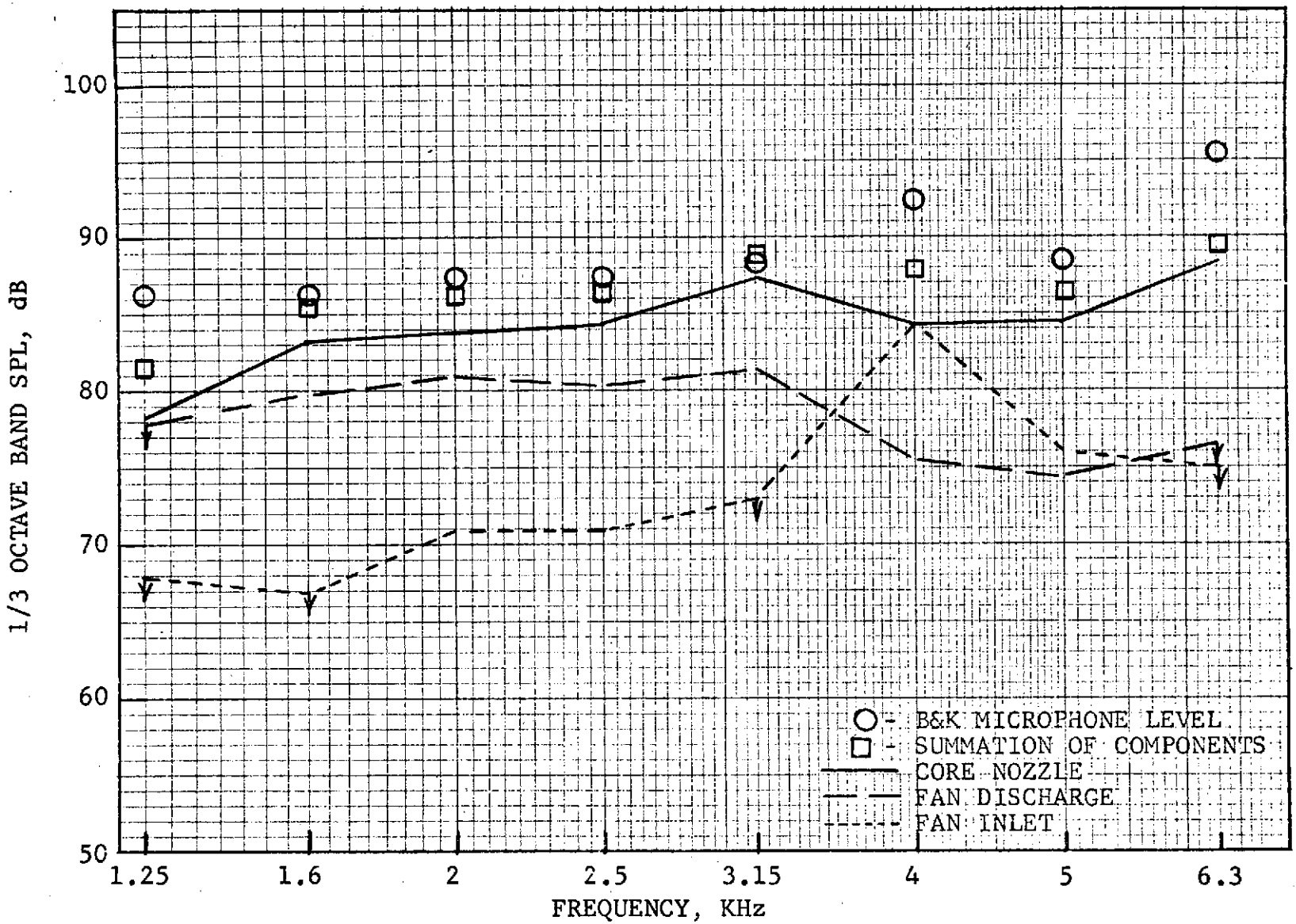

Figure 381. Engine C Broadband Noise Directivity from Directional Array Fully Suppressed Fan, Hardwall Nozzle, Approach Speed 120° from Inlet.

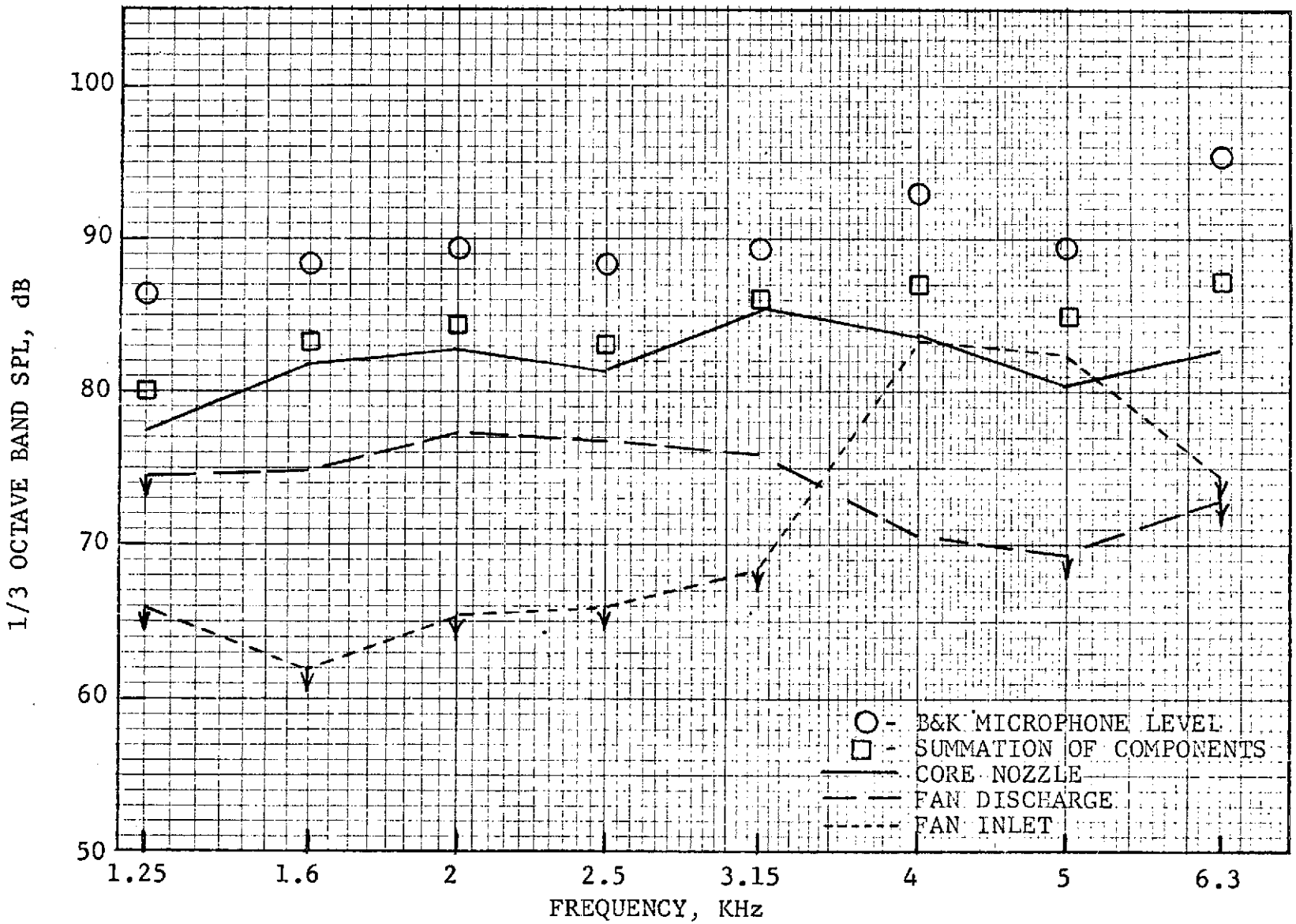

Figure 382. Engine C Broadband Noise Directivity from Directional Array Fully Suppressed Fan, Hardwall Nozzle, Approach Speed 130° from Inlet.

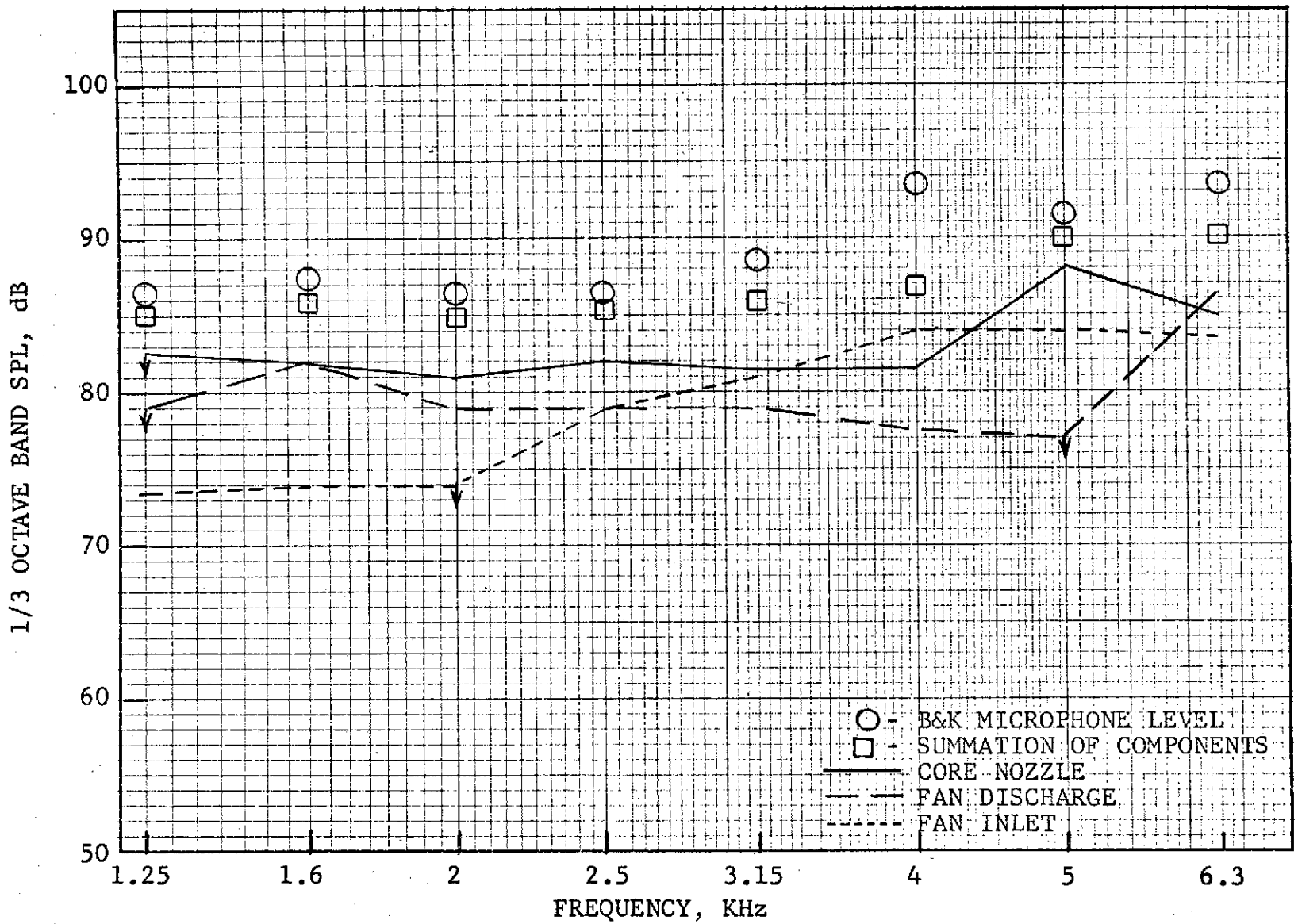

Figure 383. Engine C Broadband Noise Directivity from Directional Array Fully Suppressed Fan, Hardwall Nozzle, Takeoff Speed 50° from Inlet.

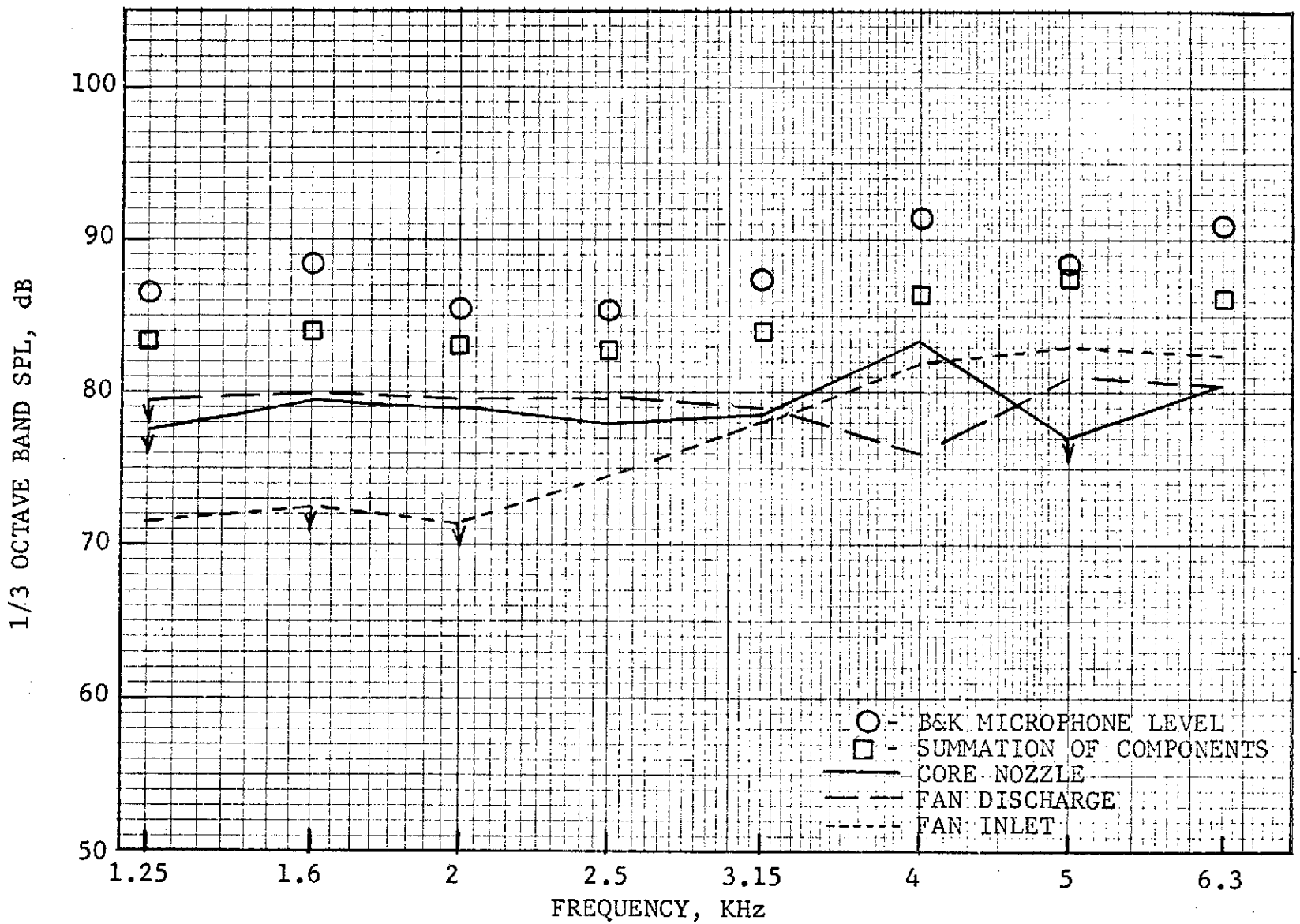

Figure 384. Engine C Broadband Noise Directivity from Directional Array Fully Suppressed Fan, Hardwall Nozzle, Takeoff Speed 60° from Inlet.

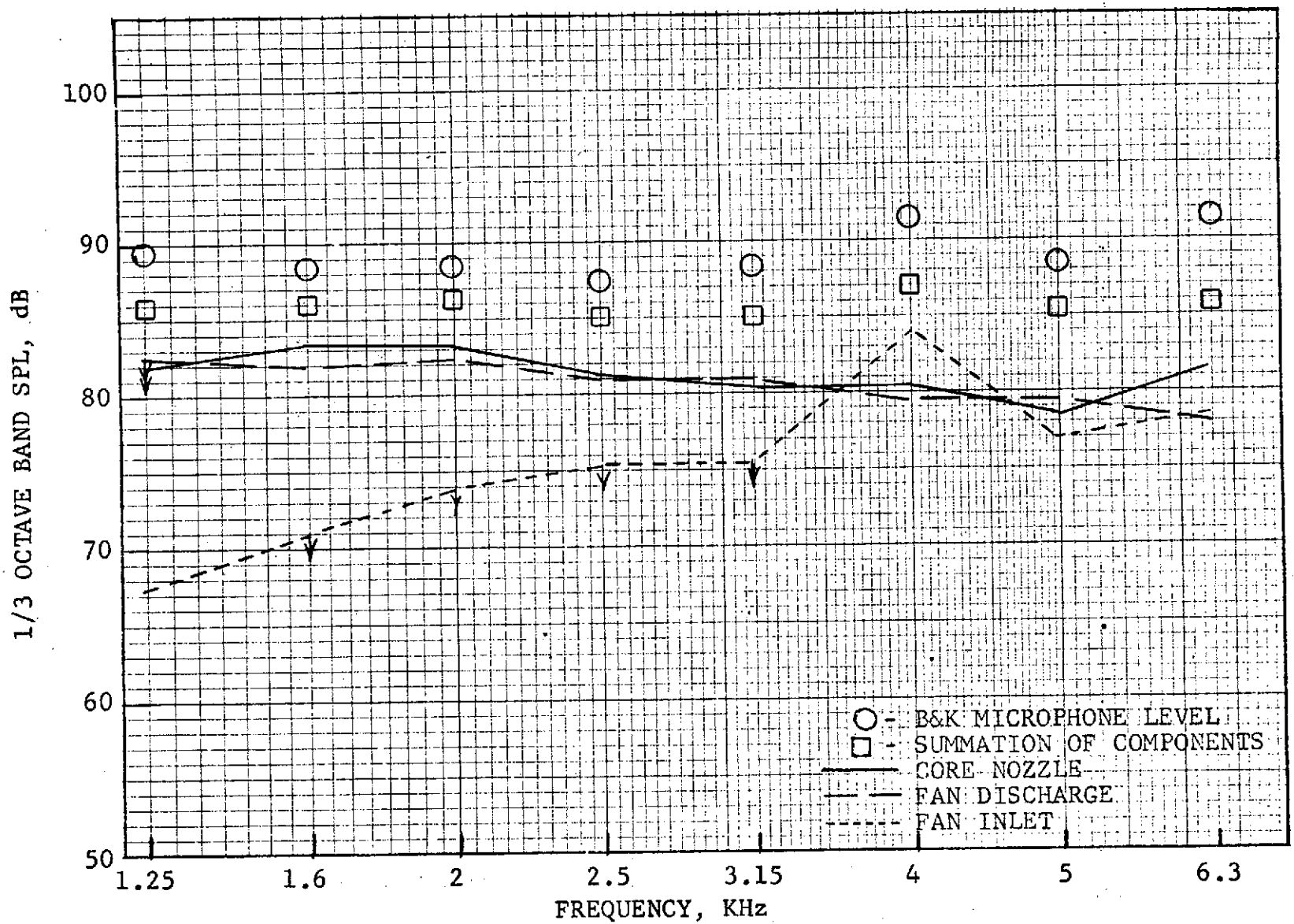

Figure 385. Engine C Broadband Noise Directivity from Directional Array Fully Suppressed Fan, Hardwall Nozzle, Takeoff Speed 90° from Inlet.

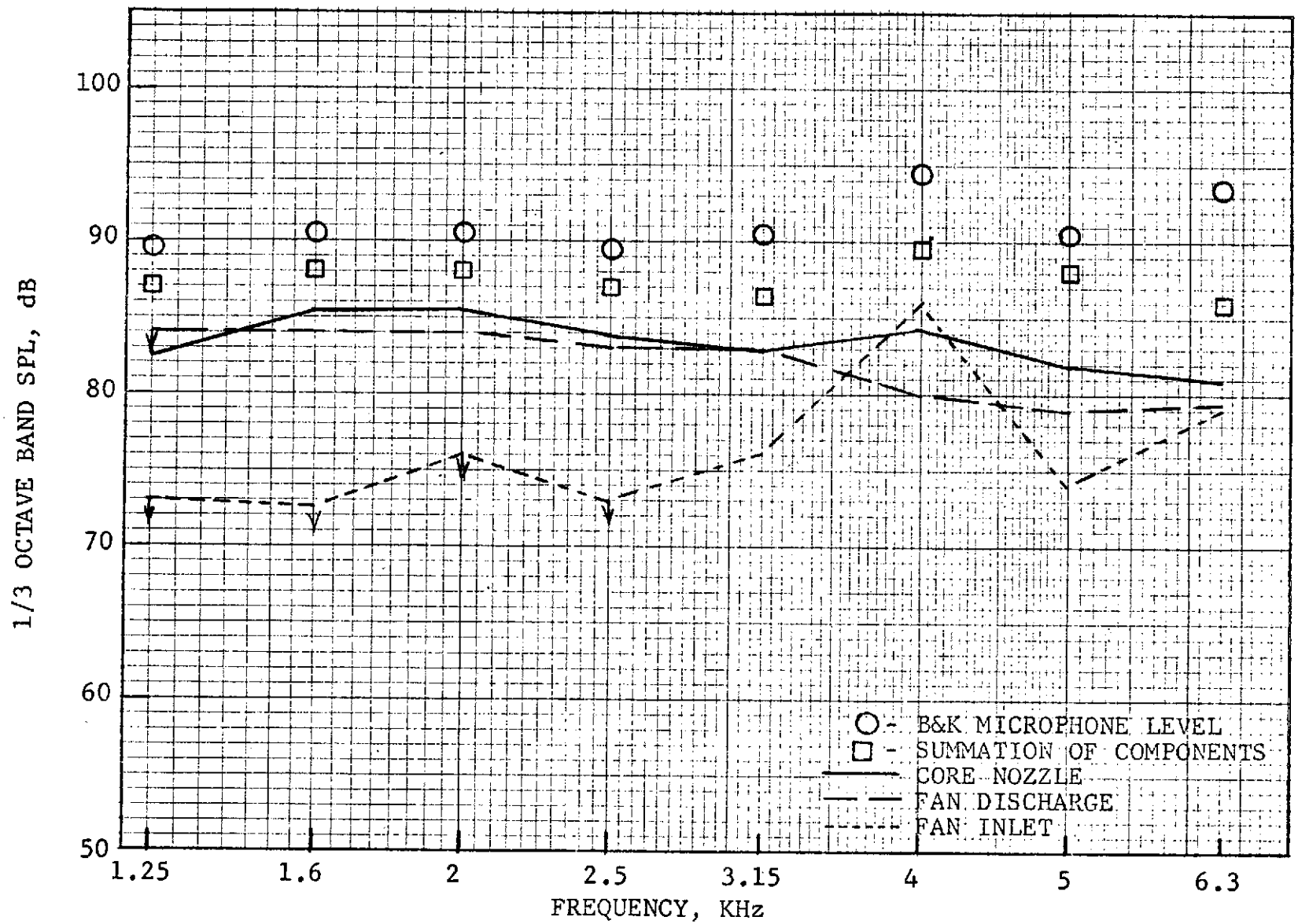

Figure 386. Engine C Broadband Noise Directivity from Directional Array Fully Suppressed Fan, Hardwall Nozzle, Takeoff Speed 100° from Inlet.

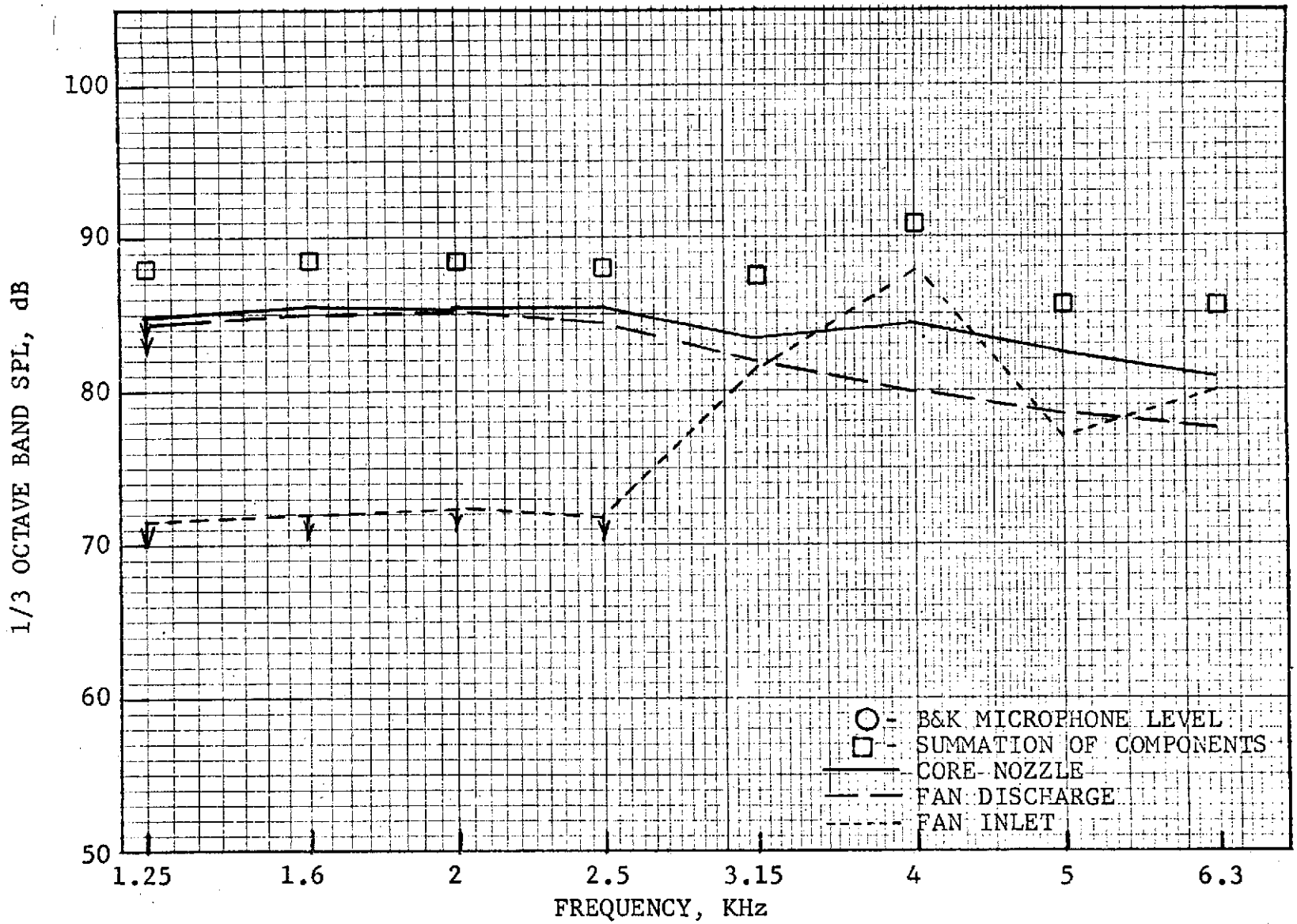

Figure 387. Engine C Broadband Noise Directivity from Directional Array Fully Suppressed Fan, Hardwall Nozzle, Takeoff Speed 110° from Inlet.

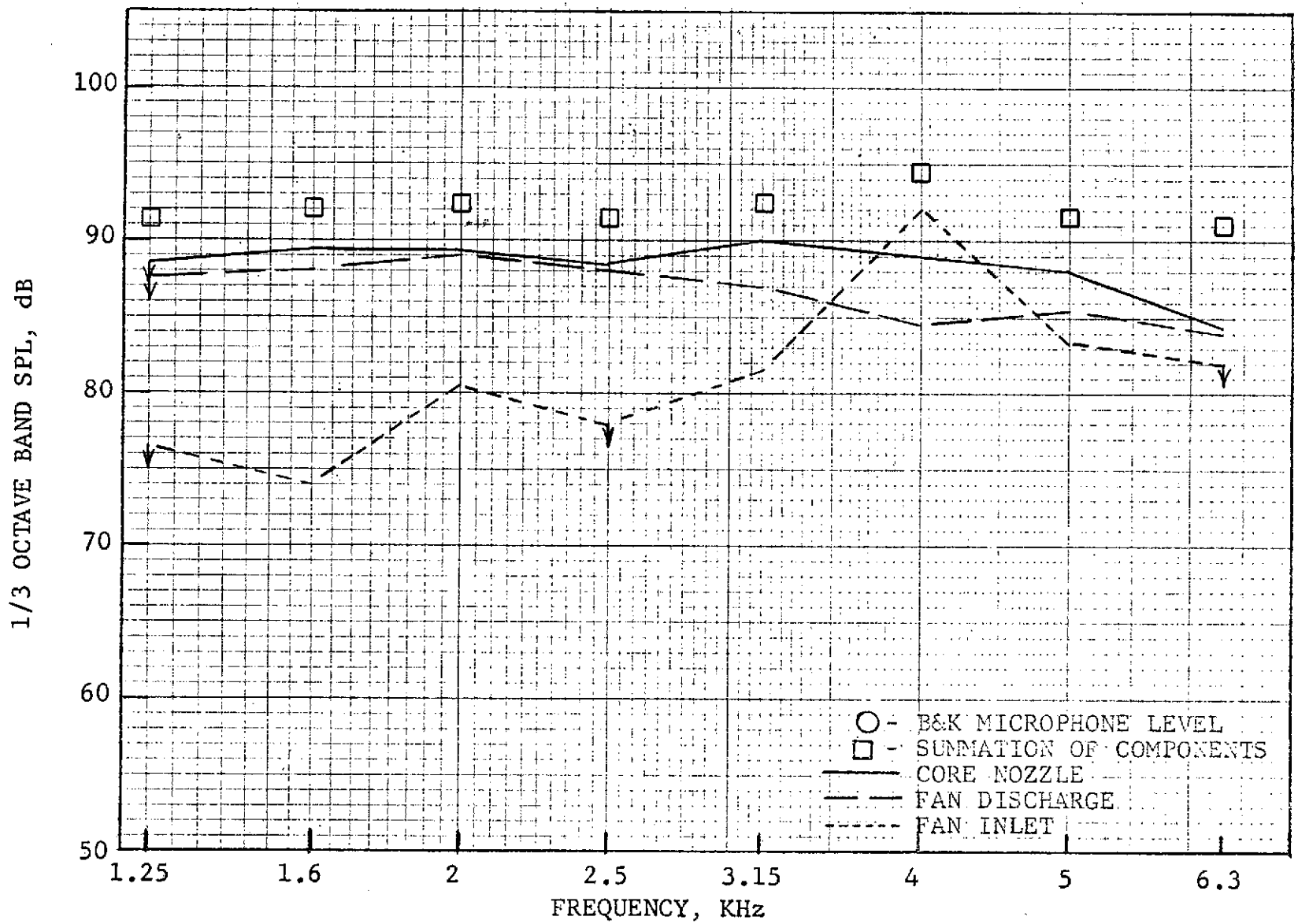

Figure 388. Engine C Broadband Noise Directivity from Directional Array Fully Suppressed Fan, Hardwall Nozzle, Takeoff Speed 120° from Inlet.

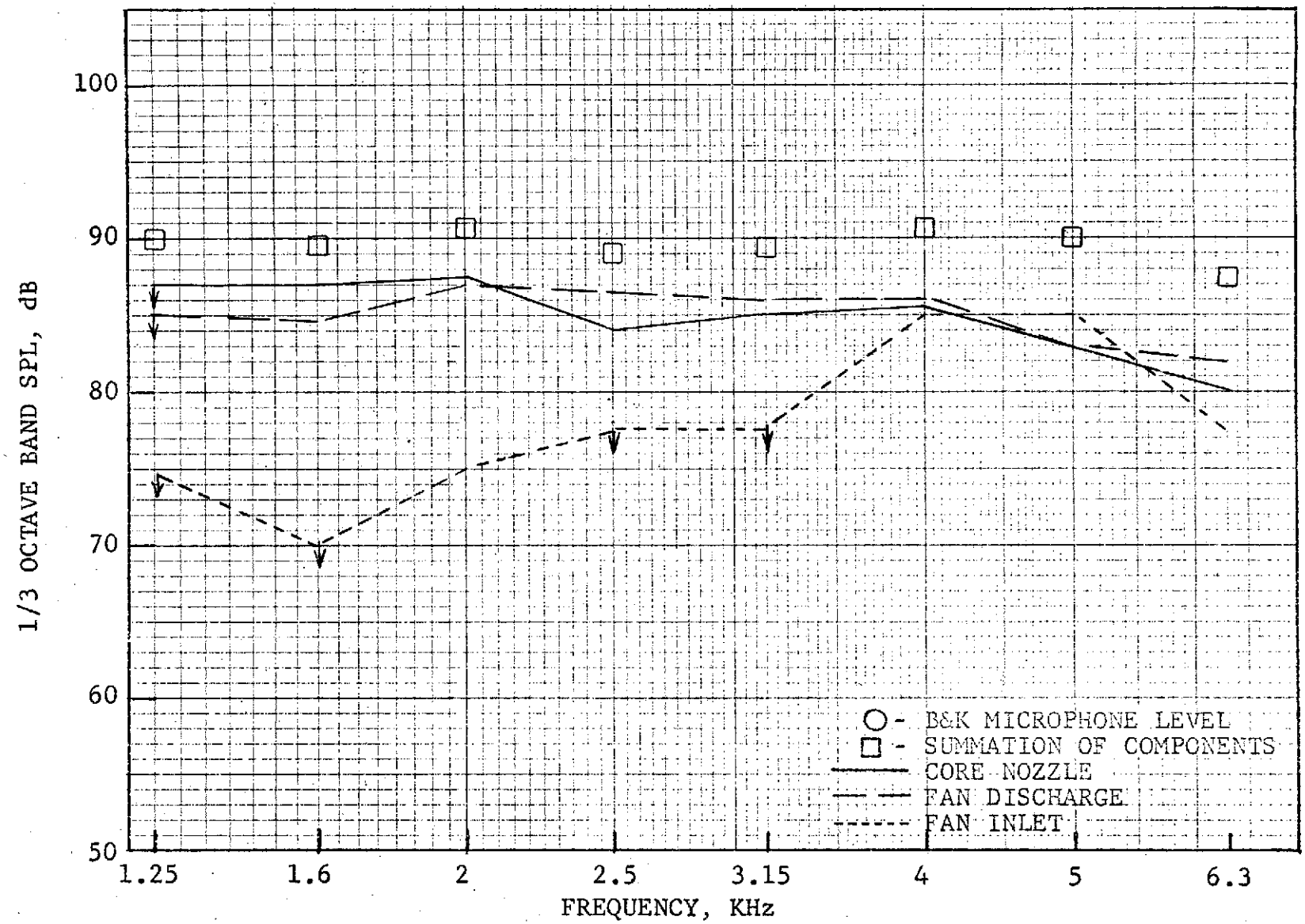

Figure 389. Engine C Broadband Noise Directivity from Directional Array Fully Suppressed Fan, Hardwall Nozzle, Takeoff Speed 130° from Inlet.

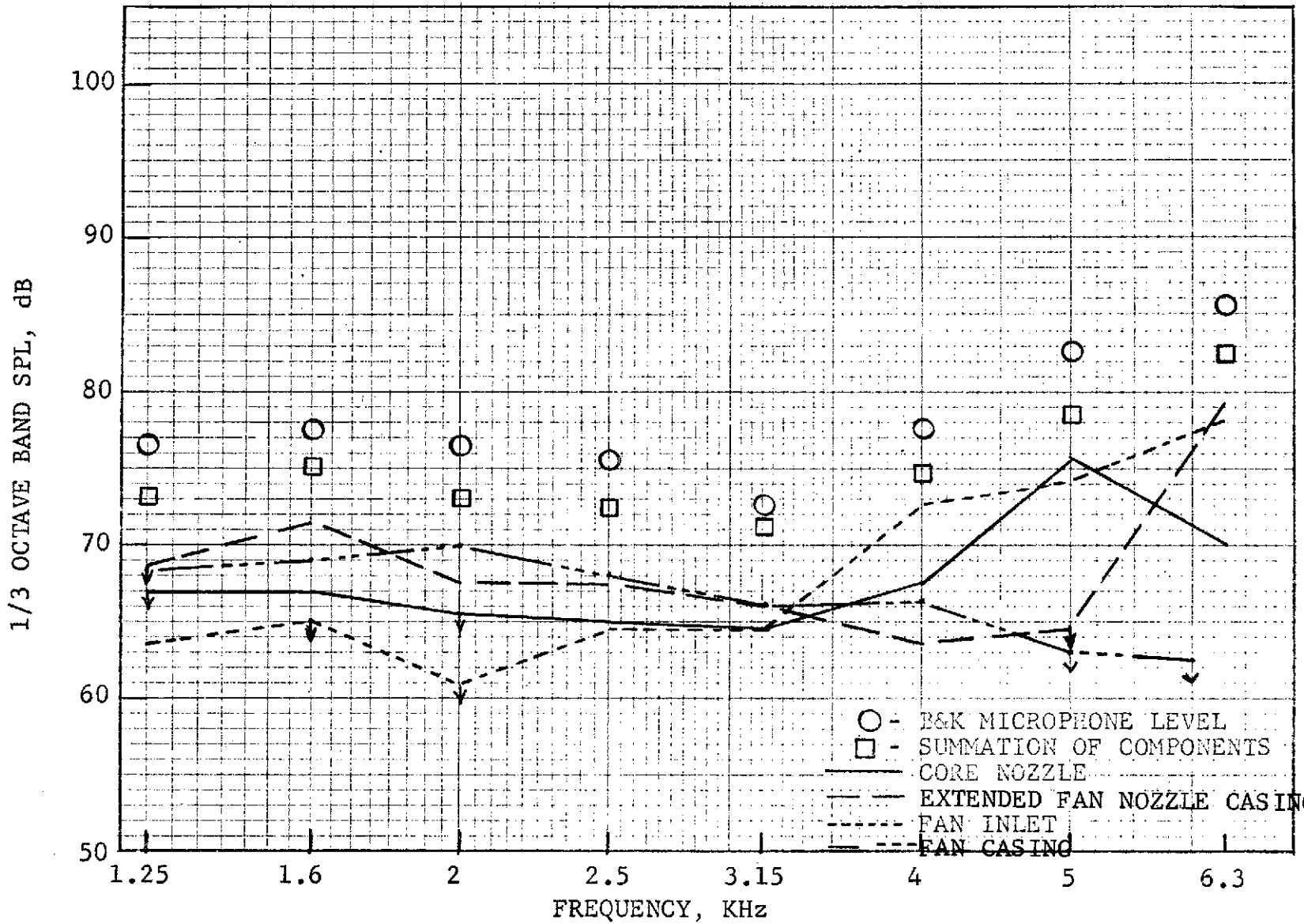

Figure 390. Engine C Broadband Noise Directivity from Directional Array Fully Suppressed Configuration, Coplanar Nozzle, Approach Speed 50° From Inlet.

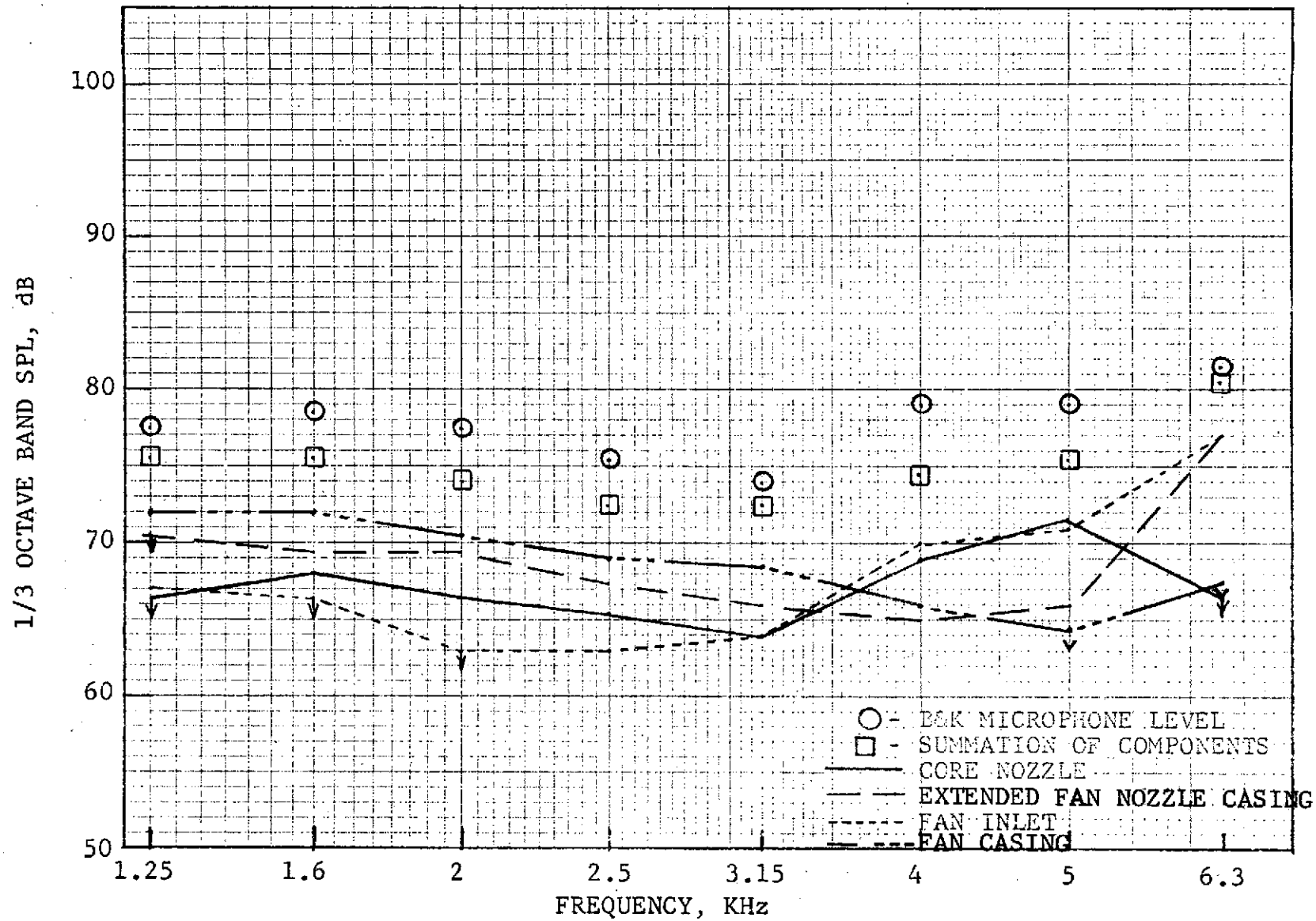

Figure 391. Engine C Broadband Noise Directivity from Directional Array Fully Suppressed Configuration, Coplanar Nozzle, Approach Speed 60° from Inlet.

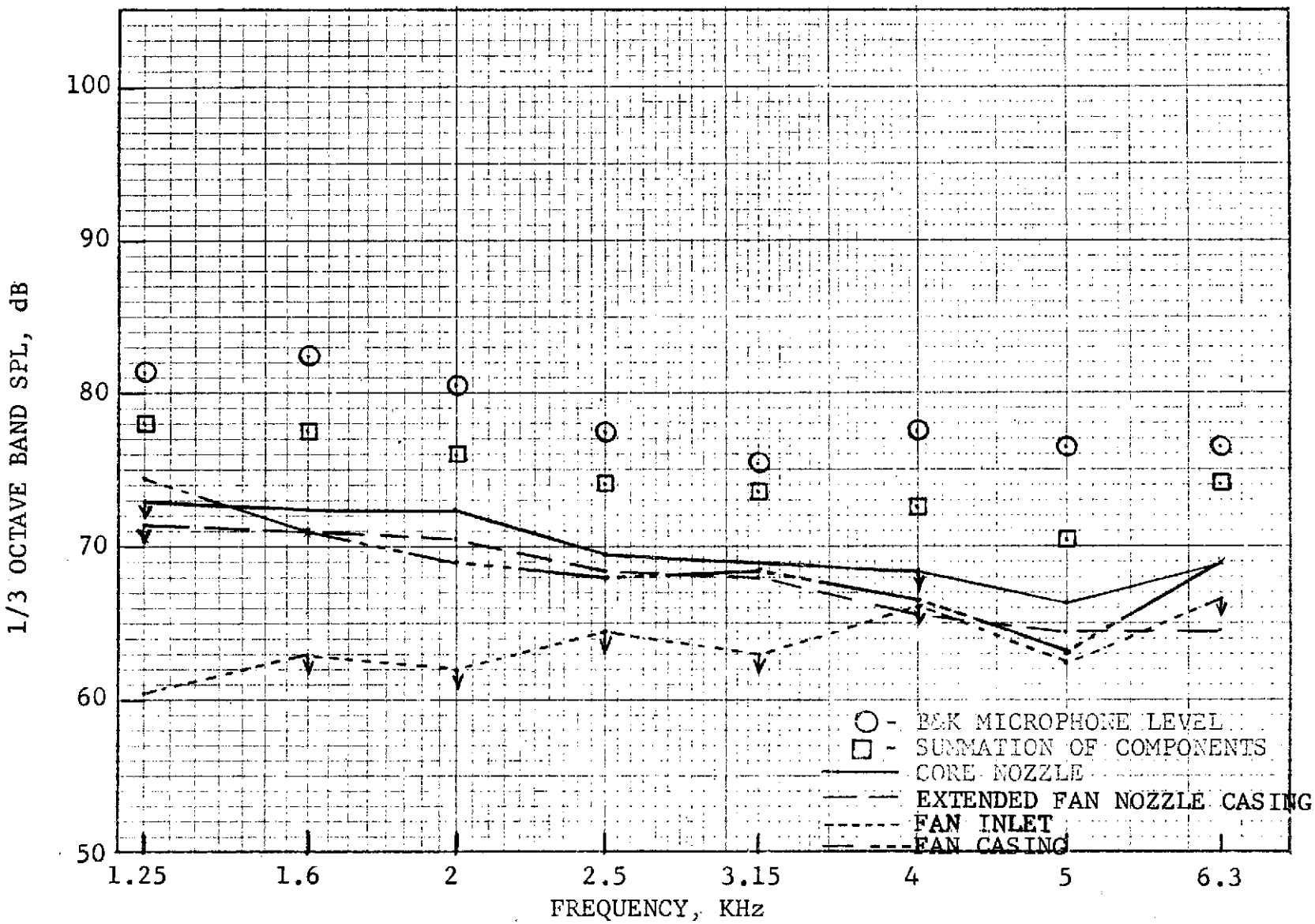

Figure 392. Engine C Broadband Noise Directivity from Directional Array Fully Suppressed Configuration, Coplanar Nozzle, Approach Speed 90° from Inlet.

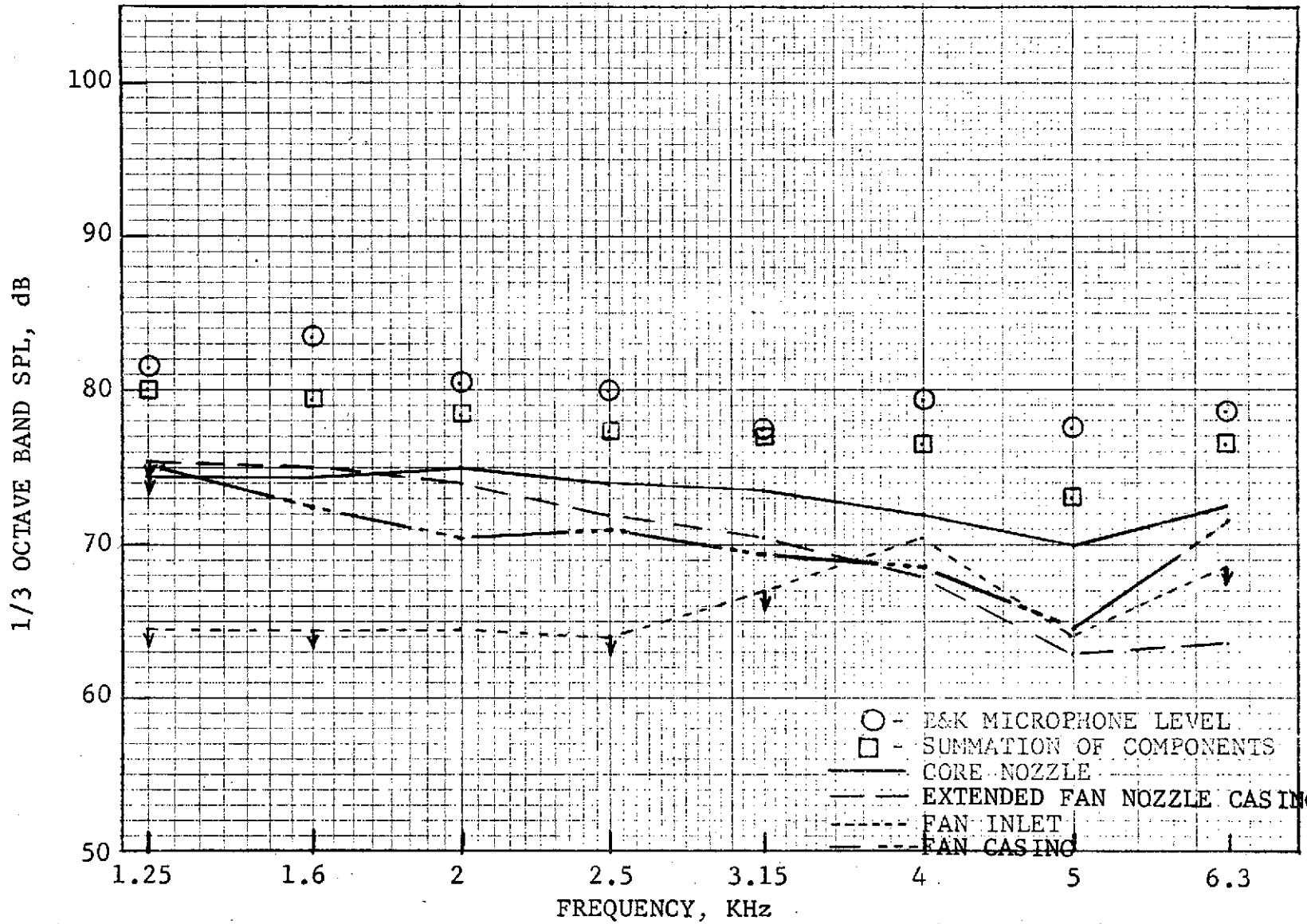

Figure 393. Engine C Broadband Noise Directivity from Directional Array Fully Suppressed Configuration, Coplanar Nozzle, Approach Speed 100° from Inlet.

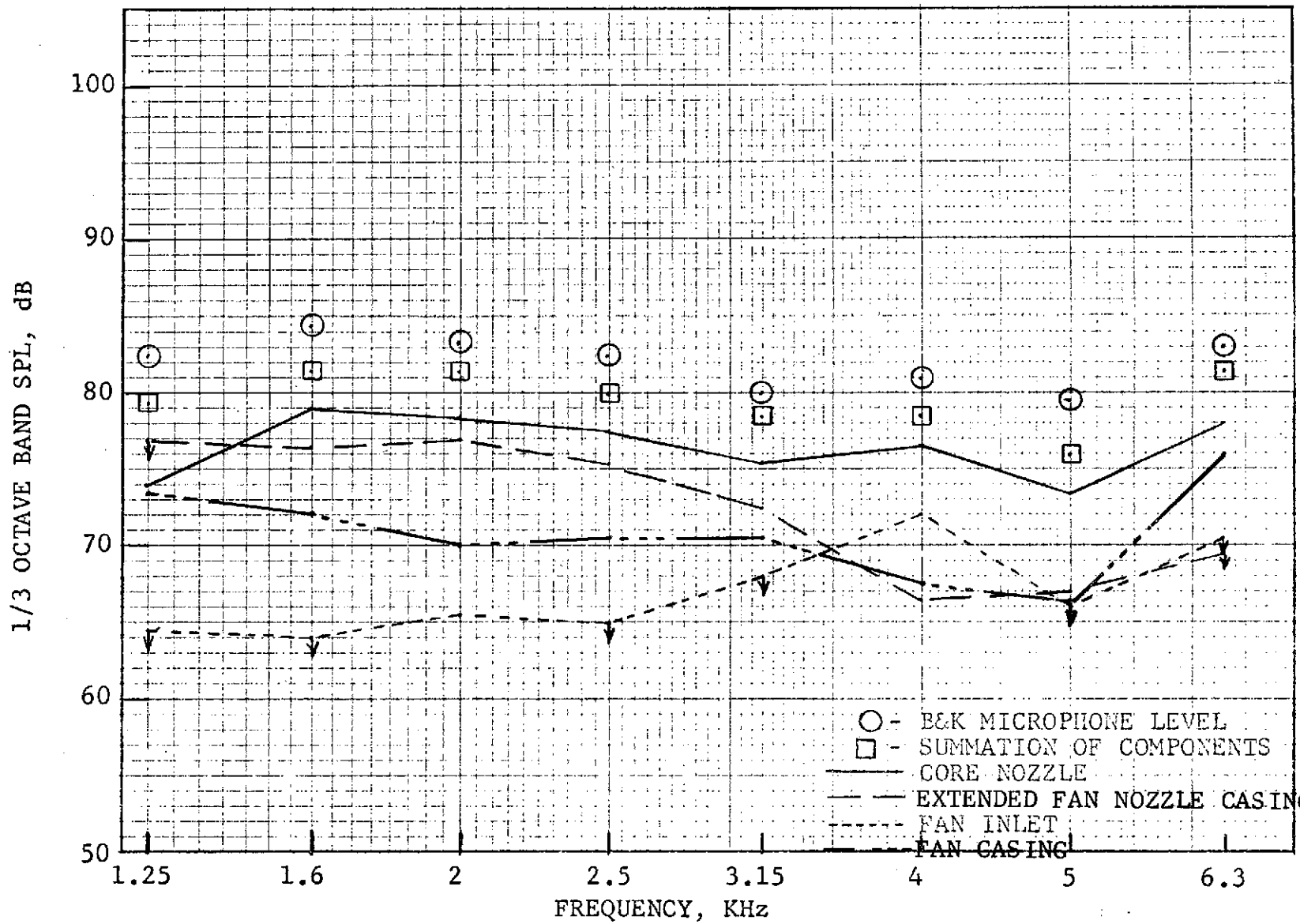

Figure 394. Engine C Broadband Noise Directivity from Directional Array Fully Suppressed Configuration, Coplanar Nozzle, Approach Speed 110° from Inlet.

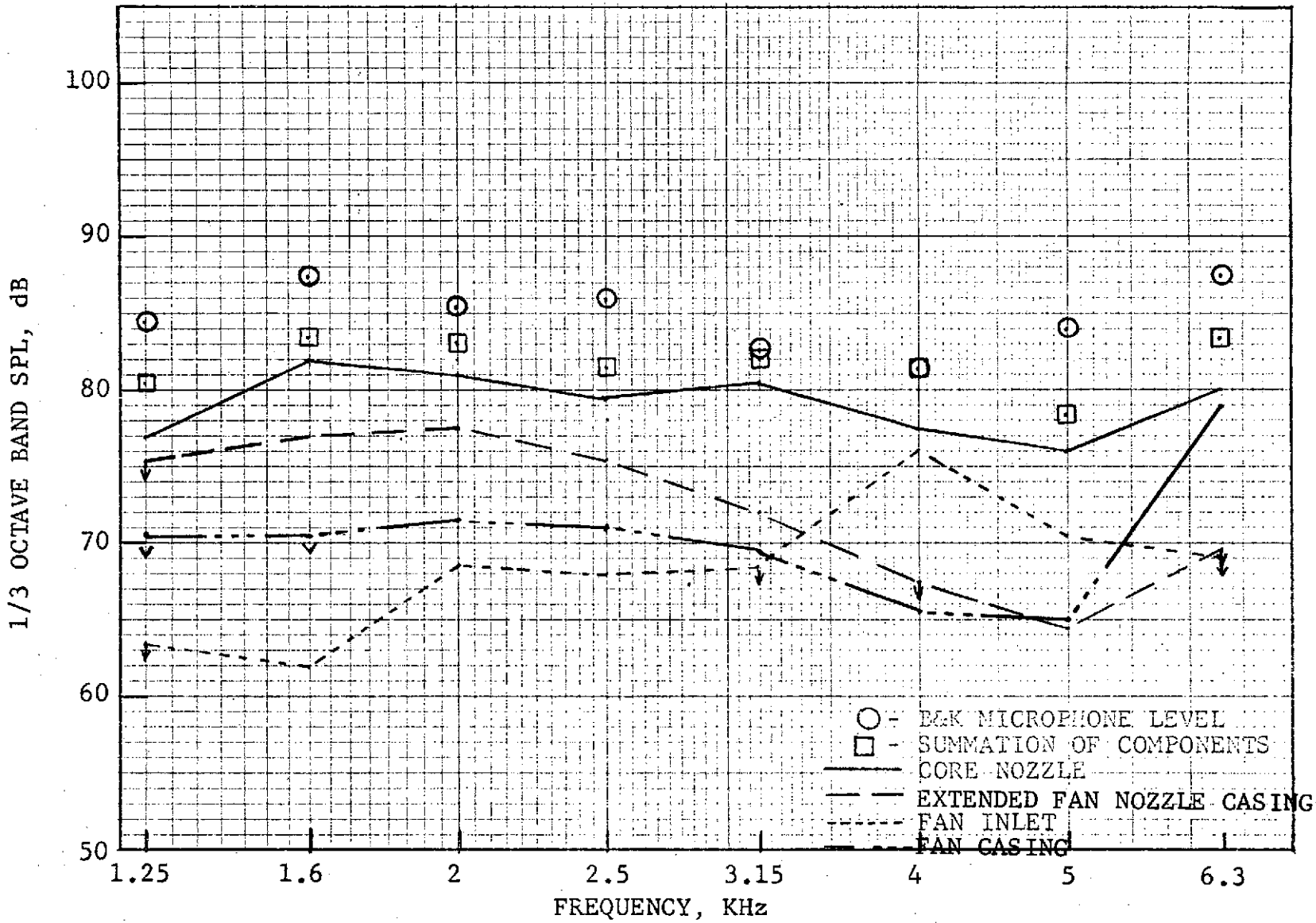

Figure 395. Engine C Broadband Noise Directivity from Directional Array Fully Suppressed Configuration, Coplanar Nozzle, Approach Speed 120° from Inlet.

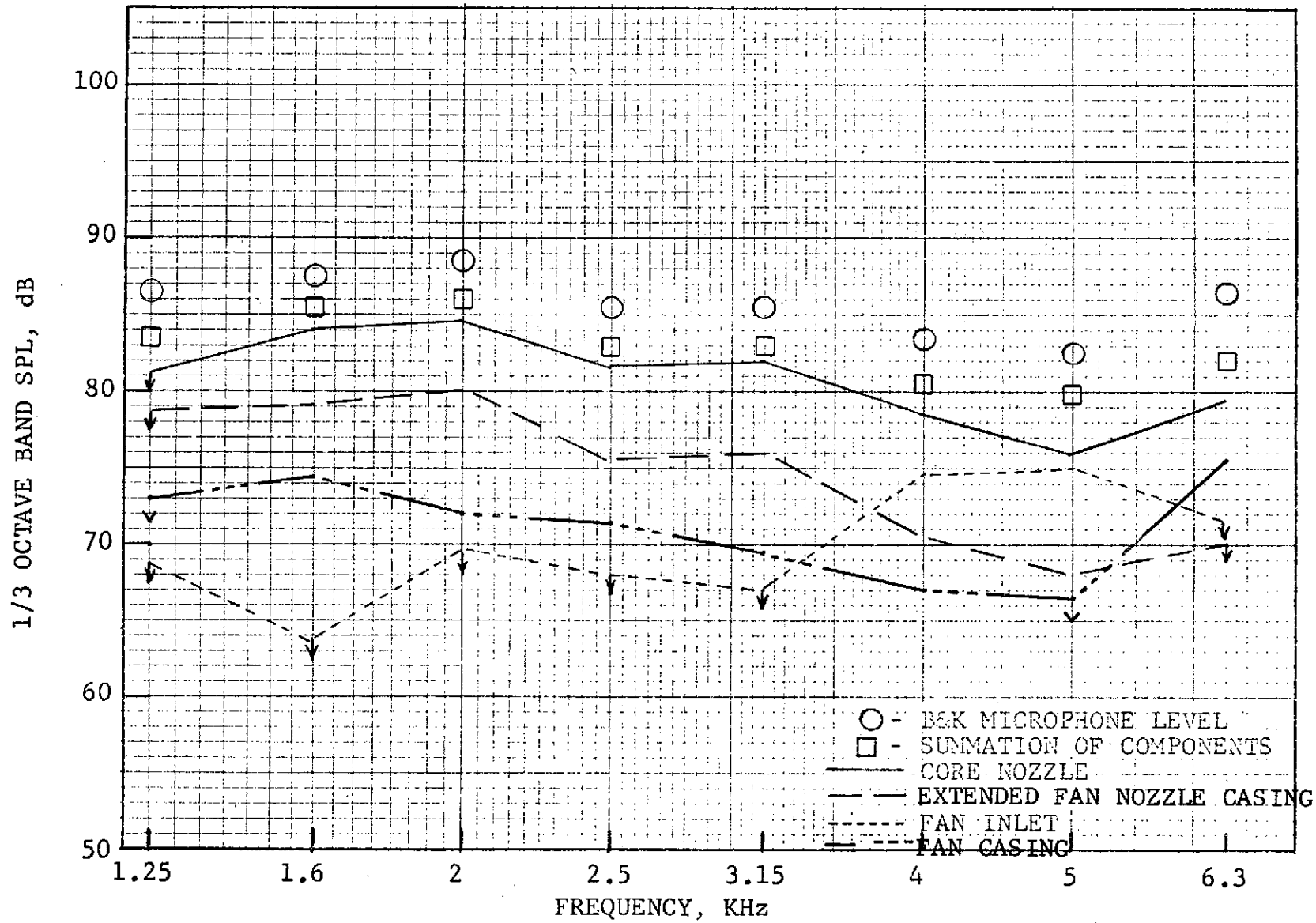

Figure 396. Engine C Broadband Noise Directivity from Directional Array Fully Suppressed Configuration, Coplanar Nozzle, Approach Speed 130° from Inlet.

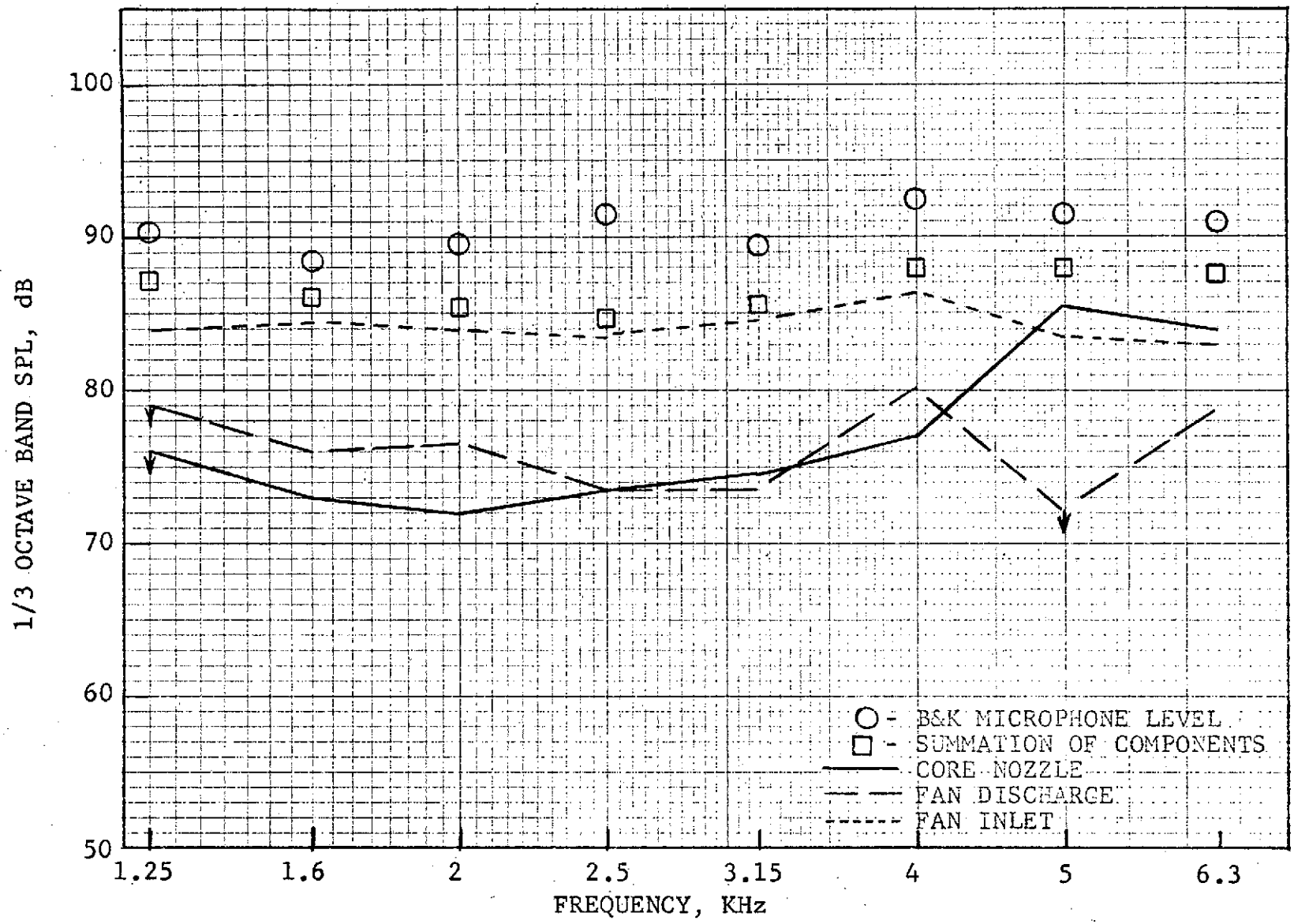

Figure 397. Engine C Broadband Noise Directivity from Directional Array Baseline Fan Configuration, Treated Core, Approach Speed 50° from Inlet.

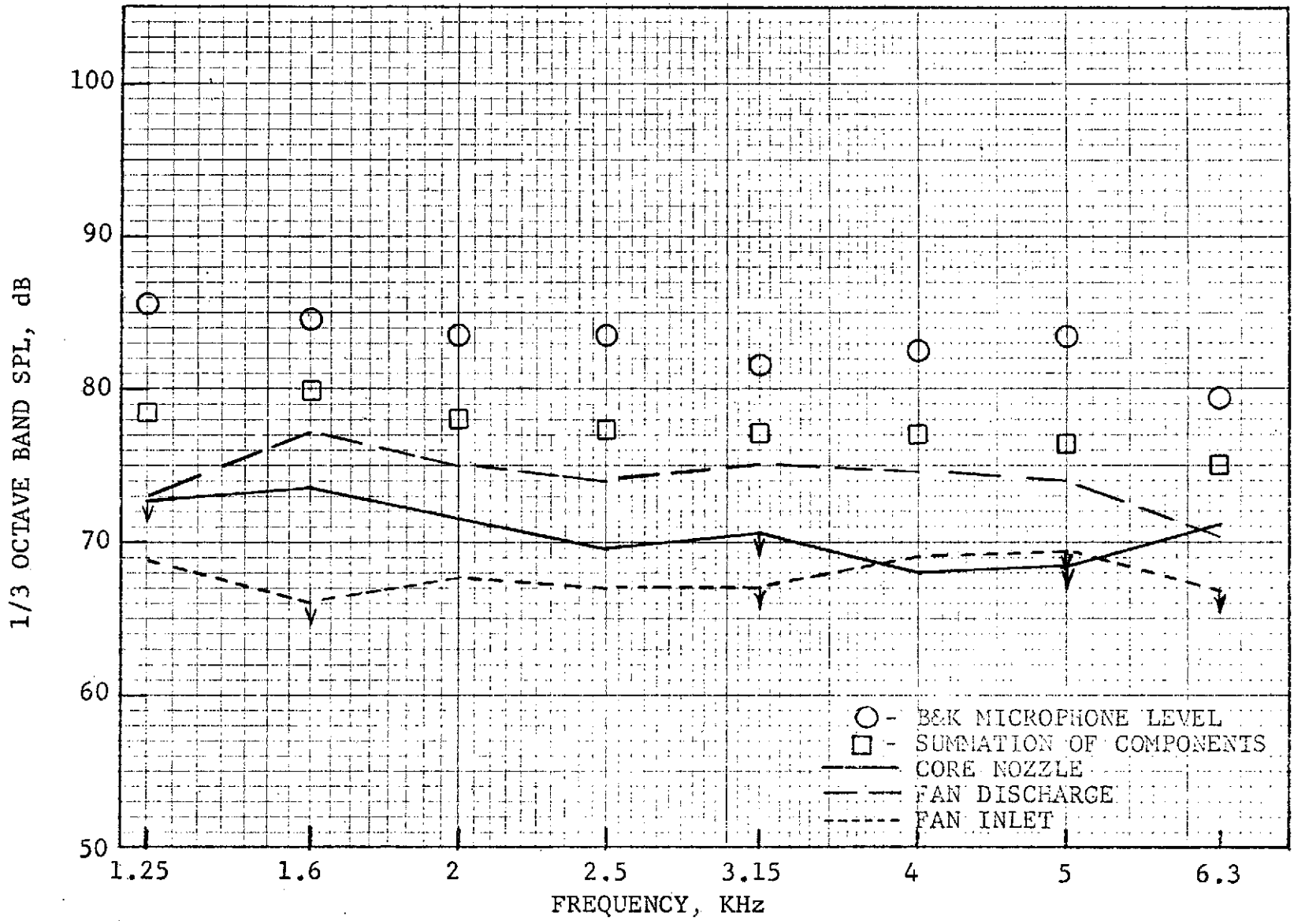

Figure 398. Engine C Broadband Noise Directivity from Directional Array Baseline Fan Configuration, Treated Core, Approach Speed 90° from Inlet.

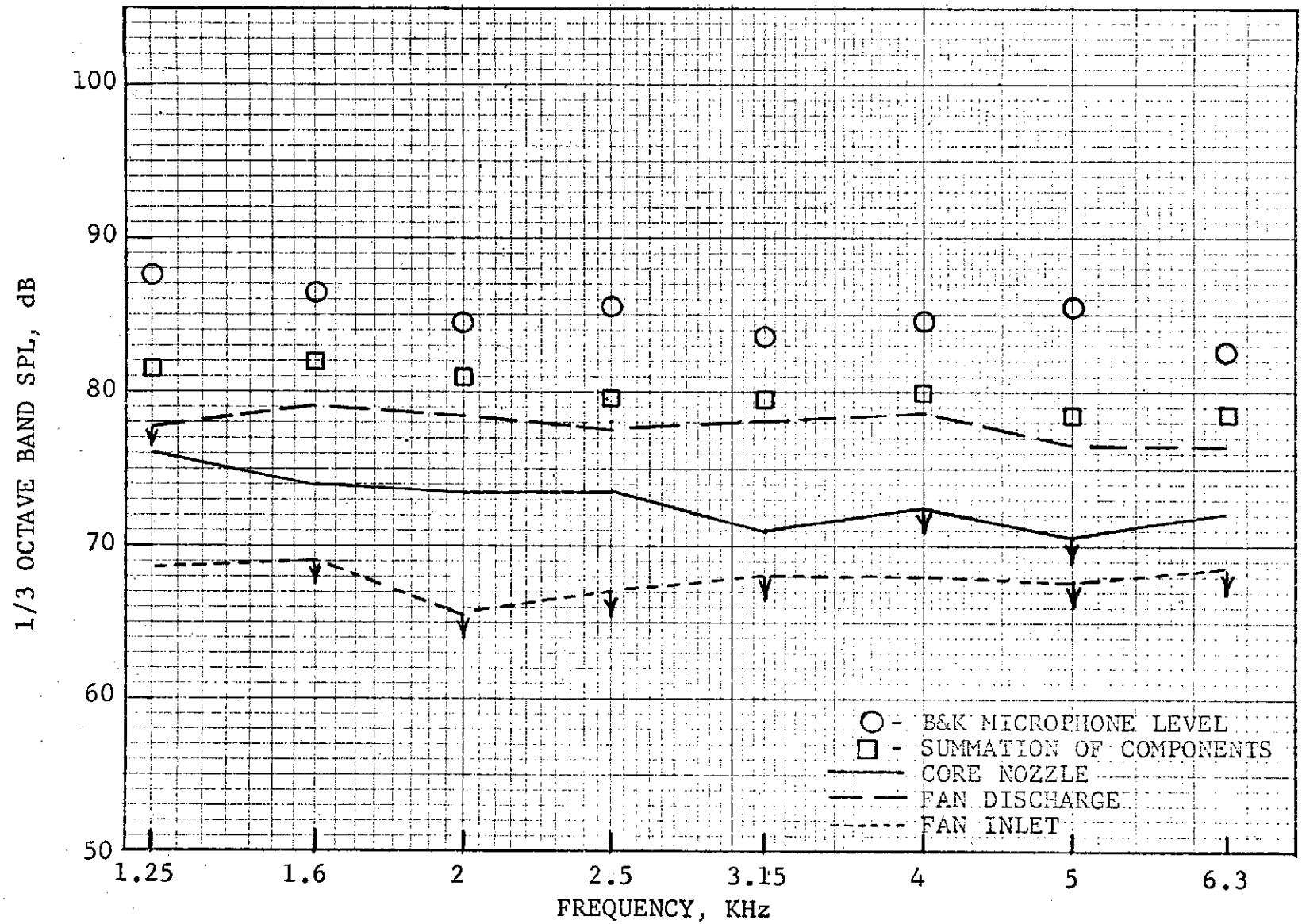

Figure 399. Engine C Broadband Noise Directivity from Directional Array Baseline Fan Configuration, Treated Core, Approach Speed 100° from Inlet.

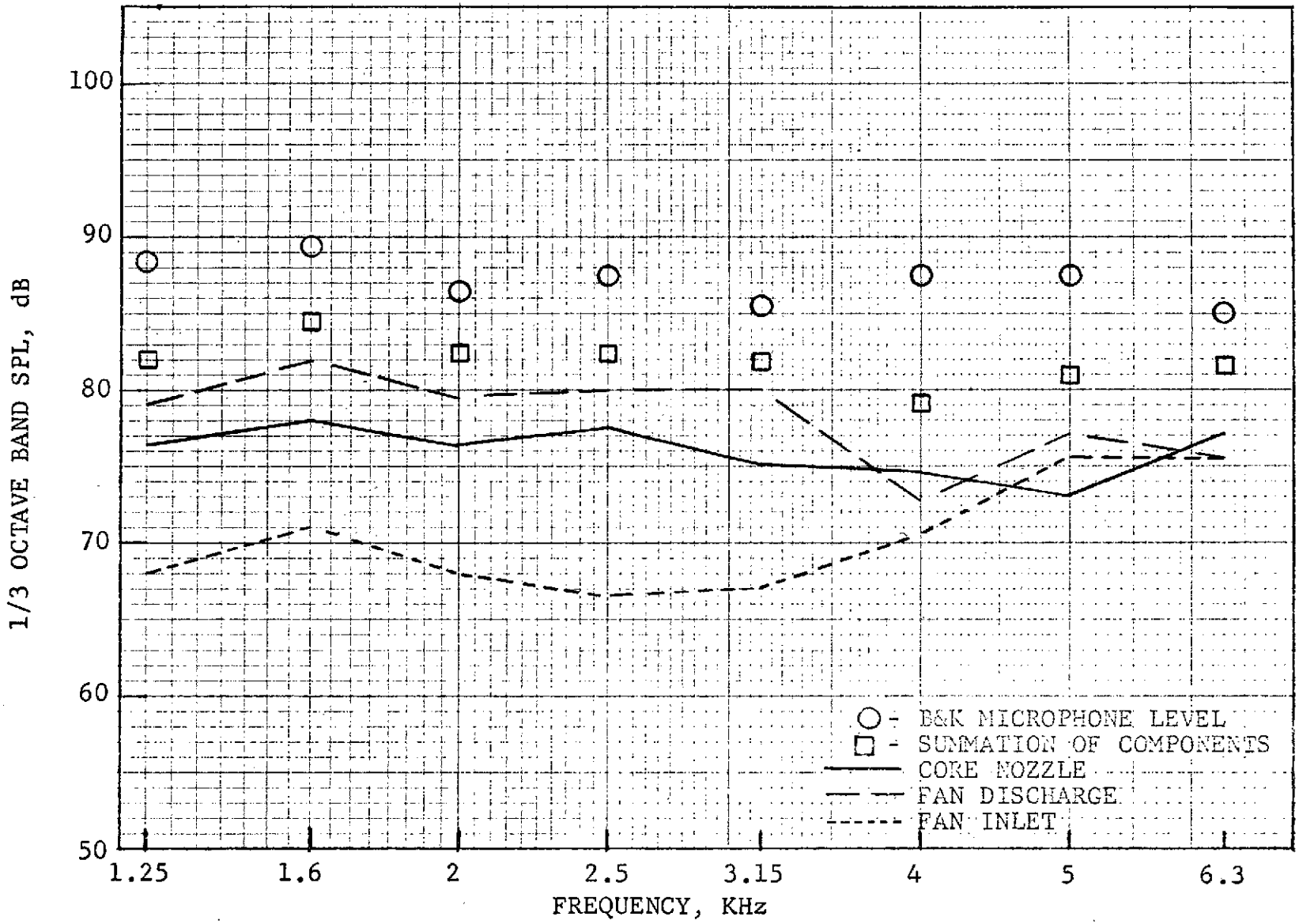

Figure 400. Engine C Broadband Noise Directivity from Directional Array Baseline Fan Configuration, Treated Core, Approach Speed 110° from Inlet.

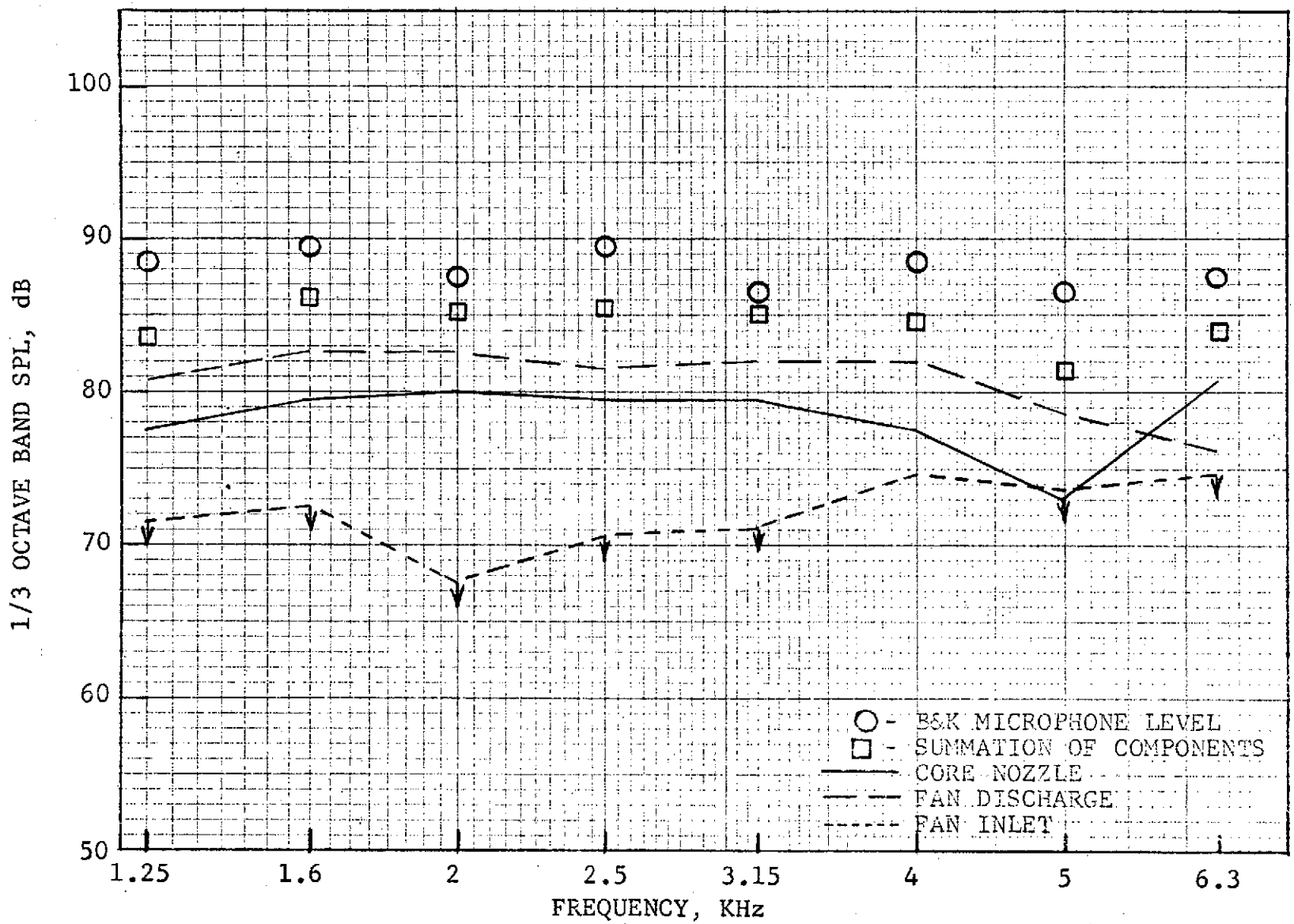

Figure 401. Engine C Broadband Noise Directivity from Directional Array Baseline Fan Configuration, Treated Core, Approach Speed 120° from Inlet.

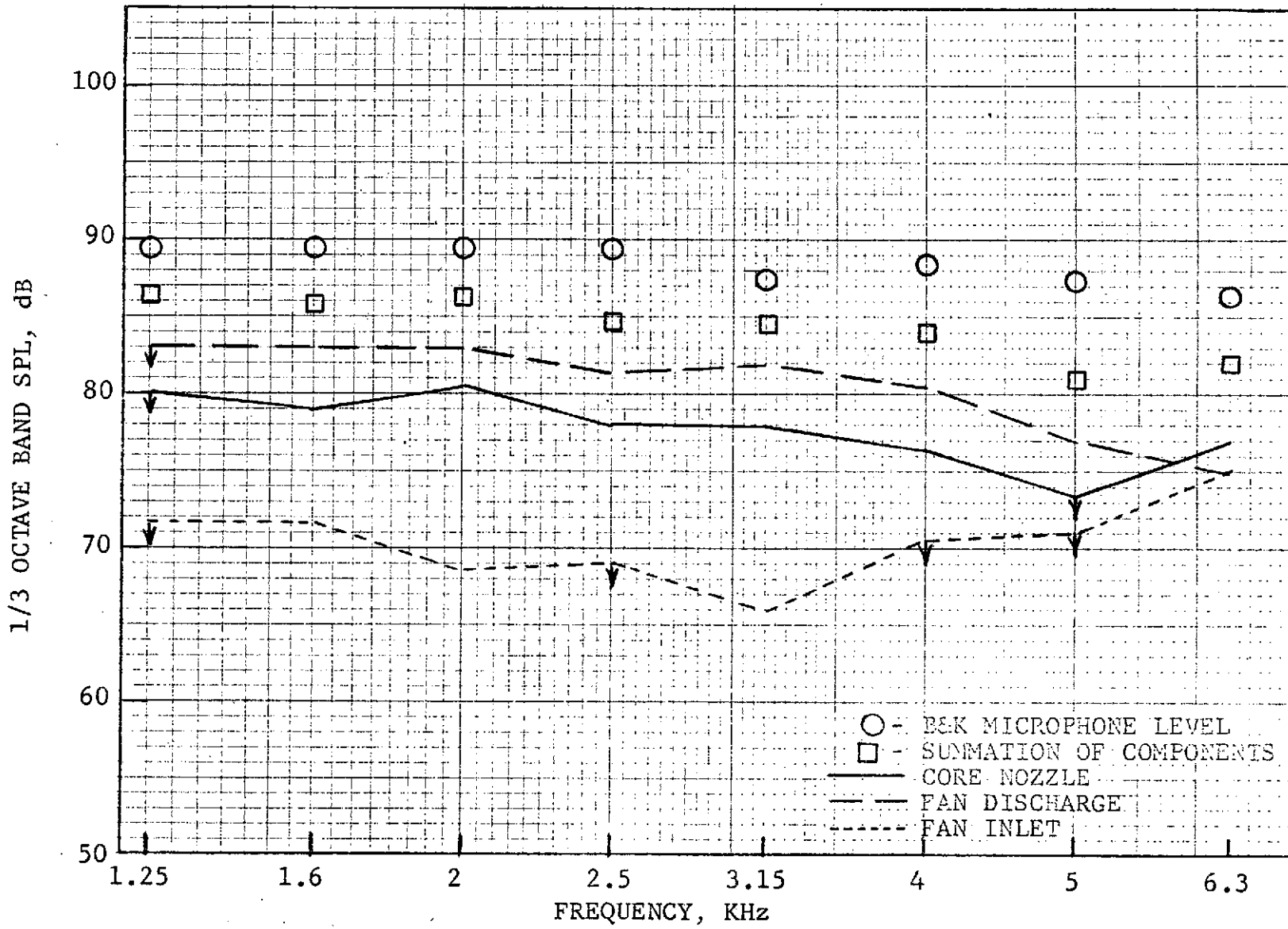

Figure 402. Engine C Broadband Noise Directivity from Directional Array Baseline Fan Configuration, Treated Core, Approach Speed 130° from Inlet.

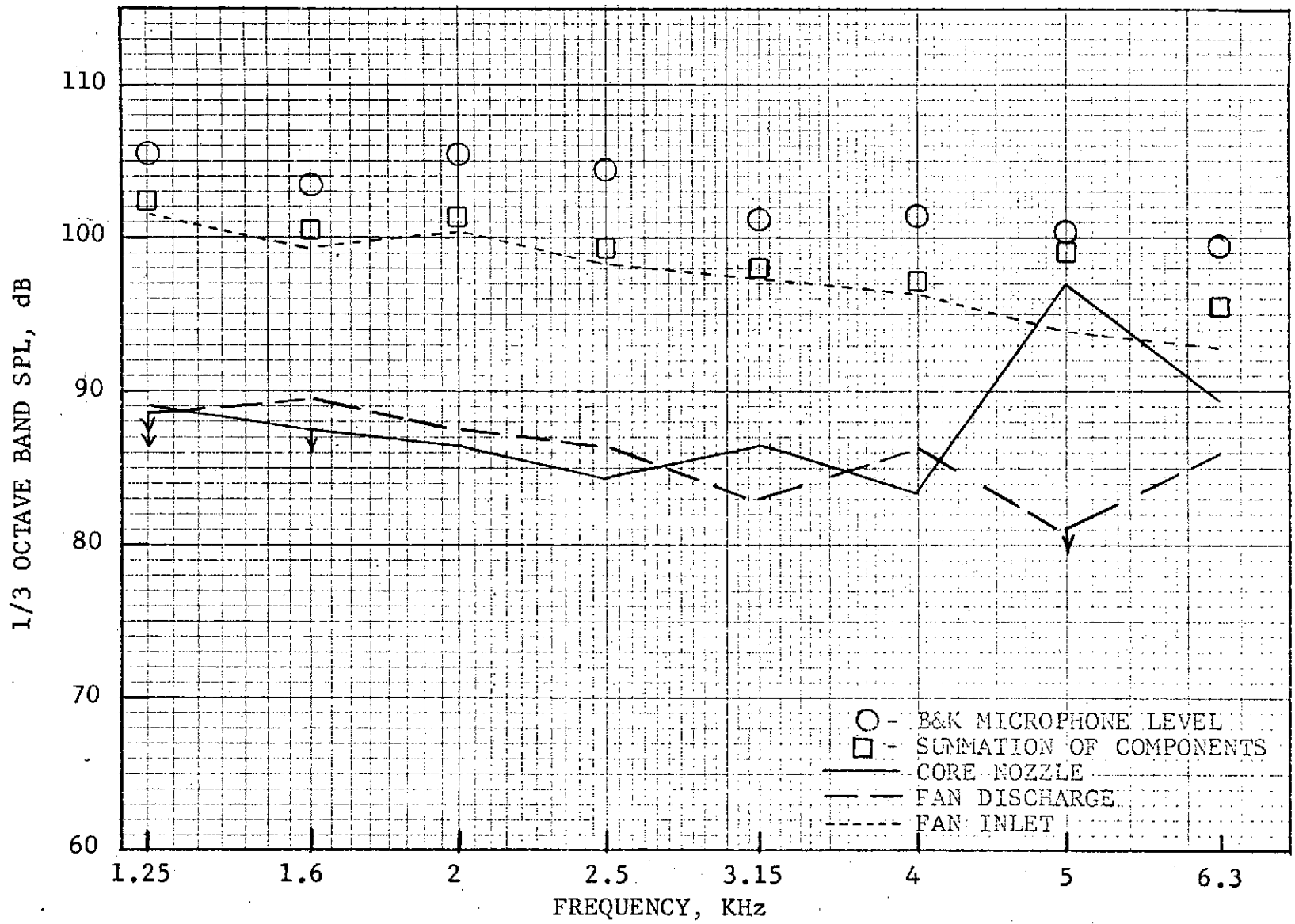

Figure 403. Engine C Broadband Noise Directivity from Directional Array Baseline Fan Configuration, Treated Core, Takeoff Speed 50° from Inlet.

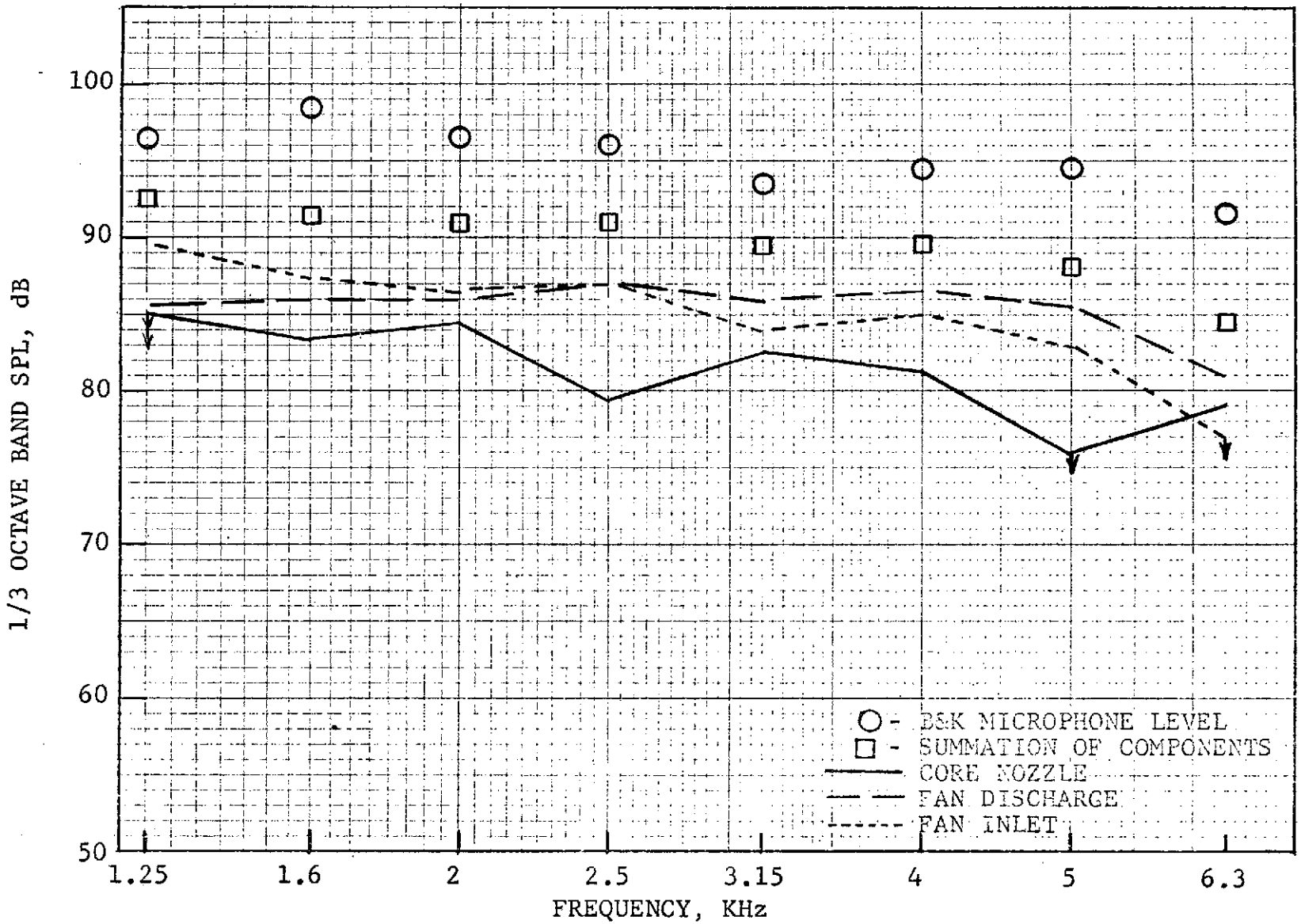

Figure 404. Engine C Broadband Noise Directivity from Directional Array Baseline Fan Configuration, Treated Core, Takeoff Speed 90° from Inlet.

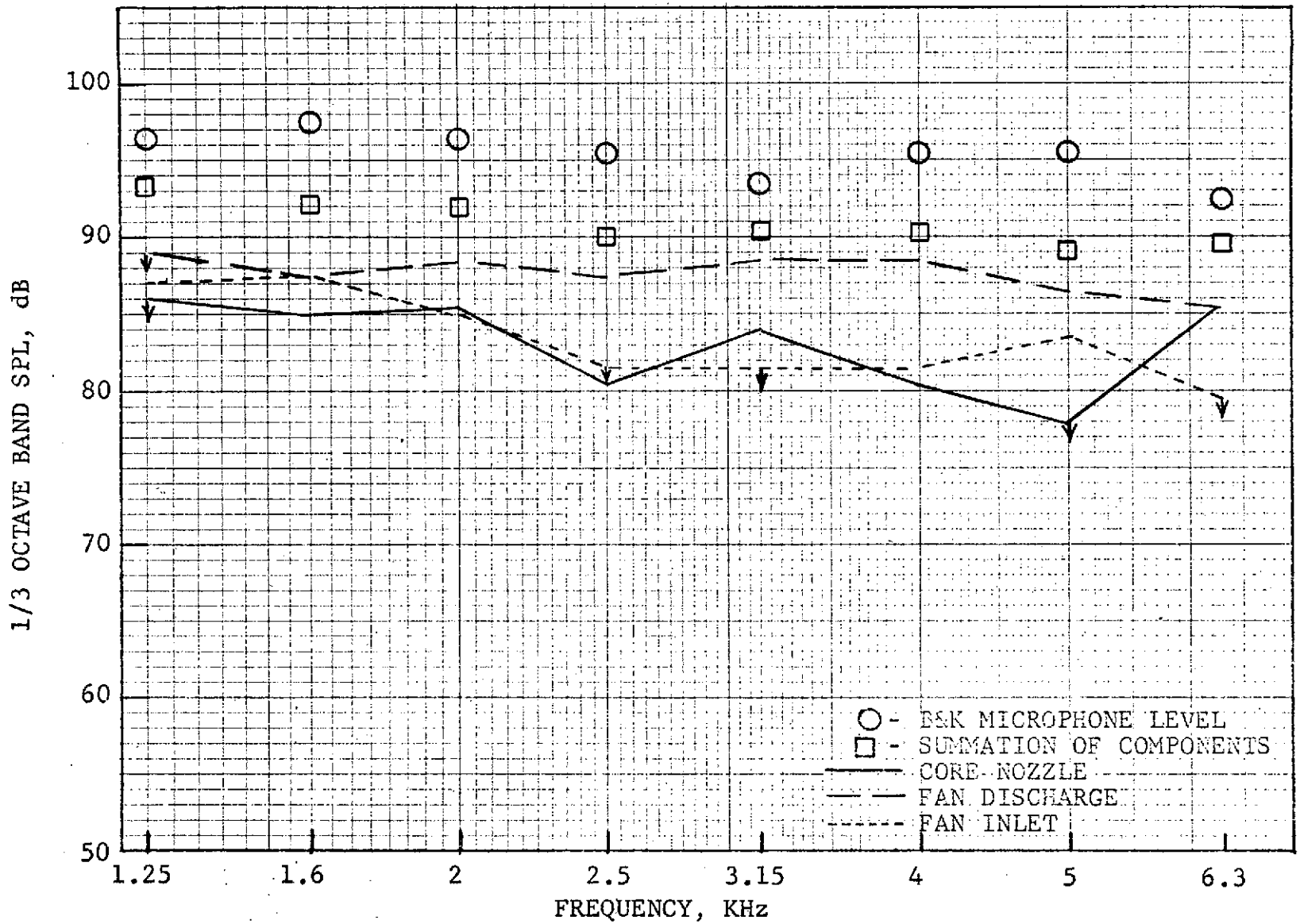

Figure 405. Engine C Broadband Noise Directivity from Directional Array Baseline Fan Configuration, Treated Core, Takeoff Speed 100° from Inlet.

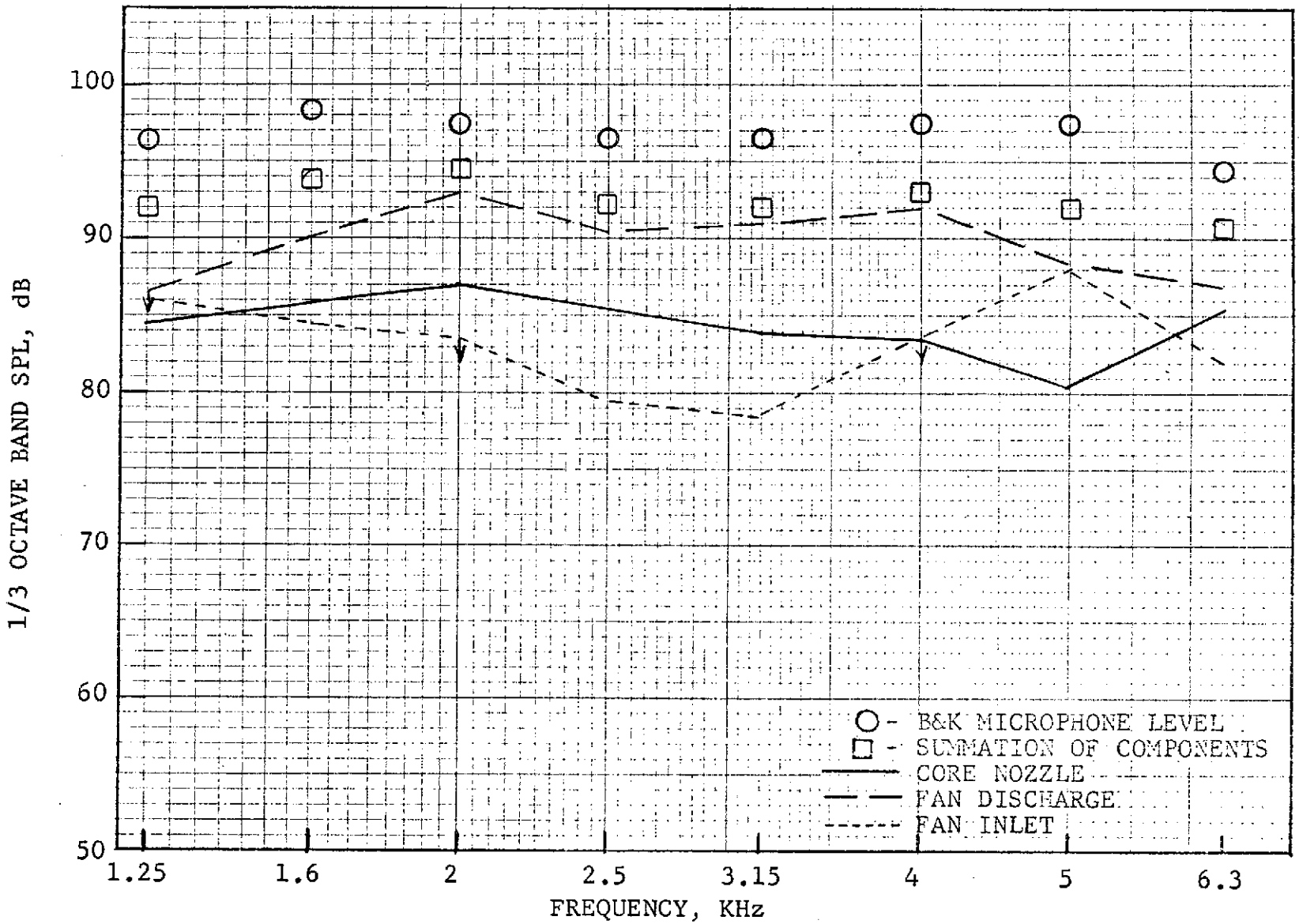

Figure 406. Engine C Broadband Noise Directivity from Directional Array Baseline Fan Configuration, Treated Core, Takeoff Speed 110° from Inlet.

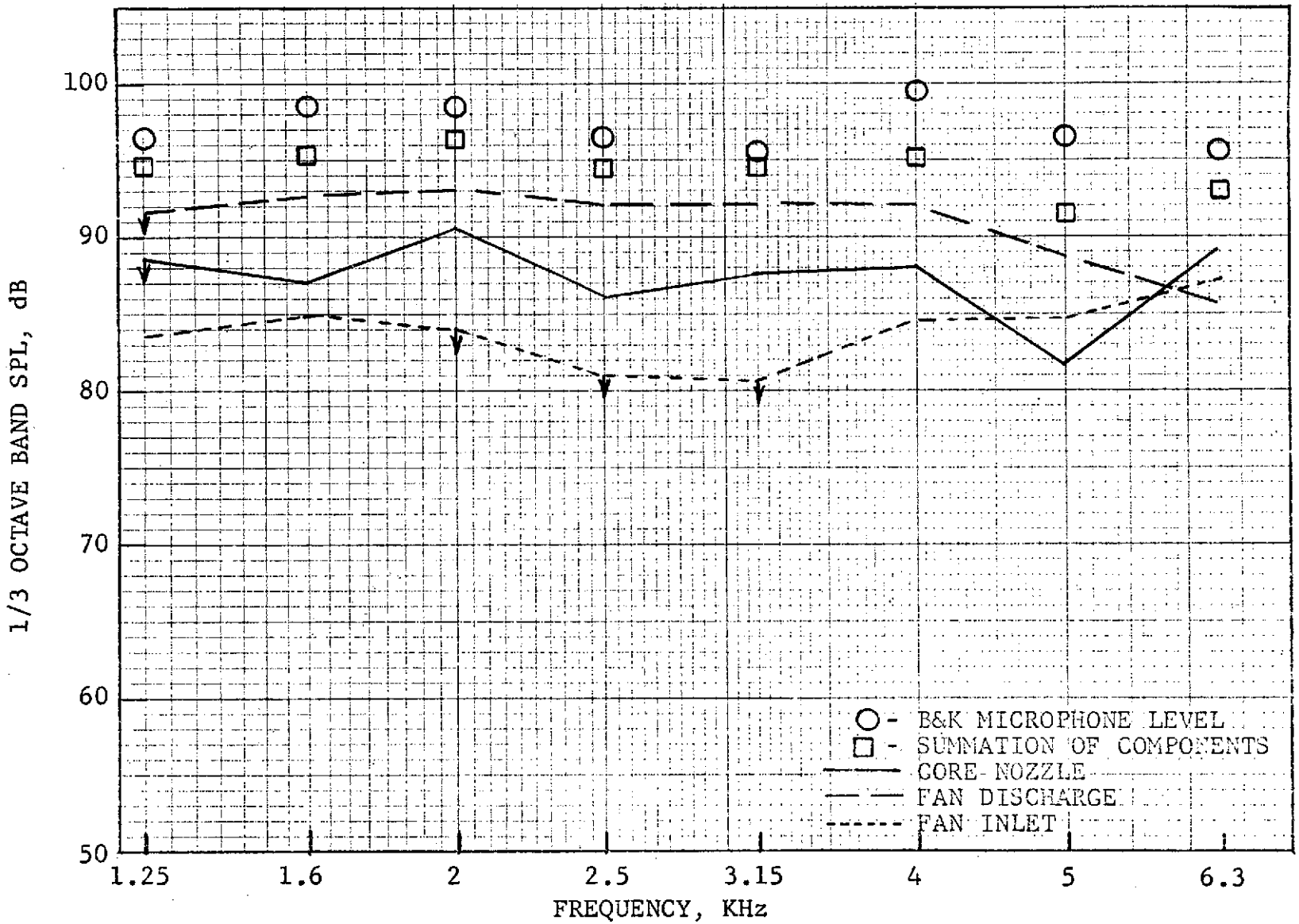

Figure 407. Engine C Broadband Noise Directivity from Directional Array Baseline Fan Configuration, Treated Core, Takeoff Speed 120° from Inlet.

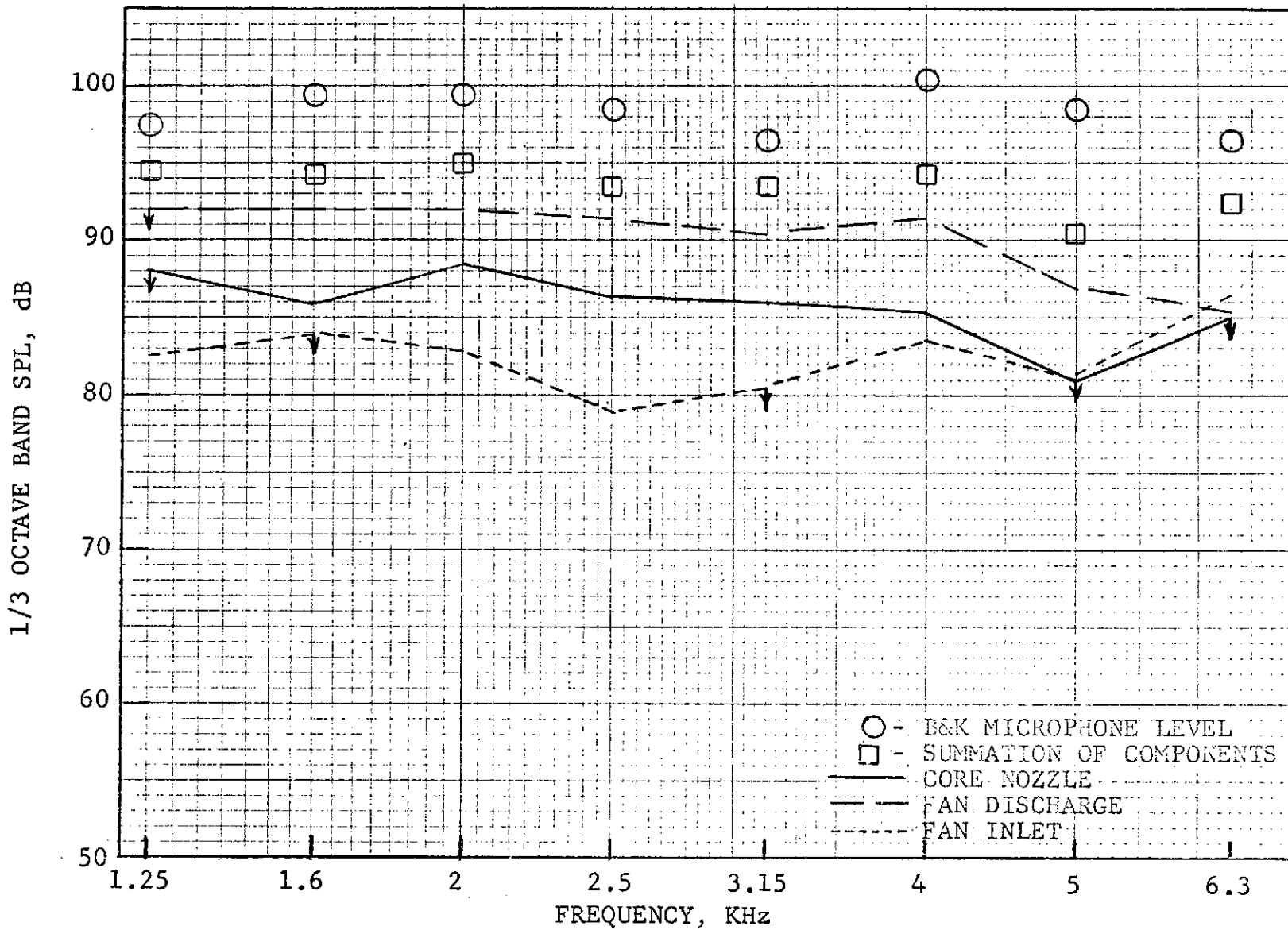

Figure 408. Engine C Broadband Noise Directivity from Directional Array Baseline Fan Configuration, Treated Core, Takeoff Speed 130° from Inlet.

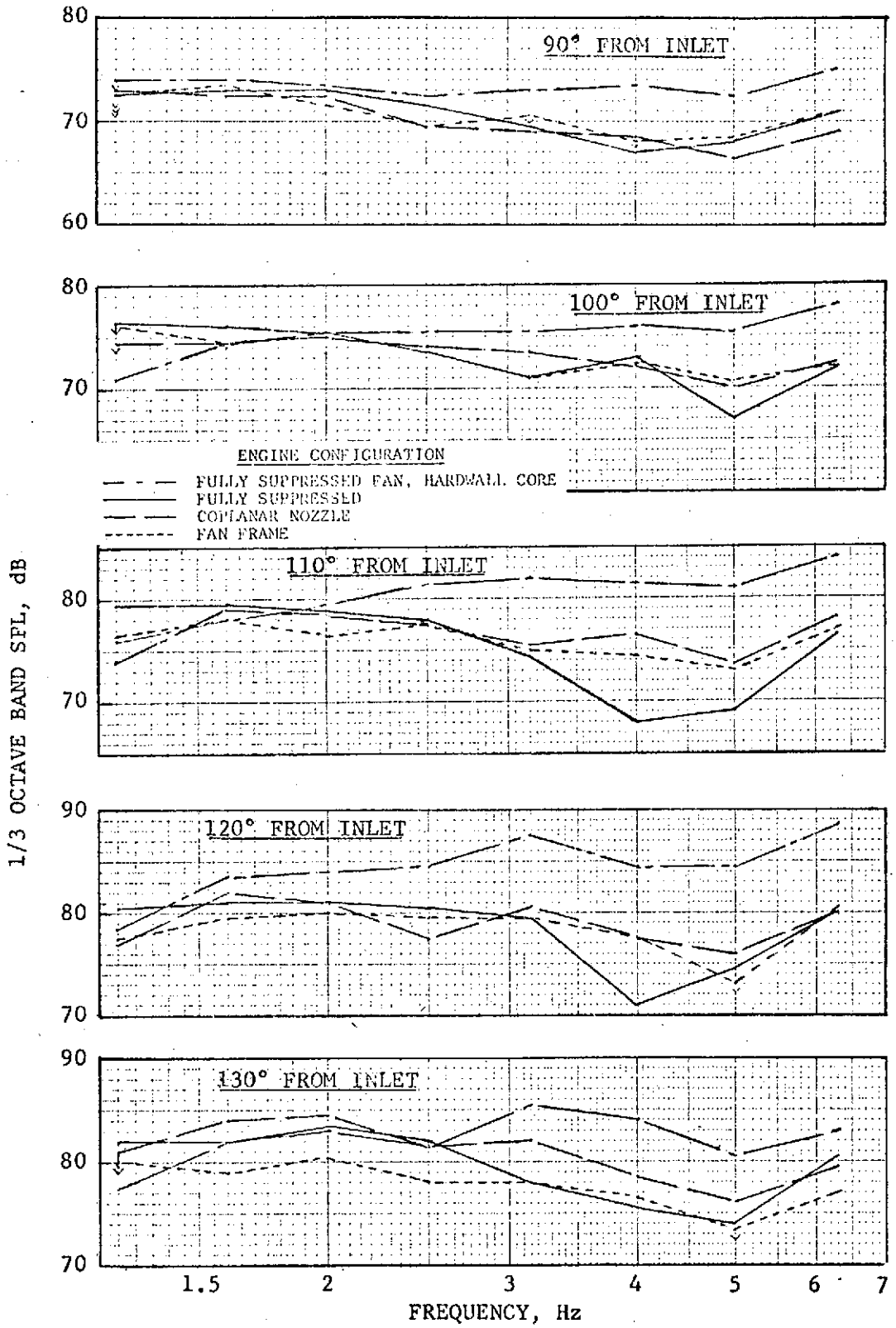

Figure 409. Engine C Core Nozzle Radiated Broadband Noise Spectra from Directional Array (Approach Power).

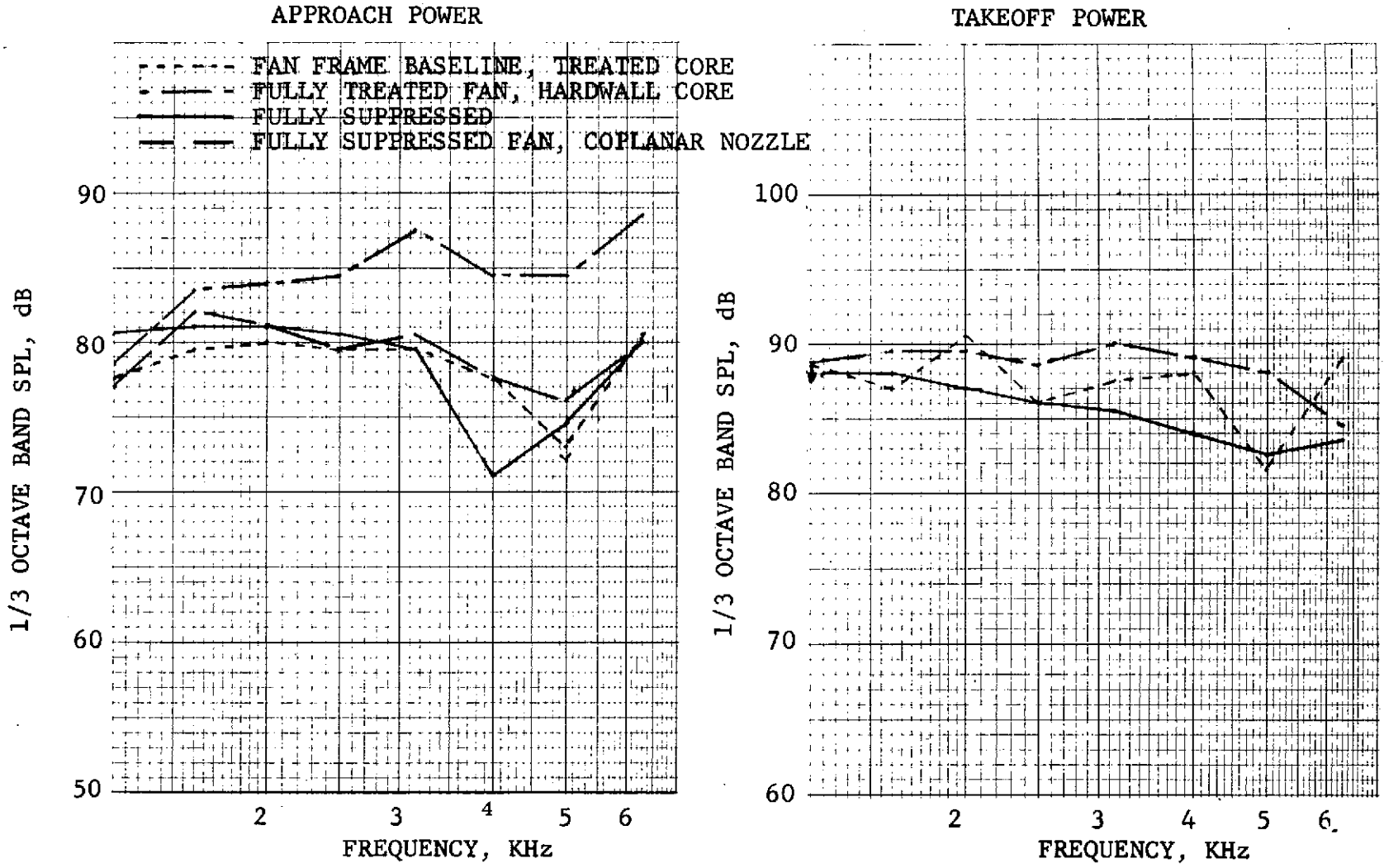

Figure 410. Engine C Core Radiated Broadband Noise at 120 Degrees.

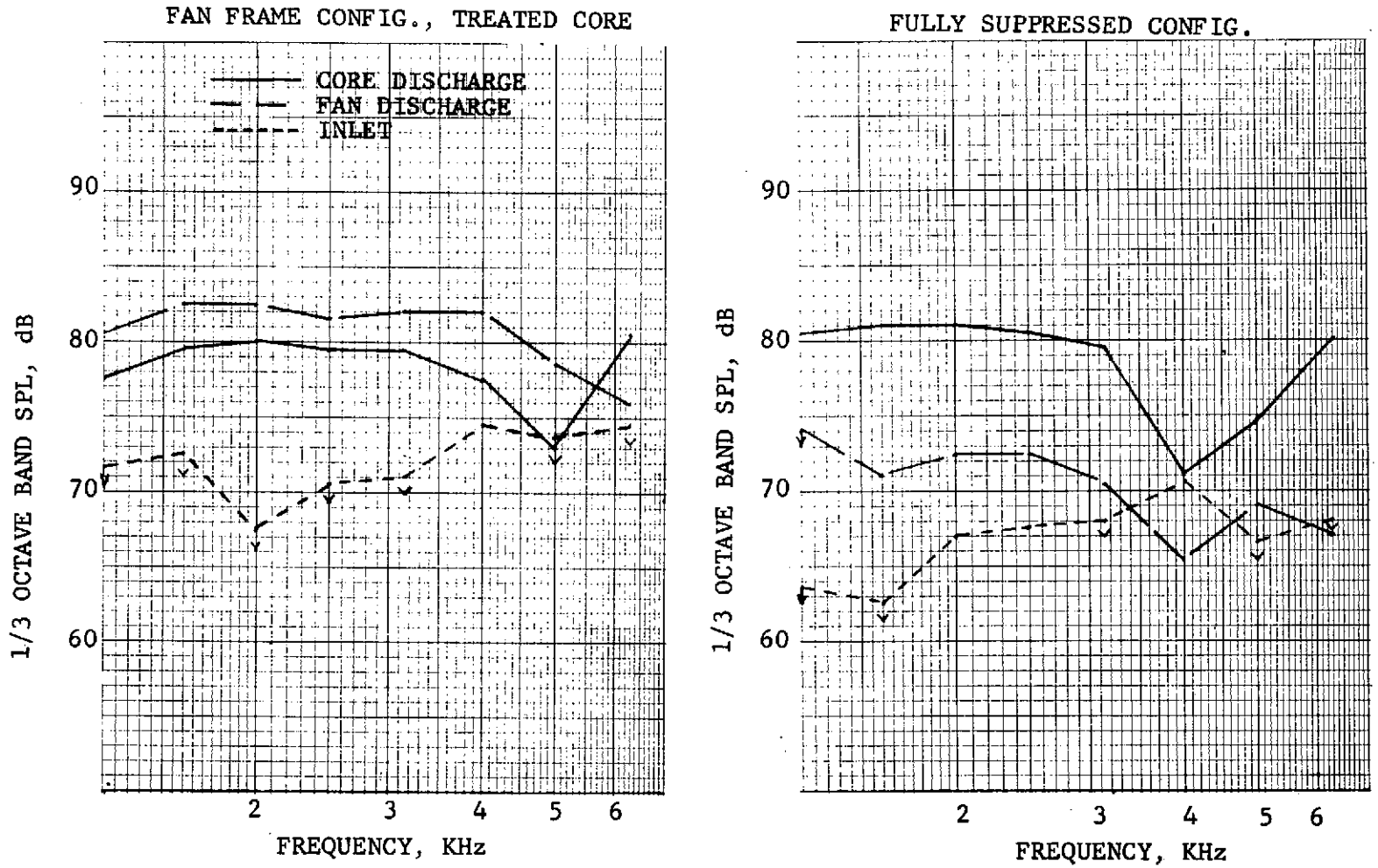

Figure 411. Engine C Broadband Source Amplitudes, Approach Power (120 Degrees, 30.5m (100') Arc).

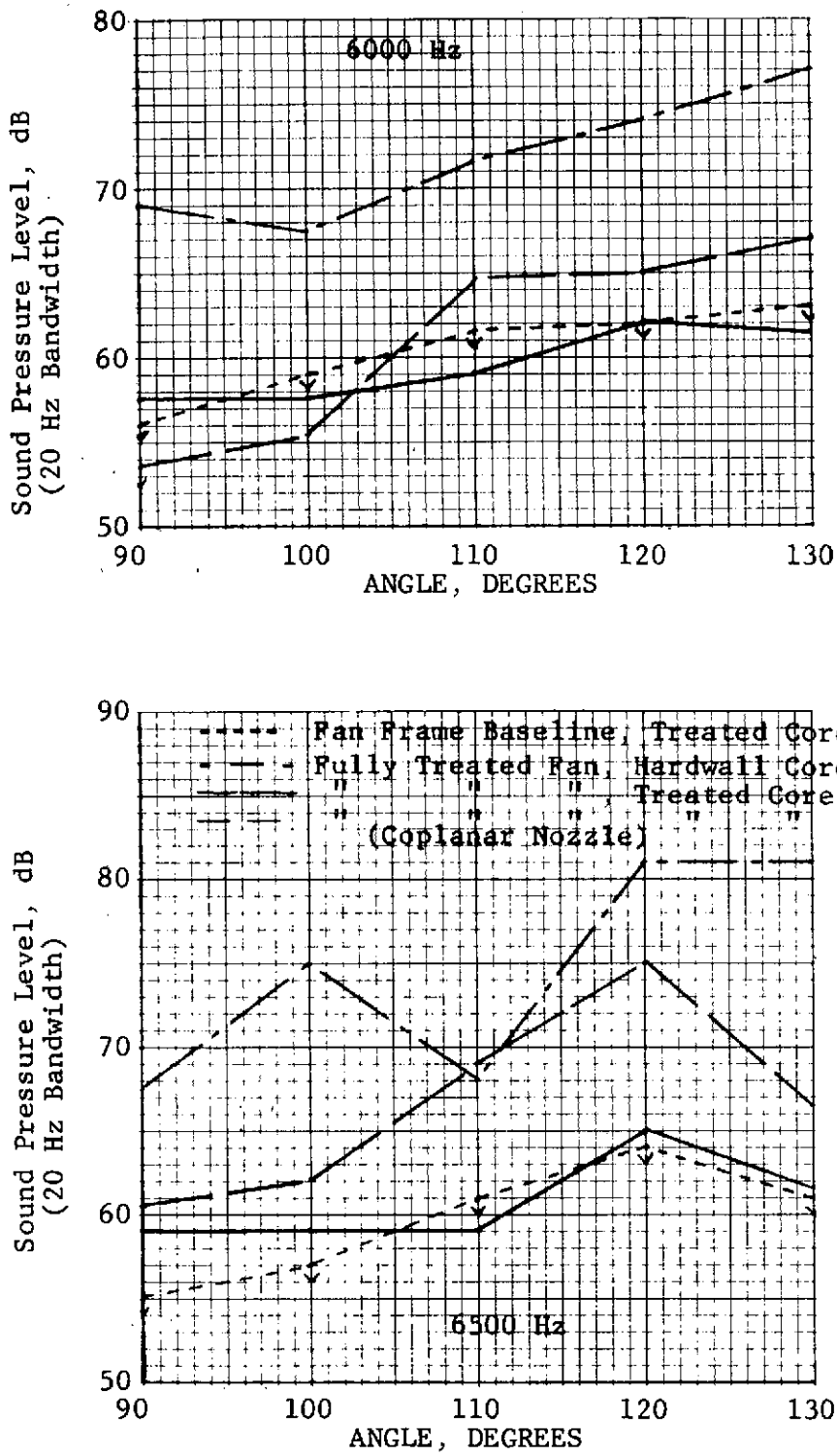

Figure 412. Engine C B&K Microphone Measured Turbine Tones (30.5m (100') Arc, Approach Power).

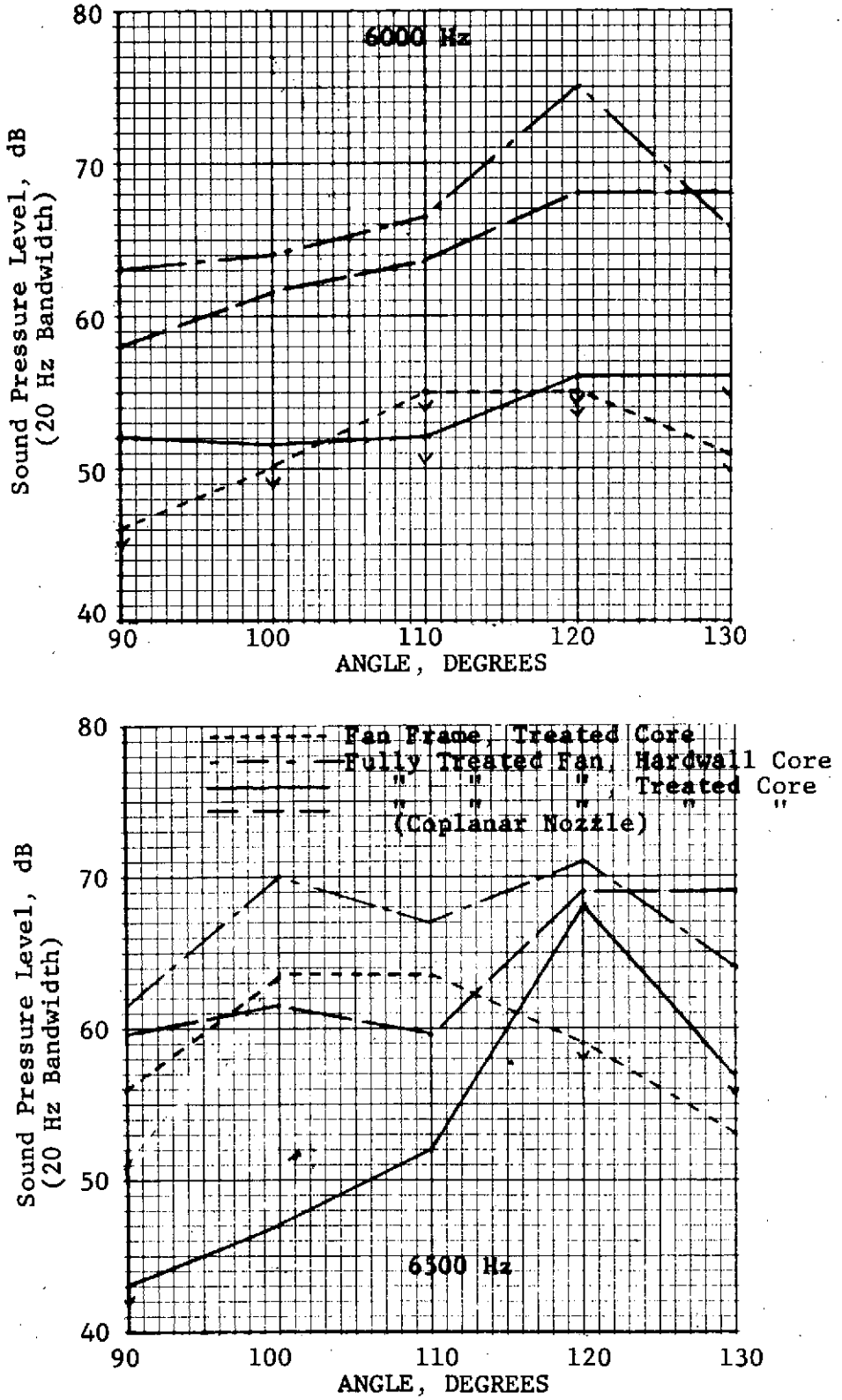

Figure 413. Engine C Directional Array Measured Turbine Tones (30.5m (100') Arc Approach Power).

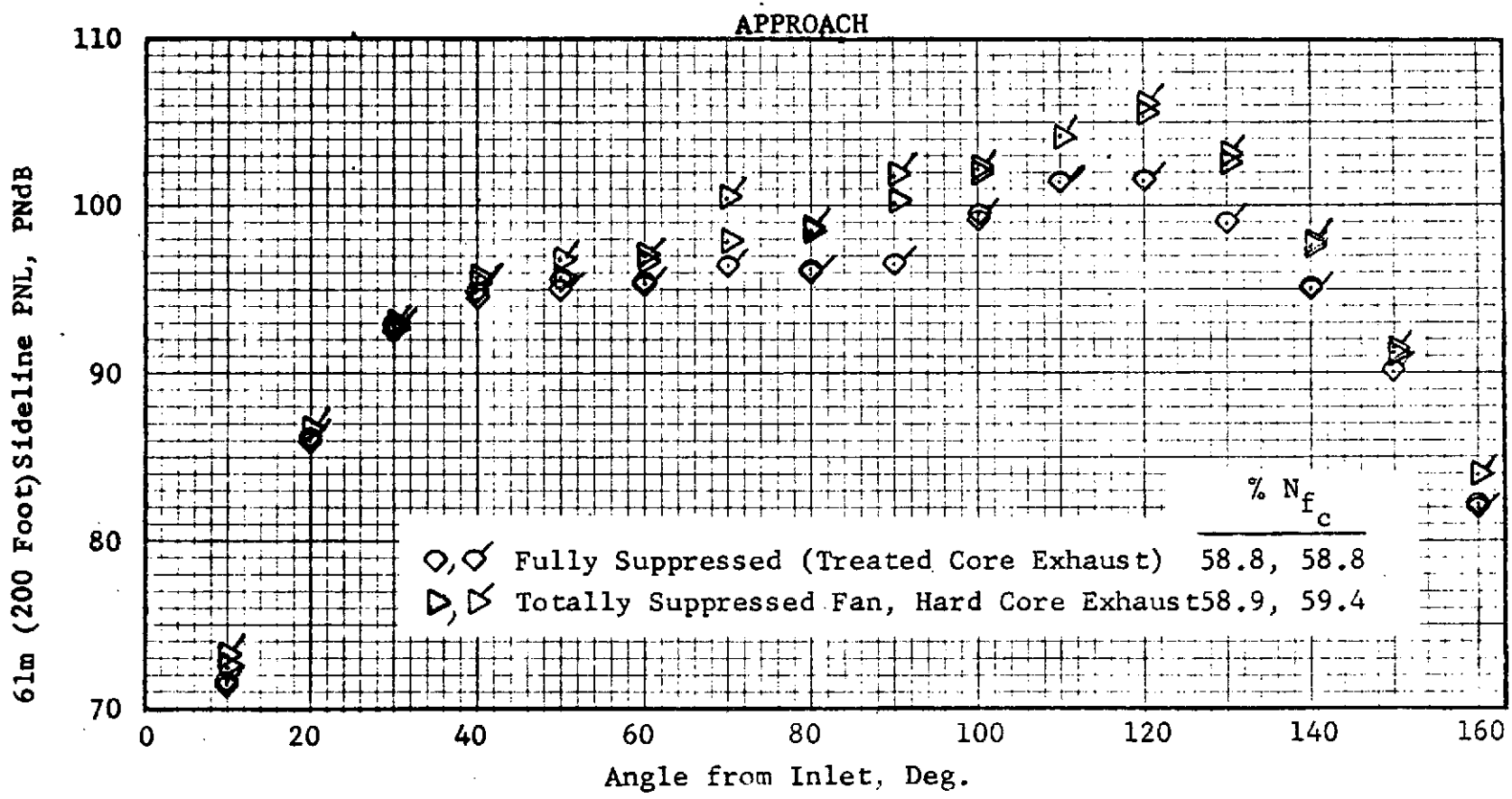

Figure 414. Engine C Perceived Noise Levels for a Single Engine Effect of Core Exhaust Treatment Standard Day.

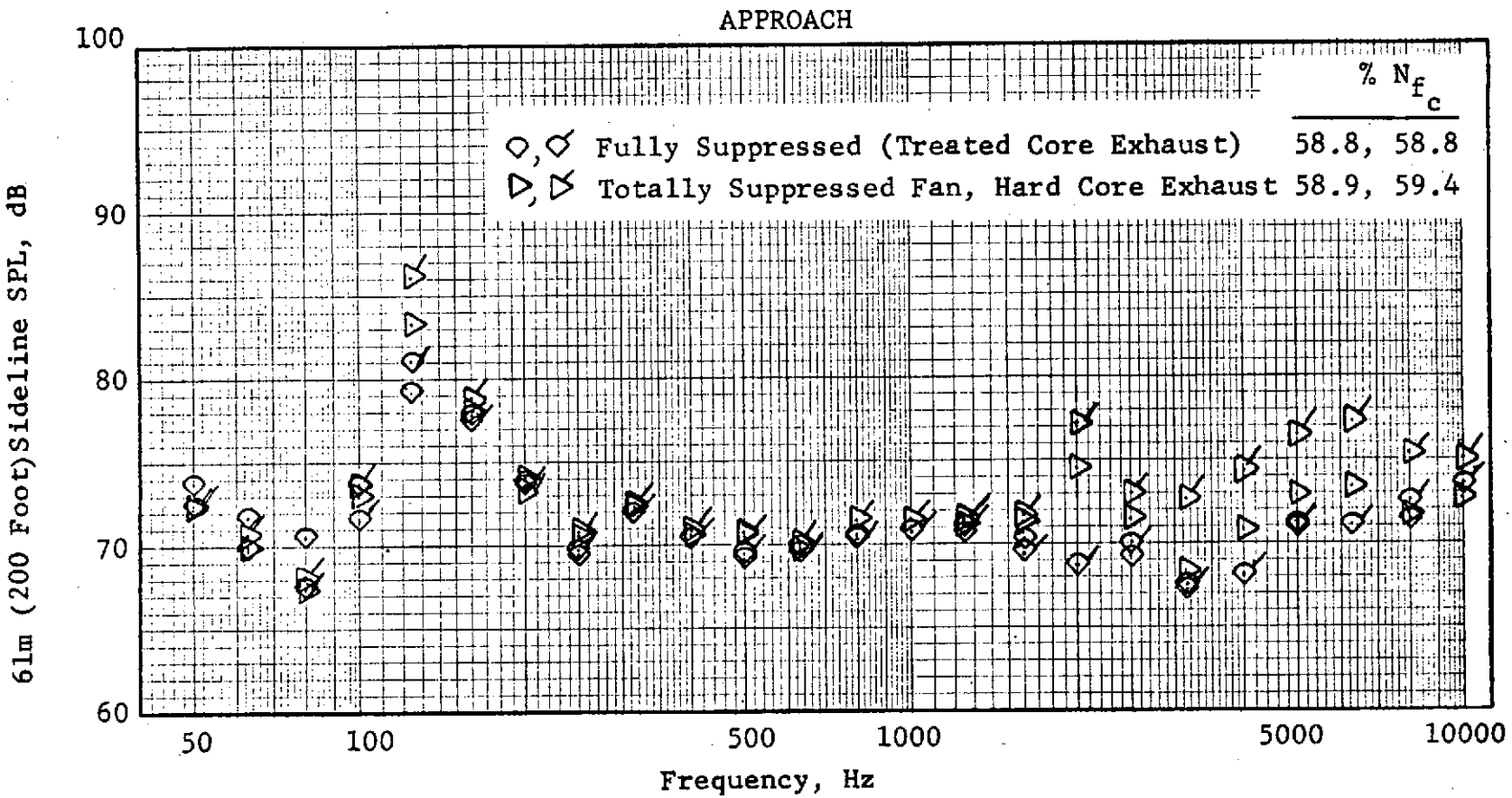

Figure 415. Engine C Sound Power Level Spectra at 70° Effect of Core Exhaust Treatment Standard Day.

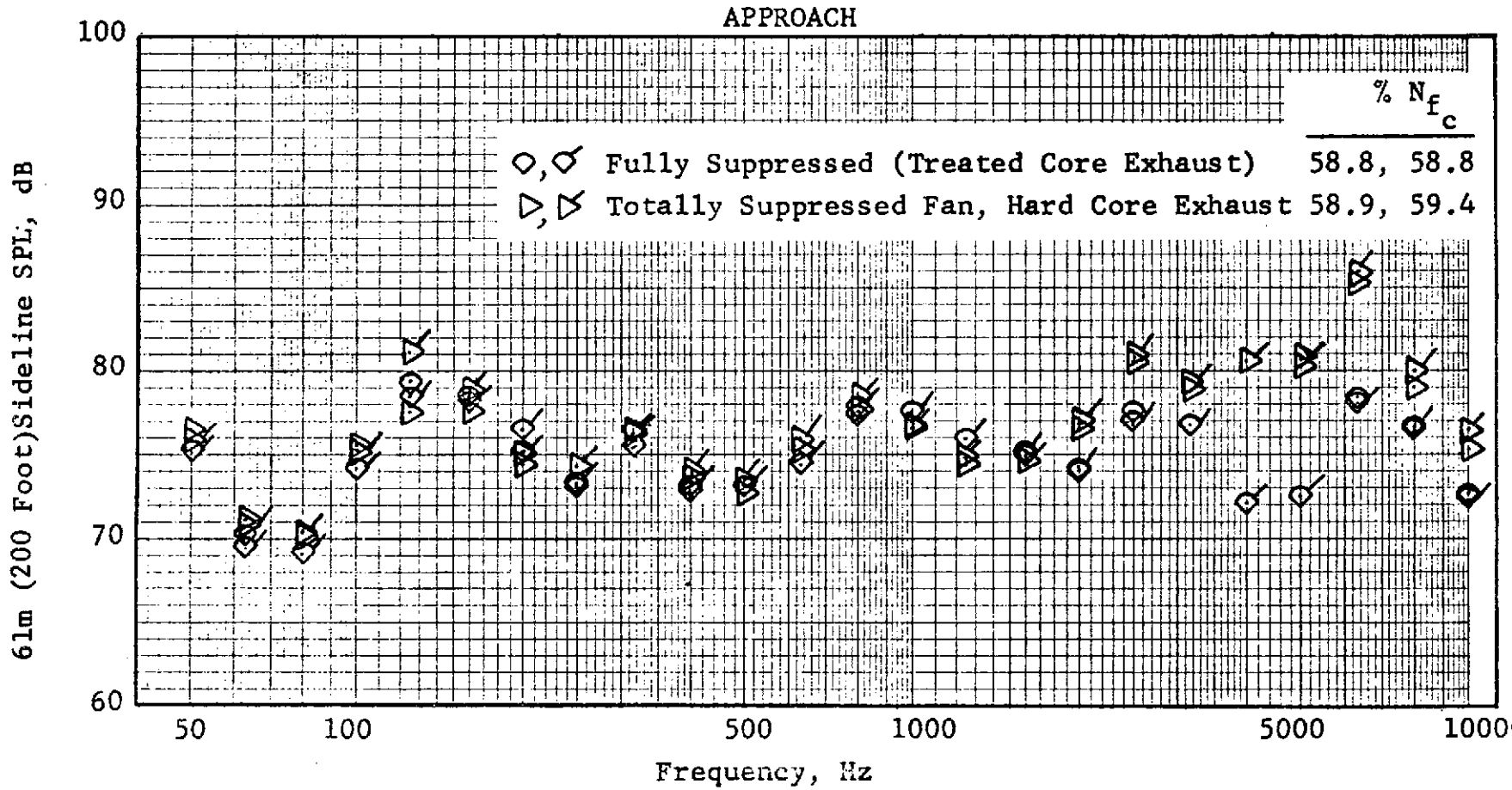

Figure 416. Engine C Sound Power Level Spectra at 120° Effect of Core Exhaust Treatment Standard Day.

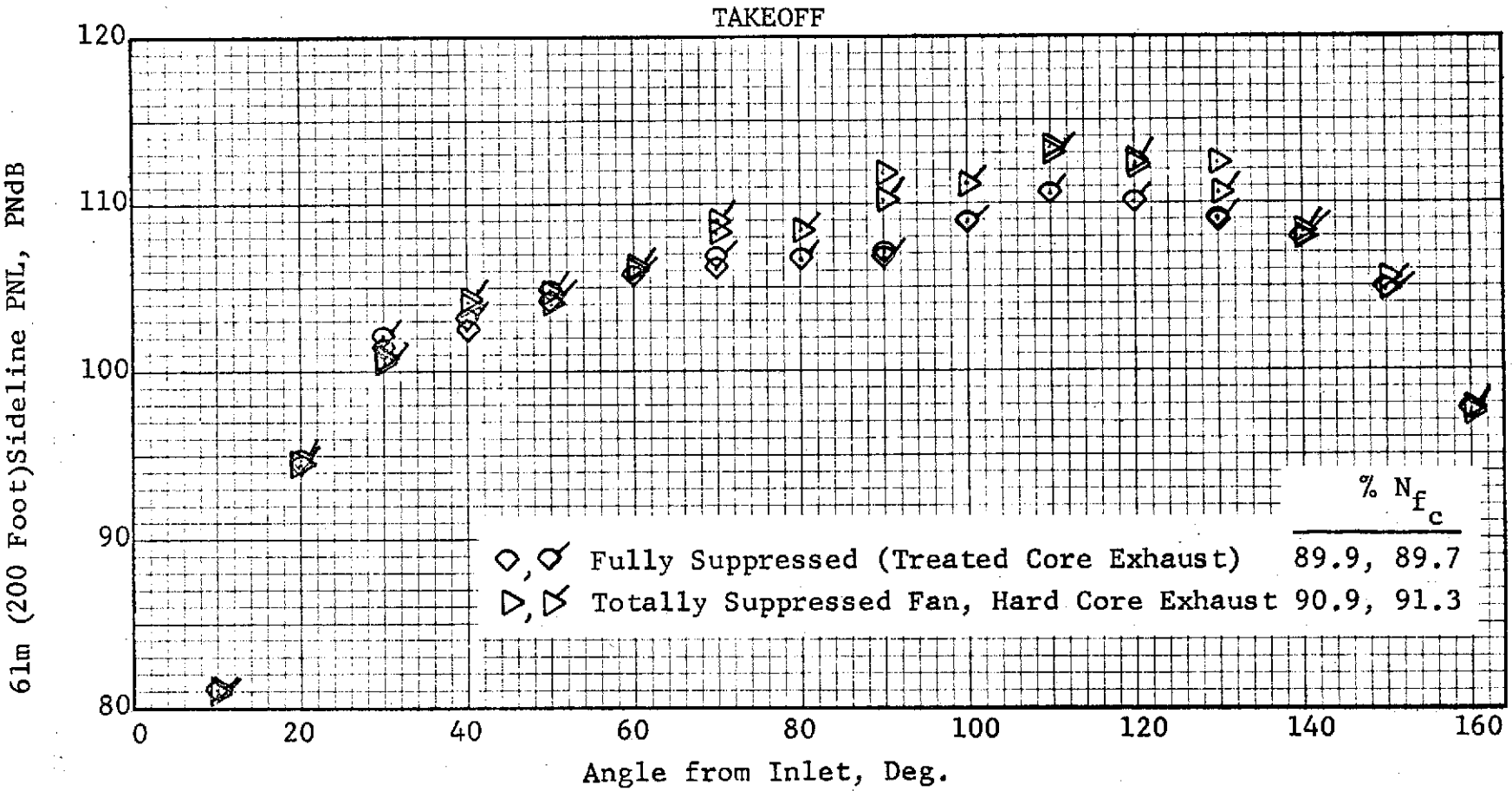

Figure 417. Engine C Perceived Noise Levels for a Single Engine Effect of Core Exhaust Treatment Standard Day.

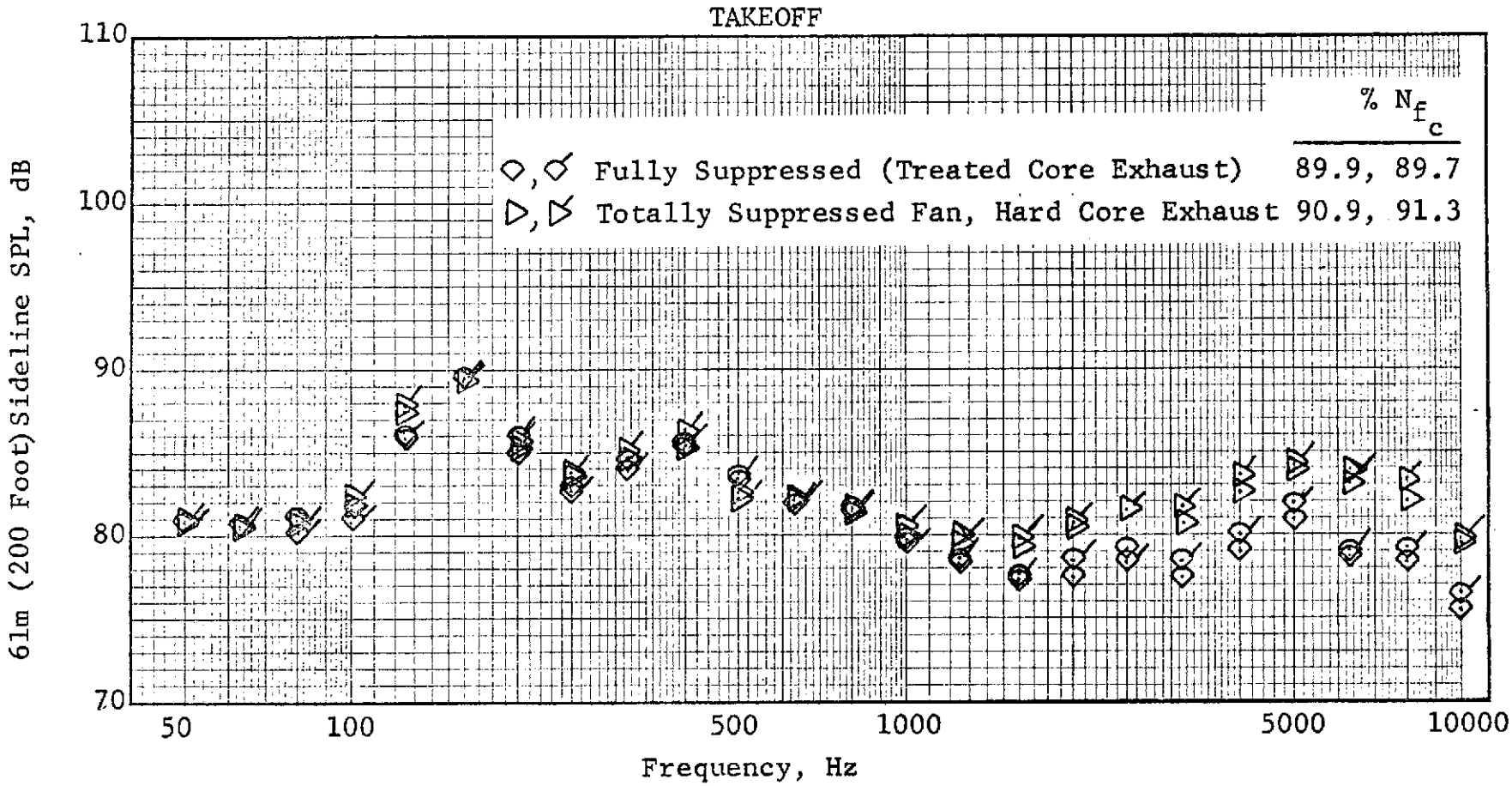

Figure 418. Engine C Sound Power Level Spectra at 70° Effect of Core Exhaust Treatment Standard Day.

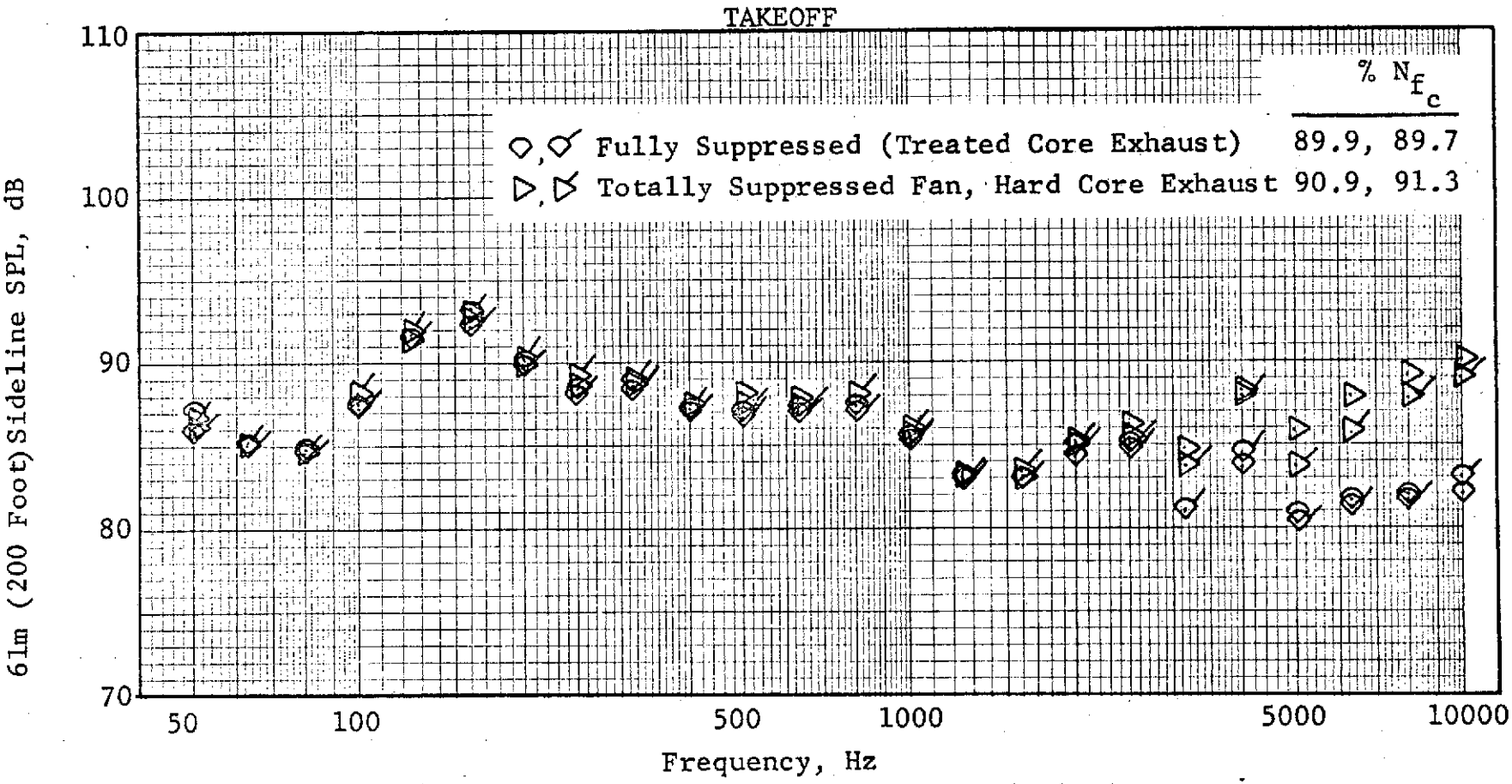

Figure 419. Engine C Sound Power Level Spectra at 110° Effect of Core Exhaust Treatment Standard Day.

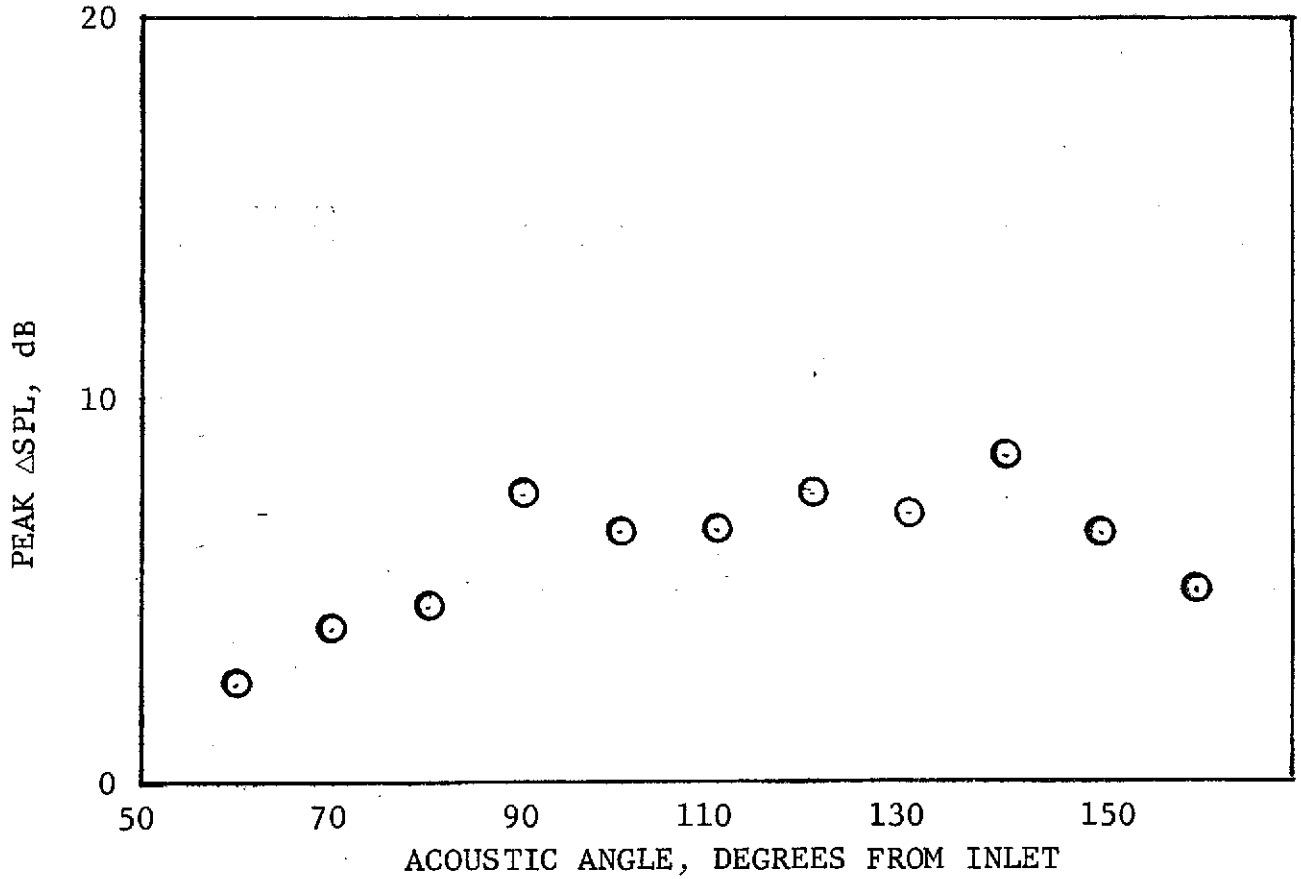

Figure 420. Engine C Turbine Suppression Directivity 50% Speed.

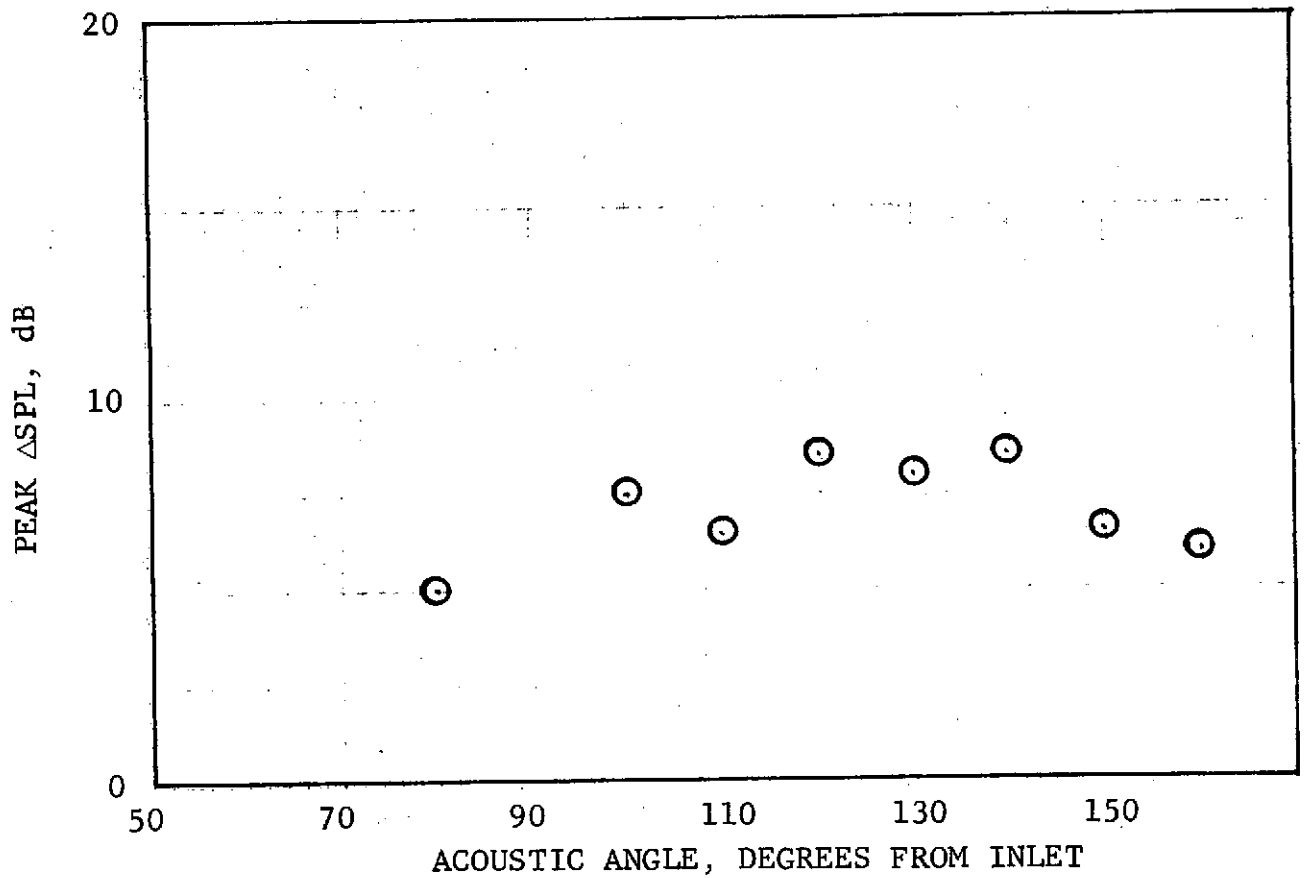

Figure 421. Engine C Turbine Suppression Directivity 60% Speed.

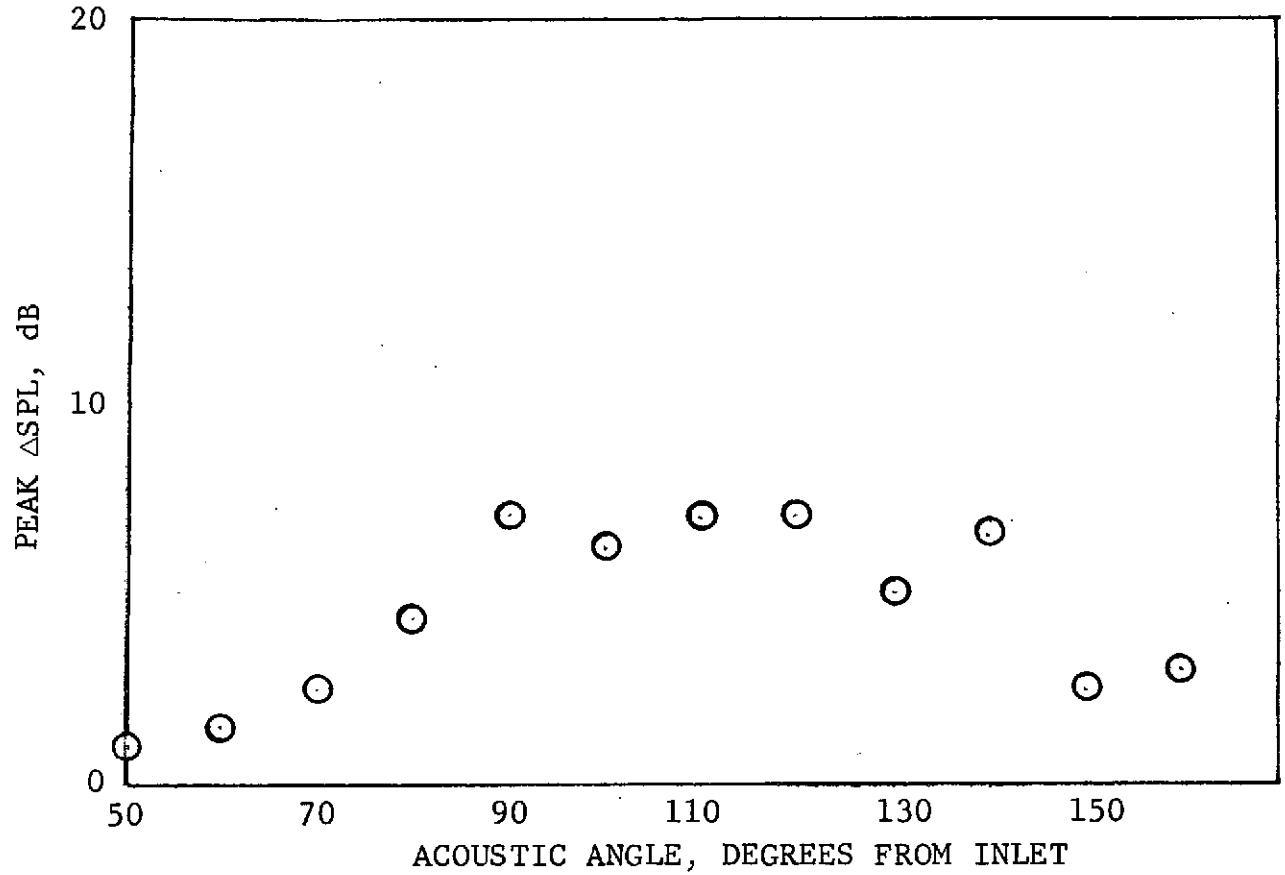

Figure 422. Engine C Turbine Suppression Directivity 80% Speed.

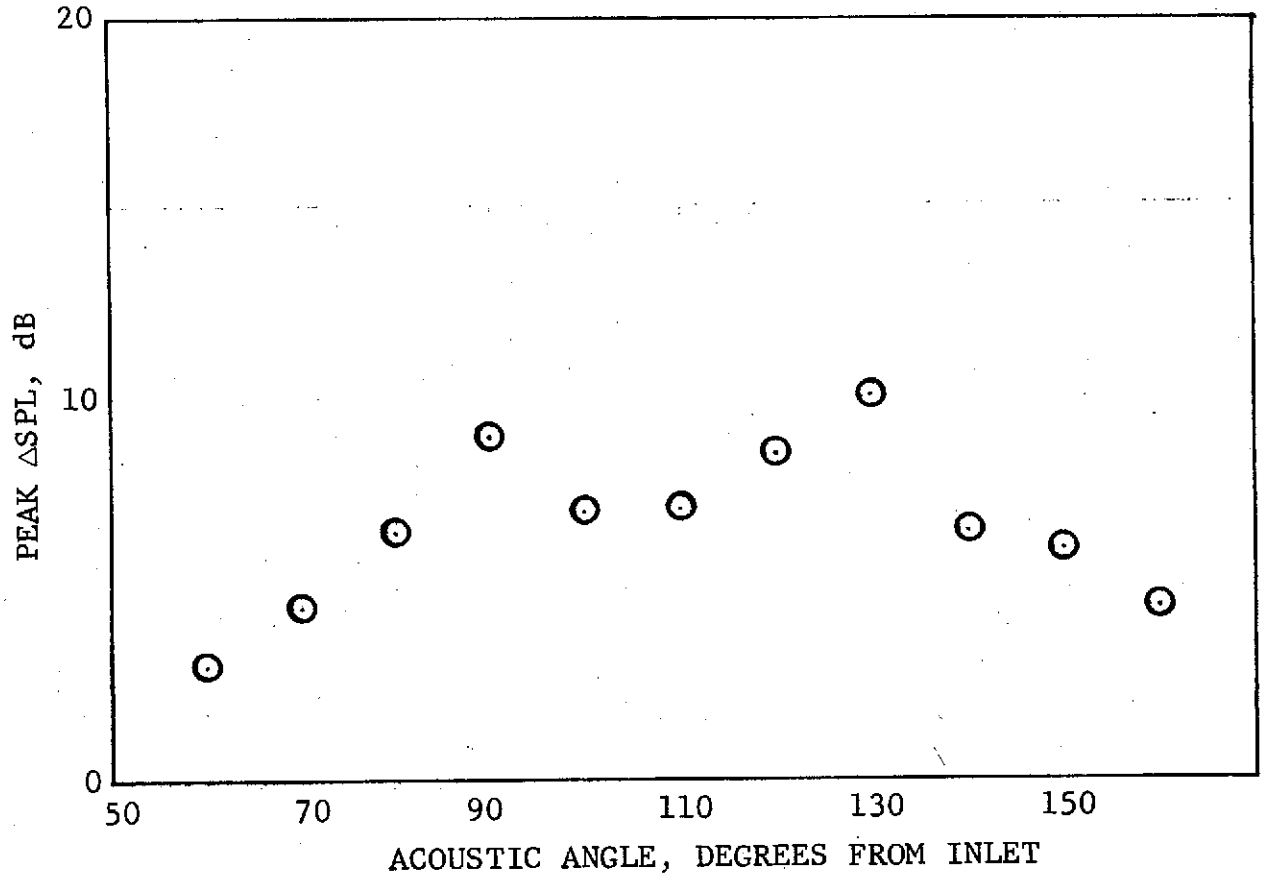

Figure 423. Engine C Turbine Suppression Directivity 90% Speed.

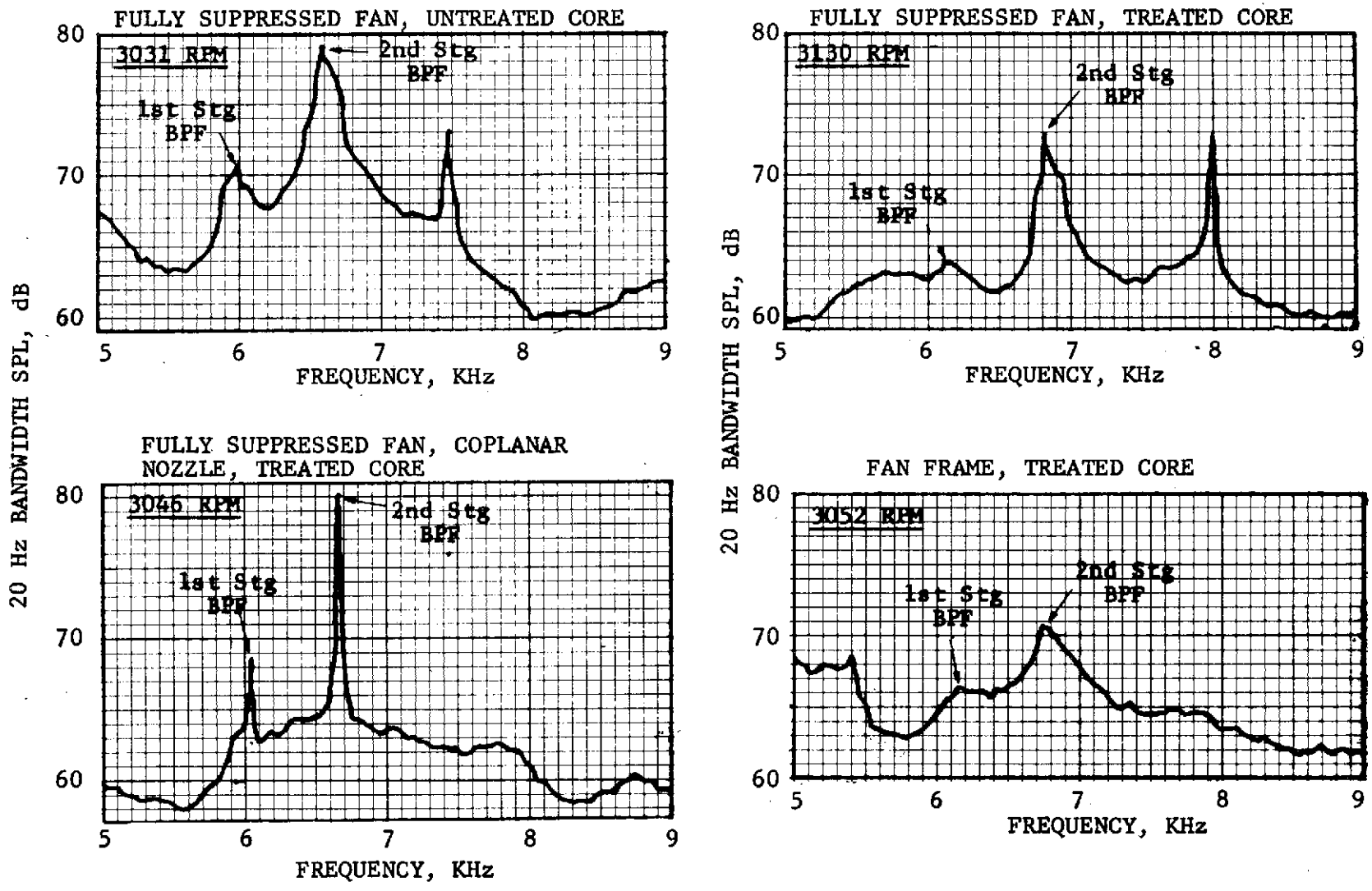

Figure 424. Engine C Farfield Narrowbands Showing Turbine Tones (Approach Power, 120°, 45.7m (150') Arc).

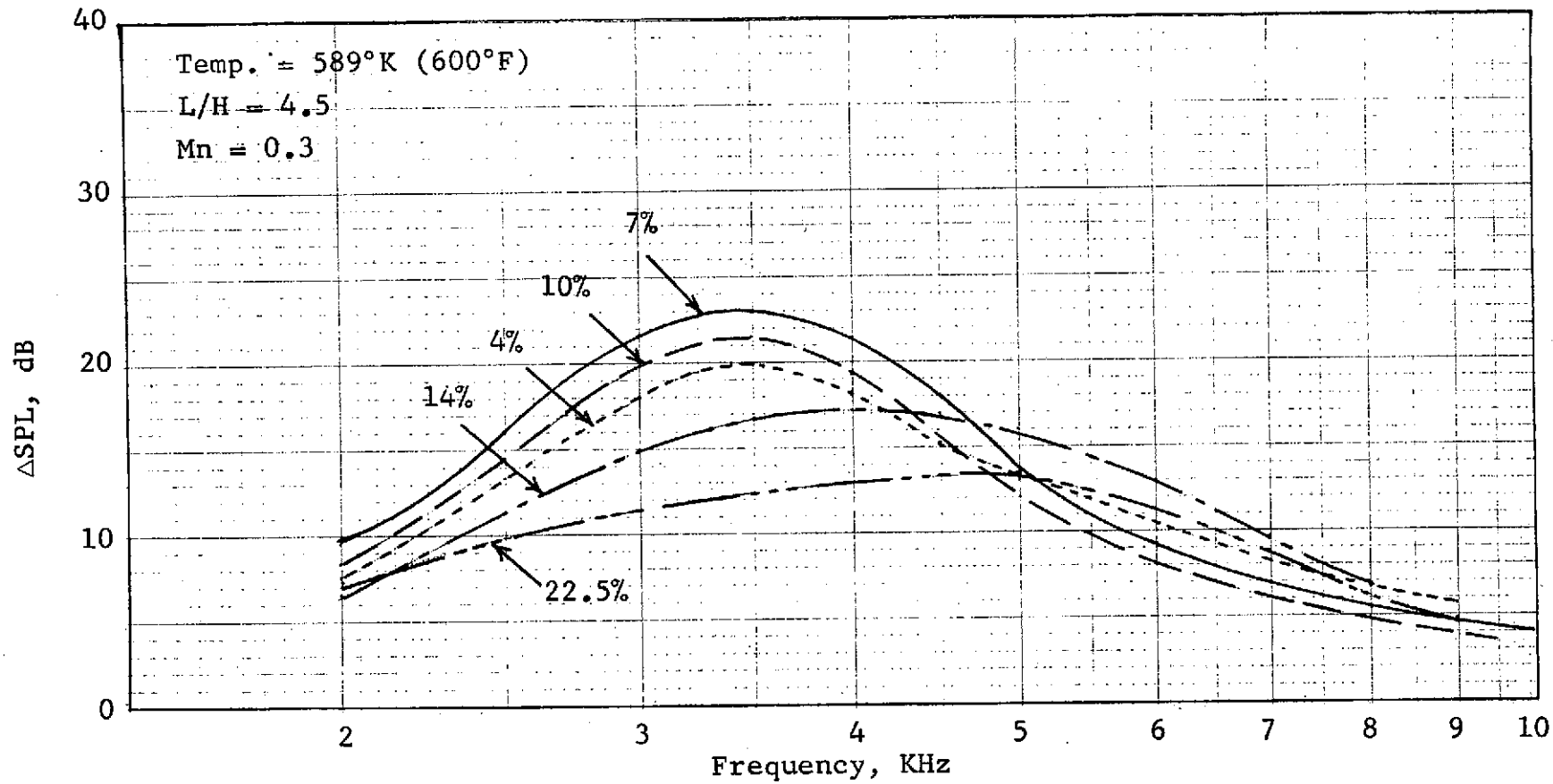

Figure 425. High Temperature Duct Results, Panel Thickness = .0127m (1/2").

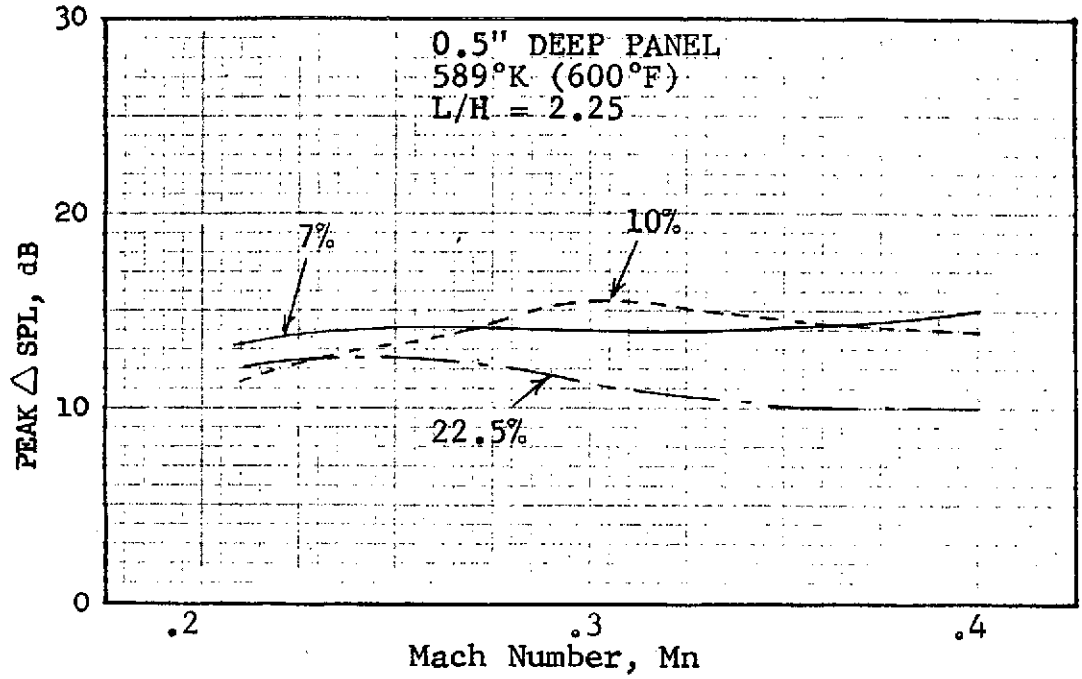

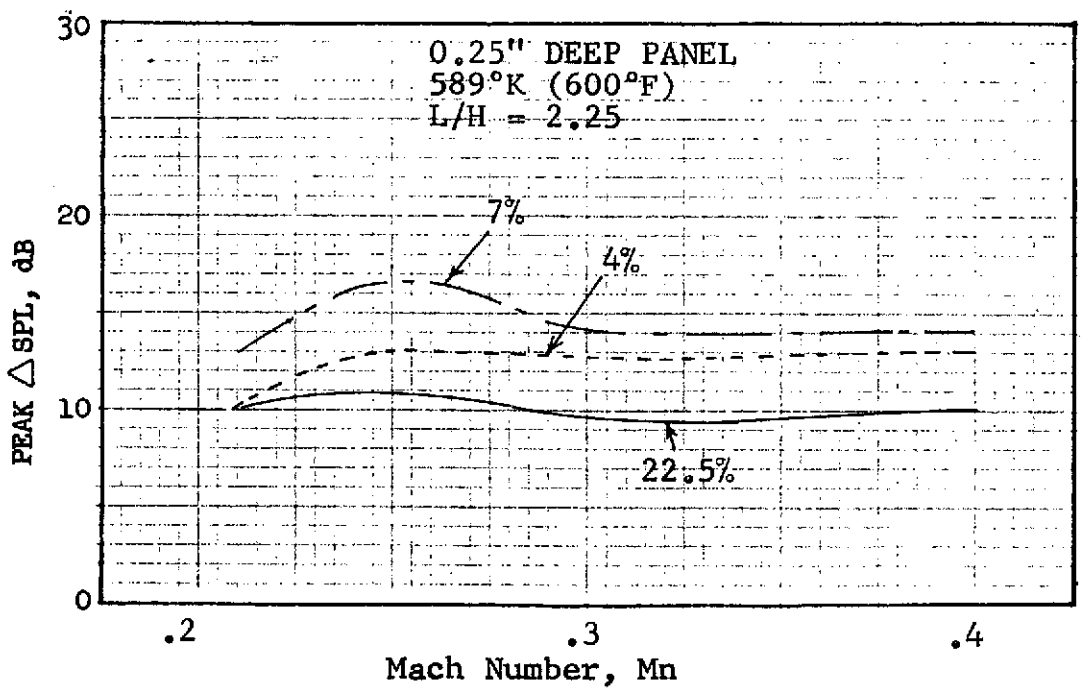

Figure 426. Peak Transmission Loss Variation with Mach Number for Different Porosities.

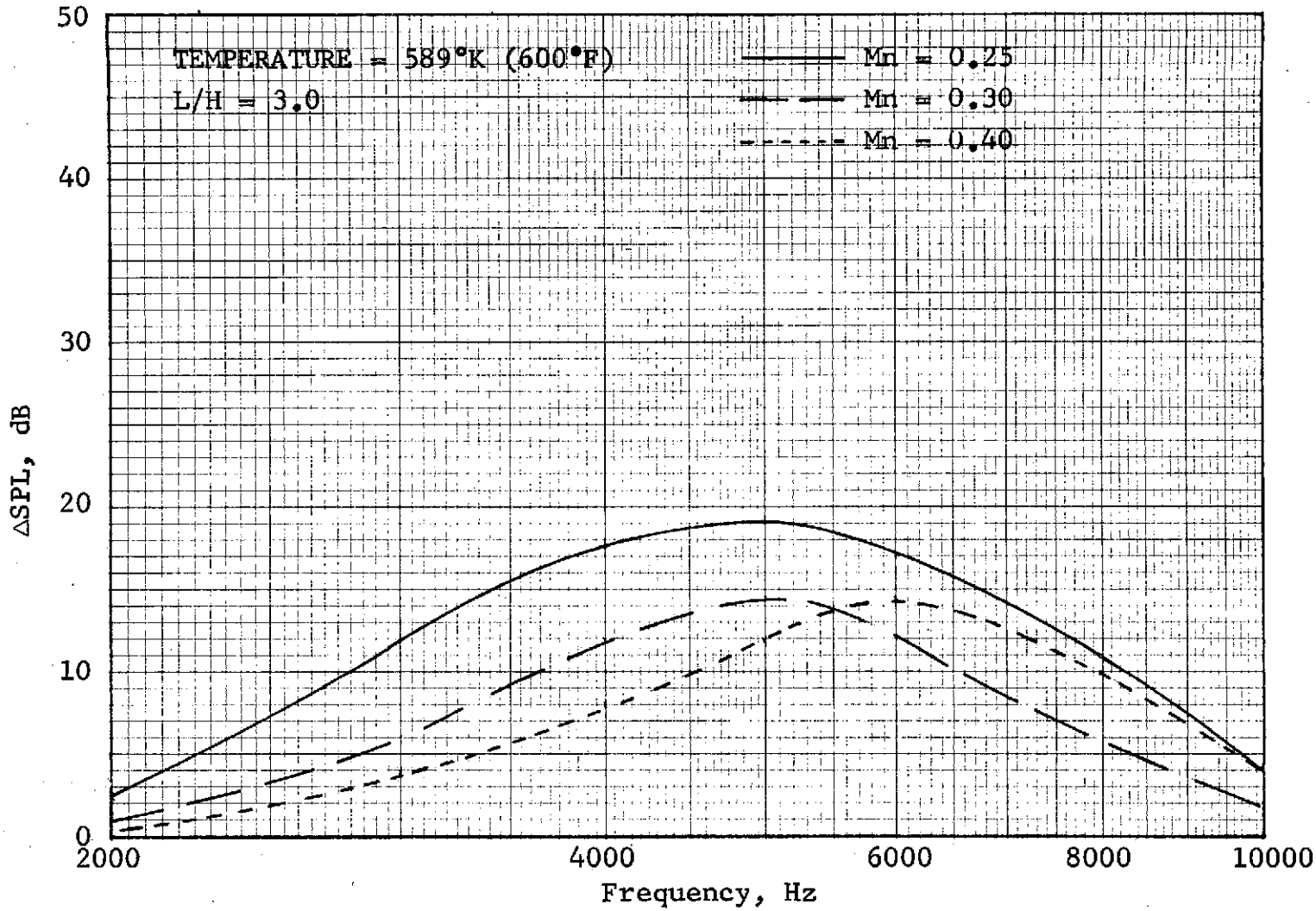

Figure 427. Mach Number Effect on Attenuation for SDOF Configuration No. 19.

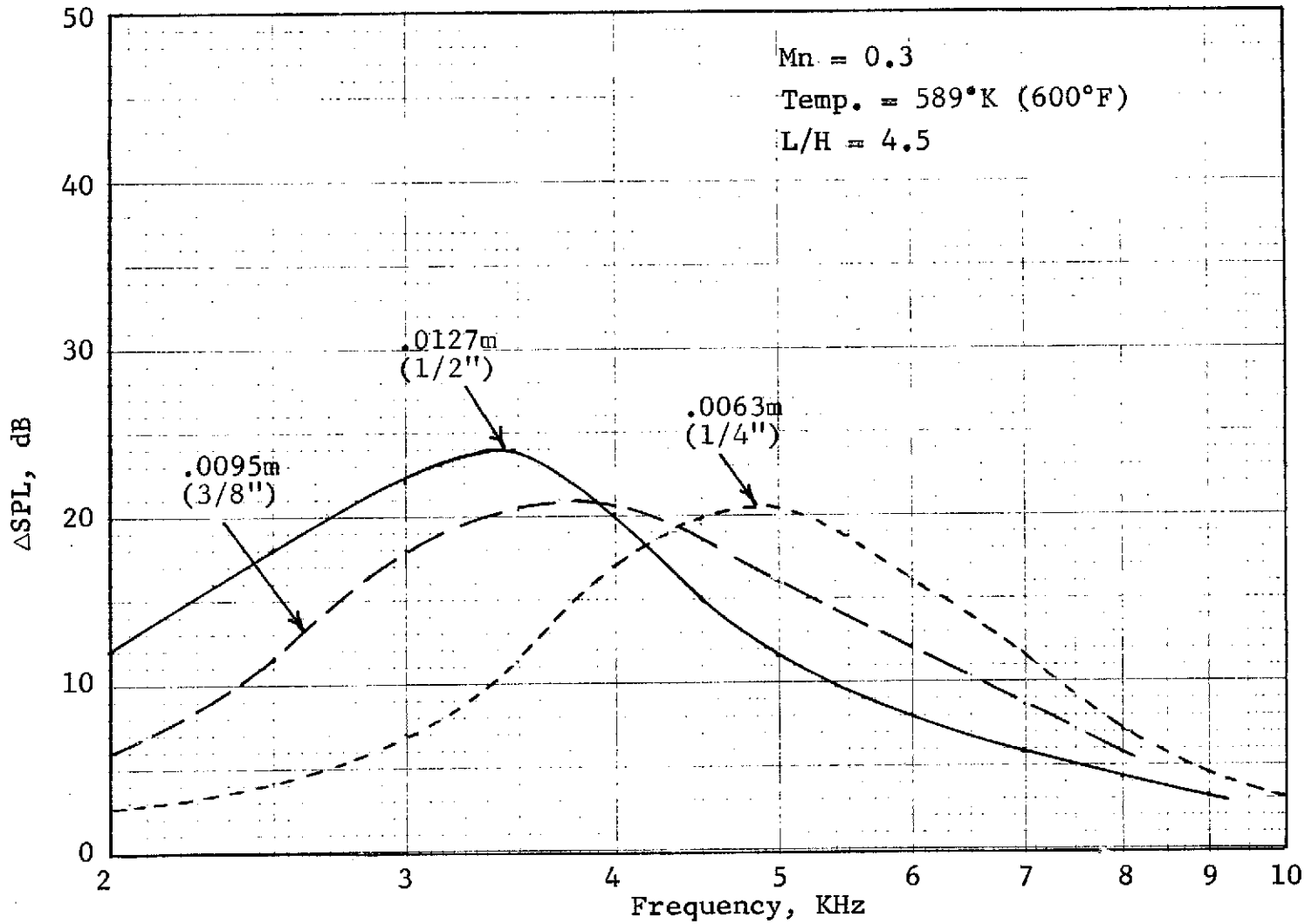

Figure 428. Sound Pressure Level Suppression Vs. Core Depth for 7% Porosity Face Plate Panel.

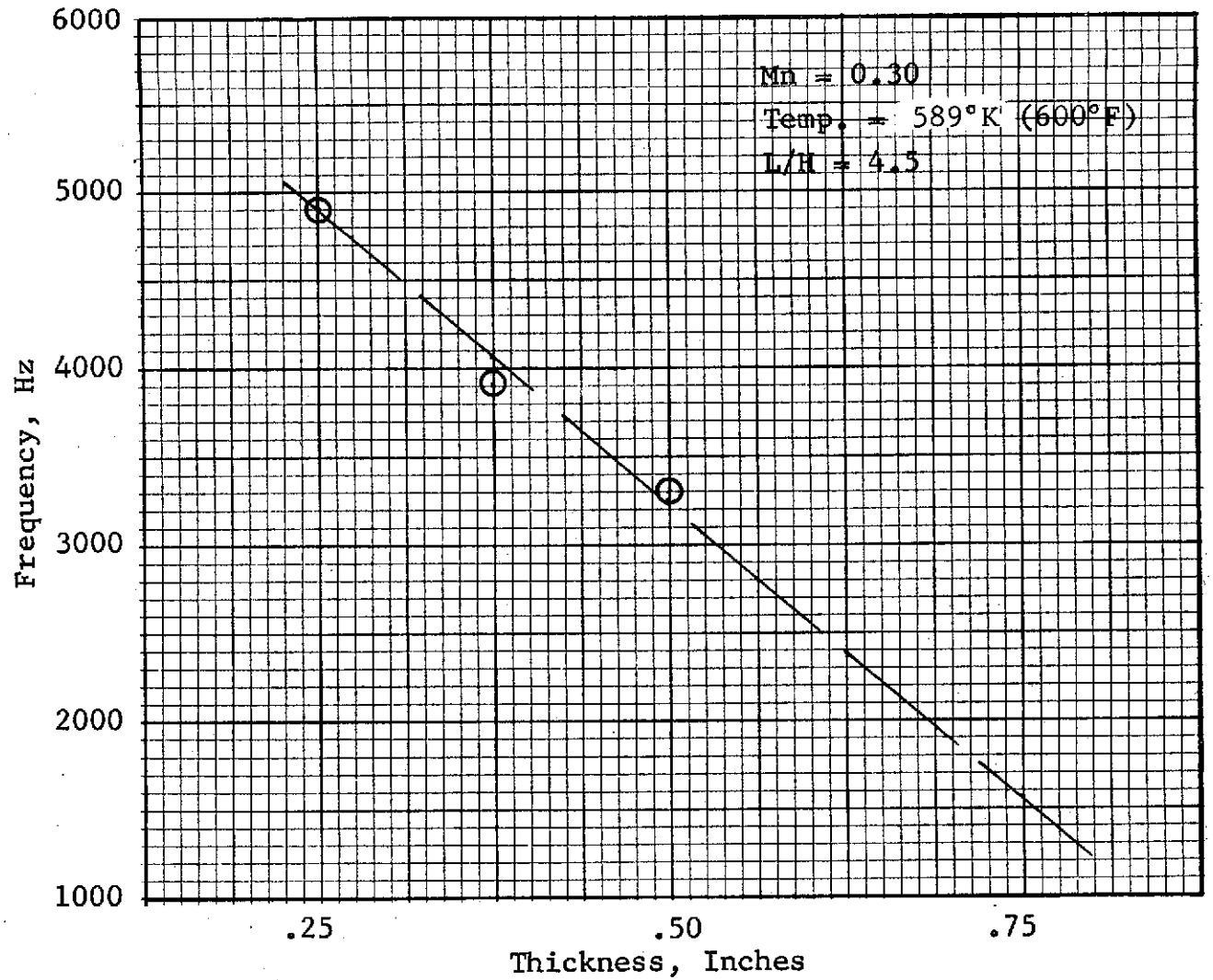

Figure 429. Peak Suppression Frequency Vs. Core Depth for 7% Porosity Face Place Panel.

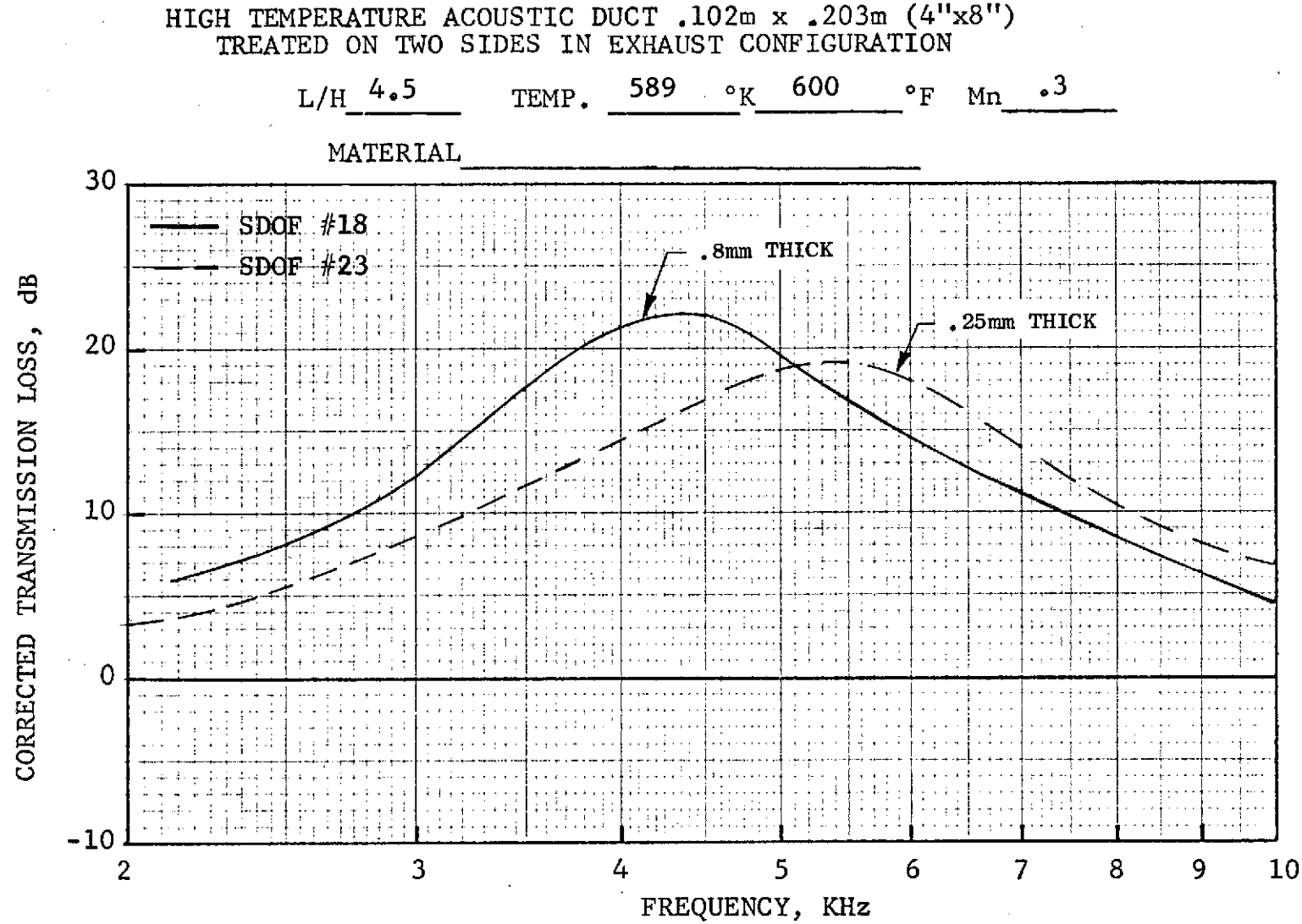

Figure 430. Corrected Transmission Loss Vs. Frequency Effect of Face Plate Thickness on Transmission Loss.

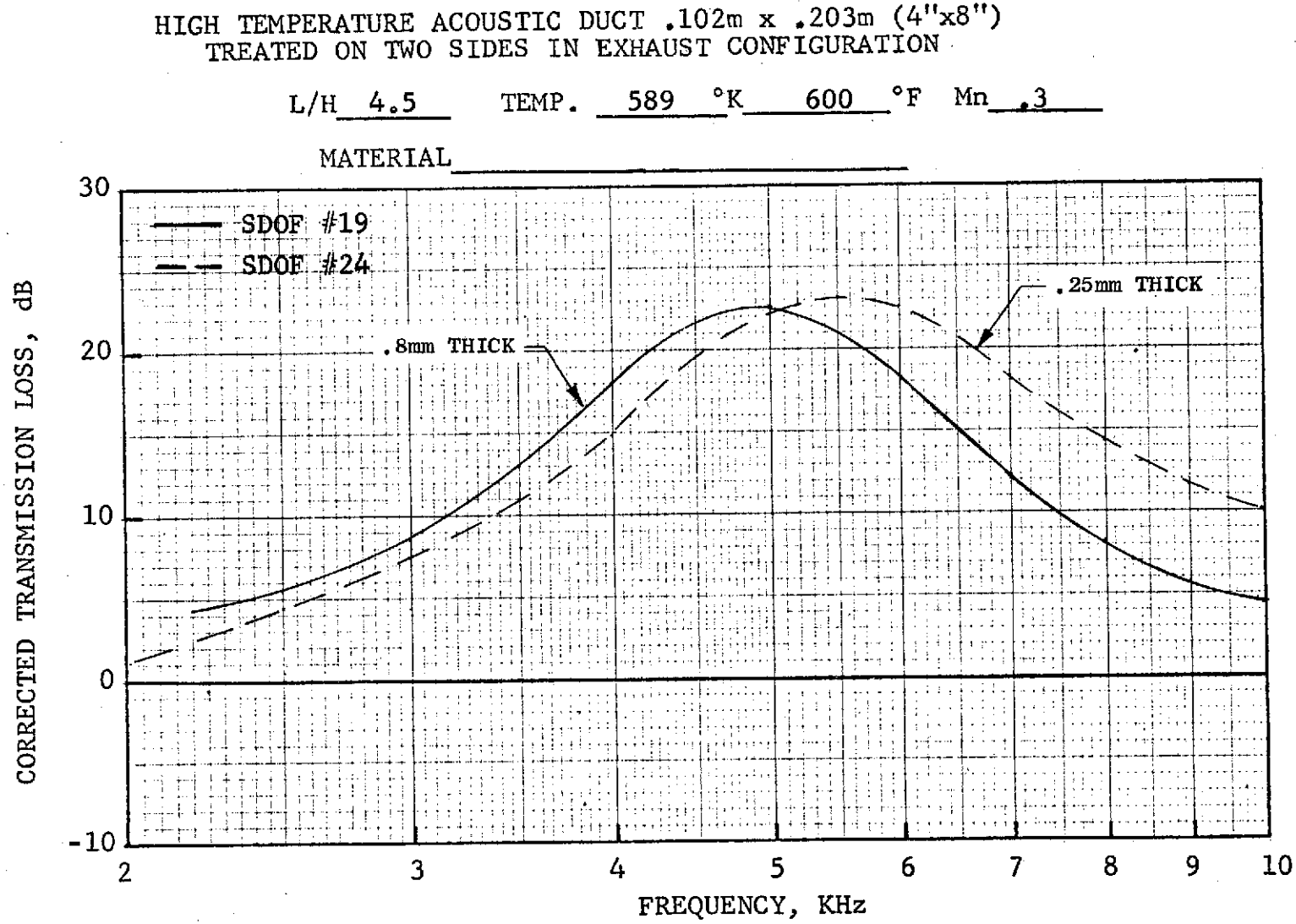

Figure 431. Corrected Transmission Loss Vs. Frequency Effect of Face Plate Thickness on Transmission Loss.

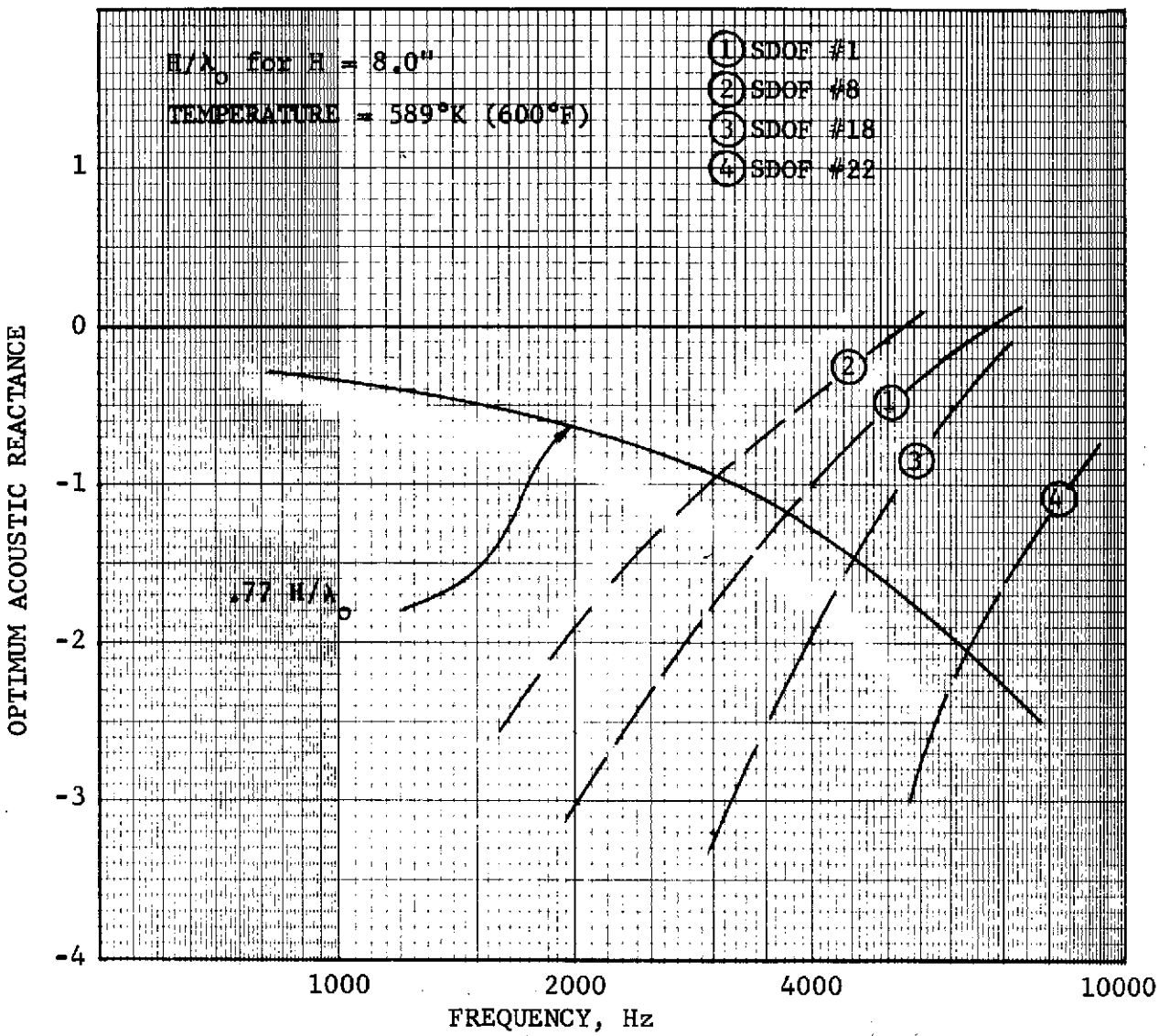

Figure 432. Optimum Transmission Loss Vs. Frequency for SDOF Resonators in a 20.3cm (8") Duct.

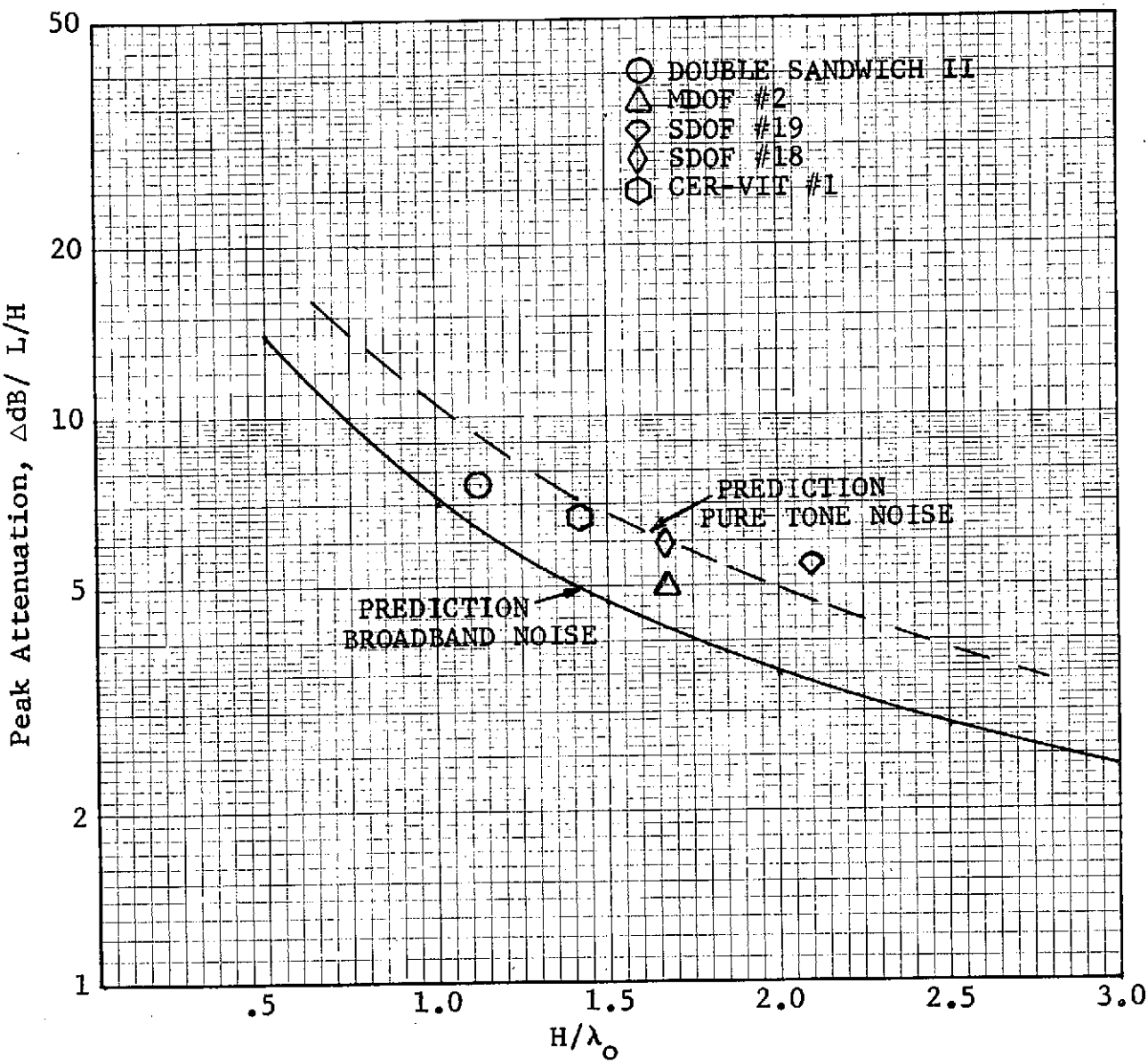

Figure 433. Peak Attenuation Vs. H/λ_o Parameter.

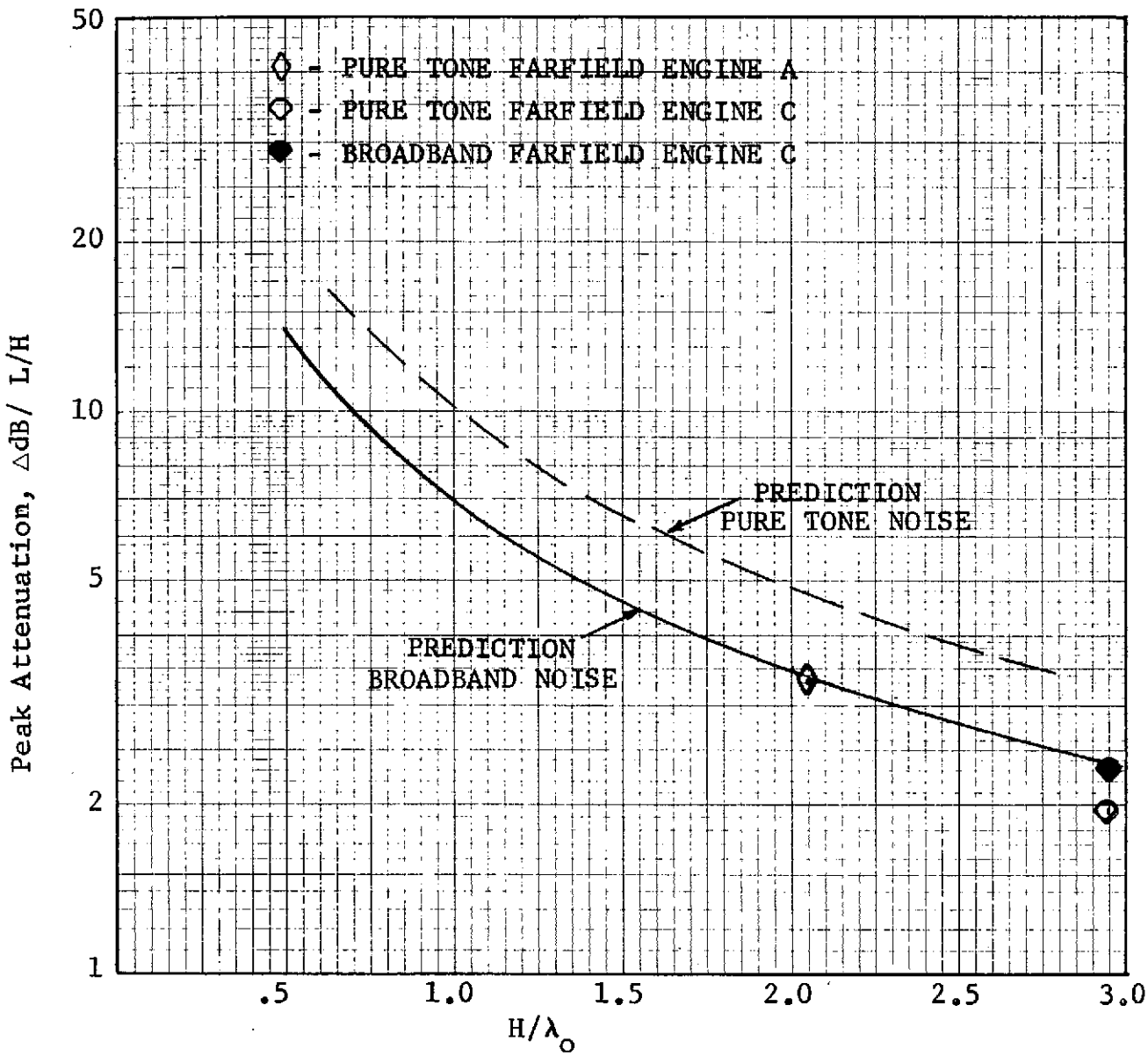

Figure 434. Peak Attenuation Vs. H/λ_o Parameter.

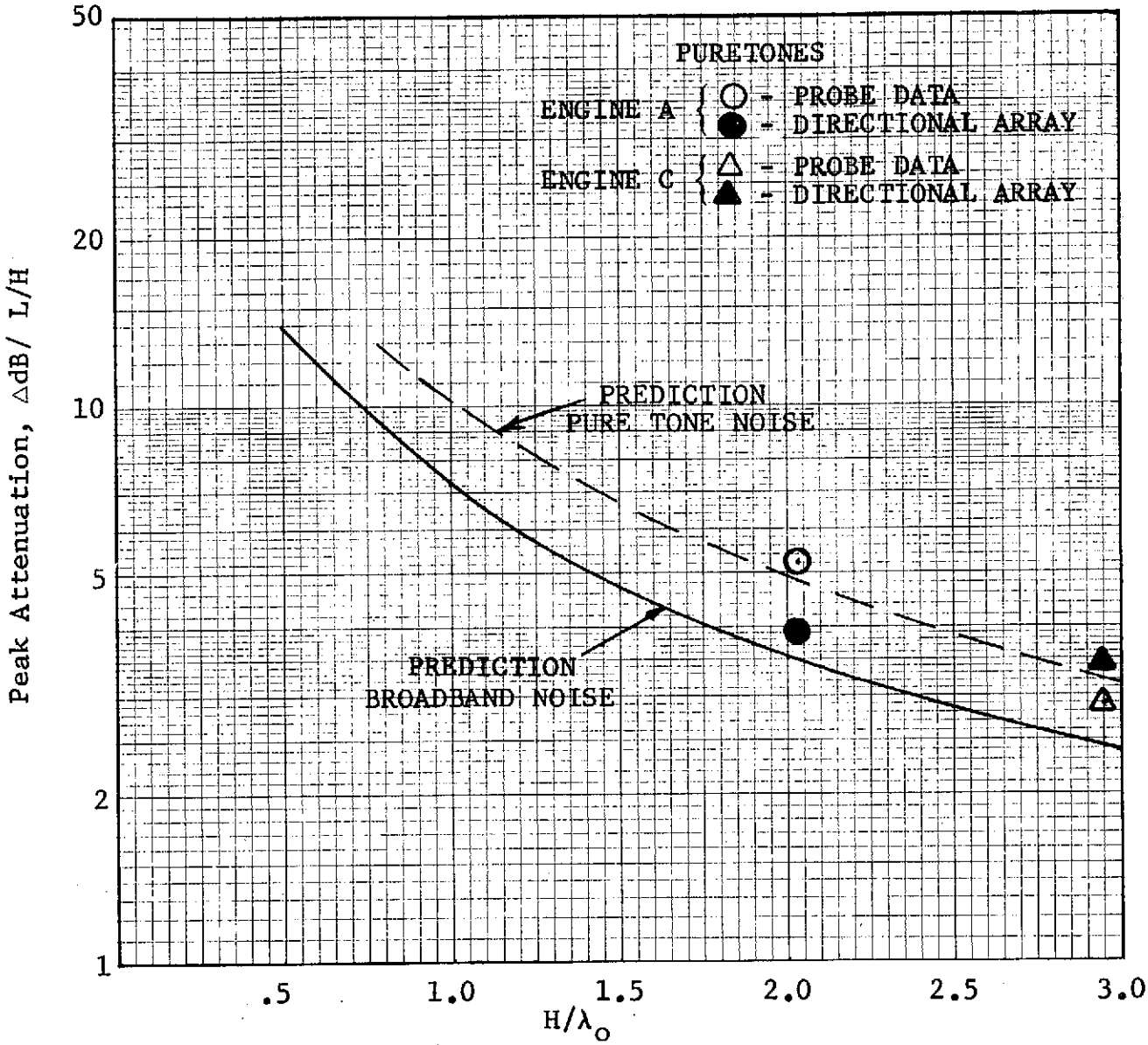

Figure 435. Peak Attenuation Vs. H/λ_o Parameter.

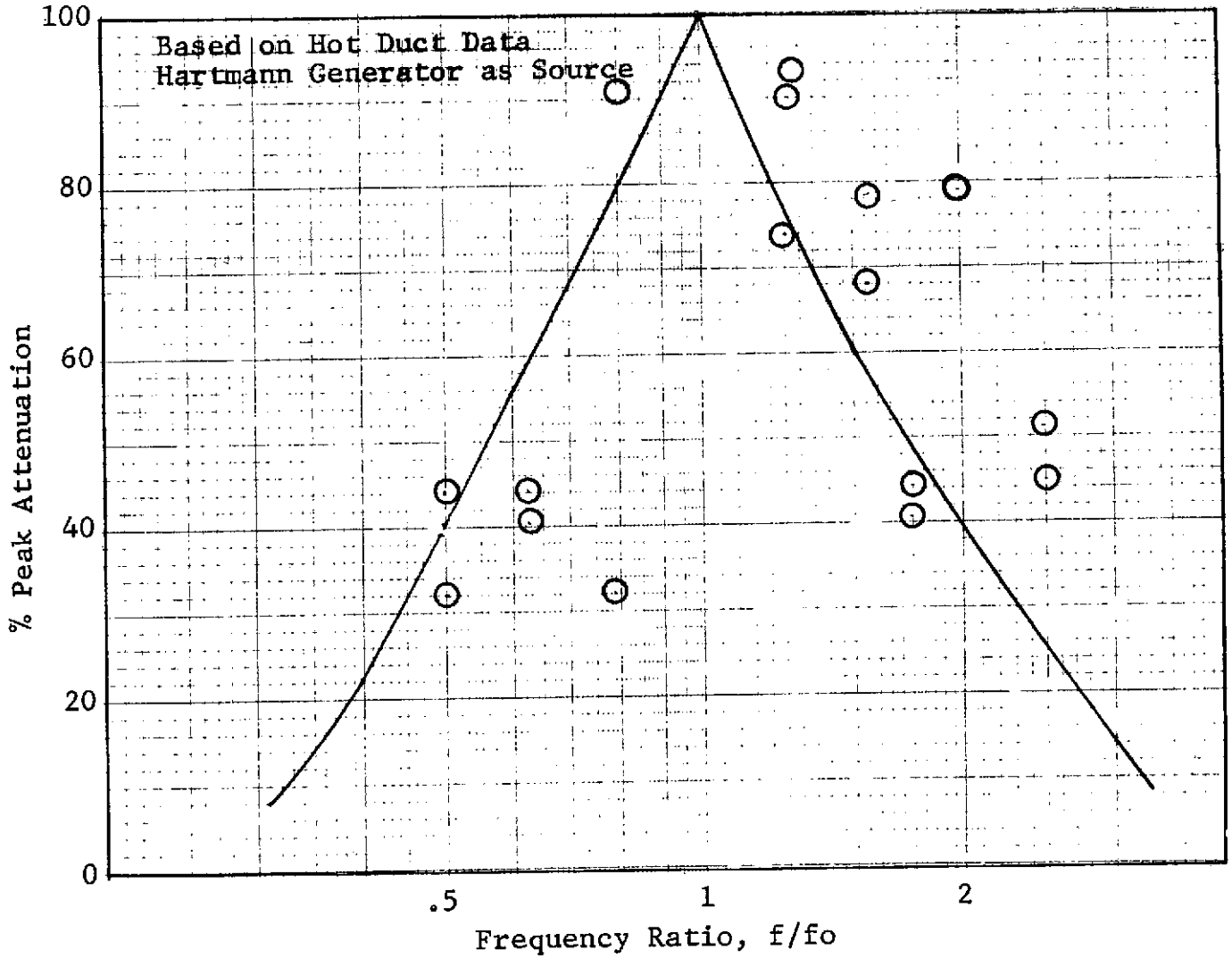

Figure 436. Percent Bandwidth Curve Based on Duct and Engine Data at $H/\lambda \approx 1.0$.

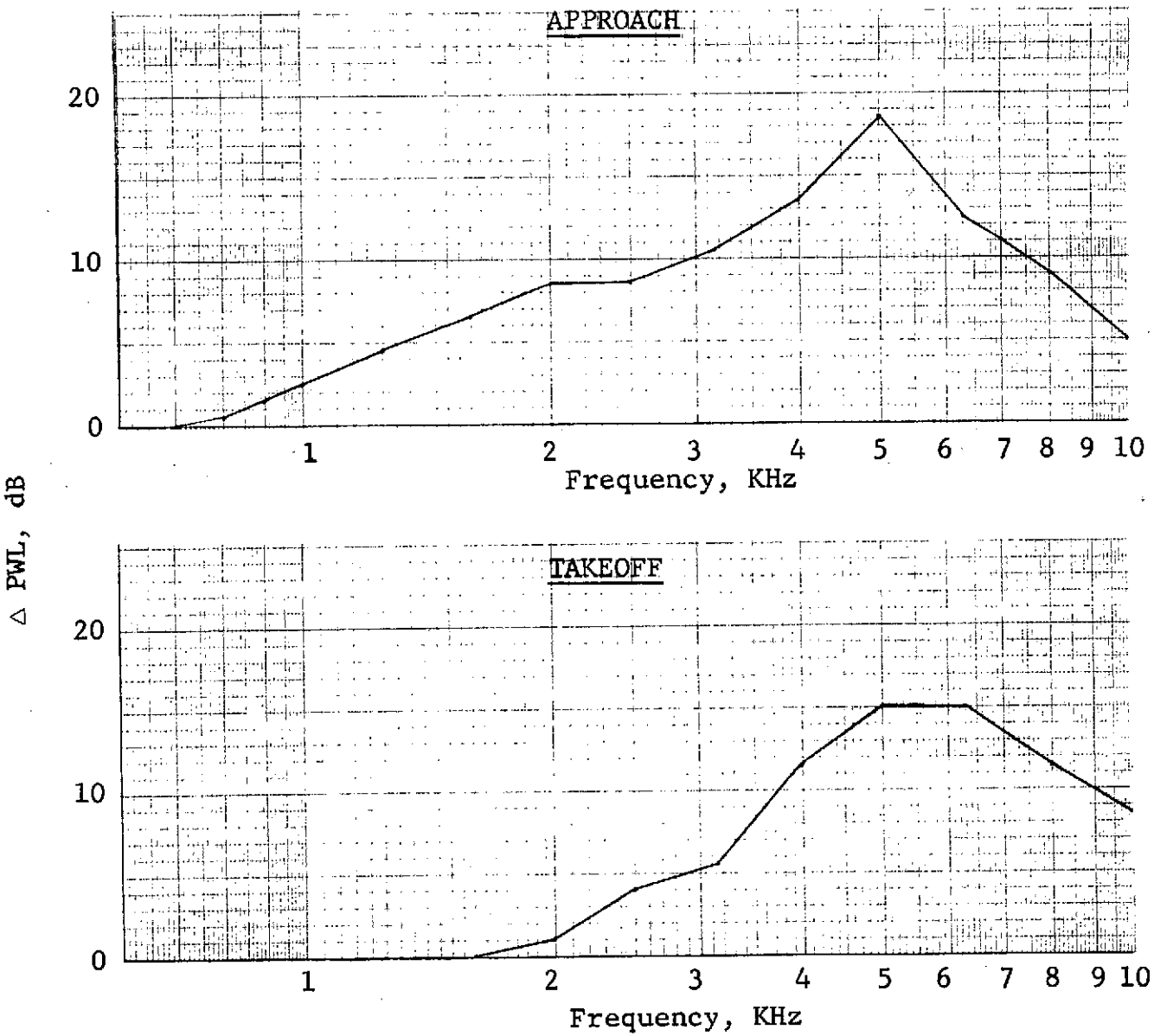

Figure 437. Engine C Predicted Turbine Treatment Suppression.

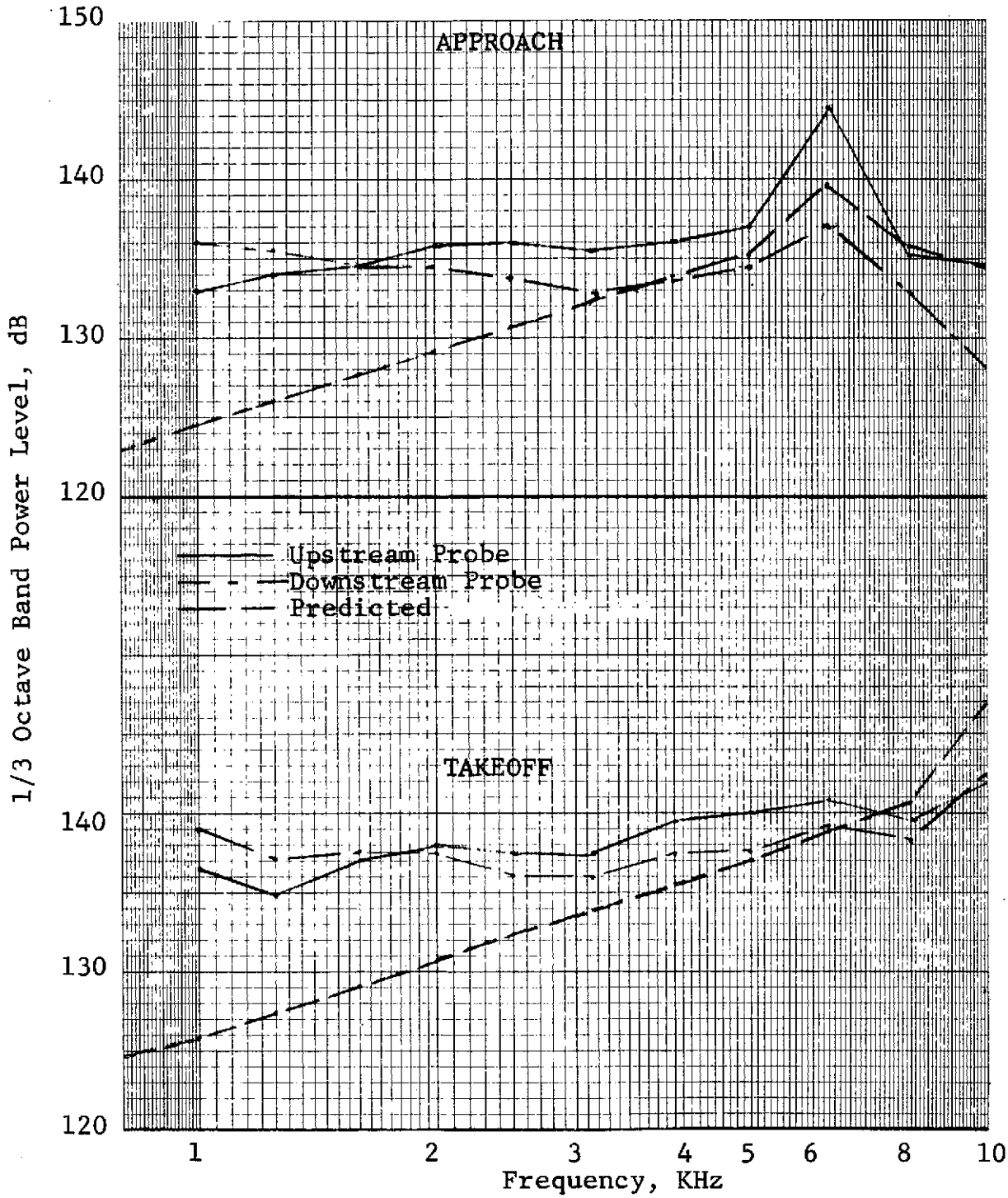

Figure 438. Engine C Turbine Probe and Predicted 1/3 OB Power Levels.

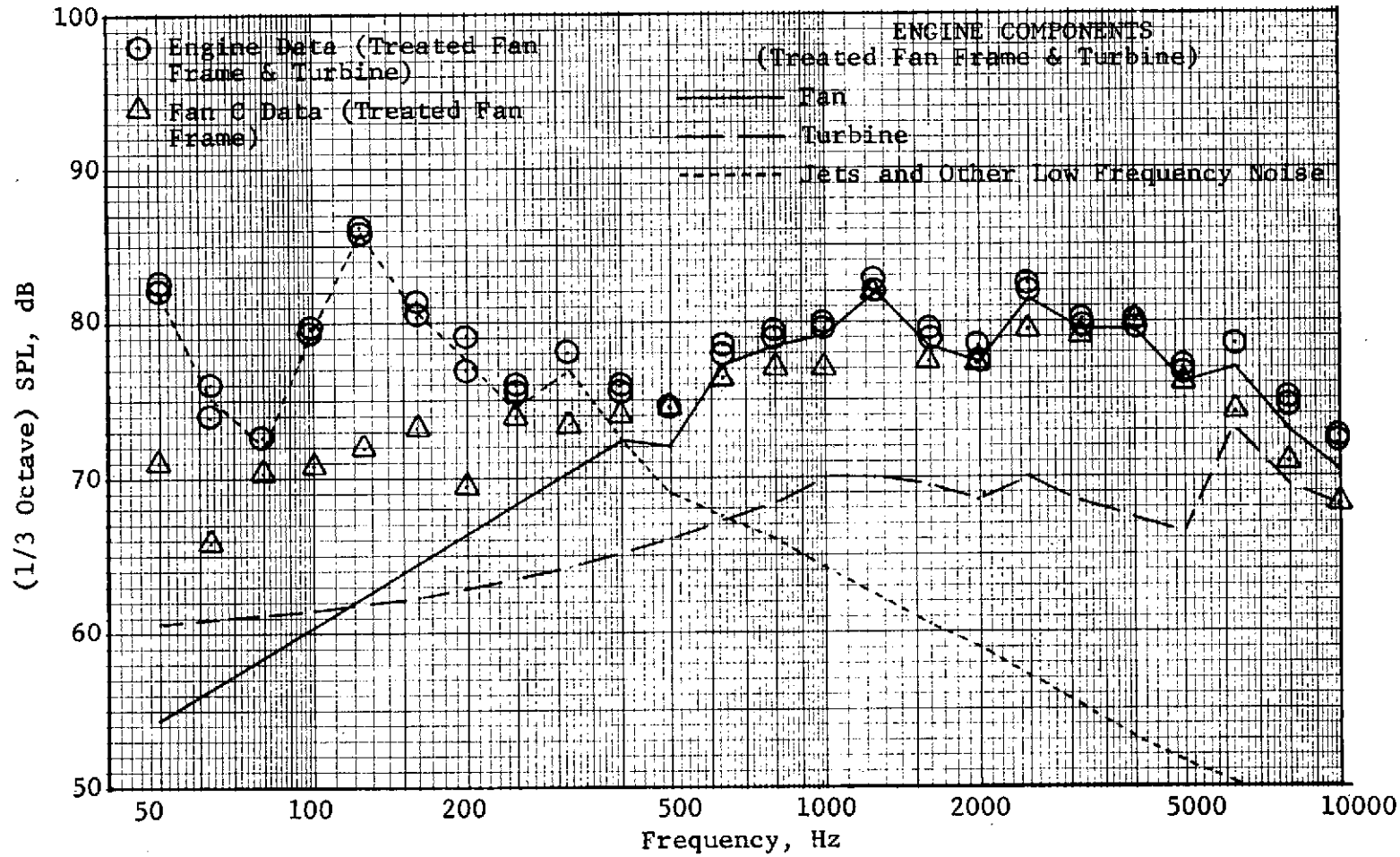

Figure 439. Engine C Component Amplitudes Derived from Probe and Farfield Data (Approach Power, 120°, 61m (200') Sideline).

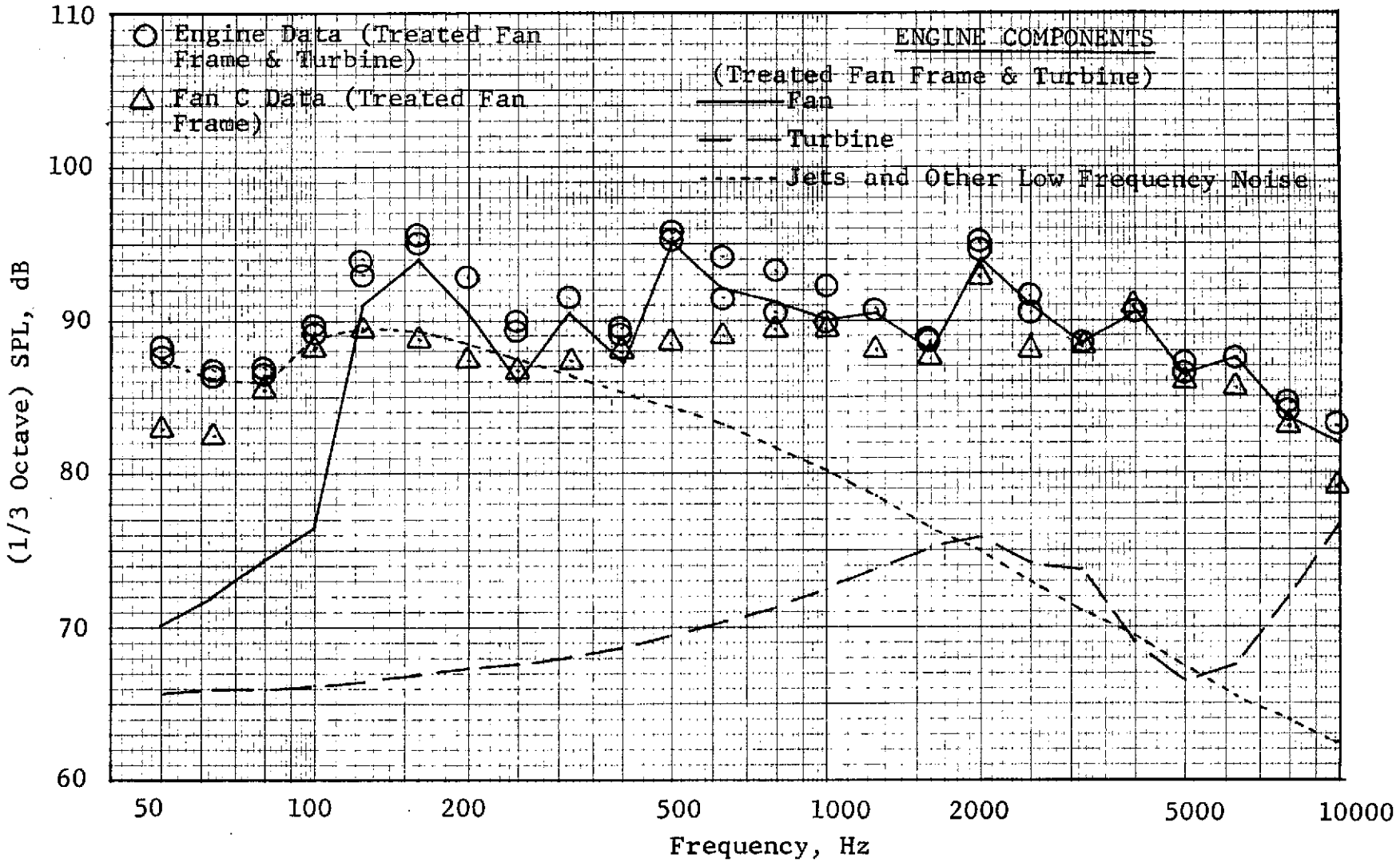

Figure 440. Engine C Component Amplitudes Derived from Probe & Farfield Data (Takeoff Power, 120°, 61m (200') Sideline).

NOMENCLATURE LIST

B & K	Bruel and Kjaer Precision Instruments
BPF	Blade Passing Frequency
Broadband Noise	1/3-Octave Band SPL minus pure tone component
CTL	Corrected Transmission Loss, dB
dB	Decibel, re 0.0002 dynes/cm^2
g	Acceleration of Gravity
H/λ_o	Duct Height/Wavelength of Sound in Stationary Medium
Hz	Hertz (cycles per second)
L/H	Length to Duct Height Ratio
LPT	Low Pressure Turbine
M	Duct Mach Number
N_{f_c}	Fan Speed, corrected to standard day
MDOF	Multiple-Degree-of-Freedom
P_o	Ambient Pressure
PNL	Perceived Noise Level; at calculated annoyance weighted sound level, PNdB
Porosity (σ)	Percent Open Area (perforated face plate)
PWL	Power Level; re 10^{-13} watts
QEP	Quiet Engine Program
R	Universal Gas Constant
rpm	Revolutions Per Minute
SDOF	Single-Degree-of-Freedom
Standard Day	288° K (59° F) Temperature and 70% Relative Humidity
SPL	Sound Pressure Level; a level of sound pressure that occurs in a specified frequency range at any instant of time

NOMENCLATURE LIST - Concluded

T_o	Ambient Dry Bulb Temperature
ℓ	$t + 0.85d$
t	Face Plate Thickness
d	Hole Diameter
f	Frequency, Hz
V	Volume
ρ	Medium Density
c	Sonic Velocity
A	Area
γ	Ratio of Specific Heat at Constant Pressure to Specific Heat at Constant Volume $\left(\frac{c_p}{c_v}\right)$
W	Mass Flow

THE FOLLOWING PAGES ARE DUPLICATES OF ILLUSTRATIONS APPEARING ELSEWHERE IN THIS REPORT. THEY HAVE BEEN REPRODUCED HERE BY A DIFFERENT METHOD TO PROVIDE BETTER DETAIL